R&T

2001

Research and Technology

Glenn Research Center
at Lewis Field

Cleveland • Ohio

NASA/TM—2002-211333

About the cover:

Top: Left: NASA Glenn's 8- by 6-Foot Supersonic Wind Tunnel compressor was recently inspected (p. 210). Right: On-orbit view of the International Space Station taken from the space shuttle in March 2001. The System Power Analysis for Capability Evaluation (SPACE) computer model of the space station's electrical power system was validated this year (pp. 205–206).

Middle: The core hot section foil-air bearing was successfully tested in the level 1 milestone on the path to the first Oil-Free turbine aircraft engine (p. 2).

Bottom: Left: Astronauts working at Bay 10 on the Hubble Space Telescope during the telescope's third servicing mission. The physical and thermal properties of Teflon FEP retrieved from the telescope were evaluated (pp. 66–67). Right: The Numerical Propulsion System Simulation (NPSS) Version 1 was designated co-winner of the NASA Software of the Year Award for 2001 (pp. 228–229).

Research & Technology 2001

National Aeronautics and Space Administration

Glenn Research Center
Cleveland, Ohio 44135-3191

NASA/TM—2002-211333

Trade names or manufacturers' names are used in this report for identification only. This usage does not constitute an official endorsement, either expressed or implied, by the National Aeronautics and Space Administration.

Available from

NASA Center for Aerospace Information
7121 Standard Drive
Hanover, MD 21076

National Technical Information Service
5285 Port Royal Road
Springfield, VA 22100

Available electronically at http://www.grc.nasa.gov/WWW/RT

Introduction

The NASA Glenn Research Center at Lewis Field, in partnership with U.S. industries, universities, and other Government institutions, is responsible for developing and transferring critical technologies that address national priorities in aeropropulsion and space applications. Our work is focused on research for new aeropropulsion technologies, aerospace power, microgravity science fluids and combustion, electric propulsion, and communications technologies for aeronautics, space, and aerospace applications.

As NASA's premier Center for aeropropulsion, aerospace power, and turbomachinery, our role is to conduct world-class research and to develop and transfer key technologies to U.S. industries. We contribute to economic growth and national security through safe, superior, and environmentally compatible U.S. civil and military aircraft propulsion systems. Our Aerospace Power Program supports all NASA enterprises and major programs, including the International Space Station, Advanced Space Transportation, and new initiatives in human and robotic exploration.

Glenn Research Center leads NASA's research in the microgravity science disciplines of fluid physics, combustion science, and acceleration measurement. Almost every space shuttle science mission has had an experiment managed by the Center, and we have started to conduct a wide array of similar experiments on the International Space Station.

We are committed to enabling U.S.-based aerospace and nonaerospace industries to benefit directly from the technologies developed through our programs. Technology spinoffs from our efforts are found in all aspects of our daily lives, from solar cells to pagers. Our goal is to maximize the benefit of our activities to the Nation and to optimize the return on each taxpayer's investment.

The Glenn staff consists of over 3300 civil service employees and support service contractor personnel. Scientists and engineers comprise more than half of our workforce, with technical specialists, skilled workers, and an administrative staff supporting them. We aggressively strive for technical excellence through continuing education, increased diversity in our workforce, and continuous improvement in our management and business practices so that we can expand the boundaries of aeronautics, space, and aerospace technology.

The Glenn Research Center is a unique facility located in the southwest corner of Cleveland, Ohio. Situated on 350 acres of land adjacent to the Cleveland Hopkins International Airport, Glenn comprises more than 140 buildings, including 24 major facilities and over 500 specialized research and test facilities. Additional facilities are located at Plum Brook Station, which is about 50 miles west of Cleveland.

Knowledge is the end product of our activities. The R&T report helps make this knowledge fully available to potential users—the aircraft engine industry, the space industry, the energy industry, the automotive industry, the aerospace industry, and others. It is organized so that a broad cross section of the community can readily use it. Each article begins with a short introductory paragraph that should prove valuable for the layperson. These articles summarize the progress made during the year in various technical areas and portray the technical and administrative support associated with Glenn's technology programs.

We hope that this information is useful to all. If additional information is desired, readers are encouraged to contact the researchers identified at the end of each article and to visit NASA Glenn on the World Wide Web at http://www.grc.nasa.gov. This document is available online (http://www.grc.nasa.gov/www/RT).

Donald J. Campbell
Director

NASA Glenn Research Center Senior Management

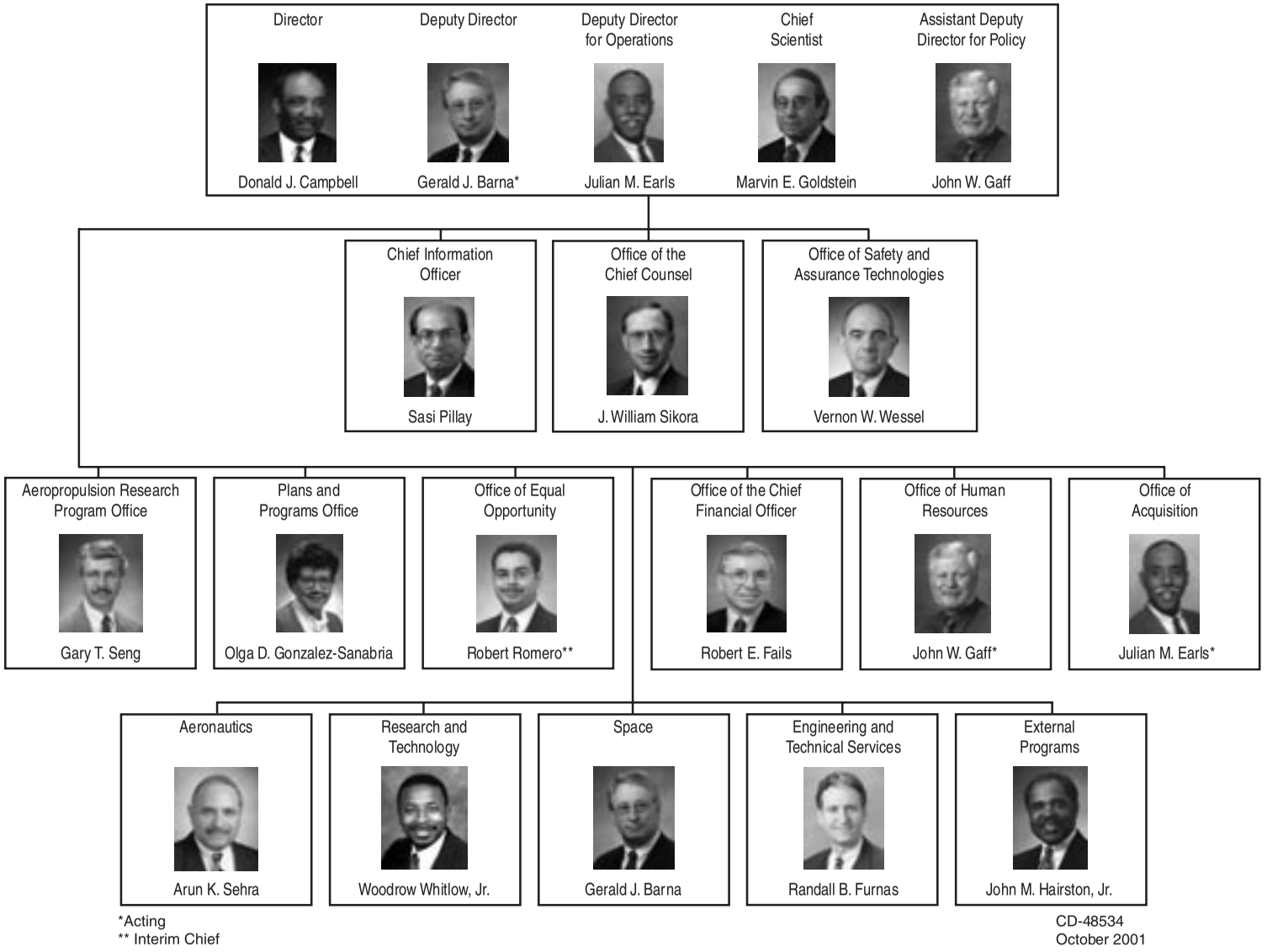

*Acting
** Interim Chief

CD-48534
October 2001

NASA Glenn Research Center at Lewis Field

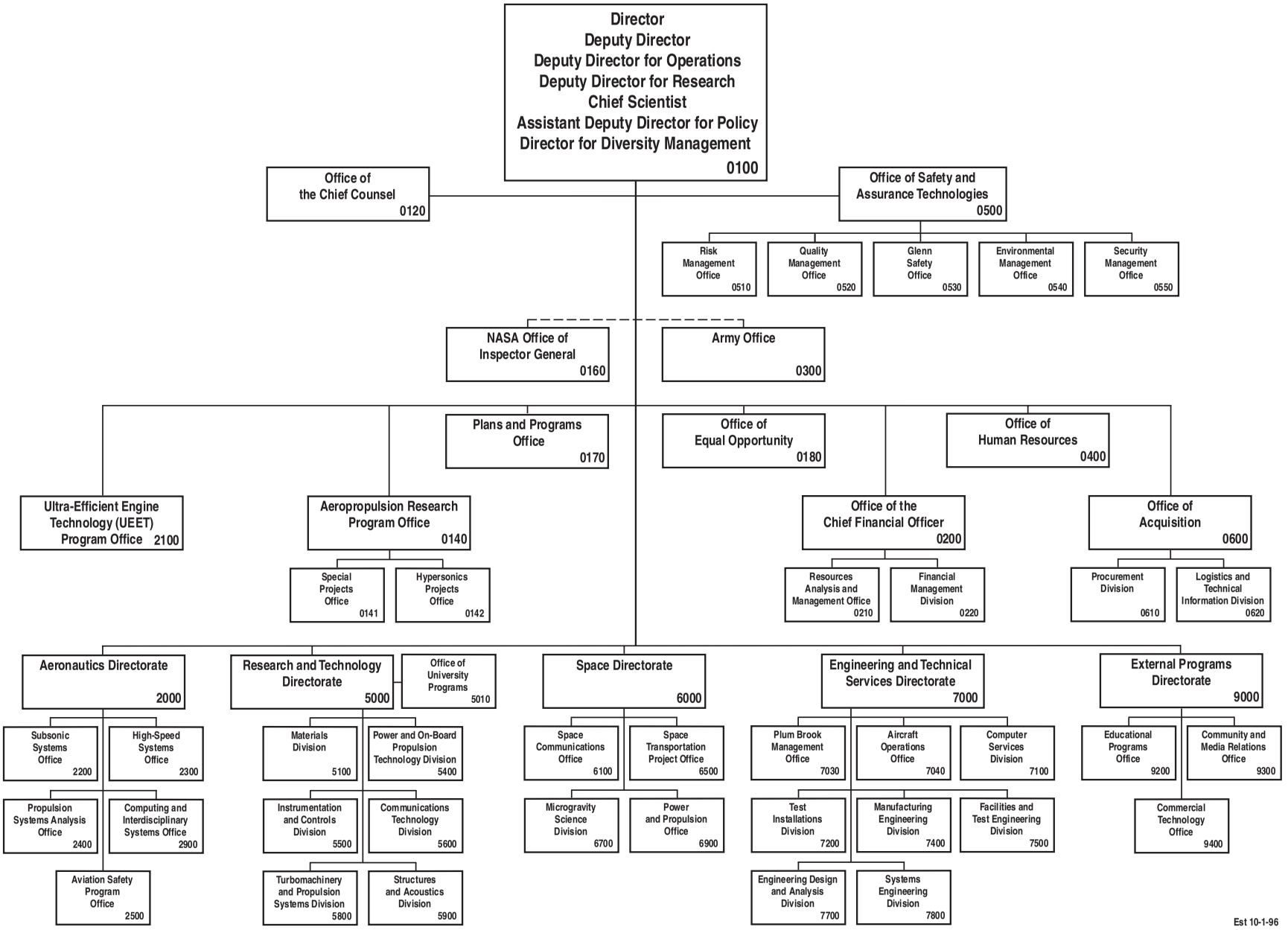

Est 10-1-96
CD-44972
Rev. 9-20-01

Contents

Aeronautics

Subsonic Systems

Oil-Free Turbomachinery Team Passed Milestone on Path to the First Oil-Free Turbine Aircraft Engine 2

Propulsion Systems Analysis

Advanced Engine Cycles Analyzed for Turbofans With Variable-Area Fan Nozzles Actuated by a Shape Memory Alloy 3
Preliminary Integrated Safety Analysis of Synthetic Vision Conducted 4

Computing and Interdisciplinary Systems

NASA Participated in the Japan 2001 Science, Creativity and the Young Mind Workshop 5

Research and Technology

Materials

New High-Performance SiC Fiber Developed for Ceramic Composites 8
Architectures for High-Performance Ceramic Composites Being Improved 9
Techniques Optimized for Reducing Instabilities in Advanced Nickel-Base Superalloys for Turbine Blades 10
Long-Term Creep of a Thin-Walled Inconel 718 Stirling Power-Convertor Heater Head Assessed 12
γ -TiA1 Shown To Have Sufficient Durability To Allow the Design of a Robust Low-Pressure Turbine Blade 13
Major Effects of Nonmetallic Inclusions on the Fatigue Life of Disk Superalloy Demonstrated 15
Dual Microstructure Heat Treatment of a Nickel-Base Disk Alloy Assessed 16
Strength and Fracture Toughness of Solid Oxide Fuel Cell Electrolyte Material Improved 17
Ceramic Propellant Injectors Designed and Fabricated 19
Tensile Strength and Microstructure of $A1_2O_3$-ZrO_2 Hypo-Eutectic Fibers Studied 19
Lightweight, Actively Cooled Ceramic Matrix Composite Thrustcells Successfully Tested in Rocket Combustion Lab 21
Ceramic Composite Intermediate Temperature Stress-Rupture Properties Improved Significantly 22
Single-Crystal Elastic Constants of Yttria (Y_2O_3) Measured to High Temperatures 23
Environment-Conscious Ceramics (Ecoceramics) Technology Received 2001 R&D 100 Award 24
Polymer/Silicate Nanocomposites Developed for Improved Thermal Stability and Barrier Properties 25
High-Glass-Transition-Temperature Polymides Developed for Reusable Launch Vehicle Applications 27
NASA Glenn/AADC Collaboration Optimized Erosion Coatings for Inlet Guide Vanes 28
Novel Molecular Architectures Developed for Improved Solid Polymer Electrolytes for Lithium Polymer Batteries 29
Ti-48A1-2Cr-2Nb Evaluated Under Fretting Conditions 30
Oxidation Behavior of GRCop-84 Copper Alloy Assessed 31
Knowledge of Pest Resistance of SiC/BN/SiC Composites Improved 33
Effects of Microalloying on the Microstructures and Mechanical Properties of Directionally Solidified Ni-33(at.%)Al-31Cr-3Mo Eutectic Alloys Investigated 34
Cyclic Oxidation Modeling Program Rewritten for MS Windows 37
Effect of Environment on the Stress-Rupture Behavior of a C/SiC Composite Studied 39
Thermal Cyclic Behavior of Thermal and Environmental Barrier Coatings Investigated Under High-Heat-Flux Conditions 41

Power and On-Board Propulsion Technology

Quantum Dots Investigated for Solar Cells 44
Silicon Carbide Solar Cells Investigated 45
Floating Potential Probe Deployed on the International Space Station 46
Carbon Nanotube Anodes Being Evaluated for Lithium Ion Batteries 47
Atmospheric-Pressure-Spray, Chemical-Vapor-Deposited Thin-Film Materials Being Developed for High Power-to-Weight-Ratio Space Photovoltaic Applications 49
Photovoltaic Engineering Testbed Designed for Calibrating Photovoltaic Devices in Space 50
Advanced Power Technologies Developed for the Starshine 3 Satellite 52
High-Power Electromagnetic Thruster Being Developed 53
Magnetohydrodynamic MACH Code Used to Simulate Magnetoplasmadynamic Thrusters 55
Next-Generation Ion Propulsion Being Developed 57
Modular 5-kW Power-Processing Unit Being Developed for the Next-Generation Ion Engine 58
13-kV Ion-Extraction System Being Developed for Inert Gas Ion Engines 59
Deep Space 1 Ion Engine Completed a 3-Year Journey 59
Flywheel Charge/Discharge Control Developed 60
Intelligent dc-dc Convertor Technology Developed and Tested 61
Solid-Body Fuse Developed for High-Voltage Space Power Missions 62
Sensitive Technique Developed Using Atomic Force Microscopy to Measure the Low-Earth-Orbit Atomic Oxygen Erosion of Polymers 63
MISSE PEACE Polymers: An International Space Station Environment Exposure Experiment Being Conducted 65
Physical and Thermal Properties Evaluated of Teflon FEP Retrieved From the Hubble Space Telescope During Three Servicing Missions 66
Facility and Methods Developed for Simulated Space Vacuum Ultraviolet Exposure Testing of Polymer Films 68
High-Temperature Intercalated Graphite Fiber Conductors Fabricated 69
Solar Selective Coatings Developed for Space Power Applications 70
Cryogenic Electronics Being Developed for Space Operation 71
Integrated Stirling Convertor and Hall Thruster Test Conducted 72
Stirling Research Laboratory Providing Independent Performance Verification of Convertors for a Stirling Radioisotope Generator 73
Refractive Secondary Solar Concentrator Demonstrated High-Temperature Operation 74
Operation of a Thin-Film Inflatable Concentrator System Demonstrated in a Solar Thermal Vacuum Environment 76

Instrumentation and Controls

High-Temperature Gas Sensor Array (Electronic Nose) Demonstrated 78
Bulk Micromachined 6H-SiC High-g Piezoresistive Accelerometer Fabricated and Tested 80
Interferometer-Controlled Optical Tweezers Constructed for Nanotechnology and Biotechnology 82
Fiber-Optic Pressure Sensor With Dynamic Demodulation Developed 83
Tip-Clearance Vortex Characterized With Three-Dimensional Digital Particle Image Velocimetry 84
Active Control of Combustor Instability Shown to Help Lower Emissions 85
Life-Extending Control for Aircraft Engines Studied 87
Hybrid Neural-Network—Genetic Algorithm Technique for Aircraft Engine Performance Diagnostics Developed and Demonstrated 88

Communications Technology

Command and Control of Space Assets Through Internet-Based Technologies Demonstrated 91
Mobile Router Developed and Tested 92

TCP Pacing Developed 93
Digital Distortion Caused by Traveling-Wave-Tube Amplifiers Simulated 94
High-Power, High-Frequency Si-Based (SiGe) Transitors Developed 96
Low-Loss, High-Isolation Microwave Microelectromechanical Systems (MEMS) Switches Being Developed 97
Overall Traveling-Wave-Tube Efficiency Improved by Optimized Multistage Depressed Collector Design 98
Power-Efficient, High-Current-Density, Long-Life Thermionic Cathode Developed for Microwave Amplifier Applications 99
Microelectromechanical Systems (MEMS) Actuator-Based, Polarization Reconfigurable Patch Antenna Demonstrated 100
622-Mbps Orthogonal Frequency Division Multiplexing (OFDM) Digital Modem Implemented 101

Turbomachinery and Propulsion Systems

Vortex Generator Model Developed for Turbomachinery 103
Fan Stall Flutter Flow Mechanism Studied 104
Centrifugal Compressor Surge Margin Improved With Diffuser Hub Surface Air Injection 105
Effect of Variable Chord Length on Transonic Axial Rotor Performance Investigated 106
Heated Surface Temperatures Measured by Infrared Detector in a Cascade Environment 108
Pulse Detonation Engine Test Bed Developed 109
One-Dimensional Spontaneous Raman Measurements of Temperature Made in a Gas Turbine Combustor 110
High-Pressure Gaseous Burner (HPGB) Facility Completed for Quantitative Laser Diagnostics Calibration 112
Spray and High-Pressure Flow Computations in the National Combustion Code (NCC) Improved 115
Sector Tests of a Low-NO_x, Lean, Direct-Injection, Multipoint Integrated Module Combustor Concept Conducted 116
Transonic Resonance Demonstrated To Be a Source of Internal Noise From Mixer-Ejector Nozzles 117
Influence of Turbulence on the Restraint of Liquid Jets by Surface Tension in Microgravity Investigated 119
Liquid Oxygen Propellant Densification Unit Ground Tested With a Large-Scale Flight-Weight Tank for the X–33 Reusable Launch Vehicle 120
Aeroacoustic Flow Phenomena Accurately Captured by New Computational Fluid Dynamics Method 122
CAD/CAE Integration Enhanced by New CAD Services Standard 124
Turbopump Performance Improved by Evolutionary Algorithms 126

Structures and Acoustics

High-Fidelity Micromechanics Model Developed for the Response of Multiphase Materials 127
Higher-Order Theory—Structural/MicroAnalysis Code (HOT–SMAC) Developed 128
Deformation, Failure, and Fatigue Life of SiC/Ti-15-3 Laminates Accurately Predicted by MAC/GMC 130
MAC/GMC Code Enhanced for Coupled Electromagnetothermoelastic Analysis of Smart Composites 131
Influence of Cooling Channel Geometry on the Thermal Response in Silicon Nitride Plates Studied 133
Integrated Nondestructive Evaluation and Finite Element Analysis Predicts Crack Location and Shape 134
Scanning Electron Microscope Mapping System Developed for Detecting Surface Defects in Fatigue Specimens 136
Life Prediction/Reliability Data of Glass-Ceramic Material Determined for Radome Applications 137
Vibration Monitoring Techniques Applied to Detect Damage in Rotating Disks 138
New Approach to Ultrasonic Spectroscopy Applied to Flywheel Rotors 140
High-Strength Composite Fabric Tested at Structural Benchmark Test Facility 141
Initial Mechanical Testing of Superalloy Lattice Block Structures Conducted 143
Scanning Ultrasonic Spectroscopy System Developed for the Inspection of Composite Flywheels 144
CARES/*Life* Used for Probabilistic Characterization of MEMS Pressure Sensor Membranes 145
Aeroelastic Calculations of Quiet High-Speed Fan Performed 147
Fail-Safe Operation of a High-Temperature Magnetic Bearing Investigated for Gas Turbine Engine Applications 149
Linear-Quadratic-Gaussian Regulator Developed for a Magnetic Bearing 150

Self-Tuning Impact Dampers Designed for Turbomachinery Blade Vibration Suppression 151
Finite Element Analysis of Morphing Piezoelectric Structures Studied 152
Advanced Vibration Analysis Tools and New Strategies for Robust Design of Turbine Engine Rotors 153
Neural Network and Regression Soft Model Extended for PAX–300 Aircraft Engine 155
Excellent Ballistic Impact Properties Demonstrated By New Fabric 156
New Fan Engine Noise-Reduction Concept Using Trailing Edge Blowing of Fan Blades Demonstrated 157
Gear Damage Detection Integrating Oil Debris and Vibration Measurement Technologies Developed 159
Rudder/Fin Seals Investigated for the X–38 Re-Entry Vehicle 160
NASA Space Mechanisms Handbook and Reference Guide Expanded Into CD–ROM Set 162
Comparison Made of Operating Characteristics of Spiral Bevel Gears Manufactured Using Different Methods 163
Gear Crack Propagation Path Studies—Guidelines Developed for Ultrasafe Design 165
Gear Transmission Error Measurement System Made Operational 166
Proof-of-Concept Traction Drive Designed for Planetary Exploration 168
Atomistic Modeling of Semiconductors: Si, C, and 3C-SiC 169
Mystery of Foil Air Bearings for Oil-Free Turbomachinery Unlocked: Load Capacity Rule-of-Thumb Allows Simple Estimation of Performance 171
Heat Treatment Used to Strengthen Enabling Coating Technology for Oil-Free Turbomachinery 172

Space

Space Communications

ACTS Operations Extended Through a University-Based Consortium 174
Architecture Studies Done for High-Rate Duplex Direct Data Distribution (D4) Services 175
Aeronautical Satellite-Assisted Process for Information Exchange Through Network Technologies (Aero-SAPIENT) Conducted 176

Microgravity Science

Bi-Component Droplet Combustion Experiment Designed 181
Combustion of Interacting Droplet Arrays Being Studied 182
Dynamics of Diffusion Flames in von Karman Swirling Flows Studied 183
Flow and Transport of Granular Materials Studied 185
Dynamic Light-Scattering Probe Used for the Very Early Detection of Cataracts and To Measure Response to Therapy (or Treatment) 186
New Method Developed to Measure Contact Angles of a Sessile Drop 188
Phase-Shifting Liquid Crystal Interferometers Demonstrated 189
Microscale Heaters Detailed Boiling Behavior in Normal Gravity and Microgravity 190
Novel Optical Technique Developed and Tested for Measuring Two-Point Velocity Correlations in Turbulent Flows 192
Advanced Microgravity Acceleration Measurement Systems Being Developed 194
Physics of Colloids in Space: Microgravity Experiment Launched, Installed, and Activated on the International Space Station 195
Gas/Liquid Separator Being Developed for Microgravity 198
Compact Video Microscope Imaging System Implemented in Colloid Studies 200
Light Microscopy Module: On-Orbit Microscope Planned for the Fluids Integrated Rack on the International Space Station 202

Power and Propulsion

Flywheel Energy Storage System Designed for the International Space Station 204
International Space Station Power System Model Validated 205
Solar Electric Propulsion Technologies Being Designed for Orbit Transfer Vehicle Applications 207

Engineering and Technical Services

Facilities and Test Engineering

8- by 6-Foot Supersonic Wind Tunnel Compressor Inspected 210
Sonic Boom Testing Performed in NASA Glenn Research Center's 10- by 10-Foot Supersonic Wind Tunnel 211
Small Hot Jet Acoustic Rig Commissioned Into Service 212

Engineering Design and Analysis

Acoustically Enhanced Electroplating Being Developed 213
Hybrid Power Management Program Continued 214
Novel Engineering and Fabrication Techniques Tested in Low-Noise-Research Fan Blades 216
High-Flow Jet Exit Rig Designed and Fabricated 217
Understanding of the Dynamics of the Stirling Convertor Advanced by Structural Testing 219
Preliminary Sizing Completed for Single-Stage-To-Orbit Launch Vehicles Powered By Rocket-Based Combined Cycle Technology 221
CORBASec Used to Secure Distributed Aerospace Propulsion Simulations 222
Observer-Based Magnetic Bearing Controller Developed for Aerospace Flywheels 223
Commercial Off-The-Shelf Microelectromechanical Systems (MEMS) Flow-Measurement Probes Fabricated and Assembled 224

Commercial Technology

Numerical Propulsion Systems Simulation (NPSS): An Award Winning Propulsion System Simulation Tool 228

Appendixes

Definitions of NASA Headquarters Program Offices 231
Definitions of Programs and Projects 232
Index of Authors and Contacts 234

2001

Aeronautics

Subsonic Systems

Oil-Free Turbomachinery Team Passed Milestone on Path to the First Oil-Free Turbine Aircraft Engine

The Oil-Free Turbine Engine Technology Project team successfully demonstrated a foil-air bearing designed for the core rotor shaft of a turbine engine. The bearings were subjected to test conditions representative of the engine core environment through a combination of high speeds, sustained loads, and elevated temperatures. The operational test envelope was defined during conceptual design studies completed earlier this year by bearing manufacturer Mohawk Innovative Technologies and the turbine engine company Williams International. The prototype journal foil-air bearings were tested at the NASA Glenn Research Center.

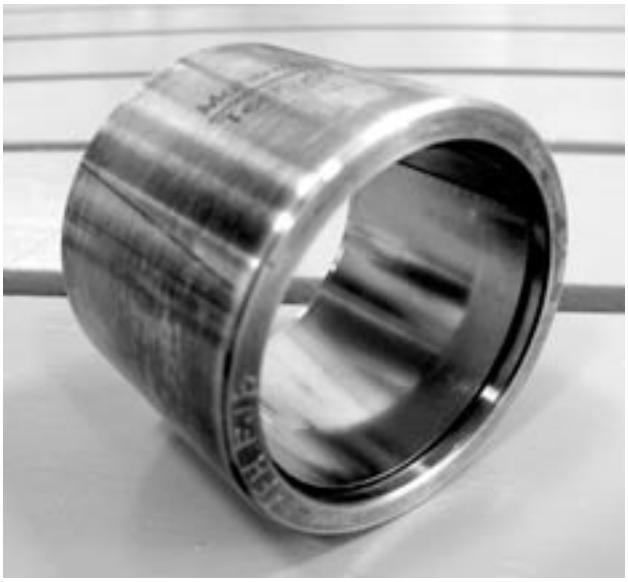

Core hot section foil-air bearing successfully tested in the level 1 milestone.

Glenn is working with Williams and Mohawk to create a revolution in turbomachinery by developing the world's first Oil-Free turbine aircraft engine. NASA's General Aviation Propulsion project and Williams International recently developed the FJX–2 turbofan engine that is being commercialized as the EJ–22. This core bearing milestone is a first step toward a future version of the EJ–22 that will take advantage of recent advances in foil-air bearings by eliminating the need for oil lubrication systems and rolling element bearings. Oil-Free technology can reduce engine weight by 15 percent and let engines operate at very high speeds, yielding power density improvements of 20 percent, and reducing engine maintenance costs. In addition, with NASA coating technology, engines can operate at temperatures up to 1200 °F.

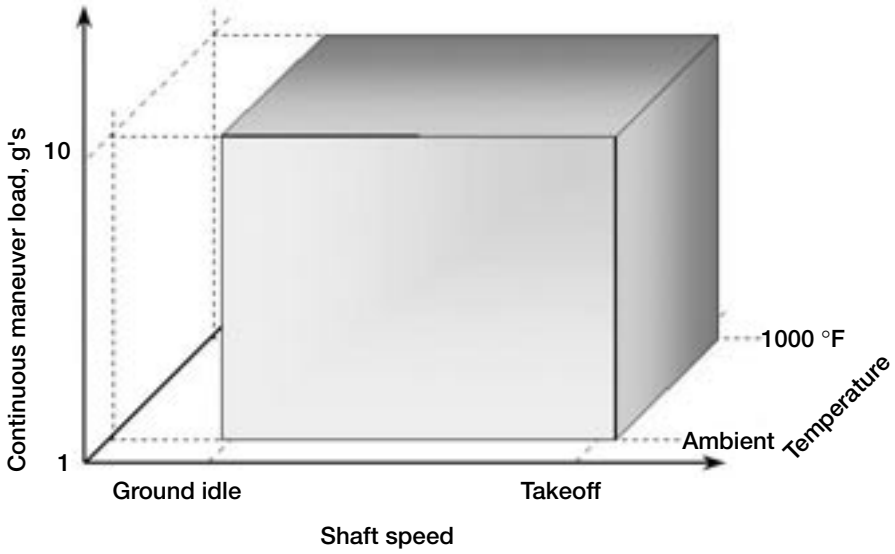

Bearing test envelope exceeded the range of normal engine operating conditions.

Although the project is still a couple of years from a full engine test of the bearings, this milestone shows that the bearing design exceeds the expected environment, thus providing confidence that an Oil-Free turbine aircraft engine will be attained. The Oil-Free Turbomachinery Project is supported through the Aeropropulsion Base Research Program.

Find out more about this research:
http://www.grc.nasa.gov/www/oilfree

Glenn contacts: Dr. Christopher DellaCorte, 216–433–6056, Christopher.DellaCorte@grc.nasa.gov; and Bruce L. Bream, 216–433–6532, Bruce.L.Bream@grc.nasa.gov

Author: Bruce L. Bream

Headquarters program office: OAT

Programs/Projects:
Aeropropulsion Base R&T, UEET

Propulsion Systems Analysis

Advanced Engine Cycles Analyzed for Turbofans With Variable-Area Fan Nozzles Actuated by a Shape Memory Alloy

Advanced, large commercial turbofan engines using low-fan-pressure-ratio, very high bypass ratio thermodynamic cycles can offer significant fuel savings over engines currently in operation. Several technological challenges must be addressed, however, before these engines can be designed. To name a few, the high-diameter fans associated with these engines pose a significant packaging and aircraft installation challenge, and a large, heavy gearbox is often necessary to address the differences in ideal operating speeds between the fan and the low-pressure turbine. Also, the large nacelles contribute aerodynamic drag penalties and require long, heavy landing gear when mounted on conventional, low wing aircraft. Nevertheless, the reduced fuel consumption rates of these engines are a compelling economic incentive, and fans designed with low pressure ratios and low tip speeds offer attractive noise-reduction benefits.

Another complication associated with low-pressure-ratio fans is their need for variable flow-path geometry. As the design fan pressure ratio is reduced below about 1.4, an operational disparity is set up in the fan between high and low flight speeds. In other words, between takeoff and cruise there is too large a swing in several key fan parameters—such as speed, flow, and pressure—for a fan to accommodate.

One solution to this problem is to make use of a variable-area fan nozzle (VAFN). However, conventional, hydraulically actuated variable nozzles have weight, cost, maintenance, and reliability issues that discourage their use with low-fan-pressure-ratio engine cycles. United Technologies Research, in cooperation with NASA, is developing a revolutionary, lightweight, and reliable shape memory alloy actuator system that can change the on-demand nozzle exit area by up to 20 percent. This "smart material" actuation technology, being studied under NASA's Ultra-Efficient Engine Technology (UEET) Program and Revolutionary Concepts in Aeronautics (RevCon) Program, has the potential to enable the next generation of efficient, quiet, very high bypass ratio turbofans.

NASA Glenn Research Center's Propulsion Systems Analysis Office, along with NASA Langley Research Center's Systems Analysis Branch, conducted an independent analytical assessment of this new technology to provide strategic guidance to UEET and RevCon. A 2010-technology-level high-spool engine core was designed for this evaluation. Two families of low-spool components, one with and one without VAFN's, were designed to operate with the core. This "constant core" approach was used to hold most design parameters constant so that any performance differences between the VAFN and fixed-nozzle cycles could be attributed to the VAFN technology alone. In this manner, the cycle design regimes that offer a performance payoff when VAFN's are used could be identified.

The NASA analytical model of a performance-optimized VAFN turbofan with a fan pressure ratio of 1.28 is shown in the figure below. Mission analyses of the engines were conducted using the notional, long-haul, advanced commercial twinjet shown in the figure on the next page. A high wing design was used to accommodate the large high-bypass-ratio engines. The mission fuel reduction benefit of very high bypass shape-memory-alloy VAFN aircraft was calculated to be 8.3 percent lower than a moderate bypass cycle using

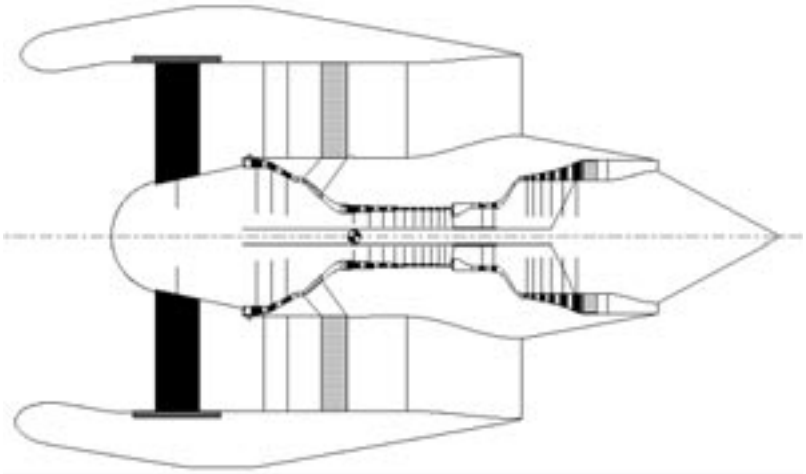

Analytical NASA model of low-fan-pressure-ratio advanced turbofan with a variable-area fan nozzle.

Notional long-haul advanced commercial twinjet using a high wing design to accommodate large, high-bypass-ratio engines.

a conventional fixed nozzle. Shape-memory-alloy VAFN technology is currently under development in NASA's UEET and RevCon Programs.

Find out more about this research:
UEET: http://www.ueet.nasa.gov

RevCon: http://www.dfrc.nasa.gov/Projects/revcon/

Glenn contact:
Jeffrey J. Berton, 216–977–7031,
Jeffrey.J.Berton@grc.nasa.gov

Author: Jeffrey J. Berton

Headquarters program office: OAT

Programs/Projects: UEET, Revolutionary Concepts in Aeronautics

Preliminary Integrated Safety Analysis of Synthetic Vision Conducted

The goal of the NASA Aviation Safety Program is to develop and demonstrate technologies that could help reduce the aviation fatal accident rate by a factor of 5 by the year 2007 and by a factor of 10 by the year 2022. Integrated safety analysis of day-to-day operations and risks within those operations will provide an understanding of the Aviation Safety Program portfolio beyond what is now available. Synthetic vision is the first of the Aviation Safety Program technologies that has been analyzed by the Logistics Management Institute under a contract with the NASA Glenn Research Center. These synthetic vision analyses include both a reliability analysis and a computer simulation model.

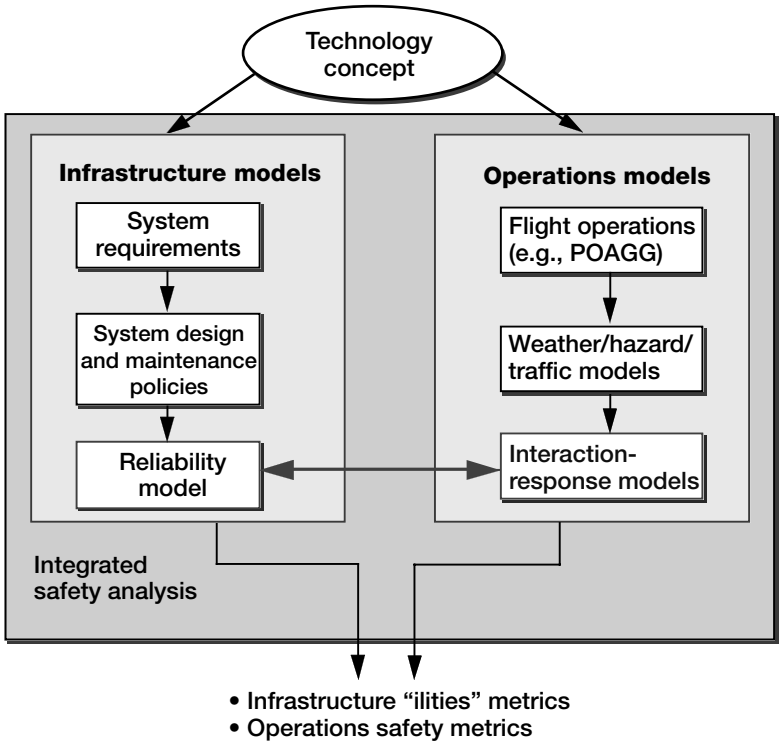

Integrated safety analysis ("ilities" refers to reliability and availability).

An integrated safety analysis must be able to estimate the safety benefits from competing technologies for existing operations and to investigate the safety implications of using new technologies to enable higher-capacity operations. The flow diagram depicts the methodology of an integrated safety analysis.

The reliability and interaction-response models are the two principal analytic components of the integrated safety analysis. These models are used to develop the safety statistics necessary to determine whether the system meets acceptable safety levels.

A combination of reliability modeling plus simulation provides significant computational benefits over either method alone. Reliability models have difficulty addressing dynamic parameters such as pilot response and changing environment, whereas the simulation of low-probability failures leads to an impractical number of computer runs. Using reliability models to estimate equipment failure rates and simulations to estimate the results when those failures occur adds dynamics to the reliability analysis and makes the simulation computationally tractable.

Synthetic vision presents computer-generated views of the external environment to the pilot. The presentation is completely artificial. Typically it is based on a geographical and cultural data base, supplemented by dynamic traffic information. Several systems in addition to the synthetic vision equipment are necessary for synthetic vision operation, and these were included in the reliability analysis.

The simulation model is used to determine the probability of an accident given the existence of a system failure. Simulation is also the primary tool for investigating the impact of human response to equipment failure and the impact of human-initiated error. Two reliability scenarios were analyzed: terrain avoidance and traffic avoidance.

The Logistics Management Institute is continuing the analyses of synthetic vision. Other Aviation Safety Program technologies that are being analyzed include

- Weather accident prevention technologies, including Aviation Weather Information (AWIN) and turbulence detection
- System-wide accident prevention technologies, including human performance and maintenance technologies

The simulation models will allow users to change input—such as the flight path, terrain, aircraft speed and location, equipment, and human factors. The output of the models will show how the new technologies affect the system risk and, ultimately, the probability of an accident. All reliability models and computer simulation models are scheduled to be complete by December 2002.

Find out more about this research:
NASA Aviation Safety Program:
http://avsp.larc.nasa.gov

Glenn's Aviation Safety Program:
http://www.grc.nasa.gov/WWW/avsp/

Logistics Management Institute:
http://www.lmi.org

Glenn contact:
Mary S. Reveley, 216–433–6511,
Mary.S.Reveley@grc.nasa.gov

Author: Mary S. Reveley

Headquarters program office: OAT

Programs/Projects: AvSP

Computing and Interdisciplinary Systems

NASA Participated in the Japan 2001 Science, Creativity and the Young Mind Workshop

During the week of July 23, 2001, a workshop called the Japan 2001 Science, Creativity and the Young Mind took place at Bristol University in Bristol, England. Coordinated by the Clifton Scientific Trust, it brought together 60 British and Japanese students and provided them with a forum for learning and interacting. All the students were chosen from geographical areas of social deprivation, where university education is not seen as a natural progression for students. One of the aims of the workshop was to give the combined group a new view of themselves as potential scientists and an ambition to succeed at the highest level.

Joe Kolecki as seen by the students at Bristol University.

Members of the Glenn Research Center's Learning Technologies Project participated with six of the students and their team leaders as a Space Science Team. Four interactive videoconferencing sessions were held between the NASA Glenn Research Center and Bristol University on four consecutive days. During the sessions, students raised questions concerning various theories about the probable formation of volcanoes on Mars. Of specific interest was if the great Tharsis volcanoes might be the result of an ancient collision of planetary proportions, or if plate tectonic movement, evidence for which was recently discovered by NASA's Mars Global Surveyor Spacecraft, might account for them.

The basic philosophy of the four days was that science involves developing focused questions whose answers are to be sought through a combination of theory and experimentation. Using facts about Mars and terrestrial volcanoes, the students were challenged to extrapolate from the known to the unknown. It was apparent that the students experienced firsthand the excitement of real-life scientific investigation. They immersed themselves completely in their activities, to the point of even working through lunch periods, breaks, and after hours. Their final presentations exceeded all expectations on both sides of the Atlantic Ocean! A final report of their findings will be available from the Learning Technologies Project (LTP) web site.

In summary, the Japan 2001 workshop demonstrated effective collaboration between young people of diverse cultures, and showed that, given an exciting challenge and necessary resources, students will far exceed set goals and expectations. It also demonstrated, in a highly visible, international context, the effectiveness of using technology (ISDN videoconferencing, e-mail, data sharing, and the Internet) in an educational setting.

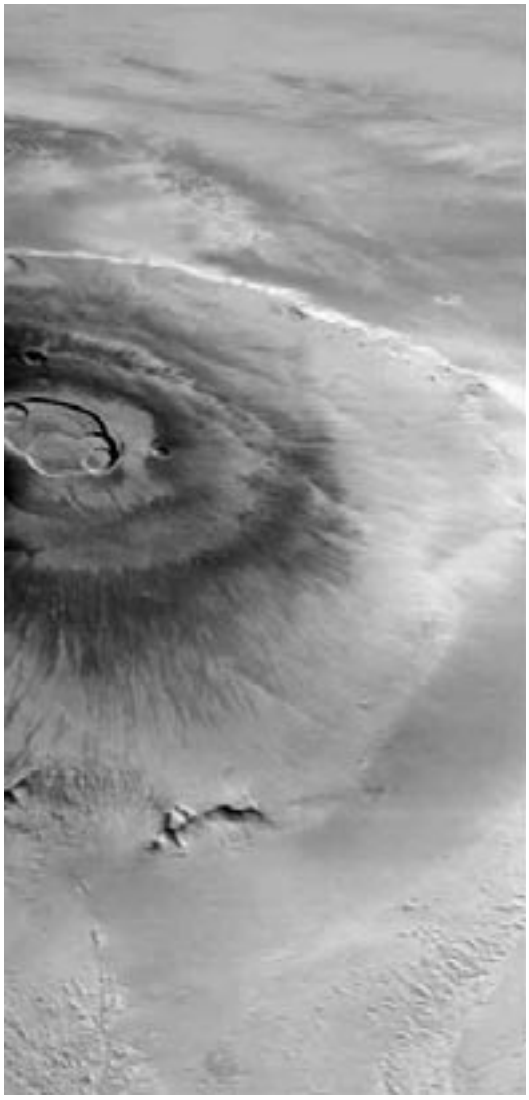

Martian volcano Olympus Mons, 1998.

LTP is a partner in NASA's educational technology program unit, an electronic community center that fosters interaction, collaboration, and sharing among educators, learners, and scientists. Glenn's LTP distance learning program, called NASA Virtual Visits, uses videoconferencing, the Internet, and interactions with experts to motivate science students by providing real-world experiences. Glenn's LTP is supported in this effort by the staff of the Integrated Design and Analysis Center, a facility developed by Glenn's Systems and Analysis Branch to support collaborative engineering between NASA, industry, and academia. A special thanks is extended to the External Programs Directorate for providing a Mars backdrop for the Japan 2001 event.

Find out more on the World Wide Web:

Japan 2001 Science, Creativity and the Young Mind Workshop:
http://www.clifton-scientific.org/j2001/indexN.htm

Glenn Learning Technologies Project: http://www.grc.nasa.gov/WWW/K-12/

Glenn contact: Joe Kolecki, 216–433–2296, Joseph.C.Kolecki@grc.nasa.gov

RSIS contact: Ruth Petersen, 216–433–9714, Ruth.A.Petersen@grc.nasa.gov

Authors:
Joseph C. Kolecki and Ruth A. Petersen

Headquarters program office: OAT

Programs/Projects: HPPCP, LTP

Special recognition:
Invited to co-present at Poskole ICT Conference in April 2002 along with Lawrence Williams on behalf of the Charles University, Prague, and Dr. Eric Albone, Clifton Scientific Trust, UK.

2001

Research and Technology

Materials

New High-Performance SiC Fiber Developed for Ceramic Composites

Sylramic-iBN fiber is a new type of small-diameter (10-μm) SiC fiber that was developed at the NASA Glenn Research Center and was recently given an R&D 100 Award for 2001. It is produced by subjecting commercially available Sylramic (Dow Corning, Midland, MI) SiC fibers, fabrics, or preforms to a specially designed high-temperature treatment in a controlled nitrogen environment for a specific time. It can be used in a variety of applications, but it currently has the greatest advantage as a reinforcement for SiC/SiC ceramic composites that are targeted for long-term structural applications at temperatures higher than the capability of metallic superalloys.

The commercial Sylramic SiC fiber, which is the precursor for the Sylramic-iBN fiber, is produced by Dow Corning, Midland, Michigan. It is derived from polymers at low temperatures and then pyrolyzed and sintered at high temperatures using boron-containing sintering aids (ref. 1). The sintering process results in very strong fibers (>3 GPa) that are dense, oxygen-free, and nearly stoichiometric. They also display an optimum grain size that is beneficial for high tensile strength, good creep resistance, and good thermal conductivity (ref. 2). The NASA-developed treatment allows the excess boron in the bulk to diffuse to the fiber surface where it reacts with nitrogen to form an in situ boron nitride (BN) coating on the fiber surface (thus the product name of Sylramic-iBN fiber). The removal of boron from the fiber bulk allows the retention of high tensile strength while significantly improving creep resistance and electrical conductivity, and probably thermal conductivity since the grains are slightly larger and the grain boundaries cleaner (ref. 2). Also, as shown in the graph, these improvements allow the fiber to display the best rupture strength at high temperatures in air for any available SiC fiber. In addition, for CMC applications under oxidizing conditions, the formation of an in situ BN surface layer creates a more environmentally durable fiber surface not only because a more oxidation-resistant BN is formed, but also because this layer provides a physical barrier between contacting fibers with oxidation-prone SiC surface layers (refs. 3 and 4).

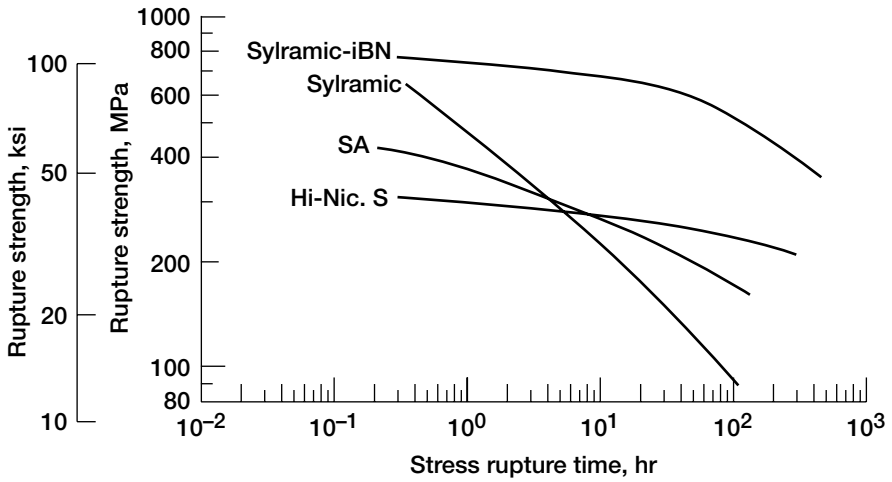

Rupture strength behavior for various high-performance SiC fibers at 1400 °C in air. SA, Tyranno SA fiber from UBE Industries; Hi-Nic. S, Hi-Nicalon Type S fiber from Nippon Carbon.

This year, Glenn demonstrated that the in situ BN treatment can be applied simply to Sylramic fibers located within continuous multifiber tows, within woven fabric pieces, or even assembled into complex product shapes (preforms). SiC/SiC ceramic composite panels have been fabricated from Sylramic-iBN fabric and then tested at Glenn within the Ultra-Efficient Engine Technology Program. The test conditions were selected to simulate those experienced by hot-section components in advanced gas turbine engines. The results from testing at Glenn demonstrate all the benefits expected for the Sylramic-iBN fibers. That is, the composites displayed the best thermostructural performance in comparison to composites reinforced by Sylramic fibers and by all other currently available high-performance SiC fiber types (refs. 3 and 5). For these reasons, the Ultra-Efficient Engine Technology Program has selected the Sylramic-iBN fiber for ongoing efforts aimed at SiC/SiC engine component development.

References
1. Lipowitz, J., et al.: Structure and Properties of SYLRAMIC™ Silicon Carbide Fiber—A Polycrystalline, Stoichiometric β–SiC Composition. Ceram. Eng. Sci. Proc., vol. 18, issue 3, 1997, pp. 147–157.
2. Yun, Hee Mann; and DiCarlo, James A.: Comparison of the Tensile, Creep, and Rupture Strength Properties of Stoichiometric SiC Fibers. Ceram. Eng. Sci. Proc., vol. 20, issue 3, 1999, pp. 259–272.
3. Yun, H.M., et al.: Tensile Behavior of SiC/SiC Composites Reinforced by Treated Sylramic SiC Fibers. Ceram. Eng. Sci. Proc., vol. 22, issue 3, 2001, pp. 521–531.
4. DiCarlo, James A.; Yun, Hee Mann; and Brennan, John, J.: SiC/SiC Composites With Improved BN Coating on Fibers. NASA Tech Brief LEW 16864, 2000.
5. DiCarlo, J.A., et al.: SiC/SiC Material Development Under the NASA UEET Program. Proceedings of 25th Annual Cocoa Beach Conference, restricted sessions, 2001. (Available from the NASA Glenn UEET Office.)

Glenn contact:
Dr. James A. DiCarlo, 216–433–5514, James.A.DiCarlo@grc.nasa.gov

Authors: Dr. James A. DiCarlo and Dr. Hee Mann Yun

Headquarters program office: OAT

Programs/Projects: UEET

Special recognition:
R&D 100 Award for 2001

Architectures for High-Performance Ceramic Composites Being Improved

A major thrust of the Ultra-Efficient Engine Technology (UEET) Program at the NASA Glenn Research Center is to develop advanced hot-section engine components using SiC/SiC ceramic matrix composites (CMC's) with thermostructural capability to 2400 °F (1315 °C). In previous studies, UEET determined that the higher the ultimate tensile strength (UTS) of the as-fabricated CMC, the greater its structural performance at 2400 °F (ref. 1). Thus efforts have been ongoing within UEET to understand and develop fiber architecture approaches that can improve the UTS of SiC/SiC CMC's.

Under UEET, SiC/SiC test panels and demonstration engine components are currently produced by the multi-ply layup of two-dimensional fabric pieces. The fabric is typically formed of multifilament tows containing high-performance Sylramic (Dow Corning) SiC fiber that is woven into two-dimensional five-harness satin fabric with 20 ends per inch in the 0° and 90° directions. In some cases, fabric pieces containing woven Sylramic fiber tows are thermally treated at NASA to form Sylramic-iBN fibers that contain a very thin in-situ-grown boron nitride layer on their surfaces (ref. 2). The final SiC/SiC panels and components are fabricated at the CMC vendor by compressing the fabric pieces in tools and then depositing a thin BN interphase coating on the fibers by chemical vapor deposition. The last step at the vendor is to infiltrate the BN-coated fiber architecture with SiC and silicon matrix constituents to form a dense product.

Because the as-produced Sylramic fiber tows are sized with a thin polymer coating to facilitate handling and weaving, the individual fibers within the tows and fabric are in close contact with each other. This contact is further increased during fabric compression. One important recent finding is that increasing Sylramic fiber tow width in a fabric increases the UTS of the final SiC/SiC CMC. This effect is presumably related to minimizing fiber/fiber contact, which can be detrimental to CMC strength because of the boron-rich chemistry and roughness of the Sylramic fiber surface (refs. 2 and 3). Tows can be spread by mechanically agitating the Sylramic fabric prior to CMC fabrication or by simply thermally treating the Sylramic fabric as in the formation of the Sylramic-iBN fibers. However, CMC's with the treated Sylramic-iBN fabric are even stronger than CMC's with mechanically spread Sylramic tows. The extra strength capability is presumably related to the in situ BN on the fiber surface, which adds compliance to the fiber surfaces and is more resistant to oxygen impurities introduced during the chemical vapor deposition BN process (refs. 2 and 3).

As shown in the table, another important finding is that the use of fabric with tows having less than the standard of 20 ends per inch

EFFECTS OF FABRIC ENDS PER INCH ON CMC PROPERTIES

Fabric ends per inch	Minimum ply height (Sylramic-iBN), mil	Maximum fiber fraction, percent	Average CMC UTS (8 plies), ksi	UTS per V_f*,[a] ksi
20	10.0	38	60	316
16	8.4	37	62	335
12	7.2	35	65	371

[a]Fiber volume fraction in stress direction, V_f*.

provides advantages in terms of reduced ply height and increased ply and CMC strength. The reduced ply height provides more control of part thickness by allowing more plies for a given thickness and by reducing interlaminar residual stresses between plies. The increased ply strength is presumably related to a reduced number of interlaced 90° tows, which, in turn, reduces the crimp angle on the high-modulus fibers in the 0° tows. Also, as shown in the table, although fabric with fewer ends per inch reduced the maximum fiber fraction in an eight-ply CMC panel, CMC UTS actually increased because of increased ply strength. Thus, using fabric with fewer ends per inch has several advantages, including providing a significantly higher strength per fiber fraction in the CMC (last column in the table). Consequently, ongoing UEET efforts will attempt to use architectural approaches for components that minimize fiber-fiber contacts and fiber bending within the final composite microstructure.

References

1. DiCarlo, J.A., et al.: SiC/SiC Material Development Under the NASA UEET Program. Proceedings of 25th Annual Cocoa Beach Conference, restricted sessions, 2001. (Available from the NASA Glenn UEET Office.)
2. Yun, Hee Mann; and DiCarlo, James A.: Comparison of the Tensile, Creep, and Rupture Strength Properties of Stoichiometric SiC Fibers. Ceram. Eng. Sci. Proc., vol. 20, issue 3, 1999, pp. 259–272.
3. Yun, H.M., et al.: Tensile Behavior of SiC/SiC Composites Reinforced by Treated Sylramic SiC Fibers. Ceram. Eng. Sci. Proc., vol. 22, issue 3, 2001, pp. 521–531.

Glenn contact:
Dr. James A. DiCarlo, 216–433–5514, James.A.DiCarlo@grc.nasa.gov

Authors: Dr. Hee Mann Yun and Dr. James A. DiCarlo

Headquarters program office: OAT

Programs/Projects: UEET, improved architectures for high-performance ceramic composites

Techniques Optimized for Reducing Instabilities in Advanced Nickel-Base Superalloys for Turbine Blades

The High-Speed Research (HSR) Airfoil Alloy program developed fourth-generation single-crystal superalloys with up to an 85 °F increase in creep rupture capability over current production airfoil alloys. Recent results have been generated at the NASA Glenn Research Center on these fourth-generation alloys, but in coated form, for subsonic turbine blade applications under NASA's Ultra-Efficient Engine Technology (UEET) Program. One goal for UEET is to optimize the airfoil alloy/thermal barrier coating system for 3100 °F turbine inlet temperatures. The state-of-the art turbine blade airfoil system consists of a superalloy single crystal that provides the basic mechanical performance of the airfoil. A thermal barrier coating is used to reduce the temperature of the base superalloy, and a bondcoat is deposited between the base material and the thermal barrier coating. The bondcoat improves the oxidation and corrosion resistance of the base superalloy and improves the spallation resistance of the thermal barrier coating. A commercial platinum aluminide bondcoat was applied to the HSR-developed alloys, and a diffusion zone developed as a result of interaction between the bondcoat and the superalloy.

Optimized strength is obtained for superalloys when the refractory element content is high and the limits of microstructural stability are approached or exceeded slightly.

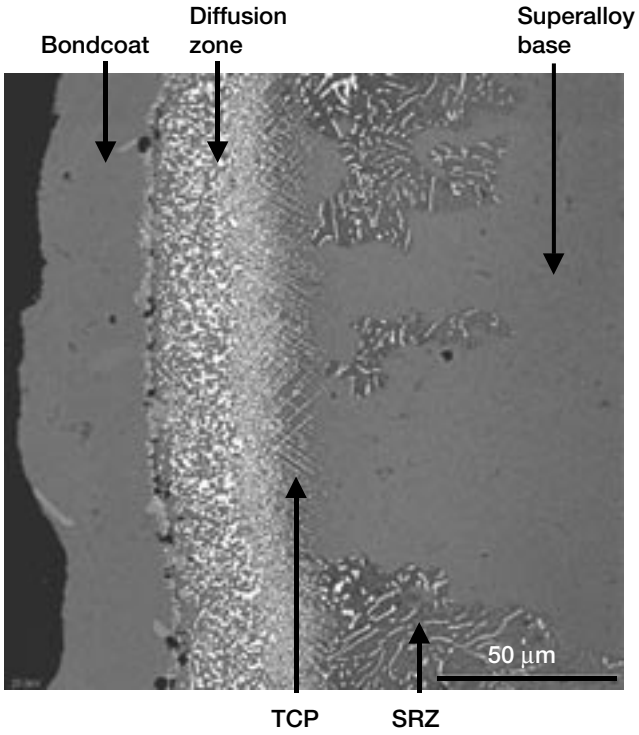

Fourth-generation alloys are susceptible to the formation of topologically close packed phases and a secondary reaction zone.

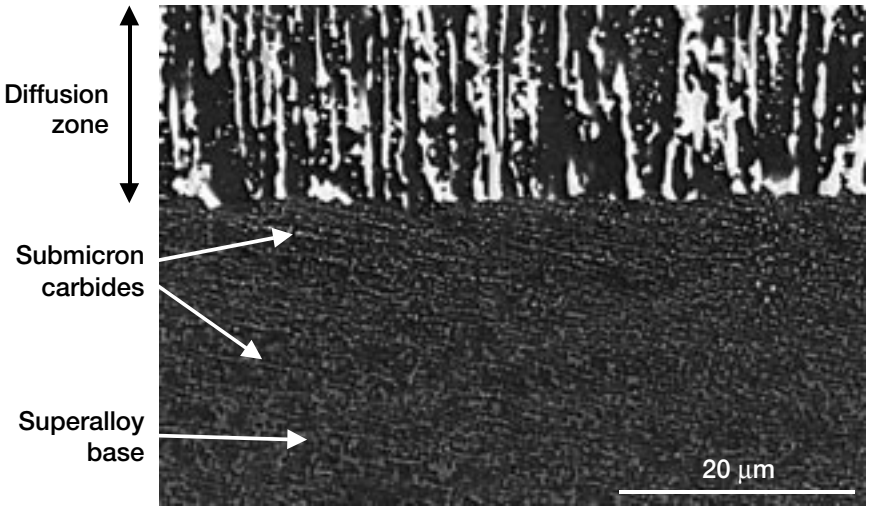

Successful carburization eliminates instabilities under the diffusion zone by forming submicron carbides and changing the local chemistry of the superalloy. Carburization is most effective when it is preceded by a stress relief heat treatment and adequate surface preparation.

For fourth-generation alloys, instability leads to the formation of topologically close packed (TCP) phases, which form internally in the superalloy, and a secondary reaction zone (SRZ), which forms under the diffusion zone. There was a concern that excessive quantities of either TCP or SRZ might decrease the mechanical properties of the superalloy, with SRZ thought to be particularly detrimental and its formation unpredictable. Thus, an SRZ-reduction effort was initiated in the NASA UEET Program so that methods developed during the HSR project could be optimized further to reduce or eliminate the SRZ.

An SRZ is a three-phase constituent composed of TCP and stringers of gamma phase in a matrix of gamma prime. An incoherent grain boundary separates the SRZ from the gamma-gamma prime microstructure of the superalloy. The SRZ is believed to form as a result of local chemistry changes in the superalloy due to the application of the diffusion aluminide bondcoat. Locally high surface stresses also appear to promote the formation of SRZ. Thus, techniques that change the local alloy chemistry or reduce surface stresses have been examined for their effectiveness in reducing SRZ. These SRZ-reduction steps are performed on the test specimen or the turbine blade before the bondcoat is applied. Stress-relief heat treatments developed at NASA Glenn have been demonstrated to reduce significantly the amount of SRZ that develops during subsequent high-temperature exposures. Stress-relief heat treatments reduce surface stresses by recrystallizing a thin surface layer of the superalloy. However, in alloys with very high propensities to form SRZ, stress relief heat treatments alone do not eliminate SRZ entirely. Thus, techniques that modify the local chemistry under the bondcoat have been emphasized and optimized successfully at Glenn. One such technique is carburization, which changes the local chemistry by forming submicron carbides near the surface of the superalloy. Detailed characterizations have demonstrated that the depth and uniform distribution of these carbides are enhanced when a stress relief treatment and an appropriate surface preparation are employed in advance of the carburization treatment. Even in alloys that have the propensity to develop a continuous SRZ layer beneath the diffusion zone, the SRZ has been completely eliminated or reduced to low, manageable levels when this combination of techniques is utilized.

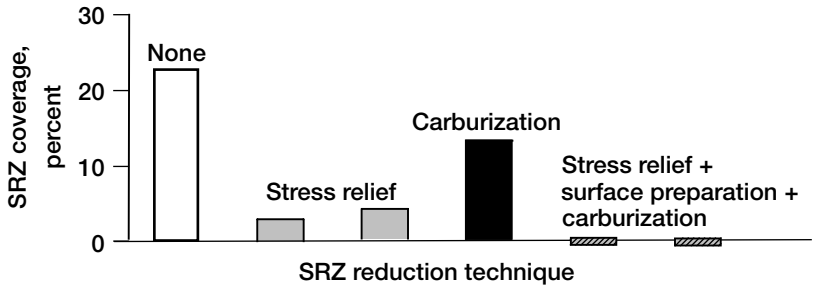

The amount of secondary reaction zone (SRZ) that forms during high-temperature exposures has been significantly reduced by a stress relief heat treatment, and it has been completely eliminated when a combination of stress relief, adequate surface preparation, and subsequent carburization is used.

Now that the techniques to mitigate SRZ have been established at Glenn, TCP phase formation is being emphasized in ongoing work under the UEET Program. The limits of stability of the fourth-generation alloys with respect to TCP phase formation are currently being defined along with high-temperature creep rupture properties. In addition, a regression model is being developed at Glenn for the prediction of the presence of TCP phase in the microstructure and SRZ under the diffusion zone. The model is based on a design-of-experiments methodology with emphasis on the potential synergistic effects of alloying elements.

Glenn contact:
Dr. Rebecca A. MacKay, 216–433–3269, Rebecca.A.MacKay@grc.nasa.gov

Authors: Dr. Rebecca A. MacKay, Dr. Ivan E. Locci, Dr. Anita Garg, and Frank J. Ritzert

Headquarters program office: OAT

Programs/Projects: UEET

Long-Term Creep of a Thin-Walled Inconel 718 Stirling Power-Convertor Heater Head Assessed

The Department of Energy and NASA have identified Stirling power convertors as candidate power supply systems for long-duration, deep-space science missions. A key element for qualifying the flight hardware is a long-term durability assessment for critical hot section components of the power convertor. One such critical component is the power convertor heater head. The heater head is a high-temperature pressure vessel that transfers heat to the working gas medium of the convertor, which is typically helium. An efficient heater head design is the result of balancing the divergent requirements of thin walls for increased heat transfer versus thick walls to lower the wall stresses and thus improve creep resistance and durability. In the current design, the heater head is fabricated from the Ni-base superalloy Inconel 718 (IN 718, Inco Alloys International, Inc., Huntington, WV).

Although IN 718 is a mature alloy system (patented in 1962), there is little long-term (>50,000-hr) creep data available for thin-specimen geometries. Since thin-section properties tend to be inferior to thicker samples, it is necessary to generate creep data using specimens with the same geometry as the actual flight hardware. Therefore, one facet of the overall durability assessment program involves generating relatively short-term creep data using thin specimens at the design temperature of 649 °C (1200 °F).

On the basis of more than 63,000 hr of cumulative creep testing, combined with metallurgical analysis, materials research at the NASA Glenn Research Center has resulted in a heat treatment and microstructure that optimizes the creep

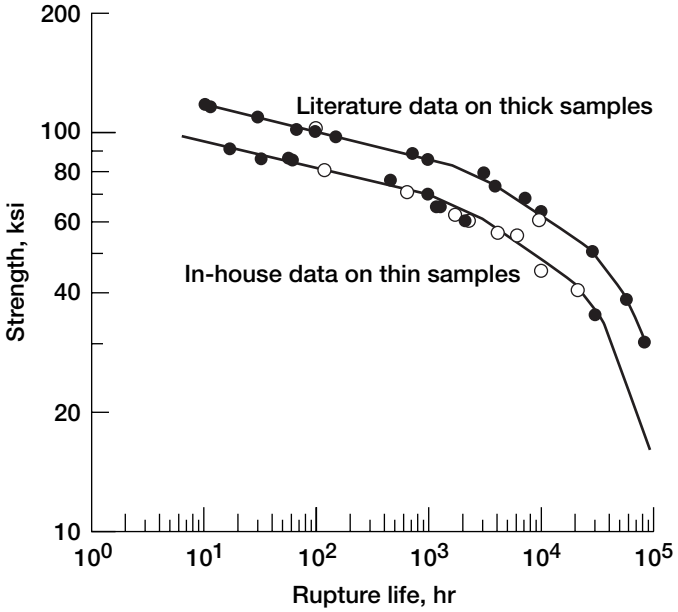

Rupture life as a function of applied stress. Comparison of the in-house data of thin specimens with literature data on thick samples demonstrates the reduction of life associated with a smaller thickness.

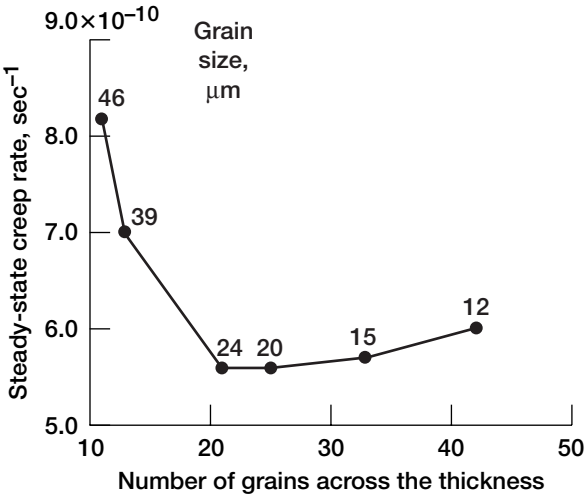

Steady-state creep rate of thin (0.05-cm-thick) IN 718 specimens as a function of grain size. Specimens tested at 649 °C with an applied stress of 414 MPa. Grain sizes are shown in parentheses. Minimum creep rate is achieved with 24-μm grains.

behavior of thin sheets of the nickel-base superalloy IN 718. For instance, creep testing of thin samples with various grain sizes provided data that allowed a determination of the ideal grain size for this application. The ideal size was determined by balancing the opposing needs of, on the one hand, having large grains so as to maximize creep life while, on the other hand, avoiding the mechanical property debit associated with large grains, which arises when there are too few grains through the wall thickness.

The overall life-prediction methodology consists of generating a material-specific data base for the Stirling power convertor application, defining the appropriate definition of failure, developing a probabilistic design methodology, and verifying the critical flight hardware using benchmark tests. For the final validation of the flight hardware design, the life models will be calibrated and verified with benchmark tests on actual heater heads under prototypical operating conditions.

Creep life predictions based on existing literature data combined with in-house test results of the actual flight hardware material indicate that heat treatment and microstructural optimization efforts increase expected life from approximately 60,000 to near 80,000 hr. Unfortunately, given the present operating conditions, even the optimized material will not achieve the goal of 100,000-hr life. On the basis of the results of the material analysis, modifications to the heater head geometry have been suggested that would allow the optimized material to achieve the desired mission life.

Glenn contact:
Dr. Randy Bowman, 216–433–3205, Randy.R.Bowman@grc.nasa.gov

Author: Dr. Randy R. Bowman

Headquarters program office: OSS

Programs/Projects:
Stirling Radioisotope Generator Project

γ-TiAl Shown To Have Sufficient Durability To Allow the Design of a Robust Low-Pressure Turbine Blade

γ-TiAl is an attractive new material for aerospace applications because of its low density and high specific strength in comparison to currently used titanium and nickel-base alloys. However, this intermetallic is inherently brittle, and long-life durability is a potential problem. As part of the aviation safety goal to reduce the aircraft accident rate, the potential for γ-TiAl to be used for robust low-pressure turbine blades has been thoroughly studied. The effect of impact damage and casting porosity on the fatigue life of cast Ti-48Al-2Nb-2Cr alloys was assessed. The Al content of TiAl can vary slightly because of the casting process, so the effect of a lower Al content on the impact resistance and resulting fatigue strength was also studied. Ti-48Al-2Nb-2Cr is one of the original cast TiAl alloys to show promising mechanical properties. However, more recently developed alloys have been developed for enhanced mechanical properties. One of these alloys, ABB–2, has a much higher strength but only half the ductility of Ti-48Al-2Nb-2Cr. The ballistic impact resistance and remnant fatigue strength of ABB–2 was determined and compared with Ti-48Al-2Nb-2Cr. In addition, the effect of fretting damage on the fatigue life of cast Ti-48Al-2Nb-2Cr was studied at the NASA Glenn Research Center.

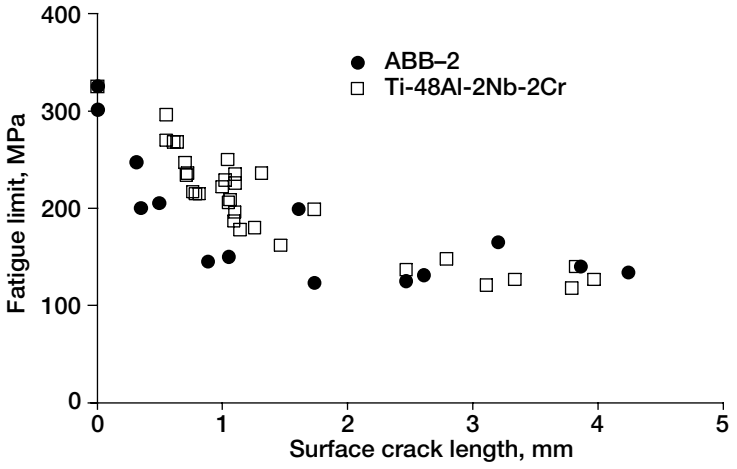

Fatigue strength of Ti-48Al-2Nb-2Cr and ABB–2 decreased with increasing surface crack length.

Ballistic impacts resulted in two forms of cracks, the severity of which depended on the impact energy. At lower impact energies, the specimens failed in fatigue from backside cracks that were perpendicular to the specimen axis. At higher impact energies,

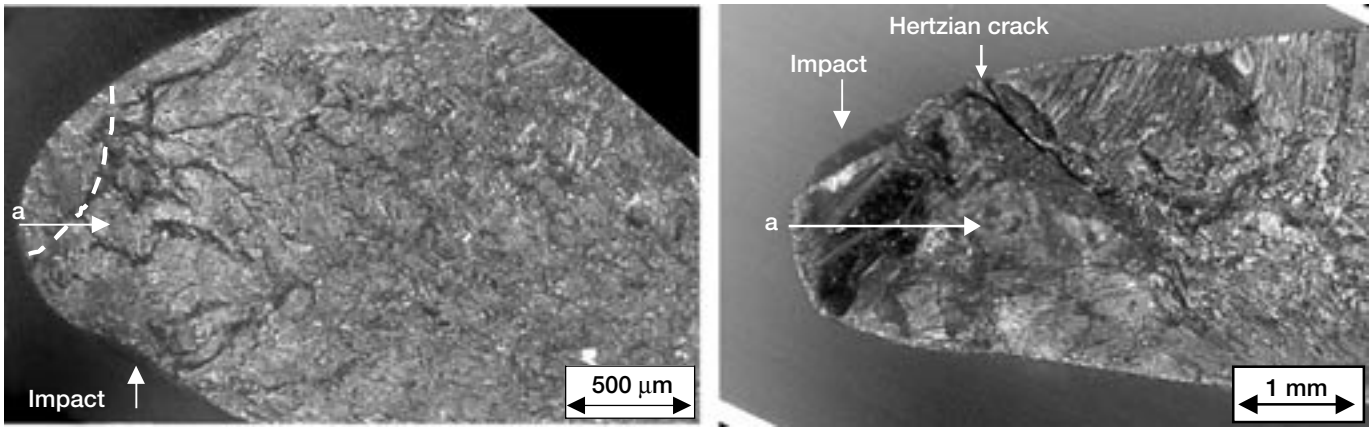

Backside crack initiation

Hertzian crack initiation

ABB–2 fatigue fracture surfaces showing backside crack initiation for low-energy impacts and front side, or hertzian, crack initiation for high-energy impacts.

the fatigue failure initiated from the hertzian cracks on the front side of the specimen (ref. 1). Hertzian and backside crack lengths were similar for a particular impact condition for both high and low Al content Ti-48Al-2Nb-2Cr alloys as well as for the ABB–2 alloy. Defect size played a large role in determining the critical fatigue loads. Increasing the defect size, regardless of whether the flaws resulted from casting porosity or from impact cracks, led to a decrease in the fatigue strength according to the $1/\sqrt{a}$ relationship described by fracture mechanics (ref. 2). The fatigue strength of Ti-48Al-2Nb-2Cr and ABB–2 showed a similar dependence on external crack length, and this was due to the fact that both materials had the same fatigue threshold stress intensity. Therefore, to improve damage tolerance, an alloy with a higher fatigue threshold is required. Within the limits of the test program, the fatigue strength of Ti-48Al-2Nb-2Cr was not affected by fretting damage (ref. 3), indicating its excellent fretting resistance. Synthesis of the entire data set in regards to its impact, chemistry, processing, fatigue, and fretting has demonstrated that TiAl has sufficient durability to allow the design of a robust low-pressure turbine blade.

References

1. Draper, S.L., et al.: The Effect of Ballistic Impacts on the High-Cycle Fatigue Properties of Ti-48Al-2Nb-2Cr (at.%). Metall. T-A, vol. 32, no. 11, 2001, pp. 2743–2758.
2. Lerch, Bradley A., et al.: Effect of Defects on the Fatigue Life of γ-TiAl. NASA/CP—1999-208915, Vol. II, HITEMP Review 1999, Paper no. 30, pp. 1–11. (Available from the NASA Glenn Subsonic Systems Office.)
3. Miyoshi, Kazuhisa, et al.: Evaluation of Ti-48Al-2Cr-2Nb Under Fretting Conditions. NASA/TM—2001-210902, 2001. http://gltrs.grc.nasa.gov/GLTRS/

Glenn contact:
Susan Draper, 216–433–3257, Susan.L.Draper@grc.nasa.gov

Authors: Susan L. Draper, Dr. Bradley A. Lerch, Dr. Kazuhisa Miyoshi, and Dr. J. Michael Pereira

Headquarters program office: OAT

Programs/Projects: Ultra Safe, RTA

Major Effects of Nonmetallic Inclusions on the Fatigue Life of Disk Superalloy Demonstrated

The fatigue properties of modern powder metallurgy disk alloys can vary because of the different steps of materials and component processing and machining. Among these variables, the effects of nonmetallic inclusions introduced during the powder atomization and handling processes have been shown to significantly degrade low-cycle fatigue life. The levels of inclusion contamination have, therefore, been reduced to less than 1 part per million in state-of-the-art nickel disk powder-processing facilities. Yet the large quantities of compressor and turbine disks weighing from 100 to over 1000 lb have enough total volume and surface area for these rare inclusions to still be present and limit fatigue life. The objective of this study was to investigate the effects on fatigue life of these inclusions, as part of the Crack Resistant Disk Materials task within the Ultra Safe Propulsion Project. Inclusions were carefully introduced at elevated levels in a nickel-base disk superalloy, U720, produced using powder metallurgy processing. Multiple strain-controlled fatigue tests were then performed on extracted test specimens at 650 °C. Analyses were performed to compare the low-cycle fatigue lives and failure initiation sites as functions of inclusion content and fatigue conditions.

Powder of the nickel-base superalloy U720 was atomized in argon at Special Metals Corporation, Inc., using production-scale high-cleanliness powder-processing facilities and handling practices. The powder was then passed through a 270-mesh screen. One portion of this powder was set aside for subsequent consolidation without introduced inclusions. Two other portions of this powder were seeded with alumina inclusions. Small, polycrystalline soft (Type 2) inclusions of about 50 μm diameter were carefully prepared and blended into one powder lot, and larger hard (Type 1) inclusions of about 150 μm mean diameter were introduced into the other seeded portion of powder. All three portions of powder were then sealed in separate containers, hot isostatically pressurized, extruded, forged into subscale disks, and heat treated. Low-cycle-fatigue specimens were then extracted, machined, and tested. Fatigue tests were performed at 650 °C in closed-loop servohydraulic testing machines using induction heating and axial extensometers. All tests were continued to failure, and fractographic evaluations were performed on all specimens to determine the crack initiation sites.

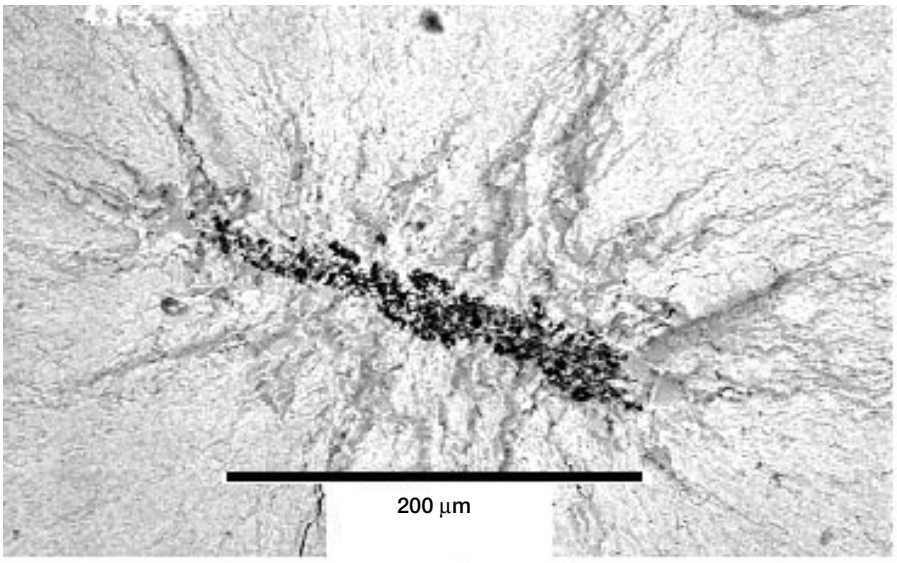

Inherent alumina nonmetallic inclusion that initiated a crack within a U720 fatigue specimen to cause failure (ref. 1). Specimen tested at 538 °C, a strain range of 0.75 percent, and a strain ratio of 0.

A large majority of the failures in specimens with introduced inclusions occurred at cracks initiating from inclusions at the specimen surface, as shown for each type of inclusion in the following bar chart. The inclusions significantly reduced fatigue life from unseeded material levels, as shown in the bar chart. These effects were found to depend on the strain range, strain ratio, and inclusion size. Tests at lower strain ranges and higher strain ratios resulted in larger effects of inclusions on life. Inclusion effects on life were thereby maximized in tests at the lowest strain range of 0.6 percent and the most positive strain ratio of 0.5. Under these conditions, small Type 2 inclusions reduced life substantially—about 20 times, whereas large Type 1 inclusions dramatically reduced life 100 times. These results clearly demonstrate that it is essential to include the effects of inclusions for realistic predictions of disk fatigue life. Important issues, including temperature dependence, crack

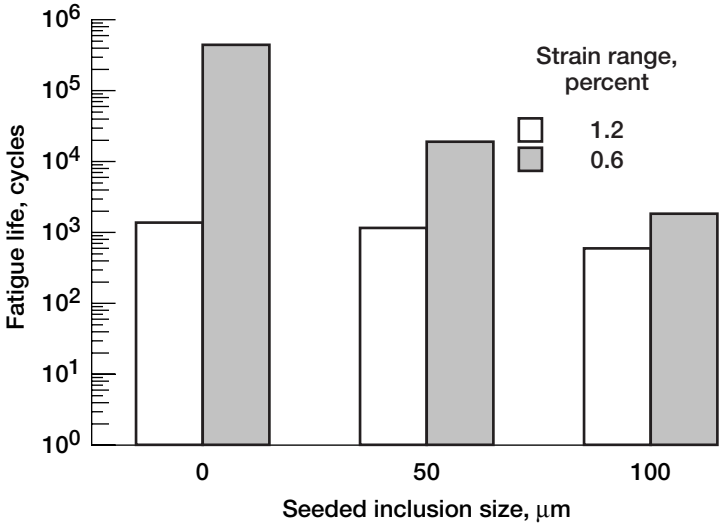

The larger seeded inclusions reduced fatigue life over 100 times in tests at a lowest strain range of 0.6 percent, a highest strain ratio of 0.5, and a temperature of 650 °C.

initiation versus propagation, surface treatments, realistic disk features and machining, and realistic disk spin testing will be addressed to accurately model inclusion effects on disk fatigue life.

Reference

1. Gabb, T.P., et al.: Assessments of Low Cycle Fatigue Behavior of Powder Metallurgy Alloy U720. The Thirty-First National Symposium on Fatigue and Fracture Mechanics. ASTM STP–1389, G.R. Halford and J.P. Gallagher, eds., 2000, pp. 110–127. (reprints available)

Glenn contacts:
Tim Gabb, 216–433–3272, Timothy.P.Gabb@grc.nasa.gov; and Jack Telesman, 216–433–3310, Jack.Telesman@grc.nasa.gov

OAI contact:
Pete Kantzos, 216–433–5202, Pete.T.Kantzos@grc.nasa.gov

U.S. Army Research Laboratory, Vehicle Technology Directorate at Glenn contacts:
Peter Bonacuse, 216–433–3309, Peter.J.Bonacuse@grc.nasa.gov; and Robert L. Barrie, 216–433–5090, Robert.L.Barrie@grc.nasa.gov

Authors:
Timothy P. Gabb, Jack Telesman, Peter T. Kantzos, Peter J. Bonacuse, and Robert L. Barrie

Headquarters program office: OAT

Programs/Projects: Ultra Safe

Dual Microstructure Heat Treatment of a Nickel-Base Disk Alloy Assessed

Gas turbine engines for future subsonic aircraft will require nickel-base disk alloys that can be used at temperatures in excess of 1300 °F. Smaller turbine engines, with higher rotational speeds, also require disk alloys with high strength. To address these challenges, NASA funded a series of disk programs in the 1990's. Under these initiatives, Honeywell and Allison focused their attention on Alloy 10, a high-strength, nickel-base disk alloy developed by Honeywell for application in the small turbine engines used in regional jet aircraft. Since tensile, creep, and fatigue properties are strongly influenced by alloy grain size, the effect of heat treatment on grain size and the attendant properties were studied in detail. It was observed that a fine grain microstructure offered the best tensile and fatigue properties, whereas a coarse grain microstructure offered the best creep resistance at high temperatures. Therefore, a disk with a dual microstructure, consisting of a fine-grained bore and a coarse-grained rim, should have a high potential for optimal performance.

Under NASA's Ultra-Safe Propulsion Project and Ultra-Efficient Engine Technology (UEET) Program, a disk program was initiated at the NASA Glenn Research Center to assess the feasibility of using Alloy 10 to produce a dual-microstructure disk. The objectives of this program were twofold. First, existing dual-microstructure heat treatment (DMHT) technology would be applied and refined as necessary for Alloy 10 to yield the desired grain structure in full-scale forgings appropriate for use in regional gas turbine engines. Second, key mechanical properties from the bore and rim of a DMHT Alloy 10 disk would be measured and compared with conventional heat treatments to assess the benefits of DMHT technology.

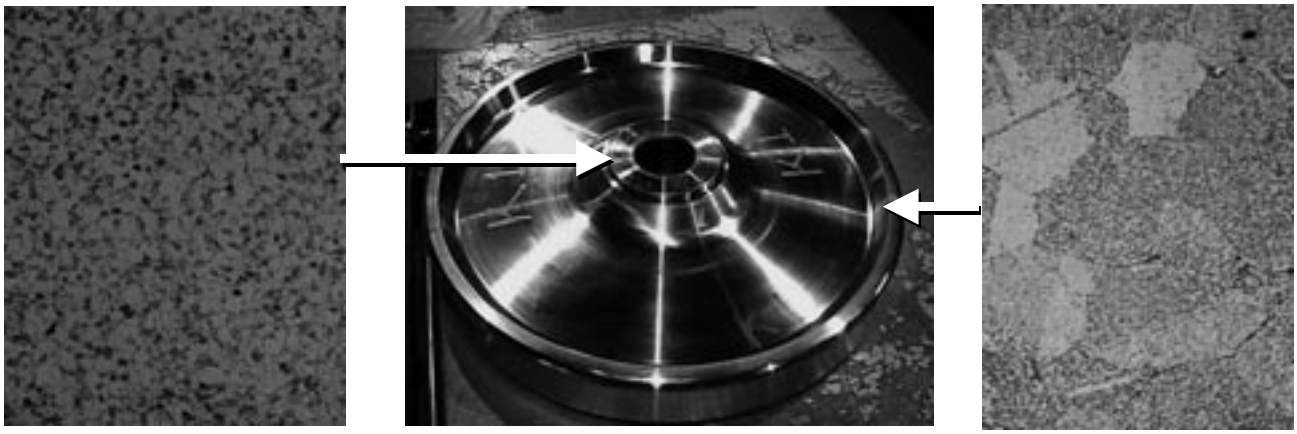

Alloy 10 DMHT disk.

At Wyman Gordon and Honeywell, an active-cooling DMHT process was used to convert four full-scale Alloy 10 disks to a dual-grain microstructure. The resulting microstructures are illustrated in the photomicrographs. The fine grain size in the bore can be contrasted with the coarse grain size in the rim. Testing (at NASA Glenn) of coupons machined from these disks showed that the DMHT approach did indeed produce a high-strength, fatigue-resistant bore and a creep-resistant rim. This combination of properties was previously unobtainable using conventional heat treatments, which produced disks with a uniform grain size.

Future plans are in place to spin test a DMHT disk under the Ultra Safe Propulsion Project to assess the viability of this technology at the component level. This testing will include measurements of disk growth at a high temperature as well as the determination of burst speed at an intermediate temperature.

Glenn contact:
Dr. John Gayda, 216–433–3273,
John.Gayda@grc.nasa.gov

Author: Dr. John Gayda

Headquarters program office: OAT

Programs/Projects: Ultra Safe, UEET

Strength and Fracture Toughness of Solid Oxide Fuel Cell Electrolyte Material Improved

Solid oxide fuel cells (SOFC) are being developed for various applications in the automobile, power-generation, and aeronautics industries. Recently, the NASA Glenn Research Center has been exploring the possibility of using SOFC's for aeropropulsion under its Zero Carbon Dioxide Emission Technology (ZCET) Program. 10-mol% yttria-stabilized zirconia (10YSZ) is a very good anionic conductor at high temperatures and is, therefore, used as an oxygen solid electrolyte in SOFC. However, it has a high thermal expansion coefficient, low thermal shock resistance, low fracture toughness, and poor mechanical strength. For aeronautic applications, the thin ceramic electrolyte membrane of the SOFC needs to be strong and tough. Therefore, we have been investigating the possibility of enhancing the strength and fracture toughness of the 10YSZ electrolyte without degrading its electrical conductivity to an appreciable extent.

We recently demonstrated that the addition of alumina to zirconia electrolyte increases its strength as well as its fracture toughness. Zirconia-alumina composites containing 0 to 30 mol% of alumina were fabricated by hot pressing. The hot pressing procedure was developed and various hot pressing parameters were optimized, resulting in dense, crack-free panels of composite materials. Cubic zirconia and

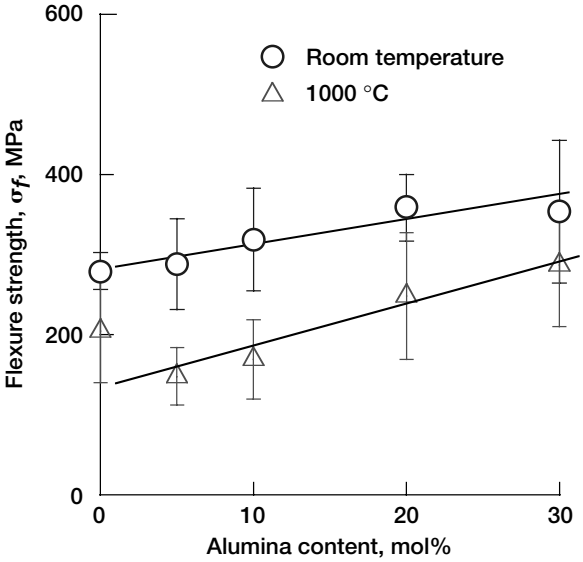

Effect of alumina additions on the strength of 10YSZ electrolyte at room temperature and 1000 °C measured in four-point flexure in ambient atmosphere with 20/40-mm spans (ASTM C1161 and 1211) at a loading rate of 50 MPa/sec in ambient air.

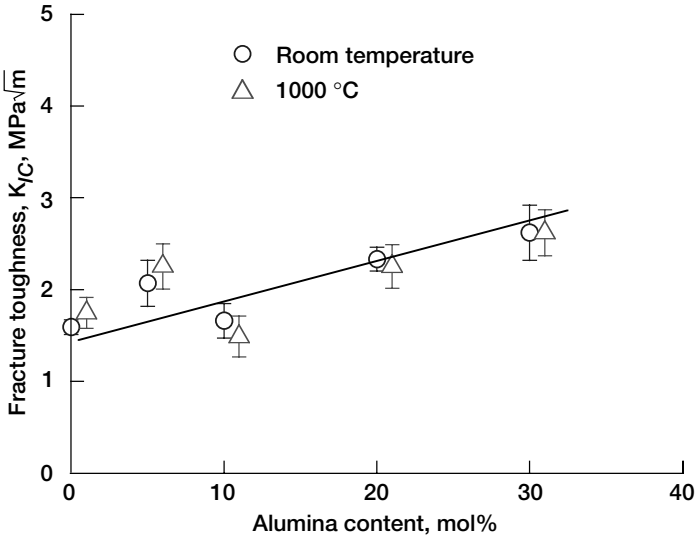

Effect of alumina additions on fracture toughness of 10YSZ electrolyte at room temperature and 1000 °C. Measurements were conducted in four-point flexure with 20/40-mm spans by the single-edge V-notched beam method in ambient atmosphere at a loading rate of 0.5 mm/min.

α-alumina were the only phases detected, indicating that there was no chemical reaction between the constituents during hot pressing at elevated temperatures. Flexure strength σ_f and fracture toughness K_{IC} of the various zirconia-alumina composites were measured at room temperature as well as at 1000 °C in air. Both properties showed systematic improvement with increased alumina addition at room temperature and at 1000 °C. Use of these modified electrolytes with improved strength and fracture toughness should prolong the life and enhance the performance of SOFC in aeronautics and other applications.

Bibliography

Bansal, N.P.; and Choi, S.R.: Processing and Mechanical Properties of Zirconia/Alumina Composites for Solid Oxide Fuel Cells. 26th Annual International Conference on Advanced Ceramics and Composites, Cocoa Beach, FL, Jan. 13–18, 2002.

Glenn contact:
Dr. Narottam P. Bansal, 216–433–3855, Narottam.P.Bansal@grc.nasa.gov

OAI contact:
Dr. Sung R. Choi, 216–433–8366, Sung.R.Choi@grc.nasa.gov

Authors: Dr. Narottam P. Bansal and Dr. Sung R. Choi

Headquarters program office: OAT

Program/Project: ZCET

Ceramic Propellant Injectors Designed and Fabricated

Ceramic propellant injectors offer the potential for order-of-magnitude weight reductions in comparison to conventional metallic injectors and may enable some NASA missions. Injectors constructed of ceramic materials have the inherent advantages of being lighter weight, more erosion resistant, and capable of higher temperature operation than current metallic designs. The use of ceramics may facilitate new designs for a broad range of combustion devices in aero and space applications. In a joint project involving NASA Glenn Research Center's Ceramics and Combustion branches and Case Western Reserve University, a rocket propellant injector faceplate was designed and fabricated using laminated object manufacturing and standard ceramic processing. A number of faceplates have been successfully hot-fire bench tested.

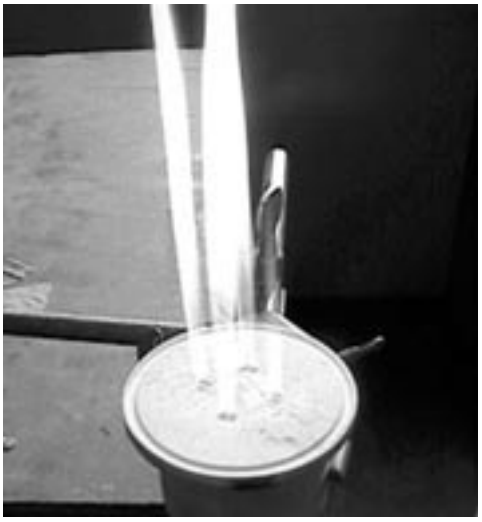

Bench test of ceramic propellant injector.

Glenn contacts:
Dr. Andrew J. Eckel, 216–433–8185, Andrew.J.Eckel@grc.nasa.gov; and
Diane Linne, 216–977–7512, Diane.Linne@grc.nasa.gov

Author: Dr. Andrew J. Eckel

Headquarters program office: OAT

Programs/Projects: DDF, STR

Tensile Strength and Microstructure of Al_2O_3-ZrO_2 Hypo-Eutectic Fibers Studied

Oxide eutectics offer high-temperature strength retention and creep resistance in oxidizing environments. Al_2O_3-ZrO_2 eutectic strengths have been studied since the 1970's (refs. 1 to 10). Directionally solidified oxide eutectics exhibit improved resistance to slow crack growth and excellent strength retention at high temperatures up to 1400 °C (refs. 1 to 10). Materials studied typically contain Y_2O_3 to metastably retain the high-temperature cubic and tetragonal polymorphs at room temperature.

Al_2O_3-ZrO_2 is of fundamental interest for creep studies because it combines a creep-resistant material, Al_2O_3, with a very low creep resistance material, ZrO_2. Results on mechanical properties and microstructures of these materials will be used to define compositions for creep testing in future work. Substantial variations from the eutectic alumina to zirconia ratio can be tolerated without a loss in room-temperature strength. The effect of increasing Y_2O_3 addition on the room-temperature tensile strength of an Al_2O_3-ZrO_2 material containing excess Al_2O_3 was examined at the NASA Glenn Research Center, where the materials were grown using Glenn's world-class laser growth facilities.

ELASTIC MODULUS FOR 68 mol% Al_2O_3 MATERIALS WITH INCREASING Y_2O_3 ADDITIONS ESTIMATED FROM THE SLOPE OF STRESS-STRAIN DATA PLOTS

Y_2O_3 content, mol%	None	1.1	3.2	5.1	7.6
Elastic modulus, GPa	270	370	320	290	310

During tensile testing, an optical extensometer was used to measure the relative displacement of two flags that define the test specimen gauge length. The elastic modulus was then estimated by curve fitting the slope of the stress-strain plot. Results for the five compositions are shown in the table. The range in moduli, 270 to 370 GPa, is large and can be explained, at least in part, by considering the variations in phase content with composition and growth defects.

Factors expected to affect eutectic strength are lamellar spacing, width of intercolony boundary regions, and associated phases, voids, and growth defects. The scale of these microstructural features extends over an order of magnitude. Interlamellar spacings are very fine, ~0.3 to ~0.2 μm, whereas pores and shrinkage cavities are several

	Y_2O_3 content, mol%		
	None	1.1	7.6
Tensile strength			
Mean (stand. dev.), GPa	0.74 (0.16)	1.34 (0.35)	1.09 (0.21)
Maximum, GPa	0.91	1.9	1.4
Minimum, GPa	0.58	0.86	0.79
Weibull modulus	5	4	9

	Y_2O_3 content, mol%		
	3.2	5.1	7.6
Tensile strength			
Mean (stand. dev.), GPa	1.1 (0.21)	1.0 (0.10)	1.0 (0.08)
Maximum, GPa	1.4	1.2	1.1
Minimum, GPa	0.8	0.8	0.9
Weibull modulus	6	10	14

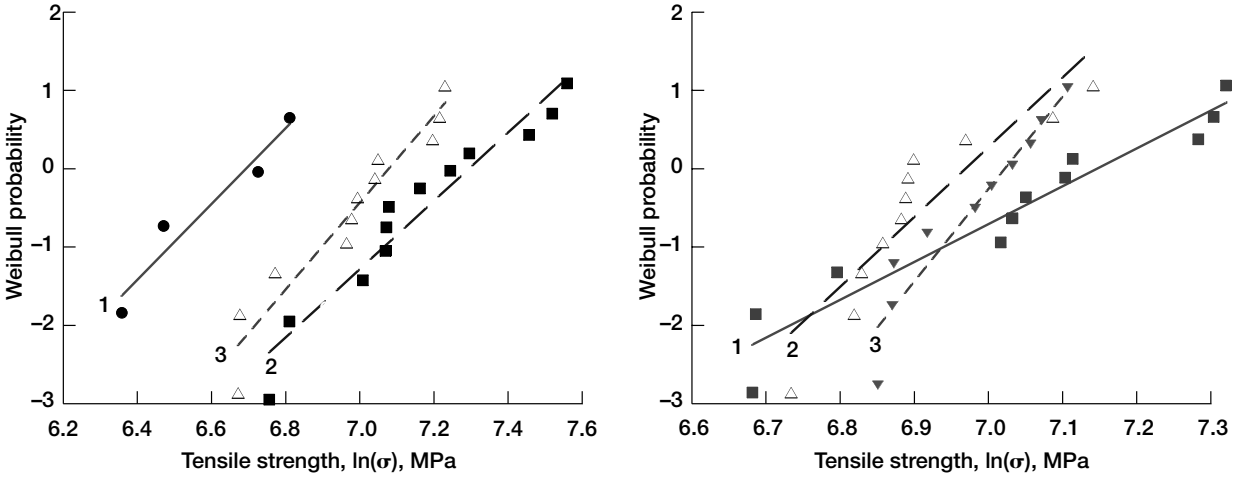

Left: Weibull probability plot of tensile strength for various compositions: (1) 68 mol% Al_2O_3 [0 mol% Y_2O_3], (2) 68 mol% Al_2O_3 [1.1 mol% Y_2O_3], (3) 68 mol% Al_2O_3 [3.2 mol% Y_2O_3]. Right: Weibull probability plot of tensile strength for various compositions: (1) 68 mol% Al_2O_3 [3.2 mol% Y_2O_3], (2) 68 mol% Al_2O_3 [5.1 mol% Y_2O_3], (3) 68 mol% Al_2O_3 [7.6 mol% Y_2O_3].

micrometers in size in materials with the highest Y_2O_3 content. The figures give the tensile strength data in the form of single-parameter Weibull probability, Ln(Ln(1/survival probability)), versus Ln(fracture stress). The figure on the left shows the test results for fibers with 68 mol% Al_2O_3 and 0 to 3.2 mol% Y_2O_3. Mean strengths range from 0.74 for no Y_2O_3 addition to a maximum of 1.3 for the 1.1 mol% Y_2O_3 addition. Fracture strength of the strongest 1.1 mol% Y_2O_3 fibers is 1.9 GPa. Strengths decline with additional Y_2O_3. The differences in the means of the first figure, although small, are significant at the 90-percent confidence level calculated using the student t-test. Strengths remain at ~1 GPa for 3.2 to 7.6 mol% Y_2O_3 materials (as shown in the figure on the right). Differences in the means for these compositions were not statistically significant. For compositions with the highest Y_2O_3 content (5.1 and 7.6 mol% Y_2O_3), there is an increase in Weibull modulus. The highest Y_2O_3 fibers contain a population of large pores and shrinkage voids within the wide colony boundaries. The defects result from the solidification conditions. Even with an apparently large flaw population contributing to failure over a narrower range of strengths, the mean strength remains approximately 1 GPa.

The Al_2O_3-ZrO_2(Y_2O_3) materials proved highly tolerant of growth defects, maintaining an average strength of 1 GPa in the presence of 1- to 2-μm pores and large shrinkage cavities, which extend with cracklike morphology along the fiber axis. Critical defects were external facets, intercolony pores, and other stress concentrators contained within the low-toughness Al_2O_3 phase that is in residual tension.

Future studies are planned to concentrate on strengthening the Al_2O_3 phase and increasing the amount of crack deflection experienced at the Al_2O_3-ZrO_2 interfaces through the use of dopants to achieve a combination of high strength and an acceptable toughness.

References

1. Schmid, F.; and Viechnicki, D.: Oriented Eutectic Microstructures in the System Al_2O_3/ZrO_2. J. Mat. Sci., vol. 5, 1970, pp. 470–473.
2. Cocks, F.H.; Pollock, J.T.A.; and Bailey, J.S.: Preparation of In Situ Composites by Edge-Defined, Film-Fed Growth (EFG) Directional Solidification. GIPXA, 1973, pp. 141–152.
3. Hulse, C.O.; and Batt, J.A.: The Effect of Eutectic Microstructures on the Mechanical Properties of Ceramic Oxides. United Aircraft Corp. UARL–N910803–10, 1974.
4. Mazerolles, L.; Michel, D.; and Portier, R.: Interfaces in Oriented Al_2O_3-ZrO_2 (Y_2O_3) Eutectics. J. Am. Ceram. Soc., vol. 69, no. 3, 1986, pp. 252–255.
5. Borodin, V.A.; Starostin, M. Yu.; and Yalovets, T.N.: Structure and Related Mechanical Properties of Shaped Eutectic Al_2O_3-ZrO_2(Y_2O_3) Composites. J. Cryst. Growth, vol. 104, 1990, pp. 148–153.
6. Bates, H.E.: EFG Growth of Alumina-Zirconia Eutectic Fibers. Ceram. Eng. Sci. Proc., July–Aug., 1992, pp. 190–197.

7. Courtright, E.L.; Haggerty, H.S.; and Sigalovsky, J.: Controlling Microstructures in $ZrO_2(Y_2O_3)$-Al_2O_3 Eutectic Fibers. Ceram. Eng. Sci. Proc., July–Aug., 1993, pp. 671–681.
8. Farmer, S.C.; Sayir, A.; and Dickerson, P.O.: Mechanical and Microstructural Characterization of Directionally-Solidified Alumina-Zirconia Eutectic Fibers. Proceedings of a Symposium on In Situ Composites: Science and Technology, TMS, Warrendale, PA, 1993, pp. 167–182.
9. Sayir, A., et al.: High Temperature Mechanical Properties of $Al_2O_3/ZrO_2(Y_2O_3)$ Fibers. Mater. Res. Soc. Symp. Proc., vol. 365, MRS, Warrendale, PA, 1995, pp. 21–27.
10. Pardo, Jose A., et al.: Piezospectroscopic Study of Residual Stresses in Al_2O_3-ZrO_2 Directionally Solidified Eutectics. J. Am. Ceram. Soc., vol. 83, no. 11, 2000, pp. 2745–2752.

Glenn contact:
Dr. Serene Farmer, 216–433–3289,
Serene.C.Farmer@grc.nasa.gov

CWRU contact:
Dr. Ali Sayir, 216–433–6254,
Ali.Sayir@grc.nasa.gov

Authors:
Dr. Serene C. Farmer and Dr. Ali Sayir

Headquarters program office: OAT

Programs/Projects: HOTPC

Lightweight, Actively Cooled Ceramic Matrix Composite Thrustcells Successfully Tested in Rocket Combustion Lab

In a joint effort between the NASA Glenn Research Center and the NASA Marshall Space Flight Center, regeneratively cooled ceramic matrix composite (CMC) thrustcells were developed and successfully tested in Glenn's Rocket Combustion Lab. Cooled CMC's offer the potential for substantial weight savings over more traditional metallic parts. Two CMC concepts were investigated. In the first of these concepts, an innovative processing approach utilized by Hyper-Therm, Inc., allowed woven CMC coolant containment tubes to be incorporated into the complex thruster design. In this unique design, the coolant passages had varying cross-sectional shapes but maintained a constant cross-sectional area along the length of the thruster. These thrusters were silicon carbide matrix composites reinforced with silicon carbide fibers.

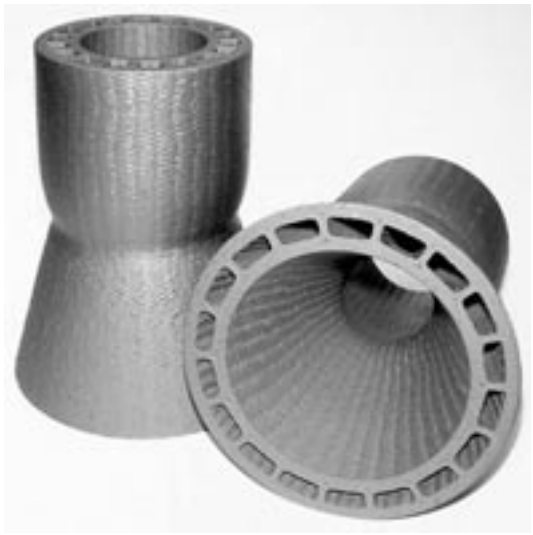

Silicon-carbide-fiber-reinforced silicon carbide matrix composites with woven cooling tubes.

The second concept, which was supplied by Ceramic Composites, Inc., utilized copper cooling coils surrounding a carbon-fiber-reinforced carbon matrix composite. In this design, a protective gradient coating was applied to the inner thruster wall. Ceramic Composites, Inc.'s, method of incorporating the coating into the fiber and matrix eliminated the spallation problem often observed with thermal barrier coatings during hot-fire testing. The focus of the testing effort was on screening the CMC material's capabilities as well as evaluating the performance of the thermal barrier or fiber-matrix interfacial coatings. Both concepts were hot-fire tested in gaseous O_2/H_2 environments. The test matrix included oxygen-to-fuel ratios ranging from 1.5 to 7 with chamber pressures to 400 psi. Steady-state internal wall temperatures in excess of 4300 °F were measured in situ for successful 30-sec test runs.

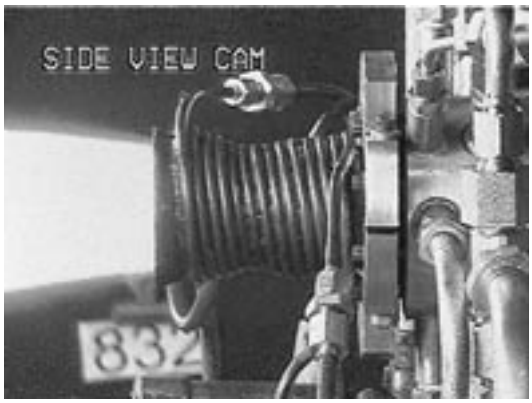

Actively cooled carbon-fiber-reinforced carbon matrix composites being hot-fire tested.

Glenn contact: Martha H. Jaskowiak, 216–433–5515,
Martha.H.Jaskowiak@grc.nasa.gov

Authors: Martha H. Jaskowiak, Sandra K. Elam, and Michael R. Effinger

Headquarters program office: OAT

Programs/Projects: STPO

Ceramic Composite Intermediate Temperature Stress-Rupture Properties Improved Significantly

Silicon carbide (SiC) composites are considered to be potential materials for future aircraft engine parts such as combustor liners. It is envisioned that on the hot side (inner surface) of the combustor liner, composites will have to withstand temperatures in excess of 1200 °C for thousands of hours in oxidizing environments. This is a severe condition; however, an equally severe, if not more detrimental, condition exists on the cold side (outer surface) of the combustor liner. Here, the temperatures are expected to be on the order of 800 to 1000 °C under high tensile stress because of thermal gradients and attachment of the combustor liner to the engine frame (the hot side will be under compressive stress, a less severe stress-state for ceramics). Since these composites are not oxides, they oxidize. The worst form of oxidation for strength reduction occurs at these intermediate temperatures, where the boron nitride (BN) interphase oxidizes first, which causes the formation of a glass layer that strongly bonds the fibers to the matrix. When the fibers strongly bond to the matrix or to one another, the composite loses toughness and strength and becomes brittle.

To increase the intermediate temperature stress-rupture properties, researchers must modify the BN interphase. With the support of the Ultra-Efficient Engine Technology (UEET) Program, significant improvements were made as state-of-the-art SiC/SiC composites were developed during the Enabling Propulsion Materials (EPM) program. Three approaches were found to improve the intermediate-temperature stress-rupture properties: fiber-spreading, high-temperature silicon- (Si) doped boron nitride (BN), and outside-debonding BN. Fibers were spread by mechanically spreading tows in the woven cloth or by heat-treating woven cloth to produce an in situ BN layer on the fibers, which naturally increases the distance between neighboring fibers. High-temperature Si-doped BN has been applied as the interphase layer to woven cloth, which is then stacked to fabricate SiC matrix composites. The Si-doped BN contains little oxygen (<1 at.%) and approximately 7 at.% Si. Outside debonding describes BN interphases that have been processed to cause interfacial debonding and sliding between the BN interphase and the SiC matrix. The interface where debonding and sliding occurs for conventional BN-interphase composites is between

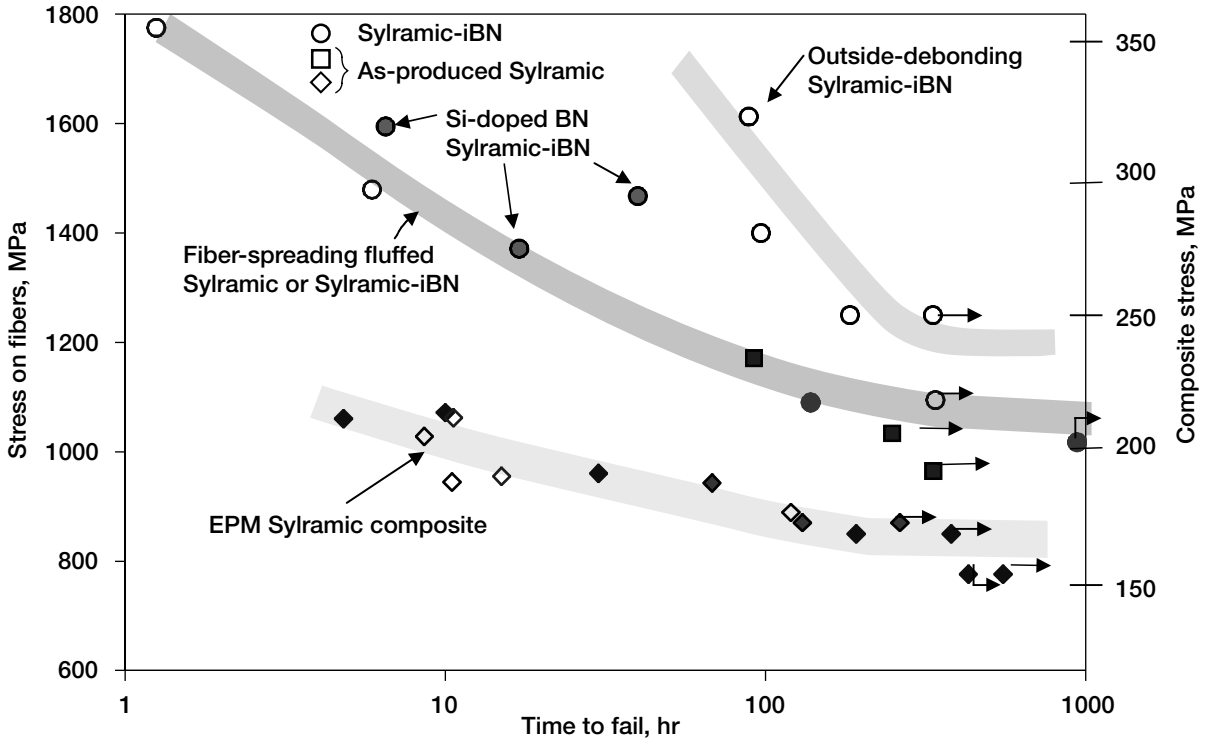

Improvements in stress-rupture at 815 °C in air.

the BN interphase and the SiC fiber. This enables the oxidizing environment to have direct access to the SiC fiber and causes more rapid strength reduction. Outside-debonding interphases dramatically slow down this process since the oxidizing environment is blocked to a great extent by the relatively thick BN interphase.

The figure compares the stress-rupture properties for current state-of-the-art material with SiC composites made with these three methods. It is evident that if these methods can be applied to new components, higher design stresses can be tolerated for the intermediate temperature regions of combustor liners. Work is continuing to combine some of these approaches and further minimize the strength reduction that occurs at intermediate temperatures.

OAI contact:
Gregory N. Morscher, 216–433–5512,
Gregory.N.Morscher@grc.nasa.gov

Glenn contact:
Janet B. Hurst, 216–433–3286,
Janet.B.Hurst@grc.nasa.gov

Authors: Gregory N. Morscher and Janet B. Hurst

Headquarters program office: OAT

Programs/Projects: UEET

Single-Crystal Elastic Constants of Yttria (Y_2O_3) Measured to High Temperatures

Yttria, or yttrium sesquioxide (Y_2O_3), has been considered for use in nuclear applications and has gained interest relatively recently for use in infrared optics. Single crystals of yttria have been grown successfully at the NASA Glenn Research Center using a laser-heated float zone technique in a fiber and rod. Such samples allow measurement of the single-crystal elastic properties, and these measurements provide useful property data for the design of components using single crystals. They also yield information as to what degree the elastic properties of yttria ceramics are a result of the intrinsic properties of the yttria crystal in comparison to characteristics that may depend on processing, such as microstructure and intergranular phases, which are common in sintered yttria. The single-crystal elastic moduli are valuable for designing such optical components. In particular, the temperature derivatives of elastic moduli allow the dimensional changes due to heating under physical constraints, as well as acoustic excitation, to be determined.

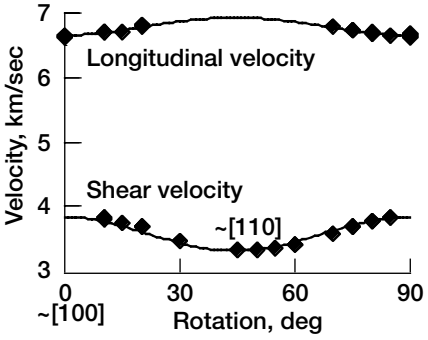

Room-temperature velocities in the {100} plane of yttria. (Copyright James Palko, University of Michigan, Ann Arbor; used with permission.)

The single-crystal elastic moduli of yttria were measured by Brillouin spectroscopy up to 1200 °C. The room-temperature values obtained were $C_{11} = 223.6 + 0.6$ GPa, $C_{44} = 74.6 + 0.5$ GPa, and $C_{12} = 112.4 + 1.0$ GPa. The resulting bulk and (Voigt-Reuss-Hill) shear moduli were $K = 149.5 + 1.0$ GPa and $G_{VRH} = 66.3 + 0.8$ GPa, respectively. Linear least-squares regressions to the variation of bulk and shear moduli with temperature resulted in derivatives of $dK/dT = -17 + 2$ MPa/°C and $dG_{VRH}/dT = -8 + 2$ MPa/°C. Elastic anisotropy was found to remain essentially constant over the temperature range studied.

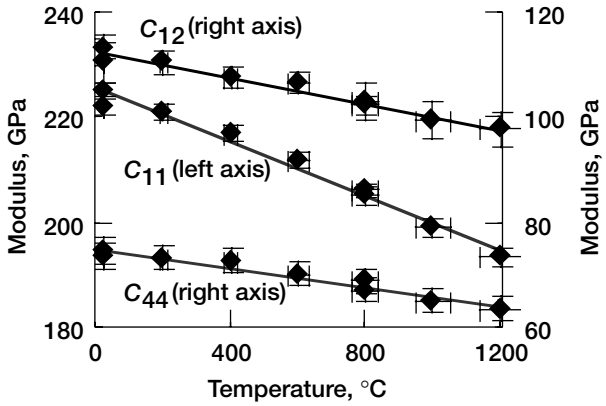

Single-crystal elastic moduli at high temperatures. (Copyright James Palko, University of Michigan, Ann Arbor; used with permission.)

MEASURED AND CALCULATED BULK PROPERTIES OF YTTRIA AT ROOM CONDITIONS

Bulk modulus, *K*, GPa	Shear modulus, *G*, GPa	Young's modulus, *E*, GPa	Poisson's ratio, ν
————	65.6 ± 0.8	172 ± 2	0.305 ± 0.003
149.5 ± 1.0	66.3 ± 0.8	173 ± 2	.307 ± 0.003
————	67.0 ± 0.8	175 ± 2	.309 ± 0.003
————	56.4	158.3	.3426
167.7	57.7	155.2	.3457
————	59.0	152.1	.3488
148.9 ± 3.0	69.2 ± 2.0	179.8 ± 4.8	.299 ± 0.004
145	67	173	.30
146.2	69.42	179.8	.2951

Bibliography
Palko, James W., et al.: Elastic Constants of Yttria (Y_2O_3) Monocrystals to High Temperatures. J. Appl. Physics, vol. 89, issue 12, 2001, pp. 7791–7796.

Case Western Reserve University contact: Dr. Ali Sayir, 216–433–6254, Ali.Sayir@grc.nasa.gov

Glenn contact:
Dr. Serene C. Farmer, 216–433–3289, Serene.C.Farmer@grc.nasa.gov

Authors:
James W. Palko, Waltraud M. Kriven, Sergey V. Sinogeikin, Jay D. Bass, and Dr. Ali Sayir

Headquarters program office: OAT

Programs/Projects: RAC

Environment-Conscious Ceramics (Ecoceramics) Technology Received 2001 R&D 100 Award

Since the dawn of human civilization, there has been a delicate balance between the use of resources as human frontiers expanded and the need to have a minimum influence on the ecosystem. The first 200 years of the industrial revolution essentially solved the problem of production. However, the massive production of goods also generated tremendous amounts of by-products and wastes. In the new millennium, to sustain a healthy life in harmony with nature, it will be extremely important for us to develop various materials, products, and processes that minimize any harmful influence on the environment.

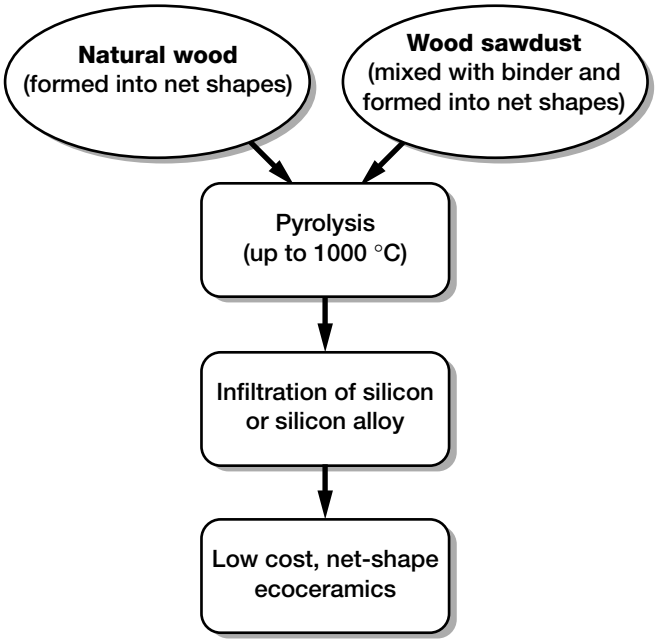

Ecoceramics technology.

Environment-conscious ceramics (ecoceramics) are a new class of materials that can be fabricated with renewable resources (wood) and wood waste material (wood sawdust). Wood is a "lignocellulosic" material formed by the photosynthetic reaction within the needles or leaves of trees. The photosynthesis process uses sunlight to take carbon dioxide from air and convert it into oxygen and organic materials. Wood has been known to be one of the best and most intricate engineering materials created by nature and known to mankind. In addition, natural woods of various types are available throughout the world. On the other hand, wood sawdusts are generated in abundant quantities by sawmills. Environment-conscious ceramic materials, fabricated via the pyrolysis and infiltration of natural wood-derived preforms, have tailorable properties with numerous potential applications. The experimental studies conducted to date on the development of materials based on biologically derived structures indicate that these materials

Complex-shaped ecoceramic components.

behave like ceramic materials manufactured by conventional approaches. These structures have been shown to be quite useful in producing porous or dense materials having various microstructures and compositions.

A schematic of ecoceramics technology is given in the figure on the preceding page. The wood pieces were dried in an oven and pyrolyzed in a furnace up to 1000 °C in a flowing-argon atmosphere to create carbonaceous preforms. The weight and dimensional changes were recorded after pyrolysis. The pyrolyzed preforms were infiltrated with silicon in a graphite element furnace under vacuum. The infiltration time and temperature depend on the melting point of the infiltrants and the dimensions and properties of the preforms. For silicon infiltration, porous preforms were infiltrated at 1450 °C for 30 min. A wide variety of wood specimens (softwood and hardwood) and wood sawdusts were used to fabricate the carbonaceous preforms. Ecoceramic technology has been used to fabricate parts with complex shapes from the machined wood or carbon specimens shown in the photograph. Detailed thermomechanical characterization of a wide variety of silicon-carbide-based ecoceramics is underway.

QSS contact:
Dr. Mrityunjay Singh, 216–433–8883, Mrityunjay.Singh@grc.nasa.gov

Glenn contact:
Dr. Stanley R. Levine, 216–433–3276, Stanley.R.Levine@grc.nasa.gov

Author: Dr. Mrityunjay Singh

Headquarters program office: OAT

Programs/Projects: CTO

Special recognition:
2001 R&D 100 Award

Polymer/Silicate Nanocomposites Developed for Improved Thermal Stability and Barrier Properties

The nanoscale reinforcement of polymers is becoming an attractive means of improving the properties and stability of polymers. Polymer-silicate nanocomposites are a relatively new class of materials with phase dimensions typically on the order of a few nanometers. Because of their nanometer-size features, nanocomposites possess unique properties typically not shared by more conventional composites. Polymer-layered silicate nanocomposites can attain a certain degree of stiffness, strength, and barrier properties with far less ceramic content than comparable glass- or mineral-reinforced polymers (ref. 1). Reinforcement of existing and new polyimides by this method offers an opportunity to greatly improve existing polymer properties without altering current synthetic or processing procedures.

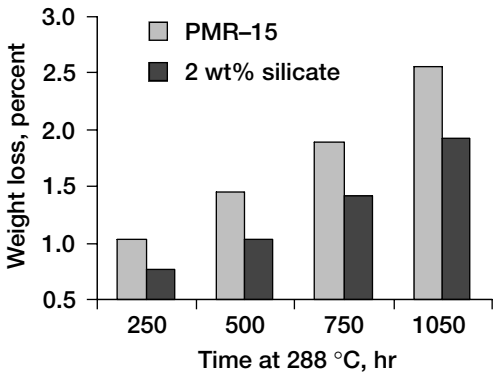

Comparison of the weight loss in carbon fabric composites with a neat PMR–15 matrix and a PMR–15/silicate matrix.

Highly crosslinked, thermally stable, thermosetting polymers have not been extensively researched as nanocomposite matrix materials. By dispersing a layered silicate into a PMR–15 matrix, there is the

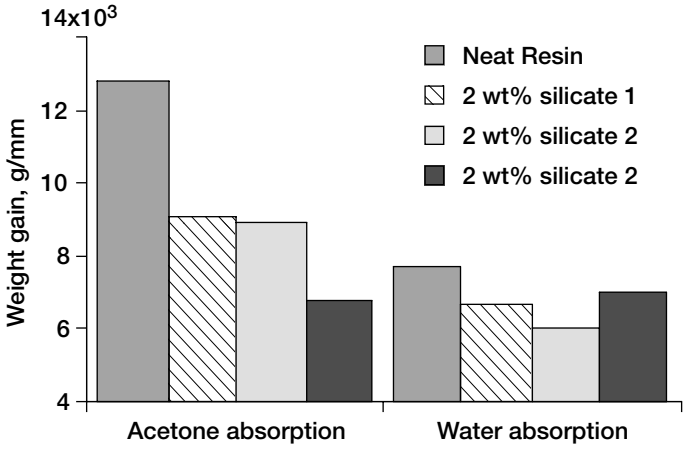

Acetone (28 hr) and water absorption (32 hr) into neat resin and polymer-silicate nanocomposites, where the structure of the ion exchange amine on the silicate varies in length and architecture.

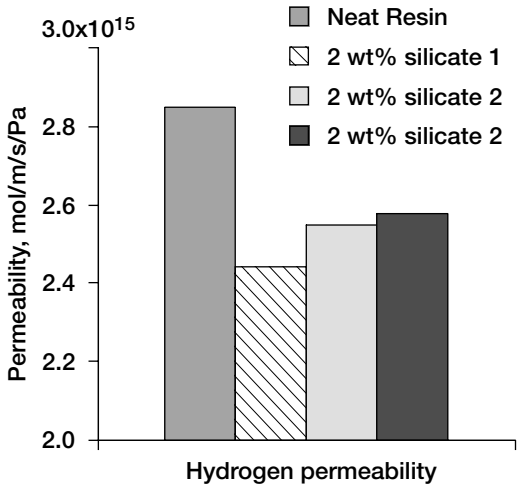

Hydrogen permeation (24 hr, 20 psi) through neat resin and polymer-silicate nanocomposites, where the structure of the ion exchange amine on the silicate varies in length and architecture.

potential to increase the use temperature and the high-temperature performance of the polymer. Nanocomposite synthesis typically requires modification of the silicate interlayer with an organic material to improve the compatibility between the clay and the polymer. An understanding of the effects of the silicate on the melt viscosity and the crosslinking of the PMR–15 oligomers is important to the selection of a silicate-organic modification system that will optimize the benefits of the nanoscale reinforcement.

Recent efforts at the NASA Glenn Research Center have led to an organically modified silicate, which on dispersion in a PMR–15 matrix, leads to a nanocomposite with up to a 12-percent increase in thermal oxidative stability. Utilization of this PMR–15 nanocomposite as a matrix to a polymer carbon fabric (T650–35) composite increases the composite's thermal stability by 25 percent in comparison to a neat PMR–15 matrix composite.

An organically modified silicate was also dispersed in a thermoplastic polyimide matrix. The silicate was modified with protonated amines of varying lengths and architecture, and several nanocomposites were prepared. Water and acetone absorption into the neat resin and the nanocomposites were investigated. In comparison to that of the neat polymer, the absorption of acetone into the nanocomposite samples decreased 30 to 47 percent after 28 hr. In water, absorption decreased 10 to 22 percent after 32 hr. Hydrogen permeability testing of these materials resulted in a 10- to 20-percent decrease in permeability. The effectiveness of the nanocomposite in decreasing absorption or permeation depended on the silicate modification. The mechanical properties of both the thermosetting and thermoplastic polyimide matrix nanocomposites are currently being evaluated.

Find out more about this research:
http://www.grc.nasa.gov/WWW/MDWeb/5150/Polymers.html

Bibliography

Burnside, S.D.; and Giannelis, E.P.: Synthesis and Properties of New Poly (Dimethylsiloxane) Nanocomposites. Chemistry of Materials, vol. 7, no. 9, 1995, pp. 1597–1600.

Glenn contact:
Sandi Campbell, 216–433–8489,
Sandi.G.Campbell@grc.nasa.gov

Author: Sandi G. Campbell

Headquarters program office: OAT

Programs/Projects:
Propulsion Systems R&T, ZCET

High-Glass-Transition-Temperature Polyimides Developed for Reusable Launch Vehicle Applications

Polyimide composites have been traditionally used for high-temperature applications in aircraft engines at temperatures up to 550 °F (288 °C) for thousands of hours. However, as NASA shifts its focus toward the development of advanced reusable launch vehicles, there is an urgent need for lightweight polymer composites that can sustain 600 to 800 °F (315 to 427 °C) for short excursions (hundreds of hours). To meet critical vehicle weight targets, it is essential that one use lightweight, high-temperature polymer matrix composites in propulsion components such as turbopump housings, ducts, engine supports, and struts. Composite materials in reusable launch vehicle components will heat quickly during launch and reentry. Conventional composites, consisting of layers of fabric or fiber-reinforced lamina, would either blister or encounter catastrophic delamination under high heating rates above 300 °C. This blistering and delamination are the result of a sudden volume expansion within the composite due to the release of absorbed moisture and gases generated by the degradation of the polymer matrix. Researchers at the NASA Glenn Research Center and the Boeing Company (Long Beach, CA) recently demonstrated a successful approach for preventing this delamination—the use of three-dimensional stitched composites fabricated by resin infusion.

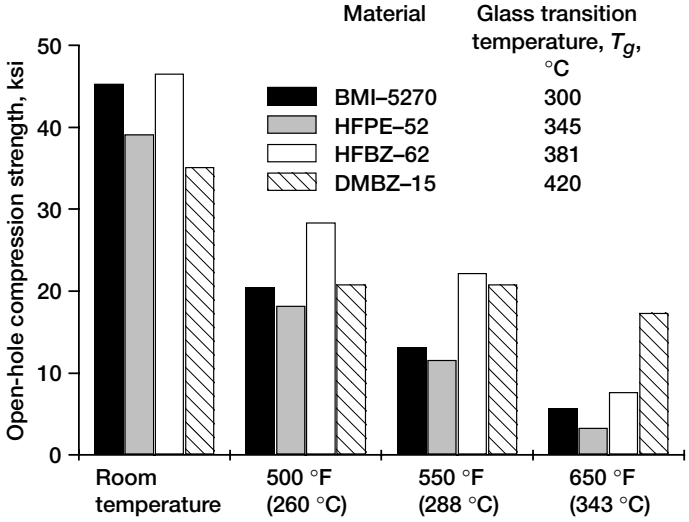

Open-hole compressive strength of stitched polyimide/AS4 composites.

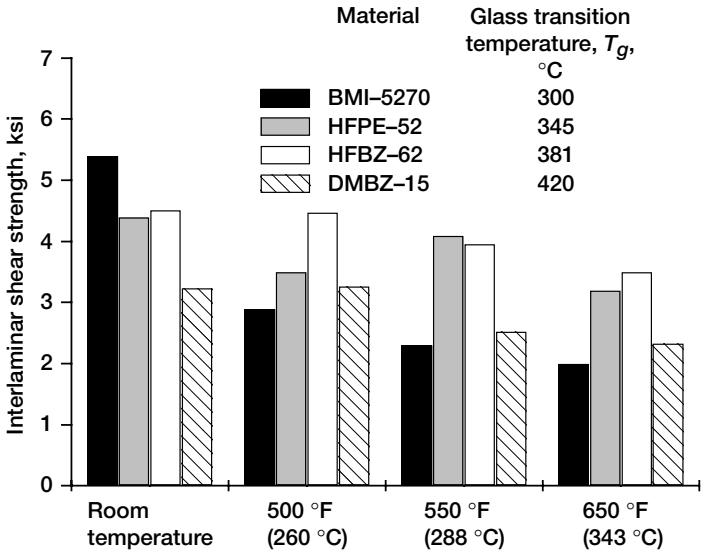

Interlaminar shear strength of stitched polyimide/AS4 composites.

Concentrated solutions of a series of Glenn-developed high-glass-transition-temperature T_g polyimides (T_g = 345 to 420 °C) were successfully infused into stitched carbon fabric preforms to fabricate composites. DMBZ–15 stitched composites display the highest open-hole compression strength at 650 °F (343 °C) of all the resins tested (see the top bar chart), whereas HFBZ composites exhibit the highest interlaminar shear strength at 650 °F (343 °C) (see the bottom bar chart). HFPE composites have shown excellent thermo-oxidative stability, as they retain 50 percent of their mechanical properties after isothermal aging at 550 °F (288 °C) for 2000 hr and maintain 60 percent of their room-temperature mechanical properties at 650 °F (343 °C). The mechanical properties of these high-T_g polyimide composites far exceed the performance of a leading commercial high-temperature bismaleimide, BMI 5270. These stitched composites hold the promise of performing at high temperatures without delamination under the high moisture and heating rate conditions encountered in many reusable launch vehicle applications.

Find out more about this research (accessible at Glenn only):
http://www.grc.nasa.gov/WWW/MDWeb/Local/People/MSCHUA.html

Glenn contact:
Dr. Kathy Chuang, 216–433–3227,
Chun-Hua.Chuang@grc.nasa.gov

Authors:
Dr. Kathy Chuang and Cory P. Ardent

Headquarter program office: OAT

Programs/Projects: STR

NASA Glenn/AADC Collaboration Optimized Erosion Coatings for Inlet Guide Vanes

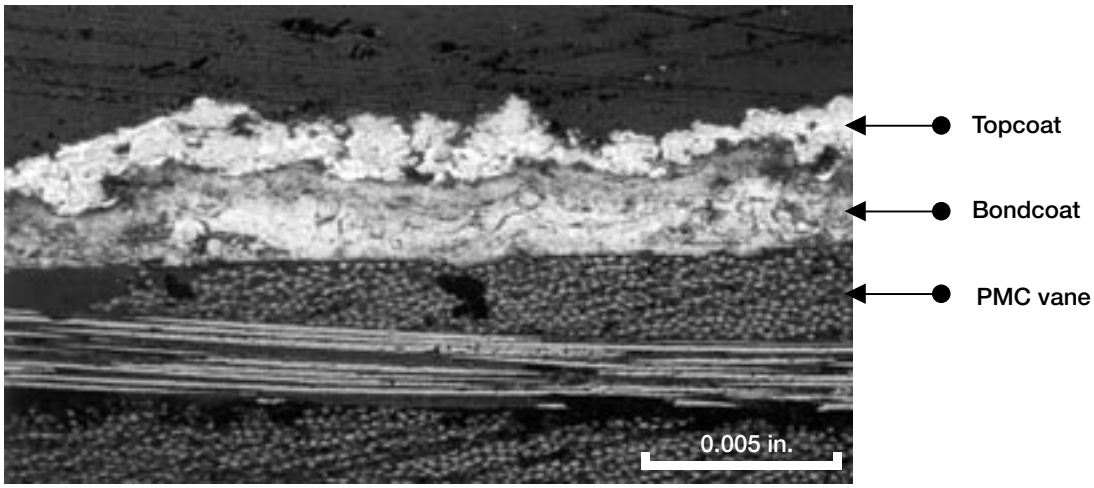

Glenn's coating on a PMC inlet guide vane.

There is a need for lightweight, durable materials and structures to reduce the weight of propulsion systems. Polymer matrix composites (PMC's) are promising materials for aerospace applications because of their high strength-to-weight ratio relative to metals. Unfortunately, they are limited to applications where they are not exposed to high-temperature oxidizing atmospheres and/or particulates from ingested air. This is because oxidation and erosion occur on the surface, leading to weight loss, nodulation, and/or cracking on the surface, and a consequent decline of mechanical properties over time.

Although prior research has shown that oxidation can be slowed when metallic or ceramic coatings are applied onto PMC's, there remains a need for erosion-resistant coatings that protect PMC's from high-velocity particulates in the engine flow path. These erosion-resistant coatings could extend the life of polymer composites. Polymer composites are heavily damaged without an erosion-resistant coating because they are not as hard as metallic engine structures.

The effectiveness and life of the coatings depends on their inherent properties as well as on the interaction between the coating and the PMC. Since polymers, in general, have high thermal expansion coefficients in comparison to metals and ceramics, failure of the coatings often occurs at this interface. The objective of this research is to develop strategies to improve this interface and tailor overlays for erosion resistance (see the photomicrograph). The bondcoat, which was developed at the NASA Glenn Research Center, is composed of zinc blended with polyimides to improve the compatibility between the PMC and the overlay material. Initial coating trials at AADC produced vanes that had poor bonding between the overlay and bondcoats. Subsequently, Glenn successfully demonstrated that high-quality plasma-sprayed erosion coating systems could be applied to these

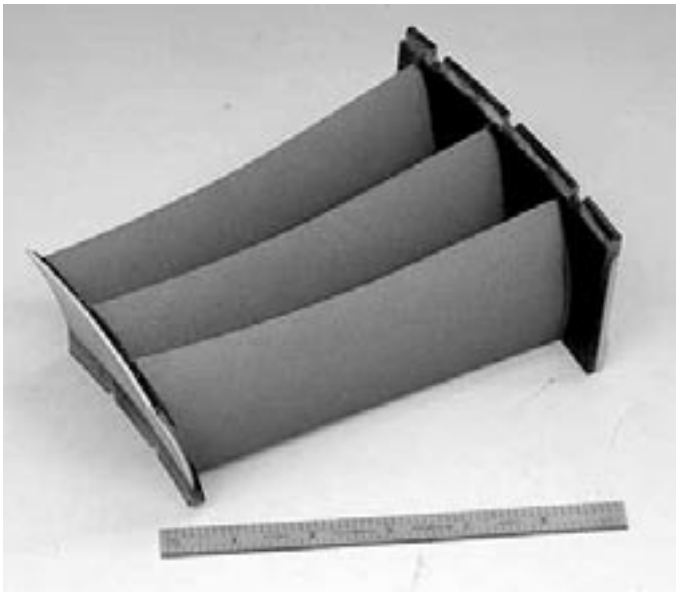

NASA Glenn erosion coating on a PMC inlet guide vane section.

guide vanes. Inlet guide vanes from AE 3007 engines fiber composites were coated using a coating system composed of a bondcoat and a hard topcoat (see the preceding photomicrograph). Optimization of the plasma spray process has led to plans for future erosion testing in gas turbine engine environments.

Glenn contact: Dr. James K. Sutter, 216–433–3226, James.K.Sutter@grc.nasa.gov

Authors: Dr. James K. Sutter, George Leissler, and Richard Horan

Headquarters program office: OAT

Programs/Projects:
Propulsion Systems R&T, HOTPC

Novel Molecular Architectures Developed for Improved Solid Polymer Electrolytes for Lithium Polymer Batteries

Lithium-based polymer batteries for aerospace applications need the ability to operate in temperatures ranging from –70 to 70 °C. Current state-of-the-art solid polymer electrolytes (based on amorphous polyethylene oxide, PEO) have acceptable ionic conductivities (10^{-4} to 10^{-3} S/cm) only above 60 °C. Higher conductivity can be achieved in the current systems by adding solvent or plasticizers to the solid polymer to improve ion transport. However, this can compromise the dimensional and thermal stability of the electrolyte, as well as compatibility with electrode materials. One of NASA Glenn Research Center's objectives in the PERS program is to develop new electrolytes having unique molecular architectures and/or novel ion transport mechanisms, leading to good ionic conductivity at room temperature and below without solvents or plasticizers.

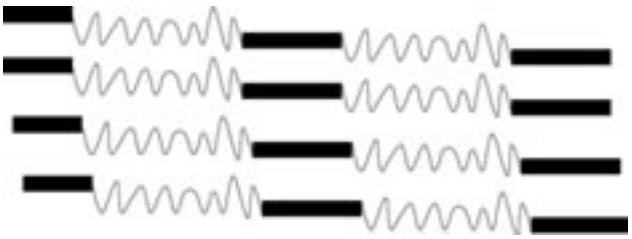

Structure of rod-coil polymers showing phase separation between incompatible rigid rods and flexible ion-conducting coils.

It is widely held that ionic conductivity is highest for amorphous (noncrystalline) polymers with low glass-transition temperatures. This is thought to be because strong coulombic forces and low free volume trap the ions in the crystalline regions. However, promising new approaches to less temperature dependent ionic conductivity in solid polymers include ways of introducing free volume and short-range order, if not crystallinity, into the system. Some of these approaches include Langmuir-Blodgett films, liquid crystals, and self-assembling monolayers.

We are combining several of these approaches to investigate new polymers with novel architectures for stable, processable polymer electrolytes with enhanced ionic conductivity over a wide range of temperatures. One approach under investigation in-house is a series of rod-coil block copolymers in which rigid polyimide rods alternate with very flexible, short PEO strands. Because of the incompatibility between the rods and coils, the blocks would tend to phase separate as much as possible. This leads to the formation of nanoscale channels of ionically conducting PEO alternating with the rigid polyimide rods. The rod regions form the mechanical support for conducting PEO coils, resulting in films with both good conductivity and mechanical integrity.

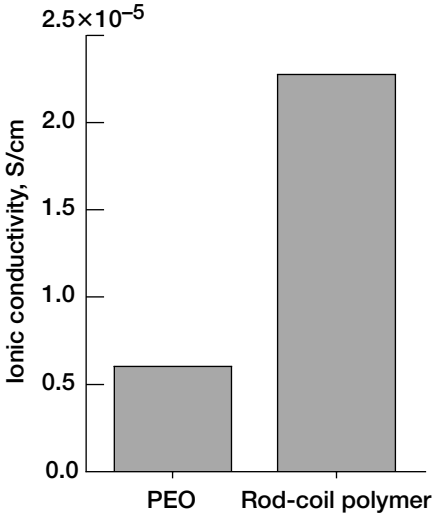

Comparison of room-temperature ionic conductivity of state-of-the-art PEO with that of a polyimide rod-coil polymer.

Rod-coil polyimides doped with lithium salts form rubbery films having glass-transition temperatures around −50 °C. Polymers with room-temperature conductivities as high as 2.3×10^{-5} S/cm have been synthesized. This is almost an order of magnitude better than measured state-of-the-art PEO. Rod-coil polymers are easily cast from 40-wt% solutions and cured into flexible, solvent-free films by heating to 200 °C. The films could be cast directly onto electrode substrates or handled as free-standing films, offering flexibility in battery fabrication.

Find out more about this research:
http://www.grc.nasa.gov/WWW/Electrochemistry/pers.html

Glenn contact:
Dr. Mary Ann B. Meador, 216–433–3221, Maryann.Meador@grc.nasa.gov

Authors:
Dr. Mary Ann B. Meador, Dr. James D. Kinder, and William R. Bennett

Headquarters program office: OAT

Programs/Projects: PERS

Ti-48Al-2Cr-2Nb Evaluated Under Fretting Conditions

Material parameters govern many of the design decisions in any engineering task. When two materials are in contact and microscopically small, relative motions (either vibratory or creeping) occur, and fretting fatigue can result. Fretting fatigue is a material response influenced by the materials in contact as well as by such variables as loading and vibratory conditions. Fretting produces fresh, clean interacting surfaces and induces adhesion, galling, and wear in the contact zone. Time, money, and materials are unnecessarily wasted when galling and wear result in excessive fretting fatigue that leads to poorly performing, unreliable mechanical systems.

Fretting fatigue is a complex problem of significant interest to aircraft engine manufacturers. It can occur in a variety of engine components. Numerous approaches, depending on the component and the operating conditions, have been taken to address the fretting problems. The components of interest in this investigation were the low-pressure turbine blades and disks. The blades in this case were titanium aluminide, Ti-48Al-2Cr-2Nb, and the disk was a nickel-base superalloy, Inconel 718 (IN 718). A concern for these airfoils is the fretting in fitted interfaces at the dovetail where the blade and disk are connected. Careful design can reduce fretting in most cases, but not completely eliminate it, because the airfoils frequently have a skewed (angled) blade-disk dovetail attachment, which leads to a complex stress state. Furthermore, the local stress state becomes more complex when the influence of the metal-metal contact and the edge of contact are considered.

At the NASA Glenn Research Center, the fretting behavior of Ti-48Al-2Cr-2Nb (γ-TiAl) in contact with nickel-base IN 718 was examined in air at temperatures from 296 to 823 K (23 to 550 °C). All fretting wear experiments were conducted at loads from 1 to 40 N, frequencies of 50, 80, 120, and 160 Hz, and slip amplitudes between 50 and 200 μm for 1 million to 20 million cycles. The interfacial adhesive bonds between Ti-48Al-2Cr-2Nb and IN 718 were generally stronger than the cohesive bonds within Ti-48Al-2Cr-2Nb. The failed Ti-48Al-2Cr-2Nb was transferred to the IN 718 at all fretting conditions, such that from 10 to 50 percent of the IN 718 contacting surface area became coated with Ti-48Al-2Cr-2Nb. The maximum thickness of the transferred Ti-48Al-2Cr-2Nb was approximately 20 μm. In reference experiments, Ti-6Al-4V transferred to IN 718 under identical fretting conditions. Compared with Ti-48Al-2Cr-2Nb transfer, the degree of Ti-6Al-4V transfer was greater, such that from 30 to 100 percent of the IN 718

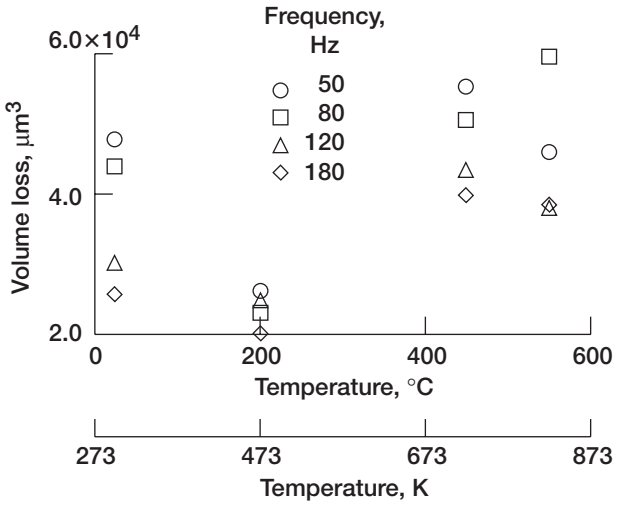

Wear volume loss of Ti-48Al-2Cr-2Nb flat in contact with an IN 718 pin in air as function of fretting temperature. Fretting conditions: load, 30 N; slip amplitude, 50 μm; total number of cycles, 1 million; environment, air.

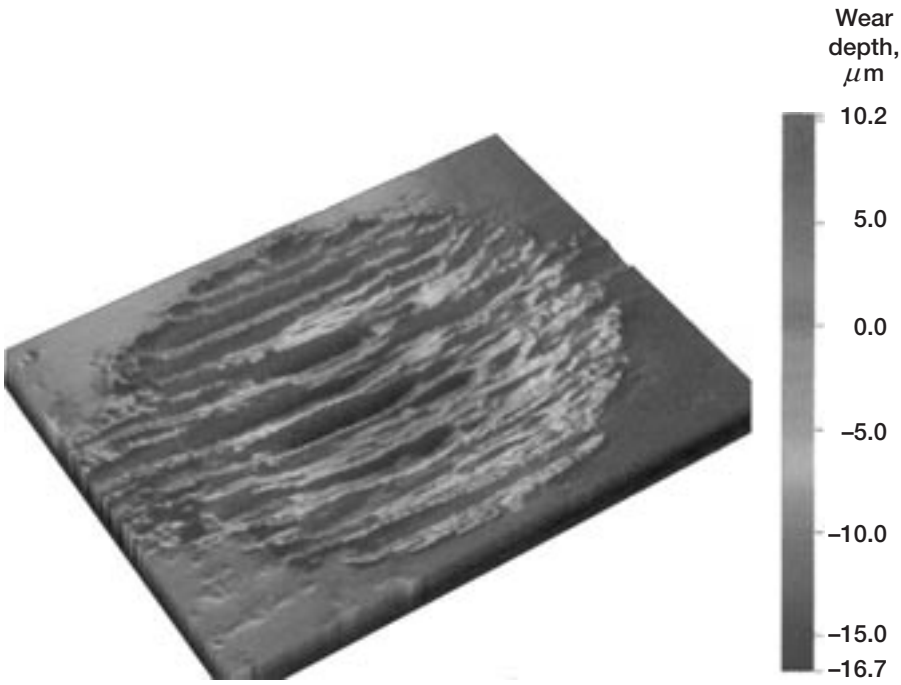

Wear scar on Ti-48Al-2Cr-2Nb flat in contact with an IN 718 pin, showing scratches. Fretting conditions: load, 30 N; fretting frequency, 50 Hz; slip amplitude, 200 μm; total number of cycles, 1 million; environment, air; and temperature, 823 K.

contacting surface area became coated with Ti-6Al-4V. The thickness of the transferred Ti-6Al-4V ranged up to 50 μm. The wear scars produced on Ti-48Al-2Cr-2Nb contained metallic and oxide wear debris, scratches, plastically deformed asperities, cracks, and fracture pits. Although oxide layers readily formed on the Ti-48Al-2Cr-2Nb surface at 823 K, cracking readily occurred in the oxide layers both within and around the contact areas. The wear volume loss of Ti-48Al-2Cr-2Nb generally decreased with increasing fretting frequency. The increasing rate of oxidation at elevated temperatures led to a drop in wear at 473 K (see the graph on the previous page). Mild oxidative wear and low wear volume were observed at 473 K. However, fretting wear increased as the temperature was increased from 473 to 823 K. At 723 and 823 K, oxide film disruption generated cracks, loose wear debris, and pits on the Ti-48Al-2Cr-2Nb wear surface. Both increasing slip amplitude and increasing load tended to produce more metallic wear debris, causing severe abrasive wear (e.g., see the photomicrograph) in the contacting metals.

Glenn contact:
Dr. Kazuhisa Miyoshi, 216–433–6078, Kazuhisa.Miyoshi@grc.nasa.gov

Authors: Dr. Kazuhisa Miyoshi, Dr. Bradley A. Lerch, Susan L. Draper, and Dr. Sai V. Raj

Headquarters program office: OAT

Programs/Projects: Ultra Safe

Oxidation Behavior of GRCop-84 Copper Alloy Assessed

NASA's goal of safe, affordable space transportation calls for increased reliability and lifetimes of launch vehicles, and significant reductions of launch costs. The areas targeted for enhanced performance in the next generation of reusable launch vehicles include combustion chambers and nozzle ramps; therefore, the search is on for suitable liner materials for these components. GRCop-84 (Cu-8Cr-4Nb), an advanced copper alloy developed at the NASA Glenn Research Center in conjunction with Case Western Reserve University, is a candidate. The current liner of the Space Shuttle Main Engine is another copper alloy, NARloy-Z (Cu-3Ag-0.1Zr). It provides a benchmark against which to compare the properties of candidate successors.

The thermomechanical properties of GRCop-84 have been shown to be superior, and its physical properties comparable, to those of NARloy-Z (ref. 1). However, environmental durability issues control longevity in this application: because copper oxide scales are not highly protective, most copper alloys are quickly consumed in oxygen environments at elevated temperatures. In consequence, NARloy-Z and most other copper alloys are prone to blanching, a degradation process that occurs through cycles of oxidation-reduction as the oxide is repeatedly formed and removed because of microscale fluctuations in the oxygen-hydrogen fuel systems of rocket engines. The Space Shuttle Main Engine lining is typically degraded by blanching-induced hot spots that lead to surface roughening, pore formation, and coolant leakage. Therefore, resistance to oxidation and blanching are key requirements for second-generation reusable launch vehicle liners. The rocket engine ambient includes H_2 (fuel) and H_2O (combustion product) and is,

hence, under reduced-oxygen partial pressures. Accordingly, our studies were expanded to include oxygen partial pressures as low as 322 parts per million (ppm) at the temperatures likely to be experienced in service.

The figure compares 10-hr weight gains of GRCop-84, NARloy-Z, and pure copper in 0.032, 2.2, and 100 percent oxygen from 550 to 750 °C. In 2.2 vol% and higher oxygen content, GRCop-84 oxidation was slower than that of NARloy-Z or Cu, but that advantage was lost or diminished in 322-ppm O_2. Over longer (50-hr) exposures in 1.0 atm O_2, however, the advantage of GRCop-84 increased significantly, its oxidation rate becoming approximately 10 times slower than those of Cu and NARloy-Z from 500 to 700 °C. Weight gains were moderate and the kinetics parabolic for all three materials in 2.2 vol% and higher oxygen content; however, in 322-ppm O_2, the scales were nonprotective below about 650 °C, as reflected in linear kinetics and large weight gains (see the figure). The superior oxidation resistance of GRCop-84 is likely related to the kinetics of extra oxygen consumption to form the additional oxides of Cr and Nb detected beneath the GRCop-84 oxide layer (ref. 2).

While we continue to evaluate the blanching resistance of GRCop-84 in other tests, these oxidation results indicate that GRCop-84 is suitable as a reusable launch vehicle liner, and in applications where it is desired to use a copper alloy but without the risk of oxidative failure.

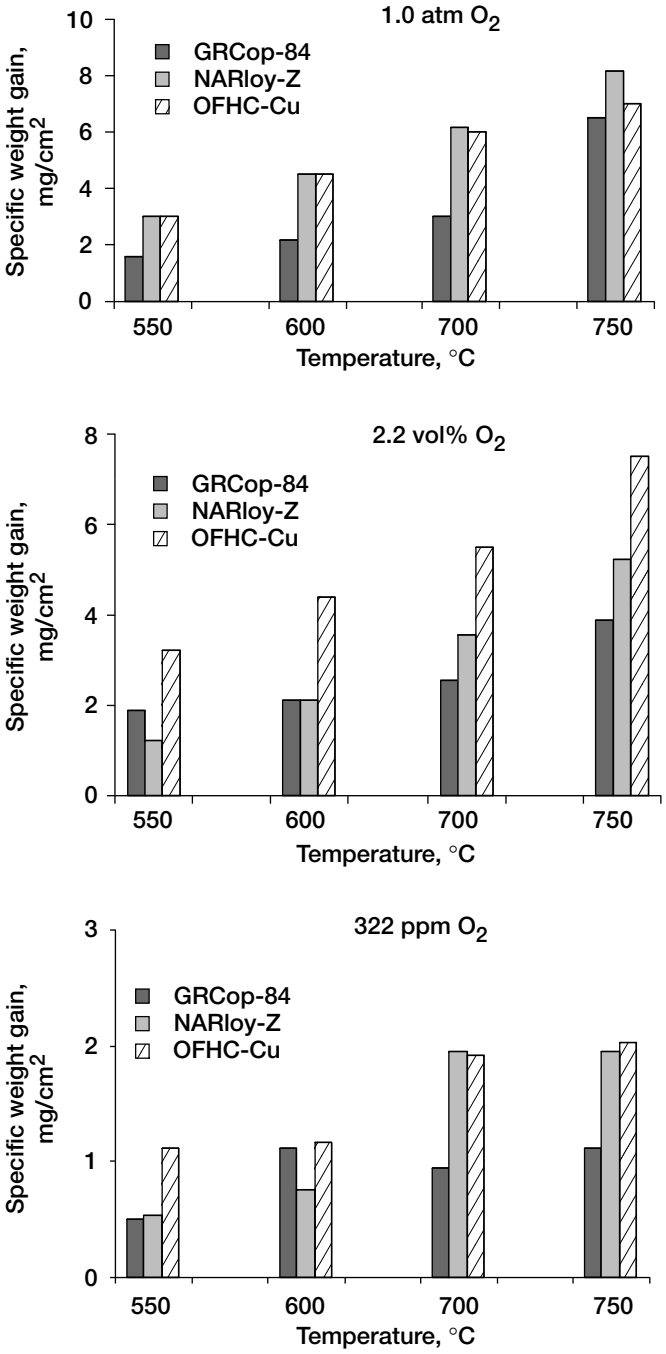

Specific weight gains of GRCop-84, NARloy-Z, and pure copper in 10-hr thermogravimetric analysis oxidation under various oxygen partial pressures.

References

1. Ellis, David L.: GRCop-84 Developed for Rocket Engines. 2000 Research & Technology, NASA/TM—2001-210605, pp. 24–25. http://www.grc.nasa.gov/WWW/RT2000/5000/5100E-ellis.html/
2. Thomas-Ogbuji, Linus U.; and Humphrey, Donald L.: Oxidation Behavior of GRCop-84 (Cu-8Cr-4Nb) at Intermediate and High Temperatures. NASA/CR—2000-210369, 2000. http://gltrs.grc.nasa.gov/GLTRS/

QSS contacts: Dr. Linus U. Thomas-Ogbuji, 216–433–6463, Linus.U.Thomas-Ogbuji@grc.nasa.gov; and Donald L. Humphrey, 216–433–5521, Donald.L.Humphrey@grc.nasa.gov

Case Western Reserve University contact: Dr. David L. Ellis, 216–433–8736, David.L.Ellis@grc.nasa.gov

Glenn contact: Leslie A. Greenbauer-Seng, 216–433–6781, Leslie.A.Greenbauer-Seng@grc.nasa.gov

Author: Dr. Linus U. Thomas-Ogbuji

Headquarters program office: OAT

Programs/Projects: STR

Knowledge of Pest Resistance in SiC/BN/SiC Composites Improved

Ceramic-matrix composites (CMC's) consisting of a silicon carbide matrix reinforced with boron-nitride- (BN-) coated silicon carbide (SiC) fibers are strong contenders for commercial and aerospace applications (in particular, the hot sections of high-performance turbine engines in advanced aircraft and generators). They have very good mechanical properties below ~600 °C and above ~1000 °C. Between those temperatures, however, the BN coating oxidizes easily, and the oxidation of the SiC matrix is too sluggish to seal off the composite with a protective layer of silica. In that temperature interval, the preferential oxidation of the BN weakens and embrittles the composite. That phenomenon, referred to as "pest" degradation, is the focus of this work, which aims to identify the causes of and remedies for pesting.

Previous work established that pesting in Hi-Nicalon (Nippon Carbon Co., Ltd., Japan)/SiC composites was caused by a layer of free carbon that undermined the oxidation resistance of the BN. New work suggests that composites containing a source of carbon are prone to severe pesting and that those that are free of elemental carbon are resistant to pesting. Pest resistance was assessed by exposing machined samples for 100 to 150 hr in an atmospheric burner rig at 600 to 1100 °C, followed by a tensile fracture test to measure residual mechanical properties and by characterization of the interphase microstructure. Whether the elemental carbon came from intrinsic or extrinsic sources, its presence induced the tensile strength to drop by over 50 percent in the burner rig, with an even more severe loss of fracture strain. The schematic figure indicates a likely mechanism by which burnoff of the carbon layer exposes the BN to accelerated flank attack by ambient oxidants. The BN is replaced with borosilicates that attack the fiber, and ultimately with silica that embrittles the composites by rigidly bonding components.

Thus, the study has shown that pesting can be prevented in SiC/BN/SiC, or at least reduced, by simply excluding free carbon. These studies continue, and plans for future work include investigating the role that carbon may play elsewhere in the interphase region.

QSS contact:
Dr. Linus U. Thomas-Ogbuji,
216–433–6463,
Linus.U.Thomas-Ogbuji@grc.nasa.gov

Glenn contact:
Dr. James A. Dicarlo,
216–433–5514,
James.A.DiCarlo@grc.nasa.gov

Author:
Dr. Linus U. Thomas-Ogbuji

Headquarters program office: OAT

Programs/Projects: UEET

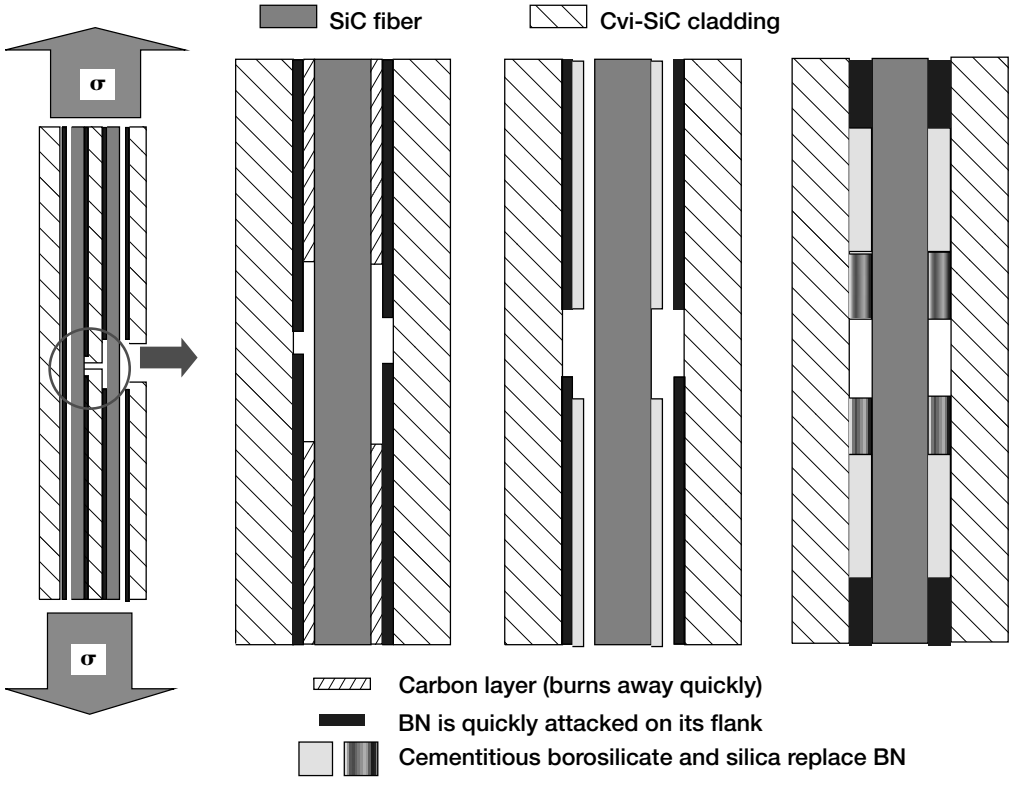

Effects of carbon in SiC/BN/SiC pesting.

Effects of Microalloying on the Microstructures and Mechanical Properties of Directionally Solidified Ni-33(at.%)Al-31Cr-3Mo Eutectic Alloys Investigated

Despite nickel aluminide (NiAl) alloys' attractive combination of oxidation and thermophysical properties, their development as replacements for superalloy airfoils in gas turbine engines has been largely limited by difficulties in developing alloys with an optimum combination of elevated-temperature creep resistance and room-temperature fracture toughness. Although single-crystal and polycrystalline NiAl alloys with superior specific creep strengths, comparable to or better than advanced superalloys, were developed by a combination of alloying and innovative processing techniques in the mid-1980's to mid-1990's, these materials had poor room-temperature fracture toughness, restricting their induction into service.

Alternatively, research has focused on developing directionally solidified NiAl-based in situ eutectic composites composed of NiAl and (Cr,Mo) phases in order to obtain a desirable combination of properties (refs. 1 to 4). Recently, it was demonstrated that the room-temperature fracture toughness K_{IC} of the directionally

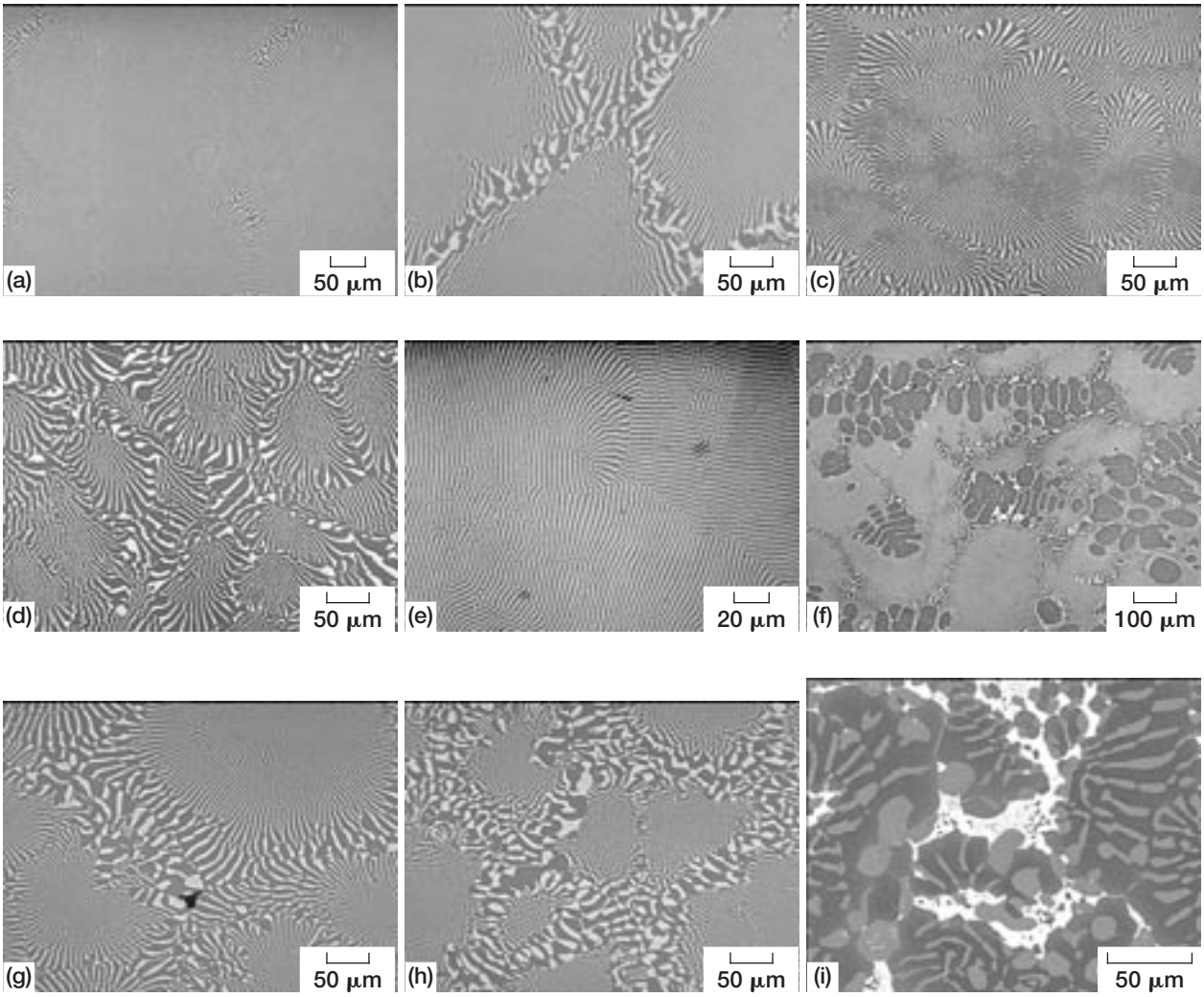

Optical (a-h) and scanning electron transverse microstructures (i) of directionally solidified Ni-33Al-(31-x)Cr-3Mo-xX alloys. (a) 0.25(at.%)Cu. (b) 0.25 Nb. (c) 0.25 Re. (d) 1.0 Re. (e) 0.5 Mn. (f) 1.0 Si. (g) 1.0 Ti. (h) 1.0 Ta. (i) 1.0 Hf. In a to h, the light phase is Cr and Mo, and the dark phase is NiAl. In i, the white phase is Hf-rich.

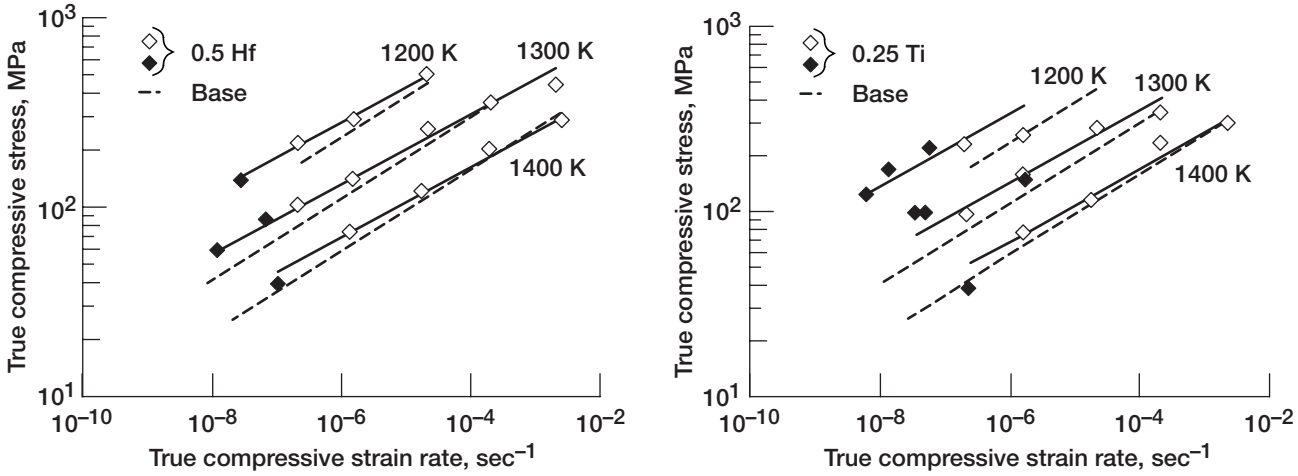

Comparison of the true compressive stress–true strain rate behavior of directionally solidified Ni-33Al-31Cr-3Mo with those for eutectic alloys grown at 12.7 mm/h between 1200 and 1400 K. The open symbols represent data from constant velocity testing, whereas the solid symbols indicate constant load creep results. Left: Ni-33Al-30.5Cr-3Mo-0.5Hf. Right: Ni-33Al-30.75Cr-3Mo-0.25Ti.

solidified Ni-33(at.%)Al-31Cr-3Mo two-phase eutectic alloy is about 17 MPa $\sqrt{m}$ (ref. 5). This is a considerable improvement over that of NiAl, for which K_{IC} ~ 6 MPa $\sqrt{m}$. However, the elevated-temperature strength of this directionally solidified eutectic alloy is still less than that of advanced nickel-based superalloys.

A systematic investigation was undertaken at the NASA Glenn Research Center to examine the effects of small additions of 11 alloying elements (Co, Cu, Fe, Hf, Mn, Nb, Re, Si, Ta, Ti, and Zr) in amounts varying from 0.25 to 1.0 at.% on the elevated-temperature strength and room-temperature fracture toughness of directionally solidified Ni-33Al-31 Cr-3Mo eutectic alloy. The alloys were grown at 12.7 mm/hr, where the unalloyed eutectic base alloy exhibited a planar eutectic microstructure (ref. 4). The different microstructures that formed because of these fifth-element additions are included in the table. The additions of these elements even in small amounts resulted in the formation of cellular microstructures, and in some cases, dendrites and third phases were observed (see the preceding photomicrographs). Most of these elemental additions did not improve either the elevated-temperature strength or the room-temperature fracture toughness over that of the base alloy. However, small improvements in the compression strength were observed between 1200 and 1400 K when 0.5 at.% Hf and 0.25 at.% Ti were added to the base alloy (see the graphs). The results of this study suggest that the microalloying of Ni-33Al-31Cr-3Mo will not significantly improve either its elevated-temperature strength or its room-temperature fracture toughness. Thus, any improvements in these properties must be acquired by changing the processing conditions.

References

1. Walter, J.L.; and Cline, H.E.: The Effect of Solidification Rate on Structure and High-Temperature Strength of the Eutectic NiAl-Cr. Metall. Trans., vol. 1, no. 5, 1970, pp. 1221–1229.
2. Yang, J.-M.: The Mechanical Behavior of In-Situ NiAl-Refractory Metal Composites. JOM, vol. 49, no. 8, 1997, pp. 40–43.
3. Raj, S.V.; Locci I.E.; and Whittenberger, J.D.: Creep Behavior of Advanced Materials for the 21st Century. Proceedings of Creep Behavior Advanced Materials for the 21st Century Symposium, R.S. Mishra, A.K. Mukherjee, and K. Linga Murty, eds., TMS, Warrendale, PA, 1999, pp. 295–310.
4. Whittenberger, J.D., et al.: Effect of Growth Rate on Elevated Temperature Plastic Flow and Room Temperature Fracture Toughness of Directionally Solidified NiAl-31Cr-3Mo. Intermetallics, vol. 7, no. 10, 1999, pp. 1159–1168.
5. Raj, S.V., et al.: Effect of Directionally-Solidified Microstructures on the Room Temperature Fracture Toughness Properties of Ni-33(at.%) Al-33Cr-1Mo and Ni-33(at.%) Al-31Cr-3Mo Eutectic Alloys Grown at Different Solidification Rates. Metall. Mater. Trans., vol. 33A, in press, 2002.

DESCRIPTION OF THE TRANSVERSE MICROSTRUCTURE IN ALIGNED REGIONS OF THE DS Ni-33Al-(31-x)Cr-3Mo-xX ALLOYS

Intended fifth element at.%	Lamellar eutectic grains	Cells	Cell diameter, mm	Cell pattern	NiAl dendrites	Intercellular regions	Globular NiAl in interdendritic regions	Distribution of fifth element		
								NiAl	(Cr, Mo)	Third phase
0.25Co	Yes				Yes			Yes		
0.25Cu		Yes	350	Radial	No	Triple points				
0.5 Cu		Yes	400	Radial	No	Yes				
1.0 Cu		Yes	250	Radial	No	Yes	Yes	Yes		
0.25Fe	Yes				No					
0.5Fe	Yes				Yes					
1.0Fe	Yes				Yes			Yes	Yes	
0.25Hf		Yes	200	Radial	Yes	Yes	Yes			
0.5Hf		Yes	250	Radial	No	Yes	Yes			
1.0Hf		Yes	200	Radial	No	Yes	Yes	Yes		Yes
0.25Mn	Yes				No					
0.5Mn	Yes				No					
1.0Mn		Yes	400	Radial	No	Yes		Not distinct		
0.25Nb		Yes	200	Straight	Yes	Yes	Some			
0.5Nb		Yes	100	Straight	Yes	Yes	Yes			
1.0Nb		A few	100	Not distinct	Yes	Yes	Yes		Yes	Yes
0.25Re		Yes	200	Nautilus	No	Not distinct				
0.5Re		Yes	150	Shell	No	Yes	Yes			
1.0Re		Yes	100	Shell	No	Yes	Yes		Yes	
0.25Si	Yes			Straight	Yes					
0.5Si		Yes		Straight	Yes	Yes				
1.0Si		Yes		Straight	Yes	Yes			Yes	
0.25Ta		Yes	300	Straight	Yes	Yes	Yes			
0.5Ta		Yes	200	Straight	Yes	Yes	Yes			
1.0Ta		Yes	150	Straight	Yes	Yes	Yes		Yes	Yes
0.25Ti		Yes	300	Radial	No	Yes				
0.5Ti		Yes	300	Radial	No	Yes				
1.0Ti		Yes	300	Radial	No	Yes	Yes	Yes		
0.25Zr		Yes	100	Shell	No	Yes	Yes			
0.5Zr		Yes	100	Shell	No	Yes	Yes		Yes	Yes

Glenn contact: Dr. Sai V. Raj, 216–433–8195, Sai.V.Raj@grc.nasa.gov

Authors: Dr. J. Daniel Whittenberger, Dr. Sai V. Raj, Dr. Ivan E. Locci, and Dr. Jonathan A. Salem

Headquarters program office: OAT

Programs/Projects: HITEMP, HOTPC

Cyclic Oxidation Modeling Program Rewritten for MS Windows

Turbine superalloy components are subject to high-temperature oxidation during operation. Protection is often conferred by coatings designed to form slow-growing, adherent oxide scales. Degradation by oxidation is exacerbated by the thermal cycling encountered during normal aircraft operations. Cooling has been identified as the major contributor to stresses in the oxidation scales, and it may often cause some oxide scale spallation with a proportional loss of protective behavior. Overall oxidation resistance is, thus, studied by the weight change behavior of alloy coupons during high-temperature cyclic oxidation in furnace or burner rig tests. The various characteristics of this behavior are crucial in understanding the performance of alloys at high temperatures. This new modeling effort helps in the understanding of the major factors involved in the cyclic oxidation process.

Weight change behavior in cyclic oxidation is typified by an initial parabolic weight gain response curve that eventually exhibits a maximum, then transitions into a linear rate of weight loss due to spalling. The overall shape and magnitude of the curve are determined by the parabolic growth rate, k_p, the cycle duration, the type of oxide scale, and the regular, repetitive spalling process. This entire process was modeled by a

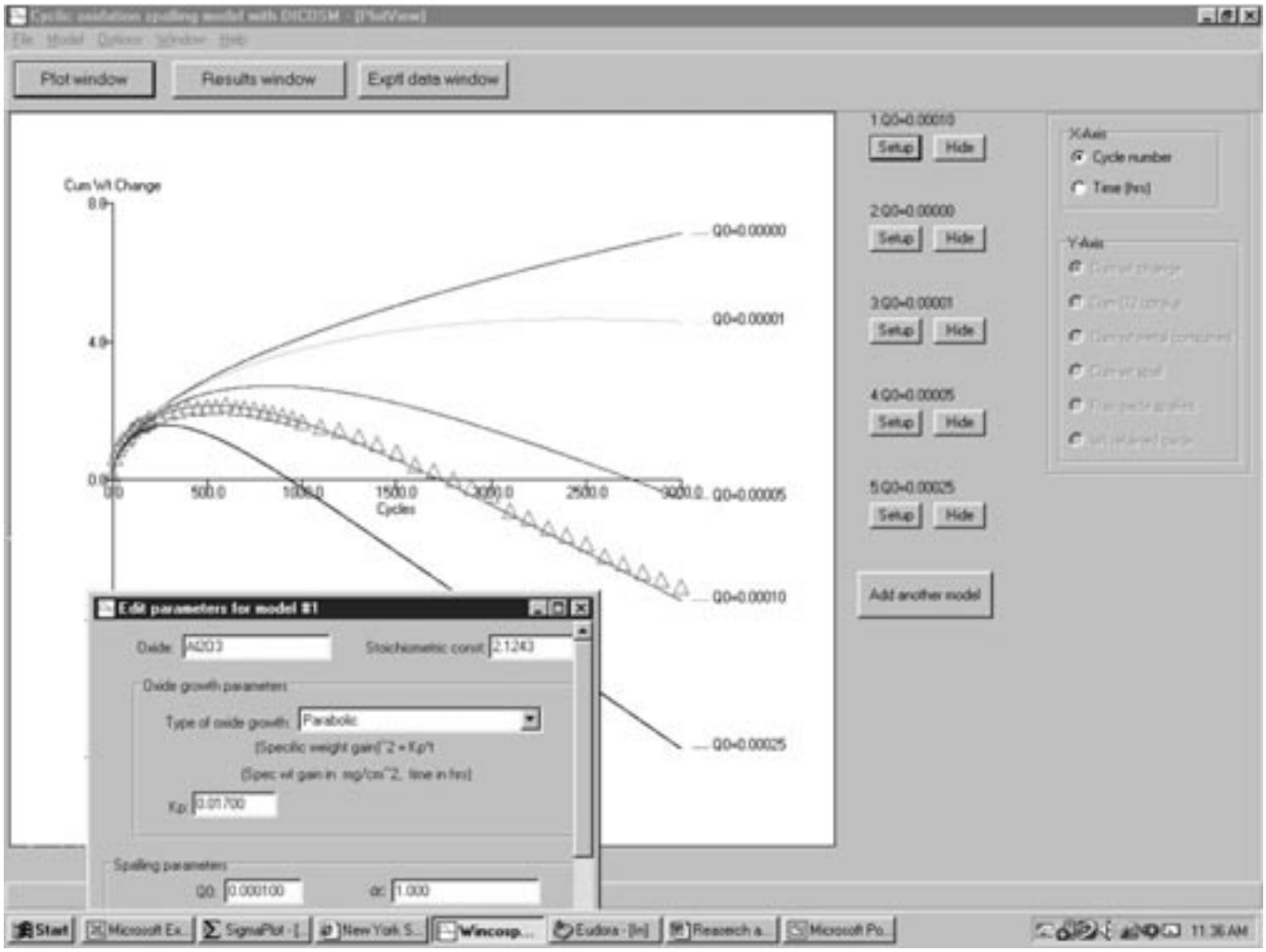

Sample screen from the COSP for Windows cyclic oxidation modeling program showing the initial setup menu and plot window. Multiple plots for various spall constants and actual data points for NiAl(Zr) oxidized at 1200 °C show good agreement for the parabolic rate constant $k_p = 0.017$ mg^2/cm^{4}h and the spall constant $Q_o = 0.0001$.

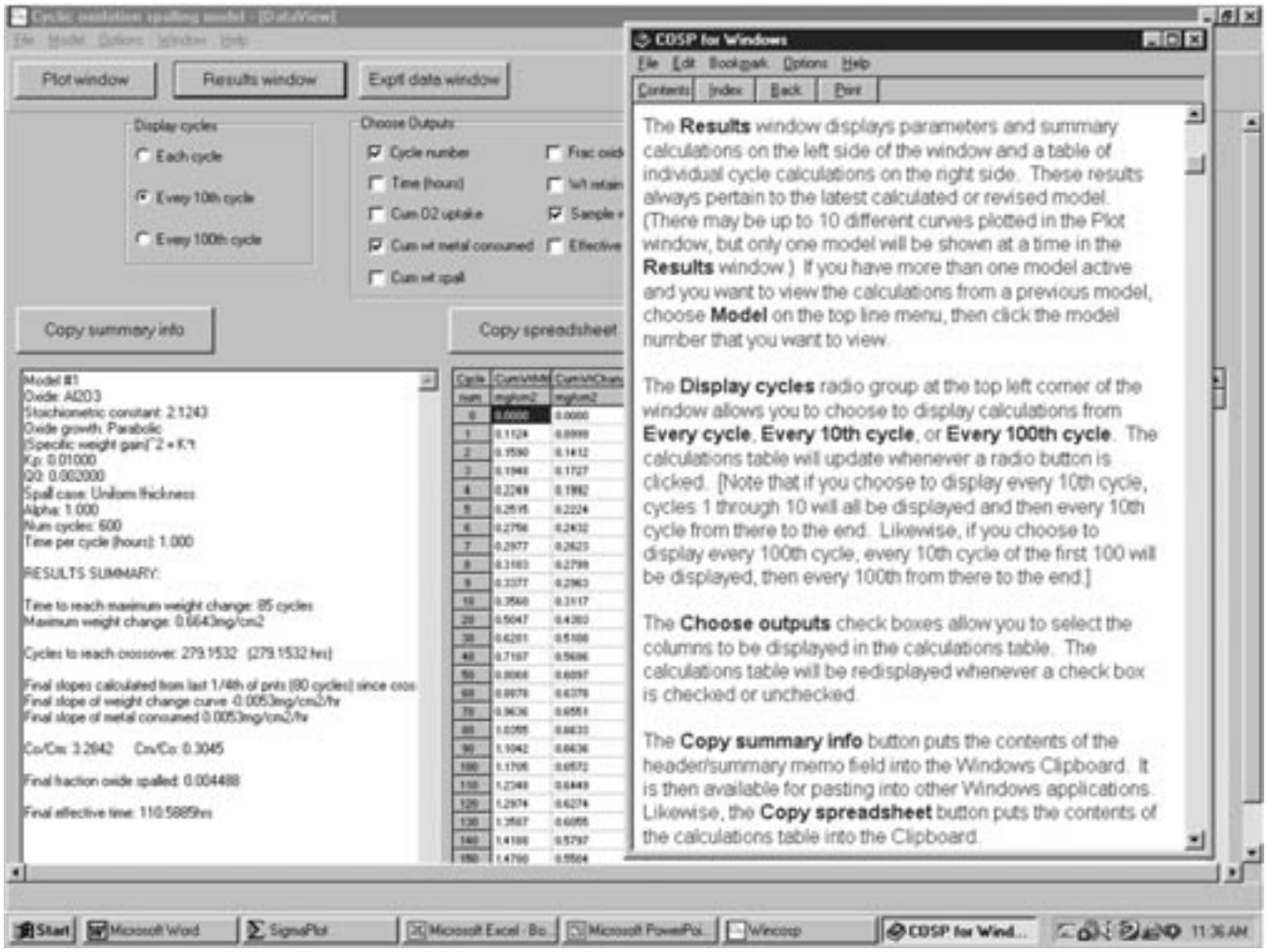

Sample screen for the results window and appropriate help text. Summary information and output data tables are presented for the selected model case.

computer program called the Cyclic Oxidation Spalling Program (COSP) previously developed at the NASA Glenn Research Center (refs. 1 and 2). Thus, by supplying appropriate oxidation input parameters, one can determine the best fit to the actual data. These parameters describe real behavior and can be used to compare alloys and project cyclic oxidation behavior for longer times or under different cycle frequencies.

This year, the program was rewritten to run under the MS Windows (Microsoft, Redmond, WA) operating system (ref. 3). This allows the major benefits of navigating between various control screens and interfacing with other applications. Point-and-click operating features include multiple drop-down menus for setting model input parameters, for importing experimental data for analysis, and for viewing quick, on-screen plots that show any of the six output parameters for up to 10 models. Families of model curves on the instant plot screen readily show the sensitivity to various input parameters and allow rapid and precise fitting to experimental curves. An example of the initial setup menu and plot window is shown in the figure on the preceding page for the weight change behavior of an aluminum oxide scale. Five model curves are presented with various spalling parameters. One curve represents the best fit to the experimental data obtained for the 1200 °C cyclic oxidation of NiAl.

The program can be operated conveniently while other MS Windows applications remain open for importing experimental weight change data, storing model output data, or plotting model curves in a graphics package. The program includes save and print options as well as a help file.

Along with the sample weight change, other salient terms are calculated—the existing scale weight and the cumulative amounts of oxygen consumed, metal consumed, and spall weight. These are all listed in a table accessed by the results window button. Key descriptive parameters (such as the number of cycles to reach the maximum weight gain and to reach zero weight change, the final weight loss slope, and the plateau in oxygen gain) are all highlighted as part of a summary text output. An example of the results table and the summary information are presented in the figure on the preceding page, along with the pertinent help topic text. The COSP for Windows program is publicly available upon request.

References

1. Lowell, C.E., et al.: COSP: A Computer Model of Cyclic Oxidation. Oxid. Met., vol. 36, nos. 1/2, 1991, pp. 81–112.
2. Smialek, J.L., et al.: Cyclic Oxidation Testing and Modelling: a NASA Lewis Perspective. NASA/TM—1999-209769, 1999. http://gltrs.grc.nasa.gov/GLTRS
3. Smialek, J.L. and Auping, J.V.: COSP for Windows—Strategies for Rapid Analyses of Cyclic Oxidation Behavior. To be published, Oxid. Met., 2002. (Also NASA/TP—2002-211108, 2002.)

Glenn contacts:
Dr. James L. Smialek, 216–433–5500, James.L.Smialek@grc.nasa.gov; and Judith V. Auping, 216–433–5016; Judith.V.Auping@grc.nasa.gov

Authors: James L. Smialek and Judith V. Auping

Headquarters program office: OAT

Programs/Projects: UEET

Effect of Environment on the Stress-Rupture Behavior of a C/SiC Composite Studied

Advanced reusable launch vehicles will likely incorporate fiber-reinforced ceramic matrix composites (CMC's) in critical propulsion and airframe components. The use of CMC's is highly desirable to save weight, improve reuse capability, and increase performance. One of the candidate CMC materials is carbon-fiber-reinforced silicon carbide (C/SiC).

In potential propulsion applications, such as turbopump rotors and nozzle exit ramps, C/SiC components will be subjected to a service cycle that includes mechanical loading under complex, high-pressure environments containing hydrogen, oxygen, and steam. Degradation of both the C fibers and the SiC matrix are possible in these environments. The objective of this effort was to evaluate the mechanical behavior of C/SiC in various environments relevant to reusable launch vehicle applications. Stress-rupture testing was conducted at the NASA Glenn Research Center on C/SiC specimens in air and steam-containing environments. Also, the oxidation kinetics of the carbon fibers that reinforce the composite were monitored by thermogravimetric analysis in the same environments and temperatures used for the stress-rupture tests of the C/SiC composite specimens.

The stress-rupture lives obtained for C/SiC tested in air and in steam/argon mixtures are shown in the following bar chart. As is typical for most materials, lives obtained at the lower temperature (600 °C) are longer than for the higher temperature (1200 °C). The effect of environment was most pronounced at the lower temperature, where the average test duration in steam at 600 °C was at least 30 times longer than the lives obtained in air. The 1200 °C data revealed little difference between the lives of specimens tested in air and steam at atmospheric pressure.

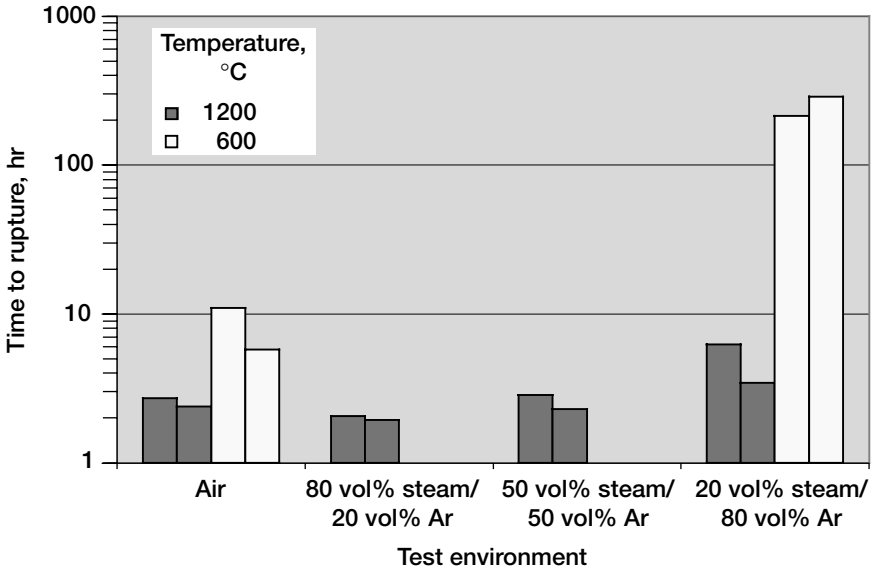

Stress-rupture data for C/SiC revealed that lives vary with test temperature and environment (stress was 10 ksi for all tests).

The damage that occurred during the stress-rupture testing at 600 and 1200 °C in steam is shown in the following photomicrographs. Little composite damage can be seen in the specimen tested at 600 °C, whereas damage, in the form of carbon fiber oxidation, was present in the specimen tested at 1200 °C. Similar damage was found in specimens tested in air. The results revealed that the oxidation rate of the carbon fibers in the various environments correlated with the composite stress-rupture lives.

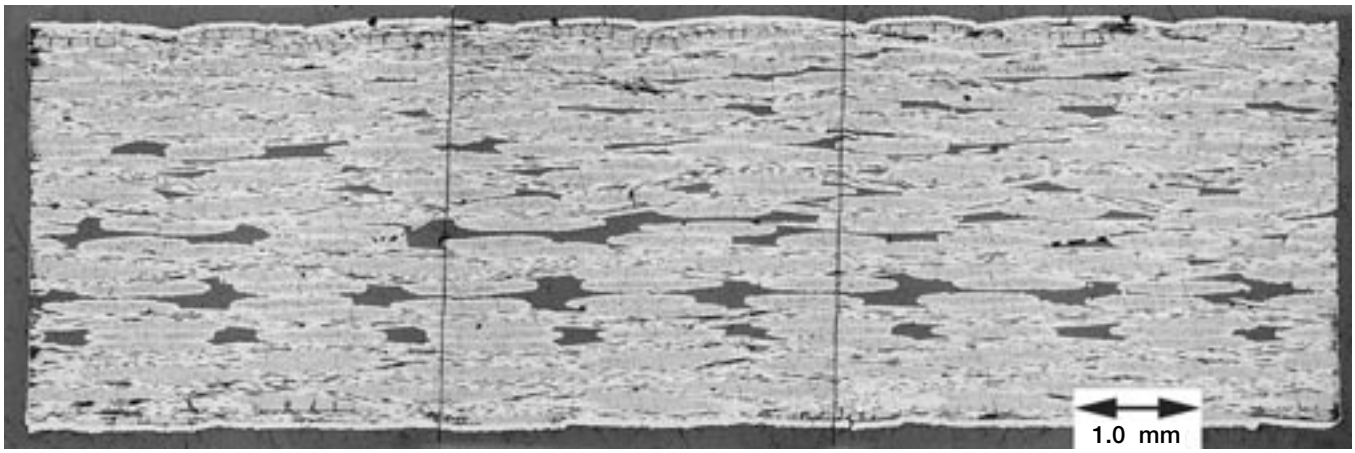

Little damage is seen in C/SiC tested in steam at 600 °C for 213 hr.

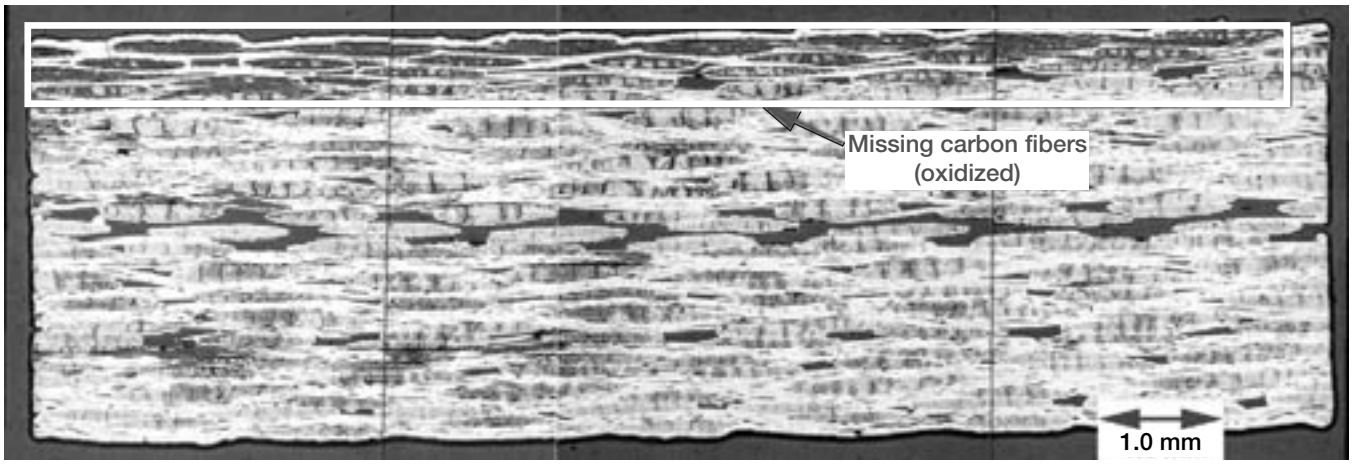

C/SiC specimen failure occurred after 2 hr in steam at 1200 °C because of carbon fiber oxidation.

Rupture testing and strength measurements studies are ongoing to guide composite life prediction method development for C/SiC as well as to provide fundamental understanding of the damage mechanisms in ceramic matrix composites in environments relevant to future launch vehicle applications.

Find out more about this research: http://www.grc.nasa.gov/WWW/EDB/

Glenn contact: Michael J. Verrilli, 216–433–3337, Michael.J.Verrilli@grc.nasa.gov

Authors: Michael J. Verrilli, J. Douglas Kiser, Dr. Elizabeth J. Opila, and Dr. Anthony M. Calomino

Headquarters program office: OAT

Programs/Projects: ASTP

Thermal Cyclic Behavior of Thermal and Environmental Barrier Coatings Investigated Under High-Heat-Flux Conditions

Environmental barrier coatings (EBC's) have been developed to protect silicon-carbide- (SiC) based ceramic components in gas turbine engines from high-temperature environmental attack (refs. 1 and 2). With continuously increasing demands for significantly higher engine operating temperature, future EBC systems must be designed for both thermal and environmental protection of the engine components in combustion gases. In particular, the thermal barrier functions of EBC's become a necessity for reducing the engine-component thermal loads and chemical reaction rates, thus maintaining the required mechanical properties and durability of these components. Advances in the development of thermal and environmental barrier coatings (TBC's and EBC's, respectively) will directly impact the successful use of ceramic components in advanced engines.

To develop high-performance coating systems, researchers must establish advanced test approaches. In this study, a laser high-heat-flux technique (ref. 3) was employed to investigate the thermal cyclic behavior of TBC's and EBC's on SiC-reinforced SiC ceramic matrix composite substrates (SiC/SiC) under high thermal gradient and thermal cycling conditions (refs. 4 and 5). Because the laser heat flux test approach can monitor the coating's real-time thermal conductivity variations at high temperature, the coating thermal insulation performance, sintering, and delamination can all be obtained during thermal cycling tests.

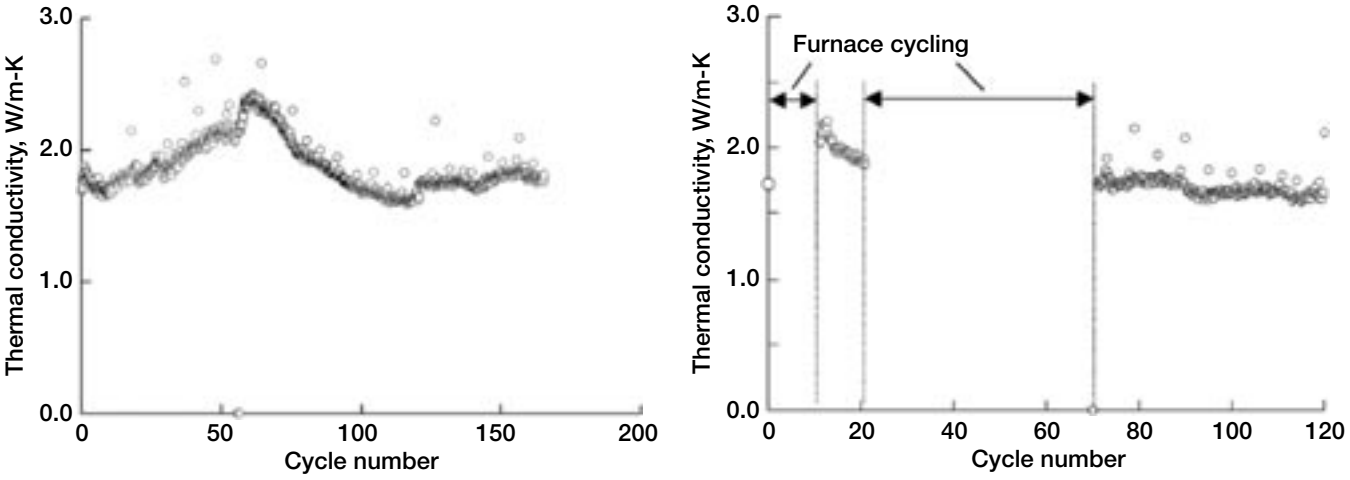

Thermal conductivity changes of the BSAS/mullite-20 wt% BSAS coating systems as a function of the cycle number. Left: Laser thermal cycling testing. Surface temperature, 1482 °C; interface temperature, 1300 °C in air; total of 166 1-hr cycles. Right: Combined furnace water vapor and laser thermal cyclic testing. Total of 120 1-hr cycles.

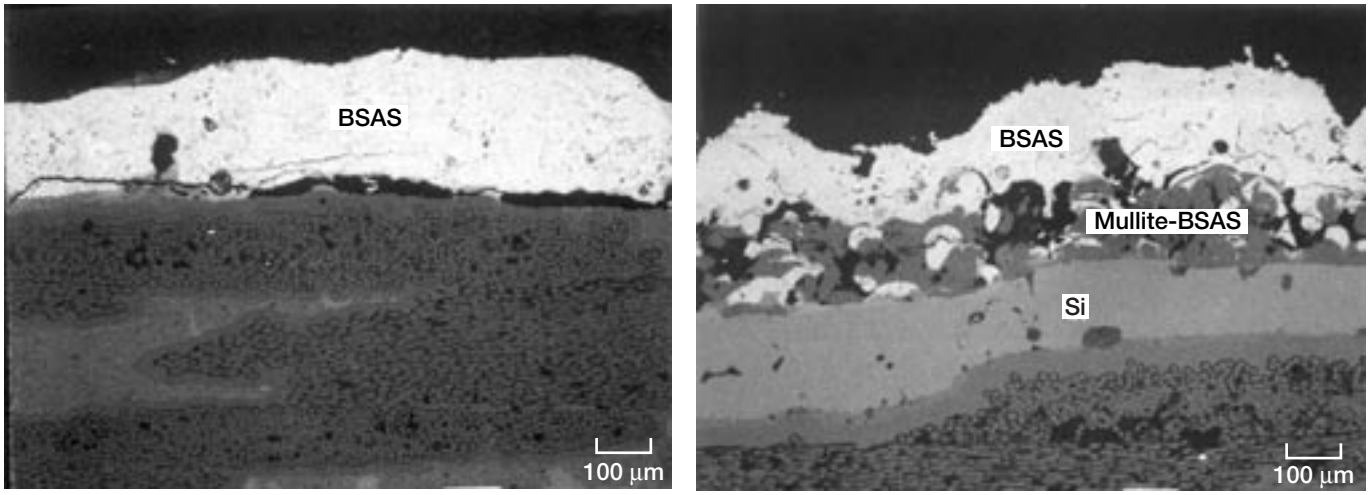

Photomicrographs of cross sections of BSAS and BSAS/mullite-20 wt% BSAS coatings after combined laser and furnace water vapor cycle testing, showing the coating interface pore structures and coating cracking and delaminations after testing. Left: BSAS coating. Right: BSAS/mullite-20 wt% BSAS two-layer coating.

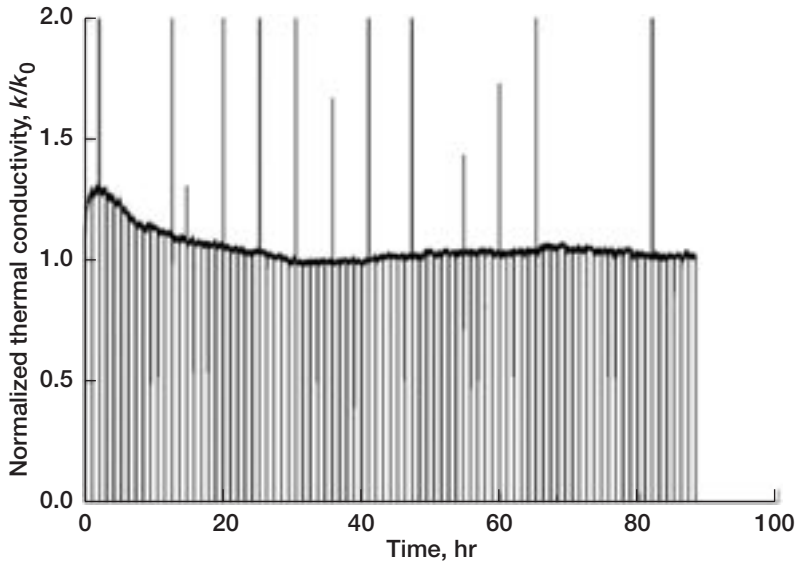

Normalized thermal conductivity of a 500-μm ZrO_2-8 wt% Y_2O_3/BSAS/BSAS+mullite/Si multilayered coating system measured during the laser thermal gradient cyclic test. The coating conductivity first rapidly increased due to coating sintering, but later decreased due to coating cracking-delamination under further thermal cycling.

Plasma-sprayed yttria-stabilized zirconia (ZrO_2-8 wt% Y_2O_3) thermal barrier and barium strontium aluminosilicate-based environmental barrier coatings (BSAS/BSAS+mullite/Si) on SiC/SiC ceramic matrix composites were investigated in this study. These coatings were laser tested in air under thermal gradients (the surface and interface temperatures were approximately 1482 and 1300 °C, respectively). Some coating specimens were also subject to alternating furnace cycling (in a 90-percent water vapor environment at 1300 °C) and laser thermal gradient cycling tests (in air), to investigate the water vapor effect. All cyclic tests were conducted using a 60-min hot-time temperature.

The graphs on the preceding page show the thermal conductivity changes of 254-μm-thick BSAS/mullite-20 wt% BSAS coating systems as a function of the cycle number. For both the laser and combined furnace-laser tested specimens, initial thermal conductivity increased considerably because of the coating sintering. However, the coating conductivity then decreased under further testing because of coating cracking and delamination. Coating sintering and delamination occurred faster under the combined furnace water vapor and laser cyclic test conditions, indicating that water vapor has a detrimental effect on coating durability. Typical failure modes and cracking morphologies of the BSAS and BSAS/mullite-20 wt% BSAS two-layer coatings under the combined furnace and water vapor cycles exposure are shown in the photomicrographs above. The coating failure was accelerated by the interface pore formation in the water vapor environments and by subsequent coating delamination under laser thermal gradient cyclic testing.

For a ZrO_2-8 wt% Y_2O_3/BSAS/BSAS+mullite/Si multilayered coating system tested under thermal gradient cyclic conditions, thermal conductivity showed a similar trend with the cycle numbers as observed for BSAS/mullite-20 wt% BSAS coating systems. The coating-sintering-induced initial conductivity increase and the subsequent coating cracking-delamination-induced conductivity decrease are clearly seen in the graph on the preceding page. However, the combined effects of the thermal expansion mismatch between the different coating layers and the substrate, along with the sintering shrinkage of the ceramic coatings, resulted in substantial wedge-shape surface cracking and coating delaminations. The failure morphologies of the coating systems are shown in the photomicrograph to the right.

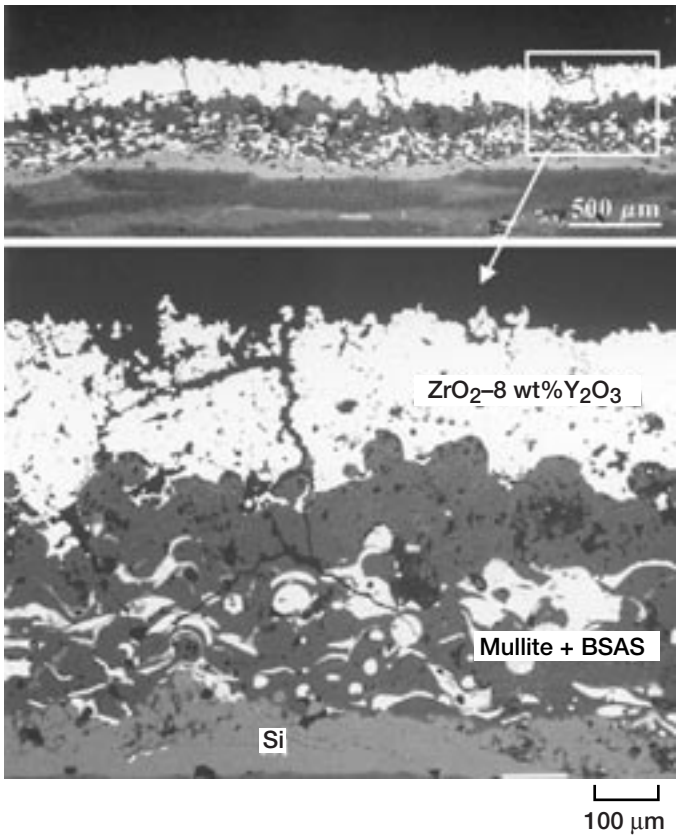

Photomicrographs of cross sections of a ZrO_2-8 wt% Y_2O_3/BSAS/BSAS+mullite/Si multilayered coating showing the coating failure morphologies after the laser cyclic test. The wedge-shape surface cracking and the coating delaminations were extensively developed under the thermal gradient cyclic test conditions.

References

1. Lee, K.N.: Key Durability Issues With Mullite-Based Environmental Barrier Coatings for Si-Based Ceramics. J. Eng. Gas Turbines Power, vol. 122, no. 4, 2000, pp. 632–636.
2. Lee, K.N.: Current Status of Environmental Barrier Coatings for Si-Based Ceramics. Surface & Coatings Technology, vol. 133–134, 2000, pp. 1–7.
3. Zhu, Dongming; and Miller, Robert A.: Thermal Conductivity and Elastic Modulus Evolution of Thermal Barrier Coatings Under High Heat Flux Conditions. NASA/TM—1999-209069, 1999. http//gltrs.grc.nasa.gov/GLTRS/
4. Zhu, Dongming; Lee, Kang N.; and Miller, Robert A.: Thermal Conductivity and Thermal Gradient Cyclic Behavior of Refractory Silicate Coatings on SiC/SiC Ceramic Matrix Composites. NASA/TM—2001-210824, 2001. http//gltrs.grc.nasa.gov/GLTRS/
5. Zhu, Dongming, et al.: Thermal Conductivity of Ceramic Thermal Barrier and Environmental Barrier Coating Materials. NASA/TM—2001-211122, 2001. http//gltrs.grc.nasa.gov/GLTRS/

OAI contact: Dr. Dongming Zhu, 216–433–5422, Dongming.Zhu@grc.nasa.gov

Cleveland State University contact:
Dr. Kang N. Lee, 216–433–5634, Kang.N.Lee@grc.nasa.gov

Glenn contact: Dr. Robert A. Miller, 216–433–3298, Robert.A.Miller@grc.nasa.gov

Authors:
Dr. Dongming Zhu, Dr. Kang N. Lee, and Dr. Robert A. Miller

Headquarters program office: OAT

Programs/Projects: UEET

Power and On-Board Propulsion Technology

Quantum Dots Investigated for Solar Cells

The NASA Glenn Research Center has been investigating the synthesis of quantum dots of CdSe and $CuInS_2$ for use in intermediate-bandgap solar cells. Using quantum dots in a solar cell to create an intermediate band will allow the harvesting of a much larger portion of the available solar spectrum. Theoretical studies predict a potential efficiency of 63.2 percent, which is approximately a factor of 2 better than any state-of-the-art devices available today (ref. 1). This technology is also applicable to thin-film devices—where it offers a potential four-fold increase in power-to-weight ratio over the state of the art.

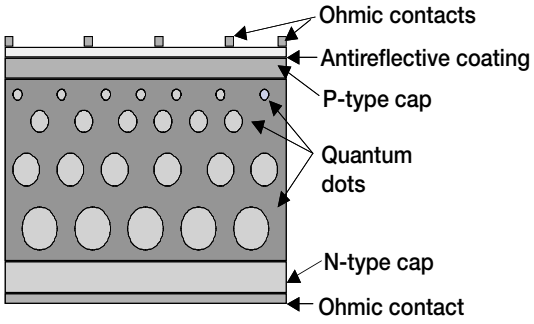

Intermediate-bandgap solar cell.

Intermediate-bandgap solar cells require that quantum dots be sandwiched in an intrinsic region between the photovoltaic solar cell's ordinary *p*- and *n*-type regions (see the top figure). The quantum dots form the intermediate band of discrete states that allow subbandgap energies to be absorbed. However, when the current is extracted, it is limited by the bandgap, not the individual photon energies. The energy states of the quantum dot can be controlled by controlling the size of the dot. Ironically, the ground-state energy levels are inversely proportional to the size of the quantum dots.

We have prepared a variety of quantum dots using the typical organo-metallic synthesis routes pioneered by Ba Wendi et al., in the early 1990's (ref. 2). The most studied quantum dots prepared by this method have been of CdSe. To produce these dots, researchers inject a syringe of the desired organometallic precursors into heated triocytlphosphine oxide (TOPO) that has been vigorously stirred under an inert atmosphere (see the bottom figure). The solution immediately begins to change from colorless to yellow, then orange and red/brown, as the quantum dots increase in size. When the desired size is reached, the heat is removed from the flask. Quantum dots of different sizes can be identified by placing them under a "black light" and observing the various color differences in their fluorescence (see the figure on the next page).

Unlike previous work in this area, Glenn used single-source precursor molecules in this synthesis process. $CuInS_2$ precursor molecules were prepared using a metasthesis reaction of an organoindium reagent in a nonaqueous solution. The precursors were used in the same process just described to produce nanoscale CuInS quantum dots for photovoltaic applications.

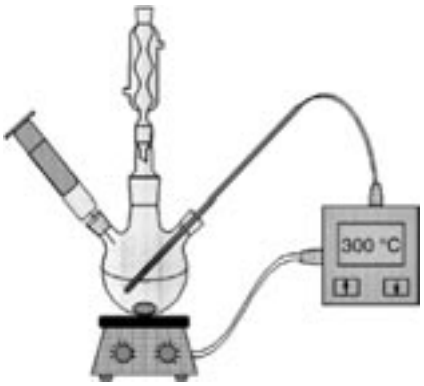

Experimental setup for chemical bath production of quantum dots.

References

1. Luque, A.; and Marti, A.: Increasing the Efficiency of Ideal Solar Cells by Photon Induced Transitions at Intermediate Levels. Phys. Rev. Lett., vol. 78, no. 26, 1997, pp. 5014–5017.
2. Murray, C.B.; Norris, D.J.; and Ba Wendi, M.G.: Synthesis and Characterization of Nearly Mono-disperse CDE (E = S, SE, TE) Semi-conductor Nanocrystallites. J. Am. Chem. Soc., vol. 115, no. 19, 1993, pp. 8706–8715.

Glenn contact:
Dr. Sheila G. Bailey, 216–433–2228, Sheila.G.Bailey@grc.nasa.gov

RIT contact: Dr. Ryne P. Raffaelle, 716–475–5149, rprsps@rit.edu

OAI contact:
Dr. Stephanie L. Castro, 216–433–3820,
Stephanie.L.Castro@grc.nasa.gov

Authors:
Dr. Ryne P. Raffaelle, Dr. Stephanie L. Castro, Dr. Aloysius F. Hepp, and Dr. Sheila G. Bailey

Headquarters program office: OAT

Programs/Projects: SSP, DDF

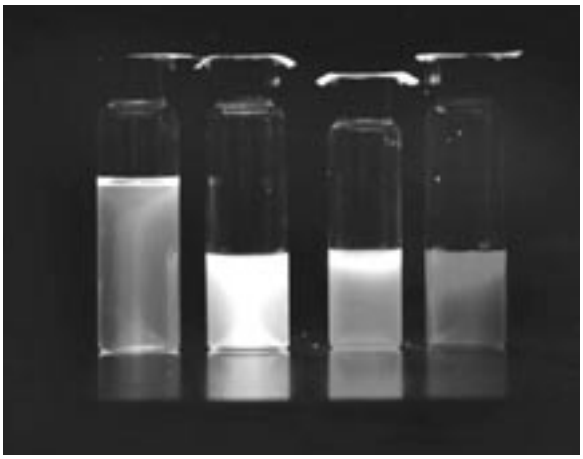

CdSe quantum dot fluorescence showing an increase in dot size going from green on the left to red on the right. This figure is shown in color in the online version of this article (http://www.grc.nasa.gov/WWW/RT2001/5000/5410bailey.html).

Silicon Carbide Solar Cells Investigated

The semiconductor silicon carbide (SiC) has long been known for its outstanding resistance to harsh environments (e.g., thermal stability, radiation resistance, and dielectric strength). However, the ability to produce device-quality material is severely limited by the inherent crystalline defects associated with this material and their associated electronic effects. Much progress has been made recently in the understanding and control of these defects and in the improved processing of this material. Because of this work, it may be possible to produce SiC-based solar cells for environments with high temperatures, light intensities, and radiation, such as those experienced by solar probes (ref. 1).

Electronics and sensors based on SiC can operate in hostile environments where conventional silicon-based electronics (limited to 350 °C) cannot function. Development of this material will enable large performance enhancements and size reductions for a wide variety of systems—such as high-frequency devices, high-power devices, microwave switching devices, and high-temperature electronics. These applications would supply more energy-efficient public electric power distribution and electric vehicles, more powerful microwave electronics for radar and communications, and better sensors and controls for cleaner-burning, more fuel-efficient jet aircraft and automobile engines.

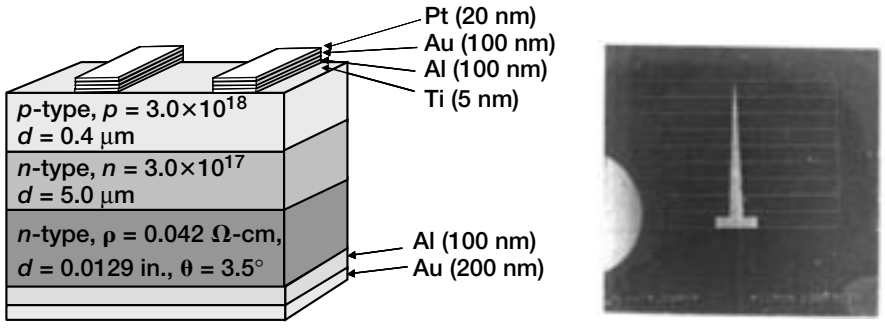

Left: SiC solar cell schematic. Right: 0.48 cm^2 SiC solar cell.

The 6H-SiC polytype is a promising wide-bandgap ($E_g = 3.0$ eV) semiconductor for photovoltaic applications in harsh solar environments that involve high-temperature and high-radiation conditions. The advantages of this material for this application lie in its extremely large breakdown field strength, high thermal conductivity, good electron saturation drift velocity, and stable electrical performance at temperatures as high as 600 °C (ref. 2).

This behavior makes it an attractive photovoltaic solar cell material for devices that can operate within three solar radii of the Sun (ref. 3).

At the NASA Glenn Research Center, several solar cells were fabricated on both thin *n*-on-*p* and thin *p*-on-*n* SiC epilayers grown by Cree Semiconductor, Inc. The contacts were made using alloys made by the sequential deposition of various metal layers followed by a rapid thermal anneal at 800 °C. The cell schematic and a resulting device are shown in the preceding figure.

The photoresponse of the cells was measured under simulated air mass zero (AM0) conditions. The current-versus-voltage behavior of the device showed a good photoresponse and diode characteristics, especially considering there is very little intensity in the solar spectrum above 3.0 eV (see the figure to the right).

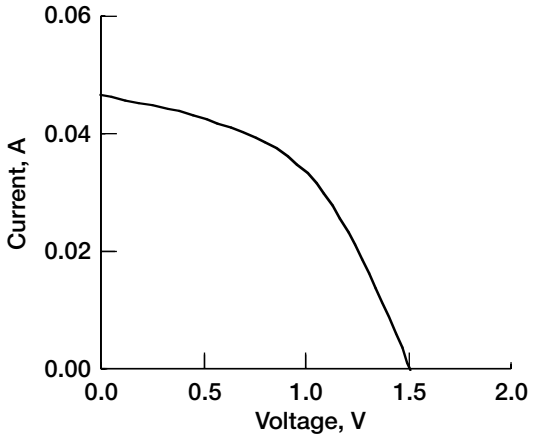

AM0 photoresponse of a thin n-on-p SiC solar cell.

References

1. Neudeck, P.G.: Progress in Silicon-Carbide Semiconductor Electronics Technology. J. Elec. Mat., vol. 24, no. 4, 1995, pp. 283–288.
2. Bhatnagar, M.; and Baliga, B.J.: Comparison of 6H-SiC, 3C-SiC, and Si for Power Devices. IEEE Trans. Electron Devices, vol. 40, no. 3, 1993, pp. 645–655.
3. Scheiman, D.A.; Landis, G.A.; and Weizer, V.G.: High-Bandgap Solar Cells for Near-Sun Missions. AIP Conf. Proc., M.S. ElGenk, ed., parts 1 and 2, 1999, pp. 616–620.

Glenn contact:
Dr. Sheila G. Bailey, 216–433–2228, Sheila.G.Bailey@grc.nasa.gov

RIT contact: Dr. Ryne P. Raffaelle, 716–475–5149, rprsps@rit.edu

Authors: Dr. Ryne P. Raffaelle and Dr. Sheila G. Bailey

Headquarters program office: OAT

Programs/Projects: TPA

Floating Potential Probe Deployed on the International Space Station

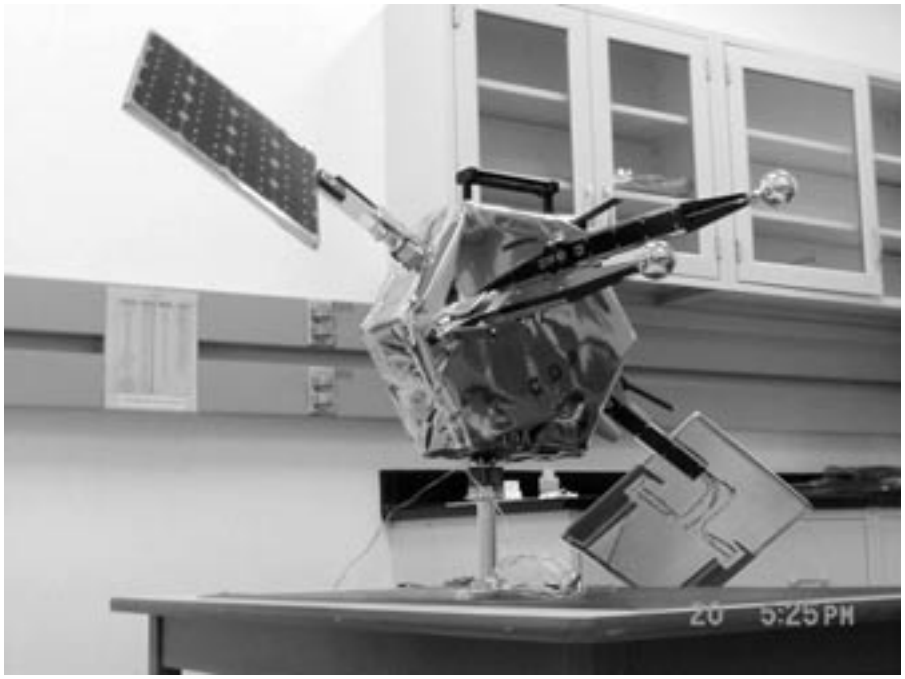

Floating Potential Probe at the NASA Kennedy Space Center before launch.

In the spring and summer of 2000, at the request of the International Space Station (ISS) Program Office, a Plasma Contactor Unit Tiger Team was set up to investigate the threat of the ISS arcing in the event of a plasma contactor outage. Modeling and ground tests done under that effort showed that it is possible for the external structure of the ISS to become electrically charged to as much as –160 V under some conditions. Much of this work was done in anticipation of the deployment of the first large ISS solar array in November 2000. It was recognized that, with this deployment, the power system would be energized to its full voltage and that the predicted charging would pose an immediate threat to crewmembers

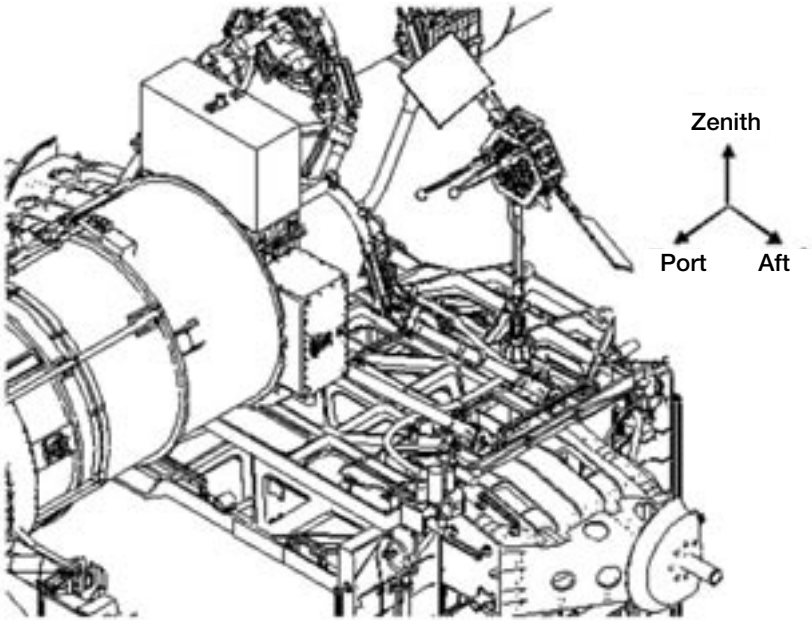

Floating Potential Probe as installed on the top of P6 on the ISS.

involved in extravehicular activities (EVA's), as well as long-term damage to the station structure, were the ISS plasma contactors to be turned off or stop functioning. The Floating Potential Probe was conceived, designed, built, and deployed in record time by a crack team of scientists and engineers led by the NASA Glenn Research Center in response to ISS concerns about crew safety. Launched on ISS mission 4A and deployed on the ISS in December 2000, the device provides a direct measurement of the electrical potential of the ISS with respect to its environment. The Floating Potential Probe has shown that, although the expected charging levels have so far not been realized, significant charging can occur, which still poses a threat to EVA astronauts, requiring a two-fault-tolerant approach during EVA.

Glenn contact: Dr. Dale C. Ferguson, 216–433–2298, Fax 216–433–6106, Dale.C.Ferguson@grc.nasa.gov

Author: Dr. Dale C. Ferguson

Headquarters program office: OAT, OSF

Programs/Projects: ISS

Carbon Nanotube Anodes Being Evaluated for Lithium Ion Batteries

The NASA Glenn Research Center is evaluating the use of carbon nanotubes as anode materials for thin-film lithium-ion (Li) batteries. The motivation for this work lies in the fact that, in contrast to carbon black, directed structured nanotubes and nanofibers offer a superior intercalation media for Li-ion batteries. Carbon lamellas in carbon blacks are circumferentially oriented and block much of the particle interior, rendering much of the matrix useless as intercalation material. Nanofibers, on the other hand, can be grown so as to provide 100-percent accessibility of the entire carbon structure to intercalation. These tubes can be visualized as "rolled-up" sheets of carbon hexagons (see the figure to the right). One tube is approximately 1/10,000th the diameter of a human hair. In addition, the high accessibility of the structure confers a high mobility to ion-exchange processes, a fundamental for the batteries to respond dynamically because of intercalation.

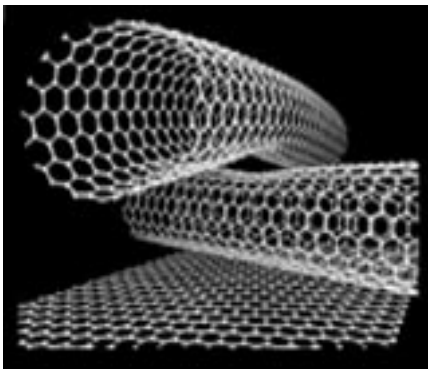

Carbon nanotube structure.

Nanotubes were grown by both laser vaporization and chemical vapor deposition (CVD). The laser vaporization method was used to provide high-purity, single-wall tubes. The CVD approach produced multiwall tubes that could be grown directly on metal foil substrates coated with suitable metal catalysts using a high-temperature furnace.

Glenn's researchers have found that evaporated nanoscale copper "islands" on nickel metal-foil substrates provide an excellent substrate for high-purity multiwall nanotube CVD growth (see the figure to the right). In addition to Li storage for high-energy-density batteries, carbon nanotubes that are deposited by CVD onto metal substrates are of high interest for a wide range of applications such as the filtering of gaseous or liquid media and as reinforcing agents in composite materials.

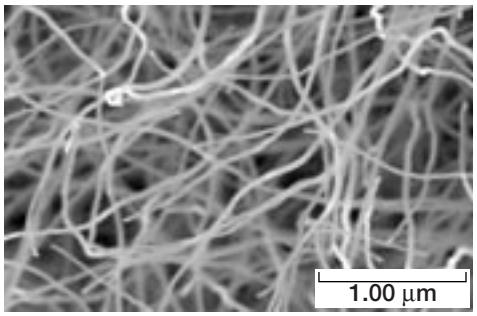

High-resolution scanning electron microscope image of CVD multiwall carbon nanotubes.

The laser vaporization nanotubes were produced in a high-temperature furnace under argon using a 755-nm alexandrite laser and a graphite target doped with Ni and Co. The resulting "soot" was purified by nitric acid refluxing followed by annealing in oxygen. Single-wall carbon nanotubes with a purity greater than 99 wt% have been prepared using this method (see the final figure) (ref. 1).

The anode surface area per mass provided by high-purity nanotube "tape" was found to be greater (by several orders of magnitude) than any conventional anode materials. This increase in area should decrease the internal battery resistance and presumably increase the attainable current densities and the cyclability of batteries utilizing these materials as anodes. The lithium capacity of high-purity carbon nanotube films was measured with a conventional three-electrode cell. Anodes were prepared by casting thin films of high-purity carbon nanotubes dispersed in poly(vinylidene fluoride) (PVDF) directly onto copper foil. The capacity, which showed excellent reversibility, was ~2000 mA-hr/g after 30 cycles. This capacity is over 5 times greater than that of graphite.

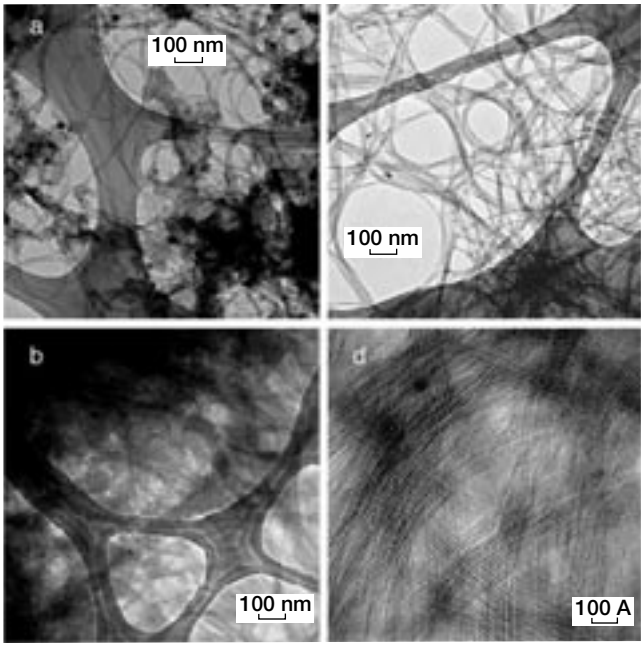

High-resolution transmission electron microscope images. (a) "Raw" laser vaporization soot. (b) Single-wall nanotube bundles after reflux. (c) High-purity (>99 wt%) single-wall carbon nanotubes. (d) Nanotube "tape."

References

1. Dillon, A.C., et al.: A Simple and Complete Purification of Single-Walled Carbon Nanotube Materials. Advanced Materials, vol. 11, no. 16, 1999, pp. 1354–1358.

Glenn contact:
Dr. Aloysius F. Hepp, 216–433–3835, Aloysius.F.Hepp@grc.nasa.gov

RIT contact: Dr. Ryne P. Raffaelle, 716–475–5149, rprsps@rit.edu

National Center for Microgravity Research contact:
Dr. Randy L. Vander Wal, 216–433–9065, Randall.L.VanderWal@grc.nasa.gov

Authors:
Dr. Ryne P. Raffaelle, Dr. Tom Gennett, Dr. Randy L. Vander Wal, and Dr. Aloysius F. Hepp

Headquarters program office: OAT

Programs/Projects: NBP

Atmospheric-Pressure-Spray, Chemical-Vapor-Deposited Thin-Film Materials Being Developed for High Power-to-Weight-Ratio Space Photovoltaic Applications

The key to achieving high specific power (watts per kilogram) space photovoltaic arrays is the development of high-efficiency thin-film solar cells that are fabricated on lightweight, space-qualified substrates such as Kapton (DuPont) or another polymer film. Cell efficiencies of 20 percent air mass zero (AM0) are required. One of the major obstacles to developing lightweight, flexible, thin-film solar cells is the unavailability of lightweight substrate or superstrate materials that are compatible with current deposition techniques. There are two solutions for working around this problem: (1) develop new substrate or superstrate materials that are compatible with current deposition techniques, or (2) develop new deposition techniques that are compatible with existing materials. The NASA Glenn Research Center has been focusing on the latter approach and has been developing a deposition technique for depositing thin-film absorbers at temperatures below 400 °C.

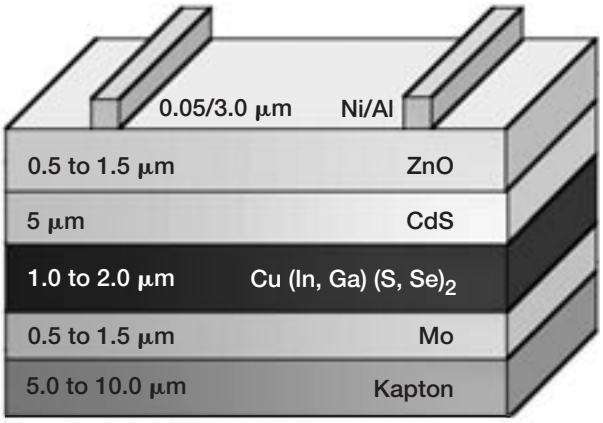

Thin-film solar cell deposited on Kapton substrate.

A chemically based approach is enabling the development of such a process by employing single-source molecular precursors and atmospheric-pressure-spray chemical vapor deposition. Thin films of $CuInS_2$ can be deposited on substrates at temperatures as low as 300 °C (see the top right figure) (ref. 1). Single-source precursors are molecules that contain all the required atoms (copper, indium, and sulfur for $CuInS_2$; or copper, indium, gallium, and selenium for $CuIn_{1-x}Ga_xSe_2$) in the correct ratio to yield the desired material when they decompose (see the figure below). The first liquid precursors for the preparation of $CuInS_2$ films were recently synthesized and utilized (ref. 2). Liquid precursors offer the advantage of even lower decomposition and deposition temperatures.

One potential configuration to achieve an efficiency at AM0 of 20 percent is a copper indium disulfide/copper indium diselenide/copper gallium diselenide ($CuInS_2/CuInSe_2/CuGaSe_2$) triple-junction

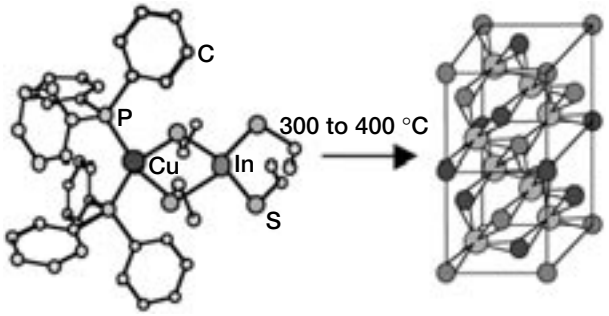

Decomposition of single-source precursor to yield $CuInS_2$.

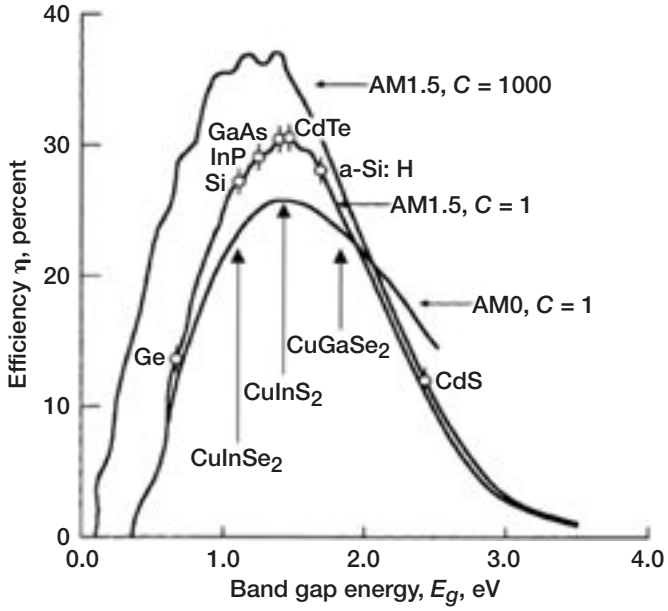

Predicted efficiency versus bandgap for thin-film photovoltaic materials for the solar spectrum in space (AM0) and on the surface of the Earth (AM1.5) at 300 K.

multiple-bandgap structure. The bandgaps for these materials are shown in the preceding graph in relation to the optimal efficiencies to be realized as a function of wavelength for the solar spectrum in space (AM0) and on the surface of Earth (AM1.5).

References

1. Harris, J.D., et al.: Using Single Source Precursors and Spray Chemical Vapor Deposition to Grow Thin-Film CuInS(2). IEEE Photovoltaic Specialists Conference, 2000, pp. 563–566.
2. Banger, K.K., et al.: Synthesis and Characterization of the First Liquid Single-Source Precursors for the Deposition of Ternary Chalcopyrite ($CuInS_2$) Thin Film Materials. Chem. Mater., vol. 13, 2001, pp. 3827–3829.

Glenn contact:
Dr. Aloysius F. Hepp, 216–433–3835, Aloysius.F.Hepp@grc.nasa.gov

Authors:
Dr. Jerry D. Harris, Dr. Ryne P. Raffaelle, Dr. Kulbinder K. Banger, Dr. Mark A. Smith, Jonathan E. Cowen, and Dr. Aloysius F. Hepp

Headquarters program office: OSS

Programs/Projects: SSP, CETDP

Photovoltaic Engineering Testbed Designed for Calibrating Photovoltaic Devices in Space

Accurate prediction of the performance of solar arrays in space requires that the cells be tested in comparison with a space-flown standard. Recognizing that improvements in future solar cell technology will require an ever-increasing fidelity of standards, the Photovoltaics and Space Environment Branch at the NASA Glenn Research Center, in collaboration with the Ohio Aerospace Institute, designed a prototype facility to allow routine calibration, measurement, and qualification of solar cells on the International Space Station, and then the return of the cells to Earth for laboratory use. For solar cell testing, the Photovoltaic Engineering Testbed (PET) site provides a true air-mass-zero (AM0) solar spectrum. This allows solar cells to be accurately calibrated using the full spectrum of the Sun.

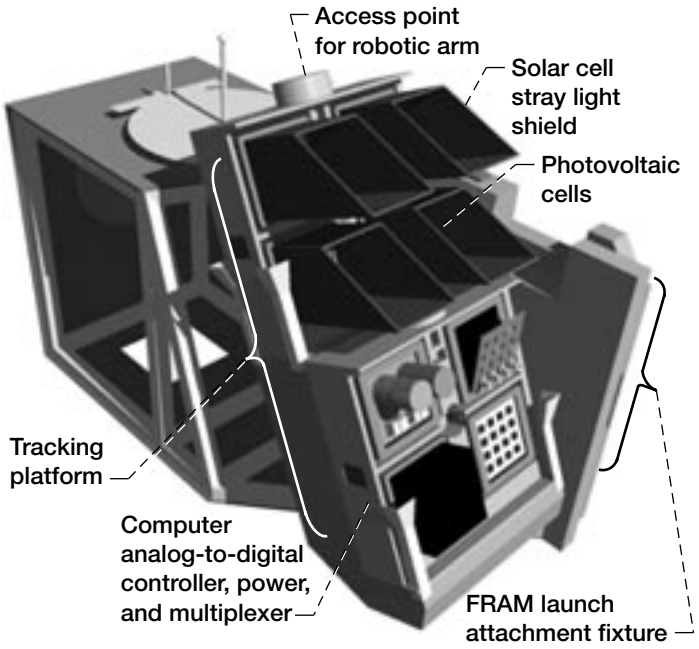

Photovoltaic Engineering Testbed (PET) facility.

Although intended for the testing and calibration of solar cells, PET could also provide a platform for conducting active experiments in a low Earth environment for either long or short durations and could provide a rapid path for the delivery and return of those experiments. Other payloads can be accommodated at sites on PET that provide a field of view in the ram, zenith, or nadir directions, to conduct active experiments in space or to operate Earth-observing instruments.

The PET facility, shown in this illustration, is designed to be located on the Japanese Experiment Module Exposed Facility (JEM–EF) of the International Space Station. PET includes an articulating platform, which provides viewing angles normal to the Sun when beta angles are between 0° and 20°. This normal-incidence Sun-viewing opportunity occurs approximately 5 days during each month.

The PET facility consists of a primary carrier structure, a Beta-Angle Tracking-Platform, command and data handling systems, interface avionics, a site for Earth-viewing instruments, and two

robotically removable trays (both of which accommodate four carriers for solar cells or carriers for other devices).

The on-orbit replaceable units are both mounted on the Beta Tracking Platform. The solar cell carriers, called multicell carriers, provide for the mounting and testing of photovoltaic cells. Optionally, other devices can be flown, such as materials or electrical, mechanical, or optical systems that require testing in a low-Earth-orbit environment. Each carrier is a self-contained element with individual interfaces for power, data, command, and mounting.

Prototype test hardware for a multicell carrier has been fabricated (as shown in the photograph). The design shown has mounting locations for twenty-eight 2- by 2-cm photovoltaic cells. The carrier includes a motorized shutter, which is typically not opened until just prior to the on-orbit test. The tracking platform also has a fixed backwards tilt of 25°, which keeps the field-of-view of the solar cells above the Earth's horizon.

Prototype multicell carrier.

Each multicell carrier contains an embedded central processor and analog-to-digital converters, power and signal conditioning, and a solar-cell voltage and load-switching controller. Utilizing custom data-acquisition electronics, the system can autonomously measure and store individual solar cell temperatures and I–V curve measurements. Several weeks of test data can be stored in nonvolatile memory. Facility instrumentation will consist of a cavity radiometer and Sun position sensors to verify the incident solar flux and orientation.

A significant capability of the PET Facility is the ability to routinely replace the carriers and trays on-orbit. Carriers will be transported to and from orbit as pressurized cargo. Carriers that have completed their mission will be placed into a protective container for return to Earth as pressurized cargo. After the completed carrier is removed, the on-orbit replaceable units will be equipped with new carriers and returned to their externally mounted location on the PET facility. This cycle will be repeated to calibrate and measure new samples as often as required by the users.

Bibliography

Landis, Geoffrey A., et al.: Design Overview of the Photovoltaic Engineering Testbed (PET). AIAA Paper 2001–4971, 2001.

Landis, G.A., et al.: The Photovoltaic Engineering Testbed: Design Options and Trade-Offs. AIP Conf. Proc., M.S. ElGenk, ed., parts 1 and 2, 2000, pp. 442–447.

Landis, G.A.; and Bailey, S.G.: Photovoltaic Engineering Testbed on the International Space Station. Second World Conference, Vienna, Austria, 1998, pp. 3564–3567.

Glenn contacts:
Dr. Geoffrey A. Landis, 216–433–2238, Geoffrey.A.Landis@grc.nasa.gov; and Dr. Sheila G. Bailey, 216–433–2228, Sheila.G.Bailey@grc.nasa.gov

OAI contacts:
Phillip P. Jenkins, 216–433–2233, Phillip.P.Jenkins@grc.nasa.gov; and J. Andrew Sexton, 440–962–3066, John.A.Sexton@grc.nasa.gov

Author: Dr. Geoffrey A. Landis

Headquarters program office:
OSF, OHSF

Programs/Projects:
Human Spaceflight

Advanced Power Technologies Developed for the Starshine 3 Satellite

The need for smaller, lightweight, autonomous power systems has recently increased with the increasing focus on microsatellites and nanosatellites. The NASA Glenn Research Center has been working on the development of such systems and recently developed several power technology demonstrations in conjunction with Project Starshine (ref. 1). The Starshine 3 microsatellite is designed to measure the density of the Earth's upper atmosphere as a function of solar activity and is primarily a passive experiment. Therefore, it did not need electrical power to successfully complete its primary mission, although a power system for future Starshine satellites was desired that could be used to power additional instruments to enhance the data collected. This created an excellent opportunity to test new power technologies capable of supplying this future need. Several Government and commercial interests teamed up with Glenn to provide Starshine 3 with a small power system using state-of-the-art components. Starshine 3 is also the inaugural flight of a novel integrated microelectronic power supply (IMPS) developed at Glenn.

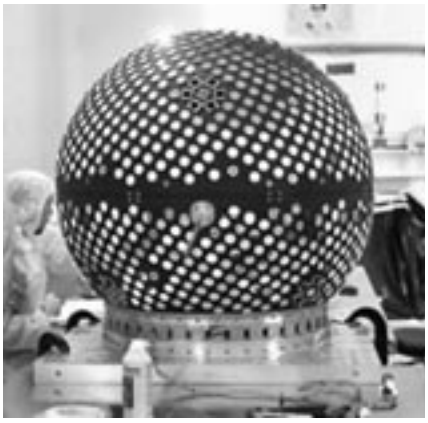

Starshine 3 satellite.

Starshine 3 is 1.0 m in diameter and has a mass of 88 kg (see the top right figure). Its surface is covered with 1500 student-polished mirrors, 31 laser retroreflectors, 48 2- by 2-cm triple-junction solar cells manufactured by Emcore Corporation, and 5 IMPS's developed at Glenn. The Starshine 3 flight marks the first time Emcore triple-junction cells have flown in space. Emcore is currently producing triple-junction cells that are 26-percent efficient at air mass zero (AM0) (ref. 2).

The Starshine 3 microsatellite was launched on a Lockheed Martin Athena I rocket from Kodiak, Alaska, on September 29, 2001. It was deployed into a 470-km orbit by a Lightband separator system developed by Planetary Systems Corp. (Washington, DC). The spacecraft has a 67° inclination, with a fixed rotational velocity of 5°/sec and an orbital period of 92 min. Data from the onboard sensors are being downloaded with a transmitter operating at a frequency of 145.825 MHz.

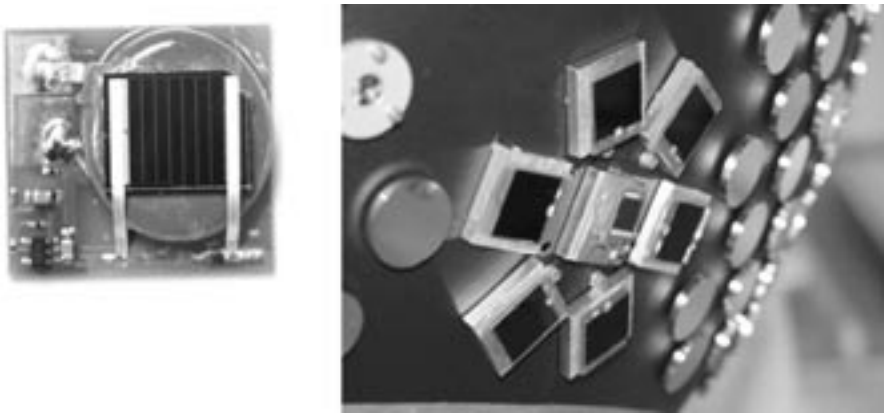

Left: Starshine 3 IMPS prototype with Panasonic battery. Right: IMPS surrounded by the Emcore triple-junction solar cells mounted on the Starshine 3 microsatellite.

The power system rechargeable battery, used for powering the satellite during the eclipse portion of the orbit, comprises three Sony 18650 lithium-ion rechargeable cells. NASA has qualified these cells for one-time (primary cells) use aboard the space shuttles, making this technology an excellent candidate for a rechargeable application. The main advantage of lithium-ion technology is its high-energy density. Lithium-ion cells weigh approximately one-fourth of what nickel-cadmium cells weigh for a given watt-hour rating.

The IMPS developed for Starshine 3 combines the generation, storage, and conditioning of power for microelectronic applications using a microphotovoltaic array, a rechargeable battery, and power management and distribution (PMAD) electronics combined into a small autonomous package. These supplies can be integrated with individual satellite components and can provide continuous power in a variety of illumination

schemes. It is a technological goal of IMPS development to have all components seamlessly integrated on a common substrate. The Starshine 3 IMPS's, which are just the first step toward this goal, will provide valuable experience in the design and operation of an IMPS in a space environment. Starshine 3 is flying the five experimental IMPS's pictured in the preceding figure. The 5-gram IMPS's are providing power for temperature sensors located around the spacecraft.

Ideally, to minimize the control electronics associated with an IMPS, researchers designed the microphotovoltaic array such that its output voltage matches the voltage needs of the battery and its current output is sufficient to charge the battery while simultaneously providing power to the load. The precise sizing of the array and battery will also depend on the anticipated illumination scheme. For example, in a typical 90-min low-Earth-orbit period, the battery will have to support the electrical load for 35 min of eclipse. During the 55-min insolation (daylight) period, the solar array will have to provide load power while fully recharging the battery. The IMPS we developed combines a seven-cell, 1-cm^2 gallium arsenide (GaAs) microphotovoltaic array produced at Glenn, with a Panasonic ML2020 rechargeable manganese dioxide lithium-ion battery (see the preceding figure) (ref. 3). This 3.0-V "coin cell" battery has a diameter of 2.0 cm, a thickness of 2.0 mm, a mass of 2.2 g, and a nominal capacity of 45.0 mA-hr.

References

1. Project Starshine. http://www.azinet.com/starshine/ (accessed Sept. 2001).
2. Solar Cells. http://www.emcore.com/html_documents/Photovoltaics.htm (accessed Sept. 2001).
3. Raffaelle, R.P., et al.: Integrated Microelectronic Power Supply (IMPS). 36th Intersociety Energy Conversion Engineering Conference, vol. 1, 2001.

Glenn contacts:
David Wilt, 216–433–6293, David.M.Wilt@grc.nasa.gov; and Dr. Aloysius F. Hepp, 216–433–3835, Aloysius.F.Hepp@grc.nasa.gov

Authors:
Dr. Ryne P. Raffaelle, Phillip P. Jenkins, David M. Wilt, David A. Scheiman, and Dr. Aloysius F. Hepp

Headquarters program office: OSS

Programs/Projects: DDF

High-Power Electromagnetic Thruster Being Developed

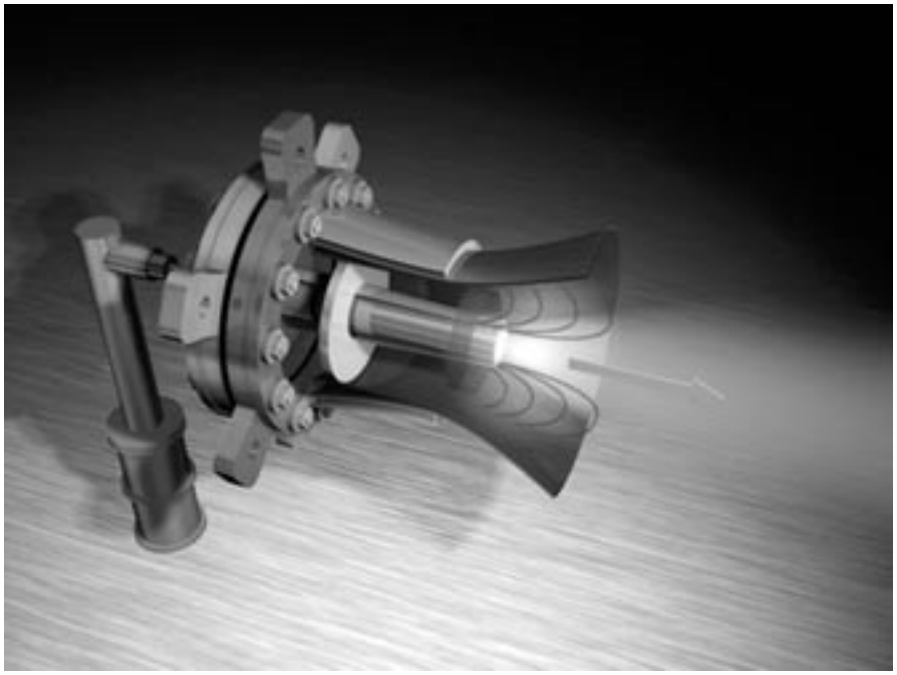

Magnetoplasmadynamic thruster. (Copyright J. MacNeill, used with permission.)

High-power electromagnetic thrusters have been proposed as primary in-space propulsion options for several bold new interplanetary and deep-space missions. As the lead center for electric propulsion, the NASA Glenn Research Center designs, develops, and tests high-power electromagnetic technologies to meet these demanding mission requirements. Two high-power thruster concepts currently under investigation by Glenn are the magnetoplasmadynamic (MPD) thruster and the Pulsed Inductive Thruster (PIT).

The MPD thruster (see the figure to the left) consists of a central cathode surrounded by a concentric anode. A high-current arc struck between the anode and cathode ionizes and accelerates a gas (plasma) propellant. In self-field versions of the thruster, an

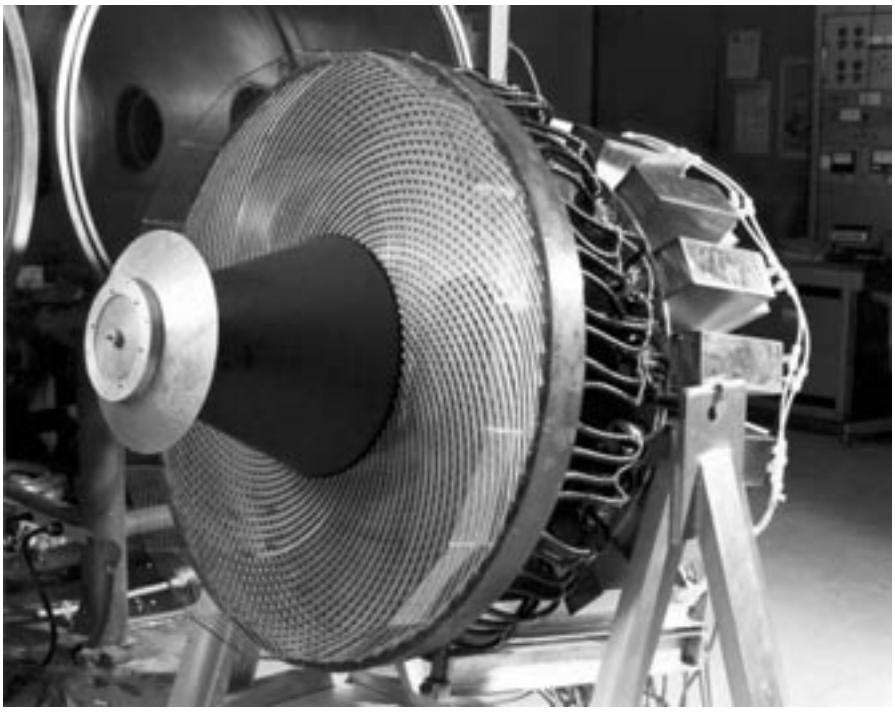

Pulsed inductive thruster. (Copyright TRW, Inc.; used with permission.)

azimuthal magnetic field generated by the current returning through the cathode interacts with the radial discharge current flowing through the plasma to produce an axial electromagnetic body force, providing thrust. In applied field-versions of the thruster, a magnetic field coil surrounding the anode is used to provide additional radial and axial magnetic fields that can help stabilize and accelerate the plasma propellant. For high-power testing at Glenn, current is supplied to the thruster by a 250-kJ capacitor bank that can provide up to 30-MW to the thruster for 2 msec. This time, though short, is sufficient to mimic steady-state thruster operation, and it allows a number of thruster designs to be quickly and economically evaluated. Planned activities include continuation of the high-power pulsed MPD experiments to improve thruster efficiencies, and refurbishment of a steady-state thruster facility to provide extended thruster operation and life testing at sub-megawatt power levels.

High-power electric propulsion team and technical support personnel.

A second high-power device under investigation, the PIT, was developed by TRW, Inc., with funding by the Department of Defense and Glenn. In its basic form, the PIT consists of a flat spiral coil covered by a thin dielectric plate (see the photograph to the left). A pulsed-gas injection nozzle distributes a thin layer of gas propellant across the plate surface at the same time that a pulsed high-current discharge is sent through the coil. The rising current creates a time-varying magnetic field, which in turn induces a strong azimuthal electric field above the coil. The electric field ionizes the gas propellant and generates an azimuthal current flow in the resulting plasma. The current in the plasma and the current in the coil flow in opposite directions, providing a mutual repulsion that rapidly blows the ionized propellant away from the plate to provide thrust. The thrust and specific impulse can be tailored by adjusting the discharge power, pulse repetition rate, and propellant mass flow, and there is minimal, if any, erosion because of the electrodeless nature of the discharge. The PIT has been tested at TRW in single-shot operation and has demonstrated 50-percent efficiency over a wide range of specific impulses. Glenn is currently using the MACH2 code to simulate PIT plasma formation and acceleration processes in an effort to better understand and improve thruster performance. Planned activities include rebuilding the single-shot PIT with solid-state switches to evaluate its performance at the high repetition rates required for in-space propulsion.

In concert with a strong numerical modeling program, the goal of the experimental high-power thruster program is to provide efficient, megawatt-class electromagnetic thrusters capable of several thousand hours of continuous operation. Because of their higher exhaust velocities, these devices can perform a variety of challenging missions with significantly less propellant than chemical rockets. For a given spacecraft launch mass, the reduced propellant mass allows more payload to be carried into orbit, requiring fewer launches and less cost for a given total mission mass. Alternatively, the lower propellant mass requirements can be used to reduce the total spacecraft mass at launch, with a corresponding reduction in launch vehicle class and associated launch costs. Providing robust and economical in-space transportation, Glenn is leading the way for these high-power plasma thrusters of the future.

OAI contacts:
Dr. Michael R. LaPointe, 216–433–6192, Michael.R.LaPointe@grc.nasa.gov; and Dr. Pavlos G. Mikellides, 440–962–3164, Pavlos.G.Mikellides@grc.nasa.gov

Glenn contact: Dr. Dhanireddy R. Reddy, 216–433–8133, Dhanireddy.R.Reddy@grc.nasa.gov

Authors: Dr. Michael R. LaPointe and Dr. Pavlos G. Mikellides

Headquarters program office: OAT, OSS

Programs/Projects: ASTP

Magnetohydrodynamic MACH Code Used to Simulate Magnetoplasmadynamic Thrusters

The On-Board Propulsion program at the NASA Glenn Research Center is utilizing a state-of-the-art numerical simulation to model the performance of high-power electromagnetic plasma thrusters. Such thrusters are envisioned for use in lunar and Mars cargo transport, piloted interplanetary expeditions, and deep-space robotic exploration of the solar system. The experimental portion of this program is described in reference 1. This article describes the numerical modeling program used to guide the experimental research. The synergistic use of numerical simulations and experimental research has spurred the rapid advancement of high-power thruster technologies for a variety of bold new NASA missions.

From its inception as a U.S. Department of Defense code in the mid-1980's, the Multiblock Arbitrary Coordinate Hydromagnetic (MACH) simulation tool has been used by the plasma physics community to model a diverse range of plasma problems—including plasma opening switches, inertial confinement fusion concepts, compact toroid formation and acceleration, z-pinch implosion physics, laser-target interactions, and a variety of plasma thrusters. The MACH2 code used at Glenn is a time-dependent, two-dimensional, axisymmetric, multimaterial code with a multiblock structure. MACH3, a more recent three-dimensional version of the code, is currently undergoing beta tests. The MACH computational mesh moves in an arbitrary Lagrangian-Eulerian (ALE) fashion that allows the simulation of diffusive-dominated and dispersive-dominated problems, and the mesh can be refined via a variety of adaptive schemes to capture regions of varying characteristic scale. The mass continuity and momentum equations model a compressible viscous fluid, and three energy equations are used to simulate nonthermal equilibrium between electrons, ions, and the radiation field. Magnetic fields are modeled by an induction equation that includes resistive diffusion, the Hall effect, and a thermal source for magnetic fields. Various models of plasma resistivity are included, along with ablation models and multiport circuit solvers. The set of equations is closed using either an ideal gas or real equation of state.

The code was used recently at Glenn to simulate the performance of megawatt-class self-field magnetoplasmadynamic thrusters with material expansion nozzles (see the top figure on the next page). Such devices may offer improved efficiency over conventional self-field thrusters through the enhanced recovery of frozen flow losses. Additional modeling efforts are underway to simulate the

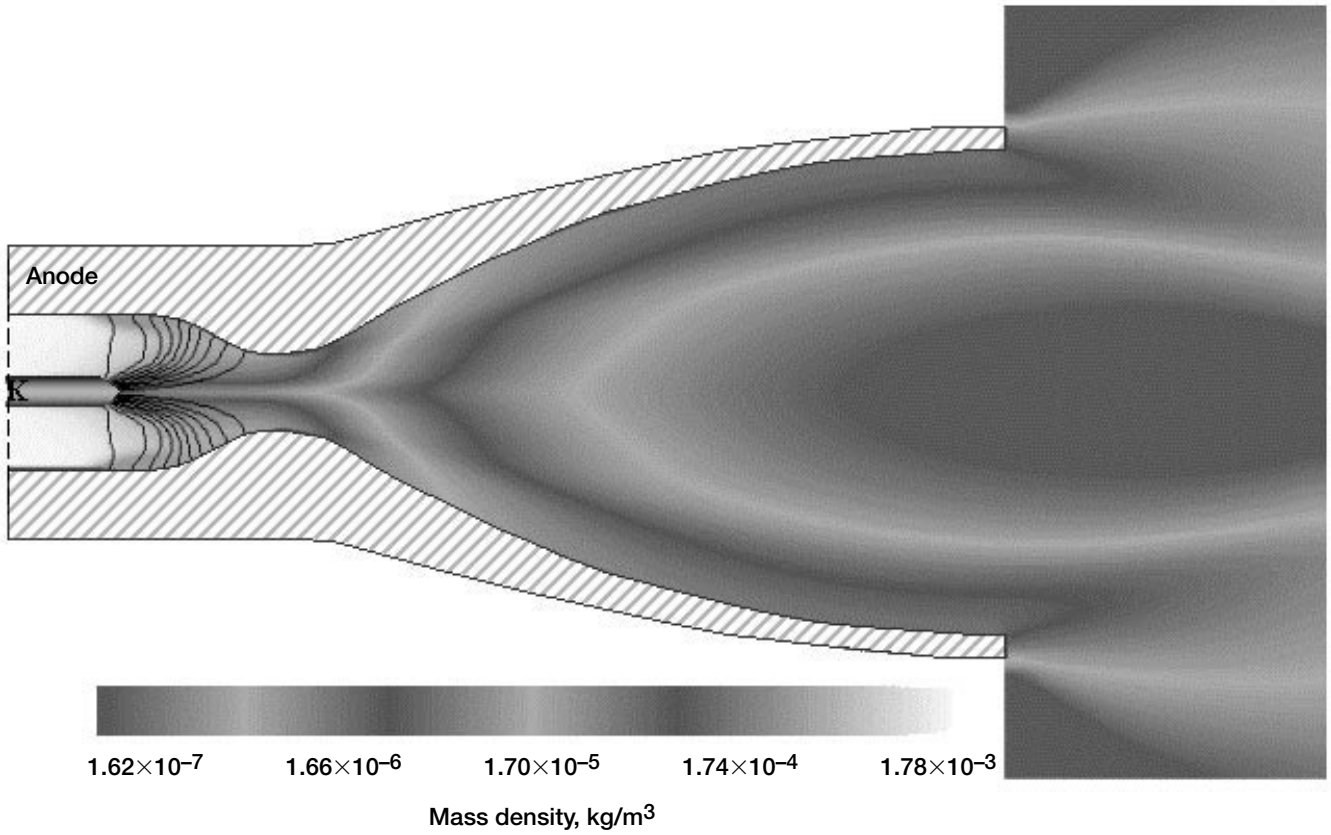

Superimposed current (line contours at 10-percent increments) and mass density (flooded contours) distributions from a MACH2 magnetoplasmadynamic thruster simulation. Hydrogen mass flow, 1.37 g/sec; thruster current, 6 kA. This figure is shown in color in the online version of this article (http://www.grc.nasa.gov/WWW/RT2001/5000/5430lapointe.html).

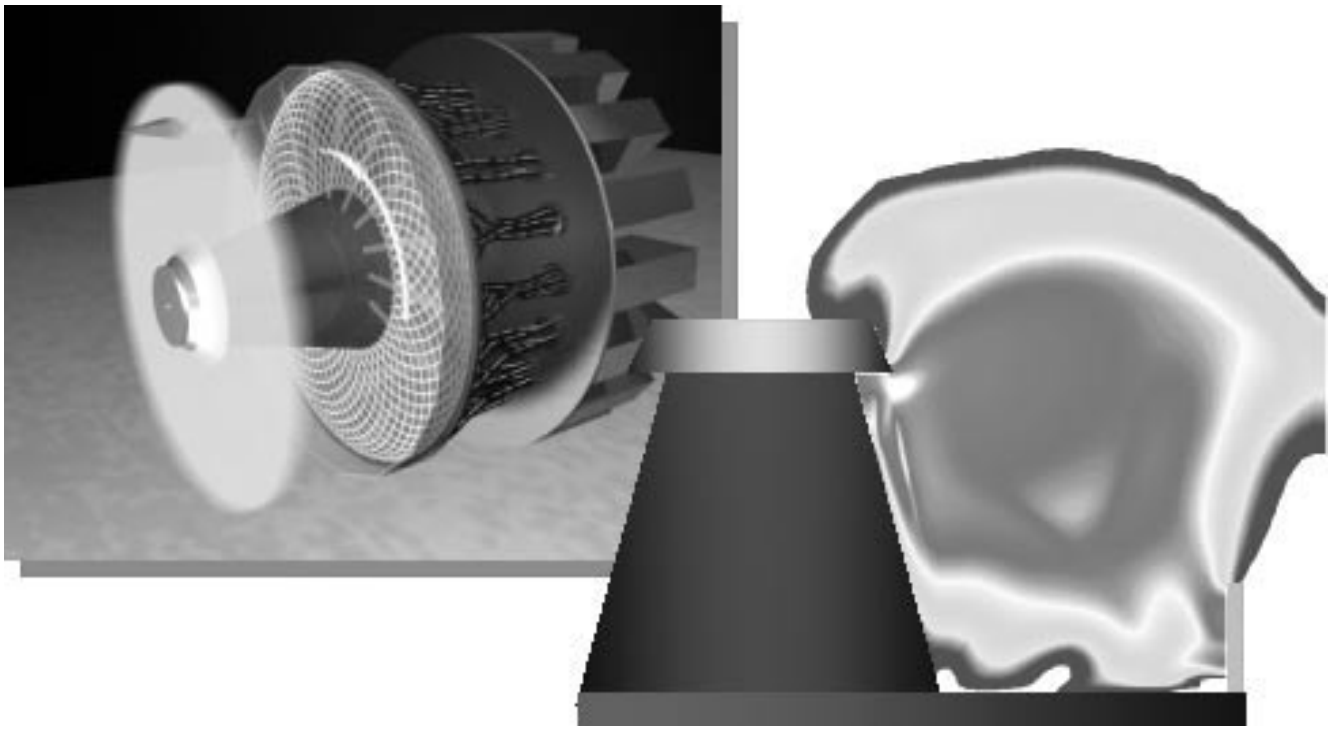

Pulsed Inductive Thruster hardware, basic acceleration mechanism, and MACH2-simulated mass density distribution. This figure is shown in color in the online version of this article (http://www.grc.nasa.gov/WWW/RT2001/5000/5430lapointe.html).

performance of the TRW Pulsed Inductive Thruster (see the bottom figure on the preceding page), an electrodeless device that may circumvent the material erosion limits of conventional plasma thrusters to provide high efficiency over a range of specific impulse values.

Reference

1. LaPointe, Michael R.; and Mikellides, Pavlos G.: High-Power Electromagnetic Thruster Being Developed. Research & Technology 2001, NASA/TM—2002-211333, 2002, pp. 51–53.

OAI contact: Dr. Michael R. LaPointe, 216–433–6192, Michael.R.LaPointe@grc.nasa.gov

Glenn contact: Dr. Dhanireddy R. Reddy, 216–433–8133, Dhanireddy.R.Reddy@grc.nasa.gov

Authors: Dr. Pavlos G. Mikellides and Dr. Michael R. LaPointe

Headquarters program office: OAT, OSS

Programs/Projects: ASTP

Next-Generation Ion Propulsion Being Developed

Left: Deep Space 1 thruster. Right: 40-cm engine.

The NASA Glenn Research Center ion-propulsion program addresses the need for high-specific-impulse systems and technology across a broad range of mission applications and power levels. One activity is the development of the next-generation ion-propulsion system as a follow-on to the successful Deep Space 1 system. The system is envisioned to incorporate a lightweight ion engine that can operate over 1 to 10 kW, with a 550-kg propellant throughput capacity. The engine concept under development has a 40-cm beam diameter, twice the effective area of the Deep Space 1 engine. It incorporates mechanical features and operating conditions to maximize the design heritage established by the Deep Space 1 engine, while incorporating new technology where warranted to extend the power and throughput capability. Prototype versions of the engine have been fabricated and are under test at NASA, with an engineering model version in manufacturing. Preliminary performance data for the prototype engine have been documented over 1.1- to 7.3-kW input power. At 7.3 kW, the engine efficiency is 0.68, at 3615-sec specific impulse. Critical component temperatures, including those of the discharge cathode assembly and magnets, have been documented and are within established limits, with significant margins relative to the Deep Space 1 engine.

The 1- to 10-kW ion thruster approach described here was found to provide the needed power and performance improvement to enable important NASA missions. The Integrated In-Space Transportation Planning (IISTP) studies compared many potential technologies for various NASA, Government, and commercial missions. These studies indicated that a high-power ion propulsion system is the most important technology for development because of its outstanding performance versus perceived development and recurring costs for interplanetary solar electric propulsion missions. One of the best applications of a high-power electric propulsion system was as

an integral part of a solar electric propulsion (SEP) stage to send a payload to outer planet targets. The IISTP studies showed that either trip time or launch vehicle class could be significantly reduced when compared with state-of-the-art systems.

Find out more about this research: http://www.grc.nasa.gov/www/ion/

Glenn contact:
Michael J. Patterson, 216–977–7481, Michael.J.Patterson@grc.nasa.gov

Authors:
Michael J. Patterson, Dr. John E. Foster, Thomas W. Haag, Luis R. Piñero, Vincent K. Rawlin, George C. Soulas, and S. Michelle Doehne

Headquarters program office: OSS

Programs/Projects:
Missions of interest include Titan Explorer, Neptune Orbiter, other interplanetary missions, and SEP.

Modular 5-kW Power-Processing Unit Being Developed for the Next-Generation Ion Engine

The NASA Glenn Research Center is developing a 5- to 10-kW ion engine for a broad range of mission applications. Simultaneously, a 5-kW breadboard power-processing unit (PPU) is being designed and fabricated by Boeing Electron Dynamic Devices, Torrance, California, under contract with Glenn. The beam supply, which processes up to 90 percent of the power into this unit, consists of four 1.1-kW power modules connected in parallel, equally sharing the output current. The modular design allows scalability to higher powers as well as the possibility of implementing an $N + 1$ redundant beam supply. A novel phase-shifted/pulse-width-modulated, dual full-bridge topology was chosen for this module design for its efficient switching characteristics.

A breadboard version of the beam power supply module was assembled. Efficiencies ranging between 91.6 and 96.9 percent were measured for an input voltage range of 80 to 160 V, an output voltage range of 800 to 1500 V, and output powers from 0.3 to 1.0 kW. This beam supply could result in a PPU with a total efficiency between 93 and 95 percent at a nominal input voltage of 100 V. This is up to a 4-percent improvement over the state-of-the-art PPU used for the Deep Space 1 mission. A flight-packaged PPU is expected to weigh no more than 15 kg, which represents a 50-percent reduction in specific mass from the Deep Space 1 design. This will make 5-kW ion propulsion very attractive for many planetary missions.

Glenn contact: Luis R. Piñero, 216–977–7428, Luis.R.Pinero@grc.nasa.gov

Authors: Luis R. Piñero, Thomas H. Bond, Don Okada, Keith Phelps, Janusz Pyter, and Steve Wiseman

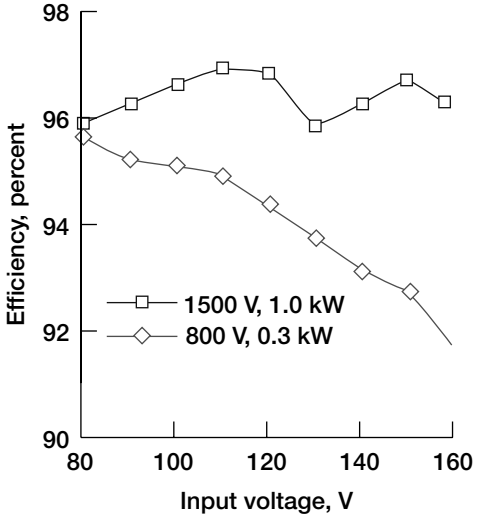

Beam power module efficiency versus input voltage.

Headquarters program office: OSS

Programs/Projects: The 5- to 10-kW ion propulsion system will benefit/enable many inner planet missions (Mars, Venus, or comet sample return), outer planets missions (Pluto Flyby, Neptune Orbiter, Titan Explorer), and GEO spacecraft (orbit insertion or NSSK).

13-kV Ion-Extraction System Being Developed for Inert Gas Ion Engines

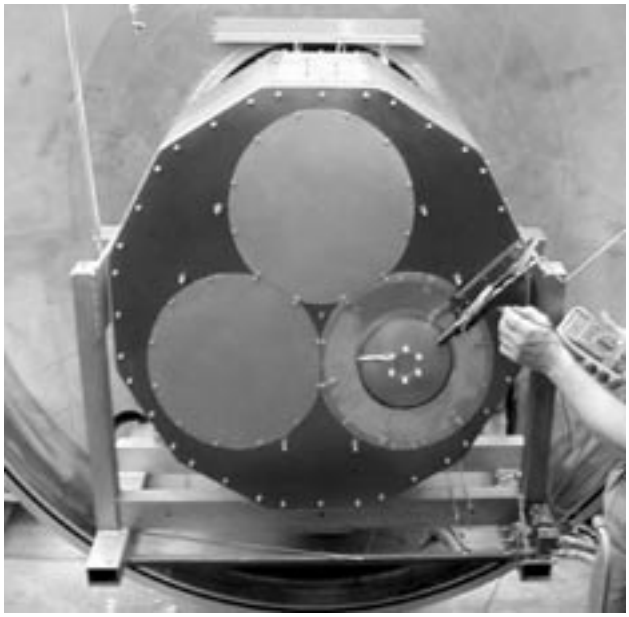

76-cm-diameter thruster with subscale grids tested to a 13,000-V beam voltage.

A high-voltage ion optics design was chosen for an assumed outer planet or interstellar precursor mission that would require a long-life, high-power, high-specific-impulse krypton ion engine. Such an engine could support energetic space missions to the outer planets or beyond. Detailed performance and lifetime analyses and several inexpensive subscale grid tests were conducted at the NASA Glenn Research Center and at the Colorado State University under a NASA Glenn grant. A subscale grid set of the selected geometry (shown in the photograph) was tested at voltages up to 13,000 V. This yielded a krypton ion beam current that would, when scaled to a full-size 50-cm diameter, produce an ion beam with a power of 30 kW at a specific impulse over 14,000 sec. The operational ion beam focusing limits, as a function of ion current per hole, were found to impose requirements of high uniformity on the discharge chamber plasma density. A full-size set of two-grid, 50-cm-diameter titanium ion optics has been fabricated and awaits testing.

Glenn contact:
Vincent Rawlin, 216–977–7462,
Vincent.K.Rawlin@grc.nasa.gov

Authors: Vincent K. Rawlin, George J. Williams, and Paul Wilbur

Headquarters program office:
OAT (Colorado State University work funded under Grant NAG3–1801)

Programs/Projects:
Backup for solar sail propulsion for OSS deep space missions

Deep Space 1 Ion Engine Completed a 3-Year Journey

A xenon ion engine and power processor system, which was developed by the NASA Glenn Research Center in partnership with the Jet Propulsion Laboratory and Boeing Electron Dynamic Devices, completed nearly 3 years of operation aboard the Deep Space 1 spacecraft. The 2.3-kW ion engine, which provided primary propulsion and two-axis attitude control, thrusted for more than 16,000 hr and consumed more than 70 kg of xenon propellant.

The Deep Space 1 spacecraft was launched on October 24, 1998, to validate 12 futuristic technologies, including the ion-propulsion system. After the technology validation process was successfully completed, the Deep Space 1 spacecraft flew by the small asteroid Braille on July 29, 1999. The final objective of this mission was to encounter the active comet Borrelly, which is about 6 miles long. The ion engine was on a thrusting schedule to navigate the Deep Space 1 spacecraft to within 1400 miles of the comet. Since the hydrazine used for spacecraft attitude control was in short supply, the ion engine also provided two-axis attitude control to conserve the hydrazine supply for the Borrelly encounter. The comet encounter took place on September 22, 2001. Dr. Marc Rayman, project manager of Deep Space 1 at the Jet Propulsion Laboratory said, "Deep Space 1 plunged into

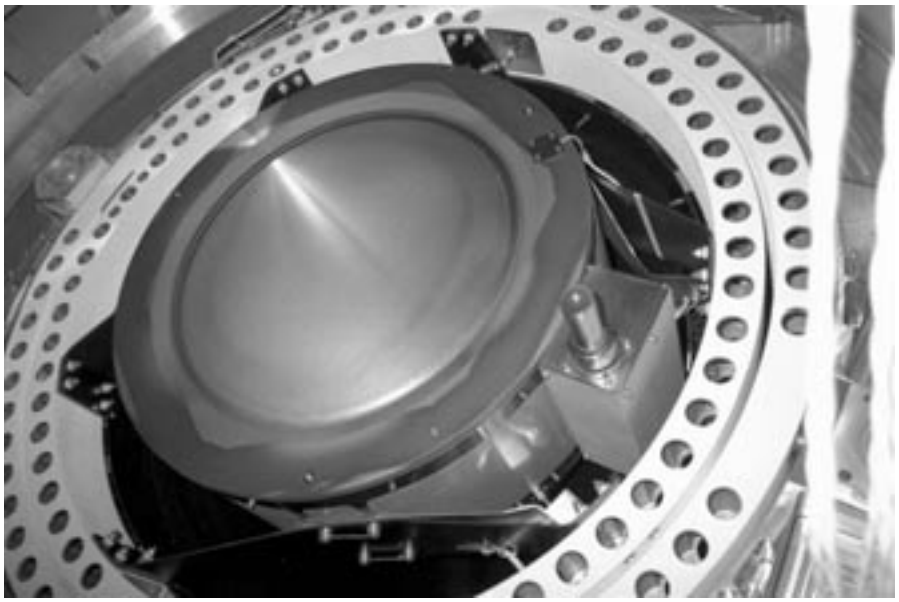

30-cm-diameter ion engine mounted to the Deep Space 1 spacecraft gimbal ring.

the heart of the comet Borrelly and has lived to tell every detail of its spine-tingling adventure! The images are even better than the impressive images of comet Halley taken by Europe's Giotto spacecraft in 1986." The Deep Space 1 mission, which successfully tested the 12 high-risk, advanced technologies and captured the best images ever taken of a comet, was voluntarily terminated on December 18, 2001.

The successful demonstration of the 2-kW-class ion propulsion system technology is now providing mission planners with off-the-shelf flight hardware. Higher power, next-generation ion propulsion systems are being developed for large flagship missions, such as outer planet explorers and sample-return missions.

Find out more about this research:
Glenn's role in Deep Space 1:
http://www.grc.nasa.gov/WWW/PAO/ds1.htm

Deep Space 1:
http://nmp.jpl.nasa.gov/ds1/

Glenn contact:
James S. Sovey, 216–977–7454, James.Sovey@grc.nasa.gov

Authors:
James S. Sovey, Michael J. Patterson, Vincent K. Rawlin, and John A. Hamley

Headquarters program office:
OAT, OSS

Programs/Projects:
Deep Space 1, NSTAR

Special recognition: Northern Ohio Live Award of Achievement, 1999; Aviation Week & Space Technology 42nd Annual Aerospace Laurels, 1999; NASA Turning Goals into Reality Award, 2001; Discover Magazine's Award for Technological Innovation, 1999.

Flywheel Charge/Discharge Control Developed

A control algorithm developed at the NASA Glenn Research Center will allow a flywheel energy storage system to interface with the electrical bus of a space power system. The controller allows the flywheel to operate in both charge and discharge modes. Charge mode is used to store additional energy generated by the solar arrays on the spacecraft during insolation. During charge mode, the flywheel spins up to store the additional electrical energy as rotational mechanical energy. Discharge mode is used during eclipse when the flywheel provides the power to the spacecraft. During discharge mode, the flywheel spins down to release the stored rotational energy.

The algorithm is based on careful control of the permanent magnet electrical motor/generator that is attached to the flywheel. In charge mode, a constant dc charging current command is provided to the flywheel system. This command is converted into an appropriate ac current command into the motor, and the flywheel spins up. In discharge mode, the flywheel system must maintain the dc bus voltage regulation in addition to supplying the load current. This is accomplished by commanding an ac current from the motor that is related to the current required by the spacecraft load and the measured dc bus value. If the dc bus voltage starts to drop, the current drawn from the motor and the deceleration of the flywheel increases. If the dc bus voltage starts to rise, the current drawn from the motor and the deceleration of the flywheel decreases. In this manner, the flywheel system can provide the necessary current to the load while maintaining the dc bus voltage.

A 350-W-hr flywheel system using magnetic bearings, an adjustable electronic load, and a dc power supply with current limiting was used at Glenn to demonstrate the concept (see the photograph).

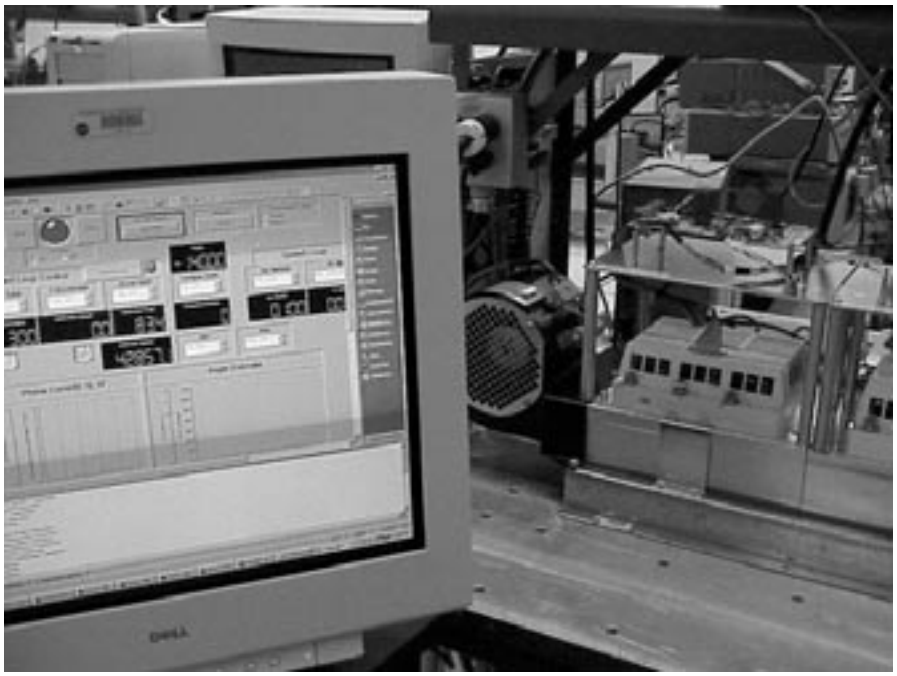

350-W-hr flywheel system.

The flywheel was accelerated to between 10,000 and 15,000 rpm under charge mode, or constant current command, conditions. Then the dc power supply was disconnected, simulating discharge mode, and the flywheel system provided the power to the load while maintaining the bus voltage regulation. Tests were conducted by adding and subtracting load while in discharge mode, and the system was shown to be able to maintain the dc bus voltage regulation.

Flywheels require a sophisticated set of power electronics and controls to allow them to be charged during sunlight and discharged during eclipse. This accomplishment provides a design for such a system that can be further developed into a product for use on satellites and the International Space Station. Future work includes developing additional algorithms to control multiple flywheels so that the attitude control and energy storage functions in future spacecraft can be combined.

Glenn contacts:
Raymond Beach, 216–433–5320, Raymond.F.Beach@grc.nasa.gov; and Barbara Kenny, 216–433–6289, Barbara.H.Kenny@grc.nasa.gov

Authors: Raymond F. Beach and Barbara H. Kenny

Headquarters program office: OAT, OSF

Programs/Projects: Flywheels

Intelligent dc-dc Converter Technology Developed and Tested

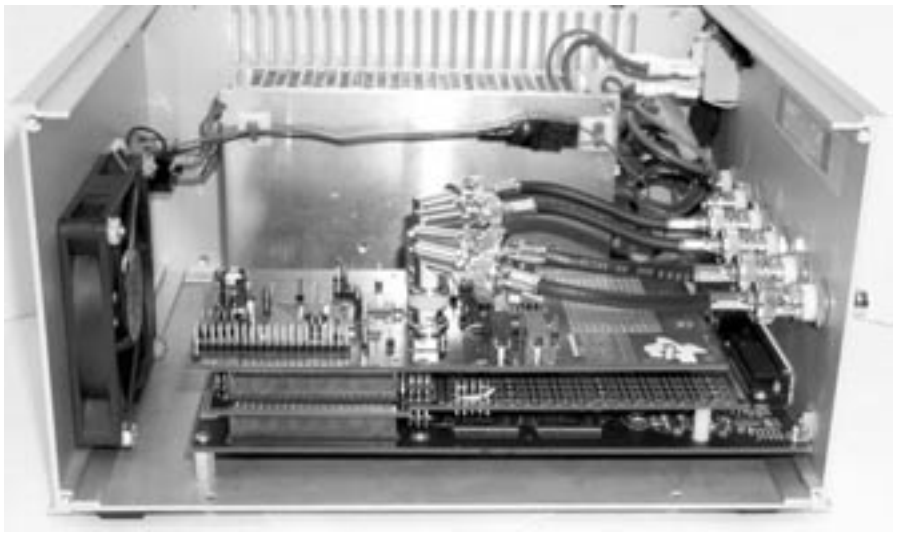

Prototype digital controller for the intelligent dc-dc converter.

The NASA Glenn Research Center and the Cleveland State University have developed a digitally controlled dc-dc converter (see the photograph) to research the benefits of flexible, digital control on power electronics and systems. Initial research and testing has shown that conventional dc-dc converters can benefit from improved performance by using digital-signal processors and nonlinear control algorithms.

A standalone digital controller has been integrated with a 1-kW full-bridge dc-dc converter to evaluate digital-control algorithms. The standalone digital controller is

made of four circuit boards packaged in one assembly: a digital-signal processor board, a complex programmable logic device board, an analog-to-digital converter board, and an analog signal isolation board. The analog signal isolation board isolates and filters the dc-dc converter output voltage signal, the analog-to-digital converter board converts the analog signal to a digital signal, and the digital-signal processor board runs the data through the nonlinear control algorithms. The complex programmable logic device board manages the pulse-width-modulation switching of the dc-dc converter transistors through four discrete digital signals.

A unique nonlinear control algorithm was developed and has shown superior performance over its linear counterpart. Using the digital controller, 1-kW dc-dc converter, and the nonlinear control algorithm, the controller has demonstrated a load transient response time improvement of 150 percent along with a 50-percent reduction in the load transient magnitude.

Future work includes the research of digital control algorithms that can tailor the converter's impedance, reduce electromagnetic interference in the system, and guarantee stable operation under all conditions. These advances will result in dc-dc converters with improved performance and electrical power systems with lower design and integration costs.

Glenn contact:
Robert M. Button, 216–433–8010,
Robert.M.Button@grc.nasa.gov

Author: Robert M. Button

Headquarters program office: OSS

Programs/Projects:
Advanced Power and On-Board Propulsion Technology Development

Solid-Body Fuse Developed for High-Voltage Space Power Missions

AEM Incorporated has completed the development, under a NASA Glenn Research Center contract, of a solid-body fuse for high-voltage power systems of satellites and spacecraft systems. High-reliability fuses presently defined by MIL–PRF–23419 do not meet the increased voltage and amperage requirements for the next generation of spacecraft. Solid-body fuses exhibit electrical and mechanical attributes that enable these fuses to perform reliably in the vacuum and high-vibration and -shock environments typically present in spacecraft applications. The construction and screening techniques for solid-body fuses described by MIL–PRF–23419/12 offer an excellent roadmap for the development of high-voltage solid-body fuses.

Conventional fuses are constructed with a wire filament that passes through a hollow cavity; solid-body fuses are designed and constructed in a manner that ensures that the overall fuse package is substantially devoid of air. The fusible element is composed of thick-film gold or silver that is deposited on a thermally and electrically insulated substrate. A complete range of

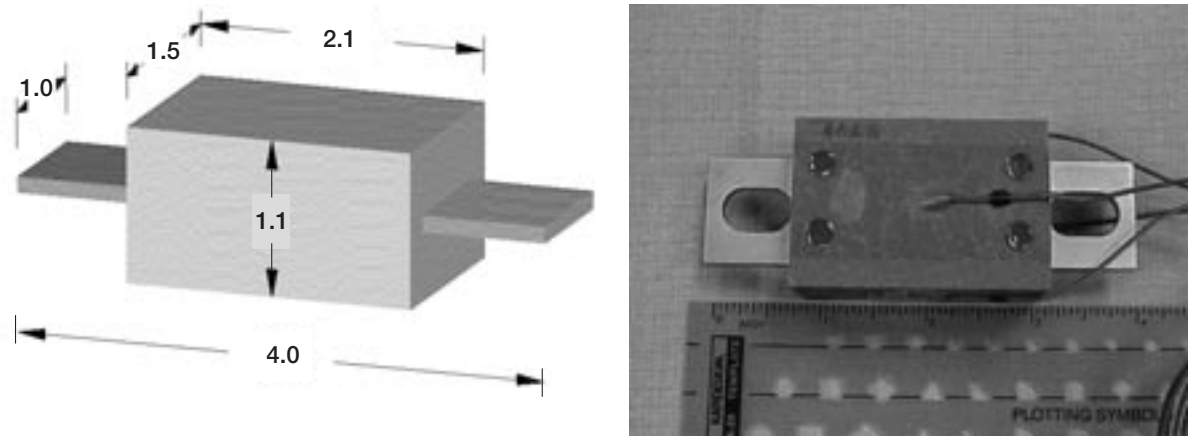

AEM's 400-V 100-A prototype fuse.

fusing values is achievable by precisely controlling the fusible element print thickness and geometry. Thick-film silver termination pads are placed at each end of the thick-film fusible element. The fusible element is completely covered with an arc-suppressive ceramic composite. Copper leads with gold plating are attached to the silver terminations with high-temperature solder. The final fuse package is insert-molded with an engineering thermoplastic to complete the fuse.

The fuses delivered to Glenn are rated at 400 Vdc at 100 A. Increased amperage can be realized if electrically paralleled fuses are used. For example, a 400-Vdc, 500-A fusing requirement would be satisfied by the installation of five electrically matched 400-Vdc, 100-A fuses. The short-circuit interrupt rating for the 400-Vdc fuses is 10,000 A. The total weight of each fuse is about 156 g, and the outside dimensions are 3.9 in. long, 1.5 in. wide, and 1 in. high.

Glenn contacts:
James L. Dolce, 216–433–8052, James.L.Dolce@grc.nasa.gov; and Anastacio N. Baez, 216–433–5318, Anastacio.N.Baez@grc.nasa.gov

Authors:
James L. Dolce and Anastacio N. Baez

Headquarters program office:
OSF (Space Shuttle Program Office)

Programs/Projects:
RLV, Orbiter Upgrade

Sensitive Technique Developed Using Atomic Force Microscopy to Measure the Low-Earth-Orbit Atomic Oxygen Erosion of Polymers

A recession measurement technique has been developed at the NASA Glenn Research Center to determine the atomic oxygen durability of polymers exposed to the space environment for short durations. Polymers such as polyimide Kapton and Teflon FEP (fluorinated ethylene propylene, DuPont) are commonly used in spacecraft because of their desirable properties, such as flexibility, low density, and in the case of FEP, low solar absorptance and high thermal emittance. Polymers on the exterior of spacecraft in the low-Earth-orbit environment are exposed to energetic atomic oxygen, resulting in erosion and potential structural loss. It is, therefore, important to understand the atomic oxygen erosion yield (*E*, the volume loss per incident oxygen atom) of polymers being considered in spacecraft design. Because long-term space exposure data are rare and very costly, short-term exposures, such as on the space shuttles, are often relied on for atomic oxygen erosion determination. The most common technique for determining *E* is through mass-loss measurements. For limited-duration exposure experiments, such as shuttle flight experiments,

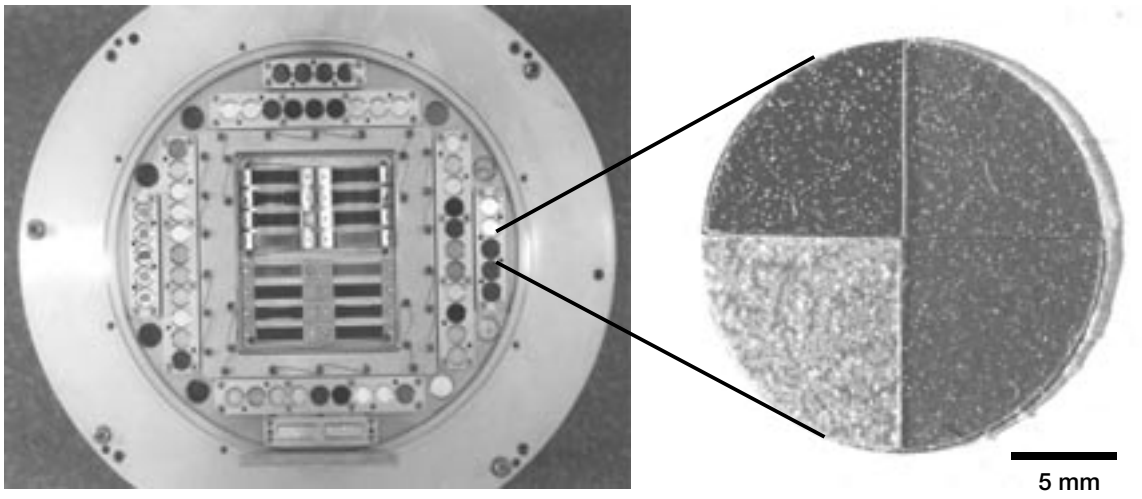

Example of a salt-sprayed, multiple-polymer flight sample prepared and flown for characterization using the AFM recession technique. This photograph shows the Limited Duration Candidate Exposure (LDCE–4) flight hardware and polymer sample prior to flight aboard the shuttle during STS–51.

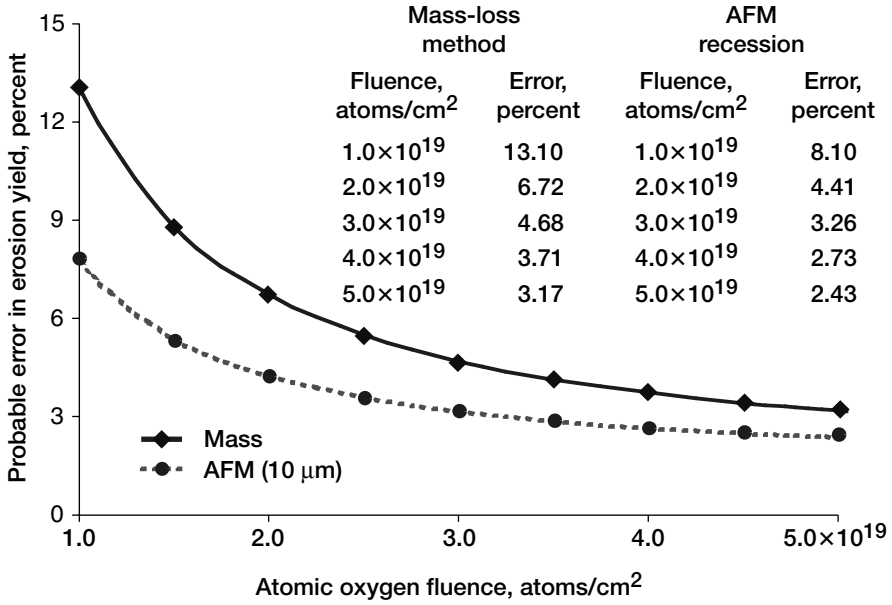

Comparison of the percent probable error in the atomic oxygen erosion yields as a function of atomic oxygen fluence for the mass loss and AFM recession (10-μm particle height) techniques for low atomic oxygen fluences.

the atomic oxygen fluence is often so small that mass-loss measurements are not sensitive enough. Therefore, a recession measurement technique has been developed at Glenn to obtain accurate erosion yields of polymers exposed to low atomic oxygen fluences.

The technique developed at Glenn is based on recession measurements. It uses the selective protection of polymer samples with intimate contact particles, combined with postflight atomic force microscopy (AFM) analysis of recession, or erosion depths, to obtain accurate erosion yields. Two methods of protection have been proposed, salt spraying and mica dusting. Specific procedures and characterization issues have been studied at Glenn with collaborative help from Hathaway Brown School for girls and Manchester College. These issues include salt spraying, salt crystal variations, potential problems with salt-rings and condensation, and mica-dusting issues. Also studied were the specific atomic force microscope (AFM) procedures necessary for this technique. For example, a salt-sprayed sample flown as part of the Limited Duration Candidate Exposure (LDCE–4) shuttle flight experiment on STS–51 was used to study the use of contact- versus noncontact-mode imaging for determining erosion depth measurements. Analyses indicate that contact-mode measurements can be used for erosion depth measurement without significantly degrading the samples.

This AFM recession technique has the advantage that very small sample areas can be used to obtain erosion yield data, and multiple polymers can be put together as one flight sample. Error analyses were computed for this technique and for the traditional erosion yield determination technique based on mass loss, and both were highly dependent on the atomic oxygen fluence as expected. The recession technique was found to be very dependent on the protective particle height in addition to the atomic oxygen fluence, and it was found to be more accurate than the mass-loss technique for protective particles less than 17 μm thick. For example, for a fluence of 1×10^{19} atoms/cm^2, the probable error in the atomic oxygen erosion yield for the AFM recession technique (using a 10-μm-thick protective particle) is approximately 60 percent of the mass loss uncertainty (7.7 versus 13.1 percent, respectively).

Glenn researchers plan to use this AFM recession depth technique to determine the erosion yield of 42 different polymers in the shuttle flight experiment Polymer Erosion and Contamination Experiment (PEACE) a collaborative experiment between Glenn and Hathaway Brown School potentially to be flown in 2002 or 2003. As part of PEACE, identical polymers will be flown and their erosion yields determined using the mass-loss technique, so a direct comparison between these two erosion yield techniques will be made.

Find out more about this research:

Glenn's Electro-Physics Branch:
http://www.grc.nasa.gov/WWW/epbranch/ephome.htm

PEACE Experiment Information:
http://www.grc.nasa.gov/WWW/RT1998/5000/5480degroh3.html

Hathaway Brown's PEACE information: http://www.hb.edu/school/upper/spotlight/srp/peace/default.htm

http://www.hb.edu/school/upper/spotlight/srp/peace/detailed_desc.htm

Glenn contacts:
Kim K. de Groh, 216–433–2297, Kim.K.deGroh@grc.nasa.gov; and Bruce A. Banks, 216–433–2308, Bruce.A.Banks@grc.nasa.gov

Authors:
Kim K. de Groh, Bruce A. Banks, Gregory W. Clark, Anne Hammerstrom, Erica Youngstrom, Carolyn Kaminski, Elizabeth Fine, and Laura Marx

Headquarters program office: OAT

Programs/Projects: ISS

MISSE PEACE Polymers: An International Space Station Environmental Exposure Experiment Being Conducted

As part of the Materials International Space Station Experiment (MISSE), 41 different polymers are being exposed for approximately 1 1/2 years to the low-Earth-orbit (LEO) environment on the exterior of the International Space Station. MISSE is a materials flight experiment sponsored by the Air Force Research Lab/Materials Lab and NASA and is the first external experiment on the space station. A similar set of 41 polymers will be flown as part of the Polymer Erosion and Contamination Experiment (PEACE)—a shuttle flight experiment that is being developed at the NASA Glenn Research Center collaboratively with the Hathaway Brown School for girls. Therefore, these 41 polymers are collectively called the MISSE PEACE Polymers. The purpose of the MISSE PEACE Polymers experiment is to determine how durable polymers are in the LEO space environment where spacecraft, such as the space station, orbit. Polymers are commonly used as spacecraft materials because of their desirable properties such as good flexibility, low density, and certain electrical properties or optical properties (such as a low solar absorptance and high thermal emittance). Two examples of the use of polymers on the exterior of spacecraft exposed to the space environment include metalized Teflon FEP (fluorinated ethylene propylene, DuPont) thermal control materials on the Hubble Space Telescope, and polyimide Kapton (DuPont) solar array blankets.

Atomic oxygen is the predominant species in LEO (below ≈1000 km), and spacecraft surfaces, such as polymers, that literally ram into the resident oxygen atoms are oxidized. Because the oxidation product for most polymers is a gas, atomic oxygen erosion results. Over time, complete loss of the polymer can occur if it is not properly protected. In addition to the obvious potential degradation to the structural stability of polymers, thin polymer thermal control materials are also threatened by atomic oxygen erosion because thermal emittance depends on polymer thickness. Therefore, the specific goal of the MISSE PEACE experiment is to accurately determine the atomic oxygen erosion yield of a wide variety of polymeric materials.

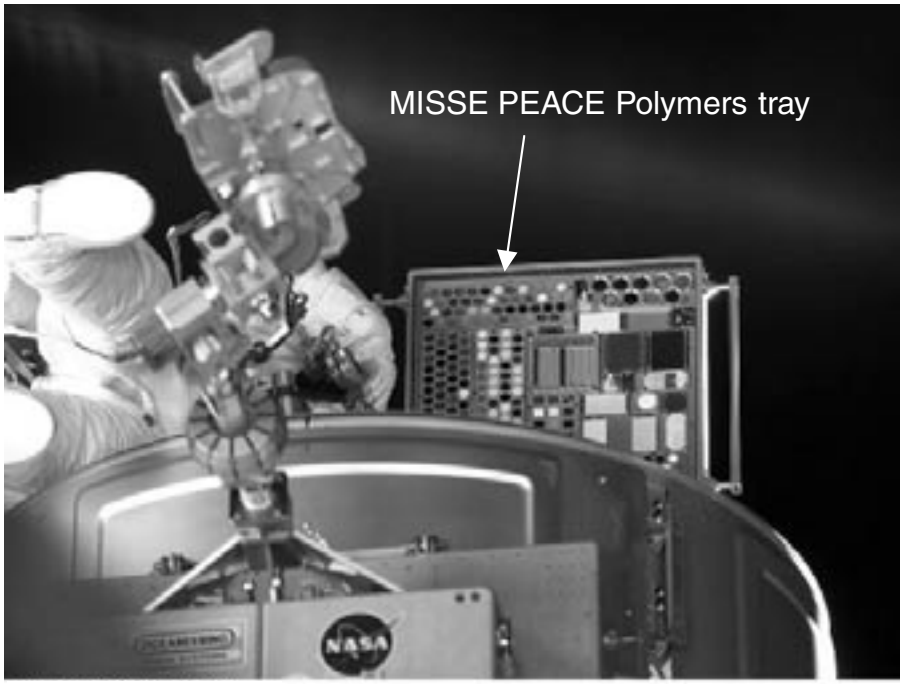

During a spacewalk on August 16, 2001, astronaut Patrick Forrester installs the Materials International Space Station Experiment (MISSE) on the International Space Station's Quest Airlock, the first external experiment on the station's hull.

Glenn invited high school students from the PEACE Team, along with some university students, to collaborate on the Glenn MISSE PEACE Polymers experiment. The polymers in the MISSE PEACE Polymers experiment range from those commonly used for spacecraft applications, such as Teflon FEP, to more recently developed polymers, such as high-temperature polyimide PMR (polymerization of monomer reactants). Polymers that are not desired for spacecraft applications are also included solely on the basis of their chemical composition. The erosion yield data obtained from this experiment will be compared with data obtained from the short-duration experiment PEACE, and with ground data. The LEO erosion yield data will be compared with erosion yield predictions made by Integrity Testing Laboratory, Inc. These predictions are made on the basis of predictive models using information about the chemical composition, structure, and densities of polymers, as well as Oxygen Index data. Having the erosion yield data for many different polymers, all characterized and

exposed to space under identical conditions, and having space data to compare with the predictive model, will be very useful to spacecraft designers in the future.

MISSE is a cooperative effort among the Air Force, NASA, and industry that underwent integration at Boeing, the NASA Marshall Space Flight Center, and the NASA Langley Research Center. It consists of 1- and 3-year exposure trays to be exposed to both atomic oxygen and solar radiation (in addition to other environmental exposures), or to solar radiation with no atomic oxygen exposure. The PEACE Polymers are on one of the two 1-yr MISSE Passive Experiment Carriers being exposed to both atomic oxygen and solar radiation. On August 16, 2001, astronauts Dan Barry and Patrick Forrester attached the two MISSE Passive Experiment Carriers (PEC's) to separate handrails on the exterior of the International Space Station airlock during a successful extravehicular activity, or space walk. NASA plans to retrieve MISSE in the fall of 2002.

Glenn contacts:
Kim K. de Groh, 216–433–2297, Kim.K.deGroh@grc.nasa.gov; and Bruce A. Banks, 216–433–2308, Bruce.A.Banks@grc.nasa.gov

Authors:
Kim K. de Groh, Bruce A. Banks, Anne Hammerstrom, Erica Youngstrom, Carolyn Kaminski, Laura Marx, Elizabeth Fine, Jonathan D. Gummow, and Douglas Wright

Headquarters program office: OAT

Programs/Projects: ISS

Physical and Thermal Properties Evaluated of Teflon FEP Retrieved From the Hubble Space Telescope During Three Servicing Missions

Mechanical properties of aluminized Teflon fluorinated ethylene propylene (FEP) thermal control materials on the Hubble Space Telescope (HST) exposed to low Earth orbit for up to 9.7 years have significantly degraded, with extensive cracking occurring on orbit. The NASA Glenn Research Center and the NASA Goddard Space Flight Center have collaborated on analyzing the physical and thermal properties of aluminized FEP (FEP-Al, DuPont) materials retrieved in December 1999 during HST's third servicing mission (SM3A). Comparisons have been made to properties of FEP-Al retrieved during the first and second HST servicing missions, SM1 and SM2, in order to determine degradation processes for FEP on HST.

Both 127-μm-thick aluminized FEP (FEP-Al) from the top multilayer insulation (MLI) layer retrieved during SM3A (exposed for 9.7 years), and 50.8-μm-thick FEP-Al patches installed during SM2 and retrieved during SM3A (exposed for 2.8 years), have numerous through-the-thickness cracks and show significant decreases in tensile properties. Various areas of 50.8-μm-thick FEP-Al patch material exposed to space for 2.8 years underwent degradation of mechanical properties similar to, or worse than, 127-μm-thick FEP-Al exposed for 9.7 years, indicating an increased rate of degradation for the thinner FEP material. The SM3A FEP-Al was not as degraded as an FEP-Al sample retrieved during SM2, which had 2.8-yr less space exposure. Ground tests conducted at Glenn and Goddard using retrieved Hubble materials have shown that the reason for the more severe embrittlement of the SM2 sample is that it experienced a significantly higher on-orbit temperature of 200 °C in comparison to the maximum of 50 °C for the SM3A FEP-Al. It was, therefore, concluded that the degradation in mechanical properties of space-exposed FEP-Al is strongly influenced by temperature.

Many through-the-thickness cracks were found in the as-retrieved SM3A FEP-Al samples, and examination of crack surface morphology led to the conclusion that all through-the-thickness cracks in the SM3A FEP-Al surfaces were produced on orbit via slow crack growth processes. A gradient in the embrittlement of both the SM3A MLI and patch materials from a top highly embrittled layer to a backside ductile layer is indicative of a significantly greater radiation dose absorbed in the surface layer and a gradually decreasing dose through the FEP thickness. Cyclic growth patterns in the cracks appear to be the result of on-orbit cyclic processes, such as temperature cycling from Sun/shadow cycles, causing cracks to propagate through the thickness of on-orbit embrittled FEP. The tests conducted indicate that irradiation (solar, x-ray, and particle radiation) of Teflon FEP in space causes chain scission, resulting in FEP embrittlement,

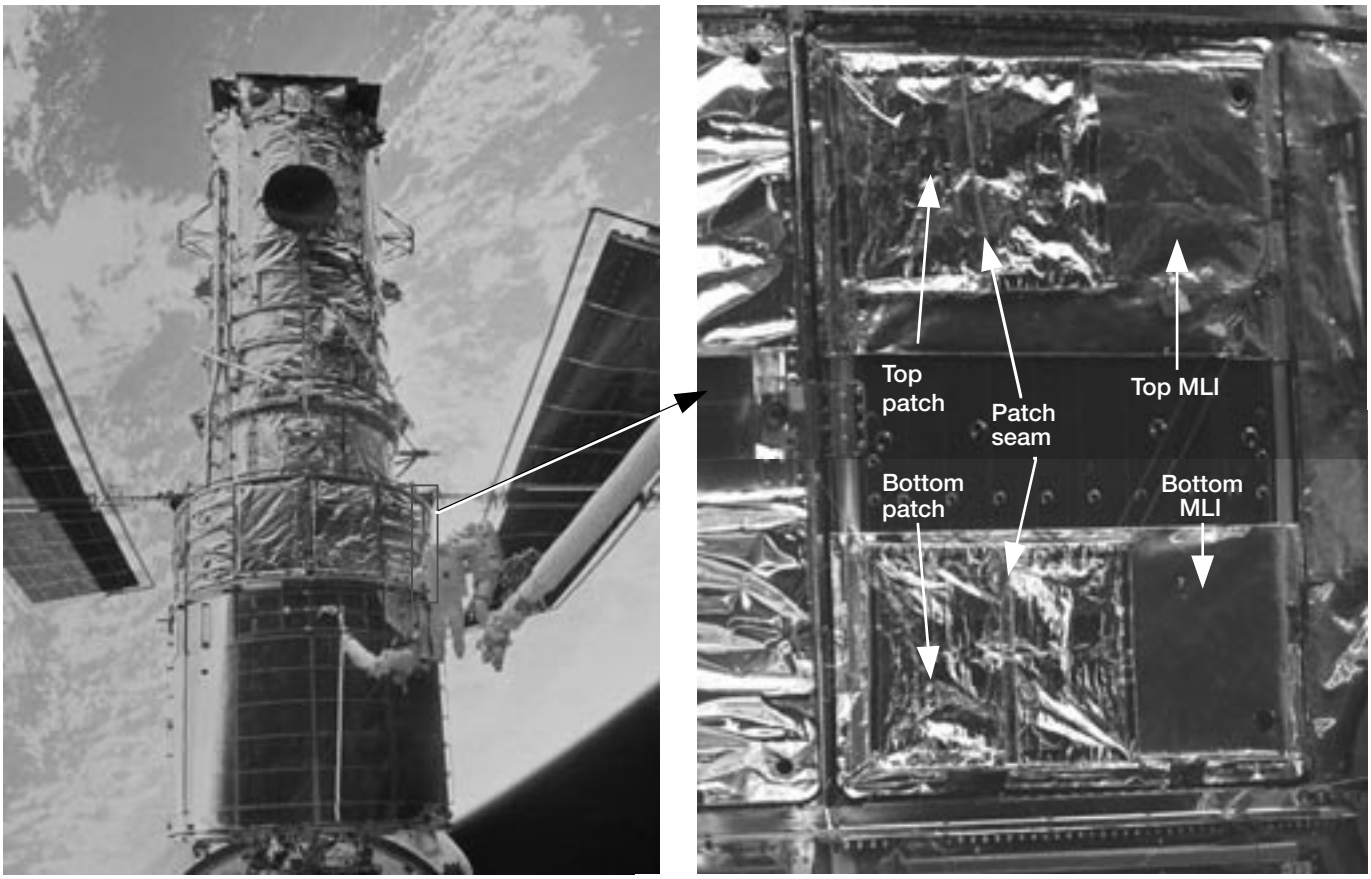

Left: Astronauts working at Bay 10 on Hubble Space Telescope (HST) during SM3A. Right: Close up of the Bay 10 multilayer insulation (MLI) and patches showing the designations of the retrieved materials, Top MLI, Top Patch, Bottom MLI, and Bottom Patch.

and that excessive heating, such as that experienced by the retrieved curled SM2 sample, allows increased mobility of the space-environment-induced scissioned short chains, with resulting increased crystallinity, density, and embrittlement.

Find out more about this research:

Hubble Space Telescope: http://hubble.gsfc.nasa.gov

Glenn's Electro-Physics Branch:
http://www.grc.nasa.gov/WWW/epbranch/ephome.htm

Glenn contacts:
Joyce A. Dever, 216–433–6294, Joyce.A.Dever@grc.nasa.gov; and Kim K. de Groh, 216–433–2297, Kim.K.deGroh@grc.nasa.gov

Authors:
Joyce A. Dever, Kim K. de Groh, Dr. James K. Sutter, Dr. James R. Gaier, Russell K. Messer, Daniel A. Scheiman, Mark W. McClendon, Michael J. Viens, L. Len Wang, Charles C. He, and Jonathan D. Gummow

Headquarters program office: OAT

Programs/Projects: HST

Facility and Methods Developed for Simulated Space Vacuum Ultraviolet Exposure Testing of Polymer Films

Vacuum ultraviolet (VUV) radiation of wavelengths between 115 and 200 nm produced by the Sun in the space environment can degrade polymer films, producing changes in their optical, mechanical, and chemical properties. These effects are particularly important for thin polymer films being considered for ultralightweight space structures, because, for most polymers, VUV radiation is absorbed in a thin surface layer. The NASA Glenn Research Center has developed facilities and methods for long-term ground testing of polymer films to evaluate space environmental VUV radiation effects. VUV exposure can also be used as part of combined or sequential simulated space environmental exposures to determine combined damaging effects with other aspects of the space environment, which include solar ultraviolet radiation, solar flare x-rays, electron and proton radiation, atomic oxygen (for low-Earth-orbit missions), and temperature effects.

Because the wavelength sensitivity of VUV damage is not well known for most materials, Glenn's VUV facility uses a broad-spectrum deuterium lamp with a magnesium fluoride window that provides output between 115 and 200 nm. Deuterium lamps of this type were characterized by the National Institute of Standards and Technology and through measurements at Glenn. Spectral irradiance measurements show that from approximately 115 to 160 nm, deuterium lamp irradiance can be many times that of air mass zero solar irradiance, and as wavelength increases above approximately 160 nm, deuterium lamp irradiance decreases in comparison to the Sun.

The facility is a cryopumped vacuum chamber that achieves a system pressure of approximately 5×10^{-6} torr. It contains four individual VUV-exposure compartments in vacuum, separated by water-cooled copper walls to

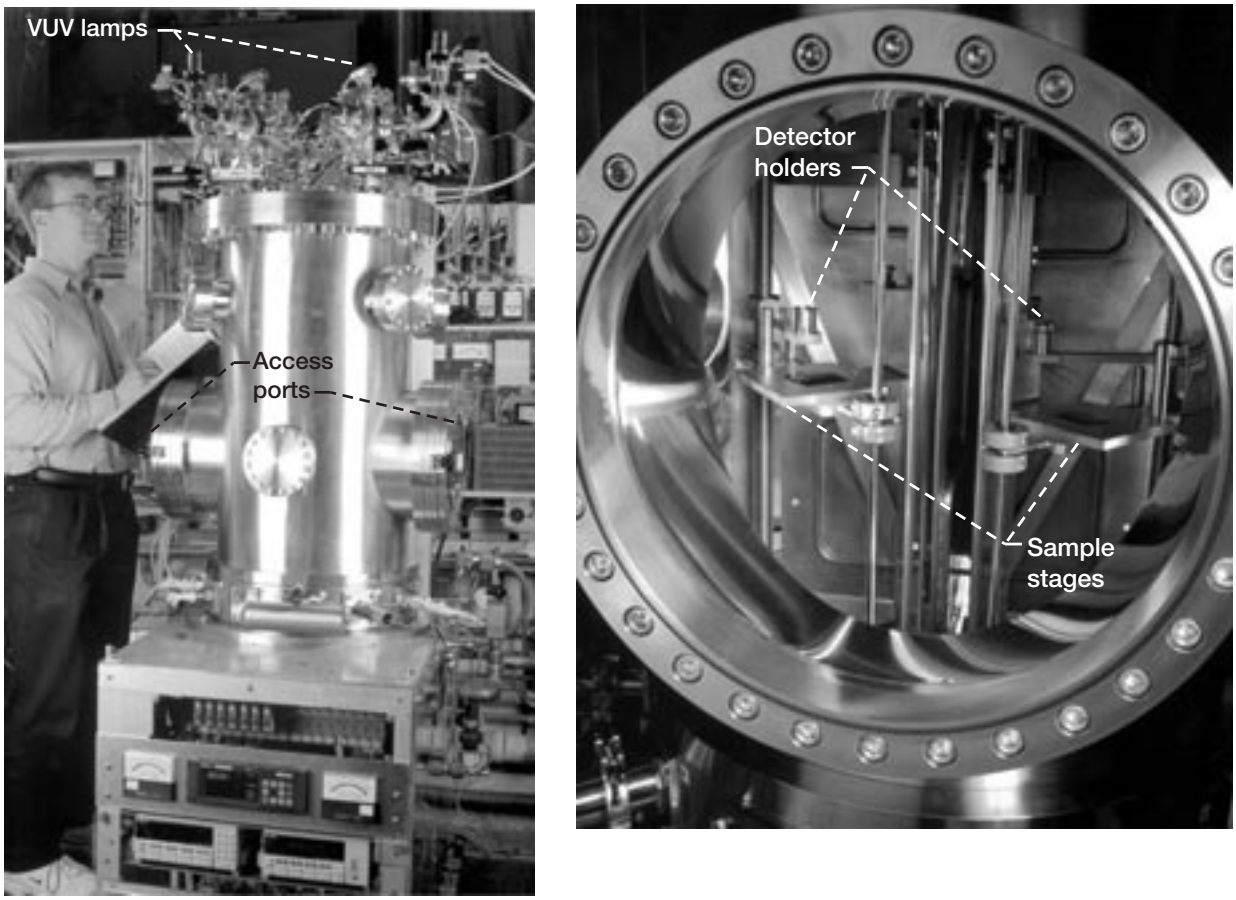

Glenn's VUV exposure facility. Left: Overview showing exterior components. Right: View of two of the four VUV exposure compartments through the access port window.

minimize VUV radiation and any sample contamination cross interactions between compartments. Each VUV-exposure compartment contains a VUV deuterium lamp, a motor-controlled sample stage coupled with a moveable cesium iodide VUV phototube, and two thermocouples for temperature measurement. The left photograph (on the preceding page) shows the vacuum chamber and exterior equipment. Each VUV lamp is located at the top of the chamber with its projection-tube pushed through an O-ring compression fitting. The lamp assemblies are located on ports that can be isolated from the rest of the vacuum chamber, permitting maintenance or replacement of the lamps without breaking vacuum in the main chamber where the samples are located. The right photograph shows a view of two of the four interior VUV-exposure compartments, including the moveable sample stages and detector holders.

Glenn is using this facility to support testing of Next Generation Space Telescope sunshield materials that is being led by the NASA Goddard Space Flight Center and to develop an understanding of the wavelength, intensity, and temperature dependence of VUV-induced polymer degradation.

Glenn contact:
Joyce A. Dever, 216–433–6294,
Joyce.A.Dever@grc.nasa.gov

Authors:
Joyce A. Dever, Anthony J. Pietromica, Thomas J. Stueber, Edward A. Sechkar, and Russell K. Messer

Headquarters program office: OAT

Programs/Projects: NGST, HST, ISS

High-Temperature Intercalated Graphite Fiber Conductors Fabricated

Composites of intercalated graphite fibers show promise to significantly reduce the weight of electromagnetic interference shielding in spacecraft and aircraft (ref. 1). Bromine-intercalated pitch-based fibers have been among the most heavily studied systems because of their attractive electrical and thermal conductivities and their stability over a wide range of environmental conditions (ref. 2). Previous studies found that the resistivity of bromine-intercalated graphite fibers began to increase when the fibers were exposed to temperatures in excess of about 200 °C in air for long periods of time. If the temperature was as high as 450 °C, the resistivity increased dramatically within a few hours (ref. 2). It remained unclear, however, whether the increase was due to deintercalation of the bromine or to air oxidation of the fibers.

Studies were initially directed toward determining the temperature at which bromine would deintercalate from the fibers, and perhaps become a hazard to both personnel and equipment. So the mass of bromine-intercalated graphite fibers was carefully monitored as it was heated in an inert atmosphere, since the fibers are known to oxidize at a lower temperature than they deintercalate. What was found was that the fibers, which are about 18-wt% bromine, did not lose any appreciable mass even at temperatures approaching 1000 °C. X-ray diffraction studies showed that there were also no changes in the overall structure of the compound. Resistivity measurements indicated that there is some slight degradation in the electronic structure, in that the resistivity increased by a few percent. Overall, the results show that these materials may be suitable for applications at temperatures at least this high, provided oxygen is excluded. This may enable their use in carbon-ceramic, and perhaps even carbon-carbon composites (ref. 3).

References
1. Gaier, James R.: Intercalated Graphite Fiber Composites as EMI Shields in Aerospace Structures. IEEE Elmagn., vol. 34, no. 3, 1992, p. 351.
2. Gaier, James R.; Slabe, Melissa E.; and Shaffer, Nanette: Stability of Bromine, Iodine Monochloride, Copper (II) Chloride, and Nickel (II) Chloride Intercalated Pitch-Based Graphite Fibers. Carbon, vol. 26, no. 3, 1988, pp. 381–387.
3. Gaier, James R.: High Temperature Stability of Bromine Intercalated Graphite Fibers. Presented at the American Carbon Society, CARBON '01, Lexington, KY, 2001.

Find out more about this research:
http://www.grc.nasa.gov/WWW/epbranch/ephome.htm

Glenn contact:
Dr. James R. Gaier, 216–433–6686,
James.R.Gaier@grc.nasa.gov

Author: Dr. James R. Gaier

Headquarters program office: OAT

Programs/Projects:
Aerospace power systems

Solar Selective Coatings Developed for Space Power Applications

A solar collector having the combined properties of high solar absorptance, low infrared emittance, and high thermal conductivity is envisioned for space power applications on minisatellites. A high solar absorptance is needed to collect as much of the incident solar radiation as possible and a low infrared emittance is needed to minimize radiant energy losses. A lightweight material having a high thermal conductivity is needed to transport the absorbed energy to where it is needed. Such a solar collector may be used with a low-temperature-differential heat engine to provide electric power to the minisatellite components or as a source of thermal energy for a thermal bus that would heat remote regions of the spacecraft.

The key to such a collector is the use of cermet coatings. Cermet coatings are composed of molecular islands of metal embedded in a three-dimensional matrix of dielectric. Recent research on molecular mixtures of aluminum and aluminum oxide at the NASA Glenn Research Center has yielded cermet coatings with a solar absorptance α of 0.797 and an infrared emittance ε of 0.131, yielding an α/ε ratio of 6. Although additional work is needed to further increase the α/ε ratio, these coatings are attractive owing to their potential durability in the space environment. The aluminum oxide surface should provide substantial protection from the atomic oxygen found in low Earth orbit. To help minimize emittance, these coatings are deposited on a smooth surface. The selected surface is aluminum that has been diamond turned to a mirror finish.

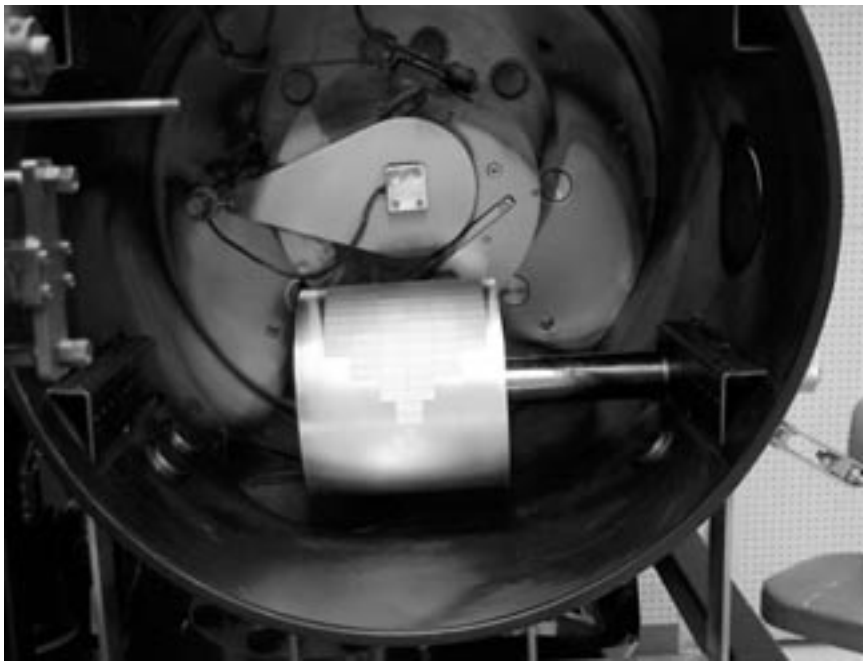

Cylindrical aluminum sputter deposition target with aluminum oxide pieces installed.

Cermet coatings are manufactured by sputter deposition. To achieve the desired variable composition, Glenn's researchers implemented a novel approach using a cylindrical target composed of aluminum and aluminum oxide. Rotating the cylinder during the deposition process yields a coating of variable composition. The figure shows a photograph of the custom-made aluminum and aluminum oxide cylindrical target installed in the sputter deposition chamber.

For more information, visit Glenn's Electro-Physics Branch online:
http://www.grc.nasa.gov/WWW/epbranch/ephome.htm

Glenn contact:
Dr. Donald A. Jaworske, 216–433–2312, Donald.A.Jaworske@grc.nasa.gov

Author: Dr. Donald A. Jaworske

Headquarters program office:
OAT, OSS (ATMS)

Programs/Projects: SRF

Cryogenic Electronics Being Developed for Space Operation

Planetary exploration missions and deep space probes require electrical power management and control systems that can operate efficiently and reliably in very low temperature environments. Presently, spacecraft operating in the cold environment of deep space carry a large number of radioisotope heating units to maintain the surrounding temperature of the onboard electronics at approximately 20 °C. Electronics capable of operation at cryogenic temperatures would not only tolerate the hostile environment of deep space but also reduce system size and weight by eliminating or reducing the radioisotope heating units and their associate structures. Thereby, such electronics would reduce system development as well as launch costs. In addition, power electronic circuits designed for operation at low temperatures are expected to result in more efficient systems than those at room temperature. This improvement results because semiconductor and dielectric materials have better behavior and tolerance in their electrical and thermal properties at low temperatures.

The Low Temperature Electronics Program at the NASA Glenn Research Center is focusing on the research and development of electrical components, circuits, and systems suitable for applications in the aerospace environment and in deep space exploration missions. Research is being conducted on devices and systems for reliable use down to cryogenic temperatures. Some of the commercial off-the-shelf as well as developed components that are being characterized include semiconductor switching devices, resistors, magnetics, and capacitors. Semiconductor devices and integrated circuits including digital-to-analog and analog-to-digital converters, dc-dc converters, operational amplifiers, and oscillators are also being investigated for potential use in low-temperature applications. For example, the figure shows the output response of an advanced oscillator at room temperature and at −190 °C. Most oscillators can operate at temperatures down to only −55 °C. It can be seen that, for this oscillator, the low temperature of −196 °C changed the leading and trailing edges of the oscillator pulses by producing overshoot.

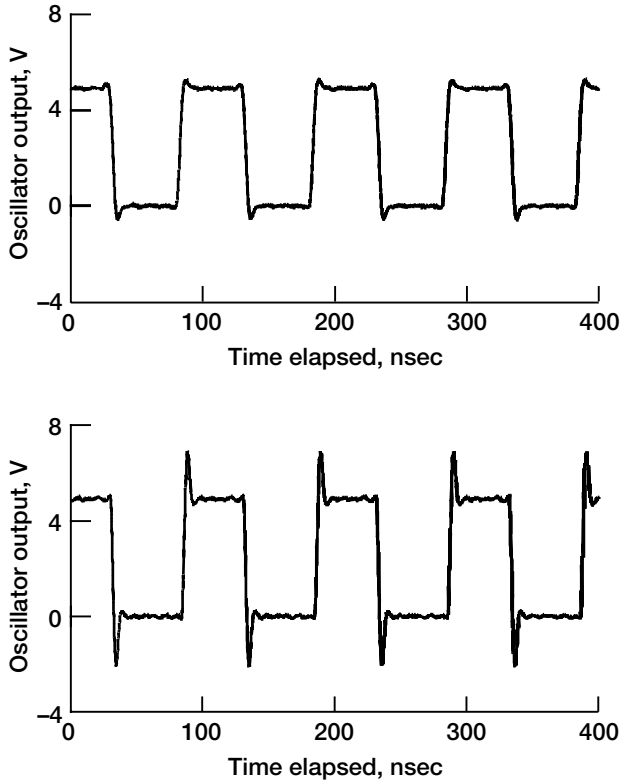

Output waveforms of an advanced oscillator. Top: Operating temperature, 25 °C. Bottom: Operating temperature, −196 °C.

The research and development efforts performed under the Low Temperature Electronics Program at Glenn are being carried out through collaboration with other Government agencies, industrial and aerospace companies, and academia. The program supports missions as well as technology development efforts at NASA's Goddard Space Flight Center and Langley Research Center, and the Jet Propulsion Laboratory.

Find out more about this research:
http://www.grc.nasa.gov/WWW/epbranch/ephome.htm

Glenn contact:
Richard L. Patterson, 216–433–8166, Richard.Patterson@grc.nasa.gov

Authors:
Richard L. Patterson, Ahmad Hammoud, and Scott S. Gerber

Headquarters program office: OAT

Programs/Projects: APOBP, NEPP, NEPAG, NGST, Galex, CloudSat

Integrated Stirling Convertor and Hall Thruster Test Conducted

An important aspect of implementing Stirling Radioisotope Generators on future NASA missions is the integration of the generator and controller with potential spacecraft loads. Some recent studies have indicated that the combination of Stirling Radioisotope Generators and electric propulsion devices offer significant trip time and payload fraction benefits for deep space missions. A test was devised to begin to understand the interactions between Stirling generators and electric thrusters. An electrically heated RG–350 (350–W output) Stirling convertor, designed and built by Stirling Technology Company of Kennewick, Washington, under a NASA Small Business Innovation Research agreement, was coupled to a 300–W SPT–50 Hall-effect thruster[1] built for NASA by the Moscow Aviation Institute (RIAME). The RG–350 and the SPT–50, shown in the figure, were installed in adjacent vacuum chamber ports at NASA Glenn Research Center's Electric Propulsion Laboratory, Vacuum Facility 8. The Stirling electrical controller interfaced directly with the Hall thruster power-processing unit, both of which were located outside of the vacuum chamber. The power-processing unit accepted the 48 Vdc output from the Stirling controller and distributed the power to all the loads of the SPT–50, including the magnets, keeper, heater, and discharge.

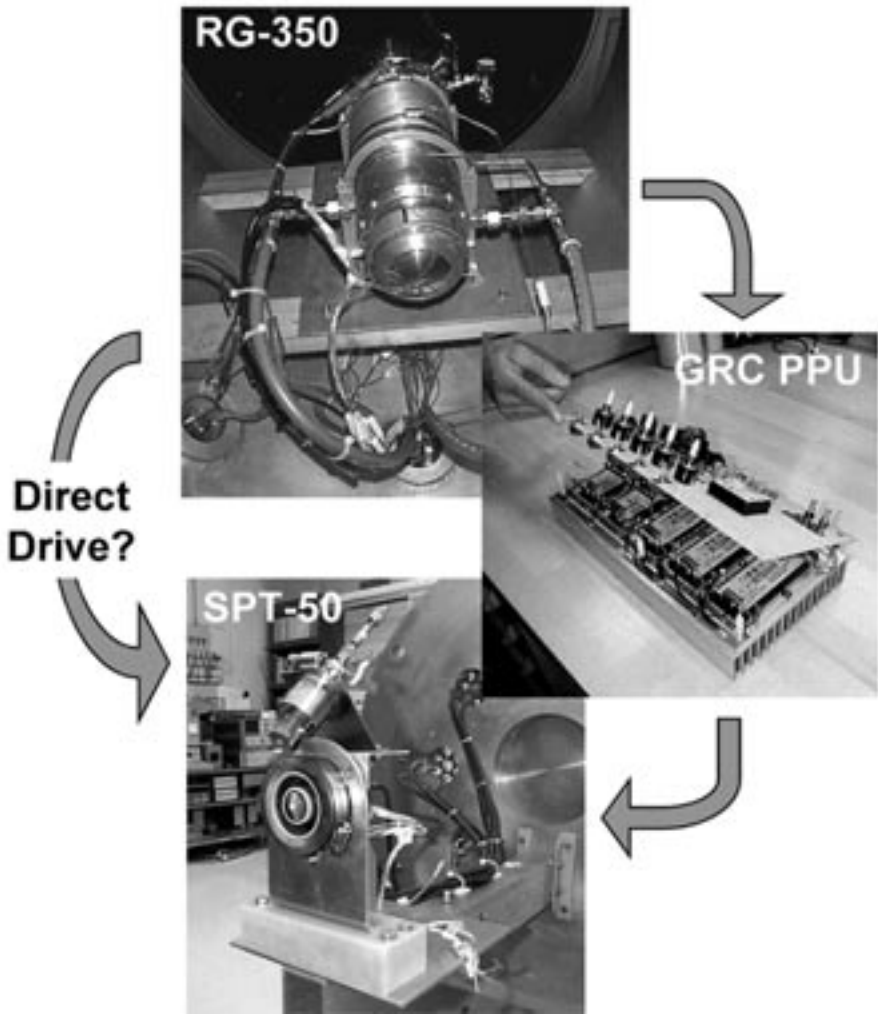

Stirling/Hall thruster integration at Vacuum Facility 8.

On February 28, 2001, the Glenn test team successfully operated the Hall-effect thruster with the Stirling convertor. This is the world's first known test of a dynamic power source with electric propulsion. The RG–350 successfully managed the transition from the purely resistive load bank within the Stirling controller to the highly capacitive power-processing unit load. At the time of the demonstration, the Stirling convertor was operating at a hot temperature of 530 °C and a cold temperature of –6 °C. The linear alternator was producing approximately 250 W at 109 Vac, while the power-processing unit was drawing 175 W at 48 Vdc. The majority of power was delivered to the Hall thruster discharge circuit operating at 115 Vdc and 0.9 A. Testing planned for late 2001 will examine the possibility of directly driving the Hall thruster discharge circuit using rectified and filtered output from the Stirling alternator.

Find out more about this research:
http://www.grc.nasa.gov/WWW/tmsb/

Glenn contact:
Lee Mason, 216–977–7106,
Lee.Mason@grc.nasa.gov

Author: Lee S. Mason

Headquarters program office: OSS

Programs/Projects:
Advanced Radioisotope Power System, In-Space Propulsion

[1]SPT, stationary plasma thruster.

Stirling Research Laboratory Providing Independent Performance Verification of Convertors for a Stirling Radioisotope Generator

The Department of Energy (DOE), Germantown, Maryland, Stirling Technology Company (STC), Kennewick, Washington, and NASA Glenn Research Center are developing a free-piston Stirling convertor for a high-efficiency Stirling Radioisotope Generator for NASA Space Science missions. This generator is being developed for multimission use, including providing electric power for unmanned Mars rovers and for deep space missions. STC is developing the 55-W Technology Demonstration Convertor (TDC) under contract to DOE. Glenn is conducting an in-house technology project to assist in developing the convertor for readiness for space qualification and mission implementation. As part of this effort, a Stirling Research Laboratory was established to test the TDC's and related technologies. A key task is providing an independent verification and validation of the TDC performance.

Four TDC's are now being tested at Glenn. Acceptance testing has been completed for all convertors, and in general, performance agreed well with that achieved by STC prior to the delivery of the convertors. Performance mapping has also been completed on two of the convertors over a range of hot-end temperatures (450 to 650 °C), cold-end temperatures (80 to 120 °C), and piston amplitudes (5.2 to 6.2 mm). These test data are available at http://www.grc.nasa.gov/WWW/tmsb. The TDC's can be tested in either a horizontal orientation with dual-opposed convertors or in a vertical orientation with a single convertor. Synchronized dual-opposed pairs are used for dynamically balanced operation that results in very low levels of vibration. The Stirling Research Laboratory also supports launch environment testing of the TDC's in Glenn's Structural Dynamics Laboratory and electromagnetic interference and electromagnetic compatibility characterization and reduction efforts. In addition, the TDC's will be used for long-term endurance testing, and preparations are underway for unattended operation.

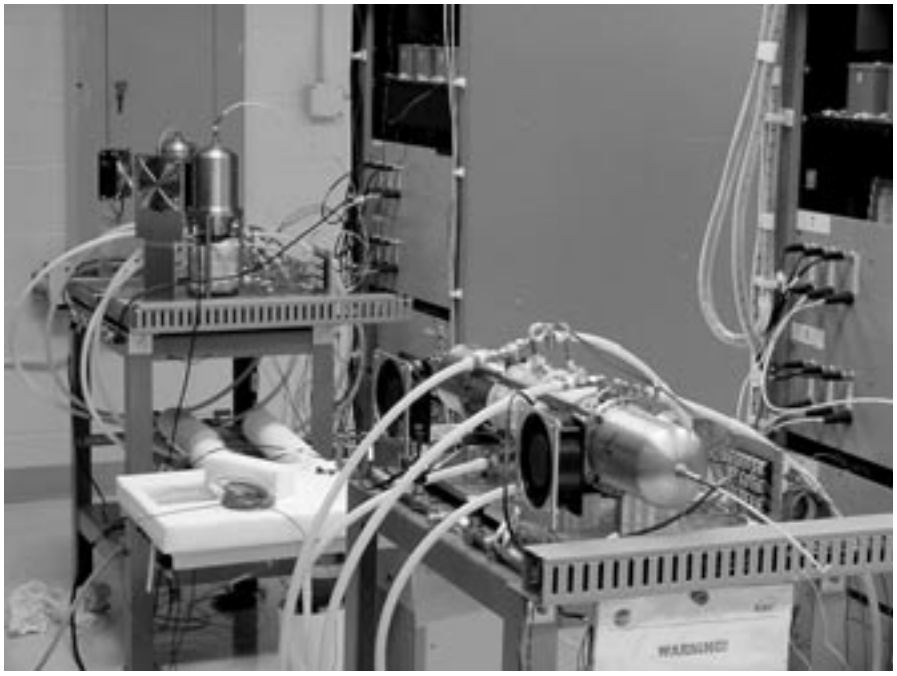

Stirling Technology Demonstration Convertors being tested at Glenn in both dual-opposed and single convertor modes of operation.

A competitive procurement by DOE for the Stirling Radioisotope Generator system integration contractor is nearing completion. Following announcement of the selected contractor, Glenn will continue to provide critical support for the overall DOE project as the work moves into system development. Other key efforts underway at Glenn are a life assessment of the TDC heater head, including creep testing of the Inconel 718 hot-end material and accelerated life testing of prototypical heater heads, long-term aging characterization of NdFeB permanent magnets used in the linear alternator, finite element analyses of the linear alternator in particular to determine the demagnetization margin of the permanent magnets, evaluation of the TDC organic materials used in the piston bearing coatings and linear alternator insulations and adhesives, support for DOE reliability assessments, and development of a multidimensional Stirling computational fluid dynamics performance code.

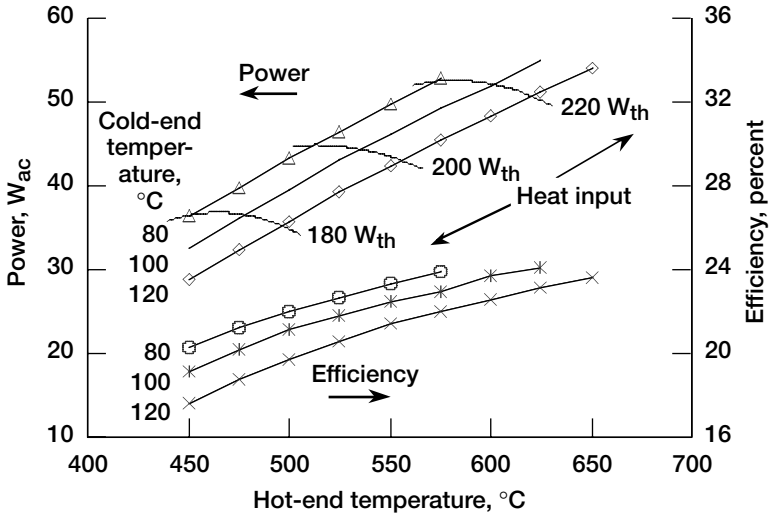

Full-stroke performance map for the Stirling Technology Demonstration Convertor.

Glenn contacts:
Richard Shaltens, 216–433–6138, Richard.K.Shaltens@grc.nasa.gov; Jeff Schreiber, 216–433–6144, Jeffrey.G.Schreiber@grc.nasa.gov; and Lanny Thieme, 216–433–6119, Lanny.G.Thieme@grc.nasa.gov

Author: Lanny G. Thieme

Headquarters program office: OSS

Programs/Projects:
Stirling Radioisotope Generator, Mars rover, Outer Planets

Special recognition: Space Technology and Applications International Forum (STAIF)—2000 Outstanding Paper Award for paper entitled "Technology Development for a Stirling Radioisotope Power System."

Find out more about this research from Glenn's Thermo-Mechanical Systems Branch: http://www.grc.nasa.gov/WWW/tmsb

References

1. Schreiber, J.G.; and Thieme, L.G.: Accomplishments in Free-Piston Stirling Tests at NASA GRC. To be published in Space Technology and Applications International Forum (STAIF–2002), 2002.
2. Thieme, L.G.; Schreiber, J.G.; and Mason, L.S.: Stirling Technology Development at NASA GRC. NASA/TM—2001-211315, 2002. (To be published in Space Technology and Applications International Forum (STAIF–2002), 2002.)

Refractive Secondary Solar Concentrator Demonstrated High-Temperature Operation

Space applications that utilize solar thermal energy—such as electric power conversion systems, thermal propulsion systems, and furnaces—require highly efficient solar concentration systems. The NASA Glenn Research Center is developing the refractive secondary concentrator, which uses refraction and total internal reflection to efficiently concentrate and direct solar energy. When used in combination with advanced lightweight primary concentrators, such as inflatable thin films, the refractive secondary concentrator enables very high system concentration ratios and very high temperatures. Last year, Glenn successfully demonstrated a secondary concentrator throughput efficiency of 87 percent, with a projected efficiency of 93 percent using an antireflective coating. Building on this achievement, Glenn recently successfully demonstrated high-temperature operation of the secondary concentrator when it was used to heat a rhenium receiver to 2330 °F.

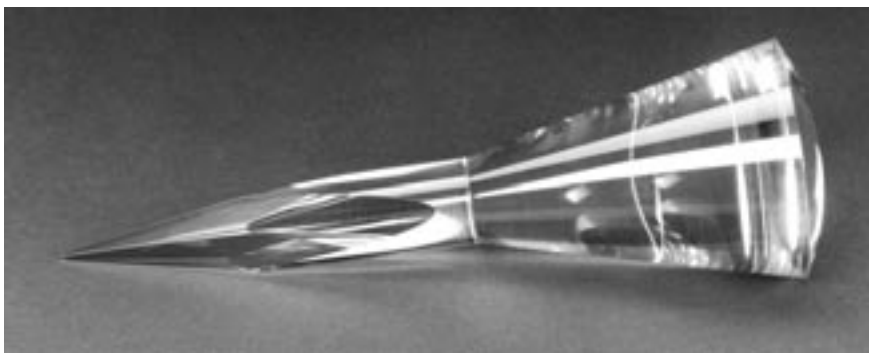

Prototype refractive secondary concentrator made of single-crystal sapphire.

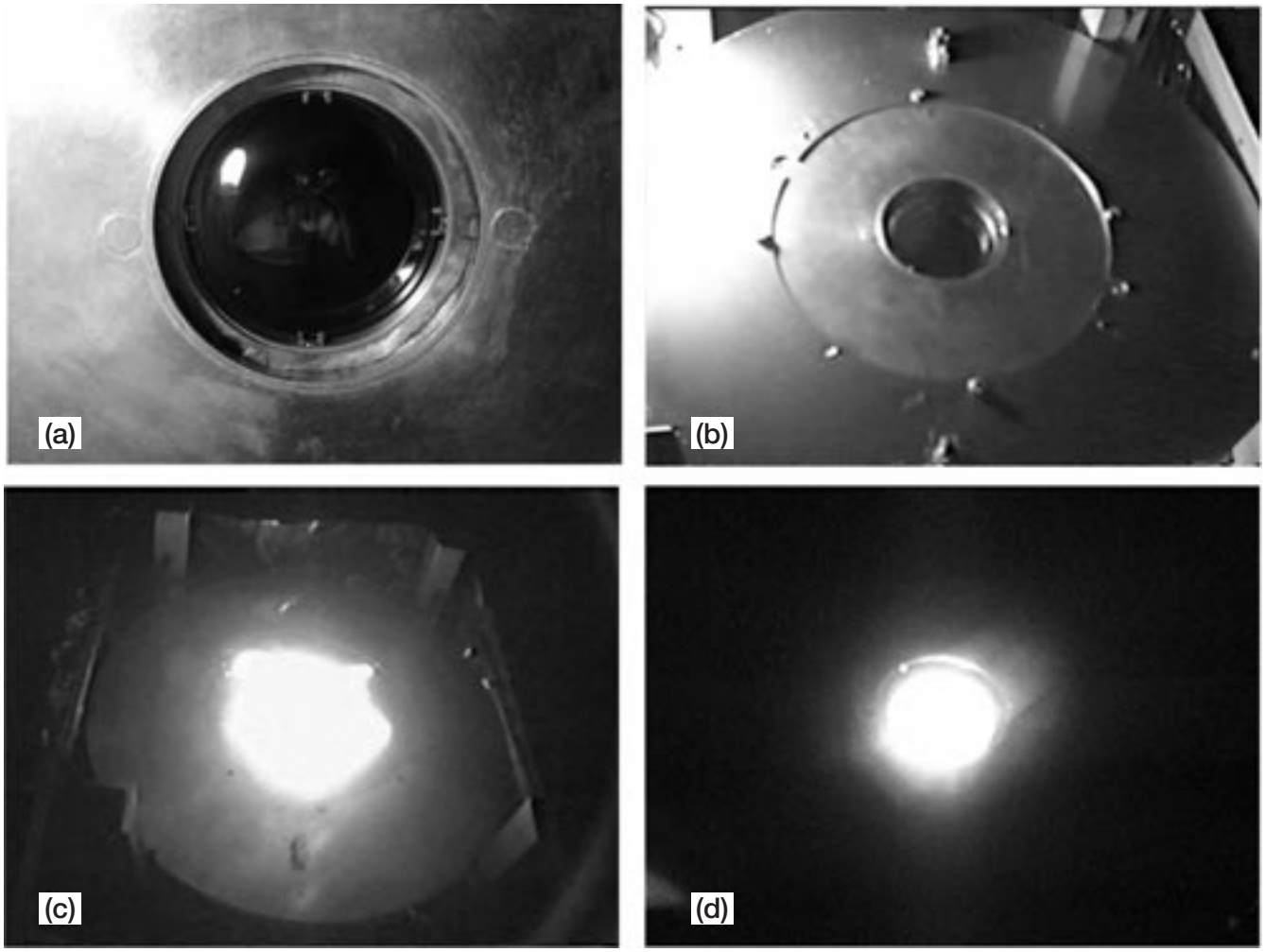

(a) Closeup of refractive secondary concentrator inlet surface. (b) Concentrator installed in receiver behind the splash shield. (c) Concentrated solar energy illuminates the secondary concentrator and splash shield. (d) With no solar illumination, the inner receiver, which reached a maximum of 2330 °F, radiates through the secondary concentrator.

The high-temperature demonstration of the concentrator was conducted in Glenn's 68-ft-long Tank 6 thermal vacuum facility equipped with a solar simulator. The facility has a rigid panel primary concentrator that was used to concentrate the light from the solar simulator onto the refractive secondary concentrator. NASA Marshall Space Flight Center provided a rhenium cavity, part of a solar thermal propulsion engine, to serve as the high-temperature receiver.

The prototype refractive secondary concentrator, measuring 3.5 in. in diameter and 11.2 in. long, is made of single-crystal sapphire. A water-cooled splash shield absorbs spillage light outside of the 3.5-in. concentrator aperture. Multilayer foil insulation composed of tungsten, molybdenum, and niobium is used to minimize heat loss from the high-temperature receiver. A liquid-cooled canister calorimeter is used to measure the heat loss through the multilayer foil insulation.

The objective of the test was to measure the resulting temperature in the receiver as the solar simulator input power was increased, demonstrating the effectiveness of the refractive secondary concentrator for high-temperature applications. Two steady-state points were attained during the test. With 460 W input to the refractive secondary concentrator (approximately 9 percent of this input power is lost because of reflection off the inlet surface), the receiver temperature reached 1620 °F. With

1.25 kW input to the refractive secondary concentrator, the receiver reached 2160 °F. While going to a third steady-state point, with 1.96 kW input to the refractive secondary, the receiver reached a maximum of 2330 °F before the receiver temperatures unexpectedly started to drop. Because of this anomaly, the test was concluded.

Posttest examination of the hardware revealed that, although the refractive secondary concentrator was intact, numerous fractures had developed in the unit. An investigation is underway to determine the cause of the fractures. Preliminary evidence suggests that the fractures may likely have been caused by either movement in the support hardware and splash shield (resulting in localized heating or cooling of the secondary concentrator) or by outgassing of the surrounding materials at high temperatures that coated onto the secondary concentrator (resulting in uneven heating of the secondary concentrator surface). Both of these issues indicate that the fractures were not due to some inherent limitation in the refractive secondary concentrator technology, and both can be easily remedied through modifications to the support hardware and the selection of appropriate materials.

Find out more at Glenn's Thermo-Mechanical Systems Branch:
http://www.grc.nasa.gov/WWW/tmsb/

Glenn contact:
Wayne A. Wong, 216–433–6318,
Wayne.A.Wong@grc.nasa.gov

Author: Wayne A. Wong

Headquarters program office:
OAT, Glenn's SRF

Programs/Projects:
Solar Thermal Power, Solar Thermal Propulsion, Solar Furnace

Operation of a Thin-Film Inflatable Concentrator System Demonstrated in a Solar Thermal Vacuum Environment

Thin-film inflatable solar concentrators offer significant advantages in comparison to state-of-the-art rigid panel concentrators, including low weight, low stowage volume, and simple gas deployment. From June 10 to 22, 2001, the ElectroMagnetic Radiation Control Experiment (EMRCE) Team used simulated solar energy to demonstrate the operation of an inflatable concentrator system at NASA Glenn Research Center's Tank 6 thermal vacuum facility. The joint Government/industry test team was composed of engineers and technicians from Glenn, the Air Force Research Laboratory, SRS Technologies, and ATK Thiokol Propulsion. The research hardware consisted of the following:

(1) **A thin-film inflatable concentrator.** This concentrator made of CP–1, a NASA-developed, flight-qualified polyimide material, was designed and fabricated by SRS Technologies as part of a Glenn Small Business Innovation Research Phase II contract. The concentrator has a front clear canopy film and a rear aluminum-coated reflector film. The two films are seamed at the edges and are held to the support ring using a network of catenaries. For the EMRCE test, a rigid aluminum ring was used to decouple the effects of the inflatable concentrator with that of the usual inflatable, thin-film torus support structure. The concentrator is elliptical to account for the diverging beam from the solar simulator.

(2) **The hexapod pointing and focus control system**. The concentrator struts are mounted on this 6-degree-of-freedom, electrical-actuator-driven, remote-controlled base. The hexapod system was developed by ATK Thiokol Propulsion.

(3) **Two rigidized support struts using two candidate technologies—ultraviolet-rigidized glass and radiation-cured isographite**. In space, the struts would be gas deployed and would only require pressurization until rigidization was complete. For this test, the struts developed by ATK Thiokol Propulsion were not attached to the other hardware so that their behavior could be isolated.

With 1-sun illumination, the 1-m-class inflatable concentrator throughput power was measured to be 685 W, within 10 percent of predictions. Other objectives achieved include the first demonstration of the hexapod focus and pointing control system in a thermal vacuum environment, thermal and geometric response characterization of the inflatable concentrator as well as the

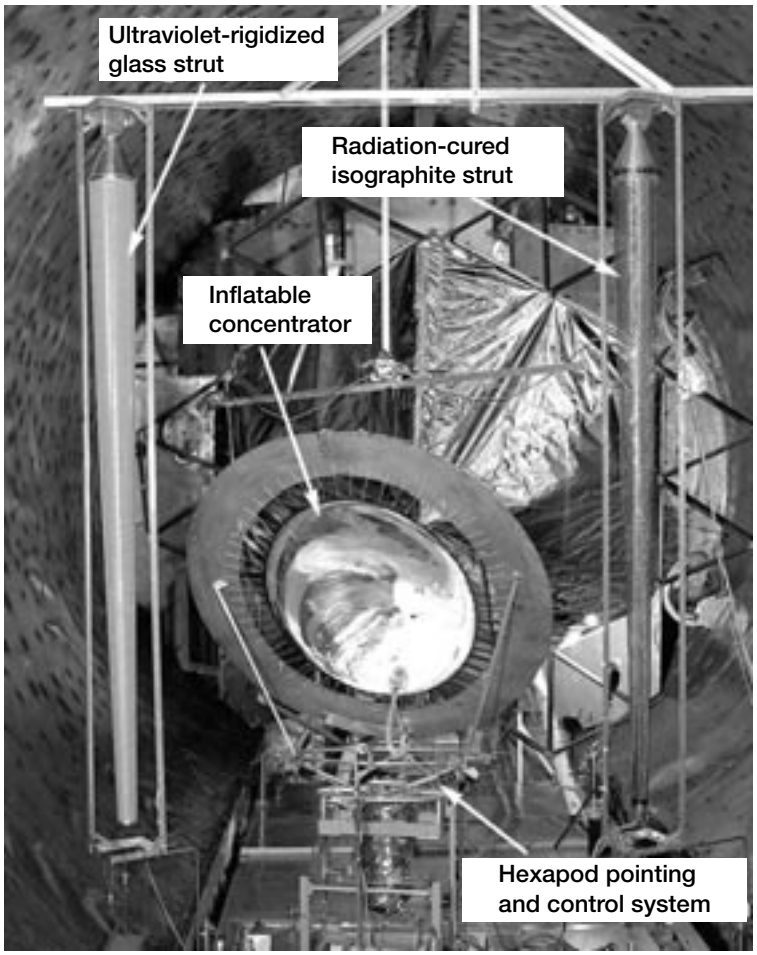

Inflatable solar concentrator, rigidized struts, and hexapod pointing and focus control system setup inside Glenn's Tank 6 Solar Thermal Vacuum Facility.

thin-film rigidized support struts, and shape measurement photogrammetry of the concentrator during the test.

EMRCE is an industry cost-shared Air Force Research Laboratory (AFRL) Dual Use Science & Technology project managed by AFRL/Wright-Patterson Air Force Base, with technical oversight by AFRL/Edwards Air Force Base. The research conducted at Glenn is the culmination of the first year of the 3-yr EMRCE project. Other partners in the EMRCE team are the NASA Marshall Space Flight Center, the Boeing Company, and the AFRL/Kirtland Air Force Base.

Find out more from Glenn's Thermo-Mechanical Systems Branch:
http://www.grc.nasa.gov/WWW/tmsb/

Glenn contact:
Wayne A. Wong, 216–433–6318,
Wayne.A.Wong@grc.nasa.gov

Author: Wayne A. Wong

Headquarters program office: OAT

Programs/Projects:
EMRCE, Solar Thermal Power, Solar Thermal Propulsion, SBIR

Instrumentation and Controls

High-Temperature Gas Sensor Array (Electronic Nose) Demonstrated

The ability to measure emissions from aeronautic engines and in commercial applications such as automotive emission control and chemical process monitoring is a necessary first step if one is going to actively control those emissions. One single sensor will not give all the information necessary to determine the chemical composition of a high-temperature, harsh environment. Rather, an array of gas sensor arrays—in effect, a high-temperature electronic "nose"—is necessary to characterize the chemical constituents of a diverse, high-temperature environment, such as an emissions stream. The signals produced by this nose could be analyzed to determine the constituents of the emission stream. Although commercial electronic noses for near-room temperature applications exist, they often depend significantly on lower temperature materials or only one sensor type. A separate development effort necessary for a high-temperature electronic nose is being undertaken by the NASA Glenn Research Center, Case Western Reserve University, Ohio State University, and Makel Engineering, Inc. The sensors are specially designed for high-temperature environments.

A first-generation high-temperature electronic nose has been demonstrated on a modified automotive engine. This nose sensor array was composed of sensors designed for high-temperature environments fabricated using microelectromechanical-systems- (MEMS-) based technology. The array included a tin-oxide-based sensor doped for nitrogen oxide (NO_x) sensitivity, a SiC-based hydrocarbon (C_xH_y) sensor, and an oxygen sensor (O_2). These sensors operate on different principles—resistor, diode, and electrochemical cell, respectively—and each sensor has very different responses to the individual gases in the environment. A picture showing the sensor head for the array is shown in the photograph on the left and the sensors installed in the engine are shown in the photograph on the right. Electronics are interfaced with the sensors for temperature control and signal conditioning, and packaging designed for high temperatures is necessary for the array to survive the engine environment.

The graph on the next page shows the individual sensor responses during the initial start of the engine, during a warm-up period, during a steady-state operation period, and at the engine turnoff. The sensors were operated at 400 °C, whereas the engine operating temperature was 337 °C. Each sensor has a different characteristic response. The oxygen sensor shows a decrease in O_2 concentration, whereas the NO_x and C_xH_y concentrations (as measured by the tin oxide and SiC sensors, respectively) increase at startup. The hydrocarbon concentrations decrease as the engine warms to steady-state, while the NO_x concentration increases before

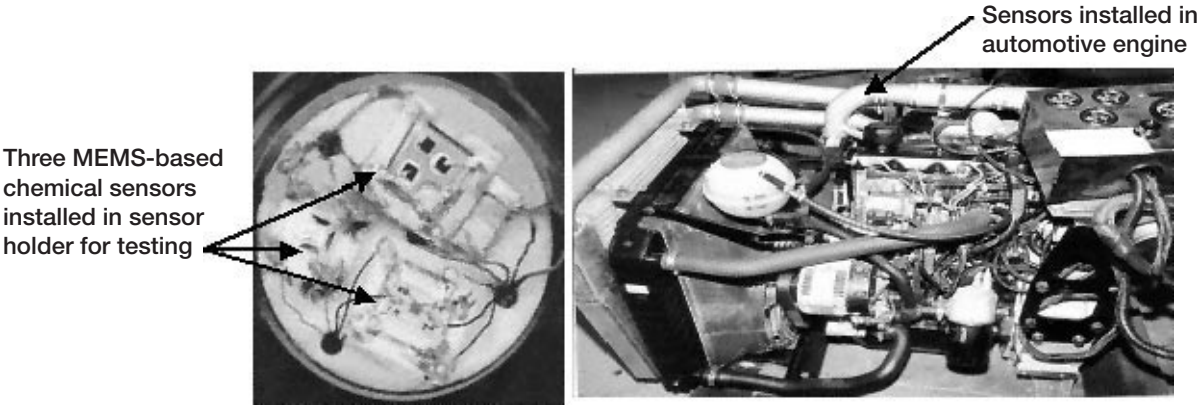

Left: Prototype high-temperature electronic nose array sensor head. Right: Sensors installed in engine.

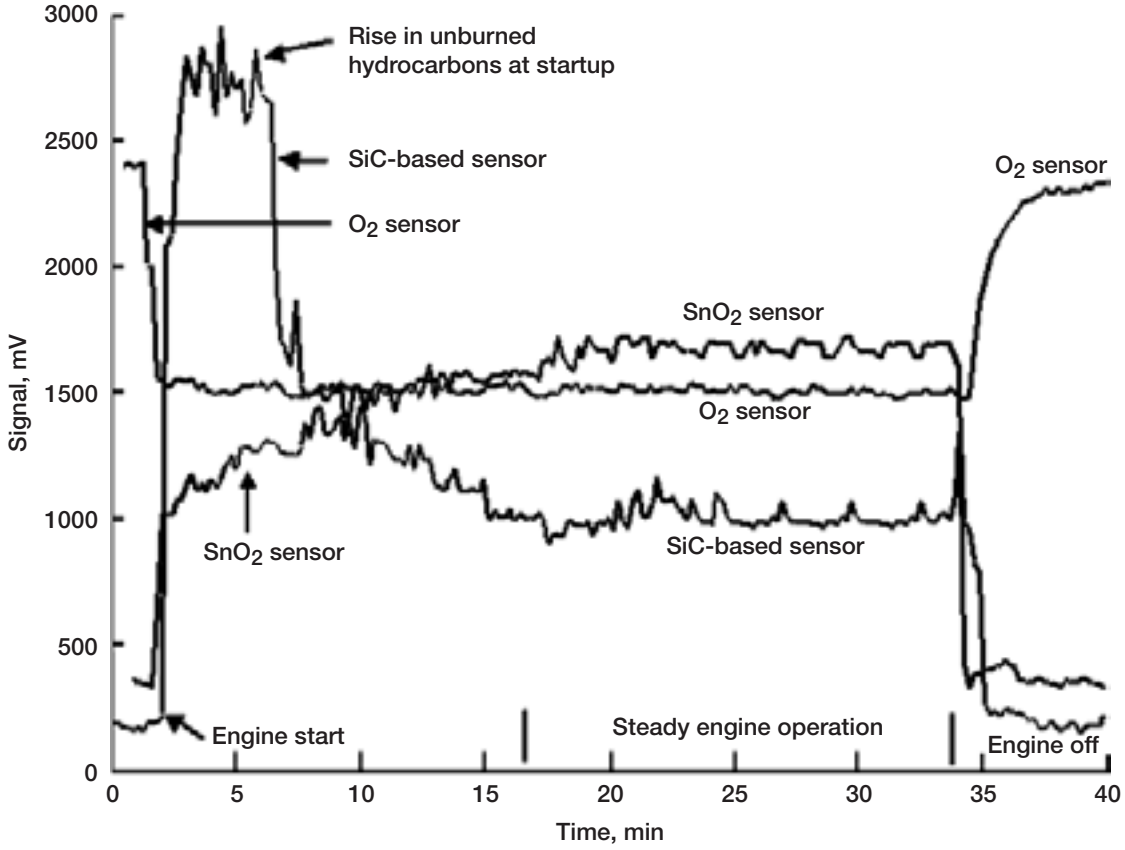

Response of a sensor array composed of a tin-oxide-based sensor (doped for NO_x sensitivity), an oxygen sensor, and a SiC-based hydrocarbon sensor in an engine environment.

stabilizing. The O_2, NO_x, and C_xH_y concentrations all return to their startup values after the engine is turned off. These results are qualitatively consistent with what would be expected for this type of engine. They also show the value of using sensors with very different response mechanisms in an electronic nose array: the information provided by each sensor was unique and monitored a different aspect of the engine's chemical behavior. Further work is planned to include the addition of more sensors and pattern recognition software for sorting out the responses of the various sensors. Neural network processing will be used to integrate and interpret this information to more accurately determine the chemical signatures of harsh, high-temperature environments. The high-temperature electronic nose integration work and demonstration was funded by the Glennan Microsystems Initiative.

Find out more about this research:
Glenn's gas sensor research: http://www.grc.nasa.gov/WWW/chemsensors/

Glennan Microsystems:
http://www.glennan.org/

Bibliography

Hunter, Gary W.; Chung-Chiun, Liu; and Makel, Darby B.: Microfabricated Chemical Sensors for Aerospace Applications. The MEMS Handbook. Mohamed Gad-el-Hak, ed., CRC Press, Boca Raton, FL, 2002, pp. 22–1—22–24.

Glenn contact:
Dr. Gary W. Hunter, 216–433–6459,
Gary.W.Hunter@grc.nasa.gov

Author: Dr. Gary W. Hunter

Headquarters program office: OAT

Programs/Projects: GMI

Bulk Micromachined 6H-SiC High-g Piezoresistive Accelerometer Fabricated and Tested

High-g accelerometers are needed in certain applications, such as in the study and analysis of high-g impact landings and projectiles. Also, these accelerometers must survive the high electromagnetic fields associated with the all-electric vehicle technology needed for aerospace applications. The choice of SiC is largely due to its excellent thermomechanical properties over conventional silicon-based accelerometers, whose material properties inhibit applicability in high electromagnetic radiation and high temperatures (>150 °C) unless more complex and sometimes costly packaging schemes are adopted (refs. 1 and 2). This work was the outcome of a NASA Glenn Research Center summer internship program, in collaboration with Cornell University and the Munitions Directorate of the U.S. Air Force in Eglin, Florida. It aimed to provide the enabling technology infrastructure (modeling, fabrication, and validation) for the implementation of SiC accelerometers designed specifically for harsh environments.

We batch-fabricated the first-generation single-crystal, 6H–SiC piezoresistive accelerometers at Glenn's Sensors and Electronics Branch and successfully tested them at the Fuzes Branch of the Munitions Directorate of the Air Force Research Laboratory at the Eglin Air Force Base. The as-fabricated 6H–SiC accelerometer chip sizes ranged from 4 to 6.25 mm^2 in area, with Wheatstone-bridge-configured piezoresistive mesa elements that were dry-etched in an *n*-type 6H–SiC epilayer grown on a *p*-type 6H-SiC substrate. A scanning electron microscope micrograph of one design concept is shown on the left, and a cross section is shown on the right to depict the relative positions of the resistors. The four sensing elements were placed longitudinally on the narrow beams, each located on the inner edge of the peripheral rigid structure and at the opposite edges of the centered inertial proof mass. The beams were fabricated by a deep reactive ion-etching process. The two wide beams control the overall stiffness and deflection of the structure. The two narrow beams that carry the piezoresistors transfer strain into the piezoresistors, effecting a change in output voltage from the Wheatstone bridge. The wider beams can be adjusted during design to control the strain level transferred to the narrow beams. Representative results from selected design concepts are shown in the following graphs. The responses of the SiC-bossed circular membrane and the simple membrane to acceleration were compared with a benchmark Endevco 7270 accelerometer (Endevco Corporation, 30700 Rancho Viejo Road, San Juan Capistrano, CA 92675).

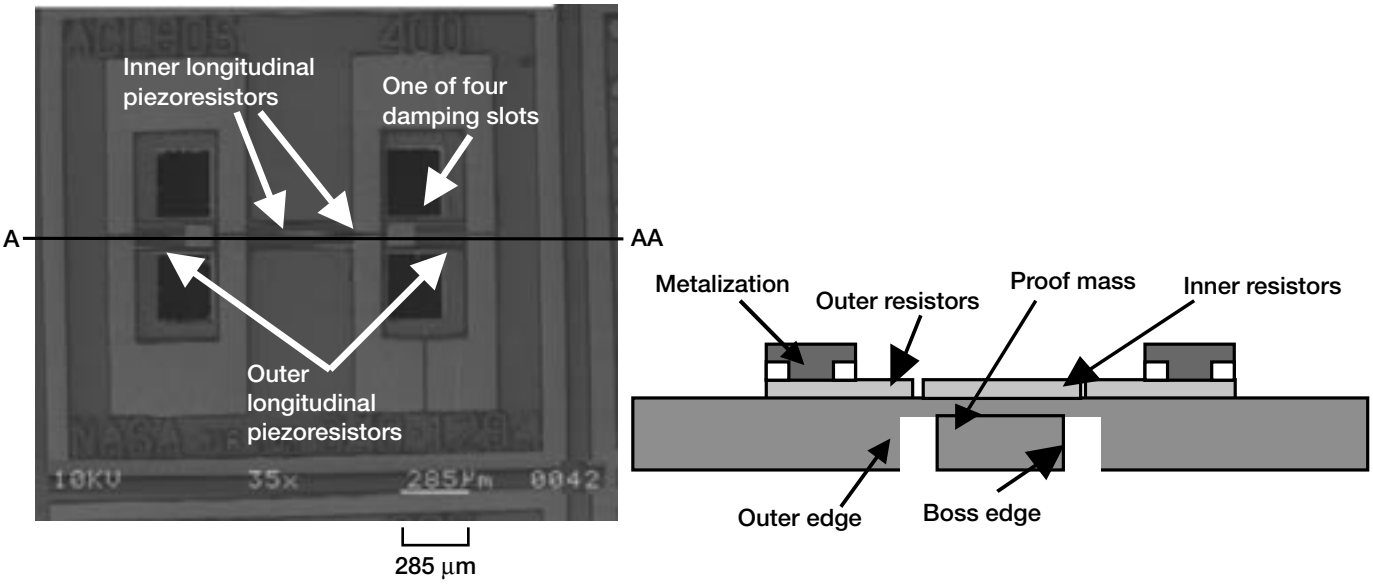

Left: Scanning electron micrograph of an accelerometer depicts the four longitudinal piezoresistors and twin suspension beams. Right: A–AA cross section of the illustration on the left indicates the relative locations of the inner and outer resistors on the narrow suspension beams.

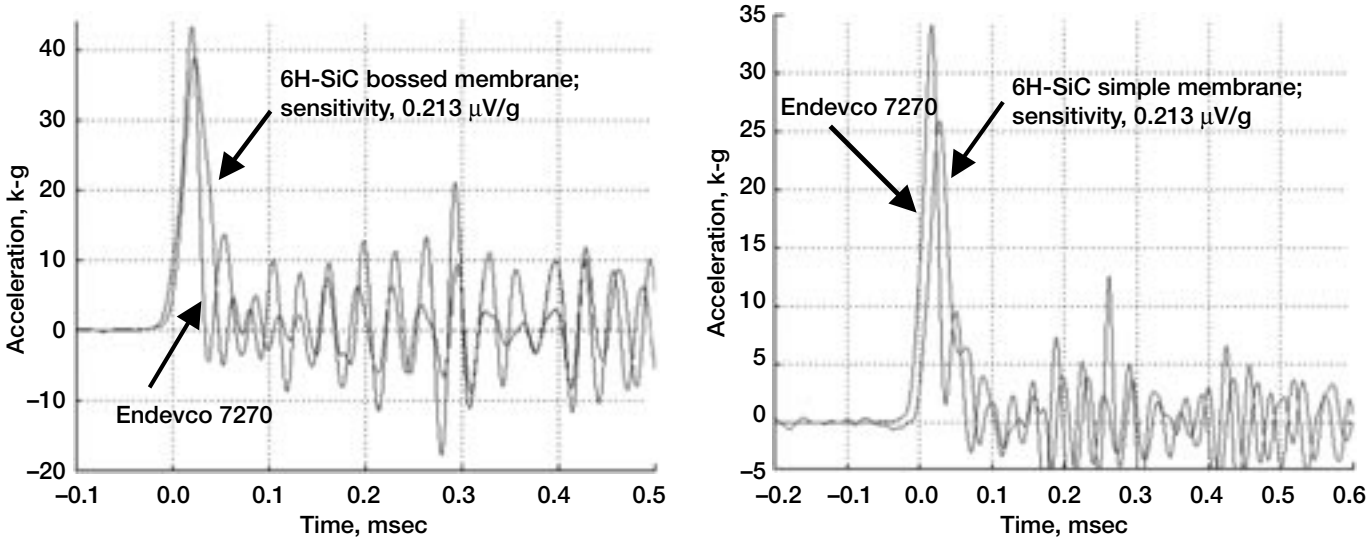

The impulse responses of the 6H-SiC for bossed (left) and simple membrane (right) accelerometers in gray are compared with the response of the benchmark Endevco 7520 accelerometer in black. This figure is shown in color in the online version of this article (http://www.grc.nasa.gov/WWW/RT2001/5000/5510okojie.html).

Although both designs tracked the benchmark very well (to within 6 μsec for the bossed membrane and 12 μsec for the simple membrane), issues such as nonlinearity, steady-state quiescence, and packaging will be investigated as ongoing work. The finite element modeling predicts SiC accelerometer operation at 300 kg (15 percent of 6H–SiC fracture strength).

This work is of significance to NASA's goal to revolutionize aviation, with objectives that include increasing aviation safety and reducing noise. The SiC accelerometers can be inserted in closer proximity than before in the hot sections of engines, rockets, and the space shuttles for in situ monitoring of extreme vibration loads. These accelerometers may also find application in high-impact landers.

In the next phase of work, we plan to streamline the design parameters based on previous results with the goal of optimizing the accelerometer performance characteristics.

Find out more about this research: http://www.grc.nasa.gov/WWW/SiC/SiC.html

References

1. Brown, T.G., et al.: Strap Down Microelectromechanical (MEMS) Sensors for High-g Munition Applications. IEEE Trans. Magn., vol. 37, no. 1, part 1, 2001, pp. 336–342.
2. Katulka, G.L., et al.: Characterization of Silicon Carbide and Commercial-Off-The-Shelf (COTS) Components for High-g Launch and EM Applications. IEEE Trans. Magn., vol. 37, no. 1, part 1, 2001, pp. 248–251.

Glenn contact:
Dr. Robert S. Okojie, 216–433–6522, Robert.S.Okojie@grc.nasa.gov

Author: Dr. Robert S. Okojie

Headquarters program office: OAT

Programs/Projects: GMI

Interferometer-Controlled Optical Tweezers Constructed for Nanotechnology and Biotechnology

A new method to control microparticles was developed in-house at the NASA Glenn Research Center in support of the nanotechnology project under NASA's Aerospace Propulsion and Power Base Research Program. A prototype interferometer-controlled optical tweezers was constructed to manipulate scanning probe microscope (SPM) tips. A laser beam passed through a Mach-Zehnder interferometer, and a microscope objective then produced an optical trap from the coaxial beams. The trap levitated and generated the coarse motion of a 10-μm polystyrene sphere used to simulate a SPM tip. The interference between the beams provided fine control of the forces and moments on the sphere. The interferometer included a piezoelectric-scanned mirror to modulate the interference pattern. The 10-μm sphere was observed to oscillate about 1 μm as the mirror and fringe pattern oscillated.

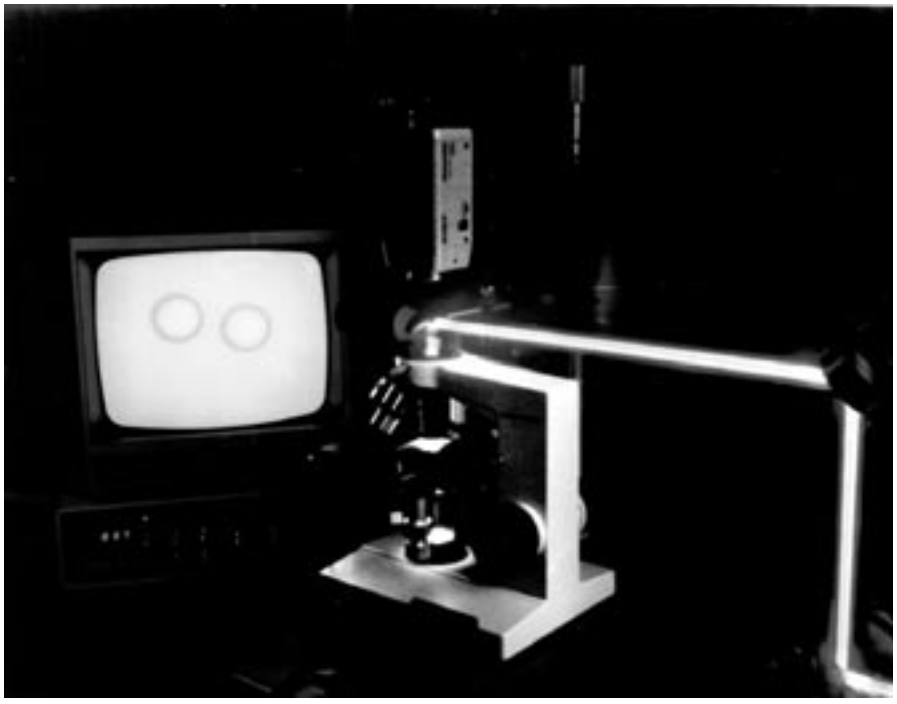

The output of a Mach-Zehnder interferometer is used to form laser tweezers that can move particles by interference phase control.

The prototype tweezers proved the feasibility of constructing a more sophisticated interferometer tweezers to hold and manipulate SPM tips. The SPM tips are intended to interrogate and manipulate nanostructures. A more powerful laser will be used to generate multiple traps to hold nanostructures and SPM tips. The vibrating mirror in the interferometer will be replaced with a spatial light modulator. The modulator will allow the optical phase distribution in one leg of the interferometer to be programmed independently at 640 by 480 points for detailed control of the forces and moments. The interference patterns will be monitored to measure the motion of the SPM tips. Neural-network technology will provide fast analysis of the interference patterns for diagnostic purposes and for local or remote feedback control of the tips. This effort also requires theoretical and modeling support in the form of scattering calculations for twin coherent beams from nonspherical particles.

Glenn contact:
Dr. Arthur J. Decker, 216–433–3639, Arthur.J.Decker@grc.nasa.gov

Author: Dr. Arthur J. Decker

Headquarters program office: OAT

Programs/Projects:
Aerospace Propulsion and Power Base Research, Microgravity Science

Fiber-Optic Pressure Sensor With Dynamic Demodulation Developed

Researchers at the NASA Glenn Research Center developed in-house a method to detect pressure fluctuations using a fiber-optic sensor and dynamic signal processing. This work was in support of the Intelligent Systems Controls and Operations project under NASA's Information Technology Base Research Program.

We constructed an optical pressure sensor by attaching a fiber-optic Bragg grating to a flexible membrane and then adhering the membrane to one end of a small cylinder. The other end of the cylinder was left open and exposed to pressure variations from a pulsed air jet. These pressure variations flexed the membrane, inducing a strain in the fiber-optic grating. This strain was read out optically with a dynamic spectrometer to record changes in the wavelength of light reflected from the grating.

The dynamic spectrometer was built in-house to detect very small wavelength shifts induced by the pressure fluctuations. The spectrometer is an unbalanced interferometer specifically designed for maximum sensitivity to wavelength shifts. An optimum path-length difference, which was determined empirically, resulted in a 14-percent sensitivity improvement over theoretically predicted path-length differences. This difference is suspected to be from uncertainty about the spectral power difference of the signal reflected from the Bragg grating.

The figure shows the output of the dynamic spectrometer as the sensor was exposed to a nominally 2-kPa peak-to-peak square-wave pressure fluctuation. Good tracking, sensitivity, and signal-to-noise ratios are evident even though the sensor was constructed as a proof-of-concept and was not optimized in any way. Therefore the fiber-optic Bragg grating, which is normally considered a good candidate as a strain or temperature sensor, also has been shown to be a good candidate for a dynamic pressure sensor.

This optical pressure sensor has been examined for aerospace applications because of the advantages of using fiber optics over traditional cabling. The replacement of copper cabling by optical fibers can reduce weight, both because glass weighs less than copper and because optical signals can be more highly multiplexed than electrical signals. Also, because they operate using light rather than electrical signals, they are not susceptible to electromagnetic interference and do not pose a sparking hazard.

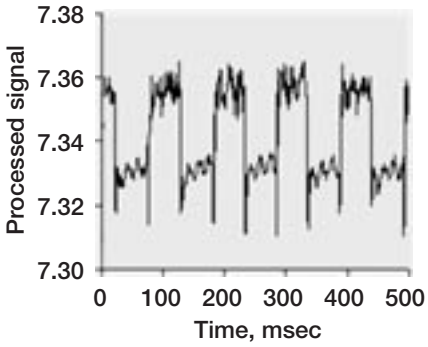

Fiber-optic Bragg grating responds well to pressure fluctuations.

Glenn contacts:
John D. Lekki, 216–433–5650, John.D.Lekki@grc.nasa.gov; and
Dr. Grigory Adamovsky, 216–433–3736, Grigory.Adamovsky@grc.nasa.gov

Author: John D. Lekki

Headquarters program office: OAT

Programs/Projects: IT Base (Intelligent Systems Controls and Operations), Aerospace Propulsion and Power Base Research (RAC)

Tip-Clearance Vortex Characterized With Three-Dimensional Digital Particle Image Velocimetry

An optical measurement technique known as Three-Dimensional Digital Particle Image Velocimetry (3-D DPIV) was used to characterize the tip clearance flow in NASA Glenn Research Center's low-speed axial compressor. 3-D DPIV is a technique in which a stereoscopic imaging system consisting of two cross-correlation cameras is used to record particles entrained in a flow as a laser light sheet is pulsed at two instances in time. Although 3-D DPIV has been used elsewhere, this is the first time it has been used to measure compressor tip clearance flows. In-house modifications of the DPIV system include the use of effective seeding technology and a novel system to perform a priori calibrations at all five measurement planes, greatly reducing facility run time.

Computational fluid dynamics predictions, which are used to guide design changes toward improving the efficiency and operating range of turbomachinery, can be verified and improved by comparison with 3-D DPIV measurements of the actual tip clearance flow. This measurement campaign dealt with the characterization of the tip clearance vortex in the first stage of a four-stage axial compressor. The tip clearance vortex is formed in compressors operating with a clearance gap between the moving rotor blade tips and the stationary casing when a leakage flow, forced from the pressure side of the blade over the blade tip, forms a vortical structure on the suction side of the blade.

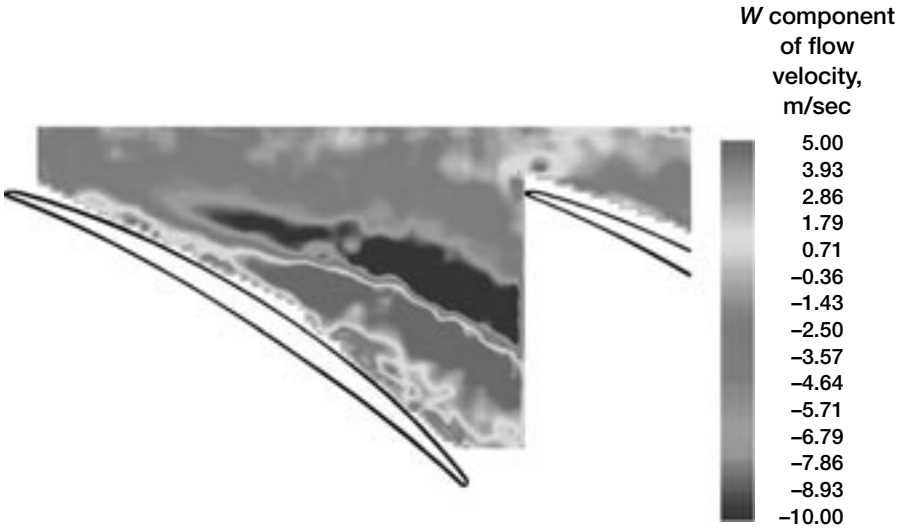

A cross section of flow within a low-speed compressor shows a strong tip clearance vortex. The color contours indicate the magnitude of the radial velocity component. The blade tips are outlined in black. This figure is shown in color in the online version of this article (http://www.grc.nasa.gov/WWW/RT2001/5000/5520wernet.html).

3-D DPIV is ideally suited to measure the clearance vortex for two reasons: (1) this technique captures the entire blade passage flow at one instant in time, so that wandering of the vortex during the measurement does not smear out velocity gradients in the flow field, and (2) the spanwise component of velocity changes sign across the vortex core, providing a more accurate measurement of the vortex location than was available with previous two-dimensional measurement approaches. These two attributes of the data will enable computational fluid dynamics researchers to validate their predictions to a level of accuracy not previously attainable.

In an effort to understand the effects of this flow phenomenon on the operation of the low-speed axial compressor, data were acquired at two mass flow coefficients: 0.395 (design operating point) and 0.35 (operating point just above stall). In order to identify the spatial extent, location, and magnitude of the tip clearance vortex for each mass flow condition, data were acquired at five equally spaced spanwise locations, from 90- to 100-percent span. The data in the figure show a cross section of the tip clearance vortex at 94-percent span and a mass flow coefficient of 0.395, where the color contours represent the radial velocity component. The blue (flow towards the hub) and red (flow towards the casing) regions illustrate the extent of the tip clearance vortex. The interface between the blue and red regions delineates the location of the vortex core.

Find out more about this research:
http://www.grc.nasa.gov/WWW/OptInstr/au/folkmpw.html

Glenn contacts:
Dr. Mark P. Wernet, 216–433–3752, Mark.P.Wernet@grc.nasa.gov; and
Dr. Anthony J. Strazisar, 216–433–5881, Anthony.J.Strazisar@grc.nasa.gov

Author: W. Trevor John

Headquarters program office: OAT

Programs/Projects:
QAT, UEET, Aerospace Propulsion and Power Base Research, Microgravity

Active Control of Combustor Instability Shown to Help Lower Emissions

In a quest to reduce the environmental impact of aerospace propulsion systems, extensive research is being done in the development of lean-burning (low fuel-to-air ratio) combustors that can reduce emissions throughout the mission cycle. However, these lean-burning combustors have an increased susceptibility to thermoacoustic instabilities, or high-pressure oscillations much like sound waves, that can cause severe high-frequency vibrations in the combustor. These pressure waves can fatigue the combustor components and even the downstream turbine blades. This can significantly decrease the safe operating life of the combustor and turbine. Thus, suppression of the thermoacoustic combustor instabilities is an enabling technology for lean, low-emissions combustors. Under the Aerospace Propulsion and Power Base Research and Technology Program, the NASA Glenn Research Center, in partnership with Pratt & Whitney and United Technologies Research Center, is developing technologies for the active control of combustion instabilities.

With active combustion control, the fuel is pulsed to put pressure oscillations into the system. This cancels out the pressure oscillations being produced by the instabilities. Thus, the engine can have lower pollutant emissions *and* long life.

The use of active combustion instability control to reduce thermo-acoustic-driven combustor pressure oscillations was demonstrated on a single-nozzle combustor rig at United Technologies. This rig has many of the complexities of a real engine combustor (i.e., an actual fuel nozzle and swirler, dilution cooling, etc.). Control was demonstrated through modeling, developing, and testing a fuel-delivery system able to pulse the fuel at the 280-Hz instability frequency. The figure at the bottom left shows the capability of this system to provide high-frequency fuel modulations. Because of the high-shear contra-rotating airflow in the fuel injector, there was some concern that the fuel pulses would be attenuated to the point where they would not be effective for control. Testing in the combustor rig showed that open-loop pulsing of the fuel was, in fact, able to effectively modulate the combustor pressure. To suppress the combustor pressure oscillations due to thermoacoustic instabilities, it is desirable to time the injection of the fuel so that it interferes with the instability. A closed-loop control scheme was developed that uses combustion pressure feedback and a phase-shifting controller to time the fuel-injection pulses. Some suppression of the pressure oscillations at the 280-Hz instability frequency was demonstrated (see the figure on the next page). However, the overall peak-to-peak pressure oscillations in the

Pulsating fuel modulations are used to suppress combustion instability.

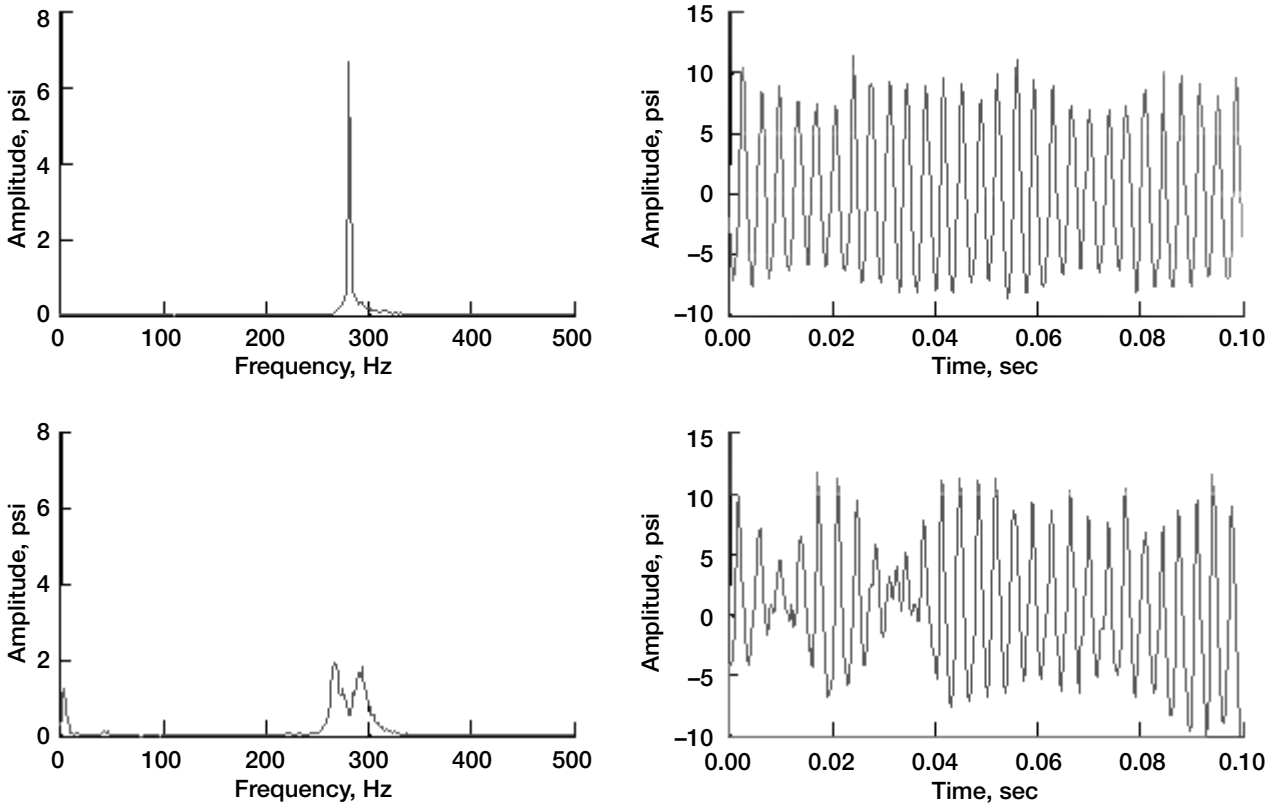

Power spectra and time history of the combustor pressure oscillations without and with instability control. Top: Without instability control; rms pressure amplitude, 5.35 psi. Bottom: With instability control; rms pressure amplitude, 5.01 psi.

combustor were only mildly reduced. Improvements to control hardware and control methods are being continued to gain improved closed-loop reduction of the pressure oscillations.

Find out more about this research:
Active Combustion Control project:
http://www.grc.nasa.gov/WWW/cdtb/projects/combustor/

Glenn's Combustion Branch: http://www.grc.nasa.gov/WWW/combustion/

Glenn contacts: John C. DeLaat, 216–433–3744, John.C.DeLaat@grc.nasa.gov; and Dr. Clarence T. Chang, 216–433–8561, Clarence.T.Chang@grc.nasa.gov

Authors: John C. DeLaat and Dr. Clarence T. Chang

Headquarters program office: OAT

Programs/Projects: Aerospace Propulsion and Power Base Research (SEC), UEET

Life-Extending Control for Aircraft Engines Studied

Current aircraft engine controllers are designed and operated to provide both performance and stability margins. However, the standard method of operation results in significant wear and tear on the engine and negatively affects the on-wing life—the time between cycles when the engine must be physically removed from the aircraft for maintenance. The NASA Glenn Research Center and its industrial and academic partners have been working together toward a new control concept that will include engine life usage as part of the control function. The resulting controller will be able to significantly extend the engine's on-wing life with little or no impact on engine performance and operability. The new controller design will utilize damage models to estimate and mitigate the rate and overall accumulation of damage to critical engine parts. The control methods will also provide a means to assess tradeoffs between performance and structural durability on the basis of mission requirements and remaining engine life.

Two life-extending control methodologies were studied to reduce the overall life-cycle cost of aircraft engines. The first methodology is to modify the baseline control logic to reduce the thermomechanical fatigue (TMF) damage of cooled stators during acceleration. To accomplish this, an innovative algorithm limits the low-speed rotor acceleration command when the engine has reached a threshold close to the requested thrust. This algorithm allows a significant reduction in TMF damage with only a very small increase in the rise time to reach the commanded rotor speed.

The second methodology is to reduce stress rupture/creep damage to turbine blades and uncooled stators by incorporating an engine damage model into the flight mission. Overall operation cost is reduced by an optimization among the flight time, fuel consumption, and component damages (see the flowchart to the left).

Recent efforts have focused on applying life-extending control technology to an existing commercial turbine engine, and doing so without modifying the hardware or adding sensors. This approach (see the figure below) makes it possible to retrofit existing engines with life-extending control technology by changing only the control software in the full-authority digital engine controller (FADEC).

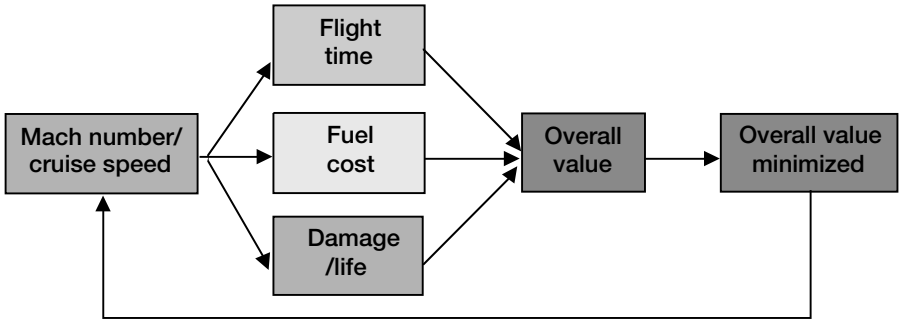

Tradeoff optimization among flight time, fuel consumption, and component damages.

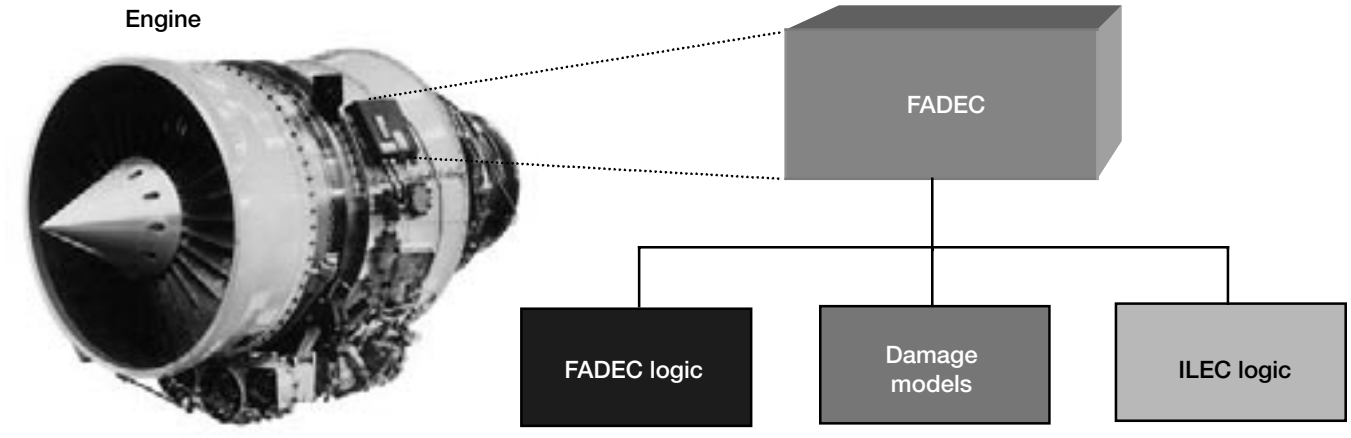

Life-extending control approach. ILEC, Intelligent Life-Extending Control.

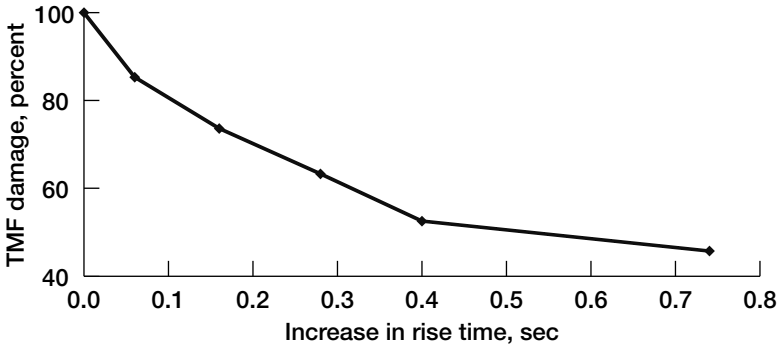

Thermomechanical fatigue (TMF) damage versus rise time.

The significant results include demonstrating a 20- to 30-percent reduction in TMF damage to the hot section by developing and implementing smart acceleration logic during takeoff. The tradeoff is an increase, from 5.0 to 5.2 sec, in the time required to reach maximum power from ground idle (see the graph).

On a typical flight profile of a cruise at Mach 0.8 at an altitude of 41,000 ft, and cruise time of 104 min, the optimized system showed that a reduction in cruise speed from Mach 0.8 to 0.79 can achieve an estimated 25- to 35-percent creep/rupture damage reduction in the engine's hot section and a fuel savings of 2.1 percent. The tradeoff is an increase in flight time of 1.3 percent (1.4 min).

Bibliography

Guo, T.-H.: A Roadmap for Aircraft Engine Life Extending Control (I). Proceedings of the American Control Conference, vol. 5, IEEE, Piscataway, NJ, 2001, pp. 3702–3705.

Scientific Monitoring, Inc.: Intelligent Engine Life Usage Control (ILEC) Demonstration Program. NASA Contract NAS3–98112, Oct. 19, 2001.

Glenn contact:
Dr. Ten-Huei Guo, 216–433–3734, Ten-Huei.Guo@grc.nasa.gov

Author: Dr. Ten-Huei Guo

Headquarters program office: OAT

Programs/Projects: IT Base

Hybrid Neural-Network–Genetic Algorithm Technique for Aircraft Engine Performance Diagnostics Developed and Demonstrated

As part of the NASA Aviation Safety Program, a unique model-based diagnostics method that employs neural networks and genetic algorithms for aircraft engine performance diagnostics has been developed and demonstrated at the NASA Glenn Research Center against a nonlinear gas turbine engine model. Neural networks are applied to estimate the internal health condition of the engine, and genetic algorithms are used for sensor fault detection, isolation, and quantification. This hybrid architecture combines the excellent nonlinear estimation capabilities of neural networks with the capability to rank the likelihood of various faults given a specific sensor suite signature. The method requires a significantly smaller data training set than a neural network approach alone does, and it performs the combined engine health monitoring objectives of performance diagnostics and sensor fault detection and isolation in the presence of nominal and degraded engine health conditions.

Aircraft engine performance is diagnosed by estimating a set of internal engine health parameters from available sensor measurements. The following relationship between the engine health parameters and the sensed parameters can be used to express the general approach:

$$y = f(p, \textit{operating condition}) + w$$

where y is a vector representing the sensed parameters (gas path

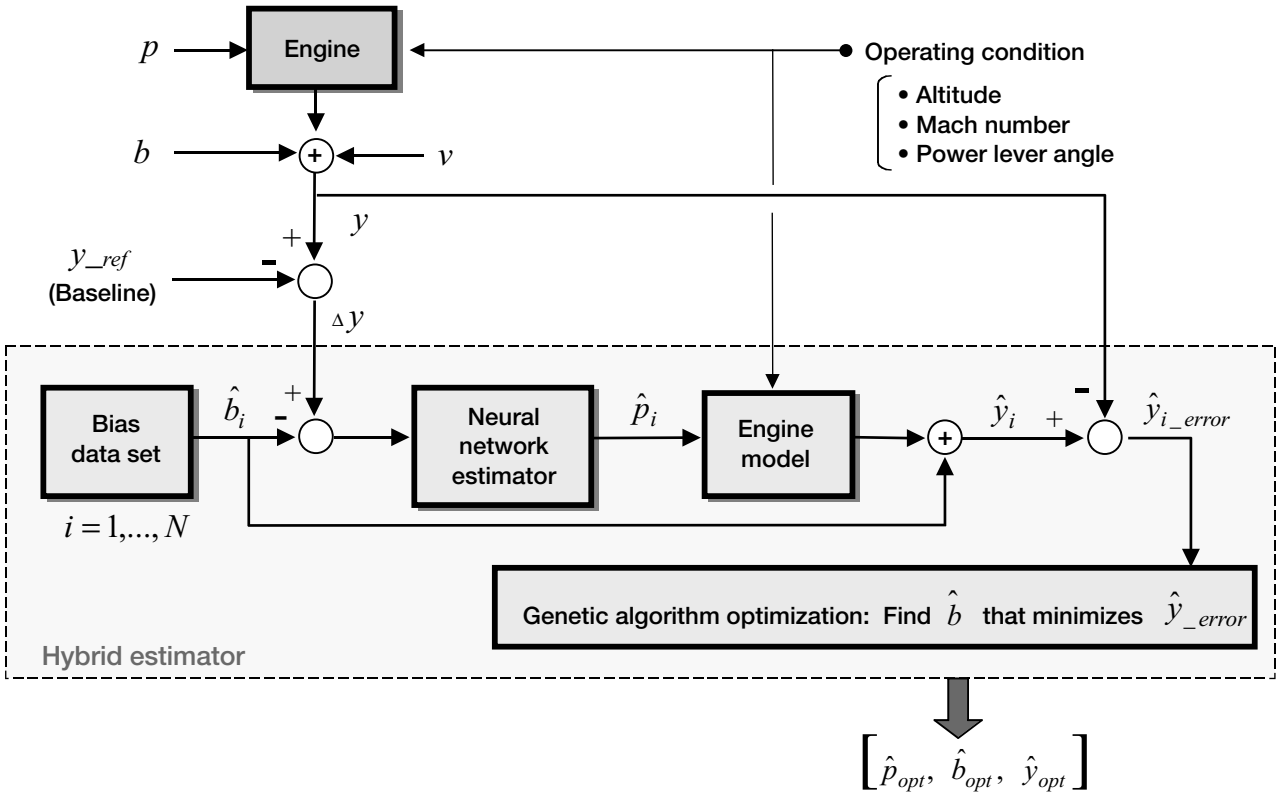

Hybrid engine health estimation architecture.

temperatures and pressures, spool speeds, fuel flow, and variable geometry), p is a vector of engine health parameters (component efficiencies and flow capacities), $f(\bullet)$ is a nonlinear function of p and the engine operating condition, and w is a vector representing measurement inaccuracies. System nonlinearities and potential sensor measurement inaccuracies make this estimation problem very challenging.

The hybrid engine health estimation architecture, as shown in the figure, is composed of a bias data set, a neural network estimator, an engine model, and the genetic algorithm optimization technique. Engine output data are based on the current operating condition and engine health parameters. These sensed parameters are corrupted by a white noise vector v and a bias vector b. To make the problem manageable, we assumed that at most one sensor could be biased at a time. The bias data set, which is composed of a large number of bias vectors, is defined a priori and is used by the genetic algorithms in the search for a bias vector $\hat{b}_i$ that matches well with an actual bias contained in the measurement vector. The neural network estimator is trained offline with noise-corrupted, but bias-free, sensor measurements to estimate engine health parameters $\hat{p}_i$. The neural network will perform sufficiently well in estimating health parameters as long as the sensor measurements do not contain any bias. For a given set of estimated health parameters and sensor bias, the engine model is executed and its output data are evaluated against the physical sensor measurements. The bias data set, the neural network estimator, and the engine model are coordinated by the genetic algorithms in the search for an optimal solution. After the search process, the searched bias vectors are ranked according to their corresponding fitness value, which is a value indicating the agreement between the measured and predicted engine output parameters. A ranked list of several plausible fault candidates can help to avoid false alarms or missed detections.

The table shows an example of the technique's estimation performance applied to a military twin-spool turbofan engine simulation, which was used to represent both the engine and the engine model shown in the figure. Here, 12 sensed engine values were used to estimate the 9 engine health parameters listed in the table. In

HEALTH PARAMETER ESTIMATION WITH AND WITHOUT BIAS DETECTION

[9.5σ bias in fuel flow.]

Health parameter	Actual condition, percent	With bias detection		Without bias detection	
		Estimated condition, percent	Error, percent	Estimated condition, percent	Error, percent
Fan efficiency	–2.900	–2.788	–3.876	–2.950	1.722
Fan flow	–1.800	–1.811	0.596	–1.819	1.076
Booster flow	0	0	-------	–0.134	-------
High-pressure compressor efficiency	–2.300	–2.172	–5.578	–2.305	0.234
High-pressure compressor flow	–1.900	–2.027	6.658	–1.497	–21.213
High-pressure turbine efficiency	–1.400	–1.614	15.254	–1.715	22.516
High-pressure turbine flow	1.000	0.875	–12.484	2.201	120.045
Low-pressure turbine efficiency	–2.000	–2.197	9.857	–2.303	15.146
Low-pressure turbine flow	2.100	2.083	–0.819	2.393	13.942

this case, a 9.5σ bias was modeled in the sensed fuel flow value. Without bias detection, the estimation errors of some engine health parameters are higher than 20 percent, and one is as high as 120 percent. With bias detection, the estimator is able to correctly identify and quantify the bias in the fuel flow. This results in greatly improved health parameter estimation accuracy with all estimation errors at 15 percent or less.

Bibliography

Simon, Donald L.: A Hybrid Neural Network-Genetic Algorithm Technique for Aircraft Engine Performance Diagnostics. AIAA–2001–3763 (NASA/TM—2001-211088, http://gltrs.grc.nasa.gov/GLTRS/), 2001.

QSS contact:
Takahisa Kobayashi, 216–433–3739, Takahisa.Kobayashi@grc.nasa.gov

Army contact:
Donald L. Simon, 216–433–3740, Donald.L.Simon@grc.nasa.gov

Authors: Takahisa Kobayashi and Donald L. Simon

Headquarters program office: OAT

Programs/Projects: AvSP

Communications Technology

Command and Control of Space Assets Through Internet-Based Technologies Demonstrated

The NASA Glenn Research Center successfully demonstrated a transmission-control-protocol/Internet-protocol- (TCP/IP) based approach to the command and control of on-orbit assets over a secure network. This is a significant accomplishment because future NASA missions will benefit by using Internet-standards-based protocols. Benefits of this Internet-based space command and control system architecture include reduced mission costs and increased mission efficiency. The demonstration proved that this communications architecture is viable for future NASA missions.

This demonstration was a significant feat involving multiple NASA organizations and industry. Phillip Paulsen, from Glenn's Project Development and Integration Office, served as the overall project lead, and David Foltz, from Glenn's Satellite Networks and Architectures Branch, provided the hybrid networking support for the required Internet connections. The goal was to build a network that would emulate a connection between a space experiment on the International Space Station and a researcher accessing the experiment from anywhere on the Internet, as shown in the figure.

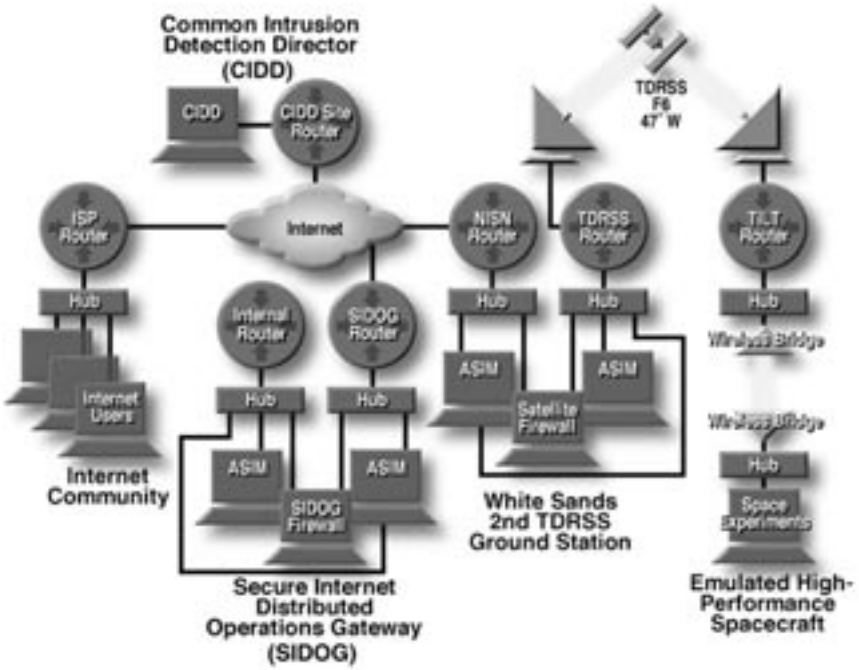

Network architecture used for Inspection 2000.

The experiment was interfaced to a wireless 802.11 network inside the demonstration area. The wireless link provided connectivity to the Tracking and Data Relay Satellite System (TDRSS) Internet Link Terminal (TILT) satellite uplink terminal located 300 ft away in a parking lot on top of a panel van. TILT provided a crucial link in this demonstration. Leslie Ambrose, NASA Goddard Space Flight Center, provided the TILT/TDRSS support. The TILT unit transmitted the signal to TDRS 6 and was received at the White Sands Second TDRSS Ground Station. This station provided the gateway to the Internet. Coordination also took place at the White Sands station to install a Veridian Firewall and automated security incident measurement (ASIM) system to the Second TDRSS Ground Station Internet gateway. The firewall provides a trusted network for the simulated space experiment.

A second Internet connection at the demonstration area was implemented to provide Internet connectivity to a group of workstations to serve as platforms for controlling the simulated space experiment. Installation of this Internet connection was coordinated with an Internet service provider (ISP) and local NASA Johnson Space Center personnel.

Not only did this TCP/IP-based architecture prove that a principal investigator on the Internet can

securely command and control on-orbit assets, it also demonstrated that valuable virtual testing of planned on-orbit activities can be conducted over the Internet prior to actual deployment in space.

Glenn contact: David A. Foltz, 216–433–5077, David.A.Foltz@grc.nasa.gov

Author: David A. Foltz

Headquarters program office: OSF (SOMO)

Programs/Projects: Secure mission operations over the Internet, including accessing experiments aboard the shuttles or the International Space Station

Mobile Router Developed and Tested

The NASA Glenn Research Center, under a NASA Space Act Agreement with Cisco Systems, has been performing joint networking research to apply Internet-based technologies and protocols to space-based communications. As a result of this research, NASA performed stringent performance testing of the mobile router, including the interaction of routing and the transport-level protocol. In addition, Cisco Systems developed the mobile router for both commercial and Government markets. The code has become part of the Cisco Systems Internetworking Operating System (IOS)—as of release 12.2 (4) T—which will make this capability available to the community at large.

The mobile router is software code that resides in a network router and enables entire networks to roam while maintaining connectivity to the Internet. This router code is pertinent to a myriad of applications for both Government and commercial sectors, including the "wireless battlefield." NASA and the Department of Defense will utilize this technology for near-planetary observation and sensing spacecraft. It is also a key enabling technology for aviation-based information applications. Mobile routing will make it possible for information such as weather, air traffic control, voice, and video to be transmitted to aircraft using Internet-based protocols. This technology shows great promise in reducing congested airways and mitigating aviation disasters due to bad weather. The mobile router can also be incorporated into emergency vehicles (such as ambulances and life-flight aircraft) to provide real-time connectivity back to the hospital and health-care experts, enabling the timely application of emergency care. Commercial applications include entertainment services, Internet protocol (IP) telephone, and Internet connectivity for cruise ships, commercial shipping, tour buses, aircraft, and eventually cars.

A mobile router, which is based on mobile IP, allows hosts (mobile nodes) to seamlessly "roam" among various IP subnetworks. This is essential in many wireless networks. A mobile router, unlike a mobile IP node, allows entire networks to roam. Hence, a device connected to the mobile router does not need to be a mobile node because the mobile router provides the roaming capabilities.

There are three basic elements in the mobile IP: the home agent, the foreign agent, and the mobile node. The home agent is a router on a mobile node's home network that tunnels datagrams for delivery to the mobile node when it is away

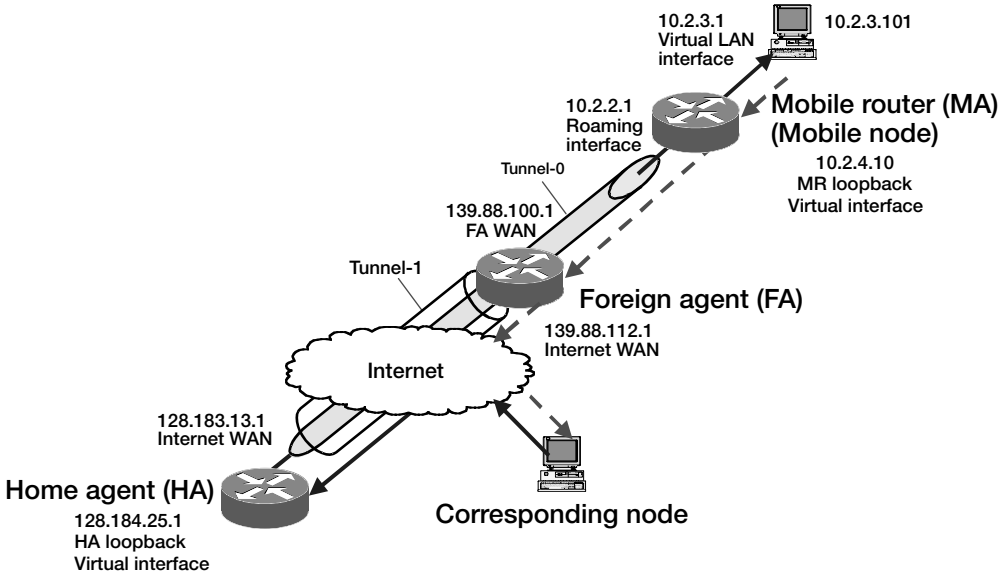

Mobile router tunneling. WAN, wide-area network; LAN, local-area network.

from home. The foreign agent is a router on a remote network that provides routing services to a registered mobile node. The mobile node is a host or router that changes its point of attachment from one network or subnetwork to another.

In mobile routing, virtual communications are maintained by the home agent, which forwards all packets for the mobile networks to the foreign agent. The foreign agent passes the packets to the mobile router, which then forwards the packets to the devices on its networks. As the mobile router moves, it will register with its home agent on its whereabouts via the foreign agent to assure continuous connectivity.

References

1. Ivancic, William D., et al.: Mobile Router Technology Development. Presented at the ACM MSWiM 2001 Technical Program, Rome, Italy, July 2001 (contains TCP handoff results).
2. Stewart, D.H., et al.: Application of Mobile Router to Military Communications. Presented at Milcom 2001, Oct. 2001.
3. Leung, K., et al.: Application of Mobile-ip to Space and Aeronautical Networks. IEEE Aerospace Conference Proceedings, vol. 2, 2001, pp. 21027–21033.

Glenn contact:
William D. Ivancic, 216–433–3494,
William.D.Ivancic@grc.nasa.gov

Author: William D. Ivancic

Headquarters program office:
OSF (SOMO)

Programs/Projects: TSIS

TCP Pacing Developed

Transmission control protocol (TCP) was conceived and designed to run over a variety of communication links, including wireless and high-bandwidth links. However, with recent technological advances in satellite and fiber-optic networks, researchers are reevaluating the flexibility of TCP. The TCP pacing and packet pair probing implementation may help overcome two of the major obstacles identified for efficient bandwidth utilization over communication links with large delay-bandwidth products.

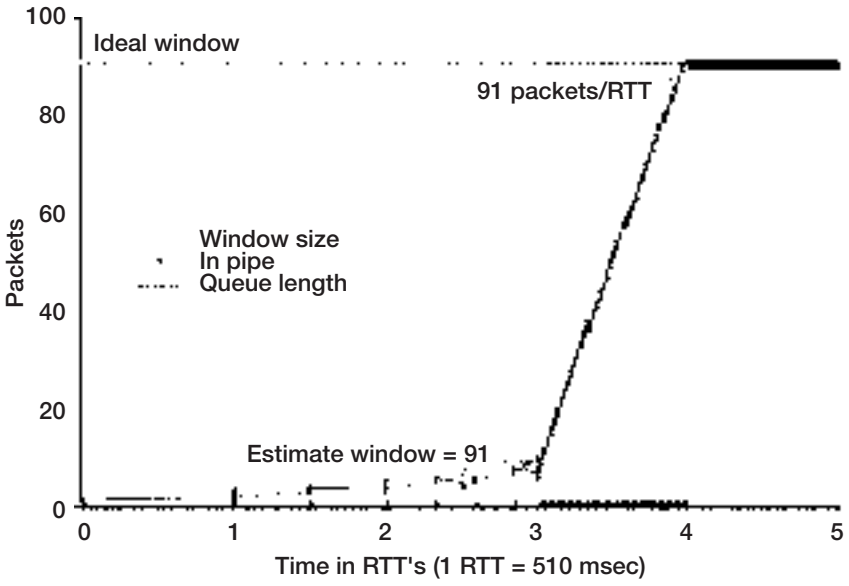

Berkeley Network Simulator time-sequence plot showing the possible rapid ascent to full bandwidth utilization when a combination of TCP pacing and packet pair probing is deployed. Single stream over a 500-msec delay link; maximum queue length, 5.

One problem common to both satellite and fiber-optic networks is that the capacity of these networks, determined by the product of the bandwidth and the delay of the network, can be more than 10 times greater than in conventional networks. The mismatch between the high capacity of these networks and available storage at the intermediate routers in the network poses unique problems for TCP. In a typical network, TCP optimizes its send rate by releasing increasingly large bursts (or windows) of packets (one burst per roundtrip time) to the receiver until it reaches its maximum window size, at which point it has reached the full capacity of the network. In a network with a high delay-bandwidth product, however, TCP's maximum window size may be larger than the queue capacity of some of the network's intermediate routers. Larger windows overload such router queues, and the routers begin to drop packets. TCP interprets dropped packets as congestion at the bottleneck and reduces its transmission rate, even

though no congestion is present. This can result in the ineffective use of available network bandwidth, negatively impacting network performance.

Paced TCP is designed to release its packets smoothly into the network over time rather than bursting its packets into the network at the transmitting host's network interface line rate. Pacing eliminates the need for excessively large queues throughout the network.

A second problem in obtaining high bandwidth efficiency over large delay-bandwidth links has to do with the slow-start algorithm of TCP. TCP determines the available bandwidth through the use of the control loop, packet send/receipt handshake. As the delay increases, it takes more time for an acknowledgment of each packet. For communications links with large delay-bandwidth products, it can take a relatively long time to reach full bandwidth utilization.

Packet-pair probing is a modification to TCP that attempts to improve network performance by extracting available bandwidth information from the spacing of the acknowledgment packets received at the transmitting host corresponding to the initial packets transmitted.

A modified version of TCP known as TCP pacing with packet pair probing has been developed in FreeBSD and is publicly available for researchers to experiment with and build on. This work was performed by BBN Technologies through the Professional, Administrative, Computing and Engineering Contract at the NASA Glenn Research Center. The software is available at http://www.ir.bbn.com/projects/pace/, with the "readme" file available separately.

References

1. Partridge, Craig; Shepard, Tim; and Coulter, Robert: Study and Simulation of Enhancements for TCP Performance Over Noisy High Latency Links. NASA/CR—1999-209167, 1999. http://gltrs.grc.nasa.gov/GLTRS
2. Partridge, Craig; Sterbenz, James; and Rockwell, Dennis: TCP Pacing/Packet Pair Probing. BBN Technologies, Cambridge, MA. Also NASA TM (to be published in 2002).

Glenn contact:
William D. Ivancic, 216–433–3494, William.D.Ivancic@grc.nasa.gov

Author: William D. Ivancic

Headquarters program office:
OSF (SOMO)

Programs/Projects: TSIS

Digital Distortion Caused by Traveling-Wave-Tube Amplifiers Simulated

Future NASA missions demand increased data rates in satellite communications for near real-time transmission of large volumes of remote data. Increased data rates necessitate higher order digital modulation schemes and larger system bandwidth, which place stricter requirements on the allowable distortion caused by the high-power amplifier, or the traveling-wave-tube amplifier (TWTA). In particular, intersymbol interference caused by the TWTA becomes a major consideration for accurate data detection at the receiver. Experimentally investigating the effects of the physical TWTA on intersymbol interference would be prohibitively expensive, as it would require manufacturing numerous amplifiers in addition to acquiring the required digital hardware. Thus, an accurate computational model is essential to predict the effects of the TWTA on system-level performance when a communication system is being designed with adequate digital integrity for high data rates.

A fully three-dimensional, time-dependent, TWT interaction model has been developed (ref. 1) using the electromagnetic particle-in-cell code MAFIA (Solution of Maxwell's equations by the Finite-Integration-Algorithm, ref. 2). It comprehensively takes into account the effects of frequency-dependent AM (amplitude modulation)/AM and AM/PM (phase modulation) conversion, gain and phase ripple due to reflections, drive-induced oscillations, harmonic generation, intermodulation products, and backward waves. This physics-based TWT model can be used to give a direct description of the effects of the nonlinear TWT on the operational signal as a function of the physical device. Users can define arbitrary excitation functions so that higher order modulated digital signals can be used as input and that computations can directly correlate intersymbol interference with TWT parameters.

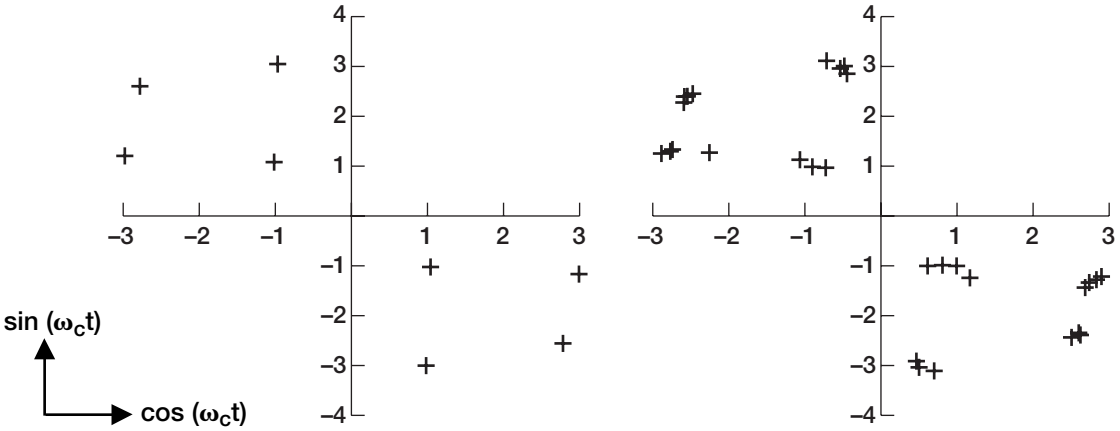

16-ary quadrature amplitude modulation (16-QAM) constellation diagram (7-dB input backoff). Left: SPW. Right: MAFIA.

Standard practice involves using communication-system-level software packages, such as SPW (ref. 3), to predict if adequate signal detection will be achieved. These models use a nonlinear, black-box model to represent the TWTA. The models vary in complexity, but most make several assumptions regarding the operation of the high-power amplifier. When the MAFIA TWT interaction model was used, these assumptions were found to be in significant error (ref. 4). In addition, digital signal performance, including intersymbol interference, was compared using direct data input into the MAFIA model and using the system-level analysis tool SPW for several higher order modulation schemes. Results show significant differences in predicted degradation between SPW and MAFIA simulations, demonstrating the significance of the TWTA approximations made in the SPW model on digital signal performance. For example, the figure compares the SPW and MAFIA output constellation diagrams for a 16-ary quadrature amplitude modulation (16-QAM) signal (data shown only for second and fourth quadrants). The upper-bound degradation was calculated from the corresponding eye diagrams (not shown). In comparison to SPW simulations, the MAFIA data resulted in a 3.6-dB larger degradation.

Find out more about this research:

Electron Device Technology Branch: http://ctd.grc.nasa.gov/5620/5620.html

Digital Communications Technology Branch:
http://ctd.grc.nasa.gov/5650/5650.html

References

1. Kory, C.L.: Three-Dimensional Simulations of PPM Focused Helical Traveling-Wave Tubes. DE Dissertation, Cleveland State Univ., 2000.
2. MAFIA Computer Simulation Technology, 2002. The Advanced Simulation Tool for Electromagnetic Analysis and Design. http://www.cst.de
3. SPW™, Signal Processing Worksystem. Comdisco Systems, Inc., Foster City, CA.
4. Kory, C.L.; and Andro, Monty: Intersymbol Interference Investigations Using a 3D Time-Dependent Traveling Wave Tube Model. IEEE Trans. Plasma Sci., vol. 30, no. 1, 2002.

Glenn contact:
Monty Andro, 216–433–3492,
Monty.Andro@grc.nasa.gov

Analex contact:
Carol L. Kory, 216–433–3512,
Carol.L.Kory@grc.nasa.gov

Authors:
Carol L. Kory and Monty Andro

Headquarters program office: OAT

Programs/Projects: CETDP

High-Power, High-Frequency *Si*-Based (*Si*Ge) Transistors Developed

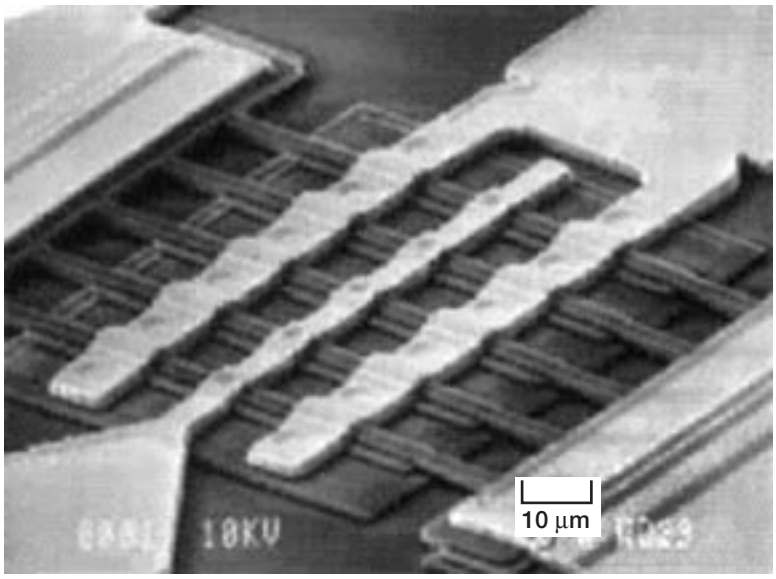

Scanning electron micrograph of a silicon-germanium heterojunction bipolar transistor.

Future NASA, DOD, and commercial products will require electronic circuits that have greater functionality and versatility but occupy less space and cost less money to build and integrate than current products. System on a Chip (SOAC), a single semiconductor substrate containing circuits that perform many functions or containing an entire system, is widely recognized as the best technology for achieving low-cost, small-sized systems. Thus, a circuit technology is required that can gather, process, store, and transmit data or communications. Since silicon-integrated circuits are already used for data processing and storage and the infrastructure that supports silicon circuit fabrication is very large, it is sensible to develop communication circuits on silicon so that all the system functions can be integrated onto a single wafer. Until recently, silicon-integrated circuits did not function well at the frequencies required for wireless or microwave communications, but with the introduction of small amounts of germanium into the silicon to make silicon-germanium (SiGe) transistors, silicon-based communication circuits are possible. Although microwave-frequency SiGe circuits have been demonstrated, there has been difficulty in obtaining the high power from their transistors that is required for the amplifiers of a transmitter, and many researchers have thought that this could not be done.

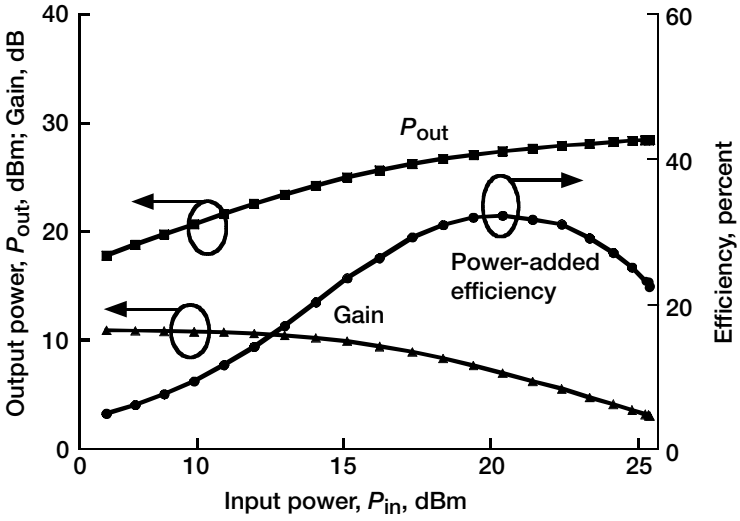

Measured output power, gain, and power-added efficiency of a 20-finger SiGe heterojunction bipolar transistor. Optimum source impedance, Γ_S, 0.816<180.2°; optimum load impedance, Γ_L, 0.828<149.5°; frequency, f, 8.4 GHz; collector-base voltage, V_{CB}, 7.0 V; emitter-base voltage, V_{EB}, 1.481 V.

The NASA Glenn Research Center and collaborators at the University of Michigan have developed SiGe transistors and amplifiers with state-of-the-art output power at microwave frequencies from 8 to 20 GHz. These transistors are fabricated using standard silicon processing and may be integrated with CMOS integrated circuits on a single chip. A scanning electron microscope image of a typical SiGe heterojunction bipolar transistor is shown in the preceding photomicrograph. This transistor achieved a record output power of 550 mW and an associated power-added efficiency of 33 percent at 8.4 GHz, as shown in the graph. Record performance was also demonstrated at 12.6 and 18 GHz.

Developers have combined these state-of-the-art transistors with transmission lines and micromachined passive circuit components, such as inductors and capacitors, to build multistage amplifiers. Currently, a 1-W, 8.4-GHz power amplifier is being built for NASA deep space communication architectures.

Glenn contact:
Dr. George E. Ponchak, 216–433–3504,
George.E.Ponchak@grc.nasa.gov

Author: Dr. George E. Ponchak

Headquarters program office: OAT

Programs/Projects: HRDD

Low-Loss, High-Isolation Microwave Microelectromechanical Systems (MEMS) Switches Being Developed

Switches, electrical components that either permit or prevent the flow of electricity, are the most important and widely used electrical devices in integrated circuits. In microwave systems, switches are required for switching between the transmitter and receiver; in communication systems, they are needed for phase shifters in phased-array antennas, for radar and communication systems, and for the new class of digital or software definable radios. Ideally, switches would be lossless devices that did not depend on the electrical signal's frequency or power, and they would not consume electrical power to change from OFF to ON or to maintain one of these two states. Reality is quite different, especially at microwave frequencies. Typical switches in microwave integrated circuits are pin diodes or gallium arsenide (GaAs) field-effect transistors that are nonlinear, with characteristics that depend on the power of the signal. In addition, they are frequency-dependent, lossy, and require electrical power to maintain a certain state. A new type of component has been developed that overcomes most of these technical difficulties. Microelectromechanical (MEMS) switches rely on mechanical movement as a response to an applied electrical force to either transmit or reflect electrical signal power.

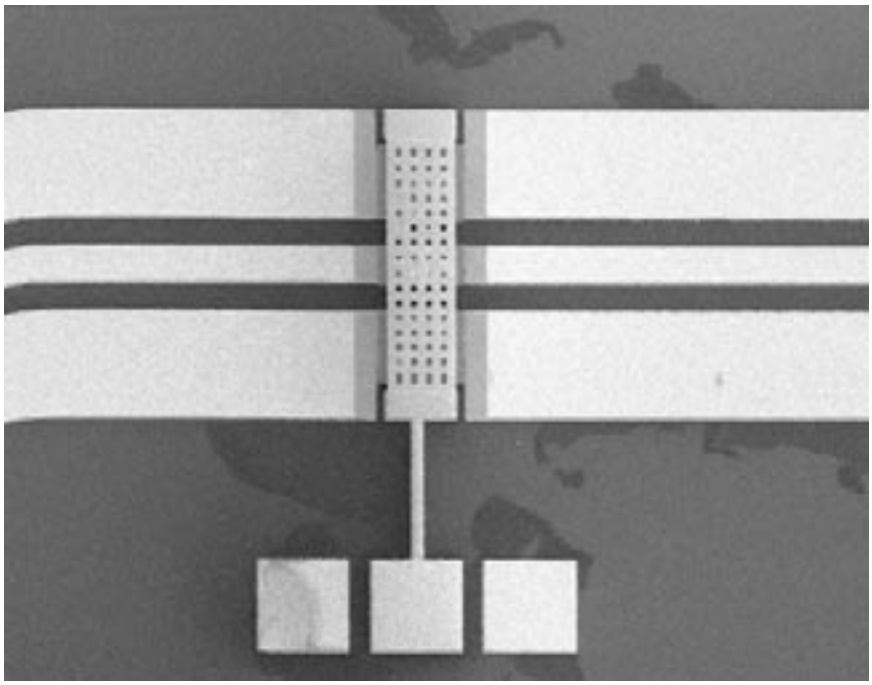

Typical MEMS switch.

The NASA Glenn Research Center has been actively developing MEMS for microwave applications for over the last 5 years. Complete fabrication procedures have been developed so that the moving parts of the switch can be released with near 100-percent yield. Moreover, the switches fabricated at Glenn have demonstrated state-of-the-art performance. A typical MEMS switch is shown in this figure. The switch extends over the signal and ground lines of a finite ground coplanar waveguide, a commonly used microwave transmission line. In the state shown in this figure, the switch is in the UP state and all the microwave power traveling along the transmission line proceeds unimpeded. When a potential difference is applied between the cantilever and the transmission line, the cantilever is pulled downward until it connects the signal line to the ground planes, creating a short circuit. In this state, all the microwave power is reflected. The following graph shows the measured performance of the switch, which has less than 0.1 dB of insertion loss and greater than 30 dB of isolation. These switches consume negligible electrical power and are extremely linear. Additional research is required to address reliability and to increase the switching speed.

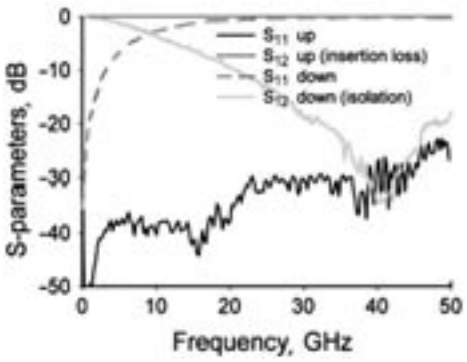

Measured characteristics of a MEMS switch in the UP and DOWN states.

Glenn contact:
Dr. George E. Ponchak, 216–433–3504,
George.E.Ponchak@grc.nasa.gov

Author: Dr. George E. Ponchak

Headquarters program office: OAT

Programs/Projects: HRDD, Glenn DDF

Overall Traveling-Wave-Tube Efficiency Improved By Optimized Multistage Depressed Collector Design

The microwave traveling wave tube (TWT) is used widely for space communications and high-power airborne transmitting sources. One of the most important features in designing a TWT is overall efficiency. Yet, overall TWT efficiency is strongly dependent on the efficiency of the electron beam collector, particularly for high values of collector efficiency. For these reasons, the NASA Glenn Research Center developed an optimization algorithm based on simulated annealing to quickly design highly efficient multistage depressed collectors (MDC's).

Simulated annealing is a strategy for solving highly nonlinear combinatorial optimization problems (ref. 1). Its major advantage over other methods is its ability to avoid becoming trapped in local minima. Simulated annealing is based on an analogy to statistical thermodynamics, specifically the physical process of annealing: heating a material to a temperature that permits many atomic rearrangements and then cooling it carefully and slowly, until it freezes into a strong, minimum-energy crystalline structure. This minimum-energy crystal corresponds to the optimal solution of a mathematical optimization problem.

The TWT used as a baseline for optimization was the 32-GHz, 10-W, helical TWT developed for the Cassini mission to Saturn (ref. 2). The method of collector analysis and design used was a 2-1/2-dimensional computational procedure that employs two types of codes, a large signal analysis code and an electron trajectory code. The large signal analysis code

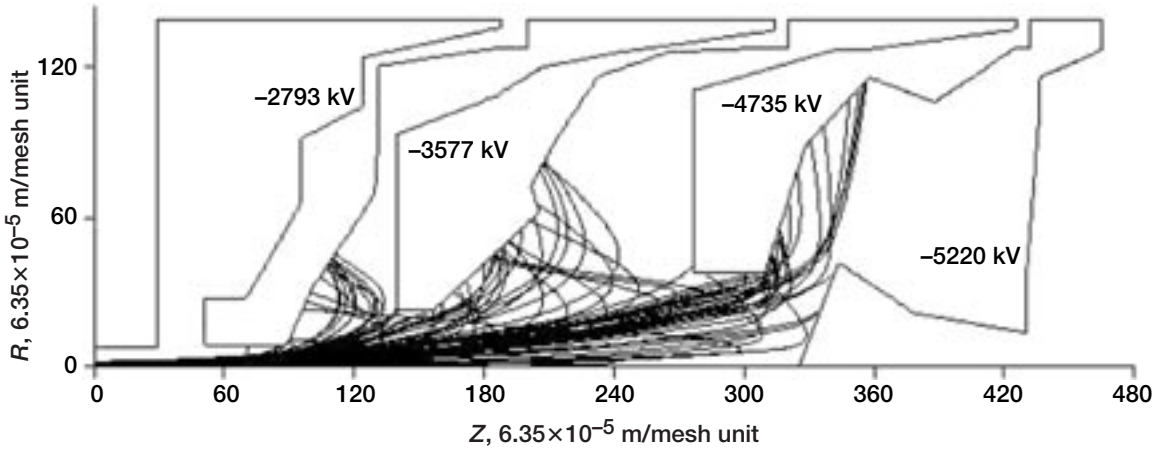

Electron trajectory plot of an optimized multistage depressed collector for a 32-GHz, 10-W traveling wave tube.

produces the spatial, energetic, and temporal distributions of the spent beam entering the MDC. An electron trajectory code uses the resultant data to perform the actual collector analysis. The MDC was optimized for maximum MDC efficiency and minimum final kinetic energy of all collected electrons (to reduce heat transfer). The preceding figure shows the geometric and electrical configuration of an optimized collector with an efficiency of 93.8 percent. The results show the improvement in collector efficiency from 89.7 to 93.8 percent, resulting in an increase of three overall efficiency points. In addition, the time to design a highly efficient MDC was reduced from a month to a few days.

All work was done in-house at Glenn for the High Rate Data Delivery Program. Future plans include optimizing the MDC and TWT interaction circuit in tandem to further improve overall TWT efficiency.

References

1. Kirkpatrick, S.; Gelatt, C.D.; and Vecchi, M.P.: Optimization by Simulated Annealing. SCI., vol. 220, 1983, pp. 671–680.
2. Curren, A.N., et al.: The Cassini Mission Ka-Band TWT. Proceedings of the 1994 IEEE International Electron Devices Meeting, 1994, pp. 783–786.

Glenn contact:
Karl R. Vaden, 216–433–8137,
Karl.R.Vaden@grc.nasa.gov

Author: Karl R. Vaden

Headquarters program office: OAT

Programs/Projects: HRDD

Power-Efficient, High-Current-Density, Long-Life Thermionic Cathode Developed for Microwave Amplifier Applications

A power-efficient, miniature, easily manufactured, reservoir-type barium-dispenser thermionic cathode has been developed that offers the significant advantages of simultaneous high electron-emission current density (>2 A/cm^2) and very long life (>100,000 hr of continuous operation) when compared with the commonly used impregnated-type barium-dispenser cathodes. Important applications of this cathode are a wide variety of microwave and millimeter-wave vacuum electronic devices, where high output power and reliability (long life) are essential. We also expect it to enable the practical development of higher purveyance electron guns for lower voltage and more reliable device operation. The low cathode heater power and reduced size and mass are expected to be particularly beneficial in traveling-wave-tube amplifiers (TWTA's) for space communications, where future NASA mission requirements include smaller onboard spacecraft systems, higher data transmission rates (high frequency and output power) and greater electrical efficiency.

The major life limitation of the impregnated-type barium dispenser cathode results from a limited supply of barium, an uneven rate of barium dispensation over cathode life, and the temperature-driven barium depletion rate, which becomes more rapid at the higher operating temperatures required for higher emission current. In contrast, the reservoir cathode has a constant rate of barium dispensation over the life of the cathode, which is limited only by the amount of barium in the reservoir, hence the capability to sustain high current densities. The capability of simultaneous high current density and very long life is being demonstrated by NASA-owned prototype reservoir cathodes now on life test at the Naval Surface Warfare Center in Crane, Indiana (ref. 1). These cathodes, operating at 2 and 4 A/cm^2, show a continuing unprecedented robust performance and stability after more than 85,000 hr of continuous operation.

The reservoir cathode described here is the result of an effort initiated and sponsored by the NASA Glenn Research Center that is now being pursued under a Small Business Innovation Research (SBIR) contract with FDE, Inc. The SBIR objective is the development of a low-cost, easily manufactured, electrical power efficient version of the NASA prototype reservoir cathode now on life test by combining the best features of the prototype with a low-heater-power, thermally

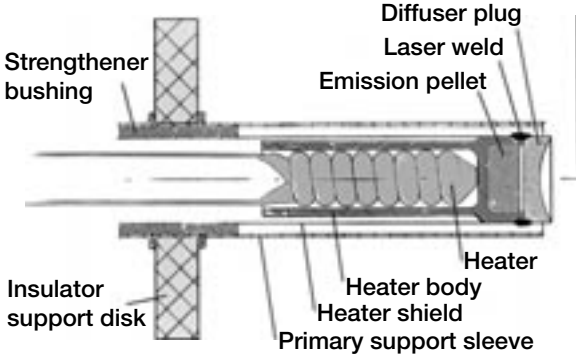

Reservoir cathode design.

efficient impregnated cathode design developed under a previous SBIR contract with FDE, Inc. (ref. 2). Foremost among these features is a thermally and chemically stable electron-emitting surface with a uniformly low work function distribution. The low-cost fabrication is based on manufacturing methods used in the highly efficient cathode ray tube industry.

Although the emphasis has been on small size (0.060 to 0.100 in. diameters) and emission current densities up to 5 A/cm^2, the basic design (shown in the figure on the preceding page) can be readily adapted to significantly larger sizes and higher current densities for both pulse and continuous operation. Glenn is pursuing the development of the reservoir cathode for microwave/millimeter-wave tube applications.

References

1. Tri-Service/NASA Cathode Life Test Facility, Annual Report, Naval Surface Warfare Center, Crane, IN, Jan. 2000–Jan. 2001.
2. Wintucky, Edwin G.: Novel Low-Cost, Low-Power Miniature Thermionic Cathode Developed for Microwave/Millimeter Wave Tube and Cathode Ray Tube Applications. Research & Technology 1998, NASA/TM—1999-208815, 1999, pp. 82–83. http://www.grc.nasa.gov/WWW/RT1998/5000/5620wintucky.html

Find out more about this research:
http://www.fdeassc.com

Glenn contact:
Edwin G. Wintucky, 216–433–3510, Edwin.G.Wintucky@grc.nasa.gov

FDE, Inc., contact:
Bernard Vancil, 503–628–0703, bernie@fdeassc.com

Author: Edwin G. Wintucky

Headquarters program office:
OAT (CTD)

Programs/Projects:
Space Communications, SBIR

Microelectromechanical Systems (MEMS) Actuator-Based, Polarization Reconfigurable Patch Antenna Demonstrated

A nearly square patch antenna with a contact actuator along a radiating edge for polarization reconfiguration was demonstrated at Ka-band frequencies at the NASA Glenn Research Center. The layout of the antenna is shown in the following sketch. This antenna has the following advantages:

(1) It can be dynamically reconfigured to receive and transmit a linearly polarized signal or a circularly polarized signal. This feature allows the substitution of multiple antennas on a satellite by a single antenna, thereby resulting in significant cost savings.

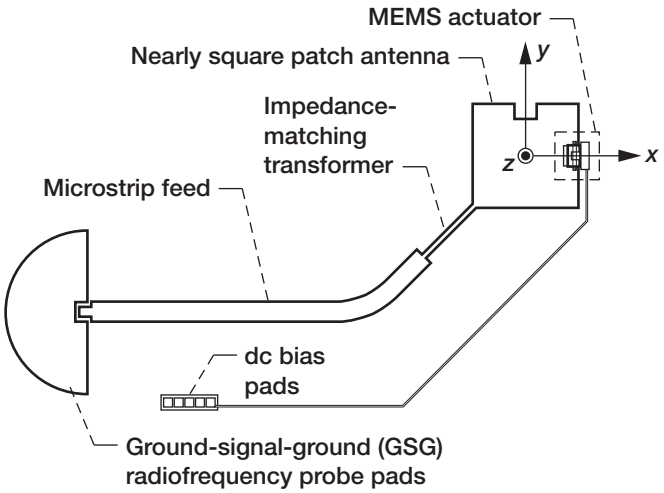

Nearly square patch antenna with integrated MEMS actuator for polarization reconfiguration. The impedance-matching transformer, feed line, and dc bias line/pads are also shown.

(2) In our approach, the polarization is switched between the two states without affecting the frequency of operation; thus, valuable frequency spectrum is conserved.

(3) The ability to switch polarization also helps mitigate propagation effects due to adverse weather on the performance of a satellite-to-ground link. Hence, polarization reconfigurability enhances link reliability.

The design and fabrication of the MEMS actuator is described in detail in reference 1. The operation of the antenna is as follows: when the MEMS actuator is turned on, the patch antenna radiates a linearly polarized signal. The measured E- and H-plane radiation patterns for this case are shown in the graph on the left (next page). When the MEMS actuator is turned off, the patch antenna radiates a circularly polarized signal. The measured radiation patterns in the

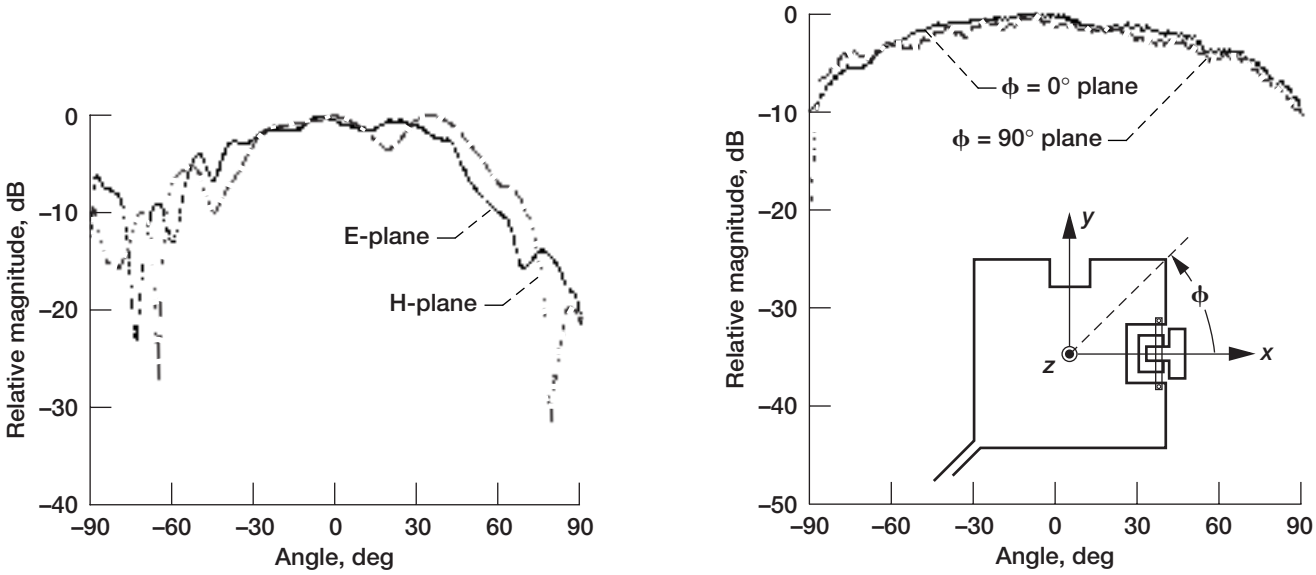

Left: Measured linearly polarized radiation patterns that result when the MEMS actuator is turned on by applying a potential at the bias pads. Right: Measured circularly polarized radiation patterns when the MEMS actuator is turned off.

two orthogonal planes are shown in the graph on the right. These results demonstrate that the polarization of a nearly square patch antenna can be dynamically reconfigured.

Reference

1. Simons, Rainee N.; Chun, Donghoon; and Katehi, Linda P.B.: Microelectromechanical Systems (MEMS) Actuators for Antenna Reconfigurability. IEEE MTT–S International Microwave Symposium Digest (NASA/CR—2001-210612), IEEE, Piscataway, NJ, 2001.

Glenn contacts:
Dr. Felix A. Miranda, 216–433–6589, Felix.A.Miranda@grc.nasa.gov; and Dr. Rainee N. Simons, 216–433–3462, Rainee.N.Simons@grc.nasa.gov

Author: Dr. Rainee N. Simons

Headquarters program office: OAT

Programs/Projects: HRDD

622-Mbps Orthogonal Frequency Division Multiplexing (OFDM) Digital Modem Implemented

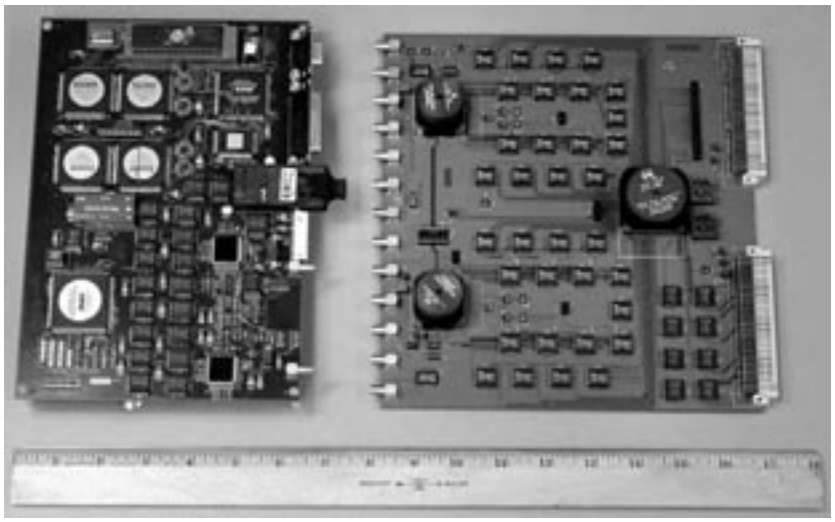

622-Mbps OFDM modulator board and OFDM demodulator front-end board.

Future generation space communications systems feature significantly higher data rates and relatively smaller frequency spectrum allocations than systems currently deployed. This requires the application of bandwidth- and power-efficient signal transmission techniques. There are a number of approaches to implementing such techniques, including analog, digital, mixed-signal, single-channel, or multichannel systems. In general, the digital implementations offer more advantages; however, a fully digital implementation is very difficult because of the very high clock

speeds required. Multichannel techniques are used to reduce the sampling rate. One such technique, multicarrier modulation, divides the data into a number of low-rate channels that are stacked in frequency. Orthogonal frequency division multiplexing (OFDM), a form of multicarrier modulation, is being proposed for numerous systems, including mobile wireless and digital subscriber link communication systems.

In response to this challenge, NASA Glenn Research Center's Communication Technology Division has developed an OFDM digital modem (modulator and demodulator) with an aggregate information throughput of 622 Mbps. The basic OFDM waveform is constructed by dividing an incoming data stream into four channels, each using either 16-ary quadrature amplitude modulation (16–QAM) or 8-phase shift keying (8–PSK). An efficient implementation for an OFDM architecture is being achieved using the combination of a discrete Fourier transform (DFT) at the transmitter to digitally stack the individual carriers, inverse DFT at the receiver to perform the frequency translations, and a polyphase filter to facilitate the pulse shaping.

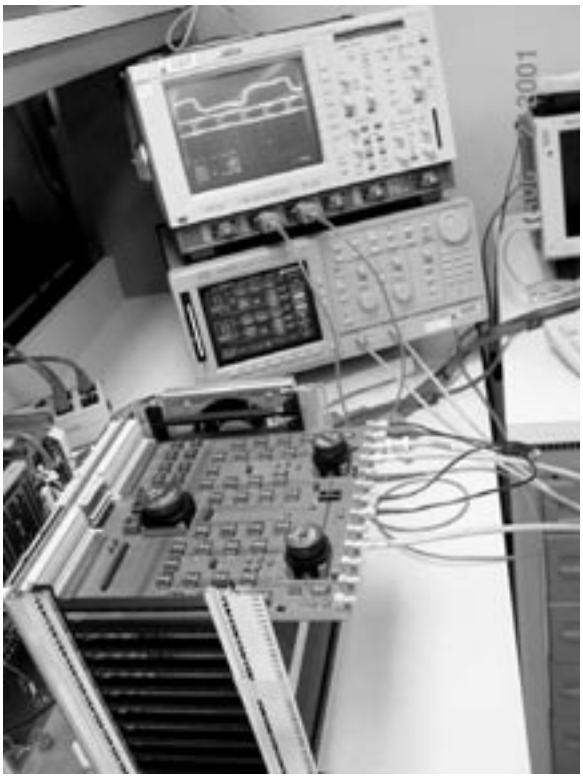

OFDM demodulator front-end board test setups.

One benefit is already evident. Because of the orthogonality of the signals, the four separate channels overlap in frequency without interfering with each other, thus reducing the system bandwidth by up to 38 percent. In addition, Glenn's researchers are working to reduce size, weight, and power while increasing throughput over state-of-the-art technology. Depending on the chosen modulation scheme, power savings of about 3 dB or more may be realized.

The OFDM modulator board consists of a microcontroller unit, a data interface, four commercial application-specific integrated circuit (ASIC) digital modulator/encoder chips, a phased lock loop, an eight-point DFT, an eight-sample polyphase filter, a high-speed multiplexer, and two digital-to-analog converters. The microcontroller unit, along with the data interface unit, divides data into four parallel channels to allow data processing at a much lower rate. It selects various modulation and coding schemes from ASIC modulator/encoder chips. The phased lock loop provides various clocks suitable for the selected modulation scheme. An eight-point complex DFT and an eight-sample polyphase filter are used to reject aliases when the signal is converted to the analog domain. This direct implementation requires filtering each channel at the sample rate and performing the DFT at the sample rate. The number of computations is greatly reduced by moving the filter function after the DFT and distributing it among the channels.

Demodulation of the OFDM signal requires the implementation of analog-to-digital converters, a high-speed demultiplexer, an eight-sample polyphase filter, an eight-point inverse DFT, a symbol synchronizer, and four single-channel demodulator/decoders. The OFDM demodulator was designed in-house at Glenn and built on an eight-layer VME (VersaModule Eurocard) compatible printed circuit board.

Bibliography
Kifle, Muli; Andro, Monty; and Vanderaar, Mark J.: An OFDM System Using Polyphase Filter and DFT Architecture for Very High Data Rate Applications. NASA/TM—2001-210813, 2001. http://gltrs.grc.nasa.gov/GLTRS/

Glenn contact:
Muli Kifle, 216–433–6521,
Fax: 216–433–8705,
Muli.Kifle@grc.nasa.gov

ZIN Technologies contact:
Dale J. Mortensen, 216–977–0348,
Fax: 216–977–0626,
dale.mortensen@zin-tech.com

Authors: Muli Kifle, Thomas P. Bizon, Nam T. Nguyen, Quang K. Tran, and Dale J. Mortensen

Headquarters program office: OAT

Programs/Projects: CETDP

Turbomachinery and Propulsion Systems

Vortex Generator Model Developed for Turbomachinery

A computational model was developed at the NASA Glenn Research Center to investigate possible uses of vortex generators (VG's) for improving the performance of turbomachinery. A vortex generator is a small, winglike device that generates vortices at its tip. The vortices mix high-speed core flow with low-speed boundary layer flow and, thus, can be used to delay flow separation. VG's also turn the flow near the walls and, thus, can be used to control flow incidence into a turbomachinery blade row or to control secondary flows.

The model was implemented in a multiblock turbomachinery analysis code called SWIFT that uses an explicit finite-difference method to solve the Navier-Stokes equations. The model uses body force terms to produce the effects of VG's on the flow, without the difficulties of gridding and solving the flow around the VG's directly. Two-dimensional calculations of VG blades were used to calibrate the model, and a full three-dimensional calculation was used to validate it.

The VG model was used to simulate three possible applications of VG's in turbomachinery. The first application used VG's as part-span splitters ahead of a transonic stator. Tall VG's (10 percent of the stator span) were used to help direct the swirling flow from an upstream rotor into the stator passage. The figure shows a segment of a stator blade row with three VG's attached to the casing just ahead of each stator passage. The stator flow field was solved in detail, but the VG's were modeled by applying body force terms on the colored areas. The particle traces show how the upstream flow is turned into the stator passage.

The second application used smaller VG's (about 2 percent of the rotor span) to improve the boundary layer and to turn the flow on the casing ahead of a rotor. Both preswirl and counterswirl configurations were investigated. The preswirl configuration increased the stall margin of the rotor, whereas the counterswirl configuration decreased the stall margin. Neither configuration had a significant effect on the efficiency.

The third application used extremely small VG's (0.014 in. or 0.36 mm high) to modify the secondary flows on the suction surface of a stator. These VG's were intended to reduce the spanwise migration of flow near the surface. They reduced the losses at midspan but increased the losses near the endwalls, such that the overall loss was slightly increased.

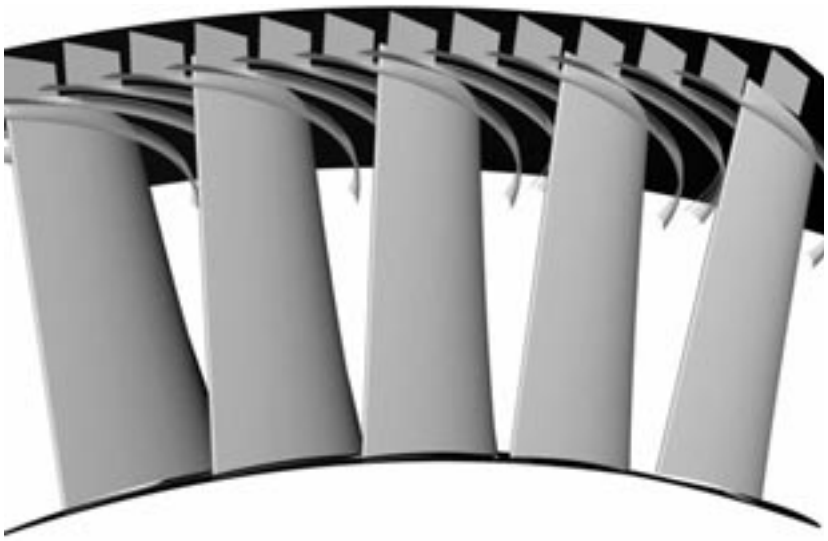

Computed particle traces from simulated vortex generators ahead of a transonic stator. This figure is shown in color in the online version of this report (http://www.grc.nasa.gov/WWW/RT2001/5800/5810chima.html).

Find out more about this research:
Turbomachinery analysis codes:
http://www.grc.nasa.gov/WWW/5810/rvc/

SWIFT multistage turbomachinery analysis code:
http://www.grc.nasa.gov/WWW/RT1996/2000/2760c.htm

Reference

1. Chima, Rodrick V.: Calculation of Multistage Turbomachinery Flow Using Steady Characteristic Boundary Conditions. AIAA Paper 98–0968, Jan. 1998. (NASA/TM—1998-206613), 1998.

Glenn contact:
Dr. Rodrick V. Chima, 216–433–5919, Rodrick.V.Chima@grc.nasa.gov

Author: Dr. Rodrick V. Chima

Headquarters program office: OAT

Programs/Projects: UEET

Fan Stall Flutter Flow Mechanism Studied

Modern turbofan engines employ a highly loaded fan stage with transonic or low-supersonic velocities in the blade-tip region. The fan blades are often prone to flutter at off-design conditions. Flutter is a highly undesirable and dangerous self-excited mode of blade oscillations that can result in high-cycle fatigue blade failure. The origins of blade flutter are not fully understood yet. Experimental data that can be used to clarify the origins of blade flutter in modern transonic fan designs are very limited.

The Transonic Flutter Cascade Facility at the NASA Glenn Research Center was developed to experimentally study the details of flow mechanisms associated with fan flutter. The cascade airfoils are instrumented to measure high-frequency unsteady flow variations in addition to the steady flow data normally recorded in cascade tests. The test program measures the variation in surface pressure in response to the oscillation of one or more of the cascade airfoils. However, during the initial phases of the program when all airfoils were in fixed positions, conditions were found where significant time variations in the pressures near the airfoil leading edges could be observed.

The variations in flow were observed in shadowgraph images of the tunnel flow and were confirmed by high-frequency electronic pressure sensors embedded in the airfoil surface. Prior to shock waves forming on the airfoils, the flow appeared uniform in the shadowgraph figure and in the surface

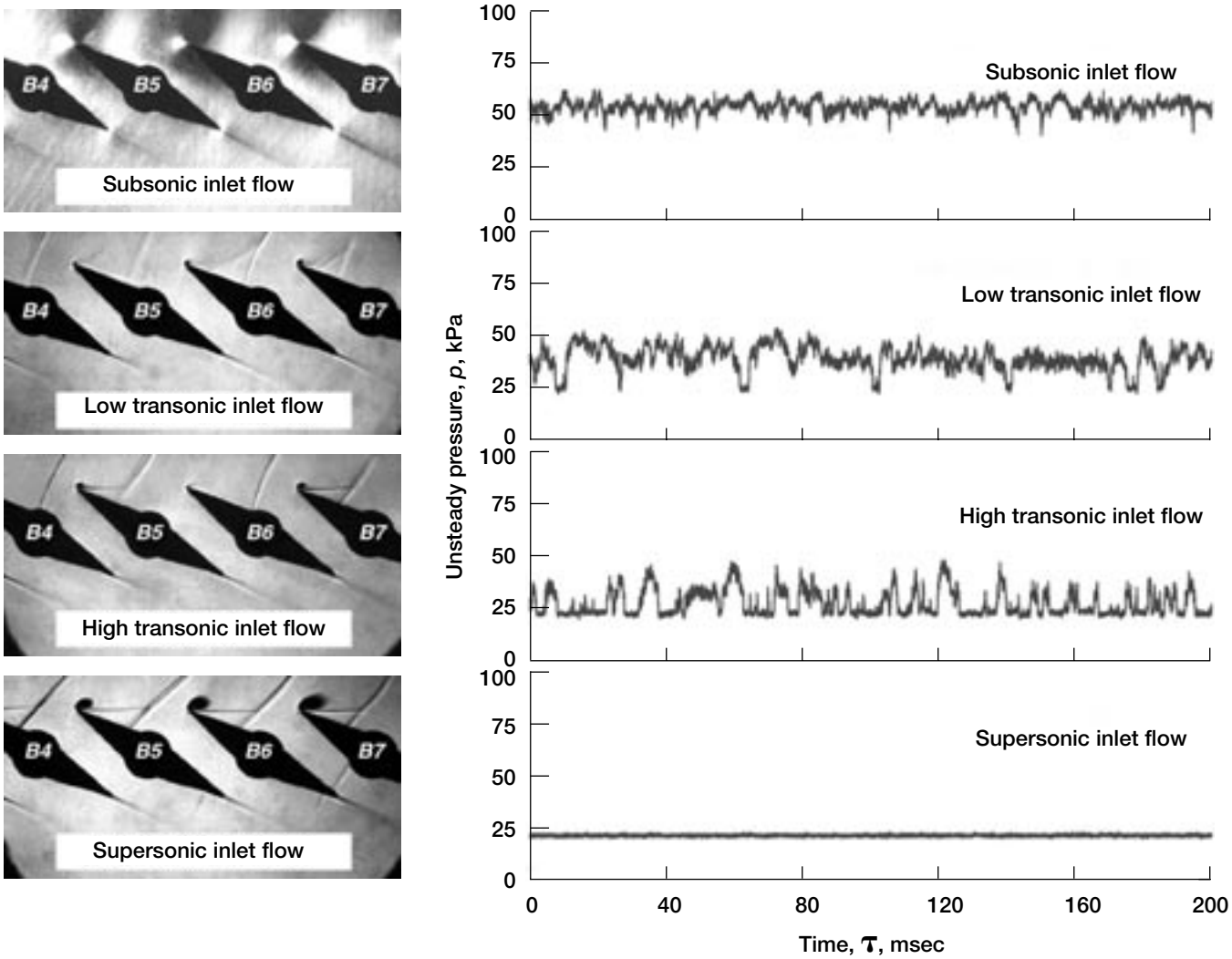

Fan flow behavior. Left: Shockwave patterns from shadowgraph flow visualization. Right: Time-resolved pressure signal on suction surface past the leading edge. Top row: Subsonic—below Mach 0.90. Middle two rows: Transonic—Mach 0.9 to 1.01. Bottom row: Supersonic—above Mach 1.01.

pressure trace from the sensors. These conditions exist for subsonic inlet flow below an inlet flow Mach number of 0.9. After the Mach number was raised slightly about unity to a value of 1.01, supersonic inlet flow was established, the shadowgraph showed a similar shockwave pattern for each airfoil, and again the pressure trace was uniform in time. While the inlet Mach number was in the low to high transonic range (between 0.90 and 1.01), the shadowgraph showed some airfoils with shock waves and some without. Also, the particular airfoils that had shock waves would vary with time. This was confirmed by the data from the sensors as the pressure level randomly alternated between two pressure levels. The lower pressure level indicated the presence of a shock wave and the higher level the absence.

The observed behavior of the cascade experiment could be very useful in the control and avoidance of stall flutter. If this behavior is an indicator or precursor to a fan entering into an area of operation where stall flutter will occur, it can be used in an active control system to control the fan. At this point, however, it is not clear if the observed behavior is common to all current fans, is only observed in this particular airfoil design, or is an artifact of the experimental arrangement. Study of these preliminary observations will continue.

QSS contact:
Dr. Jan Lepicovsky, 216–977–1402, Jan.Lepicovsky@grc.nasa.gov

Glenn contacts:
Dr. Eric R. McFarland, 216–433–5915, Eric.R.McFarland@grc.nasa.gov; and Dr. Rodrick V. Chima, 216–977–5919, Rodrick.V.Chima@grc.nasa.gov

Author: Dr. Jan Lepicovsky

Headquarters program office: OAT

Programs/Projects: Propulsion Systems R&T, SEC, UEET, RAC

Centrifugal Compressor Surge Margin Improved With Diffuser Hub Surface Air Injection

Aerodynamic stability is an important parameter in the design of compressors for aircraft gas turbine engines. Compression system instabilities can cause compressor surge, which may lead to the loss of an aircraft. As a result, engine designers include a margin of safety between the operating line of the engine and the stability limit line of the compressor. The margin of safety is typically referred to as "surge margin." Achieving the highest possible level of surge margin while meeting design point performance objectives is the goal of the compressor designer. However, performance goals often must be compromised in order to achieve adequate levels of surge margin. Techniques to improve surge margin will permit more aggressive compressor designs.

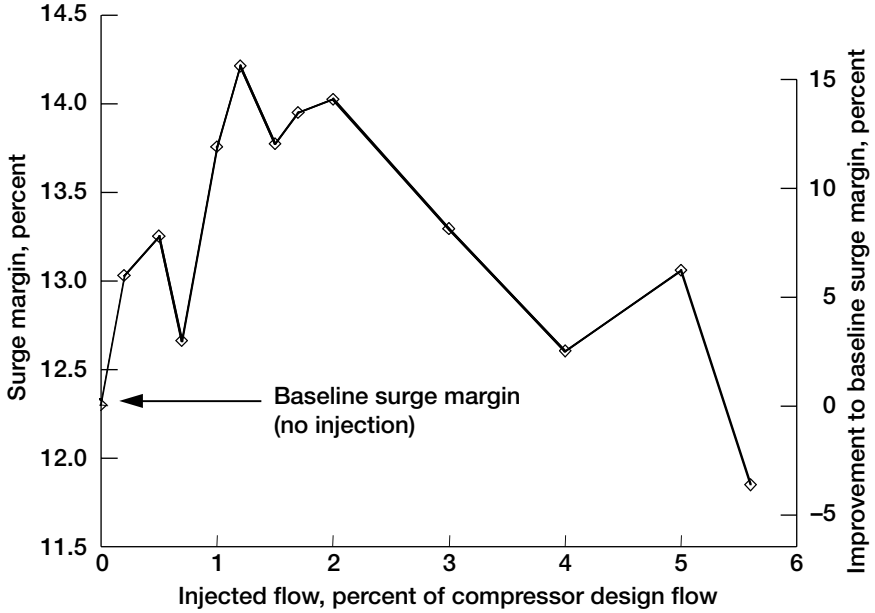

Surge margin improvement with injection that was bisected by the vane in a 4:1 pressure ratio centrifugal compressor at 100 percent of the design speed,

$$\text{Surge margin} = \frac{pr_{surge}\ \ mass\text{-}flow_{ref}}{pr_{ref}\ \ mass\text{-}flow_{surge}}.$$

Centrifugal compressor surge margin improvement was demonstrated at the NASA Glenn Research Center by injecting air into the vaned diffuser of a 4:1-pressure-ratio centrifugal compressor. Tests were performed using injector nozzles located on the diffuser hub surface of a vane-island diffuser in the vaneless region between the impeller trailing edge and the diffuser-vane leading edge. The nozzle flow path and discharge

shape were designed to produce an air stream that remained tangent to the hub surface as it traveled into the diffuser passage. Injector nozzles were located near the leading edge of 23 of the 24 diffuser vanes. One passage did not contain an injector so that instrumentation located in that passage would be preserved. Several orientations of the injected stream relative to the diffuser vane leading edge were tested over a range of injected flow rates. Only steady flow (nonpulsed) air injection was tested.

At 100 percent of the design speed, a 15-percent improvement in the baseline surge margin was achieved with a nozzle orientation that produced a jet that was bisected by the diffuser vane leading edge. Other orientations also improved the baseline surge margin. Tests were conducted at speeds below the design speed, and similar results were obtained. In most cases, the greatest improvement in surge margin occurred at fairly low levels of injected flow rate.

Externally supplied injection air was used in these experiments. However, the injected flow rates that provided the greatest benefit could be produced using injection air that is recirculating between the diffuser discharge and nozzles located in the diffuser vaneless region. Future experiments will evaluate the effectiveness of recirculating air injection.

Reference

1. Suder, K.L., et al.: Compressor Stability Enhancement Using Discrete Tip Injection. ASME J. Turbomachinery, vol. 123, no. 1, 2001, pp. 14–23.

U.S. Army Vehicle Technology Center at Glenn contact:
Gary J. Skoch, 216–433–3396, Gary.J.Skoch@grc.nasa.gov

Glenn contacts:
Loretta M. Shaw, 216–433–3931, Loretta.M.Shaw@grc.nasa.gov; and Dr. Anthony J. Strazisar, 216–433–5881, Anthony.J.Strazisar@grc.nasa.gov

Author: Gary J. Skoch

Headquarters program office: OAT

Programs/Projects: UEET

Effect of Variable Chord Length on Transonic Axial Rotor Performance Investigated

During the life of any gas turbine, blade erosion is present, especially for those units that are exposed to unfiltered air, such as aviation turbofan engines. The effect of this erosion is to reduce the blade chord progressively from the midspan to the tip region and to roughen and distort the blade surface. The effects of roughness on rotor performance have been documented by Suder et al. (ref. 1) and Roberts (ref. 2). These papers indicate that the penalty for leading-edge roughness and erosion can be significant. Turbofan operators, therefore, restore chord length at routine maintenance intervals to regain performance before deterioration is too severe to salvage blades. As the rotor blades erode, the leading edge becomes rough—blunt and distorted from the nominal shape—and the aerodynamic performance suffers. Nominal performance can be recovered by recontouring the leading edges as illustrated in the figure to the right. This process, which inherently shortens the blade chord, can be used until the blade chord erodes to the stall limit. Below this chord length, which varies among engine-compressor types, a decrease of stall margin is likely.

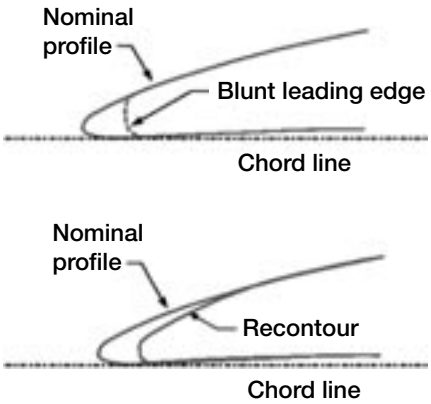

Blade leading edge. Top: Leading edge blunt because of erosion. Bottom: Recontoured leading edge.

After compressor blade rework that includes leading edge recontouring, the blades have different chord lengths, ranging from blades that are near nominal chord length down to those near the stall chord limit. Furthermore, as blades erode below the stall limit, they must be replaced with new blades that have the full nominal chord length. Consequently, a set of compressor blades with varying chord lengths will be installed into each turbofan engine that goes through a complete maintenance cycle. The question arises, "Does fan or compressor performance depend on the order in which mixed-chord blades are installed into a fan or compressor disk?"

Transonic compressor for NASA rotor35.

To investigate this issue, the aerodynamic performance of a NASA transonic compressor rotor (shown in the photograph) operating with blades of varying chord length was measured in back-to-back compressor tests in NASA Glenn Research Center's W8 Transonic Compressor Facility. One half of the rotor blades were the full nominal chord length, and the remaining half of the blades were cut back at the leading edge to 95 percent of the chord length and recontoured. The rotor aerodynamic performance was measured at 100, 80, and 60 percent of the design speed for the blade installation configurations shown in the figure to the right: (1) nominal-chord blades in half of the disk and short-chord blades in half of the disk, (2) four alternating quadrants of nominal-chord and short-chord blades, and (3) nominal-chord and short-chord blades alternating around the disk.

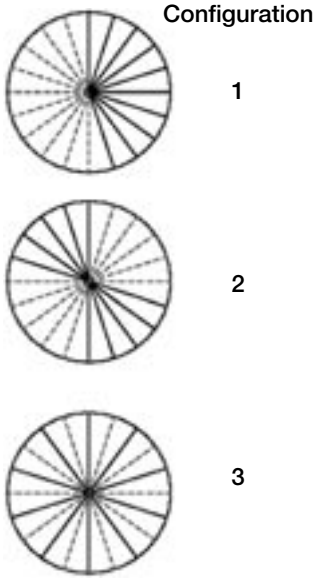

Tested blade configurations. (1) All long-chord blades grouped together; all short-chord blades grouped together. (2) Alternating quadrants of long- and short-chord blades. (3) Long- and short-chord blades alternating around the wheel.

The test results indicate only slight differences in performance with the "alternating" blade installation configuration at specific operating conditions, which are documented and discussed further in reference 3. Otherwise, there was no significant difference in performance among the various blade configurations. Since the three installation configurations tested cover the extremes of possible chord mismatch, it can be concluded that chord mismatching is not important to aerodynamic performance above the stall chord limit, which for most civil aviation engines is between 94 and 96 percent of nominal (new) chord length. This statement applies *only* to blades that have been refurbished with a leading edge recontour.

Bibliography

Suder, K.L., et al.: The Effect of Adding Roughness and Thickness to a Transonic Axial Compressor Rotor. ASME J. Turbomachinery, vol. 117, 1994, pp. 491–505.

Roberts, W.B.: Advanced Turbofan Blade Refurbishment Technique. ASME J. Turbomachinery, vol. 117, no. 4, 1995, pp. 666–667.

Roberts, W.B., et al.: The Effect of Variable Chord Length on Axial Transonic Axial Rotor Performance. ASME Paper 2002–GT–0498, 2002. To be published in the ASME J. Turbomachinery, 2002.

Glenn contacts:
Dr. Kenneth L. Suder, 216–433–5899, Kenneth.L.Suder@grc.nasa.gov;
Dr. Anthony J. Strazisar, 216–433–5881, Anthony.J.Strazisar@grc.nasa.gov; and
Scott A. Thorp, 216–433–8013, Scott.A.Thorp@grc.nasa.gov

Author: Kenneth L. Suder

Headquarters program office: OAT

Programs/Projects: UEET

Heated Surface Temperatures Measured by Infrared Detector in a Cascade Environment

Investigators have used infrared devices to accurately measure heated surface temperatures. Several of these applications have been for turbine heat transfer studies involving film cooling and surface roughness, (ref. 1), Typically, these measurements use an infrared camera positioned externally to the test section. In cascade studies, where several blades are used to ensure periodic flow, adjacent blades block the externally positioned camera's views of the test blade. To obtain a more complete mapping of the surface temperatures, researchers at the NASA Glenn Research Center fabricated a probe with an infrared detector to sense the blade temperatures. The probe size was kept small to minimize the flow disturbance. By traversing and rotating the probe, using the same approach as for total pressure surveys, one can find the blade surface temperatures. Probe-mounted infrared detectors are appropriate for measuring surface temperatures where an externally positioned infrared camera is unable to completely view the test object.

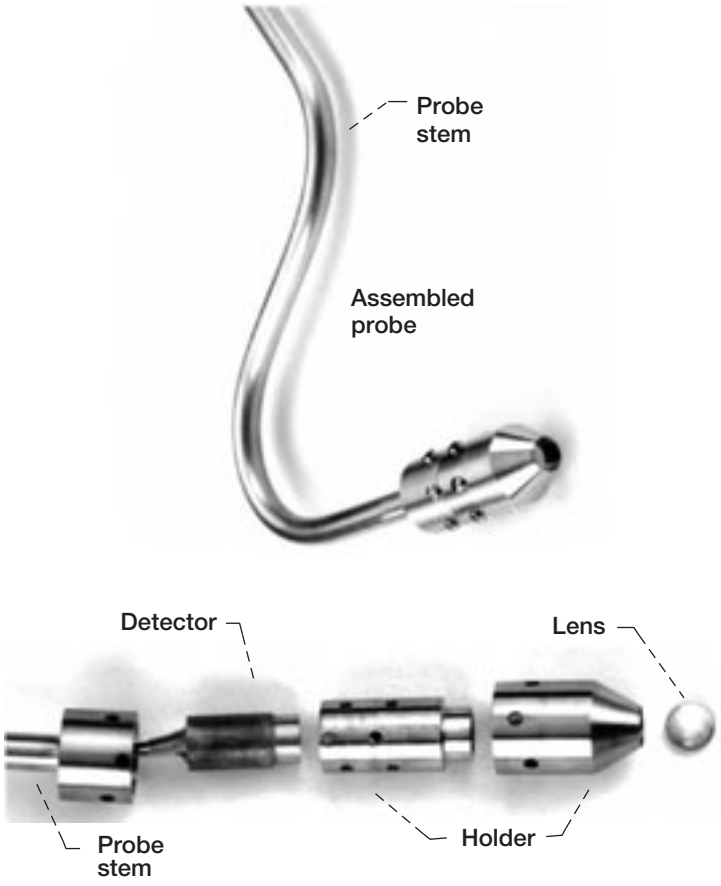

Sketch of infrared probe.

This probe (see the figure) consists of a 8-mm gallium arsinide (GaAs) lens mounted in front of a mercury-cadmium-zinc-tellurium (HgCdZnTe) detector. This type of photovoltaic detector was chosen because of its high sensitivity to temperature when the detector is uncooled. The particular application is for relatively low surface temperatures, typically ambient to 100 °C. This requires a detector sensitive at long wavelengths. The detector is a commercial product enclosed in a 9-mm-diameter package. The GaAs lens material was chosen because of its glass-like hardness and its good long-wavelength transmission characteristics. When assembled, the 6.4-mm probe stem is held in the traversing actuator. Since the entire probe is above the measurement plane, the flow field disturbance in the measurement plane is minimized. This particular probe body is somewhat wider than necessary, because it was designed to have replaceable detectors and lenses.

The signal for the detector is fed through the hollow probe body. The detector's signal goes to an externally mounted preamplifier. The detector assembly, along with a preamplifier, is calibrated as a function of the surface temperature for various detector temperatures. The output voltage is a function of both the detector and object temperatures.

Reference
1. Boyle, R.J., et al.: Infrared Low-Temperature Turbine Vane Rough Surface Heat Transfer Measurements. ASME J. Turbomachinery, vol. 123, no. 1, 2001, pp. 168–177. (Also NASA/TM—2000-210220. http://gltrs.grc.nasa.gov/GLTRS/)

Glenn contacts: Dr. Robert J. Boyle, 216–433–5889, Robert.J.Boyle@grc.nasa.gov; and Dr. Charles M. Spuckler, 216–433–2167, Charles.M.Spuckler@grc.nasa.gov

Author: Dr. Robert J. Boyle

Headquarters program office: OAT

Programs/Projects: Propulsion Systems R&T

Pulse Detonation Engine Test Bed Developed

A detonation is a supersonic combustion wave. A Pulse Detonation Engine (PDE) repetitively creates a series of detonation waves to take advantage of rapid burning and high peak pressures to efficiently produce thrust. NASA Glenn Research Center's Combustion Branch has developed a PDE test bed that can reproduce the operating conditions that might be encountered in an actual engine. It allows the rapid and cost-efficient evaluation of the technical issues and technologies associated with these engines.

The test bed is modular in design. It consists of various length sections of both 2- and 2.6-in. internal-diameter combustor tubes. These tubes can be bolted together to create a variety of combustor configurations. A series of bosses allow instrumentation to be inserted on the tubes. Dynamic pressure sensors and heat flux gauges have been used to characterize the performance of the test bed. The PDE test bed is designed to utilize an existing calorimeter (for heat load measurement) and windowed (for optical access) combustor sections. It uses hydrogen as the fuel, and oxygen and nitrogen are mixed to simulate air. An electronic controller is used to open the hydrogen and air valves (or a continuous flow of air is used) and to fire the spark at the appropriate times.

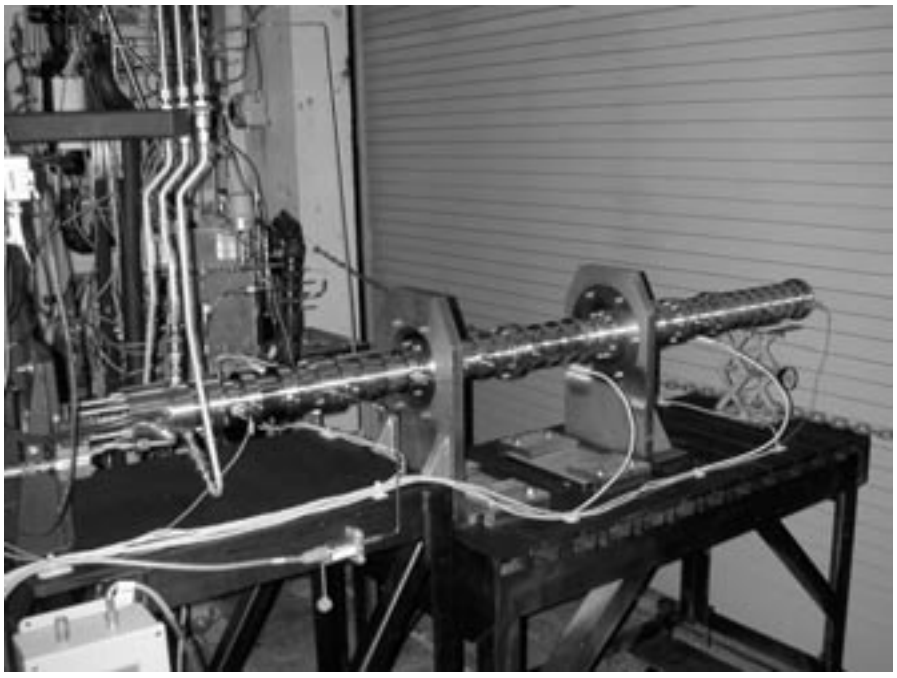

Pulse Detonation Engine testbed.

Scheduled tests on the test bed include an evaluation of the pumping ability of the train of detonation waves for use in an ejector and an evaluation of the pollutants formed in a PDE combustor. Glenn's Combustion Branch uses the National Combustor Code (NCC) to perform numerical analyses of PDE's as well as to evaluate alternative detonative combustion devices.

Glenn contact:
Kevin J. Breisacher, 216–977–7475, Kevin.J.Breisacher@grc.nasa.gov

Author: Kevin J. Breisacher

Headquarter program office: OAT

Programs/Projects:
Propulsion Systems R&T

One-Dimensional Spontaneous Raman Measurements of Temperature Made in a Gas Turbine Combustor

The NASA Glenn Research Center is working with the aeronautics industry to develop highly fuel-efficient and environmentally friendly gas turbine combustor technology. This effort includes testing new hardware designs at conditions that simulate the high-temperature, high-pressure environment expected in the next-generation of high-performance engines. Glenn has the only facilities in which such tests can be performed. One aspect of these tests is the use of nonintrusive optical and laser diagnostics to measure combustion species concentration, fuel/air ratio, fuel drop size, and velocity, and to visualize the fuel injector spray pattern and some combustion species distributions (refs. 1 to 2). These data not only help designers to determine the efficacy of specific designs, but provide a data base for computer modelers and enhance our understanding of the many processes that take place within a combustor. Until recently, we lacked one critical capability, the ability to measure temperature. This article summarizes our latest developments in that area.

Recently, we demonstrated the first-ever use of spontaneous Raman scattering to measure combustion temperatures within the Advanced Subsonics Combustion Rig (ASCR) sector rig. We also established the highest rig pressure ever achieved for a continuous-flow combustor facility, 54.4 bar. The ASCR facility (ref. 2) can provide operating pressures from 1 to 60 bar (60 atm). This photograph shows the Raman system setup next to the ASCR rig. The test was performed using a NASA-concept fuel injector and Jet-A fuel over a range of air inlet temperatures, pressures, and fuel/air ratios.

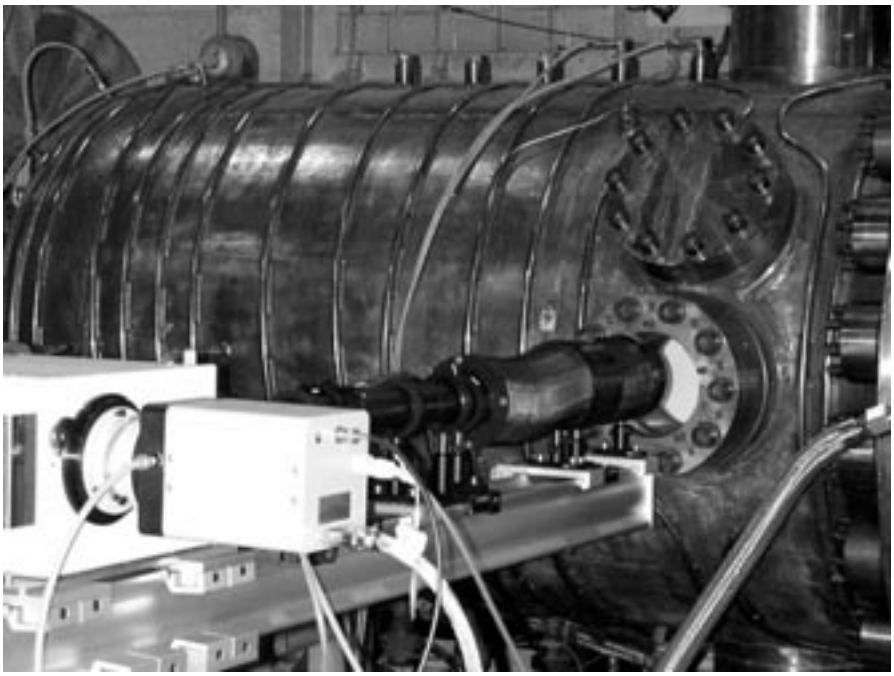

Spontaneous Raman scattering experimental setup in the Advanced Subsonics Combustion Rig.

Spontaneous Raman scattering allows one to measure combustion species (ref. 3) and/or temperature. The signal that one obtains is typically a spectrum whose peaks are linearly related to the number density of the molecular species. These peaks occur at characteristic intervals that depend on the physical characteristics of the molecular species, thus producing a fingerprint unique to that species and making this a good method for species measurement and identification. In Raman spectroscopy, that characteristic interval is the frequency shift from the laser light-scattering source. This frequency shift is related to the rotational and vibrational components of each molecule's energy at the time it encounters the laser, and it appears as a positive shift (Stokes scattering) when the molecule receives energy from the laser and a negative shift (anti-Stokes scattering) when the molecule gives up energy. The relative intensity of the Stokes and anti-Stokes peaks depends on the temperature that a system of molecules finds itself in, which follows a Boltzmann distribution. The ratio of the areas of the anti-Stokes peaks to the Stokes peaks for molecular nitrogen, an inert species whose molecular concentration remains relatively constant for any given test condition, is directly related to the temperature via Boltzmann statistics.

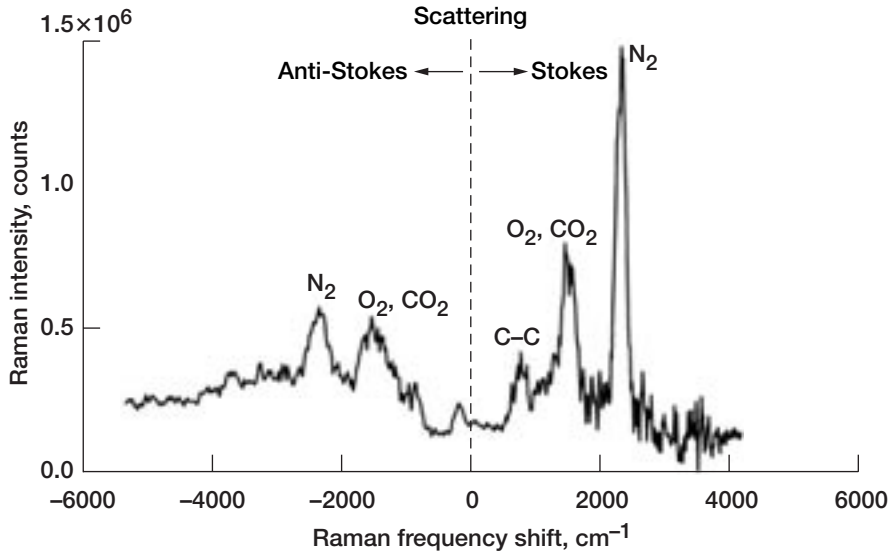

Raman spectrum acquired during combustion. The abscissa is the Raman shift in wave numbers (reciprocal centimeters). The ordinate is the Raman-scattered intensity. The combustor pressure is 54 bar, the inlet temperature is 717 K, and the fuel-to-air equivalence ratio, ϕ, is 0.35. The theoretical temperature is 1560 K, and the Raman temperature is 1500 K.

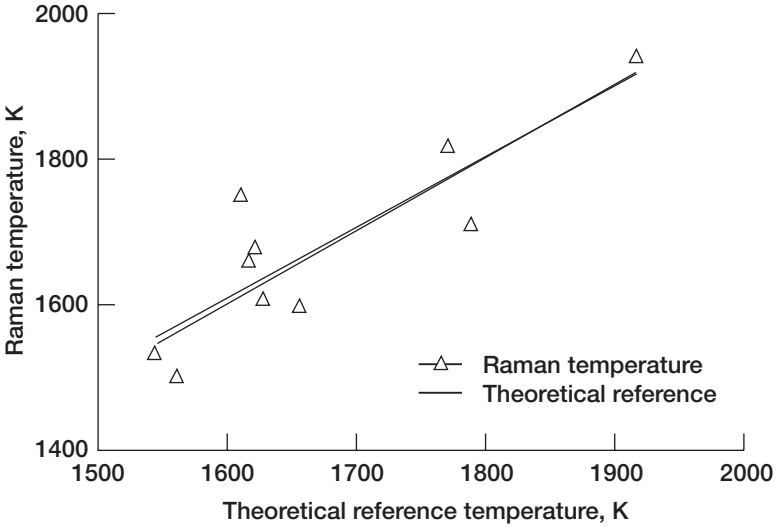

Comparison of the bulk theoretical combustion temperature to the measured Raman temperature.

The top graph shows a typical Raman spectrum obtained during the test. The inlet temperature and pressure are 720 K and 54 bar. Molecular nitrogen and oxygen are present, as well as CO_2 and fuel and its remnants as indicated by the carbon-carbon (C–C stretch). The temperatures measured using the Raman technique compare favorably with theoretical temperatures determined from the flow parameters, as shown in the bottom graph. Here, the Raman-derived temperatures are plotted with the theoretical temperatures derived from the flow conditions. Given these excellent results, we now have a very useful tool that will further enable us to develop next-generation combustor technology.

References

1. Locke, R.J., et al.: Non-Intrusive, Laser-Based Imaging of Jet-A Fuel Injection and Combustion Species in High Pressure, Subsonic Flows. Presented at the JANNAF 25th Air-breathing Propulsion Subcommittee, 37th Combustion Subcommittee, and 1st Modeling and Simulation Subcommittee Joint Meeting (NASA/TM—2001-211113), vol. 1, 2000, pp. 183–193.
2. Hicks, Yolanda R.; Locke, Randy J.; and Anderson, Robert C.: Optical Measurement and Visualization in High-Pressure, High-Temperature, Aviation Gas Turbine Combustors. NASA/TM—2000-210377, 2000. http://gltrs.grc.nasa.gov/GLTRS/
3. DeGroot, Wilhelmus A., et al.: One-Dimensional Spontaneous Raman Measurements Made in a Gas Turbine Combustor. Research & Technology 2000, NASA TM—2001-210605, pp. 76–78. http://www.grc.nasa.gov/WWW/RT2000/5000/5830degroot.html

Glenn contact:
Dr. Yolanda R. Hicks, 216–433–3410, Yolanda.R.Hicks@grc.nasa.gov

QSS contact:
Dr. Randy J. Locke, 216–433–6110, Randy.J.Locke@grc.nasa.gov

Authors:
Dr. Yolanda R. Hicks, Dr. Randy J. Locke, Dr. Wilelmus A. DeGroot, and Robert C. Anderson

Headquarters program office: OAT

Programs/Projects: UEET

High-Pressure Gaseous Burner (HPGB) Facility Completed for Quantitative Laser Diagnostics Calibration

A gas-fueled high-pressure combustion facility with optical access, which was developed over the last 2 years, has just been completed. The High Pressure Gaseous Burner (HPGB) rig at the NASA Glenn Research Center can operate at sustained pressures up to 60 atm with a variety of gaseous fuels and liquid jet fuel. The facility is unique as it is the only continuous-flow, hydrogen-capable, 60-atm rig in the world with optical access. It will provide researchers with new insights into flame conditions that simulate the environment inside the ultra-high-pressure-ratio combustion chambers of tomorrow's advanced aircraft engines. The facility provides optical access to the flame zone, enabling the calibration of nonintrusive optical diagnostics to measure chemical species and temperature. The data from the HPGB rig enables the validation of numerical codes that simulate gas turbine combustors, such as the National Combustor Code (NCC). The validation of such numerical codes is often best achieved with nonintrusive optical diagnostic techniques that meet these goals: information-rich (multispecies) and quantitative while providing good spatial and time resolution. Achieving these goals is a challenge for most nonintrusive optical diagnostic techniques.

Raman scattering is a technique that meets these challenges. Raman scattering occurs when intense laser light interacts with molecules to radiate light at a

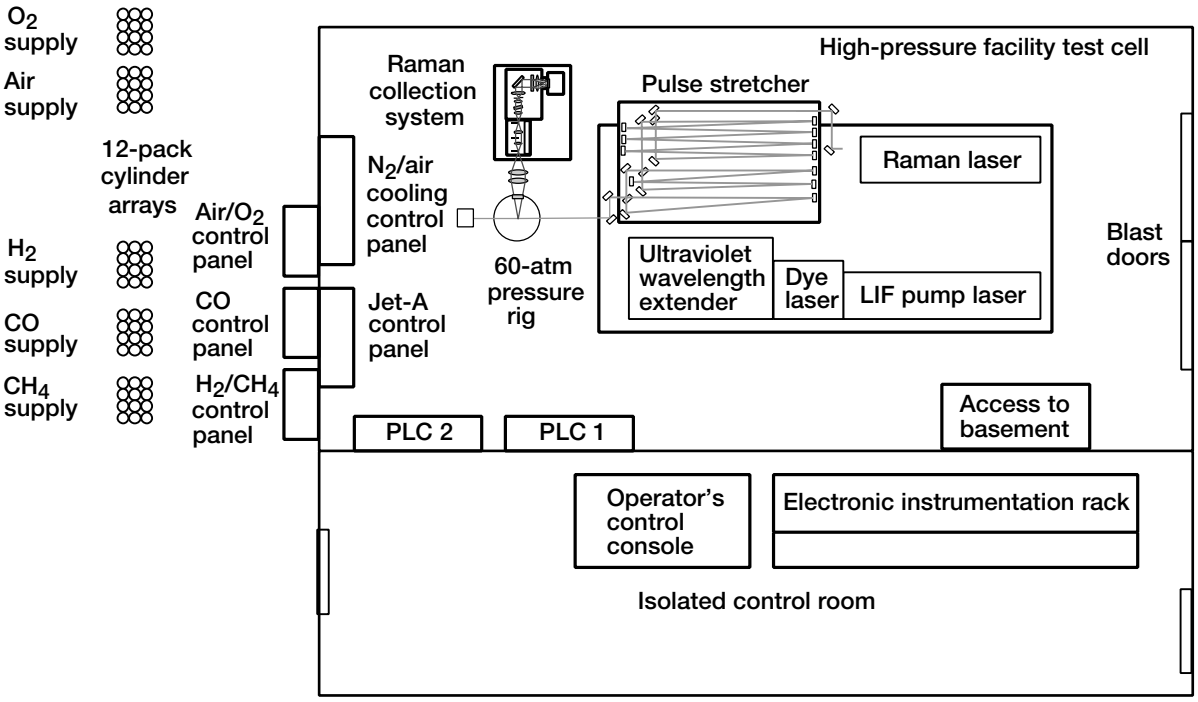

HPGB facility. This rig, along with the laser Raman scattering diagnostic equipment, and control electronics that include the programmable logic controller (PLC) is located in the main test cell. The gaseous flow control system for the fuel and oxidizer are housed in gas cabinets located outside of the test cell. The facility is remotely operated from the adjacent control room. Below a chamber pressure of 30 atm, the rig is air-cooled by dilution provided from facility compressors. At higher chamber pressures, the rig uses cooling air supplied by two compressed air trailers located outside of the building. The combustion gases (fuel and oxidizer) are provided by 12-pack cylinder arrays located outside of the test cell. LIF, laser-induced fluorescence.

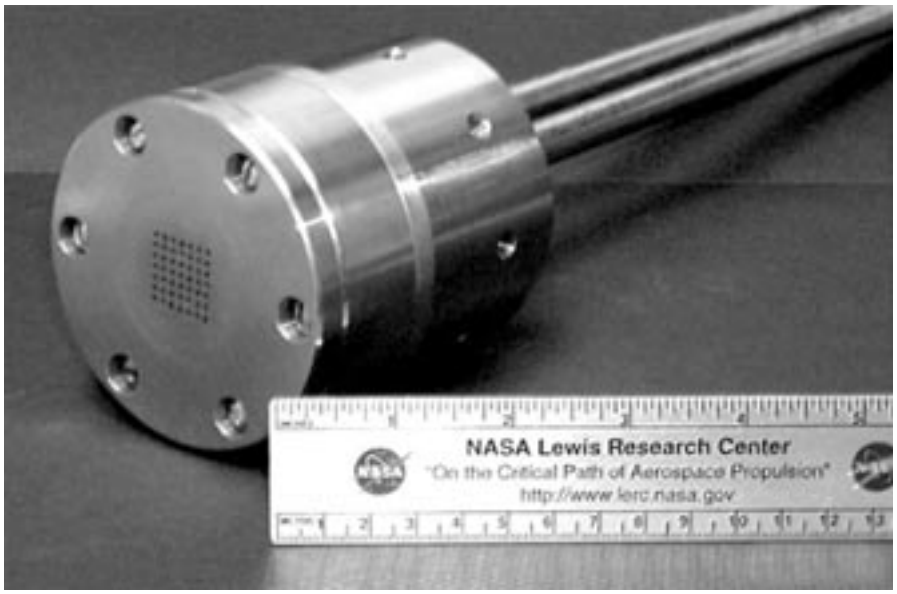

Micropremixed, self-cooled burner used to generate hot combustion products inside the high-pressure rig. The burner consists of an array of 49 premixed fuel-oxidizer jets that combine to form a larger homogeneous combustion zone.

shifted wavelength (known as the Raman shift). This shift in wavelength is unique to each chemical species and provides a "fingerprint" of the different species present. The facility will first be used to gather a comprehensive data base of laser Raman spectra at high pressures. These calibration data will then be used to quantify future laser Raman measurements of chemical species concentration and temperature in this facility and other facilities that use Raman scattering. Raman scattering is perhaps the only technique that can yield simultaneous quantitative concentration measurements of N_2, O_2, CO_2, H_2O, CO, HC's, and H_2, while also providing a measurement of the temperature in a spatially resolved volume in a single shot in time.

The figure on the preceding page shows a schematic of the facility layout. A unique micropremixed hydrogen-air burner, shown in the photograph, is mounted inside the rig. The burner design avoids the problems of flashback and meltdown normally associated with high-pressure premixed hydrogen-air operation. The burner face is constructed of high-temperature alloy and is coated with a thermal barrier coating made of a flame-sprayed zirconia ceramic (not shown). An alternate design, which utilizes a staggered array of fuel-oxidizer jets that rapidly mix outside of the burner face to provide a nonpremixed mode of operation for the burner, has also been developed. The burner is designed to generate high-temperature combustion products over a wide range of fuel and air flow rates. The facility is operated with a computer-controlled system developed with the help of engineers from Glenn's Facilities and Test Engineering Division and Engineering Design and Analysis Division.

The burner and the Raman diagnostic system was designed by Dr. Nguyen of Glenn's Combustion Branch and built in-house. In the process of building the Raman diagnostic system, a novel high-speed (8.5-μsec) electromechanical shutter was developed by Dr. Nguyen to improve the Raman signal-to-noise ratio (SNR) by 1000 times over conventional leaf shutter systems. A patent for this shutter design is currently being pursued. The Raman-scattering diagnostic system is shown schematically in the figure on the next page. The state-of-the-art design of the Raman collection system permits the detection of weak Raman signals with a 40-fold improvement in sensitivity and a 1000-fold increase in dynamic range over conventional Raman scattering systems. Recently, Dr. Jun Kojima, a National Research Council Postdoctoral Research Associate (a recent graduate of Kobe University, Japan), has been assisting Dr. Nguyen with many of the experimental aspects of this facility.

Milestones achieved for this year include completion of the gaseous burner system, obtaining a safety permit for hydrogen operation in the test cell, completion of the laser Raman scattering system, demonstration of the laser pulse-stretcher, demonstration of the shutter system, cold-flow testing (rig shakedown) to verify proper operation, and a successful first light-off with a hydrogen-air mixture at 10-atm rig pressure. The facility is now operational and in the process of beginning Raman data collection in high-pressure flames.

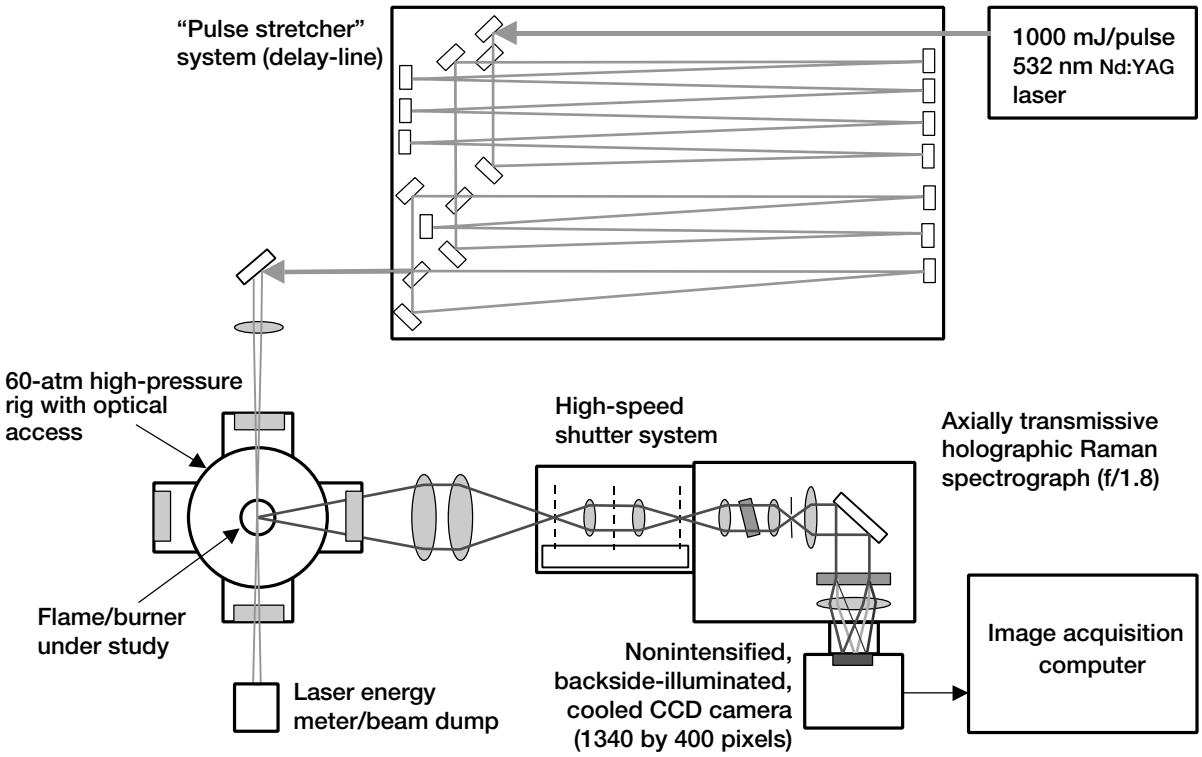

Raman diagnostic system. The Raman excitation is provided by a pulsed Nd:YAG laser that generates a green (532 nm), high-energy (1 J), and very brief (8.4 nsec) full-width, half-maximum (FWHM) pulse of light (at 10 Hz), which is then temporally "stretched" to a 75-nsec FWHM pulse using an optical delay line "pulse-stretcher" to reduce the peak intensity. The high pulse energy is necessary to provide a high signal-to-noise ratio for the weak Raman effect. The temporally stretched laser pulse is a requirement, as the intensity of the focused and unstretched laser pulse would immediately destroy the 45-mm-thick fused silica windows used on the rig and cause an optical breakdown at the focal point. The stretched laser pulse is then focused into the flame zone inside the rig where Raman-scattered light is collected at a right angle with a high-speed lens and directed into the shutter system. The high-speed shutter rejects the continuous background light through temporal gating and transmits the Raman-scattered light into the entrance slit of a high-speed (f/1.8) spectrograph fitted with a special backside-illuminated unintensified charge-coupled device (CCD) camera. The spectra, in the form of digital images from the computer-controlled CCD camera, are then stored on a computer for analysis.

Glenn contact:
Dr. Quang-Viet Nguyen, 216–977–3574, Quang-Viet.Nguyen@grc.nasa.gov

Author: Dr. Quang-Viet Nguyen

Headquarters program office: OAT

Programs/Projects: UEET, ZCET, SEC

Spray and High-Pressure Flow Computations in the National Combustion Code (NCC) Improved

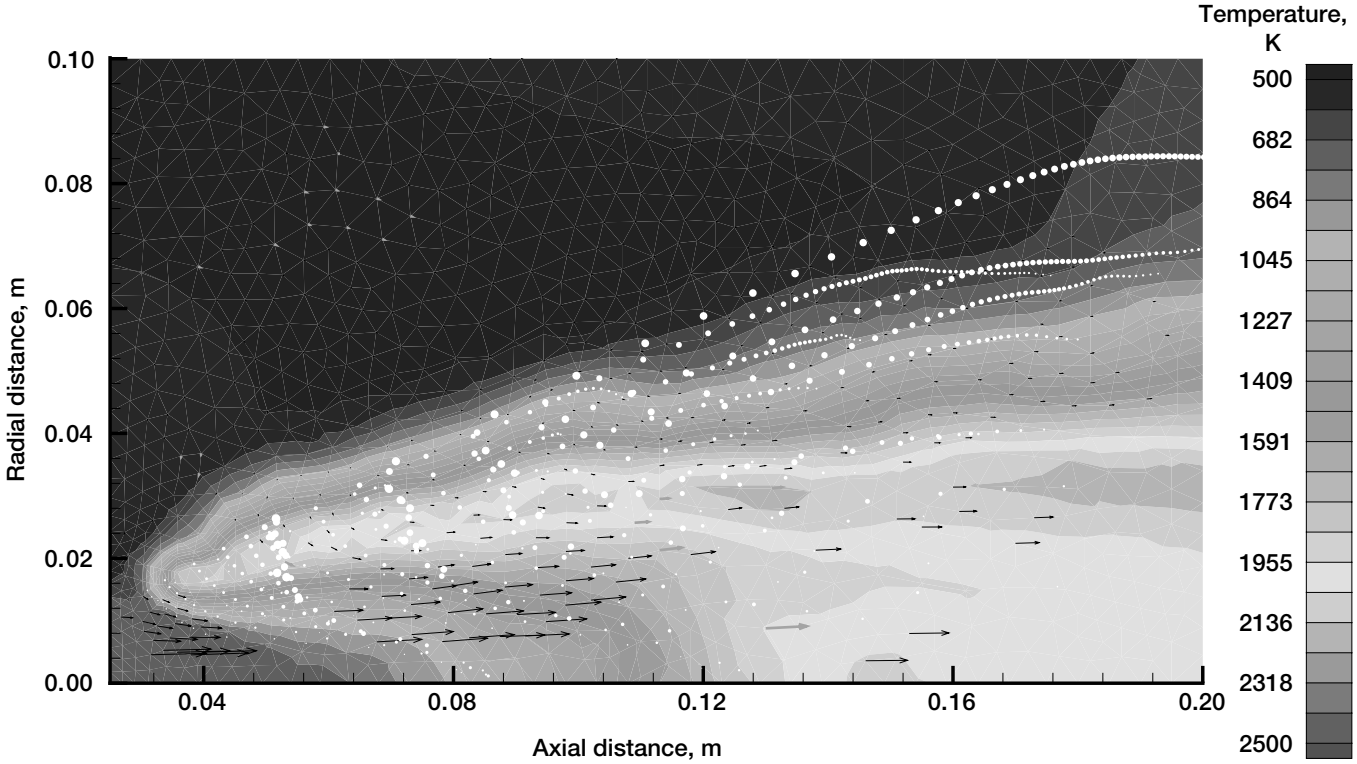

Global features of a spray flame showing temperature distribution, velocity vector plot, and droplet locations. This figure is shown in color in the online version of this article (http://www.grc.nasa.gov/WWW/RT2001/5000/5830raju.html).

Sprays occur in a wide variety of industrial and power applications and in materials processing. A liquid spray is a two-phase flow with a gas as the continuous phase and a liquid as the dispersed phase in the form of droplets or ligaments. The interactions between the two phases—which are coupled through exchanges of mass, momentum, and energy—can occur in different ways at disparate time and length scales involving various thermal, mass, and fluid dynamic factors. An understanding of the flow, combustion, and thermal properties of a rapidly vaporizing spray requires careful modeling of the rate-controlling processes associated with turbulent transport, mixing, chemical kinetics, evaporation, and spreading rates of the spray, among many other factors.

With the aim of developing an efficient solution procedure for use in multidimensional combustor modeling, researchers at the NASA Glenn Research Center have advanced the state-of-the-art in spray computations in several important ways:

(1) With the development of LSPRAY (ref. 1) and EUPDF (ref. 2), we were able to extend and demonstrate the use of the joint scalar Monte Carlo Probability Density Function (PDF) approach to the modeling of spray flames for the first time. In this approach, the mean gas-phase velocity and turbulence fields are determined with a conventional computational fluid dynamics method, the scalar fields of species and enthalpy from a modeled PDF transport equation using a Monte Carlo method, and the liquid-phase representation from a Lagrangian-based dilute spray model. The application of this method clearly demonstrated the importance of chemistry-turbulence interactions in the modeling of reacting sprays (refs. 3 and 4).

(2) To facilitate large-scale combustor applications, we extended the spray and Monte Carlo PDF computations to parallel computing and unstructured grids. The unstructured three-dimensional solver, which is designed to be massively parallel, accommodates the use of an unstructured mesh with mixed elements composed of triangular, quadrilateral, and/or tetrahedral elements. The ability to

perform the computations on unstructured meshes enables researchers to represent complex geometries with relative ease (ref. 5).

(3) To account for nonideal gas behavior under critical and supercritical conditions, we integrated a high-pressure equation of state into the gas-phase flow solver and added the effect of high pressure on transport properties in the gas phase.

The modeling approach used in LSPRAY and EUPDF provided favorable results when applied to several different spray flames representative of those encountered in both gas-turbine combustors and stratified-charge rotary combustion (Wankel) engines (refs. 3 to 5). The source code of LSPRAY and EUPDF will be available with the National Combustion Code (NCC) as a complete package. The models will be validated further at realistic temperatures and pressures.

References

1. Raju, M.S.: LSPRAY—A Lagrangian Spray Solver User's Manual, NASA/CR—97-206240, 1997.
2. Raju, M.S.: EUPDF—An Eulerian-Based Monte Carlo Probability Density Function (PDF) Solver. User's Manual. NASA/CR—1998-207401, 1998. http://gltrs.grc.nasa.gov/GLTRS/
3. Raju, M.S.: On the Importance of Chemistry/Turbulence Interactions in Spray Computations. Numer. Heat Transfer, Part B: Fundamentals, vol. 41, 2002, pp. 1–24.
4. Raju, M.S.: Application of Scalar Monte Carlo Probability Density Function Method for Turbulent Spray Flames. Numerical Heat Transfer, Part A: Applications, vol. 30, no. 8, 1996, pp. 753–777.
5. Raju, M.S.: Current Status of the Use of Parallel Computing in Turbulent Reacting Flow Computations Involving Sprays, Scalar Monte Carlo PDF and Unstructured Grids. Adv. Numer. Heat Trans., vol. 2, ch. 8, 2000, pp. 259–287.

QSS contact:
Dr. Manthena S. Raju, 216–977–1366, Manthena.Raju@grc.nasa.gov

Glenn contact:
Dr. Nan-Suey Liu, 216–433–8722, Nan-Suey.Liu@grc.nasa.gov

Author: Dr. Manthena S. Raju

Headquarters program office: OAT

Programs/Projects:
Aerospace Propulsion and Power Base Research, SEC

Sector Tests of a Low-NO_x, Lean, Direct-Injection, Multipoint Integrated Module Combustor Concept Conducted

The low-emissions combustor development described is directed toward advanced high-pressure aircraft gas-turbine applications. The emphasis of this research is to reduce nitrogen oxides (NO_x) at high-power conditions and to maintain carbon monoxide and unburned hydrocarbons at their current low levels at low power conditions. Low-NO_x combustors can be classified into rich-burn and lean-burn concepts. Lean-burn combustors can be further classified into lean-premixed-prevaporized (LPP) and lean direct injection (LDI) concepts. In both concepts, all the combustor air, except for liner cooling flow, enters through the combustor dome so that the combustion occurs at the lowest possible flame temperature. The LPP concept has been shown to have the lowest NO_x emissions, but for advanced high-pressure-ratio engines, the possibility of autoignition or flashback precludes its use. LDI differs from LPP in that the fuel is injected directly into the flame zone, and thus, it does not have the potential for autoignition or flashback and should have greater stability. However, since it is not premixed and prevaporized, good atomization is necessary and the fuel must be mixed quickly and uniformly so that flame temperatures are low and NO_x formation levels are comparable to those of LPP.

The LDI concept described is a multipoint fuel injection/multiburning zone concept. Each of the multiple fuel injectors has an air swirler associated with it to provide quick mixing and a small recirculation zone for burning. The multipoint fuel injection provides quick, uniform mixing and the small multiburning zones provide for reduced burning residence time, resulting in low NO_x formation. An integrated-module approach was used for the construction where chemically etched laminates, diffusion bonded together, combine the fuel injectors, air swirlers, and fuel manifold into a single element.

The multipoint concept combustor was demonstrated in a 15° sector test. The configuration tested had 36 fuel injectors and fuel-air mixers that replaced two fuel injectors in a conventional dual-annular combustor. During tests, inlet temperatures were up to 870 K and inlet pressures were up to 5400 kPa. A correlation was developed that related the NO_x emissions with the inlet temperature, inlet pressure, fuel-air ratio, and pressure drop. At low-power conditions, fuel staging was used so that high combustion efficiency

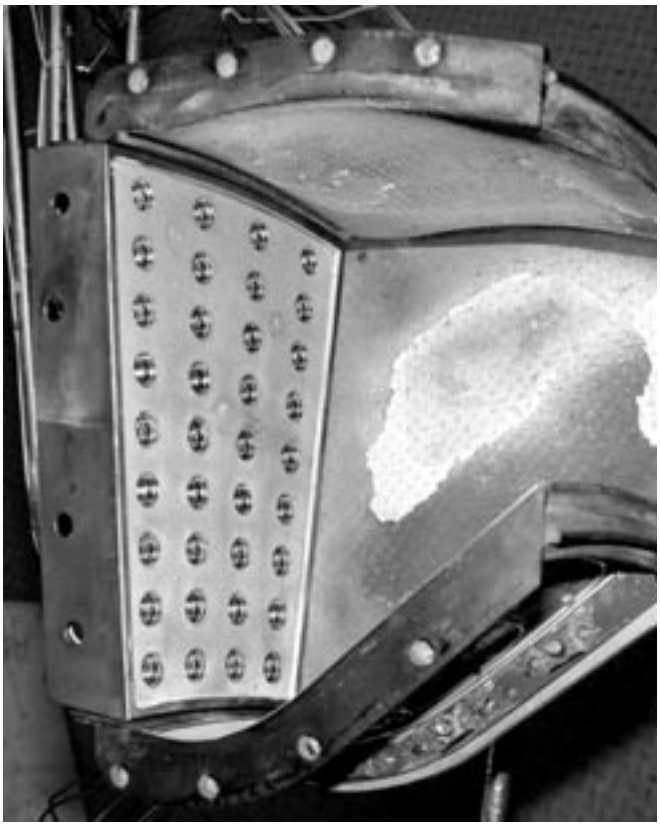

This revolutionary combustor concept employs multipoint arrays of lean-burning combustion zones to reduce NO_x emissions to extremely low levels. The multipoint array of lean direct injectors is shown integrated into a sector combustor rig.

was obtained with only one-fourth of the fuel injectors flowing. The test facility had optical access, and visual images showed the flame to be very short, approximately 25 mm long.

Glenn contact:
Robert R. Tacina, 216–433–3588, Robert.R.Tacina@grc.nasa.gov

Authors:
Robert R. Tacina, Changlie Wey, Peter Laing, and Adel Mansour

Headquarters program office: OAT

Programs/Projects: UEET

Transonic Resonance Demonstrated To Be a Source of Internal Noise From Mixer-Ejector Nozzles

Experimental studies have shown that convergent-divergent nozzles, when run at low pressure ratios, often undergo a flow resonance accompanied by the emission of acoustic tones. This "transonic resonance" phenomenon, not well recognized previously, was studied with single, round laboratory-scale nozzles, and the results were reported in reference 1. An unsteady shock occurring within the divergent section was thought to be responsible for the resonance. With increasing supply pressure, the frequency f_N of the resonance increased and "stage jumps" occurred. Within a stage, the frequency varied approximately linearly with the fully expanded jet Mach number M_j. The slope of the variation became steeper when the half-angle-of-divergence of the nozzle was decreased. Correlation equations based on the data were provided for predicting f_N. Another striking feature was that tripping the nozzle's internal boundary layer tended to suppress the resonance. A clean, smooth nozzle interior was a prerequisite for the resonance to take place prominently.

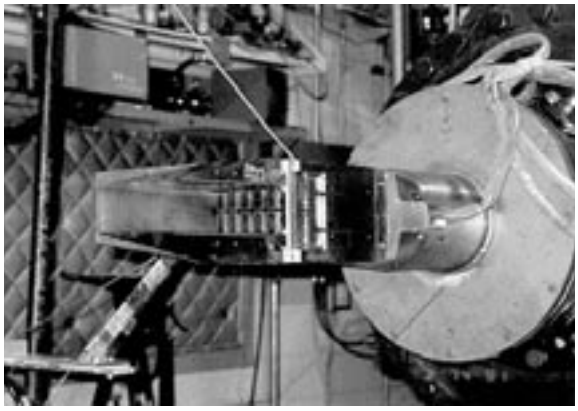

HSCT nozzle mounted in the open-jet facility.

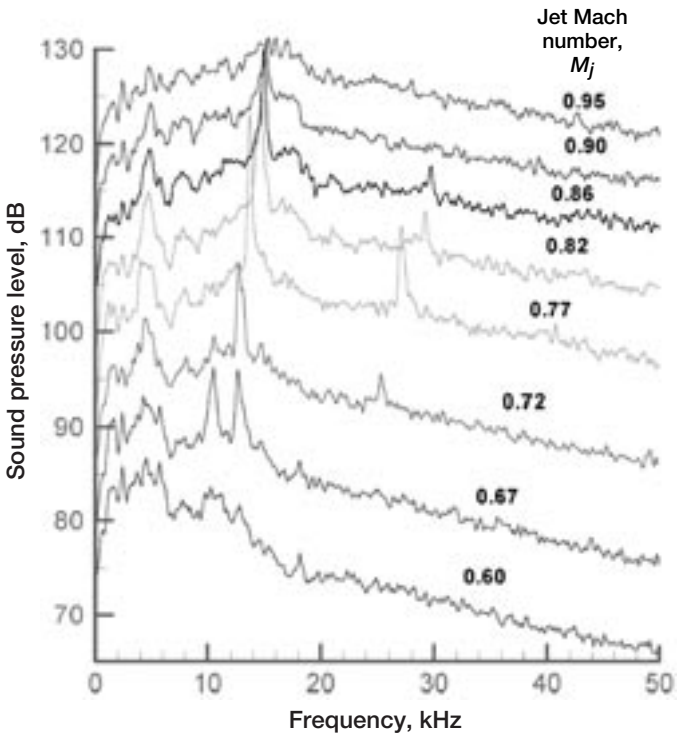

Sound-pressure-level spectra measured at different fully expanded Mach numbers (M_j).

During noise field studies with mixer-ejector nozzles in NASA's High-Speed Research program, tones were often encountered. The tones would persist in the simulated "cutback" condition (shortly after takeoff). Unfortunately, we did not understand their origin and, thus, could not develop a logical approach for suppressing them. We naturally questioned whether or not some of those tones were due to the transonic resonance. This was studied with a 1/13th scale model of the High-Speed Civil Transport nozzle. The first objective was to determine if indeed tones could be detected in the radiated noise. The next objective was to diagnose if those tones were due to the transonic resonance. Agreement of the frequencies with the correlation equation (ref. 1) and the effect of boundary layer tripping were to be used in the diagnosis.

The experiments were conducted in an open-jet facility at the NASA Glenn Research Center. The photograph on the preceding page shows the nozzle mounted on the facility. One wall of the ejector was removed so that the chutes of the primary nozzle would be visible. The noise was measured using a microphone held at a fixed location. Sound pressure spectra are shown for several values of M_j in the graph on the left. It can be seen that the frequency of the spectral peaks generally increase with increasing M_j. Furthermore, a given spectrum is marked by a peak at a lower frequency (fundamental) and by another peak to the right that is approximately the third harmonic. These are characteristic of the transonic resonance. The frequencies are compared with a prediction from the correlation equation in the graph on the right. The dimensions of the chutes are used as input in the calculations. The procedure for determining the half-angle-of-divergence for the chutes and the correlation equations is given in reference 1.

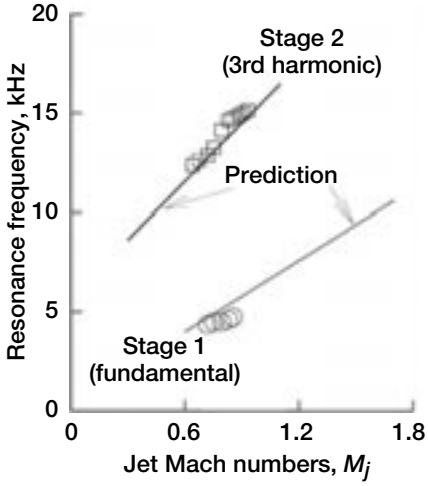

Comparison of resonance frequency (spectral peaks of second figure) with prediction.

The solid lines represent predictions for the frequencies of the fundamental and the next stage. It is clear that the observed frequencies follow the prediction well. This provides strong support to the notion that the spectral peaks are indeed due to the transonic resonance phenomenon. The effect of boundary layer trip lends further support. Boundary layer tripping near the throat of the chutes reduced the amplitudes. Because of the complex geometry and difficulties in assembling and disassembling the nozzle, the tripping effect has not been completely studied yet. The results, nevertheless, suggest that noise may be reduced simply by appropriate boundary layer tripping.

Reference

1. Zaman, K.B.M.Q.; Dahl, M.D.; and Bencic, T.J.: Experimental Investigation of 'Transonic Resonance' With Convergent-Divergent Nozzles. AIAA Paper 2001–0078, 2001.

Glenn contact:
Dr. Khairul B. Zaman, 216–433–5888, Khairul.B.Zaman@grc.nasa.gov

Author: Dr. Khairul B. Zaman

Headquarters program office: OAT

Programs/Projects:
Propulsion Systems R&T, UEET

Influence of Turbulence on the Restraint of Liquid Jets by Surface Tension in Microgravity Investigated

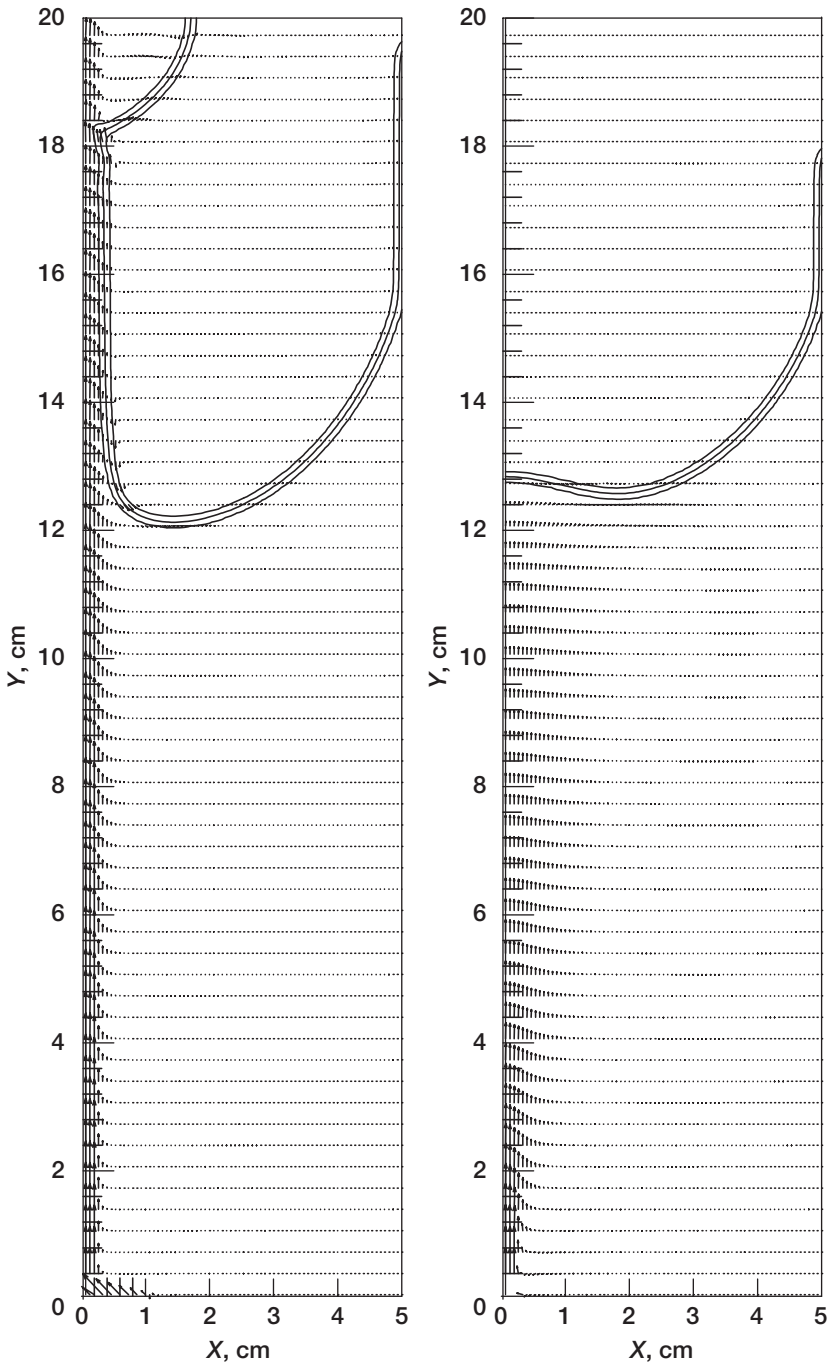

Comparison of flow modeled laminarly and with turbulent viscosity added. Time, 3.10 sec; jet flow rate, 34 cm/sec; initial fill level, 11.9 cm at the centerline; reference vector, 50 cm/sec. Left: Laminar. Right: Turbulent.

Microgravity poses many challenges to the designer of spacecraft tanks. Chief among these are the lack of phase separation and the need to supply vapor-free liquid or liquid-free vapor to the spacecraft processes that require fluid. One of the principal problems of phase separation is the creation of liquid jets. A jet can be created by liquid filling, settling of the fluid to one end of the tank, or even closing a valve to stop the liquid flow. Anyone who has seen a fountain knows that jets occur in normal gravity also. However, in normal gravity, the gravity controls and restricts the jet flow. In microgravity, with gravity largely absent, surface tension forces must contain jets.

To model this phenomenon, a numerical method that tracks the fluid motion and the surface tension forces is required. Jacqmin (ref. 1) has developed a phase model that converts the discrete surface tension force into a barrier function that peaks at the free surface and decays rapidly away. Previous attempts at this formulation were criticized for smearing the interface. This can be overcome by sharpening the phase function, double gridding the fluid function, and using a higher order solution for the fluid function. The solution of this equation can be rewritten as two coupled Poisson equations that also include the velocity.

After the code was implemented in axisymmetric form and verified by several test cases at the NASA Glenn Research Center, the drop

tower runs of Aydelott (ref. 2) were modeled. Work last year with a laminar model was found to overpredict Aydelott's results, except at the lowest Reynolds number conditions of 400. This year, a simple turbulence model was implemented by adding a turbulent viscosity based on the mixing-length hypothesis and empirical measurements of previous works. Predictions made after this change was implemented have been much closer to experimentally observed flow patterns and geyser heights. The preceding figure shows two model runs. The first, without any turbulence correction, breaks through the free surface and strikes the far end of the tank. In the second, the turbulence spreads the jet momentum over more of the free surface, enabling the surface tension forces to turn the jet back into the bulk liquid. The model geyser height with the second model is 1.1 cm. This is quite close to the 1.5-cm geyser height measured by Aydelott.

References

1. Jacqmin, David: Calculation of Two-Phase Navier-Stokes Flows Using Phase-Field Modeling. J. Comput. Phys., vol. 155, 1999, pp. 96–127.
2. Aydelott, John C.: Modeling of Space Vehicle Propellant Mixing. NASA TP–2107, 1983.

Glenn contact:
David J. Chato, 216–977–7488,
David.J.Chato@grc.nasa.gov

Author: David J. Chato

Headquarters program office: OAT

Programs/Projects: Space Launch Initiative, ASTP, Microgravity Science

Liquid Oxygen Propellant Densification Unit Ground Tested With a Large-Scale Flight-Weight Tank for the X–33 Reusable Launch Vehicle

Propellant densification has been identified as a critical technology in the development of single-stage-to-orbit reusable launch vehicles. Technology to create supercooled high-density liquid oxygen (LO_2) and liquid hydrogen (LH_2) is a key means to lowering launch vehicle costs. The densification of cryogenic propellants through subcooling allows 8 to 10 percent more propellant mass to be stored in a given unit volume, thereby improving the launch vehicle's overall performance. This allows for higher propellant mass fractions than would be possible with conventional normal boiling point cryogenic propellants, considering the normal boiling point of LO_2 and LH_2.

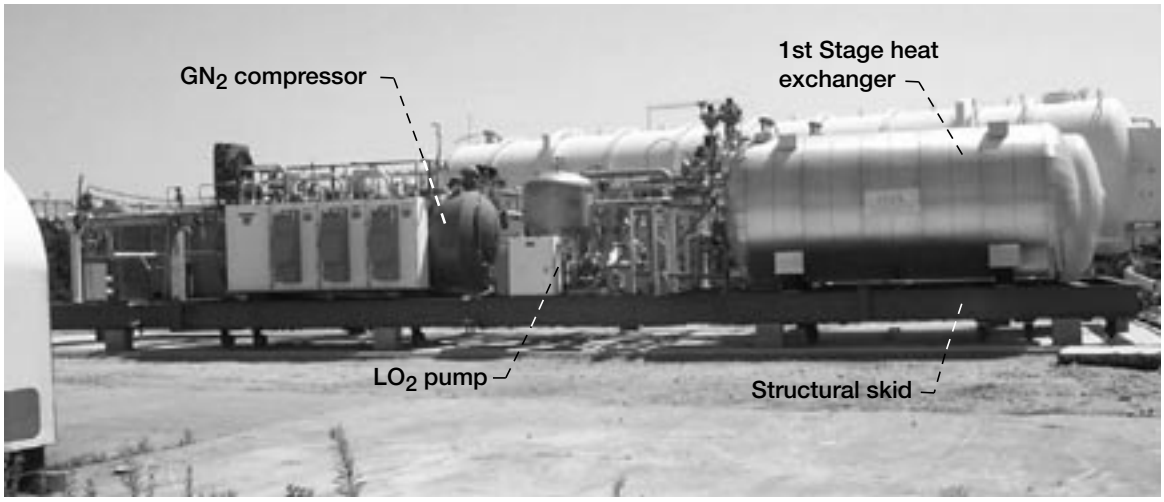

Testing has demonstrated the capability of the 30-lb_m/sec LO_2 propellant densification unit shown here, which is composed of a GN_2 cryogenic compressor, two heat exchangers in series, and an LO_2 pump. Test operations conducted with Glenn's densifier included oxygen loading, continuous production of 120 °R LO_2, fluid recirculation, and thermal stratification with the large-scale X–33 dual-lobe oxygen tank.

The Lockheed Martin propellant tank designated the Structural Test Article (STA) is a full-scale, flight-weight, prototype aluminum tank designed for the X–33 Reusable Launch Vehicle. The STA tank shown integrated with Glenn's LO_2 densification unit has a capacity of 20,000 gal of LO_2. Buildup of the South Forty Test Facility at Glenn was completed in June 2000, and densifier performance testing was completed in December 2000.

An LO_2 propellant densification unit was designed, built, and recently tested at the NASA Glenn Research Center. The steady-state demonstration and performance test series was conducted with the densifier to simulate LO_2 propellant tank loading, recirculation, and thermal stratification of the LO_2 loaded inside a flight-weight tank. The X–33-scale LO_2 densification unit as designed can process subcooled cryogen at a nominal rate of 30 lb/sec. The densifier subcools normal boiling point LO_2, thereby effectively lowering the temperature of the fluid from 168 °R to an outlet product temperature of 120 °R.

The continuous LO_2 densification production process utilizes two shell and spiral coil heat exchangers in series. Both heat exchangers employ liquid nitrogen (LN_2) as the primary coolant on the shell side. The second heat exchanger is a high-efficiency, subatmospheric, LN_2 boiling bath operating at 117 °R that cools the inlet LO_2 propellant feed stream. A three-stage centrifugal compressor operating at cryogenic inlet conditions maintains the second heat exchanger bath vapor pressure below 3.0 psia. The LO_2 propellant densification unit hardware shown in the photograph (on the preceding page) has a 30-lbm/sec production capability. The system is equipped with a cryogenic LO_2 recirculation pump for moving liquid from the propellant tank, into the densifier, and then back to the tank.

Densification performance tests started in October and were continued through early December 2000. Upon completion of Glenn's preliminary test matrix, which included densification checkout testing with LN_2, a series of loading and densification tests with LO_2 were performed for the Lockheed Martin Michoud Space Systems group. The LO_2 densifier performance tests were conducted with a large-scale Lockheed tank designated the Structural Test Article (STA) (see the photograph above) integrated with the densification unit.

Test operational and performance goals with the 30 lb_m/sec LO_2 densifier were successfully demonstrated during the course of the program. With the STA tank volume at around 20,000 gal, the initial loaded mass of normal boiling point LO_2 inside of the STA at the onset of the densification process was approximately 180,200 lb. Following completion of the 20 to 30 lb_m/sec densification flow testing, experimental results indicated that by the end of the process and based on an average bulk measured temperature of 123 °R, the final loaded mass of LO_2 was approximately 196,300 lb. This additional loaded mass of 16,100 lb represented on average an 8.9-percent increase in onboard LO_2 propellant. Test results also confirmed the presence of thermally stratified oxygen layers inside the tank. These layers varied in the vertical direction from 122 °R for the colder, denser fluid at the bottom to 166 °R for the warmer, less dense LO_2 near the top outlet of the STA tank.

Glenn research engineers and employees from Sierra Lobo, Inc., supported South Forty Facility buildup and test operations during the developmental program. This propellant research and technology work completed at Glenn has advanced the state of the technology by demonstrating the feasibility of loading, producing, and maintaining densified LO_2 onboard an operational full-scale launch vehicle propellant tank.

Bibliography

Greene, William D.; Knowles, Timothy E.; and Tomsik, Thomas M.: Propellant Densification for Launch Vehicles: Simulation and Testing 1999. AIAA Paper 99–2335, 1999.

Tomsik, Thomas M.: Performance Tests of a Liquid Hydrogen Propellant Densification Ground Support System for the X33/RLV. AIAA Paper 97–2976 (NASA TM–107469), 1997.

Lak, Tibor; Lozano, Martin; and Tomsik, Thomas M.: Advancement in Cryogenic Propulsion System Performance Through Propellant Densification. AIAA Paper 96–3123, 1996.

Glenn contact:
Thomas M. Tomsik, 216–977–7519, Thomas.M.Tomsik@grc.nasa.gov

Author: Thomas M. Tomsik

Headquarters program office: OAT

Programs/Projects:
ASTP, X–33, VentureStar

Aeroacoustic Flow Phenomena Accurately Captured by New Computational Fluid Dynamics Method

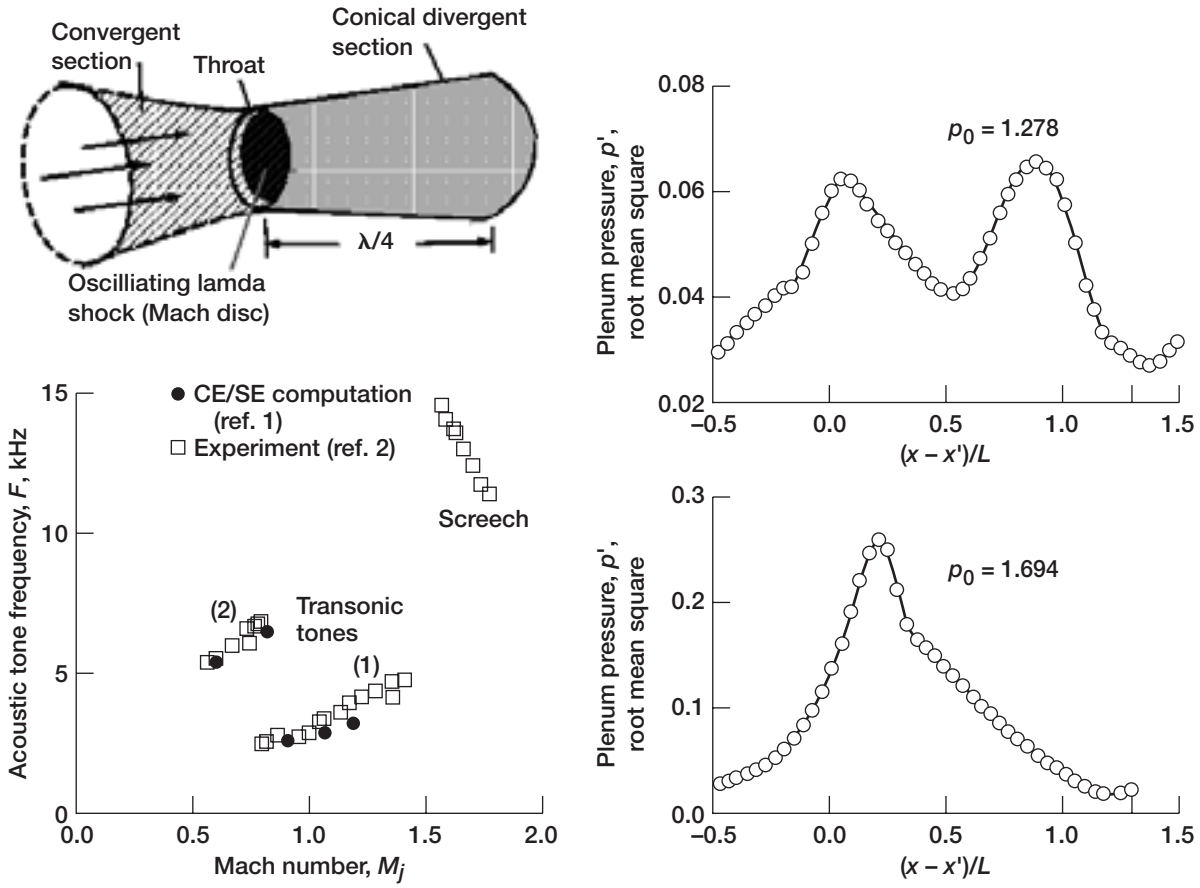

Upper left: Nozzle geometry. Lower left: Variation of tone frequency with jet Mach number. Right: Time-averaged (root mean square) amplitude of fluctuating pressure at two different plenum pressures.

One of the challenges in the computational fluid dynamics area is the accurate calculation of aeroacoustic phenomena, especially in the presence of shock waves. One such phenomenon is "transonic resonance," where an unsteady shock wave at the throat of a convergent-divergent nozzle results in the emission of acoustic tones. The space-time Conservation-Element and Solution-Element (CE/SE) method developed at the NASA Glenn Research Center can faithfully capture the shock waves, their unsteady motion, and the generated acoustic tones.

The CE/SE method is a revolutionary new approach to the numerical modeling of physical phenomena where features with steep gradients (e.g., shock waves, phase transition, etc.) must coexist with those having weaker variations. The CE/SE method does not require the complex interpolation procedures (that allow for the possibility of a shock between grid cells) used by many other methods to transfer information between grid cells. These interpolation procedures can add too much numerical dissipation to the solution process. Thus, while shocks are resolved, weaker waves, such as acoustic waves, are washed out.

In the figure on the preceding page, nozzle geometry is shown in the upper left quadrant. The convergent-divergent nozzle has diameters of 1.5, 0.3, and 0.4 in. at the inlet, throat, and exit, respectively. The throat is located 2.0-in. downstream of the inlet. The inlet is connected to a plenum with a static pressure p_0 of 1.694 psi. The lower left quadrant shows the acoustic tone frequency plotted as a function of the jet Mach number, M_j. The filled circles represent frequencies computed using a two-dimensional axisymmetric code based on the CE/SE method. The open squares represent experimental data by Zaman (ref. 1). Note that the plot shows data for both transonic tones and screech. Screech tones occur at higher jet Mach numbers. The transonic tones are of interest here. From the figure, it is evident that the results calculated by the CE/SE method show excellent agreement with the experimental data. The frequency shift with M_j, known as "staging," is captured accurately as well.

On the right side of the figure are two plots of the root mean square pressure fluctuation amplitudes at the nozzle centerline in the axial direction. The top plot is for a plenum pressure, $p_0 = 1.278$, which results in a stage-2 tone. It can be seen that a three-quarter standing wave is established within the nozzle. The bottom plot is for a plenum pressure of 1.694. Here, a one-quarter standing wave is set up, resulting in an abrupt shift in frequency. The figure to the left (on this page) shows the CE/SE method's excellent shock-capturing capability. Note the resolution of the lambda shock in the middle frame. The experimental schlieren data (right side) are taken from the experiments of C.A. Hunter at the NASA Langley Research Center (ref. 2).

The CE method is also being applied in two-dimensional axisymmetric codes to jet screech noise, turbomachinery noise, and pulse detonation engines. In all cases, excellent results have been obtained. A three-dimensional code based on CE/SE is currently being evaluated.

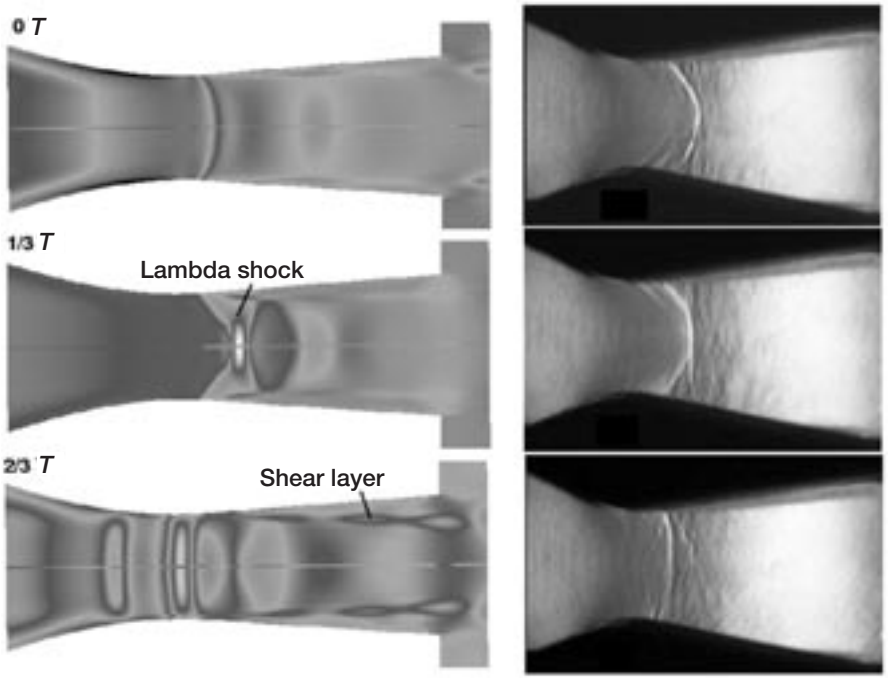

Comparison of shock structures for CE/SE computations and a similar experiment by Hunter. T represents one period of the transonic resonance oscillation.

Find out more about this research:
http://www.grc.nasa.gov/WWW/microbus/

References
1. Loh, C.Y. and Zaman, K.B.M.Q.: Numerical Investigation of 'Transonic Resonance' With a Convergent-Divergent Nozzle. AIAA Paper 2002–0077, 2002.
2. Zaman, K.B.M.Q.; Dahl, M.D.; and Bencic, T.J.: Experimental Investigation of 'Transonic Resonance' With Convergent-Divergent Nozzles. AIAA Paper 2001–0078, 2001.
3. Hunter, Craig A.: Experimental, Theoretical, and Computational Investigation of Separated Nozzle Flows. AIAA Paper 98–3107, 1998.

Bibliography
Chang, Sin-Chung: The Method of Space-Time Conservation Element and Solution Element—A New Approach for Solving the Navier-Stokes and Euler Equations. J. Comput. Phys., vol. 119, 1995, pp. 295–324.

Chang, Sin-Chung.; Wang, Xiao-Yen.; and Chow, Chuen-Yen: The Space-Time Conservation Element and Solution Element Method: A New High-Resolution and Genuinely Multidimensional Paradigm for Solving Conservation Laws. J. Comput. Phys., vol. 156, 1999, p. 89–136.

Loh, Ching-Y.; Hultgren, Lennart S.; and Chang, Sin-Chung: Wave Computation in Compressible Flow Using the Space-Time Conservation Element and Solution Element Method. AIAA J., vol. 39, no. 5, 2001, pp. 794–801.

TAIC contact:
Dr. Ching Y. Loh, 216–433–3981, Ching.Y.Loh@grc.nasa.gov

Glenn contact:
Richard A. Blech, 216–433–3657, Richard.A.Blech@grc.nasa.gov

Author: Richard A. Blech

Headquarters program office: OAT

Programs/Projects: Aerospace Propulsion and Power Base Research

CAD/CAE Integration Enhanced by New CAD Services Standard

A Government-industry team led by the NASA Glenn Research Center has developed a computer interface standard for accessing data from computer-aided design (CAD) systems. The Object Management Group, an international computer standards organization, has adopted this CAD services standard. The new standard allows software (e.g., computer-aided engineering (CAE) and computer-aided manufacturing software to access multiple CAD systems through one programming interface. The interface is built on top of a distributed computing system called the Common Object Request Broker Architecture (CORBA). CORBA allows the CAD services software to operate in a distributed, heterogeneous computing environment.

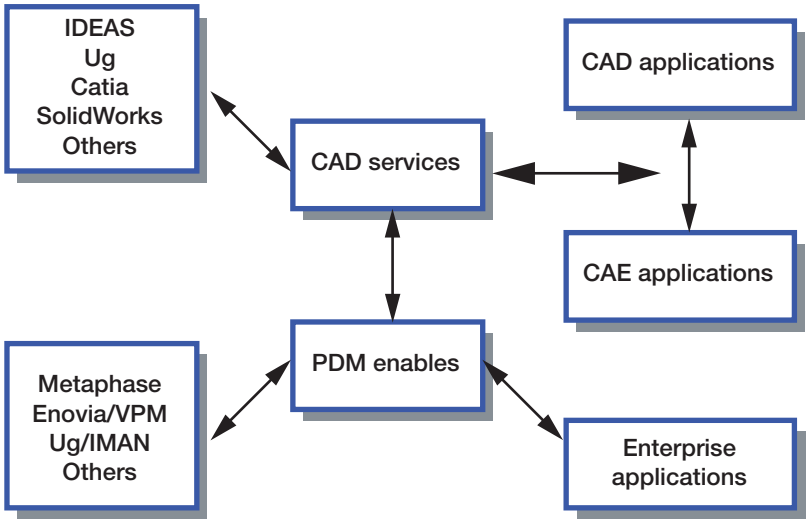

CAD systems and CAE applications link through industry standard services.

The CAD services interface provides geometry and topology data to engineering analysis and manufacturing applications and tools. It is designed around a series of high-level engineering interfaces that do not require low-level data structures to answer mechanical engineering queries. To avoid many of the problems associated with data translation, this standard provides CORBA interfaces with consistent functionality across native CAD implementations.

All queries use native CAD system geometry kernels and associated software as illustrated in the figure on the preceding page. That figure shows that this new standard provides a neutral interface across many CAD systems and also enables integration with product data manager (PDM) systems.

Some of the services provided by the CAD services interface include

(1) Geometry and topology queries for both manifold and nonmanifold geometries

(2) Parametric regeneration of solid models

(3) Tagging geometric entities with application-specific information

(4) Geometry creation

The geometry and topology queries provide precise three-dimensional location information for parts and surfaces. Parametric regeneration allows an optimization algorithm to reshape a CAD part to optimize the performance based on some engineering analysis. The geometric tagging capability allows engineering applications to tag geometry with relevant design information (for example, cost). Finally, the geometry creation capability permits system-level analyses to define detailed geometry that can be analyzed.

The primary value of the CAD services interface is that CAE applications, such as computational fluid dynamics (CFD), can access geometry in a variety of native formats without "custom" software development. All applications can use the same geometry information without translation or laborious wrapper development. This was demonstrated by using the CAD geometry illustrated in the figure to the right to generate a CFD analysis grid. This CAD/CFD integration was estimated to save several weeks in analysis development time.

Reusable launch vehicle geometry used to demonstrate CAD services.

Find out more about this research: http://mfg.omg.org/mfgcadv1ftf.htm

Glenn contact: Russell W. Claus, 216–433–5869, Russell.W.Claus@grc.nasa.gov

Author: Russell W. Claus

Headquarters program office: OAT

Programs/Projects: HPCCP, SLI

Turbopump Performance Improved by Evolutionary Algorithms

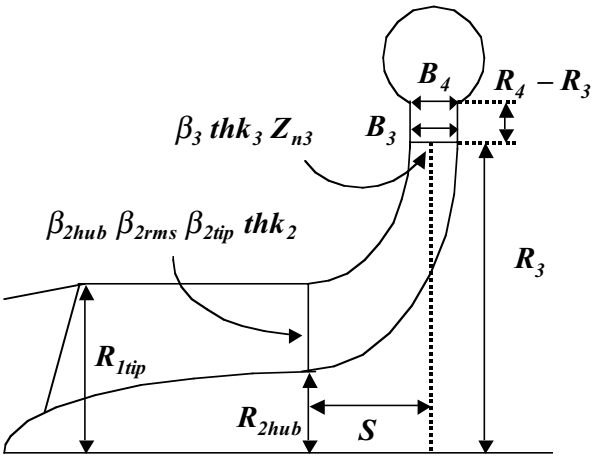

Design parameters for a multistage pump. β, relative angle from tangential; thk, normal blade thickness; R, radius; B, blade span.

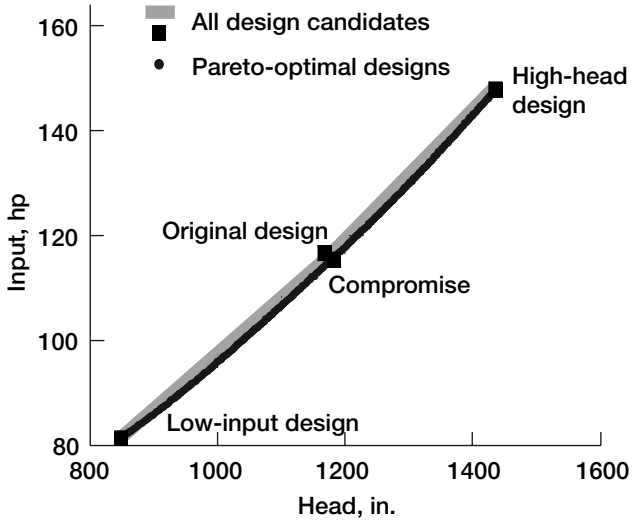

Objective function values of the multistage pump design.

The development of design optimization technology for turbomachinery has been initiated using the multiobjective evolutionary algorithm under NASA's Intelligent Synthesis Environment and Revolutionary Aeropropulsion Concepts programs.

As an alternative to the traditional gradient-based methods, evolutionary algorithms (EA's) are emergent design-optimization algorithms modeled after the mechanisms found in natural evolution. EA's search from multiple points, instead of moving from a single point. In addition, they require no derivatives or gradients of the objective function, leading to robustness and simplicity in coupling any evaluation codes. Parallel efficiency also becomes very high by using a simple master-slave concept for function evaluations, since such evaluations often consume the most CPU time, such as computational fluid dynamics. Application of EA's to multiobjective design problems is also straightforward because EA's maintain a population of design candidates in parallel. Because of these advantages, EA's are a unique and attractive approach to real-world design optimization problems.

To demonstrate the feasibility of the present approach, the redesign of the RL10A–3–3A liquid oxygen pump, shown in the top left sketch, was investigated at the NASA Glenn Research Center. The top right graph displays the Pareto-optimal solutions maximizing pressure head and minimizing input power; these include some designs that outperform the original design in both parameters by more than 1 percent. Moreover, the optimal designs give superior performance over the off-design operations (see the final graph). Detailed observation of the design results also can reveal some important design policies for the turbopump design of cryogenic rocket engines.

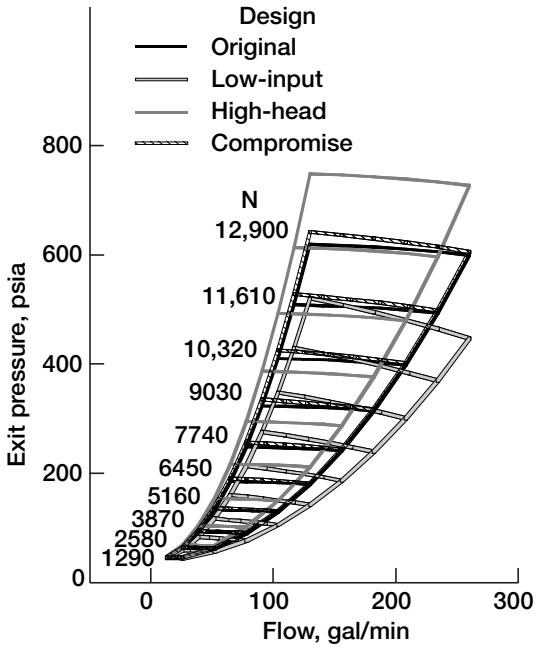

Pump overall performance map.

Glenn contact:
Dr. Meng-Sing Liou, 216–433–5855,
Meng-Sing.Liou@grc.nasa.gov

Authors: Dr. Akira Oyama and
Dr. Meng-Sing Liou

Headquarters program office: OAT

Programs/Projects:
Propulsion Systems R&T, ISE, RAC

Structures and Acoustics

High-Fidelity Micromechanics Model Developed for the Response of Multiphase Materials

A new high-fidelity micromechanics model has been developed under funding from the NASA Glenn Research Center for predicting the response of multiphase materials with arbitrary periodic microstructures (see the figure at the bottom left and refs. 1 and 2). The model's analytical framework is based on the homogenization technique, but the method of solution for the local displacement and stress fields borrows concepts previously employed in constructing the higher order theory for functionally graded materials (ref. 3). The resulting closed-form macroscopic and microscopic constitutive equations, valid for both uniaxial and multiaxial loading of periodic materials with elastic and inelastic constitutive phases, can be incorporated into a structural analysis computer code. Consequently, this model now provides an alternative, accurate method.

This new high-fidelity micromechanics model (named HFGMC, High-Fidelity Generalized Method of Cells) now enables the accurate simulation of both averaged (macro) and local (micro) stress and strain fields of heterogeneous materials such as ceramic, metal, and polymeric matrix composites employed in the aerospace, electronic, and biomedical industries. Traditional civil engineering construction materials, such as concrete and filled asphalt, can also be modeled using the developed approach. Prior to this innovation, one could accurately capture both microfields and macrofields only by using the computationally and labor intensive finite-element unit cell approach. An example of the excellent predictive capability of the averaged (or macroscopic) stress-strain response of a 25-vol%-fraction graphite/aluminum composite is shown in the graph at the bottom right. Similarly, the corresponding internal or microlevel stress and strain fields are also simulated with very good accuracy, as evidenced in the figure on the next page, where a comparison with finite-element results of the effective plastic strain are shown as well. A user-friendly interface for the model is currently under development to facilitate its use in design-oriented applications, including advanced material development and analysis.

References

1. Aboudi, J.; and Pindera, M.-J.; and Arnold, S.M.: Linear Thermoelastic Higher-Order Theory for Periodic Multiphase Materials. J. App. Mech., vol. 68, 2001, pp. 697–707.
2. Aboudi, J.; Pindera, M.-J.; and Arnold, S.M.: Higher-Order Theory for Periodic Multiphase Materials With Inelastic Phases. NASA/TM—2002-211469, 2002. http://gltrs.grc.nasa.gov/GLTRS

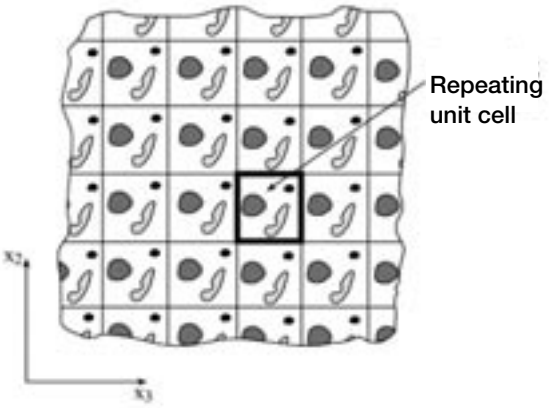

Multiphase material with periodic microstructure.

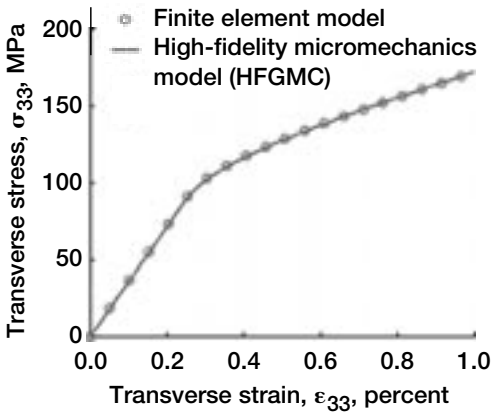

Macroscopic stress-strain response under combined biaxial loading (ref. 2).

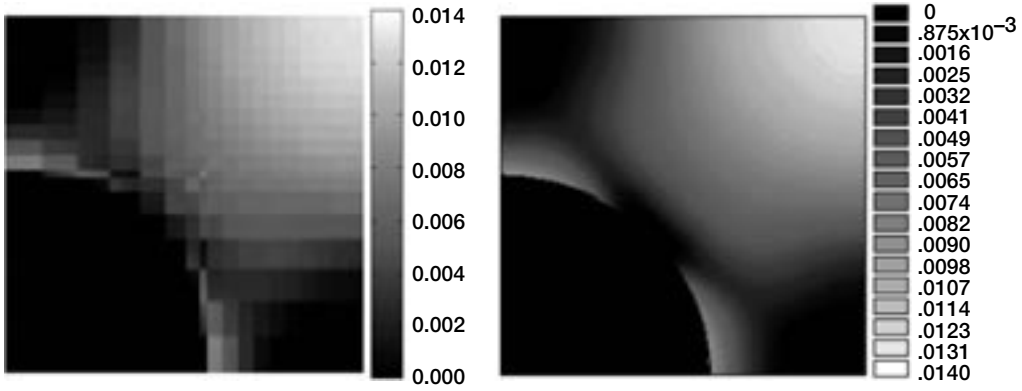

Comparison of the effective plastic strain fields obtained from the high-fidelity model and finite element analysis of a graphite/aluminum composite with 25-vol% fiber content subjected to biaxial loading (see the left figure on the preceding page) at the applied strain of 1.0 percent. This figure is shown in color in the online version of this article (http://www.grc.nasa.gov/WWW/RT2001/5000/5920arnold1.html).

3. Aboudi, J.; Pindera, M.J.; and Arnold, S.M.: Higher-Order Theory for Functionally Graded Materials. CPSOA, Part B—Engineering, vol. 30, no. 8, 1999, pp. 777–832.

Glenn contact: Dr. Steven M. Arnold, 216–433–3334, Steven.M.Arnold@grc.nasa.gov

Authors: Prof. Jacob Aboudi, Prof. Marek-Jerzy Pindera, and Dr. Steven M. Arnold

Headquarters program office: OAT

Programs/Projects: RLV, RAC

Higher-Order Theory–Structural/MicroAnalysis Code (HOT–SMAC) Developed

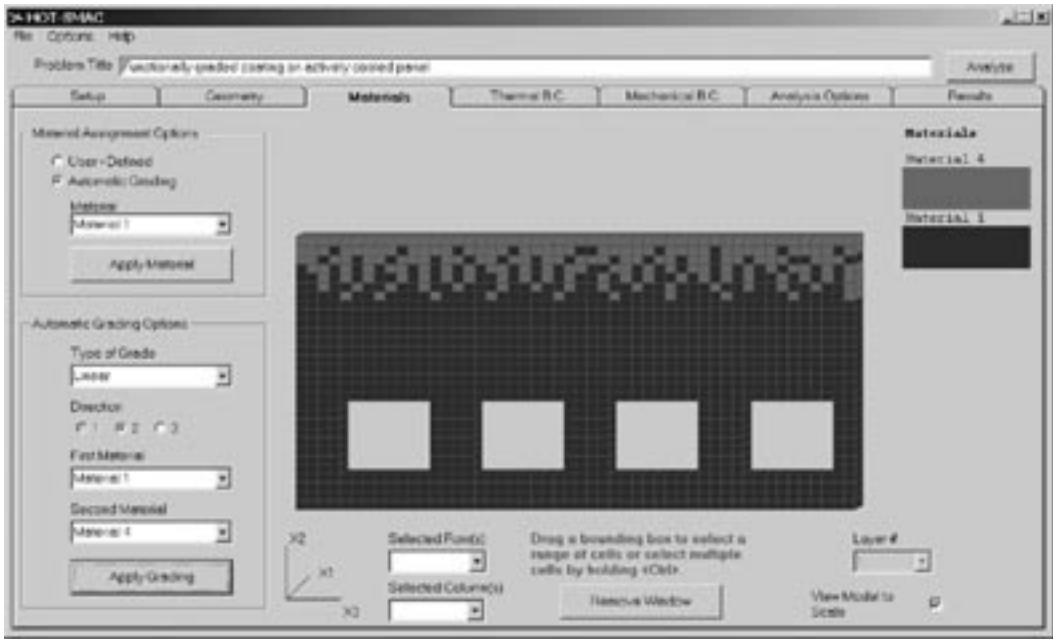

HOT–SMAC graphical user interface showing the material layout screen for a functionally graded material with a cooling channels problem.

The full utilization of advanced materials (be they composite or functionally graded materials) in lightweight aerospace components requires the availability of accurate analysis, design, and life-prediction tools that enable the assessment of component and material performance and reliability. Recently, a new commercially available software product called HOT–SMAC (Higher-Order Theory—Structural/MicroAnalysis Code) was jointly developed by Collier Research Corporation, Engineered Materials Concepts LLC, and the NASA Glenn Research Center under funding provided by Glenn's Commercial Technology Office. The analytical framework for HOT–SMAC is based on almost a decade of research into the coupled micro-macrostructural analysis of heterogeneous materials (ref. 1). Consequently, HOT–SMAC offers a comprehensive approach for analyzing/designing the response of components with various microstructural details, including certain advantages not always available in standard displacement-based finite element analysis techniques. The capabilities of HOT–SMAC include combined thermal and mechanical analysis, time-independent and time-dependent material behavior, and internal boundary cells (e.g., those that can be used to represent internal cooling passages, see the figure at the bottom of the preceding page) to name a few. In HOT–SMAC problems, materials can be randomly distributed and/or functionally graded (as shown in the figure, wherein the inclusions are distributed linearly), or broken down by strata, such as in the case of thermal barrier coatings or composite laminates. The software's user-friendly graphical user interface (see the figure) enables engineers to specify problem geometry (such as cell definition), define material distribution with a variety of techniques for distributing materials, specify general thermal and mechanical boundary conditions, and view time-dependent temperature, stress, and strain results.

This capability was recently applied to a previously solved problem (ref. 2) involving an actively cooled panel subjected to an intense flame boundary condition to validate the implementation of the recent software package. Furthermore, the figure below illustrates the kind of results available from HOT–SMAC for the free-edge region of the depicted hat-stiffened panel. Load levels determined from panel-scale structural analysis were employed as boundary conditions within HOT–SMAC. HOT–SMAC then determined the microscale in-plane shear stress field (as shown in the figure below). This type of coupled micromacroanalysis is an important strength of the HOT–SMAC software because local fields dictate local failures.

The current version of HOT–SMAC is limited geometrically to two-dimensional problems (i.e., either plane stress or generalized plane strain). A team of researchers from Glenn, the University of Virginia, the Ohio Aerospace Institute, and Collier Research plan to extend the software to three dimensions and to tightly couple it with the commercial HyperSizer structural analysis and optimization software package (Collier Research Corporation, Hampton, VA). This will enable the optimization of microscale features (e.g., the reinforcement type and the distribution) to achieve a global- or structural-scale goal.

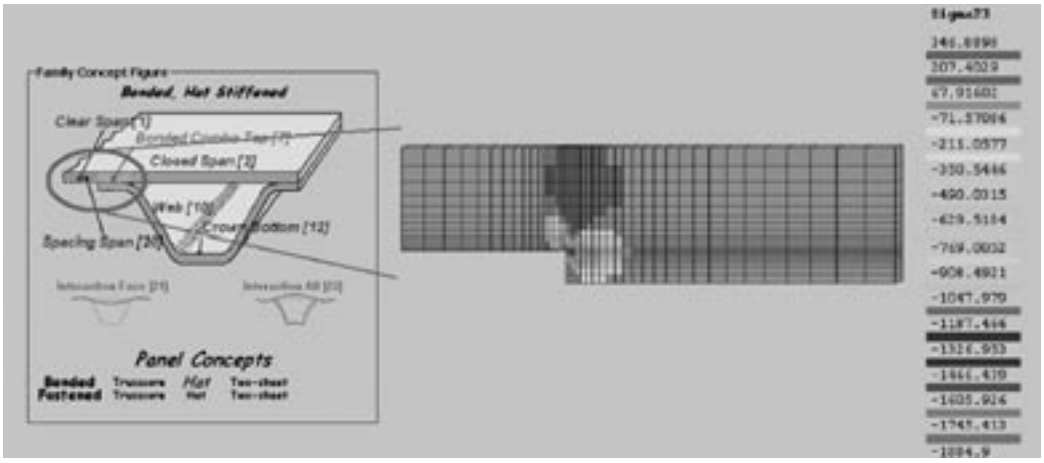

Example HOT–SMAC problem in which the in-plane shear stress field was determined for the hat-stiffened panel in the region of the flange-free edge. This figure is shown in color in the online version of this article (http://www.grc.nasa.gov/WWW/RT2001/5000/5920arnold2.html).

References

1. Aboudi, J.; Pindera, M.J.; and Arnold, S.M.: Higher-Order Theory for Functionally Graded Materials. CPSOA, Part B—Engineering, vol. 30, no. 8, 1999, pp. 777–832.
2. Arnold, Steven M.; Bednarcyk, Brett A.; and Aboudi, Jacob: Thermo-Elastic Analysis of Internally Cooled Structures Using a Higher Order Theory. NASA/TM—2001-210702, 2001. http://gltrs.grc.nasa.gov/GLTRS/

Glenn contact:
Dr. Steven M. Arnold,
216–433–3334,
Steven.M.Arnold@grc.nasa.gov

Author:
Dr. Steven M. Arnold

Headquarters program office: OAT (CTD)

Programs/Projects: CTO

Deformation, Failure, and Fatigue Life of SiC/Ti-15-3 Laminates Accurately Predicted by MAC/GMC

NASA Glenn Research Center's Micromechanics Analysis Code with Generalized Method of Cells (MAC/GMC) (ref. 1) has been extended to enable fully coupled macro-micro deformation, failure, and fatigue life predictions for advanced metal matrix, ceramic matrix, and polymer matrix composites. Because of the multiaxial nature of the code's underlying micromechanics model, GMC (ref. 2)—which allows the incorporation of complex local inelastic constitutive models—MAC/GMC finds its most important application in metal matrix composites, like the SiC/Ti-15-3 composite examined here. Furthermore, since GMC predicts the microscale fields within each constituent of the composite material, submodels for local effects such as fiber breakage, interfacial debonding, and matrix fatigue damage can and have been built into MAC/GMC. The present application of MAC/GMC highlights the combination of these features, which has enabled the accurate modeling of the deformation, failure, and life of titanium matrix composites (ref. 3).

The graph compares the room-temperature deformation and static life predicted by MAC/GMC with experimental data for five SiC/Ti-15-3 laminates (ref. 4). In these simulations, the Ti-15-3 matrix inelastic behavior is modeled using incremental plasticity theory (ref. 5) with piecewise linear postyield response. The SiC fiber failure behavior is modeled using Curtin's effective fiber-breakage model (ref. 6). The normal and shear fiber-matrix interfacial debonding, which allows the "knee" present in the [90°] and [±30°]s laminate[1] curves to be captured, is simulated with the evolving compliant interface model (ref. 7). The result of the coupling of these microscale models is the excellent macroscale agreement evident in this graph.

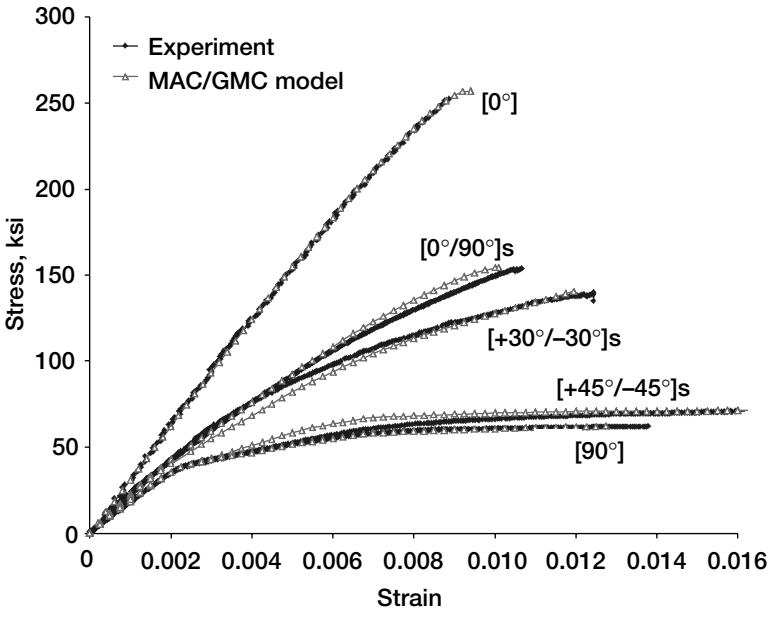

Deformation and failure of SiC/Ti-15-3 at room temperature.

[1]The letter "s" after the closing bracket indicates "symmetric."

The graph on the next page compares the elevated-temperature low-cycle fatigue (LCF) response of the SiC/Ti-15-3 laminates predicted by MAC/GMC with experimental data (ref. 8). Here, a fatigue damage model (ref. 9) was included for the matrix and the fiber (ref. 10). Again, the coupled nature of the microscale failure, debonding, and fatigue models within MAC/GMC has led to good agreement for this complex simulation.

References

1. Arnold, S.M., et al.: Micromechanics Analysis Code With Generalized Method of Cells (MAC/GMC): User Guide. Version 3, NASA/TM—1999-209070, 1999. http://gltrs.grc.nasa.gov/GLTRS/
2. Aboudi, J.: Micromechanical Analysis of Thermo-Inelastic Multiphase Short-Fiber Composites. Comp. Eng., vol. 5, no. 7, 1995, pp. 839–850.
3. Bednarcyk, B.A.; Arnold, S.M.; and Lerch, B.A.: Fully Coupled Micro/Macro Deformation, Damage and Failure Prediction for SiC/Ti-15-3 Laminates. NASA/TM—2001-211343, 2001.
4. Lerch, Bradley A.; and Saltsman, James F.: Tensile Deformation of SiC/Ti-15-3 Laminates. ASTM STP 1156, 1993, pp. 161–175.
5. Mendelson, Alexander: Plasticity: Theory and Applications. Krieger Publishing Company, Melbourne, FL, 1983.
6. Curtin, William A.: Theory of Mechanical Properties of Ceramic-Matrix Composites. J. Am. Ceram. Soc., vol. 74, no. 11, 1991, pp. 2837–2845.
7. Bednarcyk, Brett A.; and Arnold, Steven M.: A New Local Debonding Model With Application to the Transverse Tensile and Creep Behavior of Continuously Reinforced Titanium Composites. NASA/TM—2000-210029, 2000. http://gltrs.grc.nasa.gov/GLTRS/

8. Lerch, Bradley A.: Fatigue Behavior of SiC/Ti-15-3 Laminates. HITEMP Review 1990. NASA CP–10051, paper no. 35, 1990, pp. 35–1 to 35–9. (Available from the NASA Glenn Subsonic Systems Office.)
9. Arnold, S.M.; and Kruch, S.: Differential CDM Model for Fatigue of Unidirectional Metal Matrix Composites. Int. J. Damage Mech., vol. 3, no. 2, 1994, pp. 170–191.
10. McDowell, David L., ed.: Applications of Continuum Damage Mechanics to Fatigue and Fracture. ASTM STP 1315, 1997.

Glenn contact: Dr. Steven M. Arnold, 216–433–3334, Steven.M.Arnold@grc.nasa.gov

Authors: Dr. Brett A. Bednarcyk and Dr. Steven M. Arnold

Headquarters program office: OAT

Programs/Projects: RLV

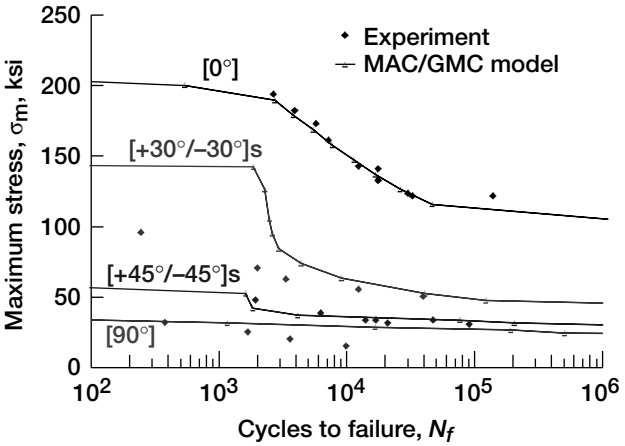

Stress-controlled LCF of 35-vol% SiC/Ti-15-3 at 800 °F.

MAC/GMC Code Enhanced for Coupled Electromagnetothermoelastic Analysis of Smart Composites

Intelligent materials are those that exhibit coupling between their electromagnetic response and their thermomechanical response. This coupling allows smart materials to react mechanically (e.g., an induced displacement) to applied electrical or magnetic fields (for instance). These materials find many important applications in sensors, actuators, and transducers.

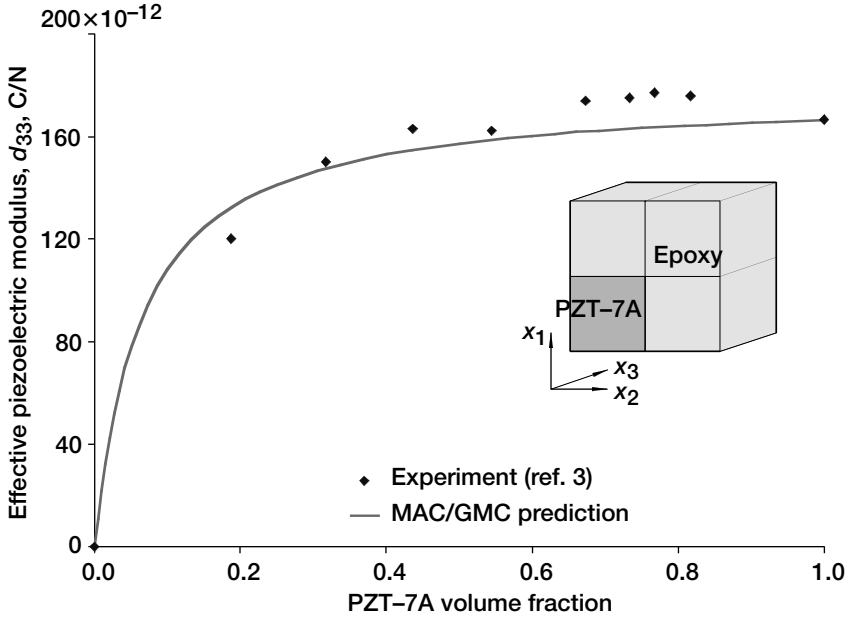

MAC/GMC prediction compared with experimental results for the "effective piezoelectric modulus" $d^*_{33} = e^*_{3k}\, S^*_{k3}$, where S_{ij} are the effective compliance components, of a continuous-fiber PZT–7A/epoxy composite.

Recently interest has arisen in the development of smart composites that are formed via the combination of two or more phases, one or more of which is a smart material. To design with and utilize smart composites, designers need theories that predict the coupled smart behavior of these materials from the electromagnetothermoelastic properties of the individual phases. The micromechanics model known as the generalized method of cells (GMC) has recently been extended to provide this important capability (ref. 1). This coupled electromagnetothermoelastic theory has recently been incorporated within NASA Glenn Research Center's Micromechanics Analysis Code with Generalized Method of Cells (MAC/GMC) (ref. 2). This software package is user friendly and has many additional features that render it useful as a design and analysis tool for composite materials in general, and with its new capabilities, for smart composites as well.

The results shown here were generated to demonstrate and validate the capabilities of the enhanced MAC/GMC code. The preceding figure compares MAC/GMC predictions with experimental results (ref. 3) for a PZT–7A/epoxy composite. The simple 2-by-2 GMC repeating unit cell depicted in the figure was employed for the analysis. Clearly, the agreement is good, indicating MAC/GMC's ability to predict the effective piezoelectric properties of smart composites. The figure to the right highlights MAC/GMC's simulated loading capabilities along with its ability to examine more refined unit cell geometries. The simulated loading is in the form of an applied electric field component, *E*3, while all other quantities besides *D*3 are held fixed at zero. Results show the amount of mechanical strain that is induced as the electric field is applied. Because of the refined unit cell geometry employed in the simulation, and the fact that the GMC theory provides predictions for the microscale fields within composite materials, the local fields shown in the final figure can be generated. The contour plots shown represent the internal fields that arise at the end of the simulation, when the applied electric field, *E*3, reaches 2.0 MV/N. It is important to note that although all global stress components on the composite are zero, MAC/GMC clearly shows that significant stresses arise internally in response to the applied electric field. This microscale capability inherent to GMC also allows the incorporation of submodels within MAC/GMC to represent local phenomena such as damage, interfacial debonding, and viscoplasticity.

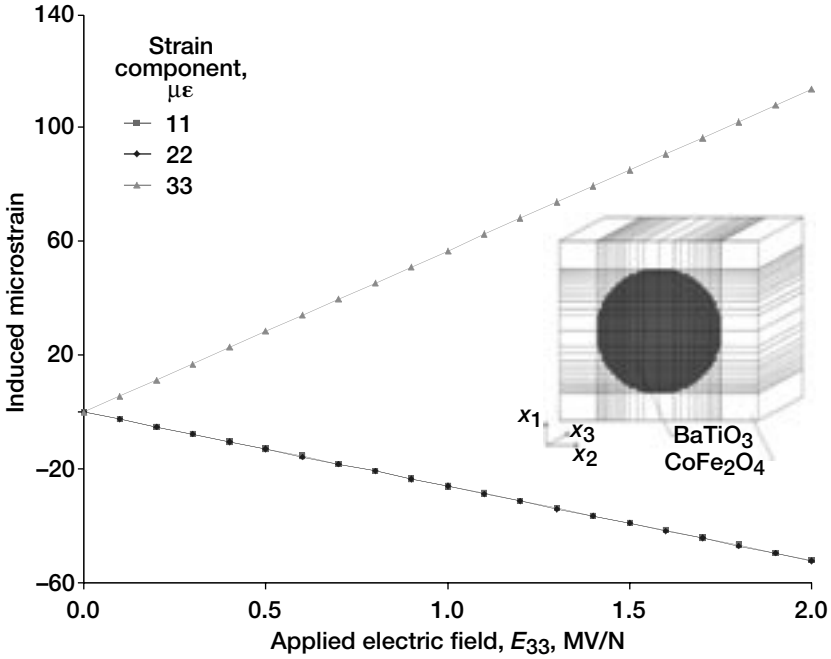

MAC/GMC prediction for the mechanical response of 35-vol% continuous-fiber $BaTiO_3/CoFe_2O_4$ to the applied electric field loading, E_{33}.

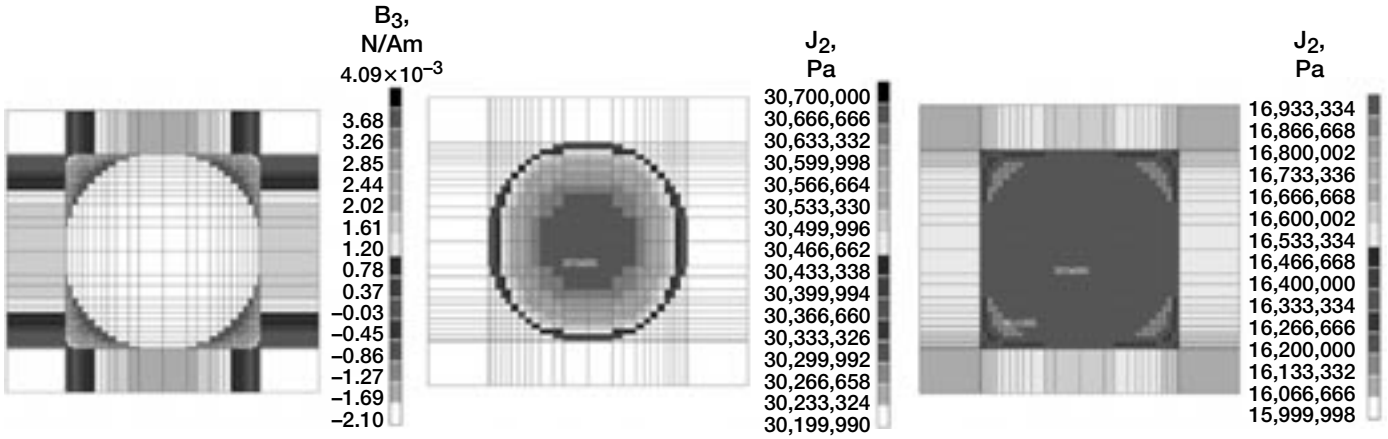

MAC/GMC prediction for the internal microfields within 35-vol% continuous-fiber $BaTiO_3/CoFe_2O_4$ at an applied electric field load level of $E_{33} = 2.0$ MV/m. B_3 = magnetic flux, $J_2 = \sqrt{(3/2)S_{ij}S_{ij}}$ where S_{ij} = stress deviator components. This figure is shown in color in the online version of this article (http://www.grc.nasa.gov/WWW/RT2001/5000/5920arnold4.html).

References

1. Aboudi, Jacob: Micromechanical Prediction of the Effective Behavior of Fully Coupled Electro-Magneto-Thermo-Elastic Multiphase Composites. NASA/CR—2000-209787, 2000. http://gltrs.grc.nasa.gov/GLTRS/
2. Arnold, S.M., et al.: Micromechanics Analysis Code With Generalized Method of Cells (MAC/GMC): User Guide. Version 3, NASA/TM—1999-209070, 1999. http://gltrs.grc.nasa.gov/GLTRS/
3. Chan, H.L.W.; and Unsworth, J.: Simple-Model for Piezoelectric Ceramic Polymer 1–3 Composites Used in Ultrasonic Transducer Applications. IEEE Trans. Ultrason. Ferroelectr. Freq. Control, vol. 36, no. 4, 1989, pp. 434–441.

Glenn contact:
Dr. Steven M. Arnold, 216–433–3334, Steven.M.Arnold@grc.nasa.gov

Authors: Dr. Brett A. Bednarcyk, Dr. Steven M. Arnold, and Prof. Jacob Aboudi

Headquarters program office: OAT

Programs/Projects: RAC

Influence of Cooling Channel Geometry on the Thermal Response in Silicon Nitride Plates Studied

Engine manufacturers are continually attempting to improve the performance and efficiency of internal combustion engines. Usually they raise the operating temperature or reduce the cooling air requirement for the hot section turbine components. However, the success of these attempts depends on finding materials that are lightweight, are strong, and can withstand high temperatures. Ceramics are among the top candidate materials considered for such harsh applications. They hold low-density, high-temperature strength, and thermal conductivity, and they are undergoing investigation as potential materials for replacing nickel-base alloys and superalloys that are currently used for engine hot-section components. Ceramic structures can withstand higher operating temperatures and a harsh combustion environment. In addition, their low densities relative to metals help reduce component mass (ref. 1).

The long-term objectives of the High Temperature Propulsion Components (HOTPC) Project are to develop manufacturing technology, thermal and environmental barrier coatings (TBC/EBC), and the analytical modeling capability to predict thermomechanical stresses in minimally cooled silicon nitride turbine nozzle vanes under simulated engine conditions. Two- and three-dimensional finite element analyses with TBC were conducted at the NASA Glenn Research Center. Nondestructive evaluation was used to determine processing defects.

TEMPERATURE VARIATION AS A FUNCTION OF COOLING CHANNEL CROSS SECTION WITH AIR COOLING

Cooling channel shape	Temperature, °C	
	Maximum	Minimum
Square	1344	976
Circular	1379	1068
Ascending-order cooling channels	1077	602

The study included conducting preliminary parametric analytical runs of heat transfer and stress analyses (ref. 2) under steady-state conditions to demonstrate the feasibility of using cooled Si_3N_4 parts for turbine applications. The influence of cooling-channel shapes (such as circular, square, and ascending-order cooling channels) on cooling efficiency and thermal stresses was investigated. Temperature distributions were generated for all cases considered under both cooling and no-cooling conditions, with air being the cooling medium.

The table shows the magnitude of the maximum and minimum temperature obtained for the plates under air cooling. Each channel's cross-sectional shape delivered a different temperature; however, the two-dimensional analyses for circular and square or equal-side rectangular holes produced close results. Moreover, the model of the panel with ascending-order cooling channels experienced the lowest temperature. A difference of near 260 °C

was found among the three cooling-hole configurations investigated. The ascending-order cooling channels arrangement showed superior performance by attaining the lowest temperature (1077 °C) in comparison to the circular (1379 °C) and square (1343 °C) channels for the same cooling-hole size. This indicates that the panel with ascending-order cooling channels is the most suitable configuration regardless of the complexity involved in its manufacture. More details pertaining to this study are reported in reference 3.

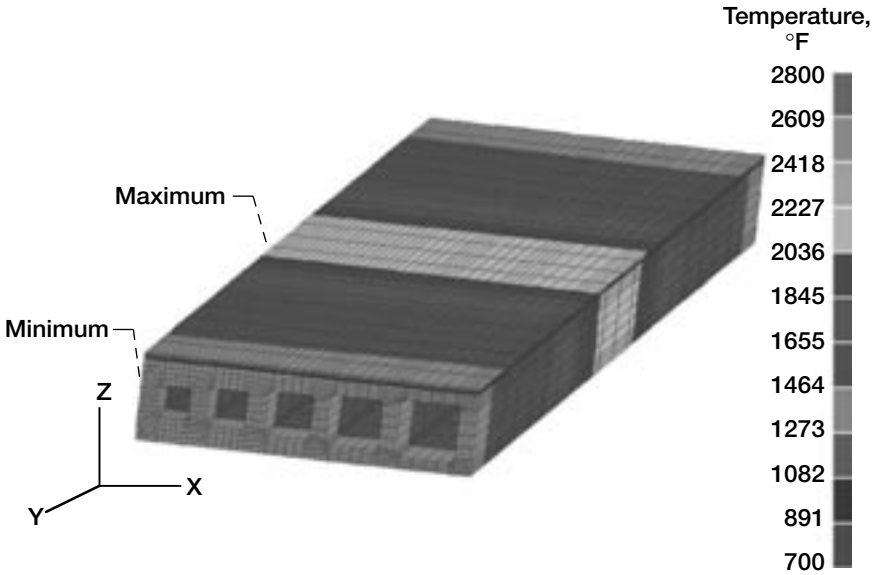

Typical temperature distribution of the panel with ascending-order cooling channels. This figure is shown in color in the online version of this article (http://www.grc.nasa.gov/WWW/RT2001/5000/5920aziz1.html).

References

1. Bhatt, R.T.: Minimally Cooled Ceramics and Fiber Reinforced Ceramic Matrix Composite Turbine Components: A Progress Report. HITEMP Review 1999, NASA/CP—1999-208915, 1999. (Available from the NASA Glenn Subsonic Systems Office.)
2. ANSYS Release 5.4: ANSYS, Inc., Canonsburg, PA, 1997.
3. Abdul-Aziz, Ali; Baaklini, George Y.; and Bhatt, Ramakrishna T.: Design Evaluation Using Finite Element Analysis of Cooled Silicon Nitride Plates for a Turbine Blade Application. NASA/TM—2001-210819, 2001. http://gltrs.grc.nasa.gov/GLTRS/

CSU contact: Dr. Ali Abdul-Aziz, 216–433–6729, Ali.Abdul-Aziz@grc.nasa.gov

U.S. Army Vehicle Technology Center at Glenn contact: Dr. Ramakrishna T. Bhatt, 216–433–5513, Ramakrishna.T.Bhatt@grc.nasa.gov

Glenn contact: Dr. George Y. Baaklini, 216–433–6016, George.Y.Baaklini@grc.nasa.gov

Authors: Dr. Ali Abdul-Aziz, Dr. Ramakrishna T. Bhatt, and Dr. George Y. Baaklini

Headquarters program office: OAT

Programs/Projects: HOTPC

Integrated Nondestructive Evaluation and Finite Element Analysis Predicts Crack Location and Shape

Composite flywheels are being developed as an alternative to expensive, short-life chemical batteries. Flywheels promise orders of magnitude increases in performance and service life in many NASA and military applications—including spacecraft, launch vehicles, aircraft power systems, uninterruptible power supplies, and planetary outposts and rovers (ref. 1). Although the technology holds great promise, there remain a number of challenges to overcome (such as rotor certification for safe life) before these advanced flywheels reach operational status. Carbon-fiber-reinforced polymer composites are the materials of choice for energy applications because of the high energy and power densities that they can achieve (ref. 2). Flywheel design topology can also allow a burst failure mode that is relatively benign in comparison with flywheels made of metallic materials (ref. 3).

A successful deployment of flywheels must address the long-term durability issue of polymer composites because of the limited availability of their fatigue characteristics and nonlinear behavior especially at elevated temperatures. Nondestructive evaluation (NDE) combined with structural analysis tools is being used at the NASA Glenn Research Center to accurately assess the applicability of using various composite materials to design a suitable rotor/flywheel assembly. However, for NDE information to be useful in structural characterization and modeling, the NDE data format must be compatible with microstructural and structural models currently being developed (ref. 4).

This study describes the finite-element analyses and the NDE modality undertaken on two flywheel rotors that were spun to burst speed. Computed

tomography and dimensional measurements were used to nondestructively evaluate the rotors before and/or after they were spun to the first crack detection. Computed tomography data findings of two- and three-dimensional crack formation were used to conduct finite-element (FEA) and fracture mechanics analyses (ref. 5). A procedure to extend these analyses to estimate the life of these components is also outlined. NDE–FEA results for one of the rotors are presented in the figures. The stress results in the top figure, which represent the radial stresses in the rim, clearly indicate that the maximum stress region is within the section defined by the computed tomography scan. Furthermore, the NDE data correlate well with the FEA results, since the crack at the bottom of the bottom figure closely follows the radial stress distribution shown in the top figure. In addition, the measurements reported, as obtained from the bottom figure, show that the NDE and FEA data are in parallel. Details pertaining to this study are more fully described in reference 6.

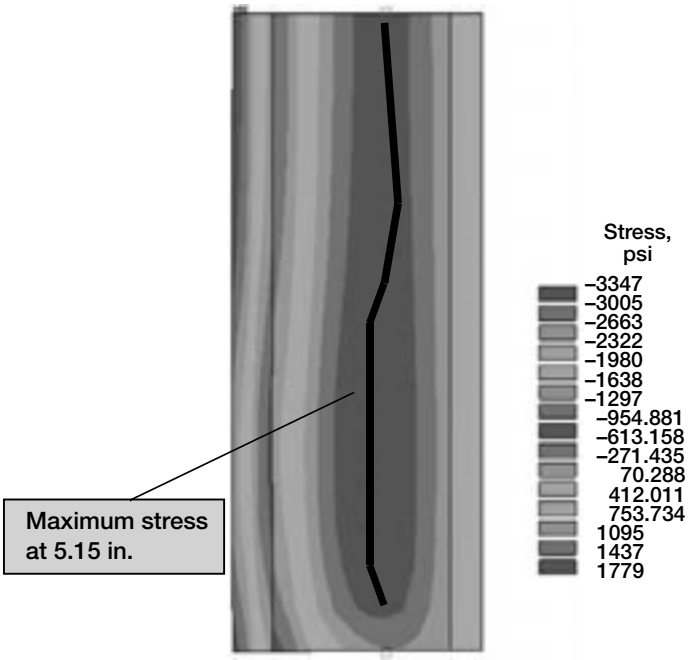

Rim radial stress distribution at 34,000 rpm for the rotor-B 30° slice (ring midplane cross section) based on ANSYS three-dimensional, finite element analysis. This figure is shown in color in the online version of this article (http://www.grc.nasa.gov/WWW/RT2001/5000/5920aziz2.html).

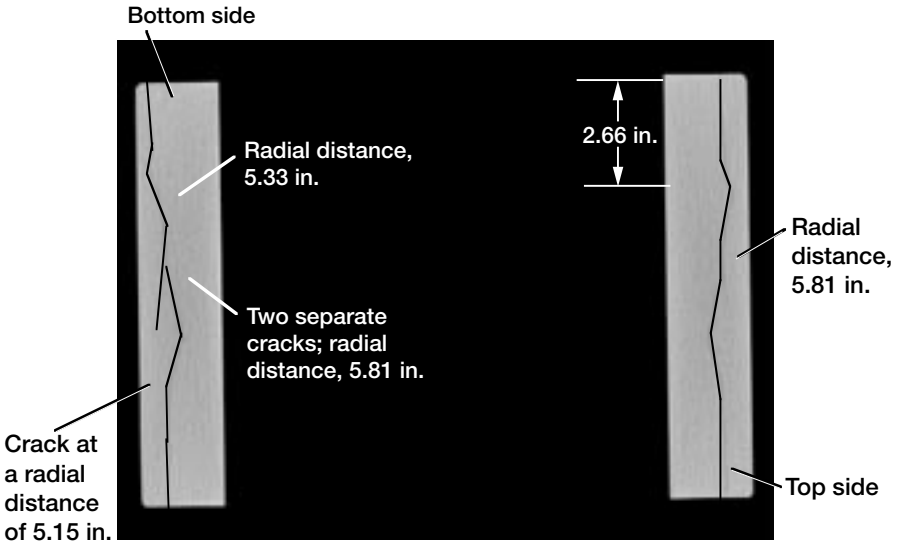

Cross-sectional computed tomography scan of rotor B showing cracking.

References

1. Ashley, Steven: Flywheels Put a New Spin on Electric Vehicles. Mech. Eng., 1993, pp. 44–51.
2. Olszewski, Mitchell, et al.: On the Fly or Under Pressure. Mech. Eng., 1988, pp. 50–58.
3. Coppa, Anthony P.: Flywheel Containment and Safety Considerations. An Assessment of Integrated Flywheel System Technology, NASA CP–2346, C.R. Keckler, et al., eds., 1984.
4. Baaklini, George Y., et al.: Structural Characterization of Metal Matrix Composites Using NDE Data. HITEMP Review 1997, NASA CP–10192, paper 41, 1997, pp. 1–15. (Available from the NASA Glenn Subsonic Systems Office.)
5. ANSYS Release 5.4: ANSYS, Inc., Canonsburg, PA, 1997.
6. Abdul-Aziz, Ali; Baaklini, George; and Trudell, Jeffrey: Structural Analysis of Composite Flywheels: An Integrated NDE and FEM Approach. NASA/TM–2001-210461, 2001. http://gltrs.grc.nasa.gov/GLTRS/

CSU contact:
Dr. Ali Abdul-Aziz, 216–433–6729, Ali.Abdul-Aziz@grc.nasa.gov

Glenn contacts:
Dr. George Y. Baaklini, 216–433–6016, George.Y.Baaklini@grc.nasa.gov; and Jeffrey J. Trudell, 216–433–5303, Jeffrey.J.Trudell@grc.nasa.gov

Authors: Dr. Ali Abdul-Aziz, Dr. George Y. Baaklini, and Jeffrey J. Trudell

Headquarters program office: OAT

Programs/Projects: FESS, RSL, Aeronautics & Space Base R&T

Scanning Electron Microscope Mapping System Developed for Detecting Surface Defects in Fatigue Specimens

An automated two-degree-of-freedom specimen positioning stage has been developed at the NASA Glenn Research Center to map and monitor defects in fatigue specimens. This system expedites the examination of the entire gauge section of fatigue specimens so that defects can be found using scanning electron microscopy (SEM). Translation and rotation stages are driven by microprocessor-based controllers that are, in turn, interfaced to a computer running custom-designed software. This system is currently being used to find and record the location of ceramic inclusions in powder metallurgy materials. The mapped inclusions are periodically examined during interrupted fatigue experiments. The number of cycles to initiate cracks from these inclusions and the rate of growth of initiated cracks can then be quantified. This information is necessary to quantify the effect of this type of defect on the durability of powder metallurgy materials. This system was developed with support of the Ultra Safe program.

Fatigue specimen mounted on translation-rotation stage.

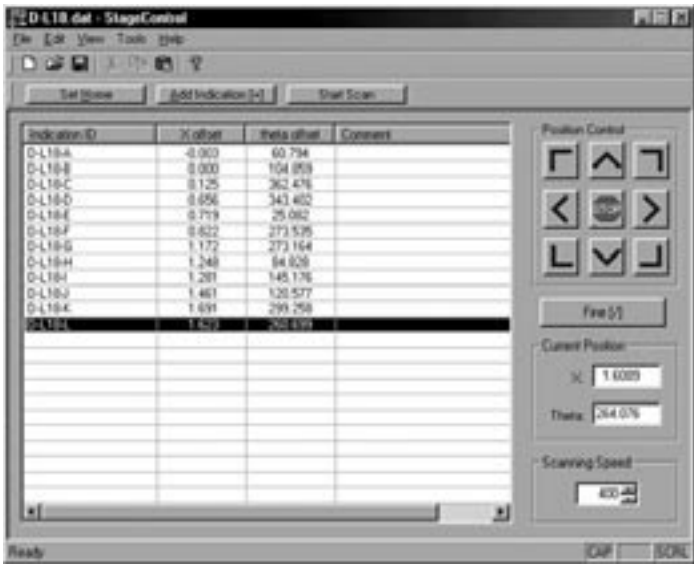

Left: User interface for StageControl software. Right: Example of an inclusion found with positioning system.

U.S. Army Vehicle Technology Center at Glenn contact:
Peter J. Bonacuse, 216–433–3309, Peter.J.Bonacuse@grc.nasa.gov

OAI contact: Peter T. Kantzos, 216–433–5205, Peter.T.Kantzos@grc.nasa.gov

Authors: Peter J. Bonacuse and Peter T. Kantzos

Headquarters program office: OAT

Programs/Projects: AvSP, Ultra Safe

Life Prediction/Reliability Data of Glass-Ceramic Material Determined for Radome Applications

Brittle materials, ceramics, are candidate materials for a variety of structural applications for a wide range of temperatures. However, the process of slow crack growth, occurring in any loading configuration, limits the service life of structural components. Therefore, it is important to accurately determine the slow crack growth parameters required for component life prediction using an appropriate test methodology. This test methodology also should be useful in determining the influence of component processing and composition variables on the slow crack growth behavior of newly developed or existing materials, thereby allowing the component processing and composition to be tailored and optimized to specific needs.

Through the American Society for Testing and Materials (ASTM), the authors recently developed two test methods to determine the life prediction parameters of ceramics. The two test standards, ASTM 1368 for room temperature and ASTM C 1465 for elevated temperatures, were published in the 2001 Annual Book of ASTM Standards, Vol. 15.01. Briefly, the test method employs constant stress-rate (or dynamic fatigue) testing to determine flexural strengths as a function of the applied stress rate. The merit of this test method lies in its simplicity: strengths are measured in a routine manner in flexure at four or more applied stress rates with an appropriate number of test specimens at each applied stress rate. The slow crack growth parameters necessary for life prediction are then determined from a simple relationship between the strength and the applied stress rate.

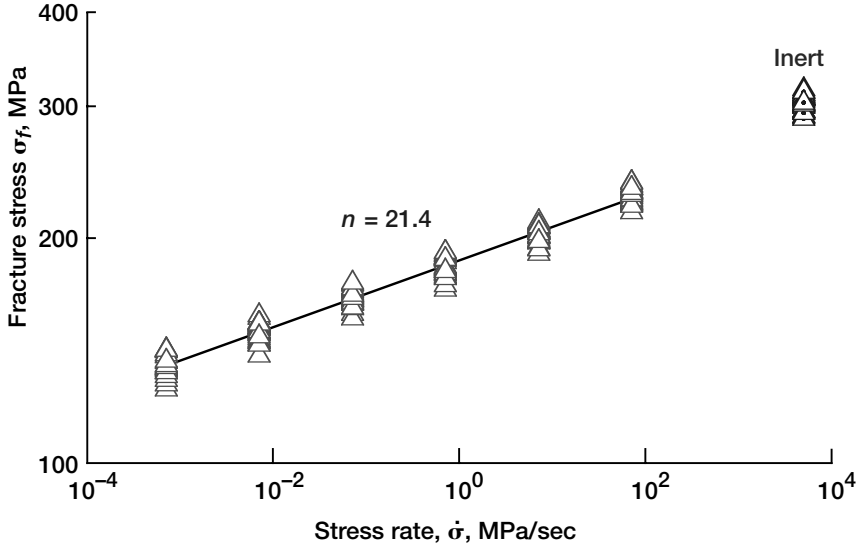

Fracture strength as a function of stress rate determined for glass-ceramic in room-temperature distilled water, in accordance with ASTM C 1368. Inert strength was determined in oil. A total of 30 test specimens were tested at each stress rate.

Extensive life prediction testing was conducted at the NASA Glenn Research Center using the developed ASTM C 1368 test method to determine the life prediction parameters of a glass-ceramic material that the Navy will use for radome applications. This project was done in cooperation with Science & Applied Technology (based in California). A wide range of applied stress rates ranging from 70 MPa/sec to 7×10^{-4} MPa/sec (six stress rates) was used, with 30 test specimens at each stress rate, totaling about 200 test specimens for the whole test matrix. The test results are shown in the graph. Peculiar to this material is that the scatter of strength was considerably small, with a resulting Weibull modulus (a measure of strength scatter) of about 45 in contrast to about 15 for typical ground ceramics. Hence, the test material was regarded as an ideal material to verify the test methodology as well as its underlying fundamentals. It can be seen from the graph that the data fit to the theory (solid line) is excellent with a correlation coefficient of 0.990, thus confirming the applicability of the test method. From the results in the graph, the corresponding life prediction parameters of the material were determined to be $n = 21$ and $D = 187$, with the units of strength in megapascals and stress rate in megapascals per second. Other material properties—such as tensile strength, fracture toughness, hardness and elastic modulus—were also evaluated. The determined life prediction parameters together with appropriate properties were further used to predict the actual component life and reliability analyses using the CARES/*Life* design software developed by Glenn. In addition,

the authors recently developed a life-prediction methodology using the exponential slow crack velocity formulation to relate its lifetime prediction parameters to those in the power-law formulation.

Ohio Aerospace Institute contact:
Dr. Sung R. Choi, 216–433–8366, Sung.R.Choi@grc.nasa.gov

Glenn contact:
Dr. John P. Gyekenyesi, 216–433–3210, John.P.Gyekenyesi@grc.nasa.gov

Authors: Dr. Sung R. Choi and Dr. John P. Gyekenyesi

Headquarters program office: OAT

Programs/Projects:
Space Act Agreement

Vibration Monitoring Techniques Applied to Detect Damage in Rotating Disks

Rotor health monitoring and online damage detection are increasingly gaining the interest of the manufacturers of aircraft engines. This is primarily due to the need for improved safety during operation as well as the need for lower maintenance costs. Applied techniques for detecting damage in and monitoring the health of rotors are essential for engine safety, reliability, and life prediction. The goals of engine safety are addressed within the NASA-sponsored Aviation Safety Program (AvSP, ref. 1). AvSP provides research and technology products needed to help the Federal Aviation Administration and the aerospace industry improve aviation safety. The Nondestructive Evaluation Group at the NASA Glenn Research Center is addressing propulsion health management and the development of propulsion-system-specific technologies intended to detect potential failures prior to catastrophe.

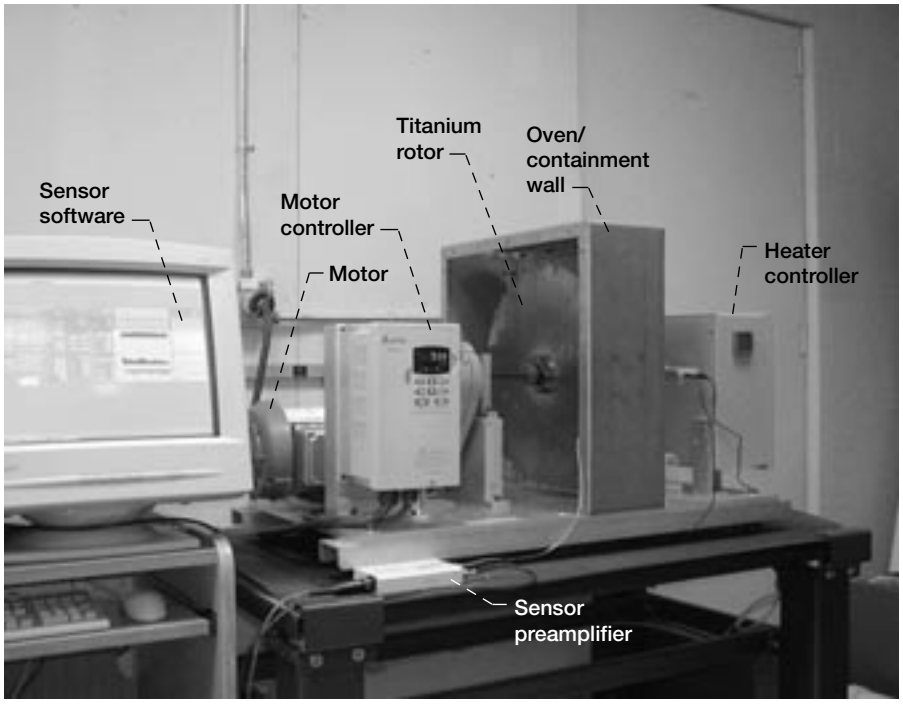

Disk spin simulation system. Note that left side containment cover is removed for viewing the rotor.

The current research is involved with experimental techniques as well as analytical results related to crack detection in rotating disks. The concept behind the crack-detection approach is based on the fact that the development of a crack is associated with the distortion in the component strain field and, consequently, with a minute unbalance. By monitoring the disk's radial vibration amplitude and phase online, one can see changes in the center of mass of the rotor system (ref. 2). To achieve the experimental setup necessary to verify and study this crack-detection technique, Glenn's Nondestructive Evaluation Group recently assembled a unique, two-bearing disk spin simulation system. The system, shown in the photograph, allows for elevated temperature, precision-controlled spin tests that can facilitate the application of various sensing

technologies for the in situ detection of rotor damage. Presently, interest is focused on an innovative capacitive sensing system used to monitor blade tip clearance and the corresponding change in the center of mass of the rotor system (refs. 3 and 4). The change in the center of mass, calculated utilizing the displacement data, has been shown to be sensitive to cracks as small as 1.27 mm (0.05 in.) in jet engine rotors tested in spin pits (ref. 2). Although at this point in time, the changes seen in this parameter have been characterized in only a subjective fashion. A deeper understanding of the relationship between crack progression and the change in the center of mass can be achieved with the implementation of highly controlled crack-initiation and growth tests on subscale spinning rotors. With the current disk spin simulation system, such controlled tests can be conducted.

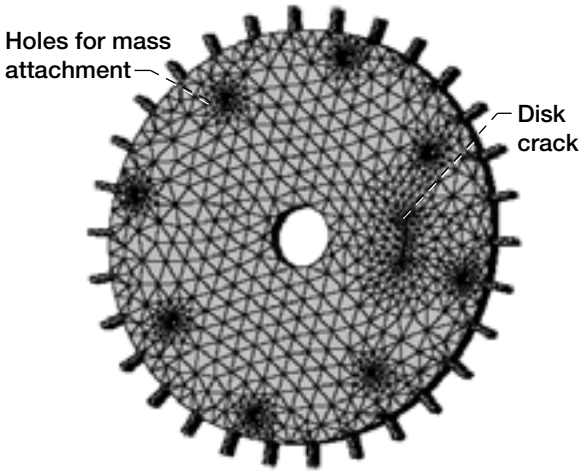

Finite element model of cracked disk used for calculating change in center of mass as a function of crack characteristics and rotational speed.

In a recent study, the sensor and the accompanying software were able to detect and precisely follow center-of-mass changes resulting from an attached mass on an 18-in.-diameter titanium disk (ref. 4). The disk had machined gear teeth to experimentally imitate a turbine's bladed disks. Furthermore, parametric finite element analyses are being conducted to optimize the experimental disk design as well as to gain an understanding of the change in the center-of-mass relationship with respect to crack characteristics and rotor speed (see the finite element model at the top right). As a result of the analytical analysis, the feasibility of measuring center-of-mass changes resulting from cracked disks was mathematically defined for the given rotor systems.

References

1. Shin, Jaiwon: The NASA Aviation Safety Program: Overview. ASME 2000–GT–0660, 2000.
2. Haase, W.C.; and Drumm, M.J.: Detection, Discrimination, and Real-Time Tracking of Cracks in Rotating Disks. Proceedings of the 9th International Symposium on Transport Phenomena and Dynamics of Rotating Machinery, Honolulu, Hawaii, Feb. 10–14, 2002.
3. Haase, W.C.; Roberge, J.K.; and Drumm, M.J.: High Bandwidth, Capacitive Sensing Preamplifier for Engine Health Monitoring. ExSell Inc., Concord, CA, 2000. http://www.exsell.org/rhm/, select *Products*, then select *Hi Band Preamp* (accessed Feb. 2002).
4. Gyekenyesi, Andrew L.; and Baaklini, George Y.: Rotor Health Monitoring and Damage Detection Utilizing a Disk Spin. Nondestructive Evaluation of Materials and Composites V, SPIE, Bellingham, WA, 2001, pp. 160–166.

Ohio Aerospace Institute contact:
Dr. Andrew L. Gyekenyesi,
216–433–8155,
Andrew.L.Gyekenyesi@grc.nasa.gov

Glenn contact:
Dr. George Y. Baaklini, 216–433–6016,
George.Y.Baaklini@grc.nasa.gov

Authors: Dr. Andrew L. Gyekenyesi and Dr. Jerzy T. Sawicki

Headquarters program office: OAT

Programs/Projects: AvSP

New Approach to Ultrasonic Spectroscopy Applied to Flywheel Rotors

Flywheel energy storage devices comprising multilayered composite rotor systems are being studied extensively for use in the International Space Station. A flywheel system includes the components necessary to store and discharge energy in a rotating mass. The rotor is the complete rotating assembly portion of the flywheel, which is composed primarily of a metallic hub and a composite rim. The rim may contain several concentric composite rings (see the figure to the right). This article summarizes current ultrasonic spectroscopy research of such composite rings and rims and a flat coupon, which was manufactured to mimic the manufacturing of the rings.

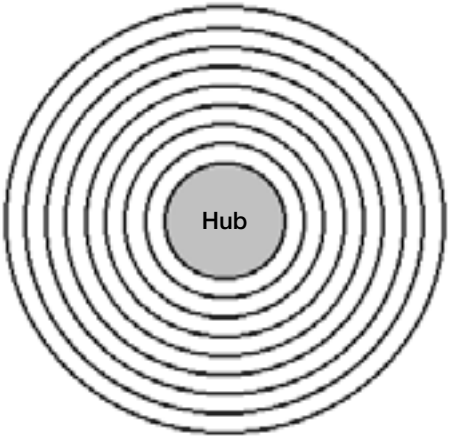

Simple rotor—metallic hub with a rim consisting of eight concentric rings.

Ultrasonic spectroscopy is a nondestructive evaluation (NDE) method for material characterization and defect detection (refs. 1 and 2). In the past, a wide bandwidth frequency spectrum created from a narrow ultrasonic signal was analyzed for amplitude and frequency changes. Tucker developed and patented a new approach to ultrasonic spectroscopy (ref. 3). The ultrasonic system employs a continuous swept-sine waveform and performs a fast Fourier transform on the frequency spectrum to create the spectrum resonance spacing domain, or fundamental resonant frequency (see the following figure). Ultrasonic responses from composite flywheel components were analyzed at Glenn to assess this NDE technique for the quality assurance of flywheel applications.

Amplitude and frequency changes in the spectrum and spectrum resonance spacing domains were evaluated from the ultrasonic responses of a flat composite coupon, thin and thick composite rings, and a multi-ring composite rim (refs. 4 and 5). Full-thickness resonance was produced in defect-free composite rings. The presence of foreign materials and of delaminations in composite rings were detected as an amplitude reduction in the spectrum domain and a change in fundamental resonant frequency. Manufacturing variations between the flat composite coupon and composite rings were detected as major differences in the response signals (see the graphs on the next page). The presence of discrete and clustered voids with widths greater than 1.7 mm (0.07 in.) was detected in thick composite rings as an amplitude reduction in the spectrum and spectrum resonance spacing.

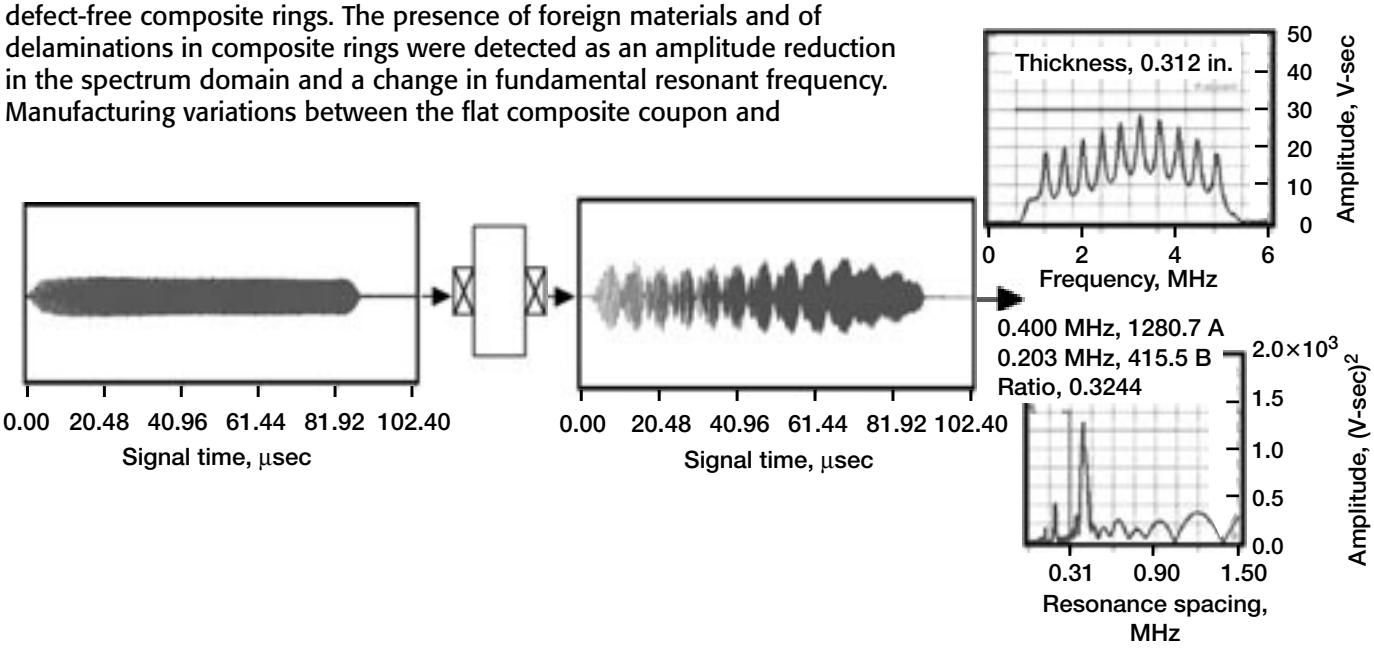

Through-transmission ultrasonic spectroscopy on a Lucite sample. Left: Digital input waveform in the time domain. Center: Digital output waveform in the time domain. Right: Typical output display of the spectrum and spectrum resonance spacing domains.

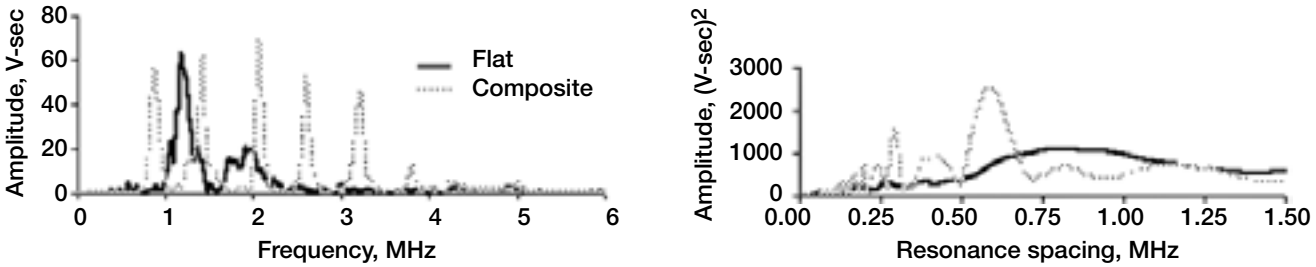

Response from a flat composite coupon compared with the response from a composite ring. Left: Spectrum. Right: Spectrum resonance spacing.

A unique detection of kissing disbonds requires further investigation, as their existence in composite rings was not confirmed destructively or corroborated with other nondestructive techniques. Voids with a width of 1.5 mm (0.06 in.) or smaller were not detected in the multi-ring composite rim. The ultrasonic responses before and after proof spin testing contained the same resonances for the four outer rings, suggesting that damage was not introduced to the rim. As a result, the signals from the multi-ring composite rim are baseline signatures to be compared after fatigue testing. On the basis of these findings, ultrasonic spectroscopy is a potential NDE tool for flight certification of flywheel rotors for the International Space Station.

References

1. Fitting, Dale W.; and Adler, Laszlo: Ultrasonic Spectral Analysis for Nondestructive Evaluation. Plenum Press, New York, NY, 1981.
2. Krautkrämer, Josef; and Krautkrämer, Herbert: Ultrasonic Testing of Materials. Second ed., Springer-Verlag, New York, NY, 1977.
3. Tucker, James R.: Apparatus and Method for Ultrasonic Spectroscopy Testing of Materials. U.S. Patent 5,591,913, Jan. 1997.
4. Harmon, Laura M.; and Baaklini, George Y.: Ultrasonic Resonance Spectroscopy of Composite Rings for Flywheel Rotors. Nondestructive Evaluation of Materials and Composites V, SPIE, Bellingham, WA, 2001, pp. 24–35.
5. Harmon, Laura M.; and Baaklini, George Y.: Ultrasonic Spectroscopy of Composite Rims for Flywheel Rotors. Review of Progress in Quantitative NDE, Bowdoin College, Brunswick, ME, vol. 21, 2001, Donald O. Thompson and Dale E. Chimenti, eds., American Institute of Physics, in press.

CSU contact:
Laura M. Harmon, 216–433–3866, Laura.M.Harmon@grc.nasa.gov

Glenn contact:
Dr. George Y. Baaklini, 216–433–6016, George.Y.Baaklini@grc.nasa.gov

Authors: Laura M. Harmon and Dr. George Y. Baaklini

Headquarters program office: OAT

Programs/Projects: FESS, RSL

High-Strength Composite Fabric Tested at Structural Benchmark Test Facility

Large sheets of ultrahigh strength fabric were put to the test at NASA Glenn Research Center's (http://www.grc.nasa.gov) Structural Benchmark Test Facility. The material was stretched like a snare drum head until the last ounce of strength was reached, when it burst with a cacophonous release of tension. Along the way, the 3-ft square samples were also pulled, warped, tweaked, pinched, and yanked to predict the material's physical reactions to the many loads that it will experience during its proposed use.

The material tested was a unique multi-ply composite fabric, reinforced with fibers that had a tensile strength eight times that of common carbon steel. The fiber plies were oriented at 0° and 90° to provide great membrane stiffness, as well as oriented at ±45° to provide an unusually high resistance to shear distortion. The fabric's heritage is in astronaut space suits and other NASA programs.

Increased demands are being made on materials for higher serviceability, more severe environments, and greater reliability. This has driven a need to better understand the mechanical properties of this composite fabric material. The

Raytheon Company, Electronics Systems Division (http://www.raytheon.com/es/es.htm) entered into a cost-reimbursable Space Act Agreement with NASA to conduct a series of tests on the fabric using Glenn's Life Prediction Branch's (http://www.grc.nasa.gov/WWW/LPB/) materials testing capabilities.

Raytheon provided 36- by 36-in. cross-shaped cruciform fabric specimens for testing in the Structural Benchmark Test Facility's 100,000-lb capacity in-plane load frame. An optical full-field strain-measurement system based on speckle-pattern correlation was employed to accurately measure material strains as the various loadings were applied.

The test program accurately characterized the stress-strain behavior of the novel fabric. Extensional and rotational elastic moduli and Poisson's ratios along the principal material axes were determined for over 120 load levels and biaxial load ratios. The test results already are proving useful in improved understanding of the material and for developing recommendations for material design changes. In the end, the testing will lead to more efficient and greater use, higher durability, longer life, and improved safety and reliability for fabric material designs.

The in-plane biaxial load frame with fabric specimen mounted.

Fabric specimen under large equibiaxial load with measured vertical displacement field superimposed.

Find out more about this research:

Raytheon Company—Electronic Systems Division:
http://www.raytheon.com/es/es.htm

Glenn's Life Prediction Branch: http://www.grc.nasa.gov/WWW/LPB/

Glenn contacts:
David L. Krause, 216–433–5465, David.L.Krause@grc.nasa.gov; and
Stephen J. Smith, 216–433–9580, Stephen.J.Smith@grc.nasa.gov

Author: David L. Krause

Headquarters program office: OAT

Programs/Projects: Space Act Agreement with Raytheon Company

Special recognition: 2001 Glenn Research Center Team Achievement Award

Initial Mechanical Testing of Superalloy Lattice Block Structures Conducted

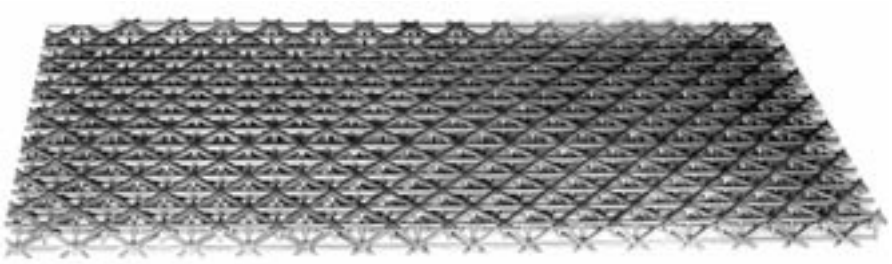

Cast Inconel 718 lattice block panel, approximately 130 by 300 by 12 mm (5 by 12 by 0.5 in.).

The first mechanical tests of superalloy lattice block structures produced promising results for this exciting new lightweight material system. The testing was performed in-house at NASA Glenn Research Center's (http://www.grc.nasa.gov) Structural Benchmark Test Facility, where small subelement-sized compression and beam specimens were loaded to observe elastic and plastic behavior, component strength levels, and fatigue resistance for hundreds of thousands of load cycles.

Current lattice block construction produces a flat panel composed of thin ligaments arranged in a three-dimensional triangulated trusslike structure. Investment casting of lattice block panels has been developed and greatly expands opportunities for using this unique architecture in today's high-performance structures. In addition, advances made in NASA's Ultra-Efficient Engine Technology Program (http://www.ueet.nasa.gov) have extended the lattice block concept to superalloy materials. After a series of casting iterations, the nickel-based superalloy Inconel 718 (IN 718, Inco Alloys International, Inc., Huntington, WV) was successfully cast into lattice block panels; this combination offers light weight combined with high strength, high stiffness, and elevated-temperature durability.

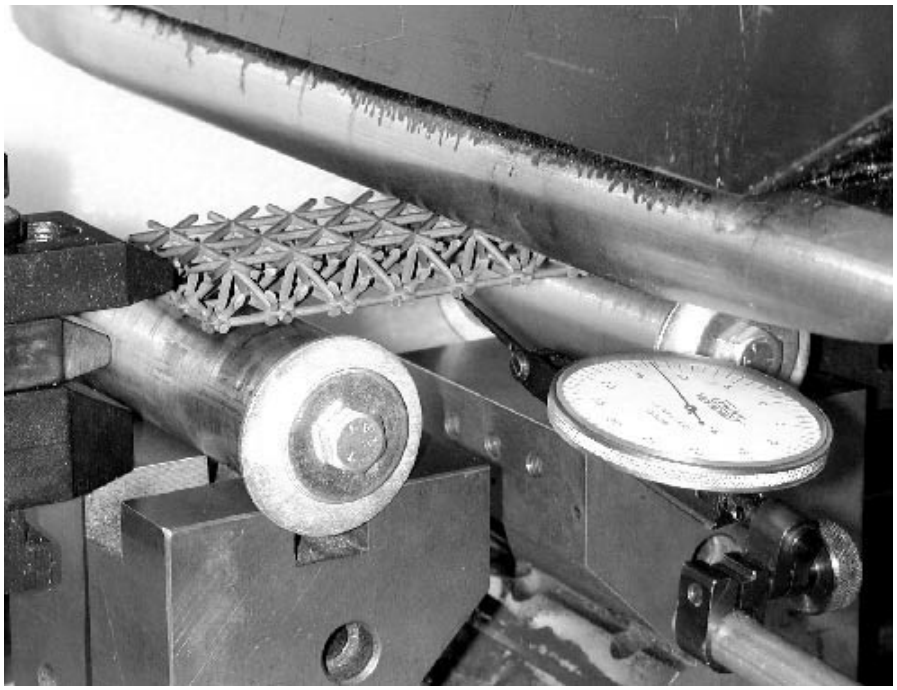

Lattice block specimen installed in test machine for bending fatigue test.

For tests to evaluate casting quality and configuration merit, small structural compression and bend test specimens were machined from the 5- by 12- by 0.5-in. panels. Linear elastic finite element analyses were completed for several specimen layouts to predict material stresses and deflections under proposed test conditions. The structural specimens were then subjected to room-temperature static and cyclic loads in Glenn's Life Prediction Branch's (http://www.grc.nasa.gov/WWW/LPB/) material test machine. Surprisingly, the test results exceeded analytical predictions: plastic strains greater than 5 percent were obtained, and fatigue lives did not depreciate relative to the base material. These assets were due to the formation of plastic hinges and the redundancies inherent in lattice block construction, which were not considered in the simplified computer models. The fatigue testing proved the value of redundancies since specimen strength was maintained even after the fracture of one or two ligaments.

This ongoing test program is planned to continue through high-temperature testing. Also scheduled for testing are IN 718 lattice block panels with integral face sheets, as well as specimens cast from a higher temperature alloy.

The initial testing suggests the value of this technology for large panels under low and moderate pressure loadings and for high-risk, damage-tolerant structures. Potential aeropropulsion uses for lattice blocks include turbine-engine actuated panels, exhaust nozzle flaps, and side panel structures.

Finite element model of a bend test specimen showing contours of expected deflections.

Find out more about this research:

Ultra Efficient Engine Technology: http://www.ueet.nasa.gov/

Glenn's Life Prediction Branch:
http://www.grc.nasa.gov/WWW/LPB/

Glenn contacts:
David L. Krause, 216–433–5465, David.L.Krause@grc.nasa.gov;
J. Daniel Whittenberger, 216–433–3196, John.D.Whittenberger@grc.nasa.gov;
Pete T. Kantzos, 216–433–5202, Pete.T.Kantzos@grc.nasa.gov; and
Mohan G. Hebsur, 216–433–3266, Mohan.G.Hebsur@grc.nasa.gov

Authors: David L. Krause and
Dr. J. Daniel Whittenberger

Headquarters program office: OAT

Programs/Projects: UEET

Scanning Ultrasonic Spectroscopy System Developed for the Inspection of Composite Flywheels

Composite flywheels are being considered as replacements for chemical batteries aboard the International Space Station. A flywheel stores energy in a spinning mass that can turn a generator to meet power demands. Because of the high rotational speeds of the spinning mass, extensive testing of the flywheel system must be performed prior to flight certification. With this goal in mind, a new scanning system has been developed at the NASA Glenn Research Center for the nondestructive inspection of composite flywheels and flywheel subcomponents. The system uses ultrasonic waves to excite a material and examines the response to detect and locate flaws and material variations.

Results of an ultrasonic spectroscopy scan of a plastic cylinder with intentionally seeded flaws.

The ultrasonic spectroscopy system uses a transducer to send swept-frequency ultrasonic waves into a test material and then receives the returning signal with a second transducer. The received signal is then analyzed in the frequency domain using a fast Fourier transform. A second fast Fourier transform is performed to examine the spacing of the peaks in the frequency domain. The spacing of the peaks is related to the standing wave resonances that are present in the material because of the constructive and destructive interferences of the waves in the full material thickness as well as in individual layers within the material. Material variations and flaws are then identified by changes in the amplitudes and positions of the peaks in both the frequency and resonance spacing domains. This work, conducted under a grant through the Cleveland State University, extends the capabilities of an existing point-by-point ultrasonic spectroscopy system, thus allowing full-field automated inspection.

Shown in the preceding figure is the result of an ultrasonic spectroscopy scan of a plastic cylinder used as a proof-of-concept specimen. The cylinder contains a number of flat-bottomed holes of various sizes and shapes. The scanning system was able to successfully detect all the defects in the material. Ultrasonic spectroscopy results for a

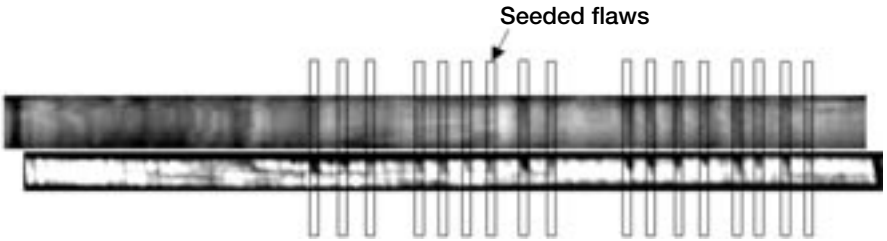

Scanning results for a nondestructive evaluation standard specimen. Top: Ultrasonic spectroscopy results. Bottom: Standard ultrasonic C-scan. Flaw locations are highlighted by boxed areas.

second specimen are shown in the figure above along with a conventional ultrasonic C-scan. The second specimen is a section of a flywheel subcomponent that has a series of drilled holes and notches. This specimen is employed as a defect detection standard to evaluate the various nondestructive evaluation methods under consideration. Scanning results demonstrate the ability of the system to detect flaws on the order of 10 mils in the radial direction and 5 mils in the circumferential direction.

Work conducted to date has shown that scanning ultrasonic spectroscopy is a viable tool for the inspection of composite flywheel systems. Ongoing development work is focused on refining the system and scanning parameters for improved resolution and defect detection.

Glenn contacts:
Richard E. Martin, 216–433–3684, Richard.E.Martin@grc.nasa.gov; and Dr. George Y. Baaklini, 216–433–6016, George.Y.Baaklini@grc.nasa.gov

Authors: Richard E. Martin and Dr. George Y. Baaklini

Headquarters program office: OAT

Programs/Projects: FESS, RSL

CARES/*Life* Used for Probabilistic Characterization of MEMS Pressure Sensor Membranes

Microelectromechanical systems (MEMS) devices are typically made from brittle materials such as silicon using traditional semiconductor manufacturing techniques. They can be etched (or micromachined) from larger structures or can be built up with material deposition processes. Maintaining dimensional control and consistent mechanical properties is considerably more difficult for MEMS because feature size is on the micrometer scale. Therefore, the application of probabilistic design methodology becomes necessary for MEMS. This was demonstrated at the NASA Glenn Research Center and Case Western Reserve University in an investigation that used the NASA-developed CARES/*Life* brittle material design program to study the probabilistic fracture strength behavior of single-crystal SiC, polycrystalline SiC, and amorphous Si_3N_4 pressurized 1-mm-square thin-film diaphragms. These materials are of interest because of their superior high-temperature characteristics, which are desirable for harsh environment applications such as turbine engine and rocket propulsion system hot sections.

FILM ISOTROPIC PROPERTIES FOR ELASTIC MODULUS, POISSON'S RATIO, RESIDUAL STRESS, AND MEAN DIMENSIONS
[Standard deviations follow the ± character.]

Material	Poisson's ratio, ν	Elastic modulus, E, Gpa	Residual stress, σ_R, MPa	Film width, mm	Thickness, μm
1a	359	0.23	254	1.097 ±0.041	1.60 ±0.09
1b	363	.23	180	1.040 ±0.033	1.64 ±0.09
2	350	.23	120	1.049 ±0.035	2.69 ±0.17
Poly SiC	308	.16	75	1.045 ±0.038	2.86 ±0.34
Si_3N_4	274	.27	1200	1.060 ±0.030	0.20 ±0.00

The fracture strength of MEMS devices is known to be affected by the surface defects and surface roughness resulting from the manufacturing process. Such variability can directly impact the failure modes and, in turn, the reliability of the device. In this study, the effect of load and geometric variation (pressure, length, and thickness) from one tested film to the other on the stochastic nature of the strength distribution was accounted for by performing different finite element stress analyses for the various films. Four material combinations were examined (see the table): (1) different suseptor (reaction chambers) on single-crystal silicon carbide—materials 1a and 1b,

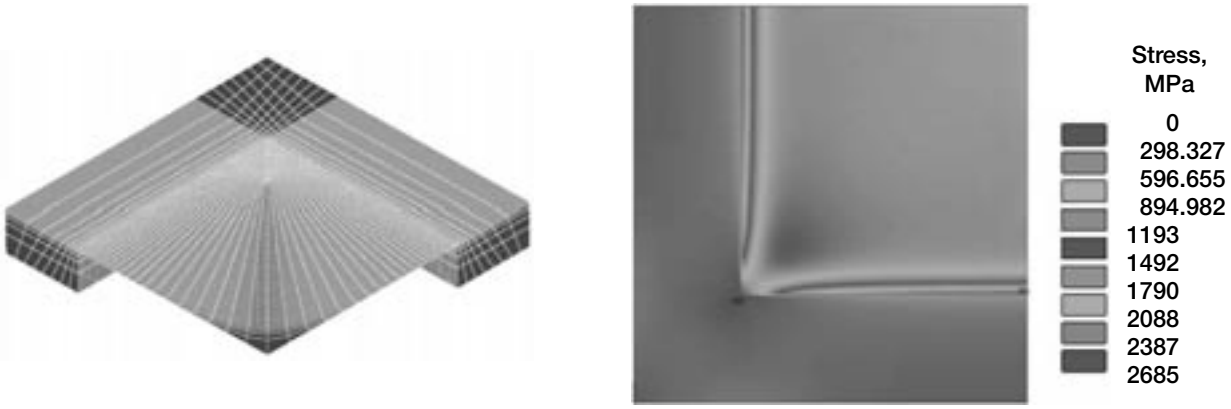

Left: Quarter model of the finite element analysis mesh for the pressure membrane and silicon substrate. The film is nominally 1 mm square and is 2 μm thick. Right: First principal stress distribution in the MEMS pressure membrane due to both the residual (thermal) and pressure loadings being applied simultaneously. The diaphragm center is at the upper right corner of the figure. This view is of the polished (externally pressurized) surface. This figure is shown in color in the online version of this article (http://www.grc.nasa.gov/WWW/RT2001/5000/5900nemeth.html).

(2) doubled growth rate on single-crystal silicon carbide—material 2, (3) polycrystalline silicon carbide—Poly SiC, and (4) amorphous silicon nitride—Si_3N_4. The table shows that the device-to-device variation of film thickness was significant.

Finite element stress modeling was carried out for 113 membranes that were burst under pressure loading conditions. Residual stress in the film, burst pressure, and film thickness were all taken into account. The finite element analysis yielded the unique fracture strength value for each of the burst films from the recorded burst pressure. The strength values for each material set were statistically analyzed using CARES/*Life*. The CARES/*Life* program was further used to characterize the probabilistic fracture strength of these materials on a per-unit-area basis by using fracture-mechanics-based multiaxial failure criteria and the results from the finite element analysis of the stress distribution throughout the film. For the single-crystal silicon carbide material, a three-dimensional reliability model based on anisotropic fracture toughness was used. These models allow experimental data to be extrapolated to other conditions of loading, stress state, and device geometry; in other words, they enable a device to be designed for optimum reliability. Such a simulation and reliability prediction approach is important to reduce product development time and to minimize the potential for costly failures during service life.

The figure to the top left shows a finite element mesh of a film. Nominal dimensions were a side length of 1 mm and a thickness of 2 μm. The films were pressurized externally or outside the cavity.

The figure to the top right shows a typical first principal stress distribution in the film. Stresses are highest at the edge because of the small thickness-to-length ratio. Average residual stresses were accounted for in the analysis, but device-to-device variations in residual stresses were not. Finite element analysis was performed for each tested film—accounting for the individual dimensional variations. This enabled associating a device fracture pressure with the strength of the film. The two-parameter Weibull distribution was used to characterize the film strength distribution for the materials as shown in the graphs on the following page. This characterization yielded the Weibull parameters for these MEMS materials.

This study showed how thin-film strength varies from device to device. It was also shown that device-to-device film thickness variations and suseptor-to-suseptor (manufacturing) variations were significant and must be considered in any analysis. Furthermore, this work illustrates the need for probabilistic-based design practices for MEMS structures and the need for probabilistic-based life-prediction tools such as the NASA-developed CARES/*Life* computer program.

Find out more about this research:
http://www.grc.nasa.gov/WWW/LPB/cares/

Glenn contact:
Noel N. Nemeth, 216–433–3215, Noel.N.Nemeth@grc.nasa.gov

Author: Noel N. Nemeth

Headquarters program office: CTO

Programs/Projects:
RAC, CTO, Third Gen, GMI

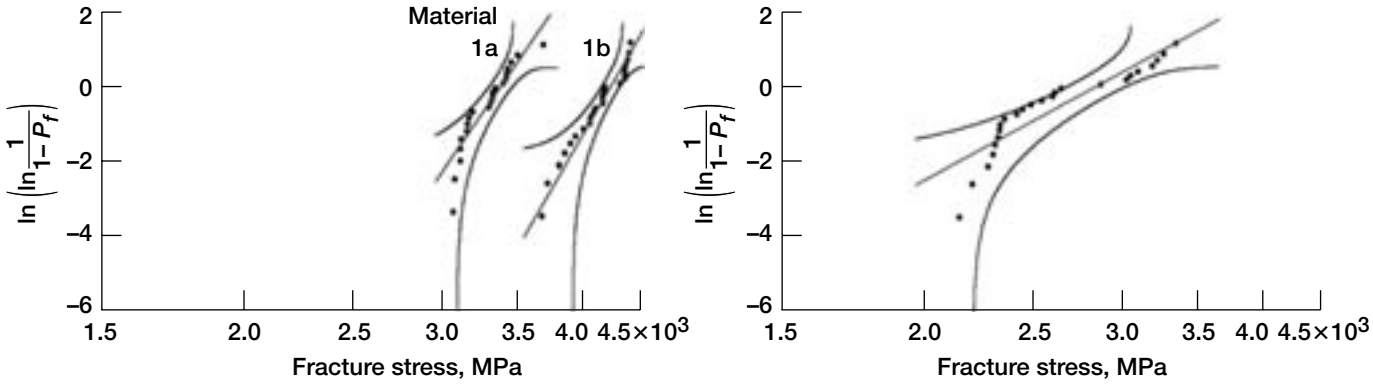

Weibull plots; P_f, probability of failure. Left: Single-crystal SiC films (materials 1a and 1b). Right: Single-crystal SiC films (material 2).

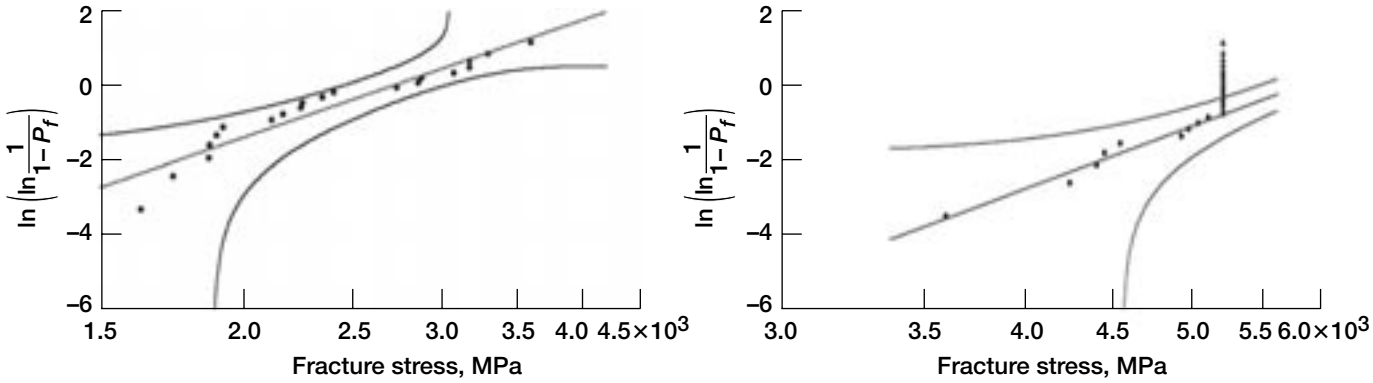

Weibull plots; P_f, probability of failure. Left: Amorphous Si_3N_4 films. Right: Polycrystalline SiC films. Unbroken films are denoted with triangular points (stacked on the right).

Aeroelastic Calculations of Quiet High-Speed Fan Performed

An advanced high-speed fan was recently designed under a cooperative effort between the NASA Glenn Research Center and Honeywell Engines & Systems. The principal design goals were to improve performance and to reduce fan noise at takeoff. Scale models of the Quiet High-Speed Fan were tested for operability, performance, and acoustics. During testing, the fan showed significantly improved noise characteristics, but a self-excited aeroelastic vibration known as flutter was encountered in the operating range. Flutter calculations were carried out for the Quiet High-Speed Fan using a three-dimensional, unsteady aerodynamic, Reynolds-averaged Navier-Stokes turbomachinery code named "TURBO." The TURBO code can accurately model the viscous flow effects that can play an important role in various aeroelastic problems such as flutter with flow separation, flutter at high loading conditions near the stall line (stall flutter), and flutter in the presence of shock and boundary-layer interaction.

Initially, calculations were performed with no blade vibrations. These calculations were at a constant rotational speed and a varying mass flow rate. The mass flow rate was varied by changing the backpressure at the exit boundary of the computational domain. These initial steady calculations were followed by aeroelastic calculations in which the blades were prescribed to vibrate harmonically in a natural mode, at a natural frequency, and with a fixed interblade phase angle between adjacent blades. The AE-prep preprocessor was used to interpolate the in-vacuum mode shapes from the structural dynamics mesh onto the computational fluid dynamics mesh and to smoothly propagate the grid deformations from the

blade surface to the interior points of the grid. The aeroelastic calculations provided the unsteady aerodynamic forces on the blade surface due to blade vibrations. These forces were vector multiplied with the structural dynamic mode shape to calculate the work done on the blade during one vibration period, then this result was converted to an aerodynamic damping. Flutter occurs when the aerodynamic damping becomes negative, if structural damping is ignored.

The results of these aeroelastic calculations are summarized in this plot of aerodynamic damping versus mass flow rate at a constant rotational speed. As the backpressure is increased, the mass flow rate through the fan decreases and the fan operating point moves towards the stall line. The aeroelastic calculations showed that the aerodynamic damping decreases as the stall line is approached, as observed during testing. In addition, the aeroelastic calculations with the TURBO code correctly predicted the aeroelastic parameters: the most unstable vibration mode and interblade phase angle, as observed during testing.

The Quiet High-Speed Fan demonstrated significant noise reductions during testing, but flutter imposed limits on its operating range. The accurate calculation of the aeroelastic characteristics using the TURBO code is a significant step toward eliminating flutter from the operating range and toward realizing the benefits of reduced fan noise. The aeroelastic calculations described here were performed under a grant by University of Toledo researchers in collaboration with Glenn's researchers.

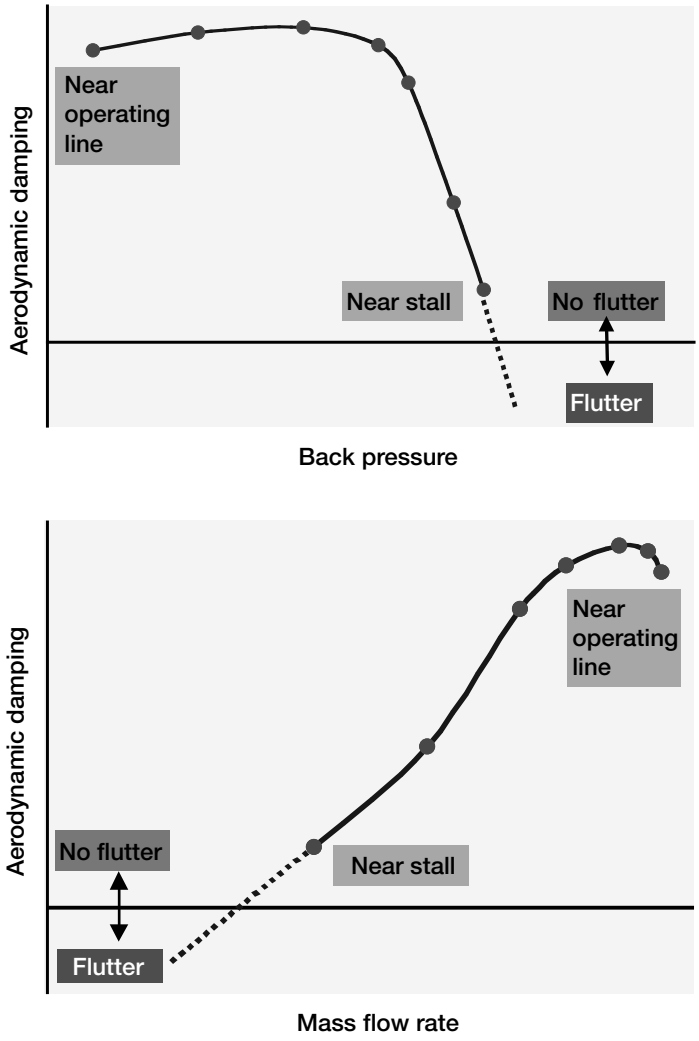

Aeroelastic characteristics as calculated using the TURBO code.

University of Toledo contacts:
Dr. Milind A. Bakhle, 216–433–6037, Milind.A.Bakhle@grc.nasa.gov; and
Dr. Rakesh Srivastava, 216–433–6045, Rakesh.Srivastava@grc.nasa.gov

Glenn contacts: Oral Mehmed, 216–433–6036, Oral.Mehmed@grc.nasa.gov; and
Dr. James B. Min, 216–433–2587, James.B.Min@grc.nasa.gov

Authors:
Dr. Milind A. Bakhle, Dr. Rakesh Srivastava, Oral Mehmed, and Dr. James B. Min

Headquarters program office: OAT

Programs/Projects: UEET, QAT, Propulsion Systems R&T

Fail-Safe Operation of a High-Temperature Magnetic Bearing Investigated for Gas Turbine Engine Applications

The Structural Mechanics and Dynamics Branch at the NASA Glenn Research Center has developed a three-axis high-temperature magnetic bearing suspension rig to enhance the safety of the bearing system up to 1000 °F. This test rig can accommodate thrust and radial bearings up to a 22.84 cm (9 in.) diameter with a maximum axial loading of 22.25 kN (5000 lb) and a maximum radial loading up to 4.45 kN (1000 lb). The test facility was set up to test magnetic bearings under high-temperature (1100 °F) and high-speed (20,000 rpm) conditions.

The magnetic bearing is located at the center of gravity of the rotor between two high-temperature grease-packed mechanical ball bearings. The drive-end duplex angular contact ball bearing, which is in full contact, acts as a moment release and provides axial stability. The outboard end ball bearing has a 0.015-in. radial clearance between the rotor to act as a backup bearing and to compensate for axial thermal expansion. There is a 0.020-in. radial air gap between the stator pole and the rotor. The stator was wrapped with three 1-kW band heaters to create a localized hot section; the mechanical ball bearings were outside this section. Eight threaded rods supported the stator. These incorporated a plunger and Bellville washers to compensate for radial thermal expansion and provide rotor-to-stator alignment. The stator was instrumented with thermocouples and a current sensor for each coil. Eight air-cooled position sensors were mounted outside the hot section to monitor the rotor. Another sensor monitored this rotation of the outboard backup bearing. Ground fault circuit interrupts were incorporated into all power amplifier loops for personnel safety. All instrumentation was monitored and recorded on a LabView-based data acquisition system. Currently, this 12-pole heteropolar magnetic bearing has 13 thermal cycles and over 26 hr of operation at 1000 °F.

For a fail-safe operation of this rig in temperature extremes, a proportional-integral-derivative (PID) controller that does not require a fault detection mechanism was tested in a passive way where the initial bias current and control gains for all six independent magnets were not changed for the remaining active magnets in the fault situations. The action of the integral term in the controller generated autonomous corrective actions for the magnet failures to return the rotor to the set point after the failure transient. The passive fault tolerance was successfully demonstrated up to the rig's maximum achievable speed of 15,000 rpm by using as few as three active magnets out of the six independent C-core magnets. Current data that were input to the

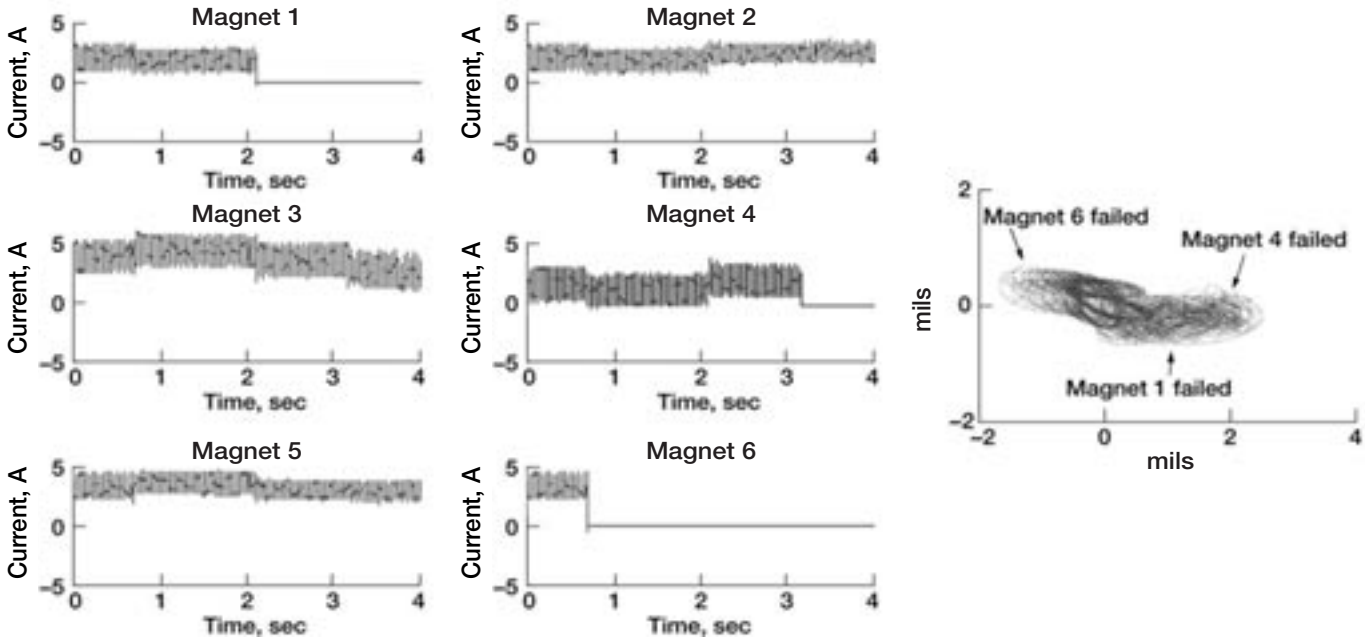

Left: Control command signals to compensate for the consecutive failure of magnets 6, 1, and 4 during operation at 12,500 rpm. Right: Transient rotor orbit plot.

power amplifiers for normal operation were also measured in terms of the rotor speed and temperature to investigate the change of actuator gain.

In comparison to a conventional active fault tolerance approach, which can handle a single magnet failure, this approach demonstrated that three active magnets out of six C-core magnets (multiple failure cases) levitated the rotor and spun it up to 15,000 rpm at 900 °F. It also showed that a passive approach could be applied to a heavily loaded magnetic bearing. This extremely valuable demonstration could help to ease the safety concerns of using high-temperature magnetic suspension technology for advanced high-speed rotating turbomachinery at temperature extremes caused by the possibility of system faults in the main bearing components.

Glenn contacts:
Dr. Benjamin B. Choi, 216–433–6040, Benjamin.B.Choi@grc.nasa.gov; and Gerald T. Montague, 216–433–6252, Gerald.T.Montague@grc.nasa.gov

Authors: Benjamin B. Choi and Gerald T. Montague

Headquarters program office: OAT

Programs/Projects: SEC, RAC

Linear-Quadratic-Gaussian Regulator Developed for a Magnetic Bearing

Linear-Quadratic-Gaussian (LQG) control is a modern state-space technique for designing optimal dynamic regulators. It enables us to trade off regulation performance and control effort, and to take into account process and measurement noise. The Structural Mechanics and Dynamics Branch at the NASA Glenn Research Center has developed an LQG control for a fault-tolerant magnetic bearing suspension rig to optimize system performance and to reduce the sensor and processing noise.

The LQG regulator consists of an optimal state-feedback gain and a Kalman state estimator. The first design step is to seek a state-feedback law that minimizes the cost function of regulation performance, which is measured by a

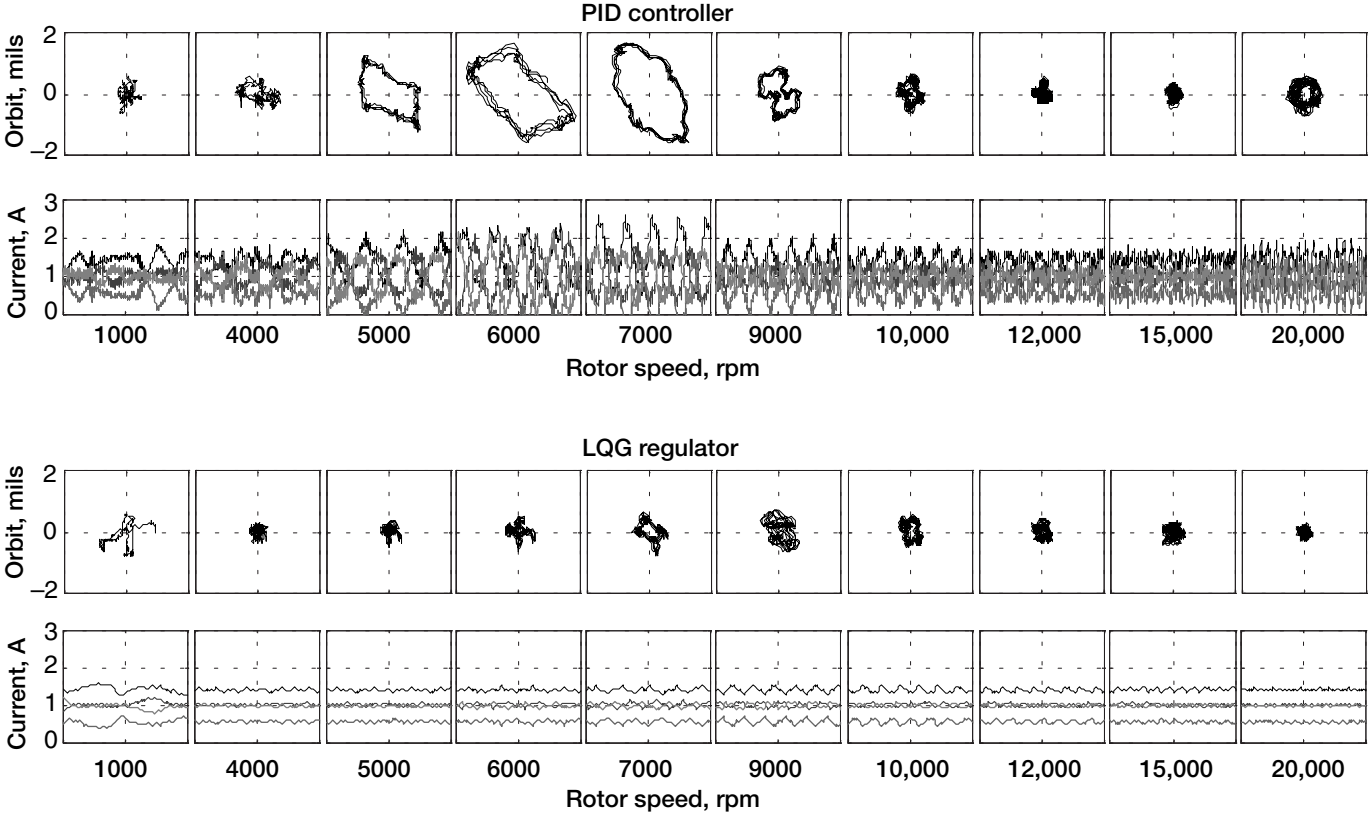

Rotor orbit and corresponding control current of PID and LQG controllers over the rig's operating range.

quadratic performance criterion with user-specified weighting matrices, and to define the tradeoff between regulation performance and control effort. The next design step is to derive a state estimator using a Kalman filter because the optimal state feedback cannot be implemented without full state measurement. Since the Kalman filter is an optimal estimator when dealing with Gaussian white noise, it minimizes the asymptotic covariance of the estimation error.

A simple second-order dynamic model was derived through an experimental transfer function of the plant model with an input of the control force and an output of the rotor displacement. An LQR with a Kalman filter was designed and implemented with the MATLAB/Simulink software. A real-time ANSI C code was generated, compiled, and downloaded to a dSPACE control system—an integrated control software and electronic control unit combination (MATLAB/Simulink software and ds1003/ds1004 alpha-combo, multiprocessor board). It was successfully demonstrated up to the rig's maximum achievable speed of 20,000 rpm. In comparison to a proportional-integral-derivative (PID) controller, which is one of the most popular classical controllers, this modern controller has the following benefits: (1) it significantly reduced the rotor orbits at critical modes, (2) it drastically improved power—saving more than 50 percent, and (3) it reduced measurement noise by more than 30 percent.

Glenn contact:
Dr. Benjamin B. Choi, 216–433–6040, Benjamin.B.Choi@grc.nasa.gov

Author: Benjamin B. Choi

Headquarters program office: OAT

Programs/Projects: SEC, RAC

Self-Tuning Impact Dampers Designed for Turbomachinery Blade Vibration Suppression

Turbomachinery blades are subject to aerodynamic forces that can lead to high-cycle-fatigue (HCF) failures. These failures will only increase as engineers begin to design blades without shrouds or as integrally bladed disks (blisks). These new designs will decrease blade damping significantly because the mechanical damping from shroud and blade joints will be eliminated. Also, it is difficult to design dampers for the engine environment with its extremely high centrifugal loads and high temperatures. The self-tuning impact damper has been designed to provide the additional damping required to avoid HCF while withstanding the harsh engine environment. In addition, the damper is placed within the engine blade itself rather than external to it.

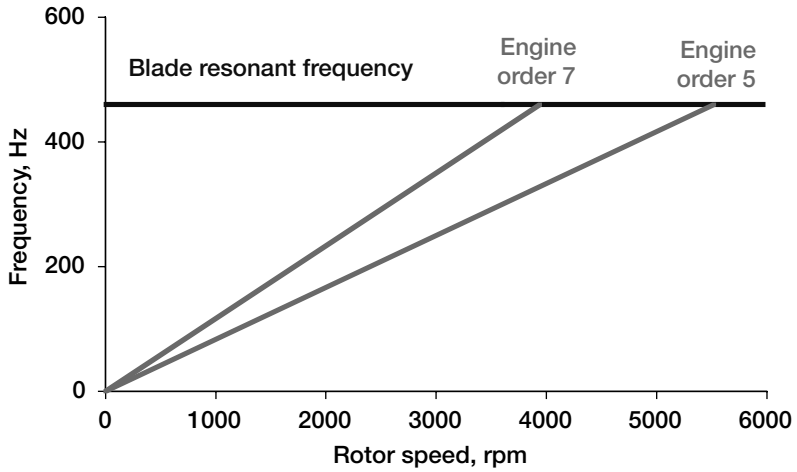

Campbell diagram showing engine order lines and blade resonance frequency.

The self-tuning impact damper combines two damping methods—the tuned mass damper and the impact damper. It consists of a ball located within a cavity in the blade. This ball rolls back and forth on a spherical trough under a centrifugal load (tuned mass damper) and can strike the walls of the cavity (impact damper). The ball's rolling natural frequency is proportional to the rotor speed and can be designed to follow an engine order line (integer multiple of rotor speed). Aerodynamic forcing frequencies typically follow these engine order lines, and a damper tuned to the engine order will most effectively reduce blade vibrations when the resonant frequency equals the engine order forcing frequency.

This damper has been tested in flat plates and turbine blades in the Dynamic Spin Facility at the NASA Glenn Research Center. During testing, a pair of plates or blades rotates in vacuum at up to 8000 rpm. Excitation is provided by one of three methods—electromechanical shakers, magnetic bearing excitation, and eddy current engine-order excitation. The first two methods apply excitation at any frequency to the shaft itself.

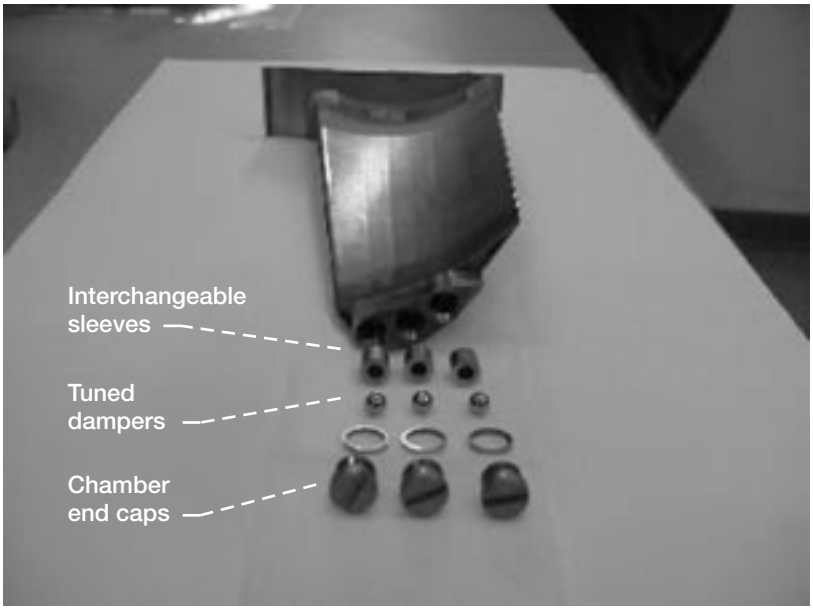

Pratt & Whitney turbine blade with three self-tuning impact dampers added to the blade tip—exploded view.

The eddy current system, manufactured by Hood Technologies and installed in fiscal year 2001, consists of magnets located circumferentially around the rotor. As a blade passes a magnet, a force is imparted on the blade. The number of magnets used equals the engine order of excitation. These magnets are remotely raised or lowered to change the magnitude of the forcing on the blades. Blade response is monitored with strain gauges and laser displacement probes.

Early tests in flat plates show that the damper is effective in reducing resonant blade response at and below the speed line crossing. Damping increased from 0.2 percent critical to about 1.0 percent critical. In fiscal year 2001, tests were performed on a pair of Pratt & Whitney low-pressure turbine blades. Preliminary results show peak resonance decreasing by 50 percent with the impact damper. In addition, very small dampers were designed such that a number of them could fit within the very thin profile of a fan blade.

Bibliography
Duffy, Kirsten P.; Mehmed, Oral; and Johnson, Dexter: Self-Tuning Impact Dampers for Fan and Turbine Blades. 6th National Turbine Engine High Cycle Fatigue (HCF) Conference Proceedings, AFRL/PRT, Wright-Patterson AFB, OH, March 5–8, 2001.

Glenn contact:
Oral Mehmed, 216–433–6036, Oral.Mehmed@grc.nasa.gov

University of Toledo contact:
Dr. Kirsten P. Duffy, 216–433–3880, Kirsten.P.Duffy@grc.nasa.gov

Authors:
Dr. Kirsten P. Duffy and Oral Mehmed

Headquarters program office: OAT

Programs/Projects: SEC

Finite Element Analysis of Morphing Piezoelectric Structures Studied

The development of morphing aerospace structures that optimize their shape offers the potential to significantly improve the performance of existing airplanes. These morphing vehicles will operate with new capabilities to reduce noise, damp vibrations, manipulate flow, and monitor damage. Piezoelectric materials represent one of the popular materials currently being investigated for applications in morphing structures.

In-house research efforts at the NASA Glenn Research Center have been directed toward developing comprehensive analytical models to facilitate the experimental characterization of piezoelectric materials. These materials present unique modeling challenges because of their complex, coupled mechanical, electrical, and thermal behaviors. To develop analytical models, we implemented a unique layerwise representation that captures the coupled responses at the constitutive level and introduces the electric potential and temperature, along with the displacements, as state variables in the analysis. This unified representation leads to the inherent capability to model both the sensory and active behavior of piezoelectric materials. Corresponding finite element equations were derived and implemented into beam, plate, and shell elements

to provide a flexible computational tool for the static and dynamic analysis of arbitrary piezoelectric structures.

Current research efforts have successfully validated the accuracy of the finite element codes with published experimental results (ref. 1). The graph shows the predicted deflection of a piezoelectric-polymer bimorph beam under various applied active voltages, along with the experimental results. Good agreement is observed between the current analysis and experiment. The bimorph beam represents one of the common actuator configurations of piezoelectric materials that will be used as elements of morphing structures.

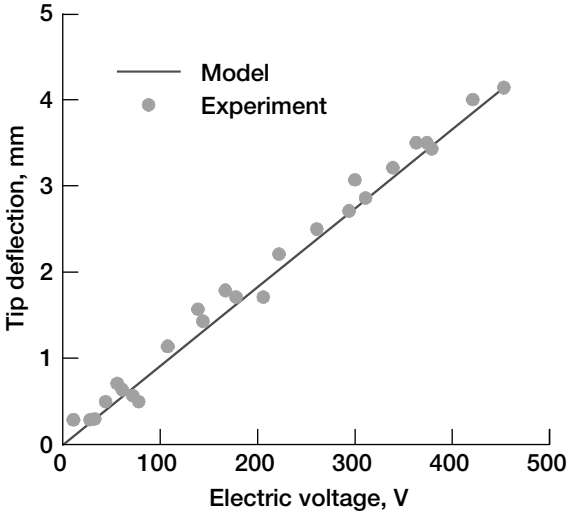

Model prediction of a piezoelectric polymer bimorph beam under applied active voltages compared with experimental results.

Reference

1. Lee, Ho-Jun: Finite Element Analysis of Active and Sensory Thermo-piezoelectric Composite Materials. NASA/TM—2001-210892, 2001. http://gltrs.grc.nasa.gov/GLTRS/

Glenn contact:
Dr. Ho-Jun Lee, 216–433–3316, Ho-Jun.Lee@grc.nasa.gov

Author: Dr. Ho-Jun Lee

Headquarters program office: OAT

Programs/Projects: RAC

Advanced Vibration Analysis Tools and New Strategies for Robust Design of Turbine Engine Rotors

The adverse effects of small, random structural irregularities among the blades, called mistuning, can result in blade forced-response amplitudes and stresses that are much larger than those predicted for a perfectly tuned rotor. Manufacturing tolerances, deviations in material properties, or nonuniform operational wear causes mistuning; therefore, mistuning is unavoidable. Furthermore, even a small mistuning can have a dramatic effect on the vibratory behavior of a rotor because it can lead to spatial localization of the vibration energy (see the photographs). As a result, certain blades may experience forced response amplitudes and stresses that are substantially larger than those predicted by an analysis of the nominal (tuned) design. Unfortunately, these random uncertainties in blade properties, and the immense computational effort involved in obtaining statistically reliable design data, combine to make this aspect of rotor design cumbersome.

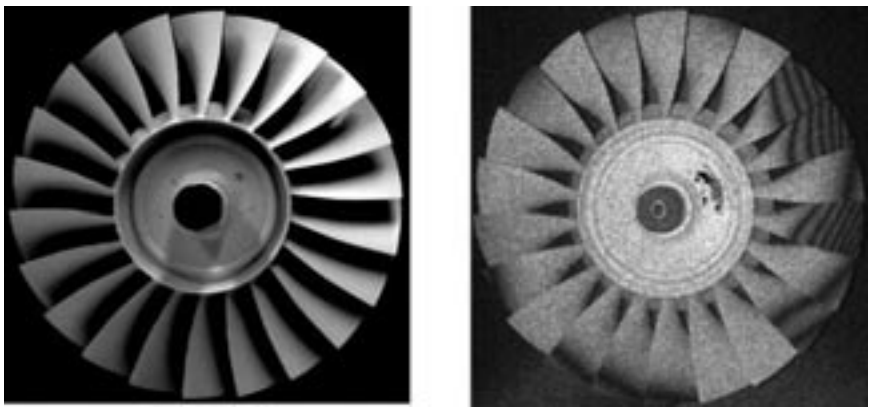

Spatial localization of mistuned bladed disks. Left: Turbine engine rotor. Right: Localized vibration.

Since the 1960's, several researchers have documented the effects of mistuning on blade vibrations by analyzing representative lumped-parameter models, using numerical, statistical, and perturbation

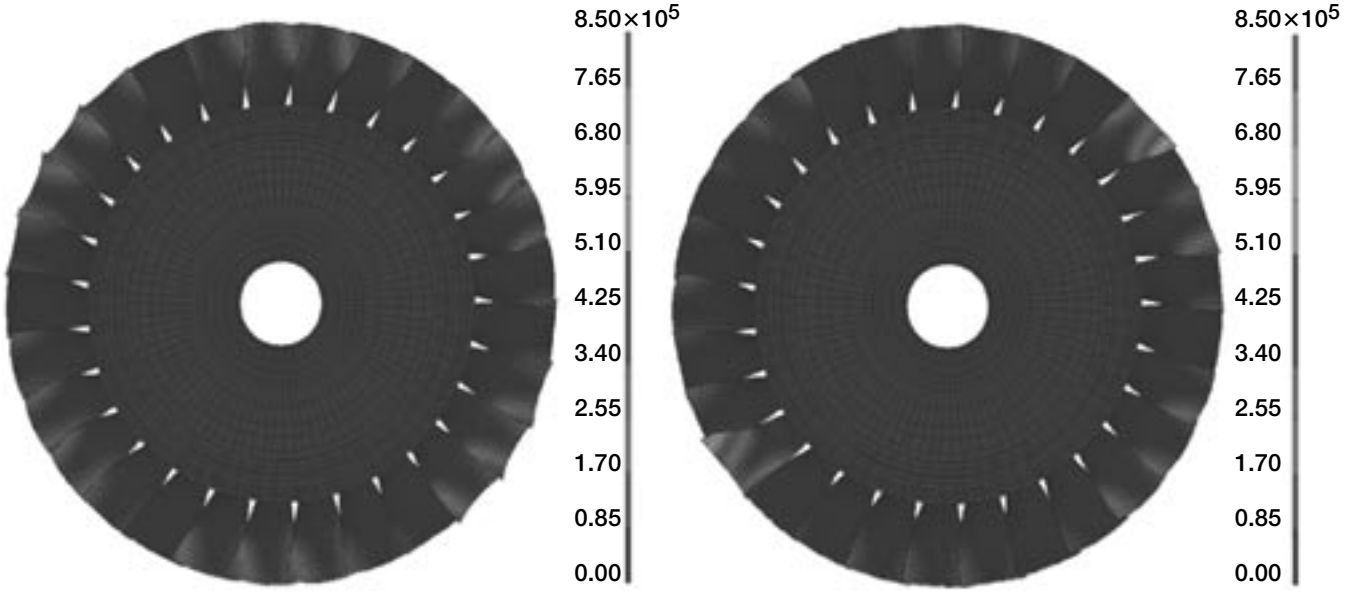

Forced response predictions for an industrial rotor by TURBO–REDUCE. Left: Tuned. Right: Mistuned. This figure is shown in color in the online version of this article (http://www.grc.nasa.gov/WWW/RT2001/5000/5930min.html).

methods. Unfortunately, to accurately represent an actual bladed disk design with a lumped-parameter model, one must perform a difficult parameter identification, which becomes infeasible as the number of model degrees of freedom increases. Hence, for models to gain practical usefulness, accurate finite element models of rotor designs must be employed in mistuning studies.

To address this issue, a team from the NASA Glenn Research Center and the University of Michigan, Ann Arbor, made several efforts to generate reduced-order models systematically from finite element models using component model synthesis methods (refs. 1 to 4). In CMS, the original structure is subdivided into small substructures, or components, for which normal modes are computed independently. The global structure is then represented by a truncated set of component modes that are assembled in a systematic fashion through compatibility constraints. This process yields highly reduced order models for bladed disks that are based on finite element models of arbitrary complexity. The effort has been particularly focused on the development of a valuable computer code named TURBO–REDUCE, which is based on a computationally efficient reduced-order modeling technique for the vibration analysis of mistuned bladed disks. The phenomenon of mode localization is well captured by the TURBO–REDUCE code (see the figure above). TURBO–REDUCE is a FORTRAN 77 computer code that has the modular features, computational efficiency, and practical implementation needed for the realistic modeling of a mistuned assembly of blades. Since the code is being actively used in industry, TURBO–REDUCE represents the current state of the art.

References

1. Kruse, M.J.; and Pierre, C.: Forced Response of Mistuned Bladed Disks Using Reduced-Order Modeling. Proceedings of the 37th AIAA/ASME Structures, Structural Dynamics, and Materials Conference, Salt Lake City, UT, 1996.
2. Kruse, M.J.; and Pierre, C.: Dynamic Response of an Industrial Turbomachinery Rotor. Proceedings of the 32nd AIAA/ASME/SAE/ASEE Joint Propulsion Conference and Exhibit, Lake Buena Vista, FL, 1996.
3. Castanier, M.P.; Ottarsson, G.; and Pierre, C.: A Reduced-Order Modeling Technique for Mistuned Bladed Disk. J. Vibration Acoustics, vol. 118, no. 3, 1997, pp. 439–447.
4. Bladh, R., Castanier, M.P.; and Pierre, C.: Reduced Order Modeling and Vibration Analysis of Mistuned Bladed Disk Assemblies With Shrouds. ASME J. Engrg. Gas Turb. Power, vol. 121, no. 3, 1999, pp. 515–522.

Glenn contact:
Dr. James B. Min, 216–433–2587, James.B.Min@grc.nasa.gov

Author: Dr. James B. Min

Headquarters program office: OAT (Glenn's GUIde Consortium)

Programs/Projects: Propulsion Systems R&T, UEET, AvSP, RLV

Neural Network and Regression Soft Model Extended for PAX–300 Aircraft Engine

In fiscal year 2001, the neural network and regression capabilities of NASA Glenn Research Center's COMETBOARDS design optimization testbed were extended to generate approximate models for the PAX–300 aircraft engine. The analytical model of the engine is defined through nine variables: the fan efficiency factor, the low pressure of the compressor, the high pressure of the compressor, the high pressure of the turbine, the low pressure of the turbine, the operating pressure, and three critical temperatures (T_4, T_{vane}, and T_{metal}). Numerical Propulsion System Simulation (NPSS) calculations of the specific fuel consumption (TSFC), as a function of the variables can become time consuming, and numerical instabilities can occur during these design calculations. "Soft" models can alleviate both deficiencies. These approximate models are generated from a set of high-fidelity input-output pairs obtained from the NPSS code and a design of the experiment strategy. A neural network and a regression model with 45 weight factors were trained for the input-output pairs. Then, the trained models were validated through a comparison with the original NPSS code. Comparisons of TSFC versus the operating pressure and of TSFC versus the three temperatures (T_4, T_{vane}, and T_{metal}) are depicted in the figures. The overall performance was satisfactory for both the regression and the neural network model. The regression model required fewer calculations than the neural network model, and it produced marginally superior results. Training the approximate methods is time consuming. Once trained, the approximate methods generated the solution with only a trivial computational effort, reducing the solution time from hours to less than a minute.

Glenn contact:
Dale A. Hopkins, 216–433–3260, Dale.A.Hopkins@grc.nasa.gov

OAI contact:
Dr. Surya N. Patnaik, 216–433–5916, Surya.N.Patnaik@grc.nasa.gov

Authors: Dr. Surya N. Patnaik and Dale A. Hopkins

Headquarters program office: OAT

Programs/Projects:
Propulsion Systems R&T

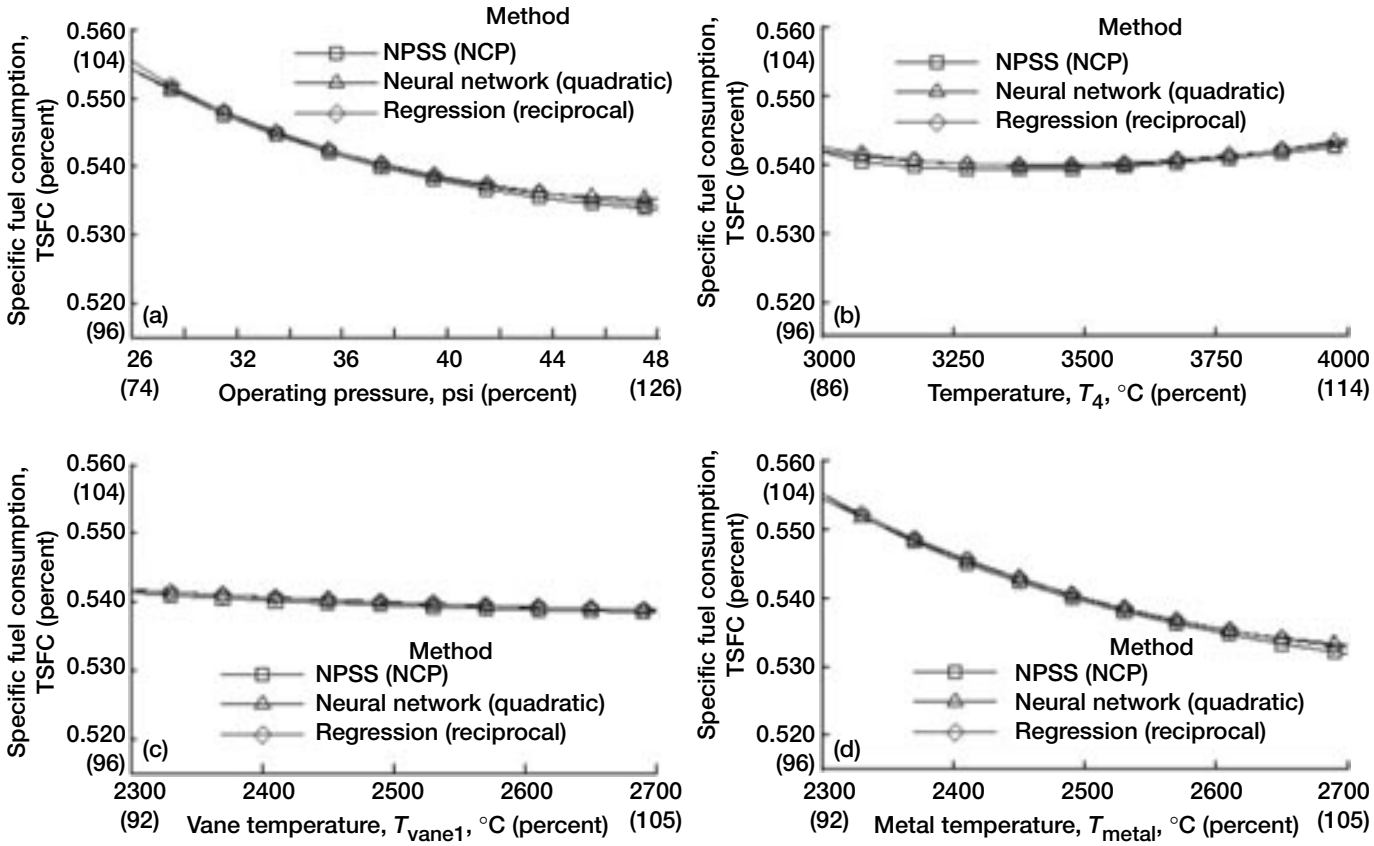

PAX–300 engine performance results compared with the specific fuel consumption (TSFC) calculated by soft models. (a) Operating pressure versus TSFC. (b) T_4 versus TSFC. (c) T_{vane} versus TSFC. (d) T_{metal} versus TSFC.

Excellent Ballistic Impact Properties Demonstrated By New Fabric

Test specimen mounted on a fixture in front of the impact gun. The specimen is supported at a slight incline so that the projectile can impact it from the inside.

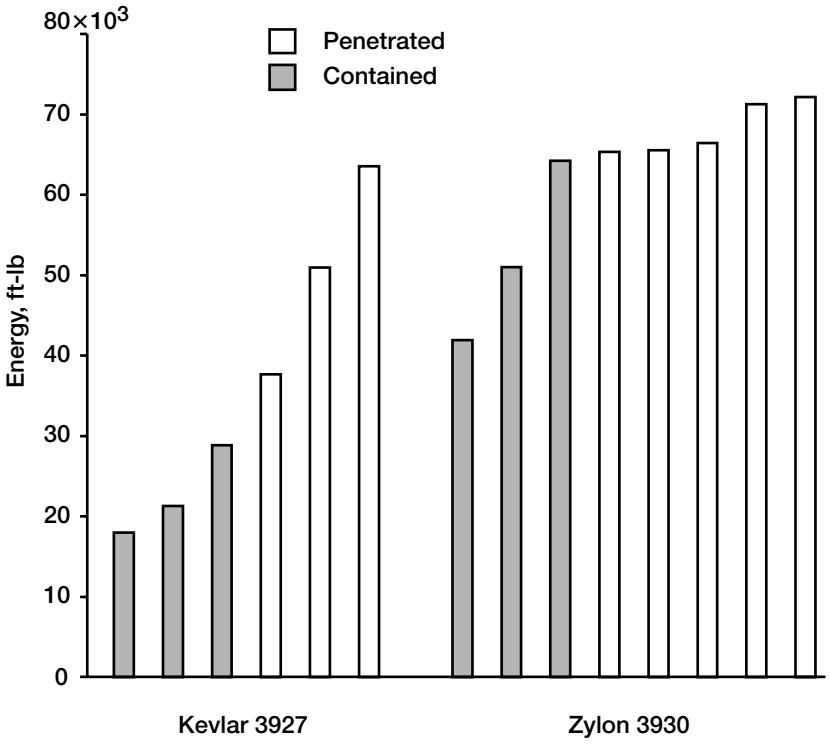

Results of impact tests on Kevlar and Zylon. Each vertical bar represents a single impact test, with the vertical axis showing the kinetic energy of the projectile.

Recently, a relatively new industrial fiber known by the trade name Zylon has been under commercial development by Toyobo Co., Ltd., Japan. In ballistic impact tests conducted at the NASA Glenn Research Center, it was found that dry fabric braided of Zylon had greater ballistic impact capacity than comparable (braid style and weight) fabric braided of Kevlar (DuPont Corp., Wilmington, DE).

To study the potential use of Zylon fabric in jet engine containment systems, the fabric was tested in Glenn's Structures and Acoustics Division Ballistic Impact Facility under conditions simulating those which occur in a jet engine blade-out event. Circular ring test specimens were fabricated by wrapping five layers of braided Zylon or Kevlar fabric around an inner ring made of a thin sheet of aluminum and a 1-in.-thick layer of aluminum honeycomb. The test specimens had an inner diameter of 40 in., an axial length of 10 in., and a wall thickness of approximately 1.5 in. A test specimen is shown in the photograph.

The test specimens were mounted on a table in front of a 40-ft-long, 8-in.-diameter gas gun such that the specimen was at a slight incline from horizontal. Titanium disks that were 4.5 in. in diameter, 0.75 in. thick, and weighed approximately 1.9 lb were shot out of the gas gun into the specimens at speeds up to 1600 ft/sec. The orientation of the test specimen allowed the projectile to impact the inside of the ring, similar to a fan blade fragment impacting the inside of a fan case. The impact tests were conducted in such a way that some of the projectiles penetrated the specimen, and some were contained (did not penetrate). Knowing the speed and mass of the projectile, we were able to determine the amount of kinetic energy that the rings could absorb before penetration occurred (sometimes referred to as the ballistic limit or ballistic threshold).

The impact test results (see the preceding bar chart) showed that rings incorporating braided Zylon fabric could absorb approximately twice as much kinetic energy as rings using Kevlar fabric of comparable weight and braid style. Each bar represents a single impact test, with the vertical axis showing the kinetic energy of the projectile. The shaded bars represent tests in which the projectile was contained (did not penetrate the specimen), whereas the open bars represent tests in which the projectile penetrated the specimen. The results indicate that the Kevlar specimens could absorb between 29,000 and 38,000 ft-lb of kinetic energy before penetration. The Zylon specimens could absorb between 64,000 and 65,000 ft-lb of energy, or approximately twice the energy that the Kevlar specimens could absorb.

Find out more about this research: http://ballistics.grc.nasa.gov/

Glenn contacts:
Dr. J. Michael Pereira, 216–433–6738, J.M.Pereira@grc.nasa.gov;
Duane M. Revilock, 216–433–3186, Duane.M.Revilock@grc.nasa.gov; and
Dale A. Hopkins, 216–433–3260, Dale.A.Hopkins@grc.nasa.gov

Authors:
J. Michael Pereira, Duane M. Revilock, and Dale A. Hopkins

Headquarters program office: OAT

Programs/Projects:
Aeronautics Base R&T, AvSP

New Fan Engine Noise-Reduction Concept Using Trailing Edge Blowing of Fan Blades Demonstrated

A major source of noise in commercial turbofan engines is the interaction of the fan blade wakes with the fan exit vanes (stators). These wakes can be greatly reduced by filling them with air blown out of the blade trailing edge. Extensive testing of this concept has demonstrated significant noise reductions. These tests were conducted on a low-speed, 4-ft-diameter fan using hollow blades at NASA Glenn Research Center's AeroAcoustic Propulsion Laboratory (AAPL).

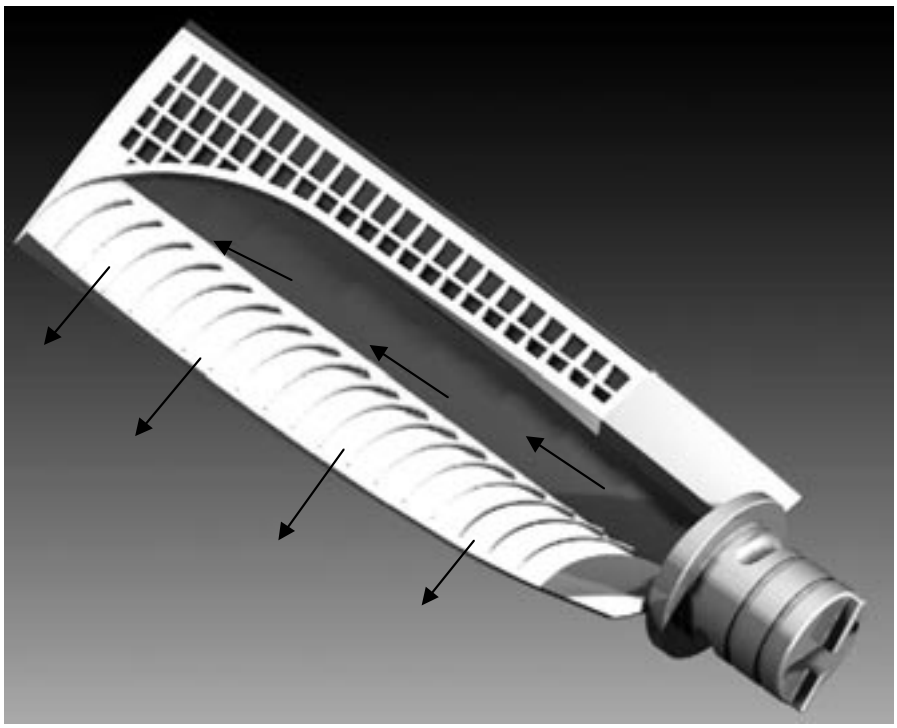

Flow path through blade with outer skin removed.

The fan was designed and fabricated using new techniques and concepts developed to support design goals. The fabrication made use of considerable rapid prototyping hardware and composites. During operation, air was injected into the hollow fan shaft and flowed into the blade though radial passages that extend to the trailing edge. The blades have composite skins with internal turning vanes and a narrow slot at the trailing edge. Up to 2 percent of the fan total flow can be injected into the slots to fill the wake.

These tests measured the internal and external (far-field) noise, the steady and unsteady velocity behind the fan blades (using hotwire anemometry), the unsteady vane surface pressures, and overall performance. The blowing flow rate was varied as well as the radial extent of the slot. Early results of these tests show that the tone noise was

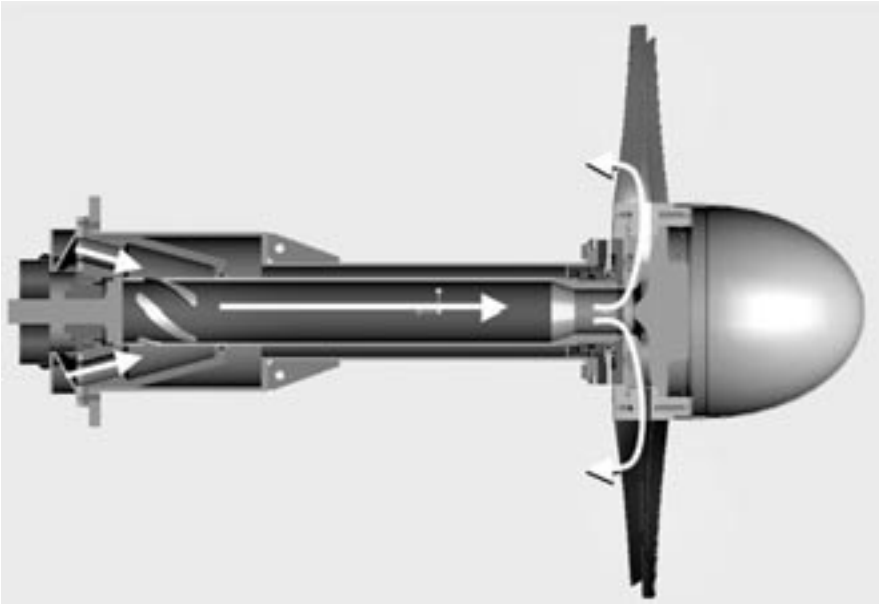

Flow path through the shaft and hub.

Fan installed in duct.

significantly reduced especially at harmonics above the fundamental blade passing frequency. Although this was primarily a noise test, there is evidence that much of the energy in the blowing airstream was recovered, as indicated by reductions in the fan shaft torque. There were also indications from the vane unsteady pressures that broadband noise might also be reduced. We hope that future tests and further analysis of the data will lead to still greater noise reductions.

Glenn contacts:
Laurence J. Heidelberg, 216–433–3859, Laurence.J.Heidelberg@grc.nasa.gov; Brian Fite, 216–433–3892, Eric.B.Fite@grc.nasa.gov

Sest, Inc., contact:
Daniel L. Sutliff, 216–433–6290, Daniel.L.Sutliff@grc.nasa.gov

Author: Laurence J. Heidelberg

Headquarters program office: OAT

Programs/Projects: Aerospace Propulsion and Power Base Research

Gear Damage Detection Integrating Oil Debris and Vibration Measurement Technologies Developed

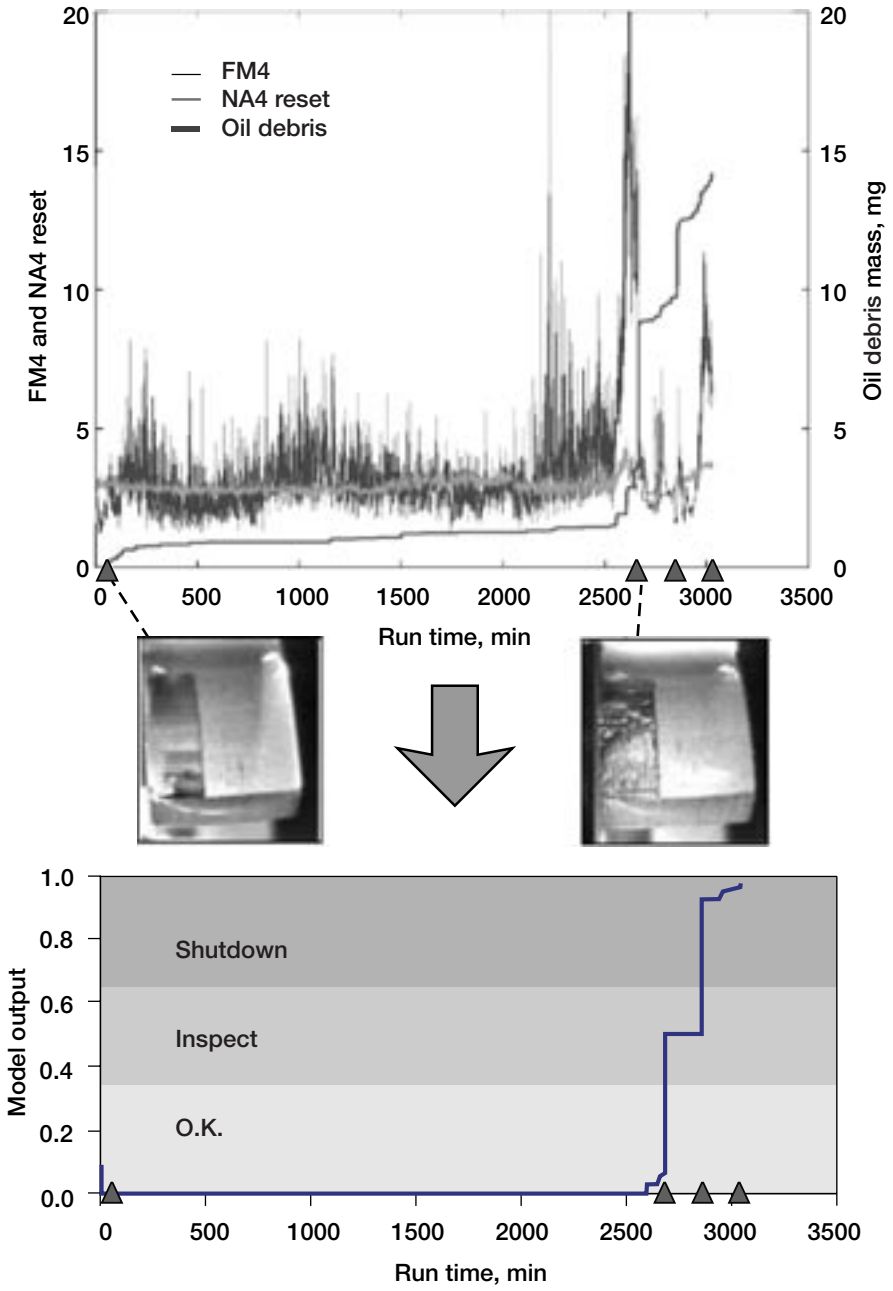

Top: Input to data fusion model. Readings were taken once per minute. Bottom: Output of the data fusion model.

The development of highly reliable health-monitoring systems is one technology area recommended for reducing the number of helicopter accidents. Helicopter transmission diagnostics are an important part of a helicopter health-monitoring system because helicopters depend on the power train for propulsion, lift, and flight maneuvering. One technique currently being tested for increasing the reliability and decreasing the false alarm rate of current transmission diagnostic tools is the replacement of simple single-sensor limits with multisensor systems integrating different measurement technologies.

The objective of this work was to integrate oil debris and vibration-based gear damage detection techniques into a health-monitoring system that can detect gear pitting damage. Vibration and oil debris data were collected from experiments in NASA Glenn Research Center's Spur Gear Fatigue Rig to demonstrate that the integration of two measurement technologies, oil analysis and vibration, results in a system with improved damage detection and decisionmaking capabilities in comparison to existing individual diagnostic tools.

Data were collected during 24 experiments using two accelerometers, an oil debris sensor, a speed sensor, and a load pressure sensor installed on the Spur Gear Fatigue Rig. The vibration data and speed data were used to calculate the gear vibration diagnostic algorithms FM4 and NA4 Reset. The oil debris mass data were collected using a commercially available inline oil debris sensor. A gear diagnostic parameter based on oil debris mass was developed as part of this work.

For this research, multisensor data fusion analysis techniques were applied to the gear damage data collected from the accelerometers and the oil debris sensor. This technique is a process similar to methods humans use to integrate data from multiple sources and senses to make decisions. Data from multiple sensors were

combined so that inferences could be made that would not be possible from a single sensor. This yielded a simple system model that discriminates between the stages of pitting wear. Results indicate that combining the two technologies, oil debris and vibration, greatly improves the detection of pitting damage on spur gears. Integrating different measurement technologies and including expert knowledge of the diagnostician into the system (i.e., understanding the strengths and weaknesses of the diagnostic tools for different applications) enables clear decisions to be made on the health of the geared system.

The two plots on the preceding page show the data collected from one experiment with pitting damage. Readings were taken once per minute. The top figure shows the vibration algorithms FM4 and NA4 Reset along with the debris measured by the oil debris sensor during one experiment with pitting damage. The triangles indicate when the gear was inspected for damage. Damage began to occur at approximately reading 2669 during this experiment. The bottom figure is the output of the data fusion model used to integrate the oil and vibration data. This plot indicates to inspect the gears at reading 2669 (after 2669 min). As the damage increases, the inspect state changes to shutdown for this experiment.

Find out more about this research: http://www.grc.nasa.gov/WWW/5900/5950/

Bibliography
Dempsey, Paula J.: A Comparison of Vibration and Oil Debris Gear Damage Detection Methods Applied to Pitting Damage. NASA/TM—2000-210371, 2000. http://gltrs.grc.nasa.gov/GLTRS/

Dempsey, Paula J.; and Zakrajsek, James J.: Minimizing Load Effects on NA4 Gear Vibration Diagnostic Parameter. NASA/TM—2001-210671, 2001. http://gltrs.grc.nasa.gov/GLTRS/

Dempsey, Paula J.: Gear Damage Detection Using Oil Debris Analysis. NASA/TM—2001-210936, 2001. http://gltrs.grc.nasa.gov/GLTRS/

Glenn contact:
Paula J. Dempsey, 216–433–3398, Paula.J.Dempsey@grc.nasa.gov

Author: Paula J. Dempsey

Headquarters Program Office: OAT

Programs/Projects:
Rotorcraft Base Program

Rudder/Fin Seals Investigated for the X–38 Re-Entry Vehicle

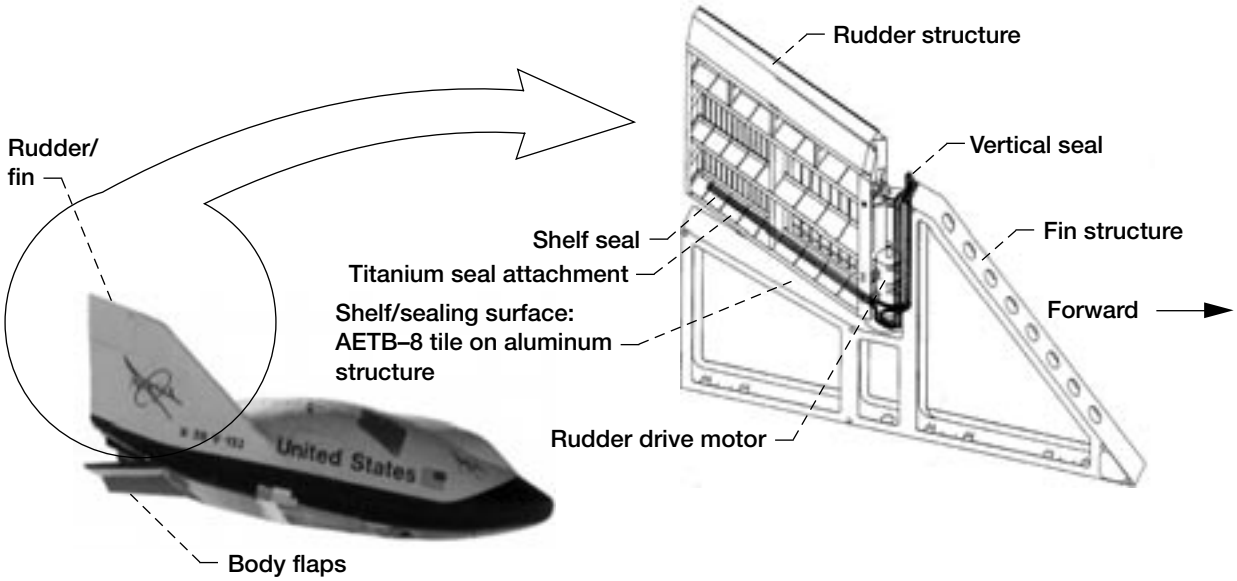

X–38 rudder/fin seal assembly with rudder/fin structure and seal locations. (AETB–8 is the shuttle tile material.)

NASA is developing the X–38 vehicle that will demonstrate the technologies required for a potential crew return vehicle for the International Space Station. This vehicle would serve both as an ambulance for medical emergencies and as an evacuation vehicle for the space station. Control surfaces on the X–38 (body flaps and rudder/fin assemblies) require high-temperature seals to limit hot gas ingestion and the transfer of

heat to underlying low-temperature structures. Working with the NASA Johnson Space Center, the Seals Team at the NASA Glenn Research Center completed a series of tests to further characterize baseline seal designs for the rudder/fin interfaces of the X–38. The structures of the rudder/fin assembly and its associated seals are shown in the illustration on the preceding page.

Tests performed at Glenn indicated that exposure of the seals in a compressed state at simulated seal re-entry temperatures resulted in a large permanent set and loss of seal resiliency. This could be of concern because the seals are required to maintain contact with the sealing surfaces while the vehicle goes through the maximum re-entry heating cycle to prevent hot gases from leaking past the seals and damaging interior low-temperature structures. To simulate conditions in which the seals may become unloaded during use, such as when they take on a large permanent set, Glenn researchers performed room-temperature flow and compression tests to determine seal flow rates, resiliency, and unit loads under minimal loads. Flow rates through an unloaded (i.e., 0-percent compression) double seal arrangement were twice those of a double seal compressed to the 20-percent design compression level. These flow rates are being used in thermal analyses to predict the effect of flow through the seals on over-all seal temperatures. Compression test results showed that seal unit loads and contact pressures were below the limits that Johnson had set as goals for the seals. In the rudder/fin seal location, the seals are in contact with shuttle thermal tiles and are moved across the tiles as the rudder is rotated during re-entry. Low seal unit loads and contact pressures are required to limit the loads on these tiles and minimize any damage that the seals could cause.

A series of tests were performed on these seals in NASA Ames Research Center's arc jet facility. The arc jet facility approximates relevant thermal environments that a seal or other structure would be subjected to during extreme heating conditions such as those experienced during space vehicle re-entry. Eleven tests were completed, including one test in which no seal was installed in the gap to examine the flow of heat down into the gap. The seal was compressed between stationary insulation tiles and a movable elevon that was rotated during the test to deflect the arc jet exhaust into the seal gap (see the figure to the right). Peak seal temperatures as high as 2000 °F were reached during the 5-min tests (see the figure on the next page). Results of these tests indicate satisfactory performance of the seal for single-use (e.g., X–38) applications. The results of these tests were shared with the NASA Johnson Space Center and are being used to validate aerothermostructural analysis codes that predict seal temperatures under these conditions.

The tests performed at Glenn have provided valuable information to Johnson about the performance of the seals that they are considering using in the rudder/fin location of the X–38 vehicle. Glenn and Johnson are currently defining what additional work needs to be done to develop the final rudder/fin seal design for the X–38 vehicle.

Find out more about this research:

Structural seals and thermal barriers: http://www.grc.nasa.gov/WWW/structuralseal/

High-temperature, flexible, fiber preform seal: http://www.grc.nasa. gov/WWW/structuralseal/InventYr/1996Inv_Yr.htm

Glenn's Mechanical Components Branch: http://www.grc.nasa.gov/WWW/5900/5950/

Bibliography

Dunlap, Patrick H., Jr., et al.: Further Investigations of Control Surface Seals for the X–38 Re-Entry Vehicle. NASA/TM—2001-210980 (AIAA Paper 2001–3628), 2001. http://www.grc.nasa.gov/WWW/structuralseal/papers/tm-2001-210980aiaa.pdf and http://gltrs.grc.nasa.gov/GLTRS/

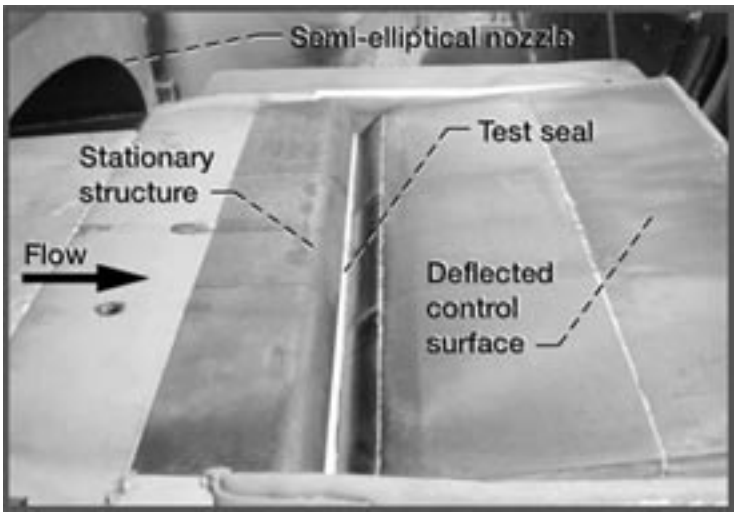

Test fixture installed in arc jet tunnel with seal installed.

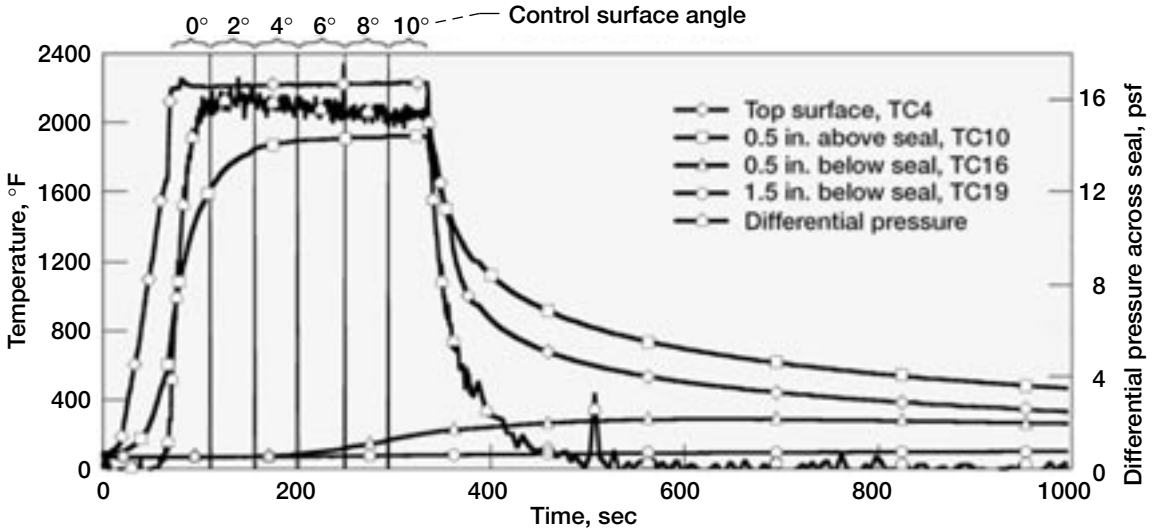

Temperatures and pressure differential measured for arc jet test with seal installed at 20-percent compression (test 5). Table angle, 6°; control surface angles, 0°, 2°, 4°, 6°, 8°, and 10°; nominal gap, 0.25 in. (Note that symbols on graph are given for identification only; data were recorded every 1 sec. TC indicates a thermocouple.)

Glenn contacts:
Patrick H. Dunlap, Jr., 216–433–3017, Patrick.H.Dunlap@grc.nasa.gov; and
Dr. Bruce M. Steinetz, 216–433–3302, Bruce.M.Steinetz@grc.nasa.gov

Authors: Patrick H. Dunlap, Jr., and Dr. Bruce M. Steinetz

Headquarters program office: OAT

Programs/Projects:
X–38, ASTP/3rd Generation RLV, Advanced Control Surface Seals, Advanced Propulsion System Seals

NASA Space Mechanisms Handbook and Reference Guide Expanded Into CD–ROM Set

NASA has been involved with the design, fabrication, testing, and operational use of space mechanisms since the earliest years of space exploration. Drawing upon the vast base of knowledge amassed since that time and in recognition of the maturity of the development of space mechanisms, a Space Mechanisms Handbook was written at the NASA Glenn Research Center that details the state-of-the-art in space mechanisms design as of 1998.

NASA's objective in developing this Space Mechanisms Handbook was to provide readily accessible information on such areas as space mechanisms design, mechanical component availability and use, testing and qualification of mechanical systems, and a listing of worldwide space mechanisms experts and testing facilities in the United States.

Recently, researchers at Glenn expanded the Handbook into a two-volume CD–ROM set in an Adobe Acrobat format.[1] In addition to the handbook, the CD's include (1) the two-volume *Space Mechanisms Lessons Learned Study*, (2) proceedings from all the NASA-hosted Aerospace Mechanisms Symposia held through the year 2000, (3) the *Space Materials Handbook*, (4) the *Lubrication Handbook for the Space Industry*, (5) the *Structural & Mechanical Systems Long-Life Assurance Design Guidelines*, (6) the *Space Environments and Effects Source-Book*, (7) the *Spacecraft Deployable Appendages* manual, (8) the *Fastener Design Manual*, (9) *A Manual for Pyrotechnic Design, Development and Qualification*, (10) the *Report on Alternative Devices to Pyrotechnics on Spacecraft*, and (11) *Gearing* (a manual). In addition, numerous other papers on tribology and lubrication are included.

By placing all these research and application results in a single, searchable CD–ROM set, we believe that we have provided a powerful information resource to

[1]The CD–ROM set is available, to qualified requestors, from Glenn's Mechanical Components Branch.

technical personnel working on space mechanical applications. In addition, we believe that this CD–ROM set will be a permanent reference resource for future space mechanisms work. The NASA Space Mechanisms Handbook and Reference Guide is available in either print or CD versions to qualified requestors who are U.S. citizens.

Find out more about this research:

Glenn's Mechanical Components Branch:
http://www.grc.nasa.gov/WWW/5900/5950/

Space Mechanism Project: http://www.grc.nasa.gov/WWW/spacemech/

Information about obtaining the handbook:
http://www.grc.nasa.gov/WWW/spacemech/CD-info.html

Glenn contact:
Fred B. Oswald, 216–433–3957,
Fred.B.Oswald@grc.nasa.gov

Author: Robert L. Fusaro (retired)

Headquarters program office: OAT

Programs/Projects: SRF/Solid Lubricated Journal Bearings as Backup Bearings for Magnetic Bearings, SRF/Torque Limited Touchdown Bearing System for Magnetic Bearings, SRF/New Concepts in Low Cost, Higher Reliability and Less Complex Flywheel Systems

Comparison Made of Operating Characteristics of Spiral Bevel Gears Manufactured Using Different Methods

Spiral bevel gears are important components on all current rotorcraft drive systems. These components are required to operate at high speeds, high loads, and for an extremely large number of load cycles. In this application, spiral bevel gears are used to redirect the shaft from the horizontal gas turbine engine to the vertical rotor. Because of the high expense of manufacturing these gears, methods that can achieve the same level of performance at reduced cost are highly desirable to aerospace gear manufacturers.

Gears manufactured for aerospace applications use high-quality materials and are manufactured to tight tolerances. Special manufacturing machine tools and computer numerically controlled coordinate measurement systems have enabled rotorcraft drive system manufacturers to produce extremely high-quality gears during their normal production. Because of low production rates for rotorcraft, these gears are manufactured in small batches, and thus are unable to benefit from the economics of high production numbers as in other industries.

In this investigation, two different manufacturing methods, face-milled and face-hobbed, were used to fabricate spiral bevel gears. For face-milled spiral bevel gears, grinding of the contacting surfaces is the final manufacturing step. At least two different specialty machines are needed to generate the teeth for face-milled spiral bevel gears. For face-hobbed gears, hard cutting is the final manufacturing process. The same machine is used to rough cut and finish cut the gears.

This study compared the operational behavior of face-milled spiral bevel gears with that of face-hobbed spiral

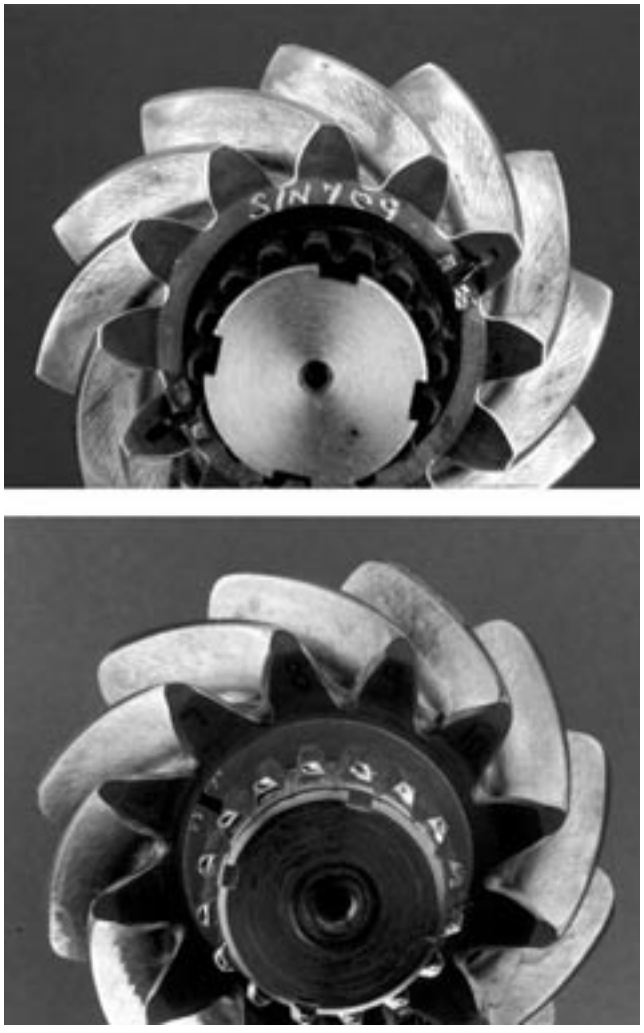

Manufactured bevel pinions for the study conducted. Top: Face-milled. Bottom: Face-hobbed.

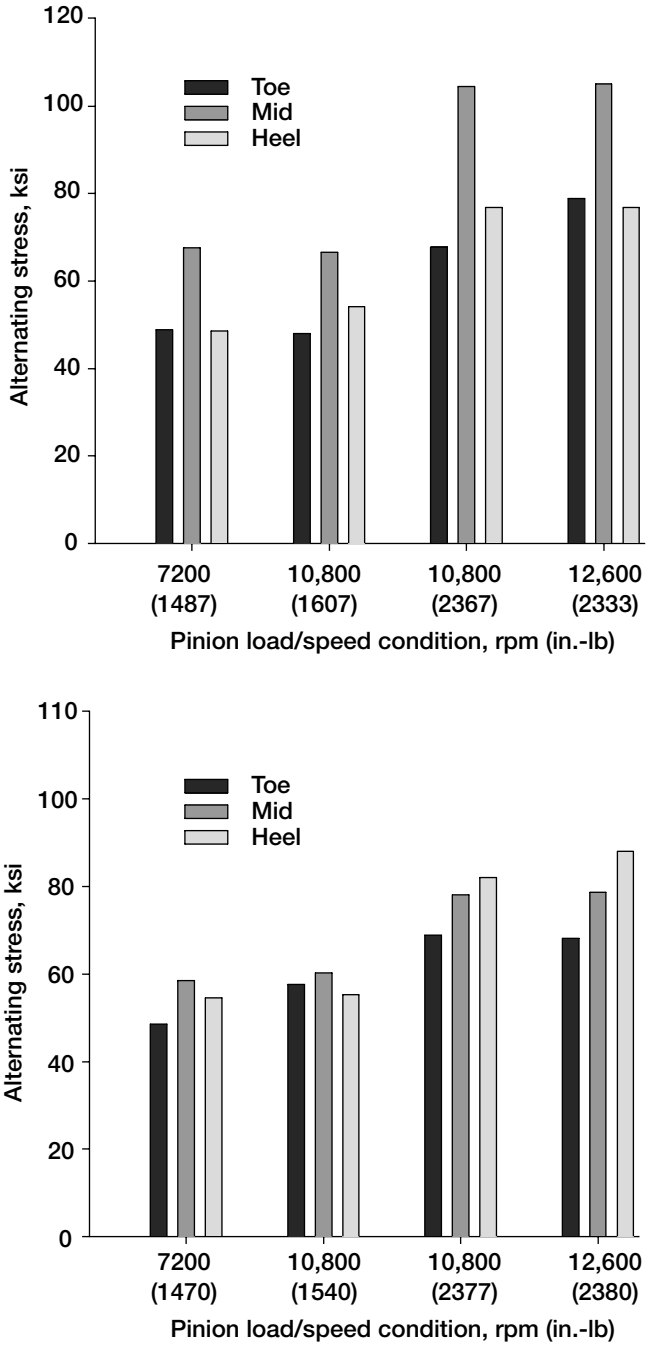

Comparison of the alternating root stress levels of spiral bevel pinions. Top: Face-milled. Bottom: Face-hobbed.

bevel gears. Test hardware was manufactured to fit within NASA Glenn Research Center's Spiral Bevel Test Facility and to aerospace quality standards. Tests were conducted for stress, vibration, and noise. A comparison of the results attained indicated that the face-hobbed gears had a lower alternating stress level with a more even distribution of loading across the teeth, and slightly reduced levels of vibration and noise. Results of this study show that the face-hobbed method is a viable and lower-cost alternative for producing aerospace-quality spiral-bevel gears.

Bibliography

Handschuh, Robert F.: Comparison of Experimental and Analytical Tooth Bending Stress of Aerospace Spiral Bevel Gears. NASA/TM—1999-208903, 1999. http://gltrs.grc.nasa.gov/GLTRS/

Handschuh, Robert F.: Testing of Face-Milled Spiral Bevel Gears at High-Speed and Load. NASA/TM—2001-210743, 2001. http://gltrs.grc.nasa.gov/GLTRS/

Handschuh, Robert F., et al.: Experimental Comparison of Face-Milled and Face-Hobbed Spiral Bevel Gears. NASA/TM—2001-210940, 2001.

Find out more about this research:
http://www.grc.nasa.gov/WWW/5900/5950/

U.S. Army Research Laboratory, Vehicle Technology Directorate at Glenn contact:
Dr. Robert F. Handschuh, 216–433–3969, Robert.F.Handschuh@grc.nasa.gov

Author: Dr. Robert F. Handschuh

Headquarters program office: OAT

Programs/Projects: Rotorcraft Base Program, Propulsion Systems R&T, NASA Ames Rotorcraft Program

Gear Crack Propagation Path Studies—Guidelines Developed for Ultrasafe Design

Effective gear designs balance strength, durability, reliability, size, weight, and cost. However, unexpected gear failures may occur even with adequate gear tooth design. To design an extremely safe system, the designer must ask and address the question "What happens when a failure occurs?" With regard to gear-tooth bending fatigue, tooth or rim fractures may occur. For aircraft, a crack that propagated through a rim would be catastrophic, leading to the disengagement of a rotor or propeller, the loss of an aircraft, and possible fatalities. This failure mode should be avoided. However, a crack that propagated through a tooth might or might not be catastrophic, depending on the design and operating conditions. Also, early warning of this failure mode might be possible because of advances in modern diagnostic systems.

An analysis was performed at the NASA Glenn Research Center to develop design guidelines to prevent catastrophic rim fracture failure modes in the event of gear-tooth bending fatigue. The finite element method was used with principles of linear elastic fracture mechanics. Crack propagation paths were predicted for a variety of gear tooth and rim configurations. The effects of rim and web thicknesses, initial crack locations, and gear-tooth geometry factors such as diametral pitch, number of teeth, pitch radius, and tooth pressure angle were considered. Design maps of tooth and rim fracture modes, including the effects of gear geometry, applied load, crack size, and material properties were developed. The occurrence of rim fractures significantly increased as the backup ratio (rim thickness divided by tooth height) decreased. The occurrence of rim fractures also increased as the initial crack location was moved down the root of the tooth. Increased rim and

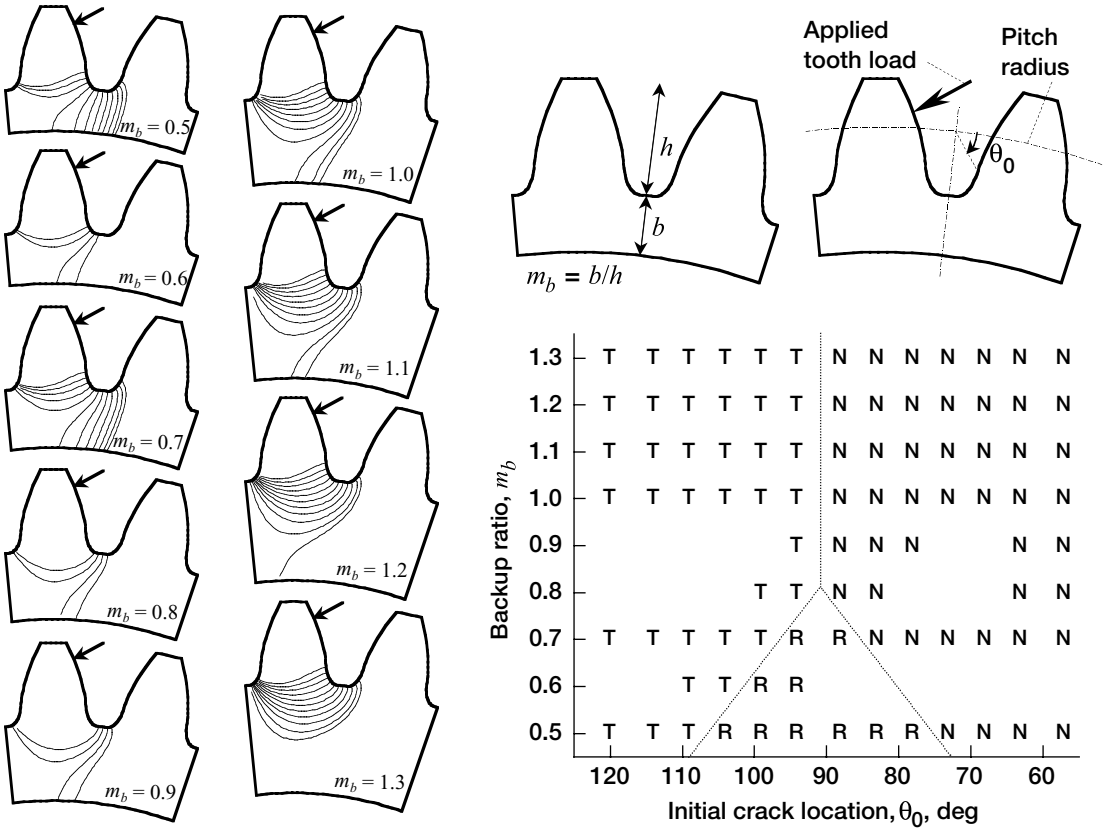

Left: Effect of backup ratio, m_b, and initial crack location on propagation path. Right: Effect of backup ratio and initial crack location on crack failure modes. Applied tooth load, 500 lb; initial crack length, 0.030 in.; stress intensity factor threshold, 5 ksi√in.; T, tooth fracture; R, rim fracture; N, no crack propagation.

web compliance increased the occurrence of rim fractures. For gears with constant-pitch radii, coarser-pitch teeth increased the occurrence of tooth fractures over rim fractures. Also, 25° pressure angle teeth increased the occurrence of tooth fractures over rim fractures in comparison to 20° pressure angle teeth. For gears with a constant number of teeth or for gears with constant diametral pitch, varying size had little or no effect on crack propagation paths.

This work was done in-house at Glenn in support of the Rotorcraft base program. The crack propagation code was developed by the Cornell Fracture Group at Cornell University.

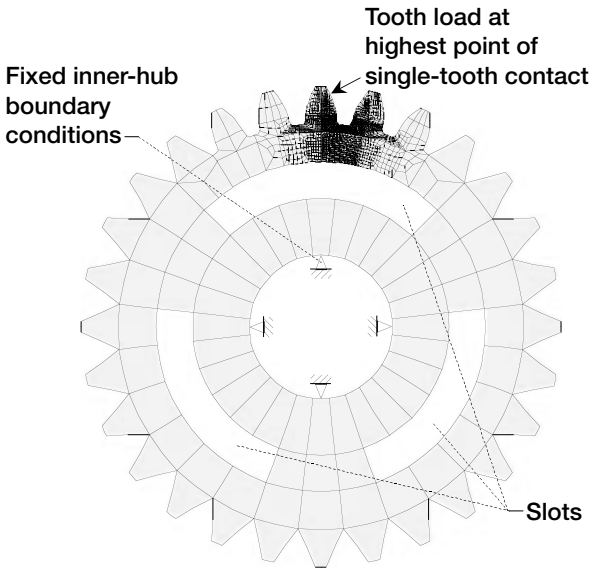

Typical finite element model of an uncracked gear used in the study. Number of teeth, 28; diametral pitch, 8; pitch radius, 1.75-in.; pressure angle, 20°; backup ratio (rim thickness divided by tooth height), m_b, 1.0.

Bibliography

Lewicki, David G., et al.: Consideration of Moving Tooth Load in Gear Crack Propagation Predictions. NASA/TM—2000-210227, 2000. http://gltrs.grc.nasa.gov/GLTRS/

Lewicki, David G.: Gear Crack Propagation Path Studies—Guidelines for Ultra-Safe Design. NASA/TM—2001-211073, 2001. http://gltrs.grc.nasa.gov/GLTRS/

Spievak, Lisa E.; Wawrzynek, Paul A.; and Ingraffea, Anthony R.: Simulating Fatigue Crack Growth in Spiral Bevel Gears. NASA/CR—2000-210062, 2000. http://gltrs.grc.nasa.gov/GLTRS/

U.S. Army Research Laboratory, Vehicle Technology Directorate at Glenn
contact: Dr. David G. Lewicki, 216–433–3970, David.G.Lewicki@grc.nasa.gov

Author: Dr. David G. Lewicki

Headquarters program office: OAT

Programs/Projects: Rotorcraft

Gear Transmission Error Measurement System Made Operational

A system directly measuring the transmission error between the meshing spur or helical gears was installed at the NASA Glenn Research Center and made operational in August 2001 (see the illustration on the next page). This system employs light beams directed by lenses and prisms through gratings mounted on the two gear shafts. The amount of light that passes through both gratings is directly proportional to the transmission error of the gears. The device is capable of resolution better than 0.1 μm (one thousandth the thickness of a human hair).

The measured transmission error can be displayed in a "map" that shows how the transmission error varies with the gear rotation (see the graph on the next page) or it can be converted to spectra to show the components at the meshing frequencies. Accurate transmission error data will help researchers better understand the mechanisms that cause gear noise and vibration and will lead to improved analytical codes.

The Design Unit at the University of Newcastle in England specifically designed the new system for NASA. It is the only device in the United States that can measure dynamic

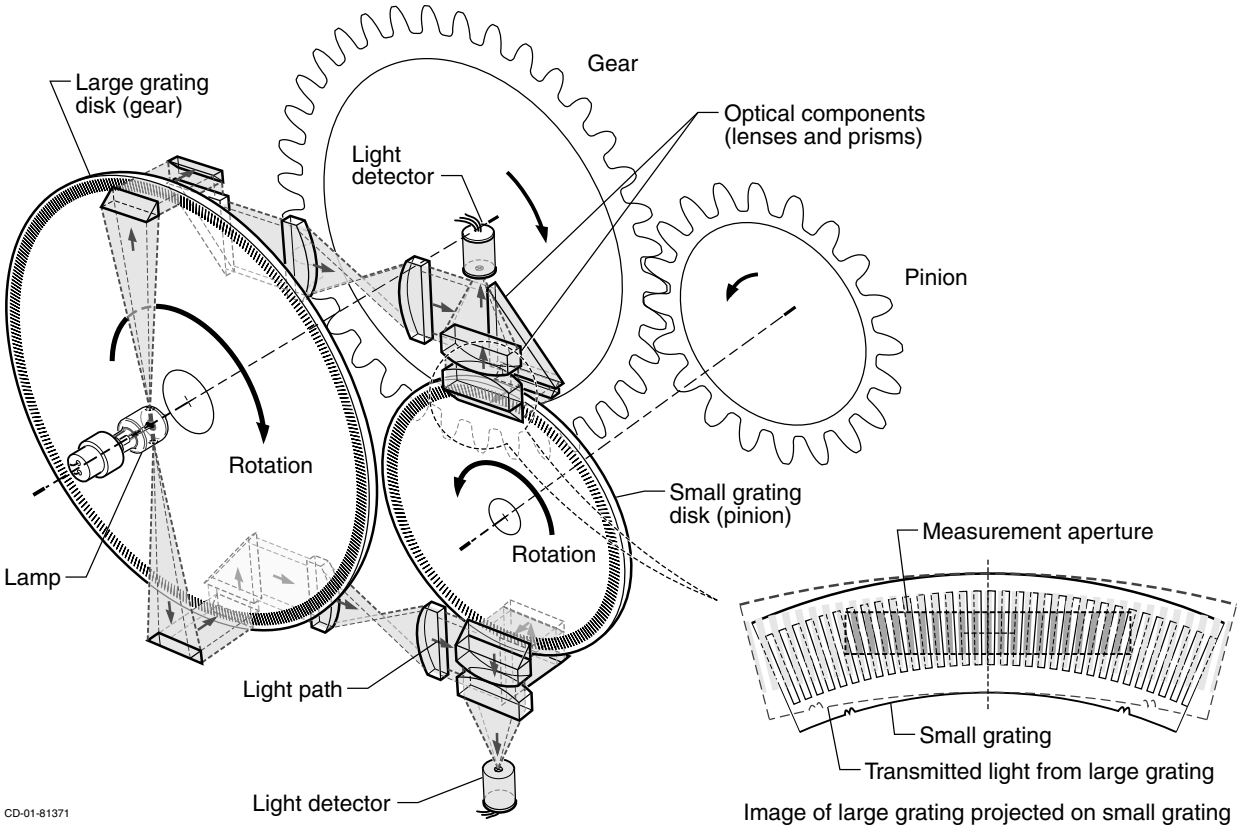

Schematic of the transmission error measurement system indicating the light path through the gratings and other optical components. At right is a representation of the light from one grating projected onto the other grating.

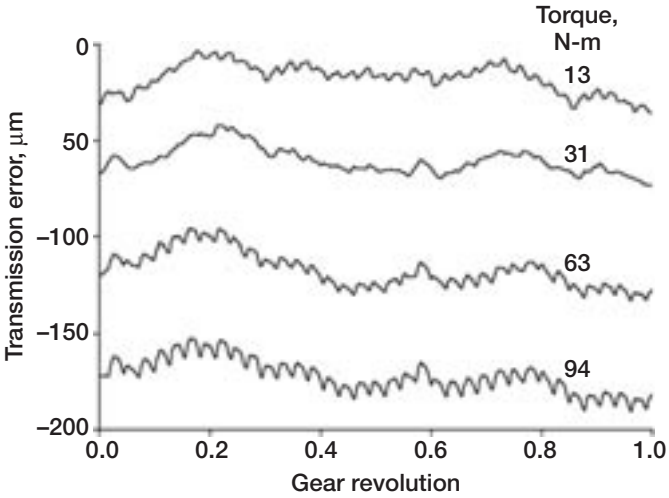

Map plot showing transmission error at four different torque levels. Note that the second trace (31 N-m) is smoother (has less high-frequency variation) than the other traces. Computer codes predict that this torque is approximately the optimum level to produce minimum tooth-to-tooth excitation of the gear system; thus, there is less vibration in the mesh.

transmission error at high rotational speeds. The new system will be used to develop new techniques to reduce dynamic transmission error along with the resulting noise and vibration of aeronautical transmissions.

Bibliography

Oswald, Fred B.: Influence of Tooth Profile Modification on Spur Gear Dynamic Tooth Strain. NASA TM–106952, 1995.

Atkins, I.; Hofmann, D.A.; and Haigh, J.: The Ultra Low Noise Gearbox. The Institute of Marine Engineers, 2000.

Find out more from Glenn's Mechanical Components Branch: http://www.grc.nasa.gov/WWW/5900/5950/

Glenn contact:
Fred B. Oswald, 216–433–3957, Fred.Oswald@grc.nasa.gov

Author: Fred B. Oswald

Headquarters program office: OAT

Programs/Projects: Rotorcraft, SILNT

Proof-of-Concept Traction Drive Designed for Planetary Exploration

Vehicles and other machines that will be designed to explore the planets and moons of our solar system will require reliable and efficient mechanical drives. Long-term operation of these drives will be challenging because of the extreme operating conditions. Some of these extreme conditions are very hot and/or very cold temperatures, wide temperature ranges, dust, vacuum or low-pressure atmospheres, and corrosive environments.

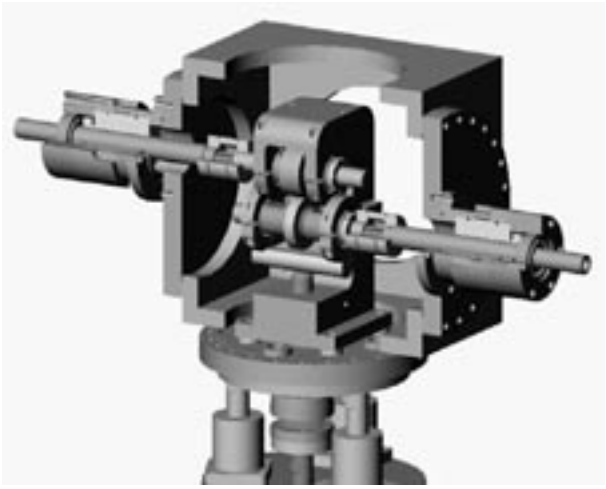

Solid model of newly designed traction drive tester mounted in a vacuum "cube." The test rollers are at center, supported by a framework. At the sides, input and output shafts pass through vacuum feedthroughs. The mechanism at the bottom applies a load to press the rollers together so they can transfer the required torque.

Because of these extreme environmental conditions, it may not be possible to use oil lubrication (including grease) for drive systems because oils vaporize at high temperatures and freeze at low temperatures. Solid lubricant films offer an alternative, but they have finite lives that depend on the contact stress and sliding speed. Heavily loaded gears operate with very high contact stress and a large amount of sliding; thus gears lubricated with solid films will not survive long enough for many drive applications.

At the NASA Glenn Research Center, we believe that traction (roller) drives either coated with solid lubricant films or made from composites provide an attractive alternative to gear drives. The rollers used in traction drives provide a tribological contact geometry that is more conducive to solid lubrication. Stresses are still high, but minimal slip occurs, so wear between the contacting surfaces is greatly reduced.

So that the use of traction drives can be evaluated under the conditions found on planetary surfaces, a prototype accelerated test rig was designed and is being built at Glenn to simulate the use of traction drives under these conditions (see the illustration). These specimens, consisting of a crowned roller running against a flat roller, will be mounted in a vacuum chamber. The roller specimens can be heated or cooled through hollow shafts. A motor driving one roller and a brake on the other roller will produce traction forces and control the slide-to-roll ratio of the contact. A mechanism will control the contact force between the two rollers.

The test rig will also be used as a screening device to evaluate roller materials, roller coatings, and composites. Various loads, speeds, and contact geometries will be evaluated in order to optimize the design of traction drives used in machines to explore planetary surfaces. The experimental program will investigate the traction (torque), wear, and endurance durability of the drive materials under various conditions of speed and applied load as well as under various simulated environmental conditions. The rig was designed so that it can test gears and bearings in addition to rollers.

In summary, this device will enable NASA to assess the feasibility of using traction drives under high and low temperatures and under various planetary atmospheric conditions, such as vacuum or low-pressure atmospheres without water vapor or oxygen. The data produced will help to advance the design of future, more complex drives.

Find out more about this research:

Space Mechanisms: http://www.grc.nasa.gov/WWW/spacemech/

Glenn's Mechanical Components Branch: http://www.grc.nasa.gov/WWW/5900/5950/

Glenn contact:
Fred B. Oswald, 216–433–3957, Fred.Oswald@grc.nasa.gov

Authors:
Fred B. Oswald, Robert L. Fusaro, Mark W. Siebert, and Ben T. Ebihara

Headquarters program office: OAT

Programs/Projects:
SRF/Solid Lubricated Vehicle Drives for Planetary Exploration

Atomistic Modeling of Semiconductors: Si, C, and 3C-SiC

An ongoing task of the Computational Materials Group (CMG) at the NASA Glenn Research Center is to enhance the role of atomistic simulations based on quantum-approximate methods in the study of new materials and their properties. One of the main goals of the activity continues to be breaching limitations that arise from the natural balance between accuracy, range of application, and computational simplicity (ref. 1). Whether that balance can be maintained while breaking new ground depends on the methods available with a minimum of constraints and limitations for the study of the energetics of arbitrary systems. The main tool used in CMG research, the Bozzolo-Ferrante-Smith (BFS) method for alloys (ref. 2), has no inherent constraint in its formulation, a feature that has allowed for successful research on various topics. In this article, we report on the latest development of the CMG program, namely, the extension and application of the BFS method to compound semiconductors, a departure from our previous research based primarily on metallic alloys.

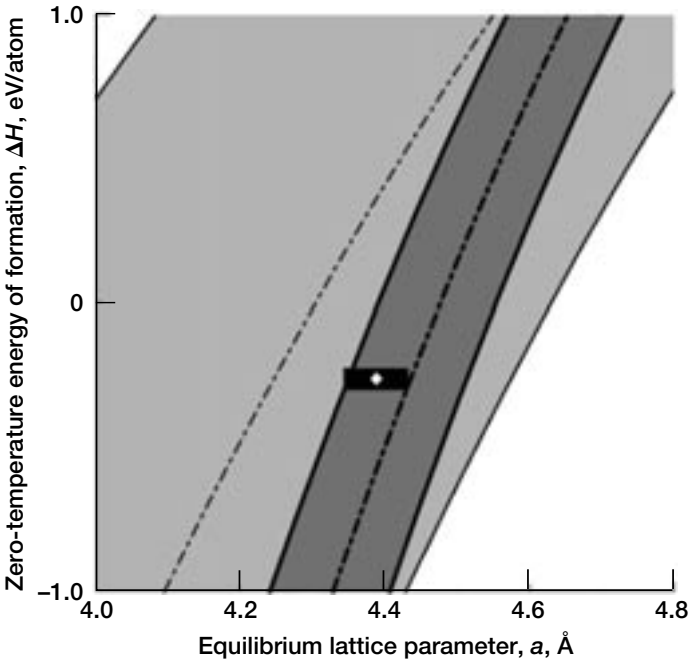

Region of validity of the BFS method: any input point (of equilibrium lattice parameter, a_0; and zero-temperature energy of formation, ΔH_0) corresponding to the shaded region ensures the determination of transferable BFS parameters. The boundaries for Si- and C-valid regions (dark and light gray shade, respectively) are given by those points where the BFS contributions to the total energy of formation are bounded by the individual cohesive energy of the individual elements, Si and C (thick and thin solid lines, respectively).

In spite of the differences between metallic systems and semiconductors, the straightforward formulation of BFS, which is based on a novel interpretation of the alloy formation process, remains unaltered, thereby providing an incisive predictive tool that is both physically sound and computationally simple. However, the particular nature of the elemental semiconductors Si and C and of the different silicon carbide (SiC) polytypes imposes a severe test of the method's accuracy because of radical differences in semiconductor and metallic bonding and because of the way such features are represented in the method.

The BFS energy calculations involve three pure element properties for each species: cohesive energy, lattice parameter, and bulk modulus. Two additional BFS perturbative parameters are determined from any pair of alloy properties. First-principles calculations using the self-consistent full-potential linearized-augmented plane wave (LAPW) method within the Generalized Gradient Correction as implemented in the WIEN97 program package (ref. 3) were used to provide the three pure element properties for Si and C, as well as the equilibrium lattice parameter and zero-temperature energy of formation of 3C-SiC, to determine the perturbative BFS parameters for Si-C.

The resulting parameters were compared with experimentally determined values where available. Once validated, these parameters will be fully transferable and applicable to any problem dealing with the SiC structure. First-principles calculations are usually accurate in predicting the value of equilibrium lattice parameters, but not as accurate in their prediction of the compressibility or the cohesive energy. These uncertainties necessarily translate into possible instabilities in the determination of the BFS perturbative parameters which should be such that the chemical energies associated with the equilibrium structure used as input (in this case, 3C-SiC) do not exceed their limiting values given by the cohesive energy of each type of atom. The preceding graph shows the regions where the BFS method is valid (i.e., if the LAPW-based point is located within the bands shown, then there is a guaranteed convergent solution to the BFS equations). The dashed curves (thick for Si, thin for C) trace the locus in the plane where the respective BFS chemical energies are zero, and the solid lines, above

and below, indicate the points where the chemical energies reach their maximum allowed value.

The graph also shows a box surrounding the original LAPW point, defined as the region in the plane for which the equilibrium lattice parameter varies by 1 percent and the energy per atom varies by 10 percent, typical uncertainties in ab initio calculations. The fact that the uncertainty box is well within a unique region of the diagram ensures the validity of the LAPW input. The applications include the determination of the surface energy and structure of Si, C, Si-terminated (Si_t), and C-terminated (C_t) SiC (100) surfaces. Atomistic analysis of the formation of Si or C dimers on Si(100), C(100), and SiC(100) was also performed.

Numerous reconstruction models, backed by experiment, have been suggested to describe each of the Si(100) and Si_t or C_t 3C-SiC(100) surfaces. There are, however, conflicting and poorly understood features, as well as lack of consensus among the different theoretical techniques used to study what are, obviously, very complex systems. BFS predictions were compared with available experiment and other theoretical methods. The predicted values for dimer lengths and dimer/surface distance are in good agreement with experimental results in all the possible dimer/surface combinations (Si/Si, Si/C, Si/SiC, etc.). Dimer reconstruction of Si(100), as shown in the sketch, is one of the most studied features and, besides its numerous applications, it is a severe test for theoretical methods. The BFS values for the dimer length and spacing, in all cases, are well within the accepted range, raising confidence on the ability of BFS to reproduce the essential features of these systems.

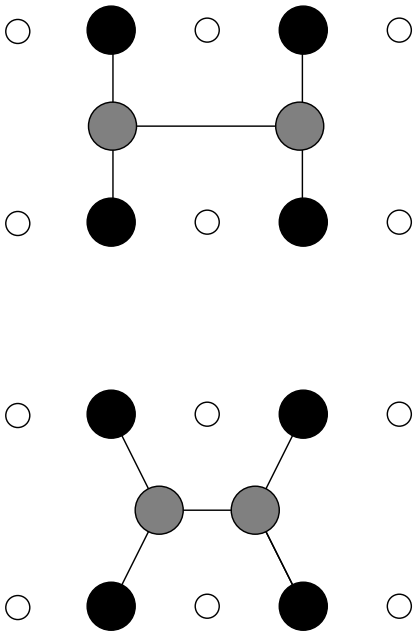

Rigid (top) and contracted (bottom) A–A dimer (A = Si, C) on a B(100) surface (B = Si, C, Si_t, or C_t 3C-SiC surface). Solid dark and light disks denote atoms in the surface and overlayer, respectively. Small circles denote atoms in the layer below the surface.

References

1. Bozzolo, Guillermo H., et al.: Software Package Completed for Alloy Design at the Atomic Level. Research & Technology 2000, NASA/TM—2001-210605, 2001, pp. 16–17. http://www.grc.nasa.gov/WWW/RT2000/5000/5100A-bozzolo.html
2. Bozzolo, G., et al.: Surface Segregation in Multicomponent Systems: Modeling of Surface Alloys and Alloy Surfaces. Comput. Mater. Sci., vol. 15, no. 2, 1999, pp. 169–195.
3. Blaha, P.; Schwarz, K.; and Sorantin, P.: Full-Potential, Linearized Augmented Plane-Wave Programs for Crystalline Systems. Comp. Phys. Comm., vol. 59, no. 2, 1990, pp. 399–415.

Find out more about this research:

Atomistic Modeling of Bulk Alloys, Surfaces and Interfaces:
http://www.grc.nasa.gov/WWW/SurfSci/bfs/bfs_index.html

Tribology & Surface Science Branch: http://www.grc.nasa.gov/WWW/SurfSci/

Ohio Aerospace Institute contact:
Dr. Guillermo Bozzolo, 440–962–3103,
Guillermo.H.Bozzolo@grc.nasa.gov

Glenn contact:
Dr. Phillip B. Abel, 216–433–6063,
Phillip.B.Abel@grc.nasa.gov

Authors: Dr. Guillermo Bozzolo,
Dr. Jorge E. Garces, and
Dr. Phillip B. Abel

Headquarters program office: OAT

Programs/Projects: HOTPC

Mystery of Foil Air Bearings for Oil-Free Turbomachinery Unlocked: Load Capacity Rule-of-Thumb Allows Simple Estimation of Performance

The Oil-Free Turbomachinery team at the NASA Glenn Research Center has unlocked one of the mysteries surrounding foil air bearing performance. Foil air bearings are self-acting hydrodynamic bearings that use ambient air, or any fluid, as their lubricant. In operation, the motion of the shaft's surface drags fluid into the bearing by viscous action, creating a pressurized lubricant film. This lubricating film separates the stationary foil bearing surface from the moving shaft and supports load. Foil bearings have been around for decades and are widely employed in the air cycle machines used for cabin pressurization and cooling aboard commercial jetliners. The Oil-Free Turbomachinery team is fostering the maturation of this technology for integration into advanced Oil-Free aircraft engines. Elimination of the engine oil system can significantly reduce weight and cost and could enable revolutionary new engine designs. Foil bearings, however, have complex elastic support structures (spring packs) that make the prediction of bearing performance, such as load capacity, difficult if not impossible.

Researchers at Glenn recently found a link between foil bearing design and load capacity performance. The results have led to a simple rule-of-thumb that relates a bearing's size, speed, and design to its load capacity. Early simple designs (Generation I) had simple elastic (spring) support elements, and performance was limited. More advanced bearings (Generation III) with elastic supports, in which the stiffness is varied locally to optimize gas film pressures, exhibit load capacities that are more than double those of the best previous designs. This is shown graphically in the figure. These more advanced bearings have enabled industry to introduce commercial Oil-Free gas-turbine-based electrical generators and are allowing the aeropropulsion industry to incorporate the technology into aircraft engines. The rule-of-thumb enables engine and bearing designers to easily size and select bearing technology for a new application and determine the level of complexity required in the bearings. This new understanding enables industry to assess the feasibility of new engine designs and provides critical guidance toward the future development of Oil-Free turbomachinery propulsion systems.

Find out more about this research: http://www.grc.nasa.gov/WWW/oilfree/

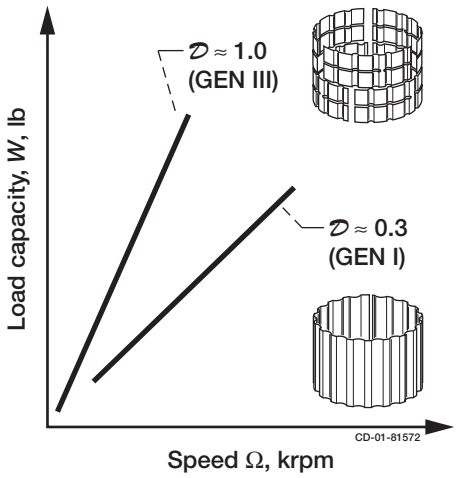

Foil bearing load capacity is enhanced by higher complexity in the elastic support (springs) structure. $W = \mathcal{D}(L \times D)(D \times \Omega)$, where W is the maximum steady-state load that can be supported (N, lb), $\mathcal{D}$ is the bearing load capacity coefficient (N/mm^3-krpm, $lb/in.^3$-krpm), L is the bearing axial length (mm, in.), D is the shaft diameter (mm, in.), and Ω is the shaft speed in 1000 rpm (krpm).

Glenn contacts:
Dr. Christopher DellaCorte, 216–433–6056, Christopher.DellaCorte@grc.nasa.gov; and Dr. Mark J. Valco, 216–433–3717, Mark.J.Valco@grc.nasa.gov

Authors: Dr. Christopher DellaCorte and Dr. Mark J. Valco

Headquarters program office: OAT

Program/Projects:
Aeropropulsion Base R&T, UEET

Heat Treatment Used to Strengthen Enabling Coating Technology for Oil-Free Turbomachinery

The PS304 high-temperature solid lubricant coating is a key enabling technology for Oil-Free turbomachinery propulsion and power systems. Breakthroughs in the performance of advanced foil air bearings and improvements in computer-based finite element modeling techniques are the key technologies enabling the development of Oil-Free aircraft engines being pursued by the Oil-Free Turbomachinery team at the NASA Glenn Research Center. PS304 is a plasma spray coating applied to the surface of shafts operating against foil air bearings or in any other component requiring solid lubrication at high temperatures, where conventional materials such as graphite cannot function.

The PS304 patented coating is a composite made from a nickel chromium binder, chrome oxide hardener, and solid lubricant additives silver and barium/calcium fluoride eutectic. This coating provides low friction and wear to sliding contacts in oxidizing and reducing atmospheres from cryogenic temperatures to over 650 °C. Recent experimental results indicate that the coating's adhesive and cohesive strengths improve by at least a factor of two following exposure to high-temperature air. Measured adhesive pulloff strength for the as-deposited coating is typically 17 MPa but rises to over 35 MPa after a 24-hr heat treatment at 532 °C. The exact strength of the heat-treated coating remains unknown because its strength exceeds that of the epoxy used in these tests to make the adhesion measurement. The heat treatment also results in a one-time coating thickness expansion of about 5 percent.

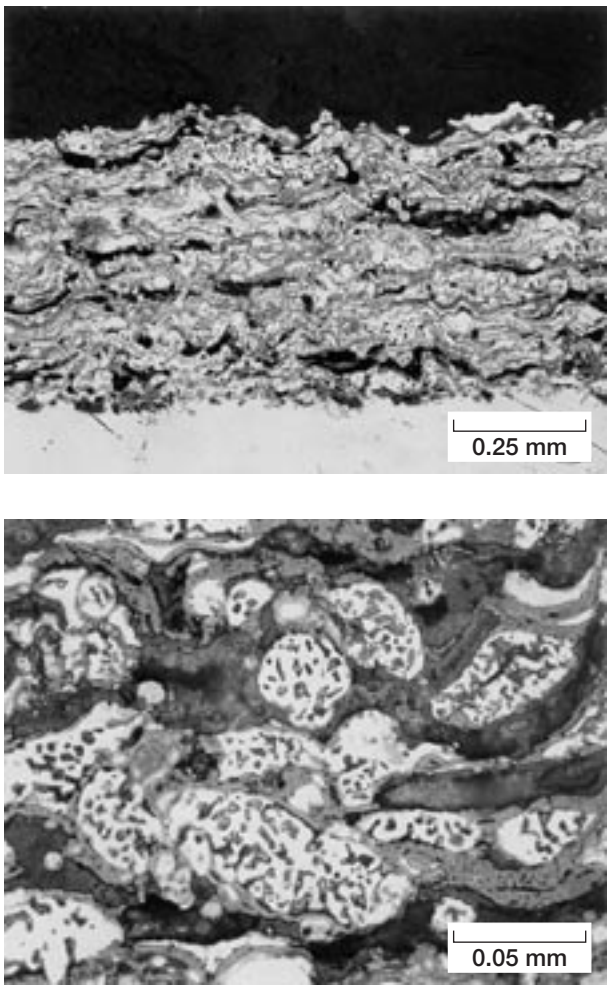

Cross section of PS304 coating following heat treatment in air at 650 °C showing the second-phase precipitate that forms in the nickel chrome binder phase.

Cross-section metallographic analyses show that the binder phase has been altered by the heat treatment. As the photomicrographs show, the nickel chrome binder phase, which originally was uniform and gray, now has distinct second-phase precipitates. These precipitates have been found to contain high levels of chromium, oxygen, and other trace elements (like silicon) when examined using scanning electron microscopy x-ray techniques. The exact nature and structure of the second phase is under continued study, but this doesn't seem to create any negative performance or durability issues. As a result of this work, a postdeposition heat treatment has been implemented for the PS304 coating, further assisting its commercial application in Oil-Free turbomachinery and other high-temperature systems.

Find out more about this research: http://www.grc.nasa.gov/WWW/oilfree/

Glenn contacts: Dr. Christopher DellaCorte, 216–433–6056, Christopher.Dellacorte@grc.nasa.gov; Brian J. Edmonds, 216–433–8963, Brian.J.Edmonds@grc.nasa.gov; and Kathleen K. Needham, 216–433–2802, Kathleen.K.Needham@grc.nasa.gov

Authors: Brian J. Edmonds and Dr. Christopher DellaCorte

Headquarters program office: OAT

Programs/Projects: Aeropropulsion Base R&T, UEET

Special recognition: U.S. Patent 5,866,518 given to Christopher DellaCorte and Brian J. Edmonds for the PS300 high-temperature solid lubricant coatings (including PS304) in February 1999.

2001

Space

Space Communications

ACTS Operations Extended Through a University-Based Consortium

The Advanced Communications Technology Satellite (ACTS) program was slated for decommissioning in October 2000. With plans in place to move the spacecraft to an orbital graveyard and then shut the system down, NASA was challenged to consider the feasibility of extending operations for education and research purposes provided that an academic organization would be willing to cover operations costs. This was determined to be viable, and in the fall of 2000, NASA announced that it would consider extending operations.

Advanced Communications Technology Satellite (ACTS).

On March 19, 2001, NASA, the Ohio Board of Regents, and the Ohio University signed a Space Act Agreement to continue ACTS operations for 2 more years with options to extend operations up to a total of 4 years. To accomplish this, the Ohio University has formed a university-based consortium, the Ohio Consortium for Advanced Communications Technology (OCACT), and acts as the managing member. The Ohio University is responsible for the full reimbursement of NASA's operations costs, and does this through consortium membership. NASA retains the operating license of the spacecraft and has two contractors supporting spacecraft and master control station operations.

This flexible arrangement between NASA and academia allows the education community to access a large communications satellite for learning about spacecraft operations and to use the system's transponders for communications applications. It also allows other organizations, such as commercial companies, to become consortium members and use the ACTS wideband Ka-band (30/20 GHz) payload. From the consortium members, six areas of interest have been identified.

(1) Space education: Use ACTS as a "laboratory" to educate students in subjects such as orbital mechanics, spacecraft control systems, spacecraft operations, radiofrequency engineering, ground station deployment and operations, and network management.

(2) Educational content: Deliver educational content (e.g., from

remote locations) to students in kindergarten through 12th grade, in collaboration with established educational content providers and foundations.

(3) Engineering verifications: Use ACTS to characterize the performance of new Ka-band hardware components and verify their designs.

(4) Final ground-station testing: Use ACTS for final preproduction testing of commercial-grade Ka-band ground stations designed and built by consortium members. These stations will be used with future Ka-band satellites.

(5) Proof-of-concept demonstrations: Demonstrate telemedicine, satellite telephony, satellite-based Internet access, and other similar applications to promote the use of Ka-band services in the future.

(6) Extended field and marketing trials: Offer and verify precommercial service in the form of extended field trials.

Extending ACTS operations by transitioning them to a university consortium provides an excellent closing chapter on ACTS. The payload continues to operate on primary systems and can continue to be a learning tool for academia while providing the only operational Ka-band system in the Western Hemisphere.

Find out more about this research:

ACTS: http://acts.grc.nasa.gov/

Ohio Consortium for Advanced Communications Technology: http://www.csm.ohiou.edu/ocact/

Glenn contacts:
Robert A. Bauer, 216–433–3431, Robert.A.Bauer@grc.nasa.gov; and Richard J. Krawczyk, 216–433–3539, Richard.J.Krawczyk@grc.nasa.gov

Authors: Robert A. Bauer and Richard J. Krawczyk

Headquarters program office: OSF (SOMO, HEDS)

Programs/Projects:
Communications Technology

Special recognition: ACTS was inducted into the Space Technology Hall of Fame in April 1997 for its contributions to the commercialization of space technology, was given a 1995 R&D 100 Award in the Significant Technology Category, and was given the prestigious Federal Technology Leadership Award in 1995.

Architecture Studies Done for High-Rate Duplex Direct Data Distribution (D4) Services

A study was sponsored to investigate a set of end-to-end system concepts for implementing a high-rate duplex direct data distribution (D4) space-to-ground communications link. The NASA Glenn Research Center is investigating these systems (both commercial and Government) as a possible method of providing a D4 communications service between NASA spacecraft in low Earth orbit and the respective principal investigators using or monitoring instruments aboard these spacecraft. Candidate commercial services were assessed regarding their near-term potential to provide a D4 type of service. The candidates included K-band and V-band geostationary orbit and nongeostationary orbit satellite relay services and direct downlink (D3) services. Internet protocol (IP) networking technologies were evaluated to enable the user-directed distribution and delivery of science data. Four realistic, near-future concepts were analyzed:

(1) A duplex direct link (uplink plus downlink communication paths) between a low-Earth-orbit spacecraft and a principal-investigator-based autonomous Earth station
(2) A space-based relay using a future K-band nongeosynchronous-orbit system to handle both the uplink and downlink communication paths
(3) A hybrid link using both direct and relay services to achieve full duplex capability
(4) A dual-mode concept consisting of both a duplex direct link and a space relay duplex link operating independently

The concepts were analyzed in terms of contact time between the NASA spacecraft and the communications service and the achievable data throughput. Throughput estimates for the D4 systems were based on the infusion

THROUGHPUT COMPARISON FOR SPACECRAFT IN INTERNATIONAL SPACE STATION ORBIT

	D4 single beam (K-band)	D4 dual beam (K-band)	Commercial X-band downlink service
Phased-array antenna beam scan, deg	50	42	50
Return link data rate, Mbps	622	1244	300
Average contact time per day, sec	337	178	337
Throughput per day, Gbits	210	221	101
Estimated cost per Gbit received	$0.13 to $0.40	$0.09 to $0.29	$0.28 to $0.83

of advanced communications technology products (single and multibeam K-band phased-arrays and digital modems) being developed by Glenn. Cost estimates were also performed using extrapolated information from both terrestrial and current satellite communications providers. The throughput and cost estimates were used to compare the concepts.

Throughput and cost information were compiled for a number of possible D3/D4 architectures using both currently available Government and commercial X-band and K-band services. Contact times were calculated for NASA low-Earth-orbit spacecraft at two different orbital inclinations, one for the International Space Station and one for polar orbiters. The table presents throughput results for three different cases at the space station's orbital inclination.

The service categories shown in columns two and three represent possible D4 service between spacecraft in low Earth orbit and the ground station using two different types of space-based transmitters in both simple duplex and relay configurations. As shown in column two, a duplex link using a single-beam phased array develops an average throughput of 210 Gbits per day, whereas a dual-beam phased array can average 221 Gbits per day (column three). Column four presents the average throughput of commercial services currently being used by NASA for direct-to-ground service. As shown, K-band services can provide greater average throughput at lower costs than the X-band service currently used.

Note that the throughput results for columns two to four are based on a 10-day average of contact times for four different ground station locations in the continental United States. Among the possible architectures, the most promising is the dual-mode combination. The dual-mode architecture combines a simplex high-data-rate direct downlink, using the user datagram protocol (UDP) instead of transmission control protocol (TCP), combined with a low-data-rate, full-duplex TCP/IP link using a satellite communications service such as Inmarsat or the Tracking and Data Relay Satellite System (TDRSS) Multiple Access. The high-data-rate link would be used for returning latency-tolerant instrument data from the spacecraft. The low-data-rate link would be used for real-time interactive commands between the principal investigator and the spacecraft and would be available all the time, instead of only when the spacecraft was in view. Copies of the study can be requested from Lawrence Wald, project manager.

Glenn contact:
Lawrence W. Wald, 216–433–5219,
Lawrence.W.Wald@grc.nasa.gov

Author: Science Applications International Corporation (SAIC)

Headquarters program office: OSF

Programs/Projects:
Satellite networking applications for HEDS and Earth Science

Aeronautical Satellite-Assisted Process for Information Exchange Through Network Technologies (Aero-SAPIENT) Conducted

Broadband satellite communications for aeronautics marries communication and network technologies to address NASA's goals in information technology base research and development, thereby serving the safety and capacity needs of the National Airspace System.

This marriage of technology increases the interactivity between airborne vehicles and ground systems. It improves decision-making and efficiency, reduces operation costs, and improves the safety and capacity of the National Airspace System.

To this end, a collaborative project called the Aeronautical Satellite Assisted Process for Information Exchange through Network Technologies, or Aero-SAPIENT, was conducted out of Tinker AFB, Oklahoma, during November and December 2000.

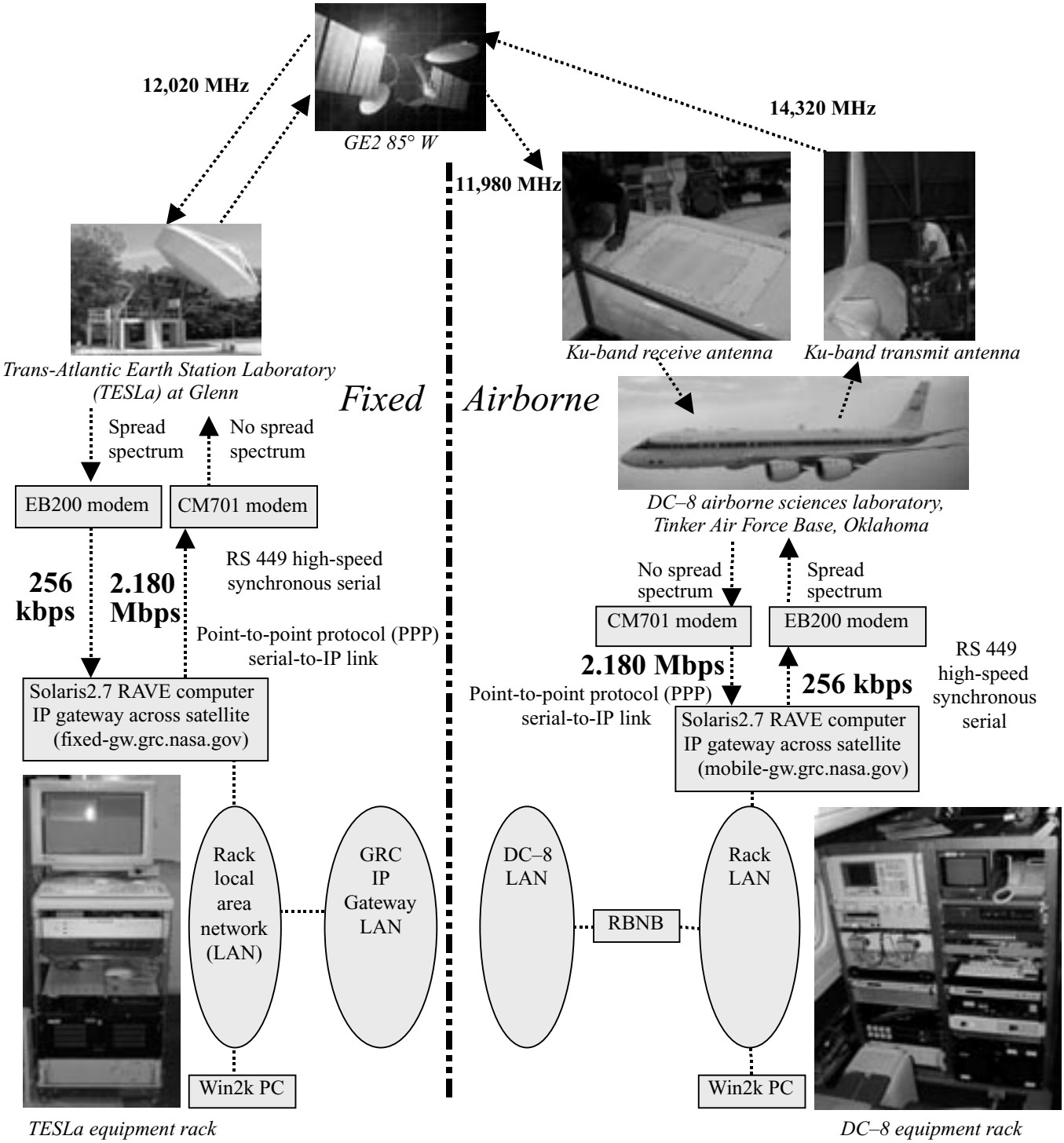

SAPIENT system overview.

The NASA Glenn Research Center provided bidirectional broadband satellite communication technology and datalink, including an electronically scanned, low-profile phased-array antenna system developed through a NASA-Boeing partnership. Glenn also contributed multiprotocol network technology, the architecture, and a suite of applications to be tested. The system architecture is depicted in the preceding figure.

The experiment flew on NASA's DC–8 Airborne Sciences Laboratory operated by the NASA Dryden Flight Research Center. Dryden also tested a Java-based measurement network and data transport

middleware concept called the Ring Buffered Network Bus, or RBNB. The RBNB provided simultaneous onboard data archival and online distribution of multiple flight data streams over the satellite link to a nationwide network of destinations on the ground. Some of these data streams were encrypted with public key infrastructure (PKI) technology.

The mission successfully demonstrated real-time data link technology to move and distribute unique and distinct flight data to multiple sites in real time while addressing multilevel priorities in a secure, high-integrity data-sharing environment. Specific to the NASA Information Technology Program, the Aero-SAPIENT project achieved these level 1 milestones: flight-demonstrated technology to move and distribute unique and distinct flight data, addressed multilevel priorities, enabled real-time distribution to three NASA Centers (Glenn, Dryden, and the Ames Research Center), and developed a communications architecture for distinct, concurrent data streams of differing priority in a secure, authenticated high-integrity environment.

This mission was a collaborative effort that successfully pioneered in-flight network communications technology, enabling various simultaneous applications to be conducted at bidirectional rates 100 times greater than what is operational in today's National Airspace System. The applications employed various link, network, and transport protocols, which included VoIP (voice), FTP (file transfer), TTCP (capacity test tool), E-mail, HTTP (web browsing, weather access, web-server-provided DC–8 Digital Air Data System), Controller-Pilot Data Link

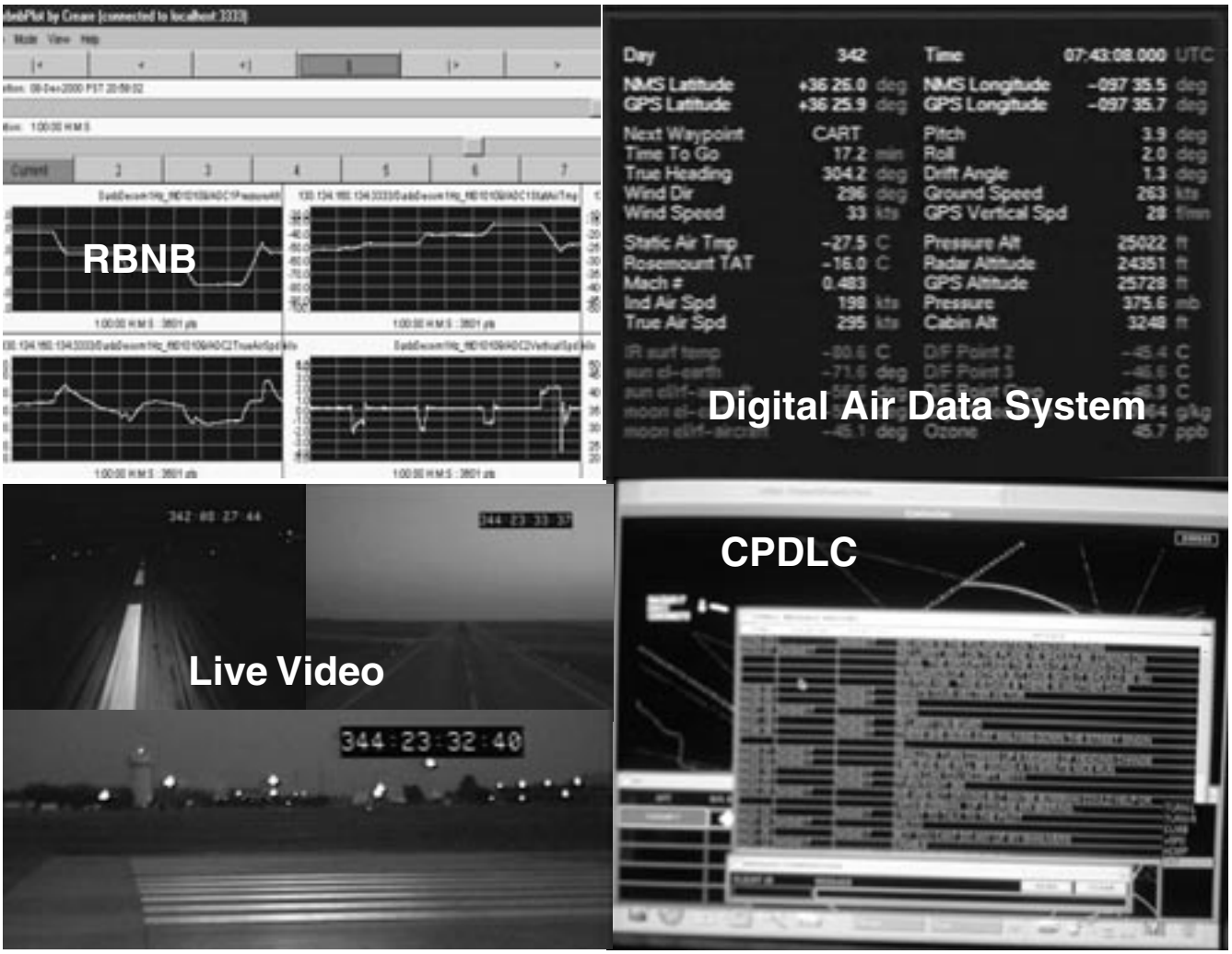

Simultaneous bidirectional applications included the Ring Buffered Network Bus (RBNB), onboard vehicle information via the Digital Air Data System, live video from several onboard cameras, and Controller-Pilot Data Link Communication (CPDLC).

Communication (using the Aeronautical Telecommunication Network, ATN, protocol), Sun Forum (duplex video, white boards, text), SSH (secured remote access), Ring Buffered Network Bus (Java middleware, cache management, stream proxy services), and authentication (PKI). Examples of some of these are shown in the preceding figure.

In addition to constructing a network architecture that included a mobile platform and simultaneous bidirectional applications, the evaluation of the physical electrical interconnect and the network performance was of particular interest in understanding a high-integrity communications environment. Because this mission was the first flight of the prototype Ku-band antenna system, the antennas were characterized in a variety of flight profiles that included different combinations of roll, pitch, and heading with regard to the geostationary satellite. The experimental link performed extremely well, yielding data transfers of approximately 2.1 Mbits/sec onto the aircraft, and 256 kbits/sec from the aircraft to the ground network that extended across the Nation. The data rates were limited by the installed firmware on the various modems used in the network, and could be increased by upgrading to the latest modem firmware revisions. Extreme flight profiles (e.g., a 45° change in roll coupled with a 50° change in heading) were purposely flown to determine the threshold of sustaining the communication link. This also provided the opportunity to understand the relationship between the antenna system performance (shown in the next graph) and the network recovery (shown in the graph on the following page), during a particular flight profile or system event.

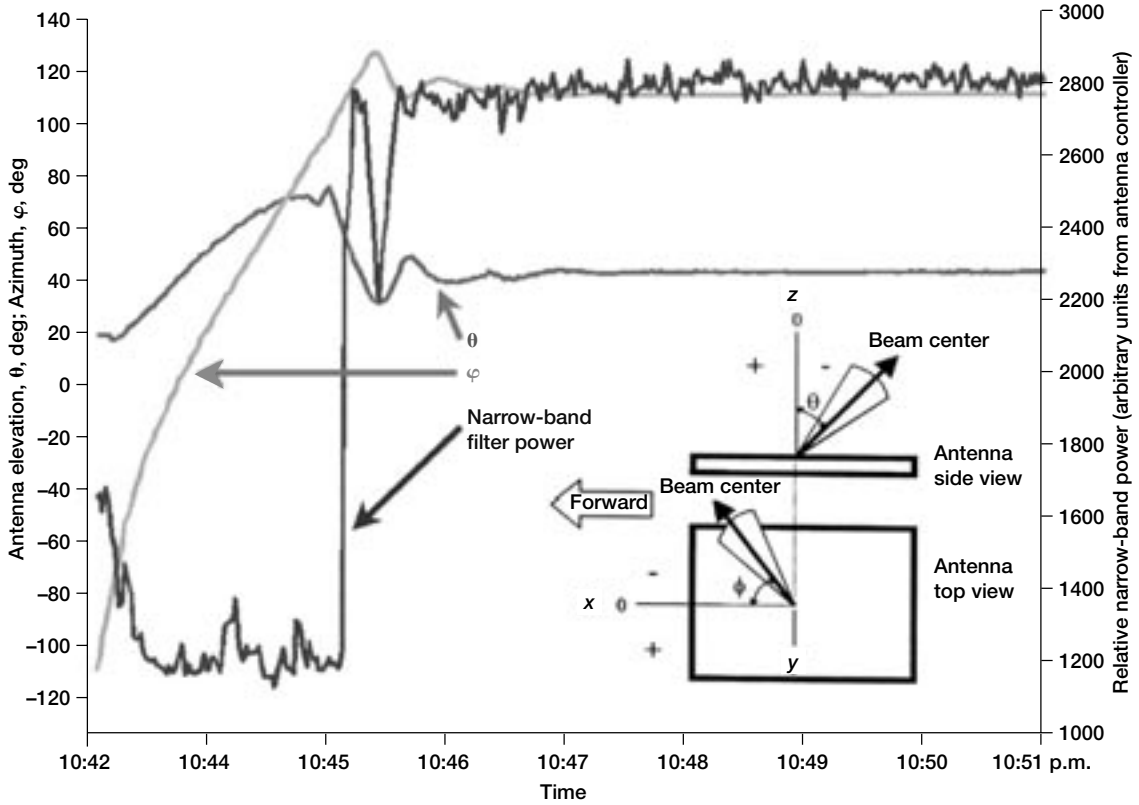

Antenna system performance conducted under a severe flight profile. December 8, 2000, Boeing antenna statistics.

These NASA technology investments for airspace safety and capacity have resulted in commercialization opportunities. Two such examples are the forthcoming Connexion by Boeing service utilizing phased-array antenna technology and the available DataTurbine software server by Creare, Inc., which is based on the Ring Buffered Network Bus concept. As a testimony to this achievement, both Glenn and Dryden were given the NASA 2001 Turning Goals Into Reality award for Commercializing Technology.

Headquarters program office: OAT

Programs/Projects: IT Base, Aero-SAPIENT (Aviation Capacity Program, AvSP)

Special recognition: 2001 NASA Turning Goals Into Reality award

Glenn contact:
Michael J. Zernic, 216–433–5286, Michael.J.Zernic@grc.nasa.gov

Author: Michael J. Zernic

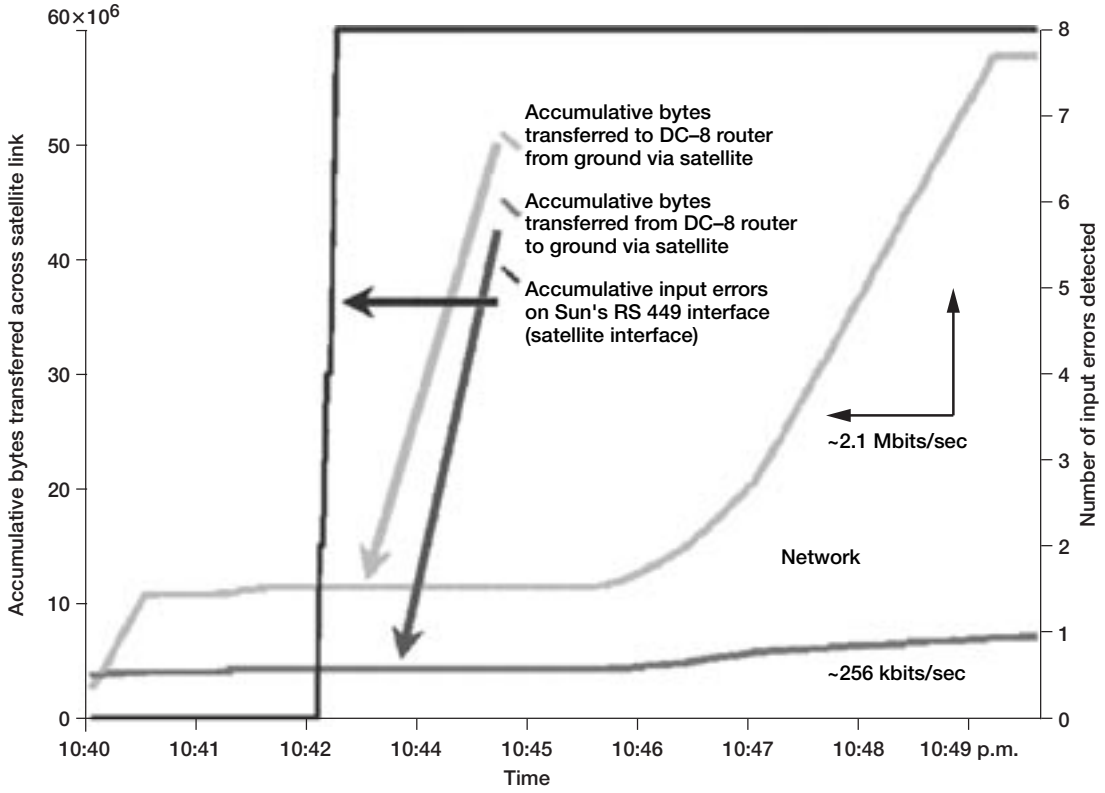

Network recovery during an interrupted communications link caused by an extreme flight profile. December 8, 2000, DC–8 airborne router satellite link utilization.

Microgravity Science

Bi-Component Droplet Combustion Experiment Designed

The combustion of liquid fuels is a major source of energy in the world today, and the majority of these fuels are burned in the form of a spray. The research at the NASA Glenn Research Center in droplet combustion has the overall goal of providing a better understanding of spray combustion by studying the smallest element in a spray, the single droplet. Practical fuels are multicomponent in nature; that is, they are composed of a large number of constituents. The Bi-Component Droplet Combustion Experiment (BCDCE) extends the work at Glenn from pure, or single-component, fuels to an idealized liquid fuel composed of two completely miscible components. The project is a collaborative effort between Glenn and Prof. B.D. Shaw of the University of California, Davis.

When a liquid droplet burns, fuel vaporizes from the droplet surface where it convects and diffuses to the flame front. A fuel component can only vaporize if it is present at the droplet surface. As a result, the combustion behavior of a multicomponent liquid fuel droplet is a strong function of the flow inside the droplet. These liquid flows can be caused by a number of factors, but the predominant force is a surface tension gradient along the surface of the droplet. These gradients can be relatively large and can cause significant motion throughout the droplet.

The BCDCE project is planned to fly onboard the International Space Station in the Multi-User Droplet Combustion Apparatus. The unique feature of this experiment is that it will be the first droplet combustion experiment to perform a detailed characterization of the flow inside a liquid fuel droplet.

The experiment will use a relatively new technique called Digital Particle Imaging Velocimetry (DPIV) to characterize the liquid flow. In this technique, very small (~5-μm-diameter) particles are dispersed throughout a liquid droplet. These particles are illuminated by a thin laser sheet. Images of the particle motion are recorded on a computer, which then tracks the motion of the particles to determine the flow characteristics.

These two images show some sample results from the DPIV apparatus. On the left is an image of the particles inside the droplet. On the right is a vector plot of the particles that results from the analysis of two consecutive images (i.e., the velocity of the particle is the distance traversed between consecutive frames divided by the time between frames).

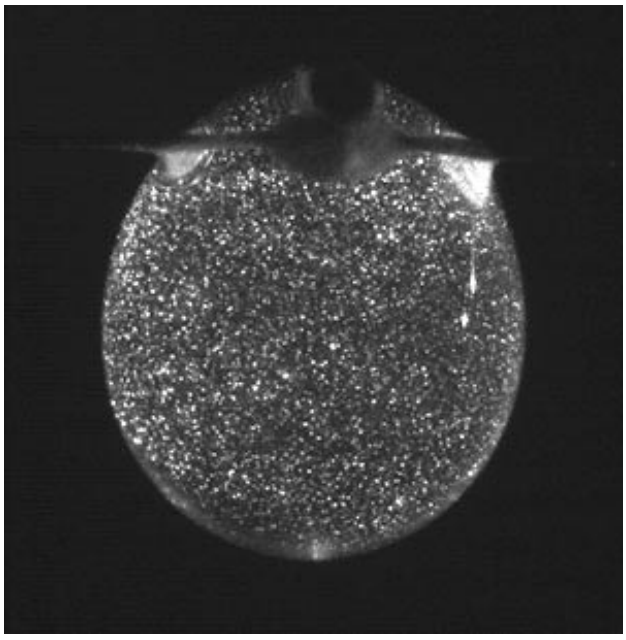

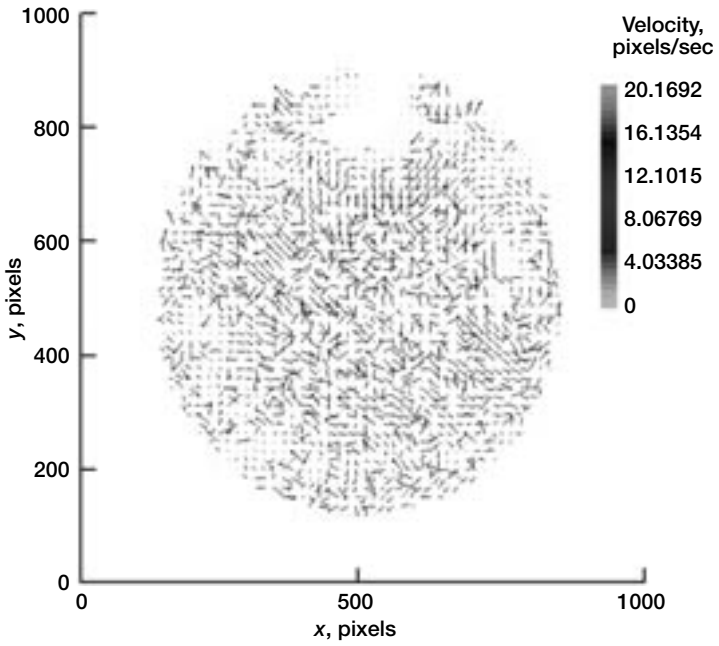

Left: Particle image. Right: Vector plot.

These data, combined with images of the flame and droplet (and other diagnostics) obtained in the Multi-User Droplet Combustion Apparatus, will be analyzed to determine the combustion characteristics of the droplet. These results will then be compared with detailed numerical predictions performed by Prof. Shaw to yield a more complete fundamental understanding of the mechanisms governing the combustion of practical fuels. This improved understanding will lead to improved efficiency for future combustors.

Glenn contact:
Dan L. Dietrich, 216–433–8759,
Daniel.L.Dietrich@grc.nasa.gov

Author: Daniel L. Dietrich

Headquarters program office: OBPR

Programs/Projects:
Microgravity Science

Combustion of Interacting Droplet Arrays Being Studied

The combustion of liquid fuels is a major source of energy in the world today, and the majority of these fuels are burned in the form of a spray. This droplet combustion project at the NASA Glenn Research Center has the overall goal of providing a better understanding of spray combustion by extending existing studies of single droplets to a regime where droplet interactions are important (as occurs in a practical spray). The Combustion of Interacting Droplet Arrays is a collaborative effort between Glenn and the National Center for Microgravity Research. The group at Glenn also collaborates with scientists at the National Institute of Advanced Industrial Science and Technology in Hokkaido, Japan.

The project is studying the combustion of a small number of droplets suspended on small quartz fibers in a 0.1-atm combustion chamber. Data consist primarily of video images of the flames and droplets. The tests are being conducted in Glenn's reduced-gravity facilities (2.2-sec and 5.2-sec drop towers) and in the Japan Microgravity Center's 10-sec drop tower (JAMIC).

These two pictures show flame images from a single droplet (top) and a binary droplet array (bottom). The droplet size is the same in both pictures (the two droplets in the binary array are also equal in size). These images clearly show that the flame surrounding the droplet array is larger, as expected, and much dimmer. The dimness of the flame surrounding the droplet array implies that the flame is much weaker. Analysis of the droplet size data shows that the burning rate of the fuel droplets in the binary array is slower than that of the single droplet, again implying a weaker flame.

Recent work on this project has focused on comparing the extinction limits of binary arrays

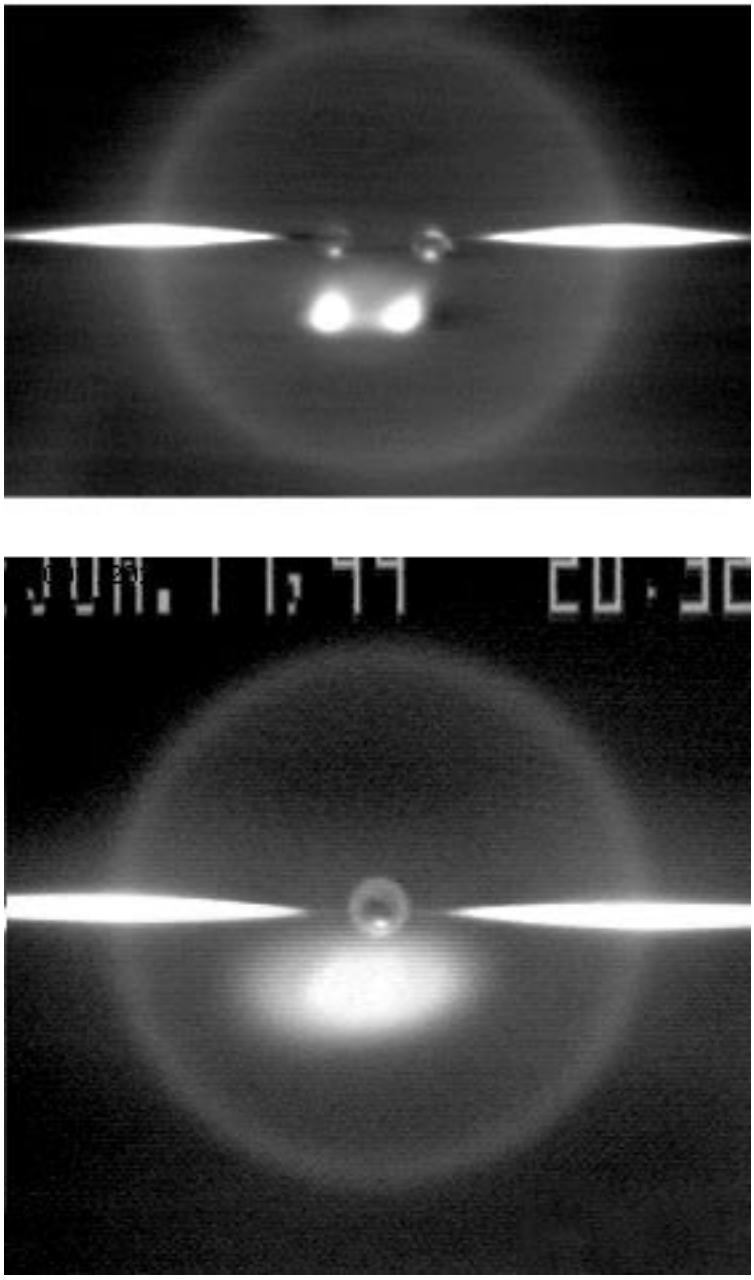

Top: Single droplet. Bottom: Binary array.

with those of single droplets. The results show that under certain ambient conditions (ambient pressure, ambient oxygen mole fraction, and diluent gas) droplet-droplet interactions can promote or enhance flame stability and that under other ambient conditions the opposite occurs (a single droplet has a more stable flame). The difference is related to the importance of radiative loss from the flame zone. For conditions where radiative loss from the flame zone is not important, interactions promote flame stability. If radiative loss is important, a single droplet will have a more stable flame. The latter condition applies to the images shown here (the single droplet has the more stable flame). The results from this work will be applied to droplet and spray combustion models to improve our ability to design spray combustors.

Glenn contact:
Dan L. Dietrich, 216–433–8759,
Daniel.L.Dietrich@grc.nasa.gov

Author: Daniel L. Dietrich

Headquarters program office: OBPR

Programs/Projects:
Microgravity Science

Dynamics of Diffusion Flames in von Karman Swirling Flows Studied

Von Karman swirling flow is generated by the viscous pumping action of a solid disk spinning in a quiescent fluid media. When this spinning disk is ignited in an oxidizing environment, a flat diffusion flame is established adjacent to the disk, embedded in the boundary layer (see the illustration to the right). For this geometry, the conservation equations reduce to a system of ordinary differential equations, enabling researchers to carry out detailed theoretical models to study the effects of varying strain on the dynamics of diffusion flames. Experimentally, the spinning disk burner provides an ideal configuration to precisely control the strain rates over a wide range.

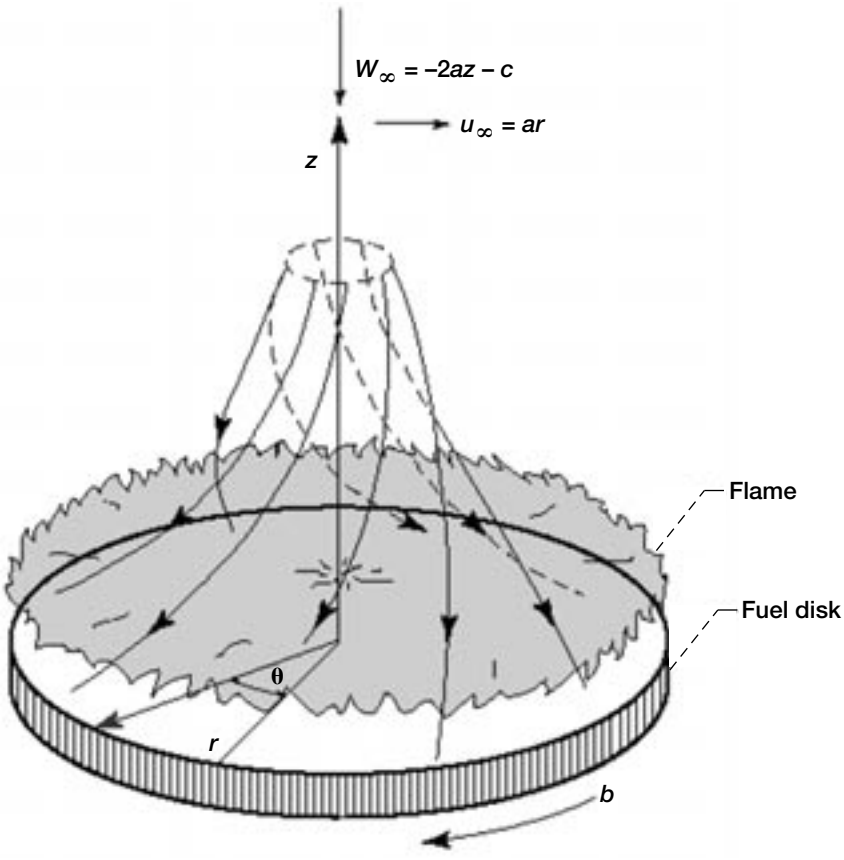

Von Karman swirling flow with an imposed forces flow, where c is the combined strain rate $(a^2 + b^2)^{1/2}$, a is the rotational speed of the disk, and b is the free-stream strain.

Our original motivation at the NASA Glenn Research Center to study these flames arose from a need to understand the flammability characteristics of solid fuels in microgravity where slow, subbuoyant flows can exist, producing very small strain rates. In a recent work (ref. 1), we showed that the flammability boundaries are wider and the minimum oxygen index (below which flames cannot be sustained) is lower for the von Karman flow configuration in comparison to a stagnation-point flow. Adding a small forced convection to the swirling flow pushes the flame into regions of higher strain and, thereby, decreases the range of flammable strain rates, as illustrated in the following graph.

Experiments using downward facing, polymethylmethacrylate (PMMA) disks spinning in air

revealed that, close to the extinction boundaries, the flat diffusion flame breaks up into rotating spiral flames (refs. 2 and 3). Remarkably, the dynamics of these spiral flame edges exhibit a number of similarities to spirals observed in biological systems, such as the electric pulses in cardiac muscles and the aggregation of slime-mold amoeba. The tail of the spiral rotates rigidly while the tip executes a compound, meandering motion sometimes observed in Belousov-Zhabotinskii reactions. The figure to the right shows a sequence of false-color images of these spiral flames.

Recently, we further explored the pattern-forming regions close to the extinction boundary using a gas-fueled, porous-disk burner (ref. 4). Experiments reveal a rich variety of complex patterns that depend on the fuel flow rate and the disk rotation speed. Theoretical models to describe these observations using activation energy asymptotics are currently underway (ref. 5).

These results will improve the interpretation of turbulent flames and flammability limits. This work is being done at the National Center for Microgravity Research at the NASA Glenn Research Center in collaboration with Prof. Forman Williams from the University of California, San Diego.

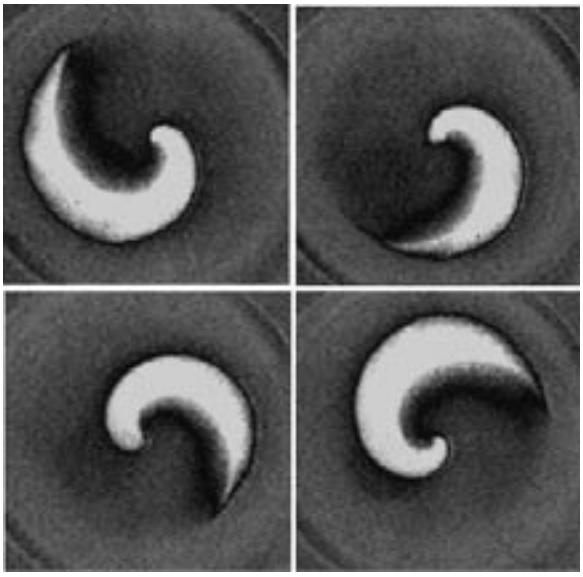

Typical false-colored images of spiral flames; the fuel disk rotates clockwise and the spiral counter-clockwise. This figure is shown in color in the online version of this article (http://www.grc.nasa.gov/WWW/RT2001/6000/6711nayagam.html).

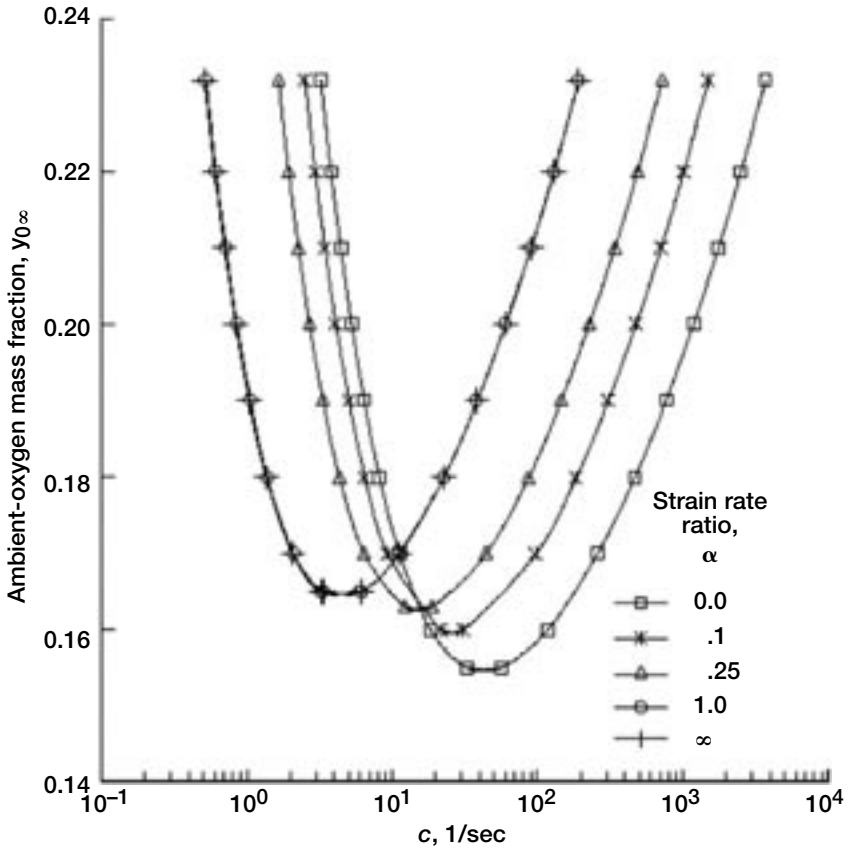

Flammability boundaries for PMMA: c is the combined strain rate $(a^2 + b^2)^{1/2}$, where a is the rotational speed of the disk, b is the free-stream strain, and α is the ratio a/b.

References

1. Nayagam, V.; and Williams, F.A.: Diffusion-Flame Extinction for a Spinning Fuel Disk in an Oxidizer Counterflow. Proceedings of the Combustion Institute, vol. 28, 2000, pp. 2875–2881.
2. Nayagam, V.; and Williams, F.A.: Rotating Spiral Edge Flames in von Karman Swirling Flows. Phys. Rev. Lett., vol. 84, no. 3, 2000, pp. 479–482.
3. Nayagam, V.; and Williams, F.A.: Diffusion-Flame Dynamics in Von Kármán Boundary Layers. Comb. Flame, vol. 125, nos. 1/2, 2001, pp. 974–981.
4. Nayagam, Vedha; and Williams, Forman A.: Pattern Formation in Diffusion Flames Embedded in von Karman Swirling Flows. Sixth International Microgravity Combustion Workshop, NASA/CP—2001-210826, 2001, pp. 97–100. http://gltrs.grc.nasa.gov/GLTRS/
5. Nayagam, Vedha; and Williams, Forman A.: Lewis-Number Effects on Edge-Flame Propagation. Accepted for publication. J. Fluid Mech., 2002.

NCMR contact:
Dr. Vedha Nayagam, 216–433–8702, Vedha.Nayagam@grc.nasa.gov

Authors: Dr. Vedha Nayagam and Forman A. Williams

Headquarters program office: OBPR

Programs/Projects: Microgravity Science

Flow and Transport of Granular Materials Studied

The flow of granular materials is of fundamental interest because of the prevalence of these materials in the pharmaceutical, agricultural, food service, and power industries, as well as others. The transport and handling operations of these materials is performed using hoppers, chutes, and belt and pneumatic conveyers. It has been estimated that related industries total one trillion dollars a year in gross sales in the United States and that they operate at only 63 percent of capacity. By comparison, industries that rely on fluid transport processes operate at 84 percent of design capacity (ref. 1).

Of particular interest to NASA, the exploration and colonization of extraterrestrial bodies will require us to address the effects of reduced gravity on granular materials, and their transport and handling operations. Specifically, granular materials found in Lunar and Martian soils can be utilized for foundation and construction purposes, and in materials processing for the extraction of valuable resources.

Granular materials exhibit very complex behavior, behaving at times like solids and at other times like fluids (liquids and gases). This dual nature leads to very complex and rich behavior, which is presently not well understood. When in a solidlike state, the load bearing is taken up heterogeneously by a finite number of stress chains, which can lead to local high-stress concentrations in the interior and walls of the system. The dynamics are such that any generated stress fluctuations, because of disturbances at the boundaries and the internal rearrangement of particles or flow conditions, are propagated as acoustic and solitary (soliton) waves along the stress chains. A prime example of a granular flow is an avalanche. Such a flow phenomenon consists of several flow regimes, ranging from the fast (dilute) flows of the particles near the top of the falling particle layer which undergo many collisions with different particles, to the slow (dense) flow near the bottom of this layer, where there is significant contact time between neighboring particles. All these stress-related and flow dynamics are very sensitive to gravitational loading conditions. It is clear that there is a great need to better understand the dynamic properties of these materials.

At the NASA Glenn Research Center, we have several research programs underway to study these related phenomena. They include (1) the impaction of two- and three-dimensional granular systems, (2) two-dimensional dense Couette flow, (3) shock absorption using granular particles, (4) detection of buried objects in granular beds, and (5) investigation of granular slug flows with electrostatic effects.

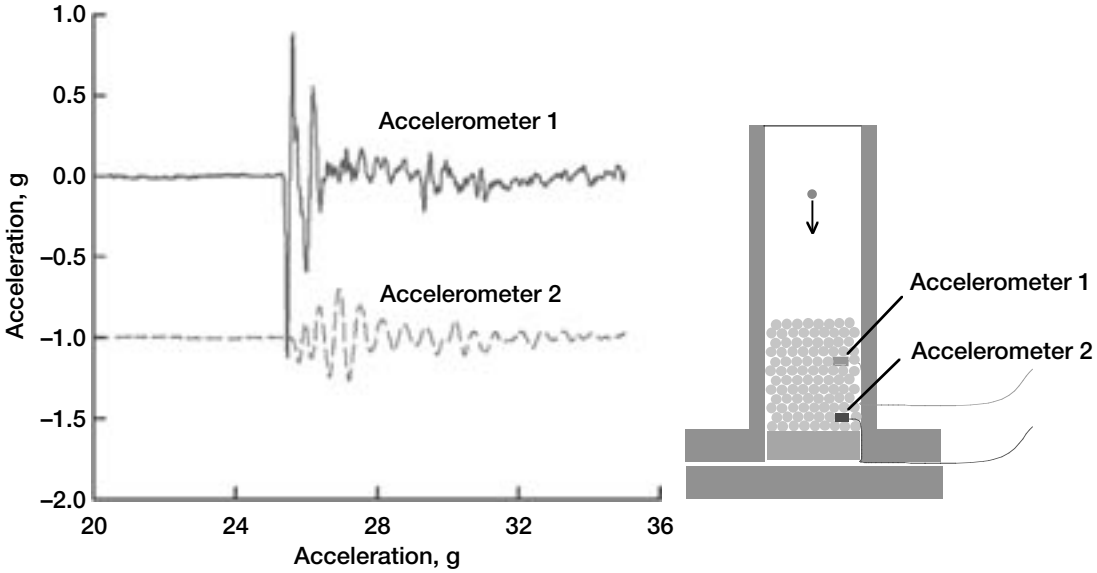

Acceleration signals from the granular bed impaction experiment. The propagation of the acoustic wave through the granular bed produces a delayed response on the second accelerometer. Data reduction of these signals will provide valuable correlation and spectral information on the acoustic wave.

For the impaction studies, acoustic waves are produced and then analyzed using time and spatial correlation measurements. For the two-dimensional granular Couette system, employing a roughened inner moving surface, photoelastic disks are used to create birefringence images to investigate the force chain fluctuations. The particles are levitated to isolate them from the frictional surface.

Granular particles also have the potential to serve as shock absorbers. We are testing a prototype shock absorber made of granular particles that can attenuate an impact load by up to 80 percent. In addition, we are using the backscattering of acoustic waves to probe granular systems for inhomogeneities such as minerals in granular soils. This method could be extended to detect different types of buried objects.

The pneumatic conveyance of granular particles, which suffers significantly from inefficient transport modes and jamming is very important to industry. As an alternative transport mode, we have started studying the slug flow mode in granular materials and the effects of electrostatics on the flow.

In support of these research efforts, we have set up and developed a few diagnostic techniques for probing the dynamics of granular systems. The first is the capability to perform high-resolution dynamic measurements of acceleration/vibrations, pressure, and forces. This technique provides valuable dynamic information on the propagation of stresses and waves, and system response. We are also using birefringence-imaging techniques to visualize force chains, and high-speed video to look at the dynamics of certain systems. Lastly, we are developing Magnetic Resonance Imaging (MRI) capabilities and hope to take advantage of this powerful technique to probe the dynamics of the interior of granular systems. To address gravitational effects, we will probably run future experiments in reduced-gravity facilities.

Reference

1. Merrow, Edward W.: A Quantitative Assessment of R&D Requirements for Solids Processing Technology. Rand Corp. Report R–3216–DOE/PSSP, 1986.

Glenn contacts:
Dr. Juan H. Agui, 216–433–5409, Juan.H.Agui@grc.nasa.gov; and
Dr. R. Allen Wilkinson, 216–433–2075, R.A.Wilkinson@grc.nasa.gov

Author: Dr. Juan H. Agui

Headquarters program office: OBPR

Programs/Projects:
Microgravity Science

Dynamic Light-Scattering Probe Used for the Very Early Detection of Cataracts and to Measure Response to Therapy (or Treatment)

Half of all blindness worldwide is due to cataracts, and 34 million Americans over the age of 65 have cataracts. This figure is expected to rise to 70 million by the year 2030. Currently, no medical treatment is available to prevent or halt the progression of a cataract; nor is there any way to reverse a cataract once it has been detected by conventional methods. The only known treatment is surgical removal of the lens. It is estimated that over $5 billion will be spent this year for the treatment of cataract patients in the United States alone.

According to Carl Kupfer, M.D., former Director of the National Eye Institute at the National Institutes of Health, "A delay in cataract formation of about 10 years would reduce the prevalence of visually disabling cataracts by about 45 percent." However, this vision remains a dream because of the lack of objective methods that can be used to detect cataracts very early and, hence, can be used for screening potential anticataract drugs. This is about to change. The National Eye Institute and NASA entered into a formal interagency agreement in late 1996 to develop and test a dynamic light-scattering (DLS) device to detect the earliest changes due to cataract formation. The new DLS probe developed by Dr. Ansari at the NASA Glenn Research Center is several orders of magnitude more sensitive than conventional clinical systems. This ultrahigh sensitivity enables the probe to detect the onset of a cataract before it has any effect on vision and allows researchers to test the effectiveness of anticataract drugs in reversing cataracts. This device (see the following illustration) was originally designed to study transport phenomena in microgravity fluid

physics experiments onboard the space shuttle orbiters and space station. It will be very useful in testing anticataract drugs to halt or reverse the progression of cataracts during longitudinal clinical trials.

In light of this development, can we find a medical cure for cataracts? According to preliminary experimental data obtained recently in collaboration with the University of Washington School of Medicine in Seattle, the answer is likely yes. Professor John Clark has been advocating the use of the drug Pantethine as an anticataract agent for many years. Determination of its efficacy has remained elusive because of the lack of reliable techniques for noninvasive and quantitative detection of early cataracts. Experiments conducted with 12 rodents using the DLS probe show promising results. The probe was used in the static mode, in which the eye of the animal (cornea to retina) was scanned at a very low, safe laser power of 80 μW to collect photons, or scattered intensity, in steps of 10 μm (see the graph). The rodents studied were control, selenite injected, and selenite plus Pantethine injected animals.[1] Selenite was used to induce cataracts. Changes (increase in light scatter) could be seen in the eye lens as early as 1 day after the selenite injections. Pantethine injections slowed down these changes. Detailed data analysis is yet to be done, and more experiments are planned to confirm these findings. It is of significant importance that these subtle molecular changes are not noticeable when the animals are examined with conventional ophthalmic instruments because their lenses are completely transparent.

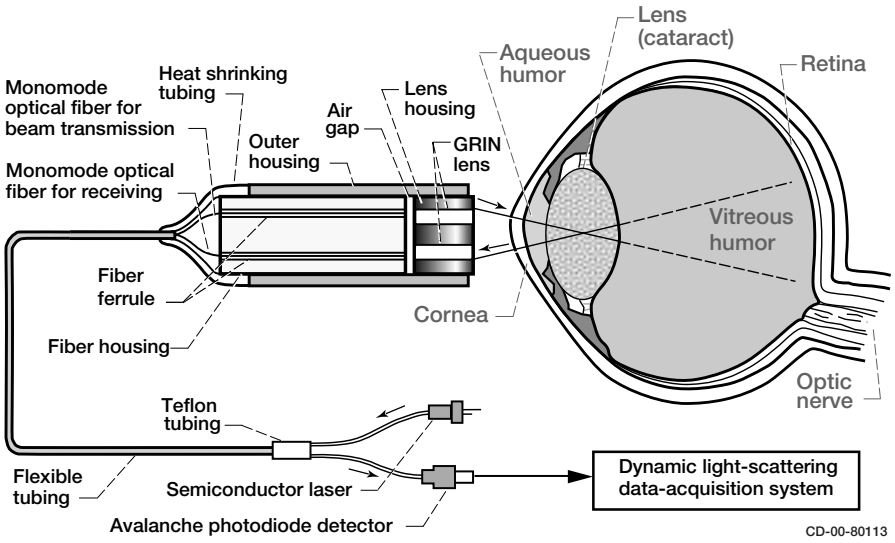

Fiber-optic probe for the early diagnosis of eye diseases.

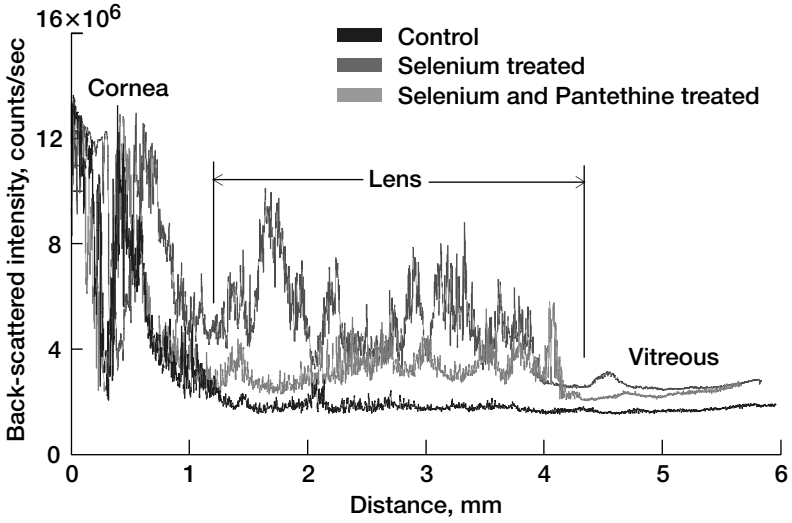

Cataract treatment in rats.

[1]Animal studies were conducted at the University of Washington in Seattle under the National Institutes of Health guidelines following the safe use of laboratory animals.

Glenn contact:
Dr. Rafat R. Ansari, 216–433–5008, Rafat.R.Ansari@grc.nasa.gov

Authors: Dr. Rafat R. Ansari, Dr. John I. Clark, and James F. King

Headquarters program office: OBPR

Programs/Projects:
Microgravity Science

Special recognition: STAIF (Space Technology and Applications International Forum) 2001 Outstanding Paper Award for the Conference on Space Radiation and Environment Effects for the paper entitled "Non-Invasive, Quantitative, and Remote Detection of Early Radiation Cataracts for Applications in Bio-Astronautics and Bio-Informatics" by Rafat R. Ansari, Frank Giblin (Oakland University), and James F. King (QSS/Glenn). U.S. Patent 5973779 awarded Oct. 26, 1999.

New Method Developed to Measure Contact Angles of a Sessile Drop

The spreading of an evaporating liquid on a solid surface occurs in many practical processes and is of importance in a number of practical situations such as painting, textile dyeing, coating, gluing, and thermal engineering. Typical processes involving heat transfer where the contact angle plays an important role are film cooling, boiling, and the heat transfer through heat pipes. The biological phenomenon of cell spreading also is analogous to a drop spreading (ref. 1). In the study of spreading, the dynamic contact angle describes the interfacial properties on solid substrates and, therefore, has been studied by physicists and fluid mechanics investigators. The dynamic contact angle of a spreading nonvolatile liquid drop provides a simple tool in the study of the free-boundary problem, but the study of the spreading of a volatile liquid drop is of more practical interest because the evaporation of common liquids is inevitable in practical processes.

The most common method to measure the contact angle, the contact radius, and the height of a sessile drop on a solid surface is to view the drop from its edge through an optical microscope. However, this method gives only local information in the view direction. Zhang and Yang (ref. 2) developed a laser shadowgraphy method to investigate the evaporation of sessile drop on a glass plate. As described here, Zhang and Chao (refs. 3 and 4) improved the method and suggested a new optical arrangement to measure the dynamic contact angle and the instant evaporation rate of a sessile drop with much higher accuracy (less than 1 percent). With this method, any fluid motion in the evaporating drop can be visualized through shadowgraphy without using a tracer, which often affects the field under investigation.

This illustration depicts an apparatus that simultaneously and synchronously records magnified ordinary top-view video images and laser-shadowgraph video images of a sessile drop. The shadowgraphs contain flow patterns indicative of thermocapillary convection (if any) within the drop. One can determine the time-dependent parameters of the drop—such as the contact diameter, contact angle, and evaporation rate—by measuring the apparent diameters in the timed sequence of images. The apparatus combines a collimated white-light beam and a collimated laser beam. A charge-coupled-device (CCD) camera connected to video system I

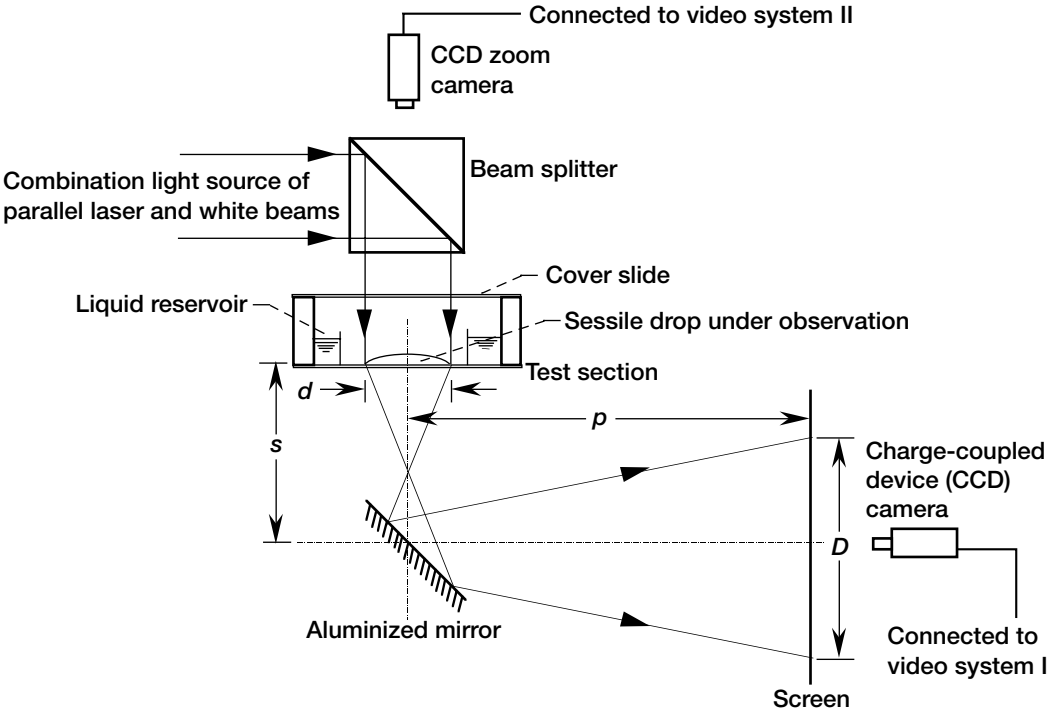

Apparatus for measuring spreading and contact angle.

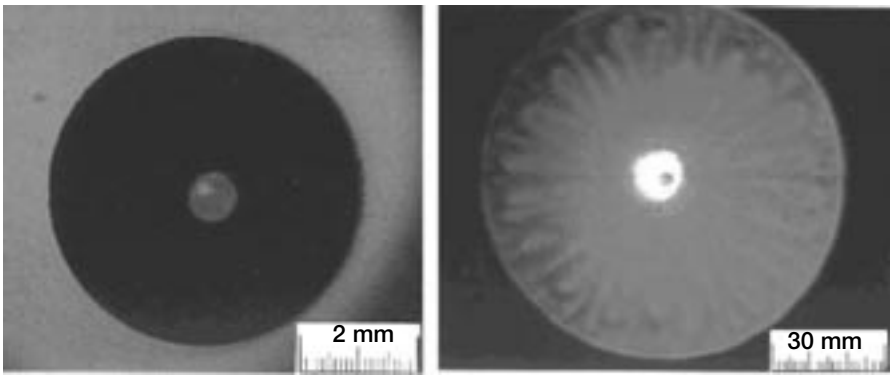

Sessile drop. Left: Typical top-view image. Right: Laser shadowgraphic image.

acquires the shadowgraph images, while a CCD zoom camera connected to video system II acquires the ordinary top-view images. Assuming that the drop takes the shape of a sphere cap, it can be considered as a plano-convex lens. The time-dependent contact angle is given by

$\theta(t) = arcsin \frac{d(t) + D(t)}{2(n-1)(s+p)}$, where n is the index of refraction of the liquid in the drop, s and p are the constant dimensions indicated in the illustration on the previous page, d is the time-dependent (t) diameter of the drop measured in the ordinary image acquired by video system II, and D is the time-dependent diameter of the shadowgraph acquired by video system I (as shown in the images above). This technology is currently under development at NASA Glenn Research Center's Fluids Physics Branch of the Microgravity Science Division.

References

1. Greenspan, H.P.: On the Motion of a Small Viscous Droplet That Wets a Surface. J. Fluid Mech., vol. 84, part 1, 1978, pp. 125–143.
2. Zhang, Nengli; and Yang, Wen-Jei: Natural Convection in Evaporating Minute Drops. J. Heat Transfer Trans. ASME, vol. 104, no. 4, 1982, pp. 656–662.
3. Zhang, Nengli; and Chao, David F.: A New Approach to Measure Contact Angle and Evaporation Rate With Flow Visualization in a Sessile Drop. NASA/TM—1999-209636, 1999. http://gltrs.grc.nasa.gov/GLTRS/
4. Chao, David F.; and Zhang, Nengli: Effects of Evaporation and Thermocapillary Convection on Volatile Liquid Droplets. J. Thermophysics Heat Trans., vol. 15, no. 4, 2001, pp. 416–420.

Glenn contact:
Dr. David F. Chao, 216–433–8320, David.F.Chao@grc.nasa.gov

Authors: Dr. David F. Chao and Dr. Nengli Zhang

Headquarters program office: OBPR

Programs/Projects:
Microgravity Science

Phase-Shifting Liquid Crystal Interferometers Demonstrated

The advent of computer control and analysis algorithms in the 1980's increased interferometric precision by two orders of magnitude with a concept called phase-shifting interferometry. These new interferometers changed the phase of the reference beam relative to the test beam by known integer multiples of fractions of π. Interferograms were recorded on CCD cameras in sets that completed one cycle of 2π. A pixel-by-pixel analysis using the intensity as a function of the phase step determined the phase at each pixel. Because the phase of the reference beam had to be shifted, essentially all these new interferometers separated the test and reference beams by a large physical distance. Although such data were advantageous for interferometry, even small vibrations degraded them.

In the mid-1990's, personnel at the NASA Glenn Research Center developed a common-path interferometer capable of phase shifting (ref. 1). A derivative of the classic Point Diffraction Interferometer, this device used a liquid crystal cell as the basis for operation. A sphere within the cell was used as the diffracting element that created the reference beam. Varying the ac voltage applied to the liquid crystal layer altered the phase of the test beam. However, the optical density of the liquid crystal varied as the voltage was applied, thus causing the transmitted intensity to change with the phase step. Furthermore, several seconds were required to complete a data set. Finally, since the cell used thousands of the spheres as spacers, locating an interference pattern free of fringe noise from other spheres was a time-consuming process of trial and error.

Beginning in 2000, personnel at Glenn and the University of Rochester's Laboratory for Laser Energetics teamed to develop

Liquid Crystal Point Diffraction Interferometers that avoid these difficulties. To date, they have demonstrated a 25-mm square cell with a total thickness, including glass, of 5.9 mm that can switch at 120 msec per phase step. It uses only four widely separated spacer spheres and minimizes the change in optical density as a function of applied voltage. The top figure is a sample interferogram recorded with this device. Further development will focus on reducing the size of the diffracting object, thus permitting the use of lenses with lower F-numbers. In addition, the team will focus on decreasing the switching time to be compatible with video frame rates.

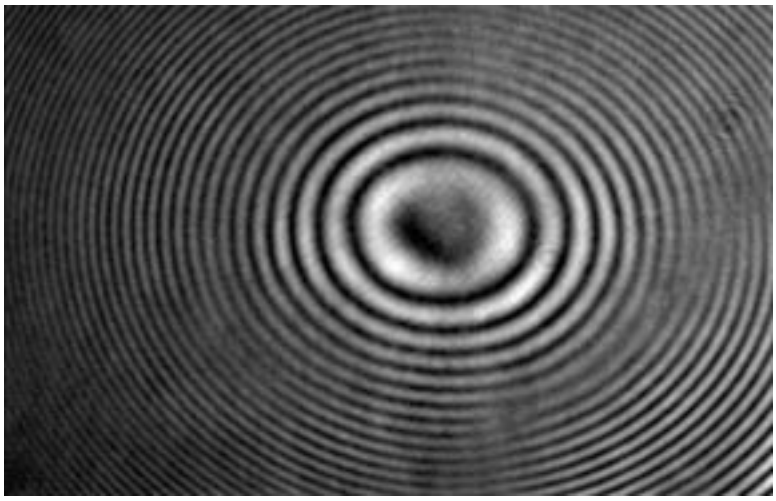

Interferogram from Liquid Crystal Point Diffraction Interferometers.

In a parallel effort, Glenn personnel demonstrated a phase-shifting shearing interferometer using a commercial liquid crystal retarder tilted 45° to incident light. This device, which was not optimized for interferometry, recorded a complete set of phase-shifted interferograms (ref. 2). The bottom figure displays the complete set of interferograms. In these images, the fiducial mark is for reference when viewing the phase shift. Since the device was not optimized for this application, spurious fringes, where the phase does not shift, are apparent in the upper right corner.

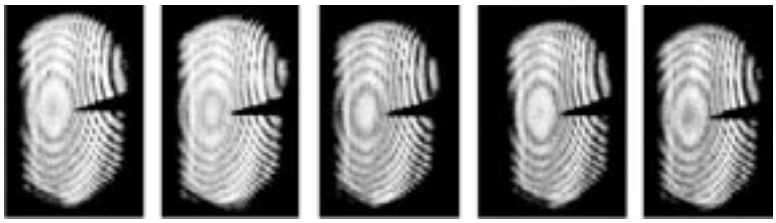

Interferogram set from the phase-shifting shearing interferometer.

References

1. Mercer, Carolyn R.; and Creath, Katherine: Liquid-Crystal Point-Diffraction Interferometer. Opt. Lett., vol. 19, no. 12, 1994, pp. 916–918.
2. Griffin, DeVon W.: Phase-Shifting Shearing Interferometer. Opt. Lett., vol. 26, no. 3, 2001, pp. 140–141.

Glenn contact:
Dr. DeVon W. Griffin, 216–433–8109,
DeVon.W.Griffin@grc.nasa.gov

Author: Dr. DeVon W. Griffin

Headquarters program office: OBPR

Programs/Projects:
Microgravity Science

Microscale Heaters Detailed Boiling Behavior in Normal Gravity and Microgravity

Pool boiling in microgravity is an area of both scientific and practical interest. Conducting tests in microgravity, as well as lunar and Martian gravity, makes it possible to assess the effect of the density difference between the vapor and liquid phases on the overall boiling process and to assess the relative magnitude of these effects in comparison to other "forces" and phenomena, such as surface tension forces, liquid momentum forces, and microlayer evaporation. The microscale heater developed under a NASA Glenn Research Center grant serves as a unique tool to probe the fundamental mechanisms associated with pool boiling.

An experimental package was designed and built by the University of Maryland and tested on the NASA Johnson Space Center KC–135 experimental aircraft and a NASA WFF Terrier Orion Sounding Rocket under NASA Grants NAG3–2228 and NCC3–783. A square array of 96 microscale

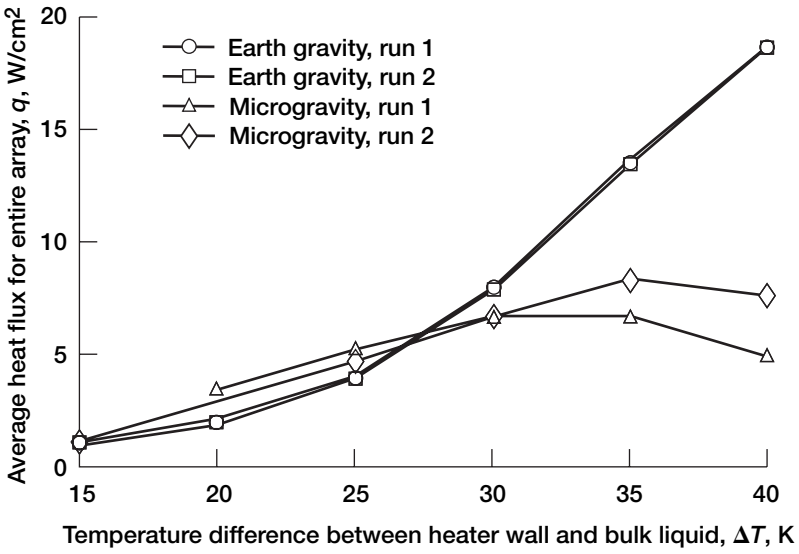

Array-averaged boiling curves at various gravity levels.

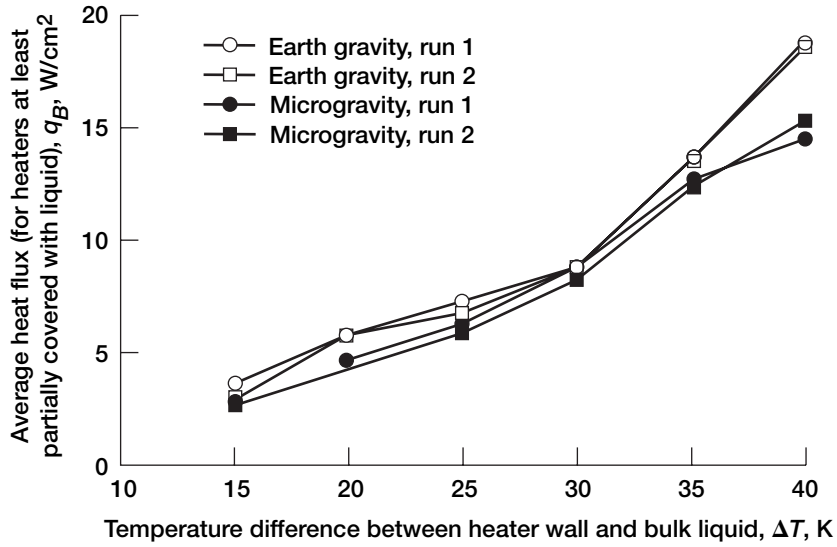

Modified-array-averaged boiling curves at various gravity levels using only heaters that were in contact with liquid or a liquid-vapor mixture.

heaters was constructed and installed into a special boiling chamber. A fluorinert, FC–72, was used as the test fluid. A variety of tests were conducted at different pressures, heater wall temperatures, bulk fluid temperatures, and gravity levels.

Data reduction indicates that gravity has little effect on boiling heat transfer when the wall temperature is no more than 25 °C above the average liquid temperature (see the top graph), even though there were vast differences in bubble behavior between gravity levels. At all these temperature differences in microgravity, a large primary bubble moved over the surface, occasionally causing boiling to occur. Smaller satellite bubbles surrounded this primary bubble. Once formed, the primary bubble's size remains constant for a given condition, indicating a balance between evaporation at the bubble base and condensation on the bubble cap. The size of the primary bubble increased with increasing temperature differences between the wall and liquid.

Modifying the preceding plot by averaging the heat flux from only heaters that had liquid contact produced boiling curves that were independent of the gravity condition (see the bottom graph). This suggests that the small-scale bubble behavior is not affected by gravity. Heat transfer from the heater surface occurred primarily through these small bubbles, and not much heat transfer was associated with the large bubble that occasionally formed on the surface when many small bubbles coalesced.

In the figures on the next page, color-coded maps that display the amount of local heat transfer are superimposed over photographic data. The bottom of the scale indicates negligible heat transfer, and the top of the scale indicates significant amounts of heat transfer. In general, the darker areas on these maps show areas of less heat transfer and the lighter areas show more. The bubble itself is an area of moderate heat transfer. Most of the heaters under the primary bubble indicated low heat transfer, suggesting that liquid dryout occurred on the heater surface. Almost all the power was consumed by the test fluid during periods when the heater was immersed either in liquid or in a two-phase mixture of vapor and liquid. Because of a surface-tension-induced flow in

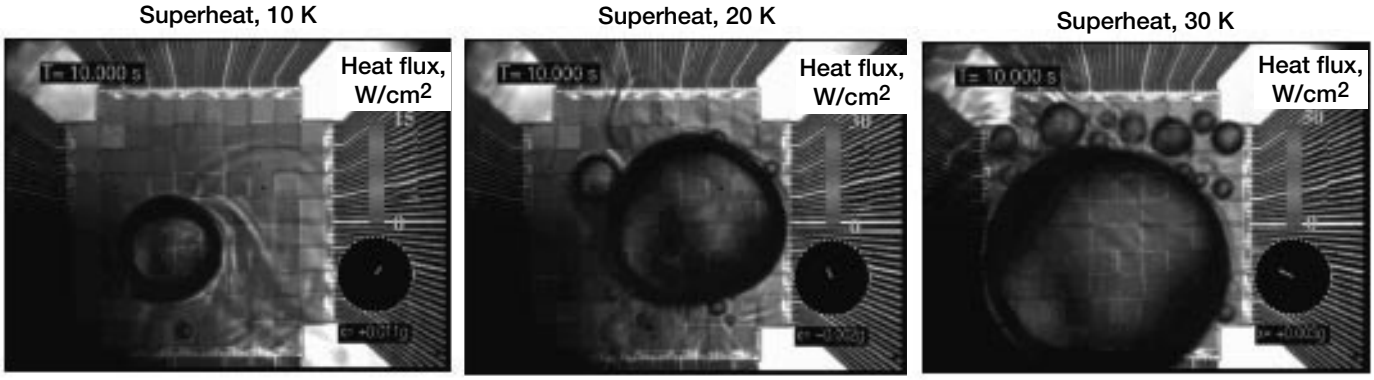

Spatially resolved heat transfer distributions relative to the position of vapor bubbles. This figure is shown in color in the online version of this article (http://www.grc.nasa.gov/WWW/RT2001/6000/6712mcquillen.html).

microgravity, a "jet" of fluid formed above the bubble into the bulk liquid and kept the bubble on the heater. As the superheat or temperature difference between the liquid and heater increased, the primary bubble became larger and more satellite bubbles were formed. By comparing these data, one can assess how the position and movement of the liquid and vapor phases affect the local heat transfer.

Find out more about this research:

Journal of Heat Transfer article, *Subcooled Pool Boiling Heat Transfer in Microgravity and Hi-g*: http://ojps.aip.org/journals/doc/JHTRAO-ft/vol_123/iss_4/620_1.html?jsessionid=1055681000550034717

Phase Change Heat Transfer Lab at University of Maryland:
http://www.glue.umd.edu/%7Ekimjh/

***Pool Boiling Heat Transfer Mechanism in Microgravity Using an Array of Surface-Mounted Heat Flux Sensors*:**
http://microgravity.grc.nasa.gov/6712/multiph/kim.htm

Glenn contact:
John B. McQuillen, 216–433–2876,
John.B.McQuillen@grc.nasa.gov

Author: John B. McQuillen

Headquarters program office: OBPR

Programs/Projects:
Microgravity Science

Novel Optical Technique Developed and Tested for Measuring Two-Point Velocity Correlations in Turbulent Flows

A novel technique for characterizing turbulent flows was developed and tested at the NASA Glenn Research Center. The work is being done in collaboration with the University of Pittsburgh, through a grant from the NASA Microgravity Fluid Physics Program. The technique we are using, Homodyne Correlation Spectroscopy (HCS), is a laser-light-scattering technique that measures the Doppler frequency shift of light scattered from microscopic particles in the fluid flow. Whereas Laser Doppler Velocimetry gives a local (single-point) measurement of the fluid velocity, the HCS technique measures correlations between fluid velocities at two separate points in the flow at the same instant of time. Velocity correlations in the flow field are of fundamental interest to turbulence researchers and are of practical importance in many engineering applications, such as aeronautics.

In analogy with a police radar gun, which measures speed from the Doppler shift of light reflected from a moving car, the HCS technique uses a laser as the source of "radar," and instead of large moving cars, detects light scattered by micrometer-sized particles that are introduced to the flow from a smoke cartridge. By combining the signals, or scattered light, from two separate points in the flow, the average velocity difference between the points can be measured. When fiber-optic probes are used to collect the scattered light, it is simple to vary the spacing between the two points. With our setup, we can probe velocity correlations at length scales from 0.2 to 32 mm. Measuring the average velocity difference, or correlations, as a

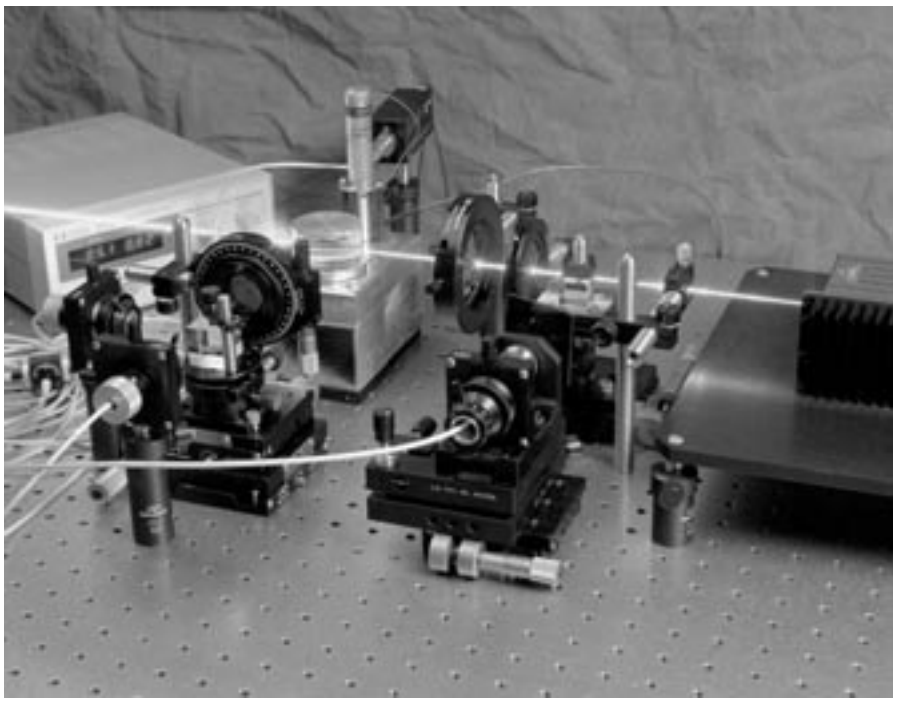

Optical system used to measure two-point velocity correlations in turbulent wind tunnel flows. A small fluid sample is used to align the optics.

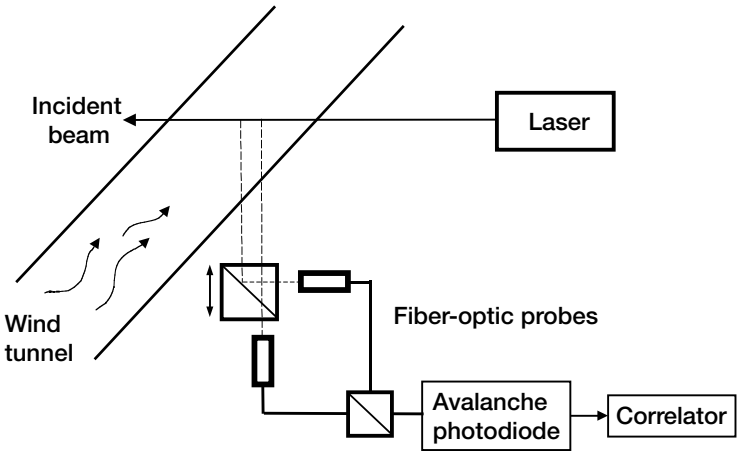

Homodyne Correlation Spectroscopy (HCS) optics. Fiber optics and a beam-splitter cube combine the scattered light from two points along the incident beam. An avalanche photodiode converts the light to an electrical signal, which is analyzed by the correlator.

function of the distance between the two points yields the structure function of the turbulent flow.

At Glenn, we tested the HCS technique with fiber-optic probes in a 20- by 20-cm wind tunnel at wind speeds from 2 to 30 m/sec. The incident laser was a 100-mW Nd:YAG laser, focused to a beam width of about 0.2 mm. Regin smoke cartridges (Shelton, CT) were used to produce a large quantity of particles at a near-constant rate. A grid mesh of 1-cm-diameter rods was used to generate the grid turbulence, which is considered a model turbulence system. By varying the wind speed and the spacing between fiber-optic probes, we successfully characterized the turbulence using this technique. Advantages of the HCS technique include characterizing turbulence at small length scales (down to 0.2 mm in our studies), nonintrusive probe of the velocity correlations, and direct measurements of two-point correlations, instead of invoking Taylor's frozen turbulence assumption.

This is the first application of the HCS technique to wind tunnel flows, and we have successfully demonstrated that the HCS technique is a powerful, simple method of characterizing velocity correlations in turbulent flows. The data obtained from the wind tunnel have been analyzed and are currently under review for publication. Some surprising results have emerged from our analysis, which could lead to a new and better understanding of turbulence.

Bibliography

Tong, P., et al.: Turbulent Transition by Photon-Correlation Spectroscopy. Phys. Rev. A, vol. 37, no. 6, 1988, pp. 2125–2133.

Zimmerli, G.A.; Min, K.Y.; and Goldburg, W.I.: Measuring the Probability Distribution of Velocity Differences Using Homodyne Correlation Spectroscopy. Proc. Soc. Photo. Opt. Instrum. Eng., vol. 3783, 1999, pp. 46–53.

Glenn contact:
Dr. Gregory A. Zimmerli, 216–433–6577, Gregory.A.Zimmerli@grc.nasa.gov

Authors: Dr. Gregory A. Zimmerli and Walter I. Goldburg

Headquarters program office: OBPR

Programs/Projects:
Microgravity Science, Aeronautics

Advanced Microgravity Acceleration Measurement Systems Being Developed

The Advanced Microgravity Acceleration Measurement Systems (AMAMS) project at the NASA Glenn Research Center is part of the Instrument Technology Development program to develop advanced sensor systems. The primary focus of the AMAMS project is to develop microelectromechanical (MEMS) acceleration sensor systems to replace existing electromechanical-sensor-based systems presently used to assess relative gravity levels aboard spacecraft. These systems are used in characterizing both vehicle and payload responses to low-gravity vibroacoustic environments. The collection of microgravity acceleration data has cross-disciplinary utility to the microgravity life and physical sciences and the structural dynamics communities. The inherent advantages of semiconductor-based systems are reduced size, mass, and power consumption, while providing enhanced stability.

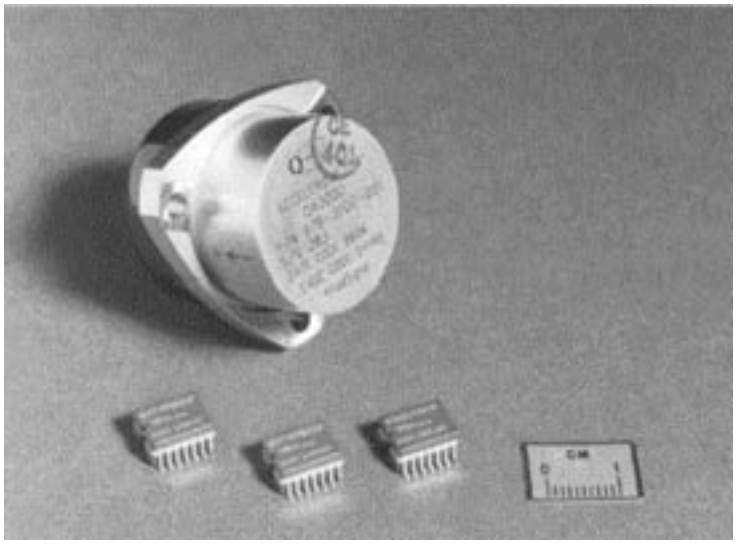

Size and volume were greatly reduced with the MEMS accelerometer. Top: Traditional force-balance accelerometer used for microgravity measurements. Bottom: MEMS accelerometer.

A market survey was conducted to examine the state of the art in MEMS accelerometers, focusing on the requirements for making low-gravity, high-resolution measurements. From this survey, the most suitable sensors were selected, and MEMS accelerometers in various stages of development have been received from vendors. In addition, appropriate signal-conditioning circuitry has been developed for the best performing sensors to facilitate benchtop and development testing. The goal of this first stage of testing is to demonstrate the capability to measure microgravity (10^{-6} g) levels during operations below 10 Hz. This frequency range is significant since the structural modes (when the structure rings) for the shuttles and the International Space Station are approximately 4.7 and 3.2 Hz, respectively.

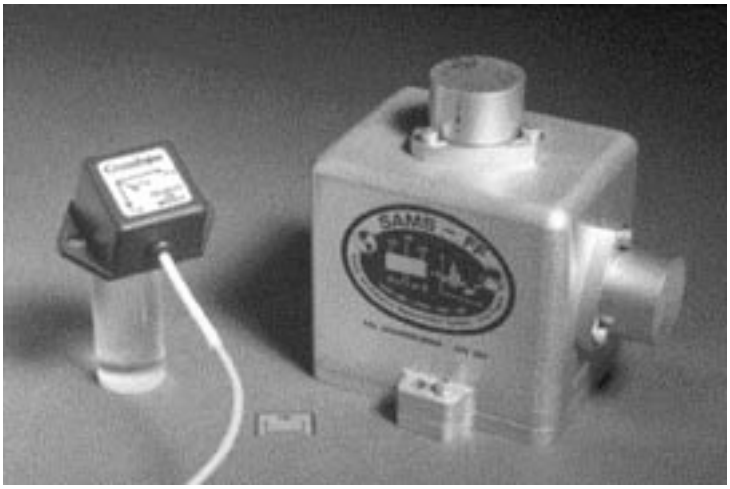

MEMS reduces the size of a triaxial accelerometer. Left: MEMS-based triaxial sensor package. Right: SAMS triaxial sensor developed specifically for microgravity-level measurements.

The initial testing results demonstrated that several of the developmental MEMS sensors have the required sensitivity. This is significant since most of the commercial sensors that were tested were sensitive to only measured levels in the milli-g (10^{-3} g) range.

Further testing will be conducted with the chosen sensors to characterize their operational capabilities beyond the 1 to 10 Hz range. Also, a prototype Triaxial Sensor Head will be designed and fabricated as a step toward space flight hardware. The Triaxial Sensor Head design requires an enclosure with three sensors that are mounted triaxially and integrated with low-noise signal-conditioning circuitry and a computer interface—all packaged into a compact size suitable to operate successfully on long-duration space flights. Once a

prototype is completed, computer algorithms will be developed to process and display the data.

Glenn contacts: Ronald J. Sicker, 216–433–6498, Ronald.Sicker@grc.nasa.gov; and Thomas J. Kacpura, 216–977–0420, Thomas.Kacpura@grc.nasa.gov

Authors: Ronald J. Sicker and Thomas J. Kacpura

Headquarters program office: OBPR

Programs/Projects: Microgravity Science

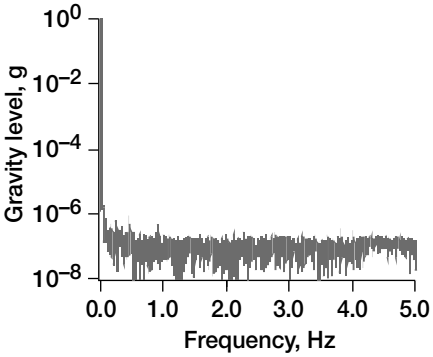

Noise floor testing of one of the development MEMS accelerometers. This graph demonstrates the ability to measure lower than 10^{-6}g during operation below 5 Hz.

Physics of Colloids in Space: Microgravity Experiment Launched, Installed, and Activated on the International Space Station

The Physics of Colloids in Space (PCS) experiment is a Microgravity Fluids Physics investigation that is presently located in an Expedite the Process of Experiments to Space Station (EXPRESS) Rack on the International Space Station. PCS was launched to the International Space Station on April 19, 2001, activated on May 31, 2001, and will continue to operate about 90 hr per week through May 2002.

PCS is concurrently gathering data on the basic physical properties of three different types of colloids to study how colloidal structures grow, the rates at which they grow, and the structures that they form. A colloidal suspension consists of fine particles (micrometer to submicrometer) suspended in a fluid, for example, paints, milk, salad dressings, and aerosols. The long-term goal of this investigation is to better understand how colloidal constituent properties affect the properties of a bulk colloidal suspension and to begin to probe the unique light-scattering properties of nano-engineered binary colloidal alloys. The potential payoffs of PCS are improvements in the properties of paints, coatings, ceramics, and food- and drug-delivery

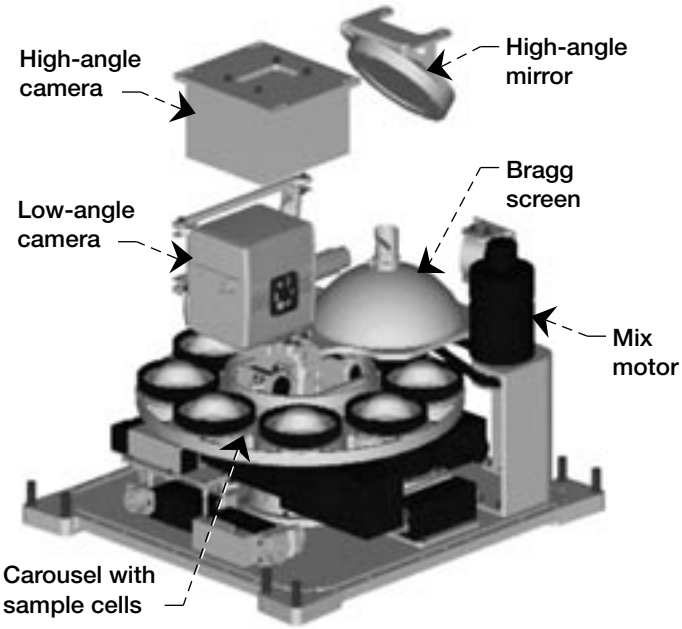

Physics of Colloids in Space (PCS) test section features.

products; improved manufacturing of products requiring either colloidal suspensions for processing or as precursors; and important first steps in the research and development of an entirely new class of materials that can passively affect the properties of light passing through them. These materials may find uses as optical switches and lasers for advanced communications and displays. This experiment is the first part of a two-stage investigation conceived by Professor David Weitz of Harvard University along with Professor Peter Pusey of the University of Edinburgh.

PCS contains eight approximately 3-milliliter colloid samples, each contained by a glass cell stationed within a remotely controllable carousel inside the PCS test section. Experiment operations consist of mixing (or homogenizing) the colloid samples to eliminate any sedimentation and to produce a uniform distribution of particles in the solution. Once mixed, particles start to self-assemble, and the diagnostic measurements are initiated. Measurements are regularly made on each sample over 1 to 2 months as its substructures (either crystallines or gels) grow and evolve. Measurements include still color digital images, high-angle static laser light scattering (or Bragg scattering), low-angle static and low-angle dynamic light scattering, fiber static and fiber dynamic light scattering, and rheology. The diagnostic data provide growth information, the shape of the structures formed, and other physical properties of the structures.

PCS is being remotely operated from the NASA Glenn Research Center's Telescience Support Center in Cleveland, Ohio, and at an established remote site at Harvard University in Cambridge, Massachusetts. The two locations permit daily remote operation of the experiment. In real time via commands uplinked from Earth to the International Space Station, the PCS commanders control such activities as which sample to interrogate, when to homogenize the sample, which diagnostic technique to employ to perform the interrogation, as well as the sequencing of sample diagnostic runs.

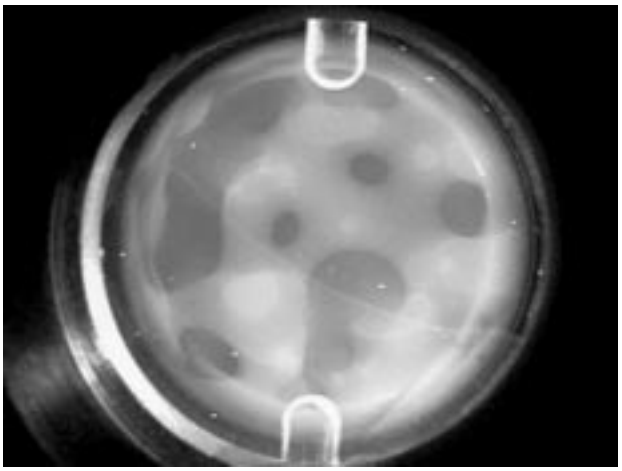

Colloid polymer critical point sample—13 hr, 24 min after being mixed. Sample shows a phase separation never seen on Earth.

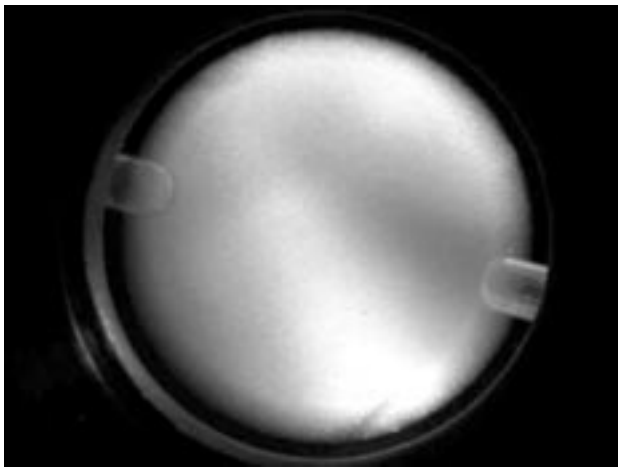

AB6 binary colloidal alloy sample—20 days, 11 hr after being mixed. Bands of color can be seen that were created by the diffraction of white light by the crystallized sample. This figure is shown in color in the online version of this article (http://www.grc.nasa.gov/WWW/RT2001/6000/6728doherty.html).

PCS completed its checkout operations on June 22, 2001. During the subsequent 13 weeks, it did an initial survey of crystal nucleation and growth on six of the eight samples and then reinitiated more detailed investigations on the two binary colloidal alloy samples. The crystalline samples (AB6, AB13, colloid polymer crystal, and colloidal glass) are all behaving as hoped for, with the growth of the crystallites having been interrogated by a host of different state-of-the-art light-scattering techniques. The colloid polymer critical point sample, as hoped, exhibits, upon homogenization, a phase separation, or demixing process, that

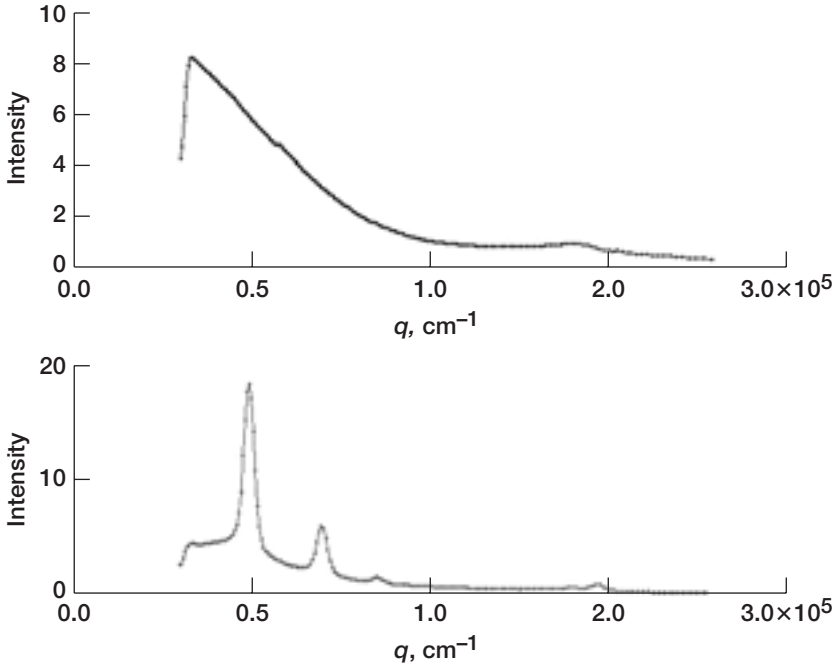

Diffraction patterns from the AB13 binary colloidal alloy sample (high-angle scattering). Intensity shown in arbitrary units; q is directly proportional to the scattering angle. Growth of Bragg peaks over time indicates the presence of crystals. Top: 0.48 hr after melting. Bottom: 255 hr after melting.

would never be seen in 1g. The colloid polymer gel sample, the last of the six samples to be homogenized, was verified to gel in microgravity, and aging of the gel was observed. Each of these six samples is to be rehomogenized to enable more detailed investigations to occur over the upcoming months on orbit.

Overall, the initial survey was successful in determining the crystallization time and other characteristics of the samples, revealing exciting areas of interest for each and confirming the diagnostic techniques to be used for the much more detailed measurements to be conducted on each sample through May 2002. Two samples yet to be interrogated, composed of colloids that gel in an irreversible manner when a salt is added, will be initiated during future PCS experiment runs. To date, experiments performed by PCS have proceeded very well with the instrumentation exceeding Professor Weitz' expectations. The PCS experiment was developed and launched and is being operated by Zin Technologies under NASA contract NAS3–99154.

Find out more about this research:

Glenn's PCS research (includes data on a sample-by-sample basis—being updated): http://microgravity.grc.nasa.gov/6712/PCS.htm

David Weitz at Harvard (introduces the principal investigator): http://www.physics.harvard.edu/fac_staff/weitz.html

Principal investigator group at Harvard (scientific focus areas of interest): http://www.deas.harvard.edu/projects/weitzlab/

Glenn's microgravity research: http://microgravity.grc.nasa.gov

Glenn's fluid physics research: http://microgravity.grc.nasa.gov/MSD/MSD_htmls/fluids.html

Glenn contacts:
Michael P. Doherty, 216–433–6641, Michael.P.Doherty@grc.nasa.gov; and Dr. Subramanian Sankaran, 216–433–9335, Subramanian.Sankaran@grc.nasa.gov

Author: Michael P. Doherty

Headquarters program office: OBPR

Programs/Projects:
Microgravity Science

Gas/Liquid Separator Being Developed for Microgravity

The examination and research of how liquids and gases behave in very low gravity will improve our understanding of the behavior of fluids on Earth. The knowledge of multiphase fluid behavior is applicable to many industries on Earth, including the pharmaceutical, biotechnology, chemical, and nuclear industries, just to name a few. In addition, this valuable knowledge applies very well to the engineering and design of microgravity materials processing and of life-support systems for extended space flight. Professors Ashok Sangani of Syracuse University and Donald Koch of Cornell University are principal investigators in the Microgravity Fluid Physics Program, which is managed and sponsored by the NASA Glenn Research Center. Their flight experiment entitled "Microgravity Observations of Bubble Interactions" (MOBI) is planned for operation in the Fluids and Combustion Facility aboard the International Space Station. They will analyze and study the physics of a sheared bubble suspension in ideal flow conditions. Plans are to measure the bubble distribution of a sheared suspension in a cylindrical couette cell and to use suspension-averaged equations of motion to compare the results with the predicted distribution. Multiple bubble suspensions will be generated during the MOBI experiment. To reduce the cost associated with delivering the many liters of water needed for the experiments to the International Space Station, researchers are developing a separator to separate the gas phase from the liquid phase and recycle the liquids.

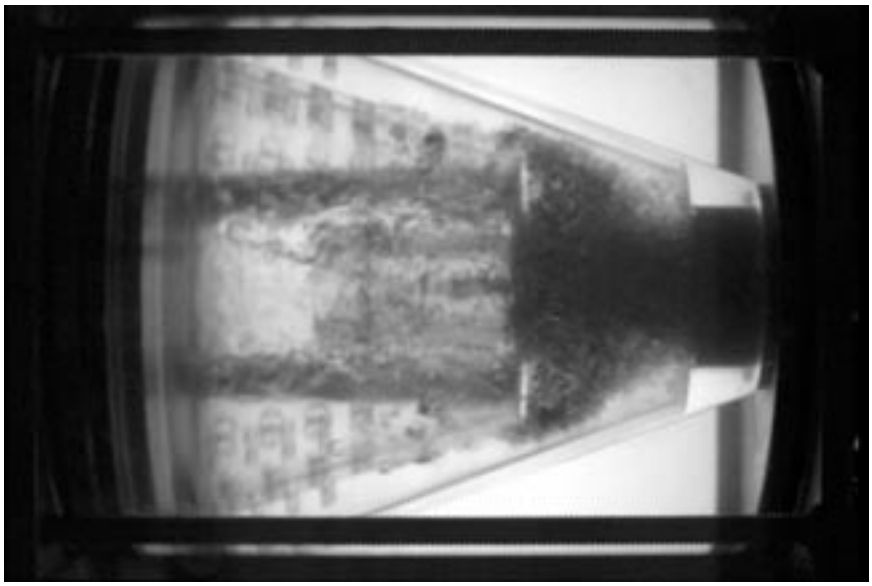

Gas-liquid separator as a mixture of air bubbles and water enter the separator between the spinning cones, forming a gas core in the center.

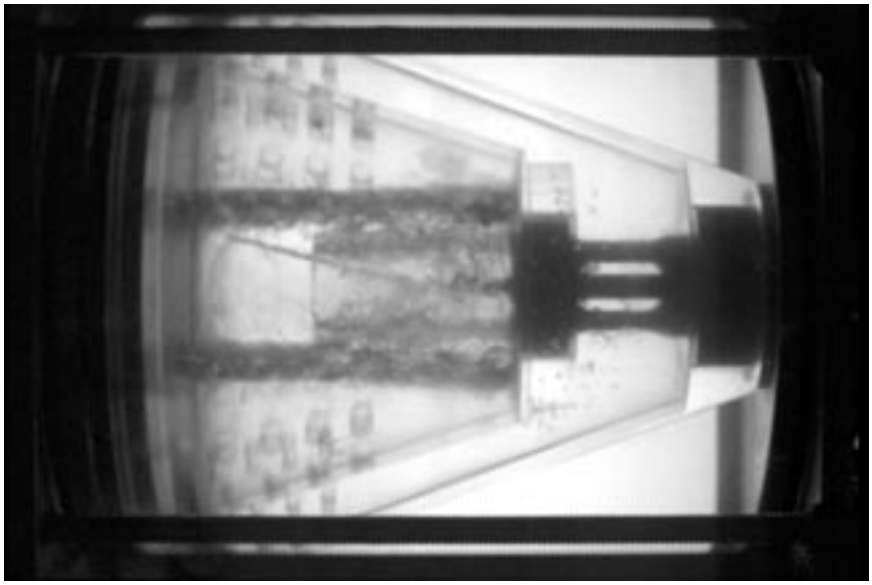

Gas-liquid separator as the air bubbles form a core in the center of the separator. The air core grows smaller as the gas is vented from the center of the separator. Bubble-free water is pumped out of the separator from the cylindrical volume outside the spinning cones.

On Earth, buoyancy causes gases and liquids to separate, with the gas on the top and the liquid on the bottom of a container. In microgravity, the buoyancy force is not present, and the separation and removal of gases from liquids requires a technical solution. A centrifugal separator concept was

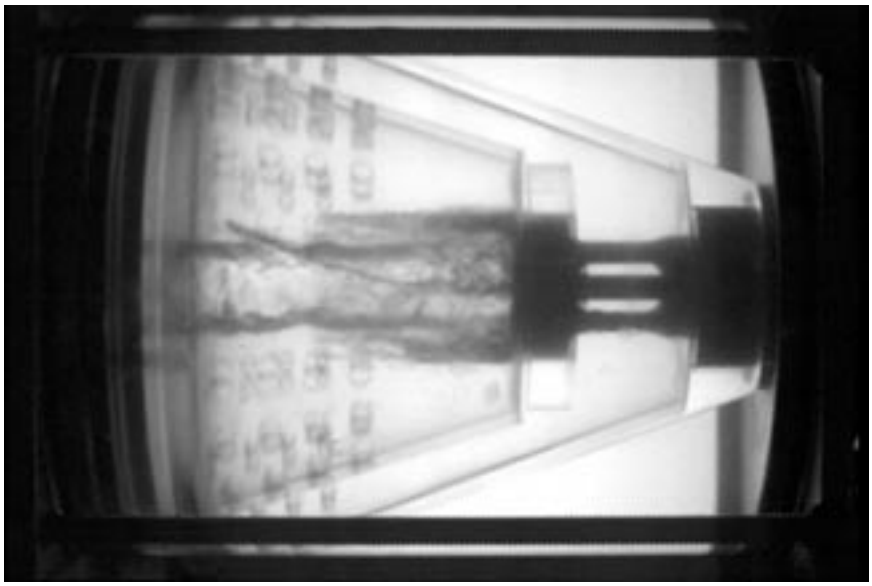

Gas-liquid separator after the air core has grown small enough that the tip of the gas/liquid detector (the bent probe in the center of the separator) is now in water, causing the gas vent valve to close. Liquid is prohibited from exiting the separator through the gas vent.

designed and fabricated by C. Frances Enterprises with support from ZIN Technologies and Glenn's Engineering Design and Analysis Division. The concept was successfully tested aboard the KC–135 microgravity facility in January and March of 2001.

The separator concept consists of an acrylic cylindrical chamber that houses two concentric acrylic cones with holes machined into the cone sides. The chamber is coupled to a motor that spins the cones at approximately 2500 rpm. When a mixture of gas and liquid enters the separator in the volume between the cones, the liquid is forced to the outside through the holes in the spinning cones and into the cylindrical chamber. The gas in the separator forms a distinct core at the center of the inner cone. A gas-liquid detector is mounted in the separator, and software is used for automatic operation. When gas is detected, a solenoid valve opens and the gas is removed by a vacuum pump. When liquid is detected, the solenoid valve closes so that no liquid is removed through the gas vent line. A pump is used to remove the gas-liquid mixture from the couette test chamber into the separator. The same pump pushes the bubble-free water back into the couette test chamber in preparation for making a new bubble suspension for the next experiment.

Find out more about this research:
http://microgravity.grc.nasa.gov/6712/multiph/bubbly.htm

Glenn contacts: Monica I. Hoffmann (Project Manager), 216–433–6765, Monica.I.Hoffmann@grc.nasa.gov; and Henry K. Nahra (Project Scientist), 216–433–5385, Henry.K.Nahra@grc.nasa.gov

Author: Monica I. Hoffmann

Headquarters program office: OBPR

Programs/Projects:
Microgravity Science

Compact Video Microscope Imaging System Implemented in Colloid Studies

The Compact Microscope Imaging System (CMIS) is a diagnostic tool with intelligent controls for use in space, industrial, medical, and security applications. CMIS can be used in situ with a minimum amount of user intervention. This system can scan, find areas of interest in, focus on, and acquire images automatically. Many multiple-cell experiments require microscopy for in situ observations; this is feasible only with compact microscope systems.

CMIS is a miniature machine vision system that combines intelligent image processing with remote control. The software also has a user-friendly interface, which can be used independently of the hardware for further postexperiment analysis.

CMIS has been successfully developed in the SML Laboratory at the NASA Glenn Research Center and adapted for use for colloid studies and is available for telescience experiments. The main innovations this year are an improved interface, optimized algorithms, and the ability to control conventional full-sized microscopes in addition to compact microscopes. The CMIS software-hardware interface is being integrated into our SML Analysis package, which will be a robust general-purpose image-processing package that can handle over 100 space and industrial applications.

CMIS provides automated online inspection of precision parts, medical imaging, examination of currency in automated teller machines, fingerprint identification in secure entry locks, automated examination of soil and water samples, automated blood and cell analysis, and improved microscopy.

Using CMIS, we were able to detect full and partial cells, which gave us information on the centroid of each cell and its position in relationship to all other cells in the image. We first use a contrast filter to determine the outer ring of each cell. We then use an adaptive background subtraction algorithm to subtract the background from the image. This distinctly separates the cells from the background while preserving the integrity of the cell perimeters. Next, we find the number of cells, their positions, and their nearest neighbors, and identify the particle closest to the center of the image. Finally, we

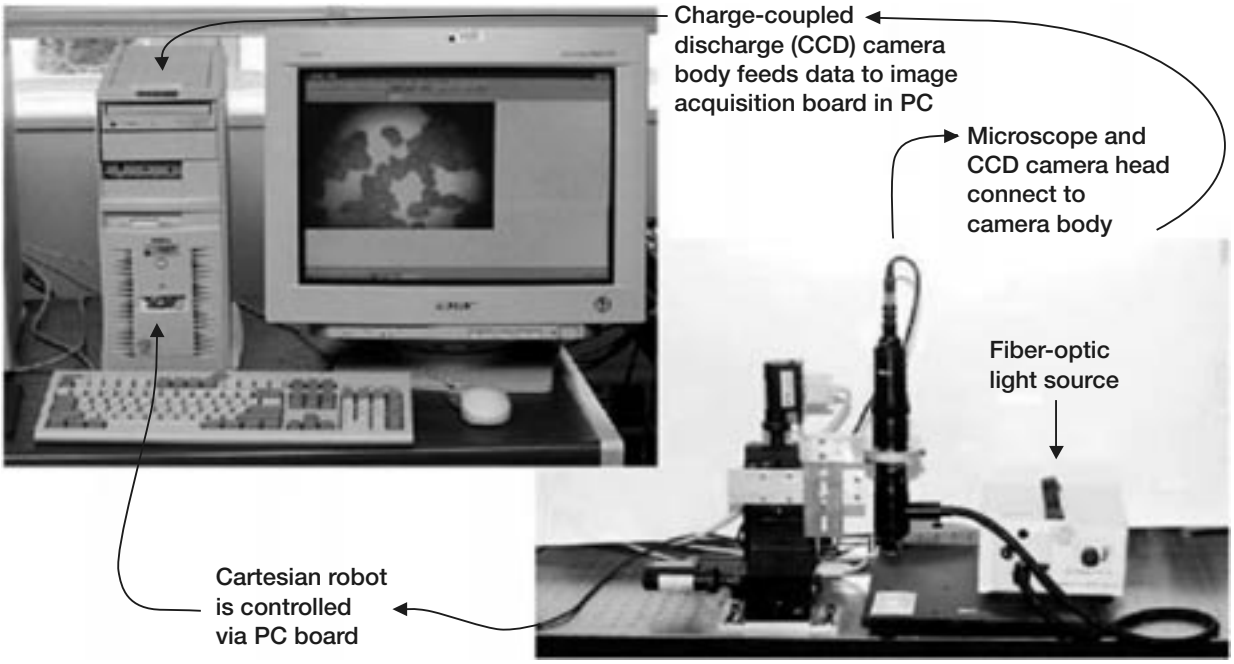

CMIS setup.

Identify each individual cell

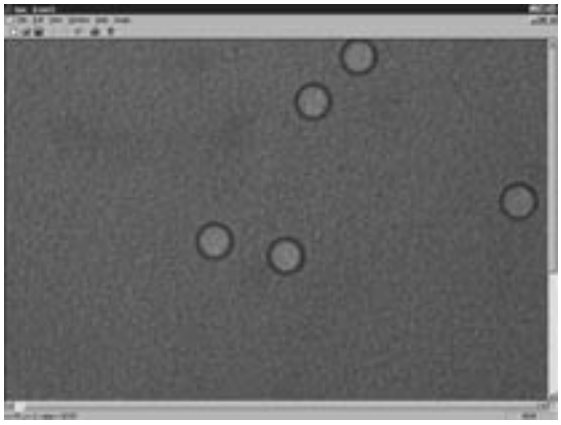

Raw data exhibiting a vertical disorder-order interface.

Background subtraction to isolate individual cells

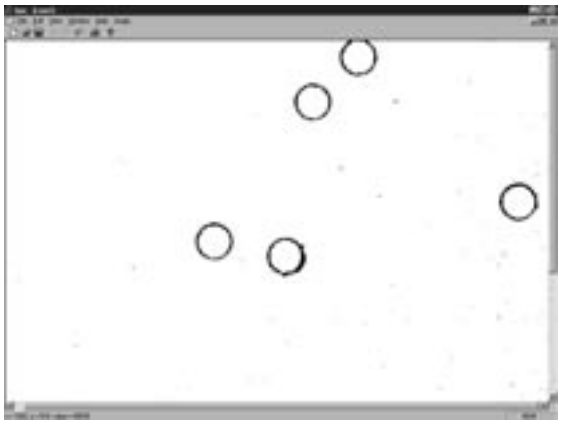

Raw data exhibiting horizontal disorder-order interface.

Label each cell as full or partial

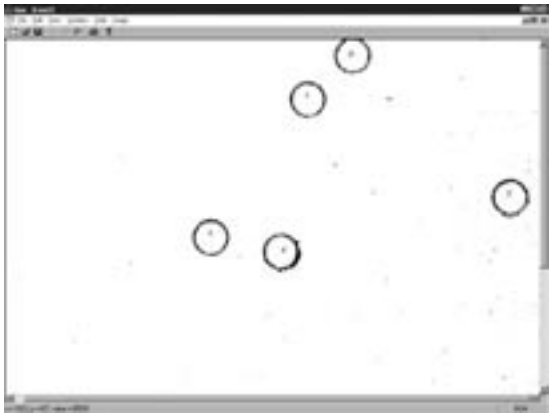

Vertical interface located by CMIS is highlighted. This figure is shown in color in the online version of this article (http://www.grc.nasa.gov/WWW/RT2001/6000/6728mcdowell.html).

Determine cell displacements in original image

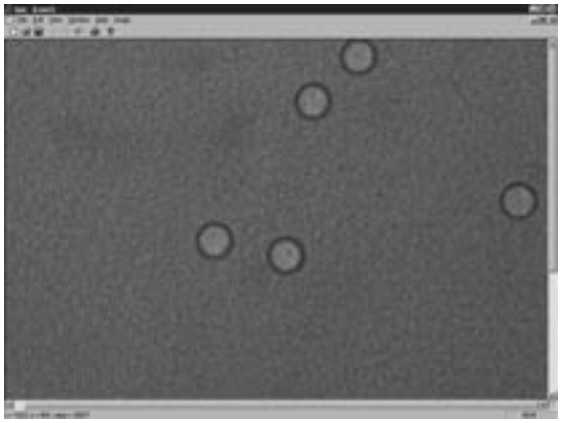

Horizontal interface located by CMIS is highlighted. This figure is shown in color in the online version of this article (http://www.grc.nasa.gov/WWW/RT2001/6000/6728mcdowell.html).

combine the identified cells with the original image and determine cell displacements.

This application is applicable to any experiment that requires cell detection, displacements, and tracking. This microscopy innovation will be incorporated into future microcopy experiments in Glenn's microgravity program.

Find out more about this research: http://cmis.grc.nasa.gov

Glenn contact: Dr. Mark McDowell, 216–433–8161, drmm@easy.grc.nasa.gov

Author: Dr. Mark McDowell

Headquarters program office: OBPR

Programs/Projects: Microgravity Science

Special recognition: Given 2000 Imaging Solution of the Year award by *Advanced Imaging* for significant advancement in the fields of medical imaging, bioscience, and scientific analysis. *Advanced Imaging* is an international magazine that highlights the latest state-of-the-art advancements in imaging processing.

Light Microscopy Module: On-Orbit Microscope Planned for the Fluids Integrated Rack on the International Space Station

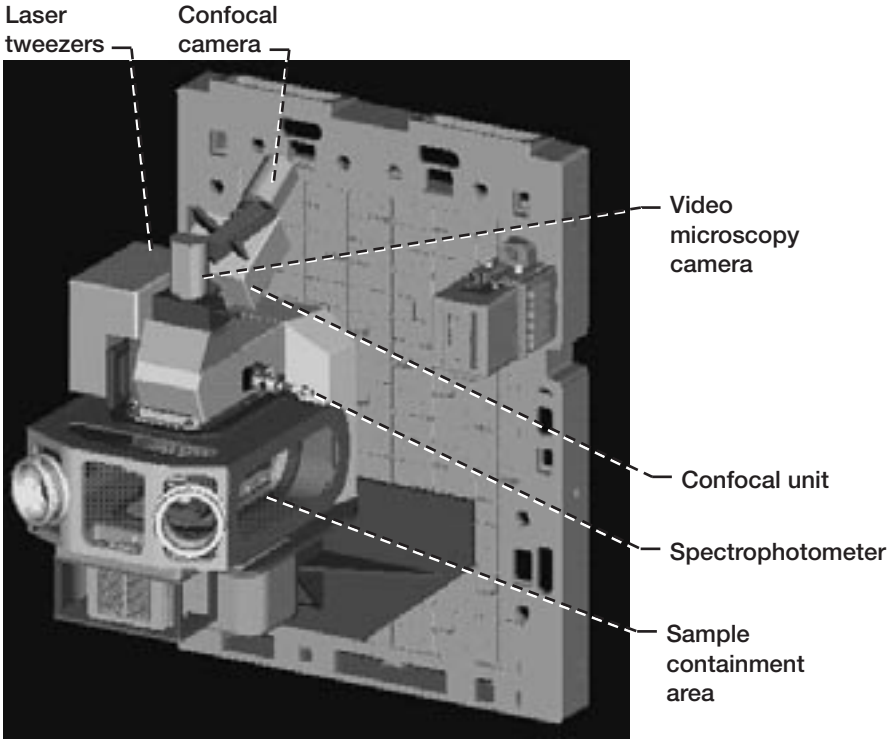

The LMM integrated with the FIR optics plate.

The Light Microscopy Module (LMM) is planned as a remotely controllable, automated, on-orbit facility, allowing flexible scheduling and control of physical science and biological science experiments within the Fluids Integrated Rack (FIR) on the International Space Station. Initially four fluid physics experiments in the FIR will use the LMM—the Constrained Vapor Bubble, the Physics of Hard Spheres Experiment-2, Physics of Colloids in Space-2, and Low Volume Fraction Entropically Driven Colloidal Assembly. The first experiment will investigate heat conductance in microgravity as a function of liquid volume and heat flow rate to determine, in detail, the transport process characteristics in a curved liquid film. The other three experiments will investigate various complementary aspects of the nucleation, growth, structure, and properties of colloidal crystals in microgravity and the effects of micromanipulation upon their properties.

Key diagnostic capabilities of LMM include video microscopy to observe sample features including basic structures and dynamics, thin film interferometry, laser tweezers for colloidal particle manipulation and patterning, confocal microscopy to provide enhanced three-dimensional visualization of colloidal crystal structures, and spectrophotometry to measure colloidal crystal photonic properties. In addition to using the confocal system, biological experiments will be able to conduct fluorescence imaging by using the fiber-coupled output of the Nd:YAG laser operating at 532-nm, the 437-nm line of a mercury arc, or appropriate narrow-band filtering of the FIR-provided metal halide white-light source.

The LMM will be a modified Leica RXA commercial research imaging light microscope with powerful laser-diagnostic hardware and interfaces, combining to form a one-of-a-kind, state-of-the-art microscopic research facility. It will combine high-resolution color video microscopy with brightfield, darkfield, phase contrast, differential interference contrast, spectrophotometry, and confocal microscopy. An auxiliary fluids container (AFC) will be fastened to the microscope body and sealed to provide a clean working space and one level of containment. Gloveports will allow access to the sample area for cleaning before opening the box and for experiment sample changeout or reconfiguration.

An equipment transfer module (ETM) will transport experiment samples from stowage to the LMM without the risk of contamination release and will be able to be configured to support various experiment modules. It will be located below the AFC, which has a pass-through for the samples. The ETM will be loaded with experiment modules on the ground, providing contained storage until the samples are used in the experiments.

The laser tweezers is a custom-built system with a 1064-nm, 1-W Nd:YAG laser, beam-focusing optics, and two acousto-optic deflectors to steer the trap within the field of view of the microscope. The acousto-optic deflector is a programmable diffraction grating, allowing high-speed scanning of the trap location, which in essence will create multiple trap locations. The tweezer beam will be coupled to the microscope via a lateral port located near the fluorescence turret, and the beam will be deflected into the objective with a dichroic mirror. This mirror will allow simultaneous tweezer and confocal microscope operations. The tweezers will be used both to probe local crystal properties, such as yield stress, as well as to create seed crystals or defects within existing crystals. Thus, they will allow researchers to directly manipulate a colloidal crystal lattice to investigate the viscosity and viscoelasticity of a fluid.

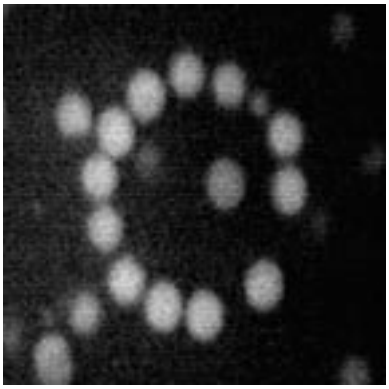

Circular array of 2.3-μm rhodamine-dyed PMMA particles trapped with scanning laser tweezers. Image taken with the confocal unit.

Confocal microscopy will use a 532-nm frequency-doubled Nd:YAG laser, a Yokogawa CSU–10 Nipkow disk confocal unit, and a 12-bit digital charge-coupled device (CCD) camera on a fluorescent-dyed sample. The crystal's three-dimensional structure will be reconstructed by assembling the slices with an image analysis program, from which colloidal growth, structure, and dynamics can be measured.

Spectrophotometry will be used to measure photonic band gaps of colloidal crystals and spectral response of biological samples. This will be done by a monochromator that is attached to the light source, has a spectral bandwidth of less than 10 nm, and is tunable over the entire visible waveband. The spectrophotometer will take advantage of the optical system within the microscope, in that it will be possible to vary the angle of the incident light on the sample within the range allowable by the numerical aperture of the objective lens.

The project is in the preliminary design phase. During 2001, the team at the NASA Glenn Research Center successfully built an integrated breadboard of the LMM. A preliminary design review will be conducted in late 2001. This work was performed under NASA contract NAS3–99155 by Northrop Grumman Information Technology.

Glenn contact:
Susan M. Motil, 216–433–8589,
Susan.M.Motil@grc.nasa.gov

Authors: Susan M. Motil, John H. Snead, and Dr. DeVon W. Griffin

Headquarters program office: OBPR

Programs/Projects:
Microgravity Science

Power and Propulsion

Flywheel Energy Storage System Designed for the International Space Station

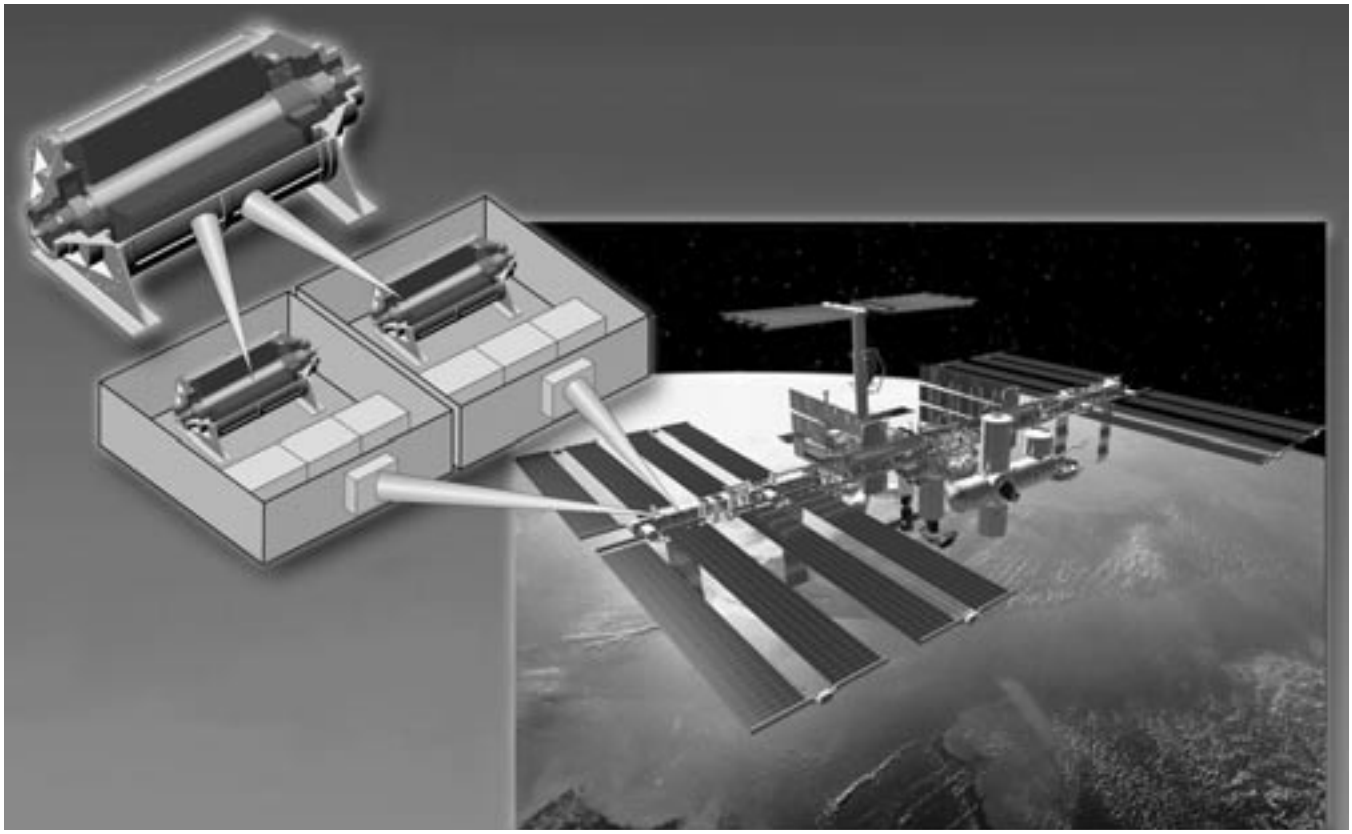

Flywheel Energy Storage System (FESS) for the International Space Station. Architecture: 1 flywheel module + 1 set of electronics = 1 flywheel energy storage unit; 2 flywheel energy storage units = 1 flywheel energy storage system.

Following successful operation of a developmental flywheel energy storage system in fiscal year 2000, researchers at the NASA Glenn Research Center began developing a flight design of a flywheel system for the International Space Station (ISS). In such an application, a two-flywheel system can replace one of the nickel-hydrogen battery strings in the ISS power system. The development unit, sized at approximately one-eighth the size needed for ISS was run at 60,000 rpm. The design point for the flight unit is a larger composite flywheel, approximately 17 in. long and 13 in. in diameter, running at 53,000 rpm when fully charged. A single flywheel system stores 2.8 kW-hr of useable energy, enough to light a 100-W light bulb for over 24 hr. When housed in an ISS orbital replacement unit, the flywheel would provide energy storage with approximately 3 times the service life of the nickel-hydrogen battery currently in use.

Significant progress was made in fiscal year 2001, including the flywheel module design, avionics design, and test facility preparation. Glenn now has assets to conduct the flywheel cyclic spin test, flywheel module test, and integrated power systems test.

An independent peer review continued to advocate the advancement of flywheel technology to benefit the ISS. However, ISS

funding is no longer available for continued development in fiscal year 2002. Plans are in place to continue development once new funding is secured.

Find out more about this research: http://acts.grc.nasa.gov/fess/

Glenn contacts:
Dr. Timothy E. Tyburski, 216–433–8616, Timothy.E.Tyburski@grc.nasa.gov; Ray F. Beach, 216–433–5320, Raymond.F.Beach@grc.nasa.gov; and Rex A. Delventhal, 216–433–5608, Rex.A.DeLventhal@grc.nasa.gov

Author: Rex A. Delventhal

Headquarters program office: OSF

Programs/Projects: ISS

International Space Station Power System Model Validated

System Power Analysis for Capability Evaluation (SPACE) is a computer model of the International Space Station's (ISS) Electric Power System (EPS) developed at the NASA Glenn Research Center. This uniquely integrated, detailed model can predict EPS capability, assess EPS performance during a given mission with a specified load demand, conduct what-if studies, and support on-orbit anomaly resolution.

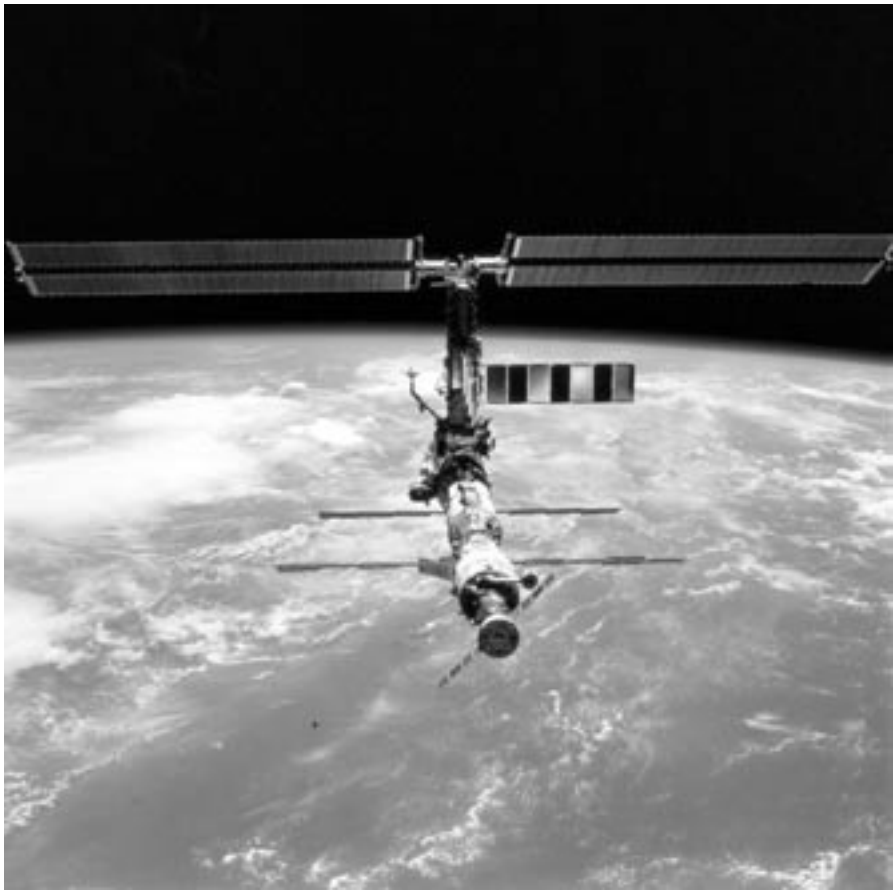

On-orbit view of the International Space Station taken from the space shuttle in March 2001.

The first U.S. power module was launched to the ISS on November 30, 2000. This module boasts two solar arrays, the largest ever flown in space, each capable of producing more than 30 kW of power. The module also contains batteries to power the ISS when it is in the Earth's shadow and the associated cables and power electronics to route power to electrical loads.

The model validation process reviewed a range of on-orbit data, compared them with SPACE input data, and output the results. Pertinent data in the downlinked data stream were determined, and several time periods with minimal data dropouts were identified. These data were gathered using tools available in Glenn's Engineering Support Room, which can be staffed by Glenn engineers to support ISS operation. SPACE input and output generated from running the SPACE code were compared with the on-orbit telemetry. The comparisons looked at all aspects of the power system, including solar array performance from both the front and back, array pointing uncertainty, battery performance, dc-to-dc converter

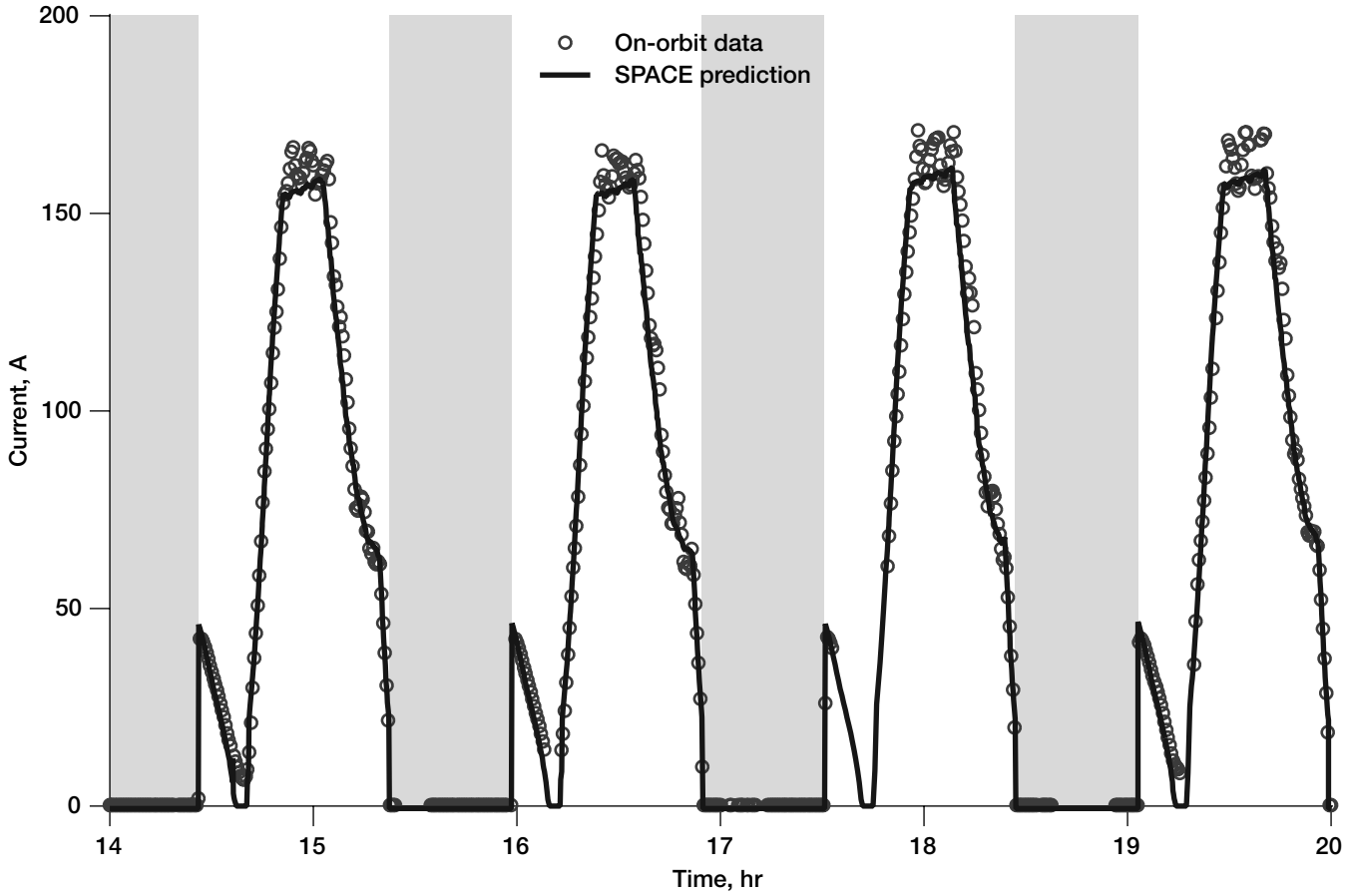

Comparison of on-orbit data with SPACE predictions for solar array output current.

efficiency, battery charge-discharge efficiency, and the overall ISS EPS system performance.

This plot compares SPACE predictions and actual ISS telemetry. It shows the usable current produced by one of the two solar arrays. During this four-orbit period, the solar arrays are in a fixed position so the current varies during the orbit. At the beginning of each sunlight period, the back of the array (which generates power less efficiently than the front) faces the Sun. As the sunlight period progresses, the Sun transitions from the back of the array to the front, and thus the current falls off, then steadily increases. During the second half of the sunlight period, the usable current decreases; once the batteries become fully charged, excess current is shunted away to prevent overcharging the batteries. The shaded areas in the plot indicate when the ISS passes through the Earth's shadow, and thus the solar arrays produce no power. The SPACE prediction matches the on-orbit data extremely well during all phases of the orbit. In fact, for the cases examined thus far, SPACE predictions of currents, voltages, and other parameters consistently match on-orbit performance within approximately 5 percent.

With this validation against the actual on-orbit performance of the ISS EPS this year, the development of SPACE has reached a significant milestone. SPACE predictions can be used with greater confidence than ever in planning future operations of the ISS.

Find out more about this research:
http://space-power.grc.nasa.gov/ppo/

Glenn contact:
Jeffrey S. Hojnicki, 216–433–5393,
Jeffrey.S.Hojnicki@grc.nasa.gov

Authors: Jeffrey S. Hojnicki and Ann M. Delleur

Headquarters program office: OSF

Programs/Projects: ISS

Solar Electric Propulsion Technologies Being Designed for Orbit Transfer Vehicle Applications

There is increasing interest in employing Solar Electric Propulsion (SEP) for new missions requiring transfer from low Earth orbit to the Earth-Moon Lagrange point, L1. Mission architecture plans place the Gateway Habitat at L1 in the 2011 to 2016 timeframe. The Gateway Habitat is envisioned to be used for Lunar exploration, space telescopes, and planetary mission staging. In these scenarios, an SEP stage, or "tug," is used to transport payloads to L1—such as the habitat module, lunar excursion and return vehicles, and chemical propellant for return crew trips. SEP tugs are attractive because they are able to efficiently transport large (>10,000 kg) payloads while minimizing propellant requirements.

To meet the needs of these missions, a preliminary conceptual design for a general-purpose SEP tug was developed that incorporates several of the advanced space power and in-space propulsion technologies (such as high-power gridded ion and Hall thrusters, high-performance thin-film photovoltaics, lithium-ion batteries, and

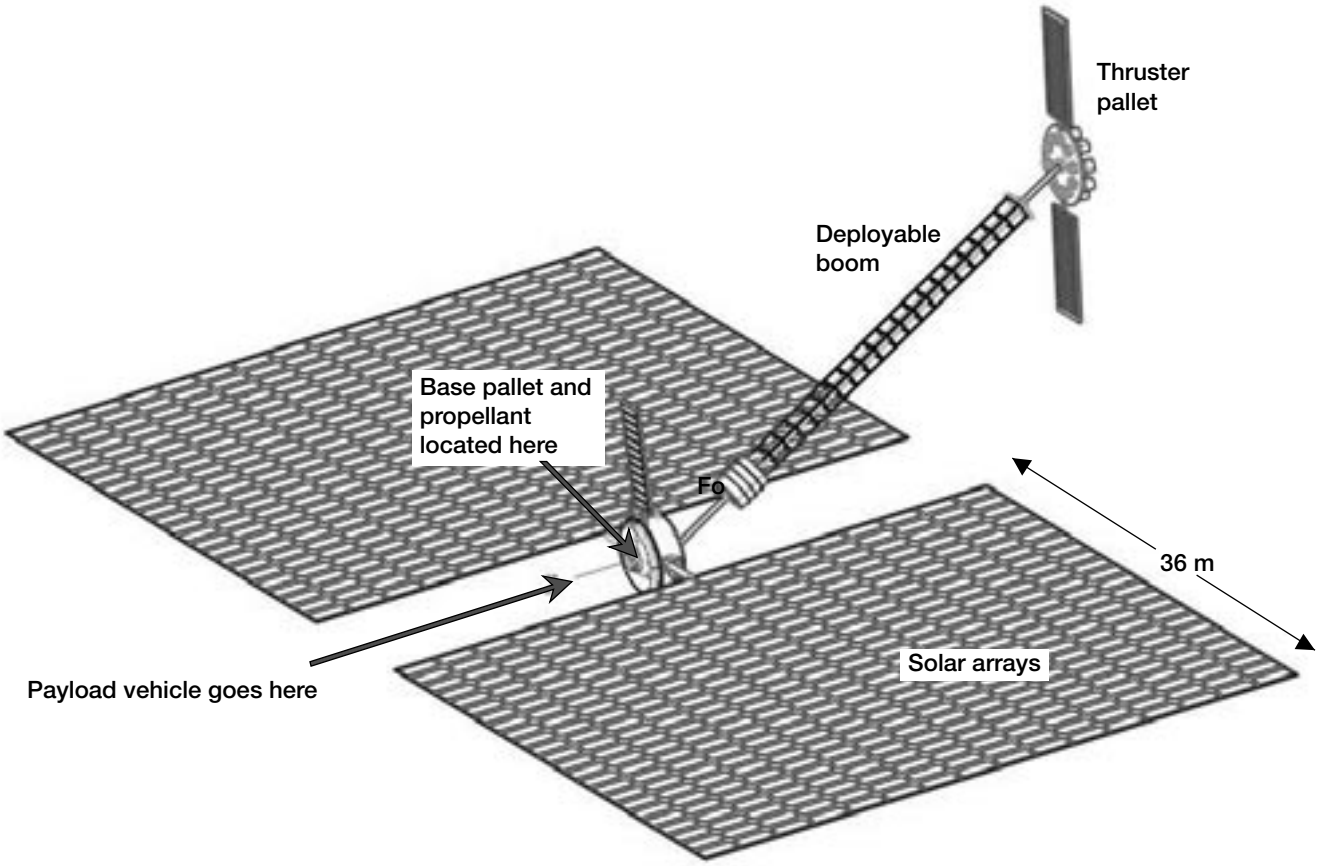

Solar Electric Propulsion (SEP) tug for the Revolutionary Aerospace Systems Concepts' Hybrid Propellant Module project. Nine 50-kW gridded ion thrusters are mounted on the deployable boom to enable the base pallet, arrays, and payload vehicle to remain in a solar inertial attitude while maintaining a constant thrust along the center of mass. The deployable boom is conformable to enable it to fit around the payload vehicle. In this case, the xenon propellant is on the payload vehicle, which is not shown. For scale, the coilable center mast section of the deployable boom (in yellow) is 20 m in length. This figure is shown in color in the online version of this article (http://www.grc.nasa.gov/WWW/RT2001/6000/6920verhey.html).

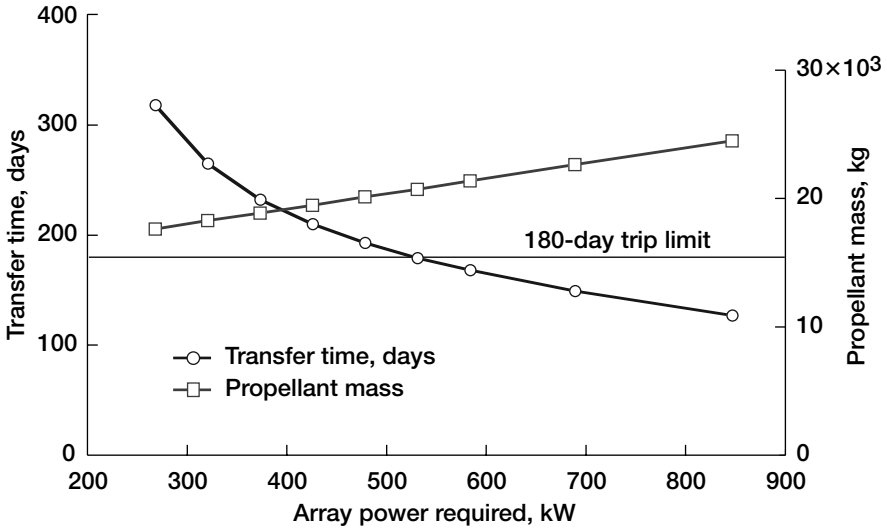

Solar Electric Propulsion (SEP) tug performance for Johnson Space Center's Gateway mission. Transfer time from low Earth orbit to Earth-Moon L1 and xenon propellant mass required for transfer are shown as functions of the power generated. At 584 kW, the tug would be able to deliver the 30 MT payload in 179 days.

advanced high-voltage power processing) being developed at the NASA Glenn Research Center. A spreadsheet-based vehicle system model was developed for component sizing and is currently being used for mission planning. This model incorporates a low-thrust orbit transfer algorithm to make preliminary determinations of transfer times and propellant requirements. Results from this combined tug mass estimation and orbit transfer model will be used in a higher fidelity trajectory model to refine the analysis.

The SEP tug system model was used in two design studies in 2001. First, the conceptual design of the Hybrid Propellant Module under the Revolutionary Aerospace Systems Concepts program at the NASA Langley Research Center required an SEP tug to transfer it to L1. This SEP tug, shown in the illustration on the previous page, would deliver a 36-metric-ton (MT) payload to L1 in 272 days. The second conceptual design activity was for the Lunar L1 Gateway mission architecture study at the NASA Johnson Space Flight Center. The SEP tug in this case would be able to deliver the required 30 MT payload to L1 within the time constraint of 180 days. The tug's performance is shown in the graph, where the transfer time as a function of power on the tug is shown, along with the xenon propellant required.

For both studies, the SEP tug performance satisfied the requirements of the respective mission designers, and the SEP concept was incorporated into the mission architectures. Further refinement of the system model, including structural and dynamic analysis and incorporation of the results of the improved orbit trajectory, is planned. The development of the SEP tug system model has been a joint effort by Glenn's Power and Propulsion Office, Power and On-Board Propulsion Technology Division, and Systems Engineering Division, through Glenn's Systems Assessment Team.

Glenn contact:
Timothy R. Sarver-Verhey,
216–977–7458, Fax 216–433–2995,
Timothy.R.Verhey@grc.nasa.gov

Authors: Timothy R. Sarver-Verhey, David J. Hoffman, Thomas W. Kerslake, Steven R. Oleson, and Robert D. Falck

Headquarters program office:
HEDS (Advanced Programs), OSF (Advanced Projects)

Programs/Projects: Advanced Power and On-Board Propulsion, Systems Engineering, Power and Propulsion

2001

Engineering and Technical Services

Facilities and Test Engineering

8- by 6-Foot Supersonic Wind Tunnel Compressor Inspected

The NASA Glenn Research Center's 8- by 6-Foot Supersonic Wind Tunnel (8×6 SWT) is NASA's only transonic propulsion wind tunnel. The test section speed range is between Mach 0.25 and 2.0. The 9- by 15-Foot Low-Speed Wind Tunnel (9×15 LWST), which has a speed range from 0 to 175 mph, is housed in the return leg of the 8×6 SWT and uses the same compressor. The 8×6 SWT uses a large, seven-stage axial flow compressor to drive the air through the tunnel. The compressor is 17 ft in diameter and is rated at 1600 m^3 (56,600 ft^3) of air/sec. It is driven by three electric motors with a combined horsepower of 87,000. A close examination of this compressor was performed in 2001, the first time since February of 1966.

The examination focused on inspections that would define the condition of the six major compressor components: the compressor rotor and stator blades, the shaft flange bolts, the rotor spacer rings, the rotor tie rods, and the casing. The kind of inspections performed were visual, dye penetrant, hardness, tightness, and ultrasonic. The visual, dye penetrant, hardness (not completed on all blades), and tightness inspections were completed on the rotor and stator blades. A hardness test was also completed on a sampling of the spacer rings. Tightness checks were completed on the shaft flange bolts and rotor tie rods. An ultrasonic inspection was completed on the rotor tie rods.

These inspections are very important because they can catch potential problems before they become significant. This inspection revealed that the compressor is in excellent condition and should give Glenn many more years of faithful service.

Find out more about this research:
http://www.grc.nasa.gov/WWW/FMPO/

Glenn contacts:
Martin J. Krupar, 216–433–5660, Martin.J.Krupar@grc.nasa.gov; and Alan A. Linne, 216–433–6751, Alan.A.Linne@grc.nasa.gov

Authors:
Martin J. Krupar and Alan A. Linne

Headquarters program office: OAT

Programs/Projects: UEET, QAT, JSF, HSR, Aeropropulsion Base R&T

8×6 SWT compressor.

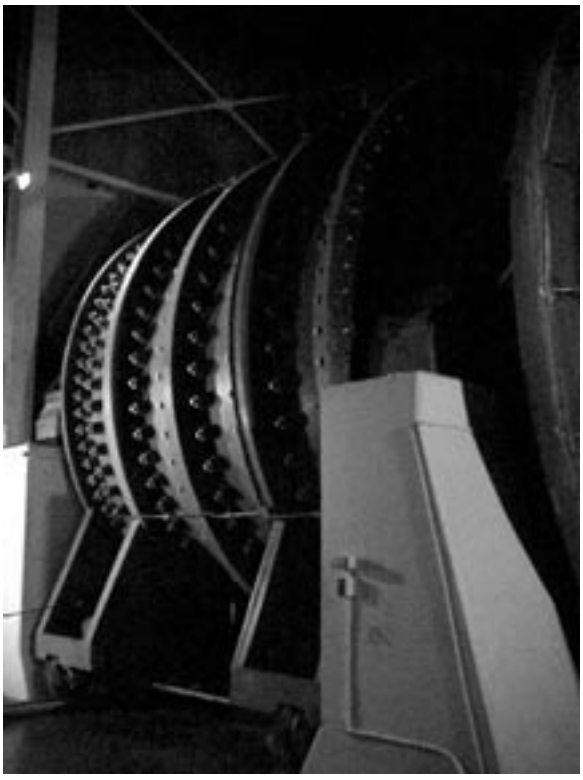

8×6 SWT rotor and stator blades.

Sonic Boom Testing Performed in NASA Glenn Research Center's 10- by 10-Foot Supersonic Wind Tunnel

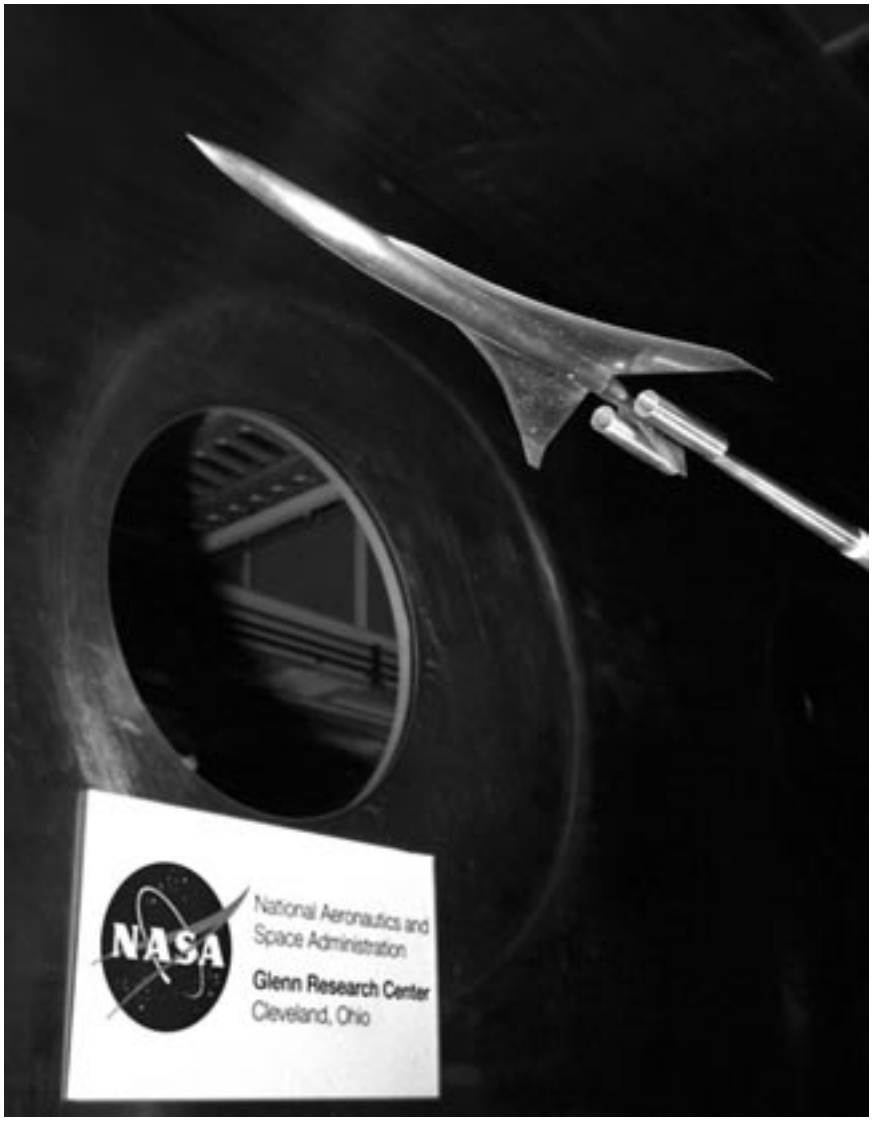

Business jet concept model installed in Glenn's 10×10 SWT test section.

One of the current impediments to the establishment of supersonic transports as a viable part of the commercial aviation fleet is the sonic boom effect. This effect is created when a vehicle achieves supersonic speeds and creates a shock wave (an immediate pressure change) that impinges on the ground. The resulting sonic boom can be both heard and felt on the ground, and it traverses the ground along the flight path of the vehicle. The environmental impact of this sonic boom effect is currently regulated by only allowing supersonic flight on over-water flight paths. The ability to measure the pressure signature of an aircraft configuration would allow researchers to identify the sources and the relative magnitude of that source on the aircraft pressure signature. It would also allow for the development and validation of computer codes to predict the sonic boom effects of an aircraft configuration.

Sonic boom pressure signature data generated by two business jet concept wind tunnel models were recorded in a test conducted in NASA Glenn Research Center's 10- by 10-Foot Supersonic Wind Tunnel (10×10 SWT) in April 2001. A static pressure survey probe was translated axially through the test section to measure the pressure signature of the model. The data were collected with two different model nacelle configurations and at various angles of attack and separation distances. The sonic boom test was a cooperative effort by Glenn and the NASA Langley Research Center to expand the sonic boom pressure signature data base and to validate the pressure signature prediction codes.

During testing, over 7300 data points were collected. Glenn's 10×10 SWT near-field pressure signature data showed the same features and pressure levels as near-field data recorded previously in Langley's 4- by 4-Foot Unitary Plan Wind Tunnel. In addition, the test provided non-far-field data for the same model configurations and attitudes. The data are being used to develop and validate pressure signature prediction codes. The codes also will be used to determine if pressure signatures can be credibly extrapolated from cruise altitude to the ground.

Business jet concept model and survey probe installation in Glenn's 10×10 SWT test section.

Find out more about Glenn's facilities: http://www.grc.nasa.gov/WWW/FMPO/

Glenn contact:
David E. Stark, 216–433–2922,
David.E.Stark@grc.nasa.gov

Army contact:
Gary A. Klann, 216–433–5715,
Gary.A.Klann@grc.nasa.gov

Author: David E. Stark

Headquarters program office: OAT

Programs/Projects:
DARPA, Quiet Supersonic Platform

Small Hot Jet Acoustic Rig Commissioned Into Service

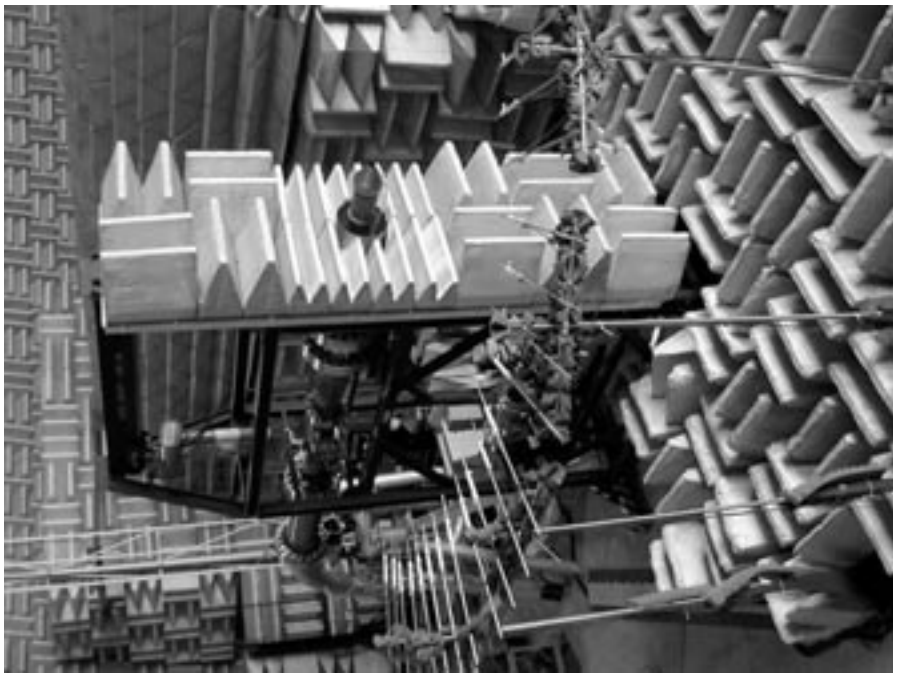

Vertical perspective of Small Hot Jet Acoustic Rig at Glenn's Aeroacoustic Propulsion Laboratory.

A new test stand, the Small Hot Jet Acoustic Rig, was commissioned into service at NASA Glenn Research Center's Aeroacoustic Propulsion Laboratory. This new rig provides researchers with an all-in-one platform with which to economically evaluate the thrust performance, acoustic performance, and plume turbulence characteristics of new nozzle concepts. It features an integral force balance, exceptionally low internal flow-noise, and provisions to conduct laser-based plume turbulence studies with Particle Imaging Velocimetry, shadowgraphs, schlieren photography, and other techniques. The rig also features an integral combustor and can deliver air to the test nozzle at temperatures ranging from

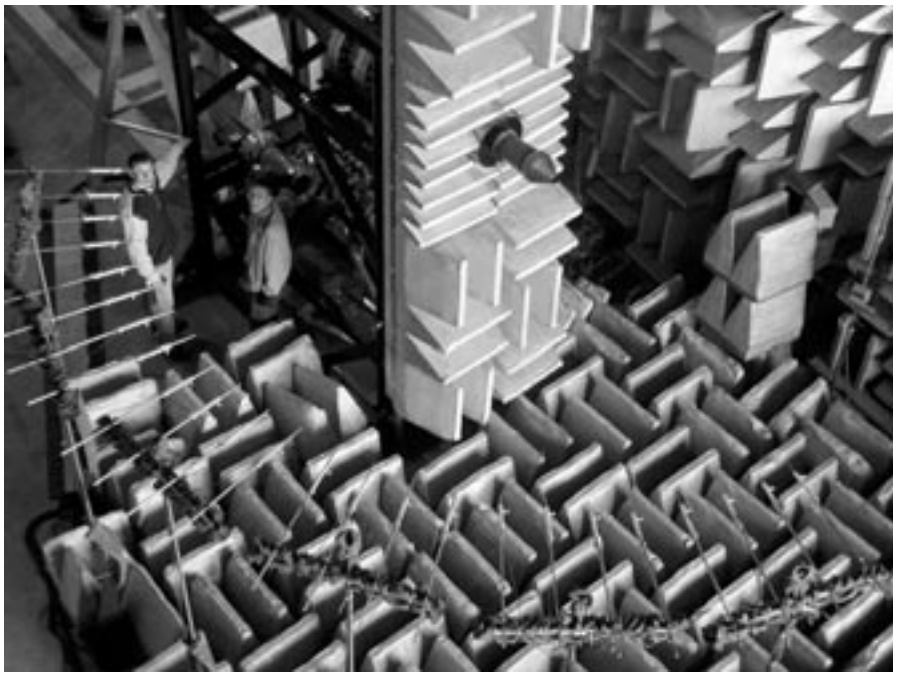

Horizontal perspective of Glenn's Small Hot Jet Acoustic Rig.

ambient to 1300 °F. The Small Hot Jet Acoustic Rig is the fourth semipermanent rig now residing in the Aeroacoustic Propulsion Laboratory. It will add to the facility's substantial list of acoustic research capabilities and improve its already impressive productivity.

Find out more about this research:
http://www.grc.nasa.gov/WWW/FMPO/

Glenn contacts:
Dr. James E. Bridges, 216–433–2693, James.E.Bridges@grc.nasa.gov; Stephen P. Wnuk, 216–433–5748, Stephen.P.Wnuk@grc.nasa.gov; and Osvaldo Rivera, 216–433–5699, Osvaldo.Rivera@grc.nasa.gov

Author: Stephen P. Wnuk

Headquarters program office: OAT

Programs/Projects: UEET, QAT

Engineering Design and Analysis

Acoustically Enhanced Electroplating Being Developed

In cooperation with the NASA Glenn Research Center, Alchemitron Corp. is developing the Acoustically Enhanced Electroplating Process (AEEP), a new technique of employing nonlinear ultrasonics to enhance electroplating. The applications range from electroplating full-panel electronic circuit boards to electroplating microelectronics and microelectromechanical systems (MEMS) devices. In a conventional plating process, the surface area to be plated is separated from the nonplated areas by a temporary mask. The mask may take many forms, from a cured liquid coating to a simple tape. Generally, the mask is discarded when the plating is complete, creating a solid waste product that is often an environmental hazard. The labor and materials involved with the layout, fabrication, and tooling of masks is a primary source of recurring and nonrecurring production costs. The objective of this joint effort, therefore, is to reduce or eliminate the need for masks.

AEEP improves selective plating processes by using directed beams of high-intensity acoustic waves to create nonlinear effects that alter the fluid dynamic and thermodynamic behavior of the plating process. It relies on two effects: acoustic streaming and acoustic heating. Acoustic streaming is observed when a high-intensity acoustic beam creates a liquid current within the beam. The liquid current can be directed as the beam is directed and, thus, users can move liquid around as desired without using pumps and nozzles. The current of the electroplating electrolyte, therefore, can be directed at distinct target areas where electroplating is desired. The current delivers fresh electrolyte to the target area while flushing away the spent electrolyte. This dramatically increases the plating rate in the

target area. In addition, acoustic heating of both the liquid in the beam and the target surface increases the chemical reaction rate, which further increases the plating rate. The combined effects of acoustic streaming and heating accelerate the deposition of plating in that area and, thus, provide an effect similar to a mask but without the costs of masking. AEEP further improves the plating process by clearing debris and bubbles from the surface by acoustic radiation pressure and acoustic streaming.

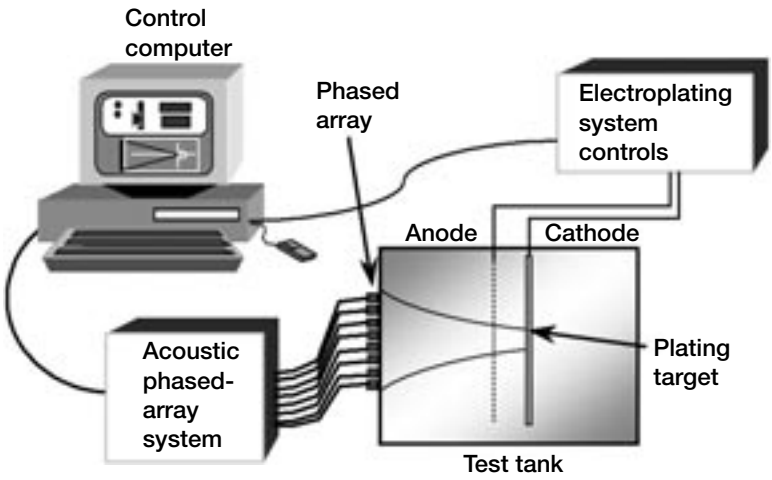

Advanced electroplating system incorporating acoustic phased-array technology.

As an alternative to the immersion form of plating just described, AEEP can also perform selective plating by using acoustic radiation pressure to create an acoustic fountain from a liquid pool. This approach raises a liquid fountain of plating solution and brings it into contact with the part suspended over a pool. The fountain can be moved around to draw a plating pattern on the part. This approach is expected to be most effective in conveyorized plating lines.

All these acoustic effects use high-frequency, high-intensity acoustic transducers and a means of directing a beam of acoustic waves. The complexity may range from a simple transducer with a fixed acoustic lens to a complex array of many elements in an acoustic phased array. Acoustic phased-array technology promises to provide the flexibility of electronically steered and focused beams. In turn, this flexibility will allow users to "draw" a pattern on the target surface under computer control. In this way, AEEP is expected to make electroplated products, which were formerly tooling and labor intensive, as simple to produce as computer-printed graphics.

Glenn contact:
Richard C. Oeftering, 216–433–2285,
Richard.C.Oeftering@grc.nasa.gov

Author: Richard C. Oeftering

Headquarters program office:
OAT (CTD)

Programs/Projects: CTO

Hybrid Power Management Program Continued

Hybrid Power Management (HPM) is the innovative integration of diverse, state-of-the-art power devices in an optimal configuration for space and terrestrial applications. The appropriate application and control of the various power devices significantly improves overall system performance and efficiency. The advanced power devices include ultracapacitors and photovoltaics. HPM has extremely wide potential with applications including power-generation, transportation, biotechnology, and space power systems. It may significantly alleviate global energy concerns, improve the environment, and stimulate the economy.

One of the unique power devices being employed by HPM for energy storage is the ultracapacitor. A capacitor is an electrical energy storage device consisting of two or more conducting electrodes separated from one another by an insulating dielectric. An ultracapacitor is an electrochemical energy storage device that has extremely high volumetric capacitance energy because of its high-surface-area electrodes and very small electrode separation. Ultracapacitors have many advantages over batteries:

(1) Batteries can be charged and discharged only about 300 times and then must be replaced. Ultracapacitors can be charged and discharged over 1 million times. The long cycle life of ultracapacitors greatly improves system reliability, and it reduces life-of-system costs.

(2) Long ultracapacitor life significantly reduces environmental impact because ultracapacitors will probably never need to be replaced and disposed of in most applications.

(3) The environmentally safe, recyclable components of ultracapacitors greatly reduce disposal concerns.

(4) The ultracapacitor's high-power density provides high power during surges and the ability to absorb high power during recharging. Ultracapacitors are extremely efficient in capturing recharging energy.

(5) Ultracapacitors are extremely rugged, reliable, and maintenance free.

(6) Ultracapacitors have excellent low-temperature characteristics.

(7) Ultracapacitors provide consistent performance over time.

(8) Ultracapacitors promote safety because they can be discharged easily and then left indefinitely in a safe discharged state.

HPM has been used in several applications at the NASA Glenn Research Center. One successful application was the NASA Hybrid Electric Transit Bus (HETB)—a 40-ft transit bus with a unique hybrid drive. At over 37,000-lb gross weight, this is the largest vehicle to ever use ultracapacitor energy storage. The ultracapacitor technology utilized for this bus is being applied to satellite actuation to replace unreliable hydraulic systems. The motor and control technology utilized for the bus is being applied to flywheel dynamometer systems.

E-Bike used in the Hybrid Power Management (HPM) program—Bike, Bus, and Beyond.

HPM also has been applied to the E-Bike—a state-of-the-art, built-from-the-ground-up, hybrid electric bicycle that was tested and documented in fiscal year 2001. The E-Bike is an inexpensive, practical way to advance the state of the art in hybrid technology.

HPM has been utilized to provide safe, long-life energy storage systems for drop tower research. In addition, it is being considered for providing reliable, long-life energy storage systems for space missions (such as the exploration of Mars) and deep space missions (such as the exploration of Europa).

Through Glenn's Commercial Technology Office, HPM is being applied to power-generation, transportation, safety, and biotechnology systems. Some specific examples include photovoltaic power generation, safety flashers, water pumping for irrigation and human consumption, and hearing aids. In fiscal year 2001, an ultracapacitor-powered highway safety flasher and an ultracapacitor-enhanced photovoltaic power station were designed, developed, and tested successfully.

Bibliography

Eichenberg, Dennis J.; Kolacz, John S.; and Tavernelli, Paul F.: Baseline Testing of the EV Global E-Bike. NASA/TM—2001-210569, 2001. http://gltrs.grc.nasa.gov/GLTRS/

Eichenberg, Dennis J.; Kolacz, John S.; and Tavernelli, Paul F.: Baseline Testing of the EV Global E-Bike SX. NASA/TM—2001-210972, 2001. http://gltrs.grc.nasa.gov/GLTRS/

Eichenberg, Dennis J.; Kolacz, John S.; and Tavernelli, Paul F.: Baseline Testing of the EV Global E-Bike With Ultracapacitors. NASA/TM—2001-211077, 2001. http://gltrs.grc.nasa.gov/GLTRS/

Glenn contact:
Dennis J. Eichenberg, 216–433–8360, Dennis.J.Eichenberg@grc.nasa.gov

Author: Dennis. J. Eichenberg

Headquarters program office: OAT (CTD)

Programs/Projects: CTO

Novel Engineering and Fabrication Techniques Tested in Low-Noise-Research Fan Blades

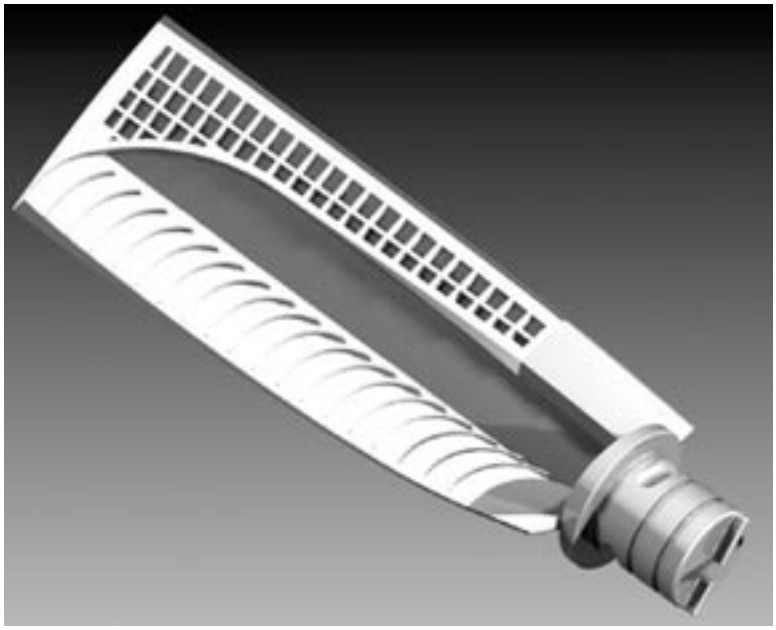

Trailing Edge Blowing blade with top skin removed. Air enters at the retainer (bottom right) and exits through turning vanes at the trailing edge (left).

A major source of fan noise in commercial turbofan engines is the interaction of the wake from the fan blades with the stationary vanes (stators) directly behind them. The Trailing Edge Blowing (TEB) project team at the NASA Glenn Research Center designed and fabricated new fan blades to study the effects of fan trailing edge blowing as a potential noise-reduction concept. The intent is to fill the rotor wake by supplying air to the rotor blade trailing edge at the proper conditions to minimize the wake deficit, and thus generate less noise. The TEB hardware is designed for the Active Noise Control Fan (ANCF) test rig in Glenn's Aeroacoustic Propulsion Laboratory.

For this test, the air is fed from an external supply through the shaft of the rig. It is distributed to the base of each blade through an impeller, where it is forced into a plenum at the core of each blade. In actual engine configuration, air would most likely be bled from the compressor, but only at times when noise is an issue, such as takeoffs and landings.

Glenn researchers designed and manufactured the blades in-house, using new techniques and concepts. The skins, which were designed for maximum strength in the directions of highest stress, were molded from multiple layers of carbon fiber. Considerable use was made of rapid prototyping techniques, such as laser sintering. The core was sintered from a lightweight polymer, and the retainer was CNC-machined (computer numerical control machined) from aluminum. All the components were joined with a cold-cure aerospace adhesive. These techniques and processes reduced the overall cost and allowed the new concept to be studied much sooner than would be possible using traditional fabrication methods.

Since this test rig did not support the use of blade-monitoring techniques such as strain gauges, extensive bench testing was required to qualify the design. The blades were examined using a variety of methods including holography, pull tests (cyclic and failure), shake tests, rap tests, and nondestructive inspection.

Acoustic testing of the ANCF fan using TEB has been ongoing since January of 2001. The fan has completed about 100 hr of testing with no structural, vibrational, or fatigue problems. Far-field acoustic measurements, in-duct mode measurements, precise hot wire surveys, and detailed performance measurements are providing data for evaluating the concept. The far-field noise data show that tone noise was reduced significantly with the initial ANCF TEB fan design. In addition, a significant reduction in

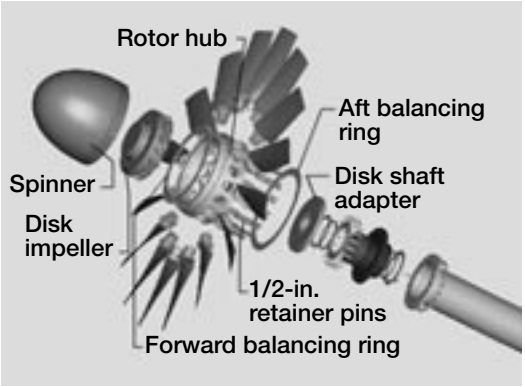

ANCF Trailing Edge Blowing test rig showing the flowpath of the air supply through the shaft into the blades.

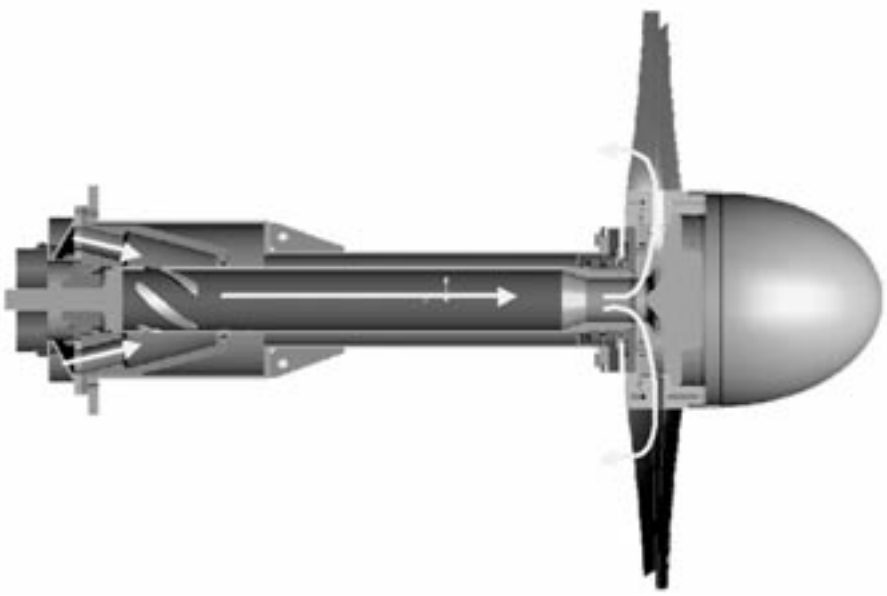

Exploded view of ANCF Trailing Edge Blowing test rig hardware. Mass flow, 2.6 lb/sec (2-percent total mass flow); pressure, 2.5 psig; rotational velocity, 2000 rpm.

unsteady stator loading has been measured, indicating the potential for stator broadband noise reduction. The acoustic benefits will be assessed and important design parameters identified to improve the ability to fully exploit any benefit provided by this technique.

On the basis of the success of trailing edge blowing, Glenn plans to continue this research with a higher speed, higher pressure ratio fan operating in an acoustic wind tunnel to simulate flight conditions.

Find out more about this research:
http://www.grc.nasa.gov/WWW/7725/

Glenn contacts: Cameron C. Cunningham, 216–433–5516, Cameron.C.Cunningham@grc.nasa.gov; Tony D. Shook, 216–433–6373, Tony.D.Shook@grc.nasa.gov; and E. Brian Fite, 216–433–3892, Eric.B.Fite@grc.nasa.gov

Author: Cameron C. Cunningham

Headquarters program office: OAT

Programs/Projects: QAT, UEET

High-Flow Jet Exit Rig Designed and Fabricated

The High-Flow Jet Exit Rig at the NASA Glenn Research Center is designed to test single-flow jet nozzles and to measure the appropriate thrust and noise levels. The rig has been designed for the maximum hot condition of 16 lbm/sec of combustion air at 1960 °R (maximum) and to produce a maximum thrust of 2000 lb. It was designed for cold flow of 29.1 lbm/sec of air at 530 °R. In addition, it can test dual-flow nozzles (nozzles with bypass flow in addition to core flow) with independent control of each flow. The High-Flow Jet Exit Rig was successfully fabricated in late 2001 and is being readied for checkout tests. The rig will be installed in Glenn's Aeroacoustic Propulsion Laboratory.

The High-Flow Jet Exit Rig consists of the following major components: a single-component force balance, the natural-gas-fueled J–79 combustor assembly, the plenum and manifold assembly, an acoustic/instrumentation/seeding (A/I/S) section, a table, and the research nozzles. The rig will be unique in that it is designed to operate uncooled. The structure survives the 1960 °R test condition because it uses carefully selected high-temperature alloy materials such as Hastelloy-X. The lower plenum assembly was designed to operate at pressures to 450 psig at 1960 °R, in accordance with the ASME B31.3 piping code. The natural gas-fueled combustor fires directly into the lower manifold. The hot air is directed through eight 1-1/2-in. supply pipes that supply the upper plenum. The flow is conditioned in the upper plenum prior to flowing to the research nozzle. The 1-1/2-in. supply lines are arranged in a U-shaped design to provide for a flexible piping system.

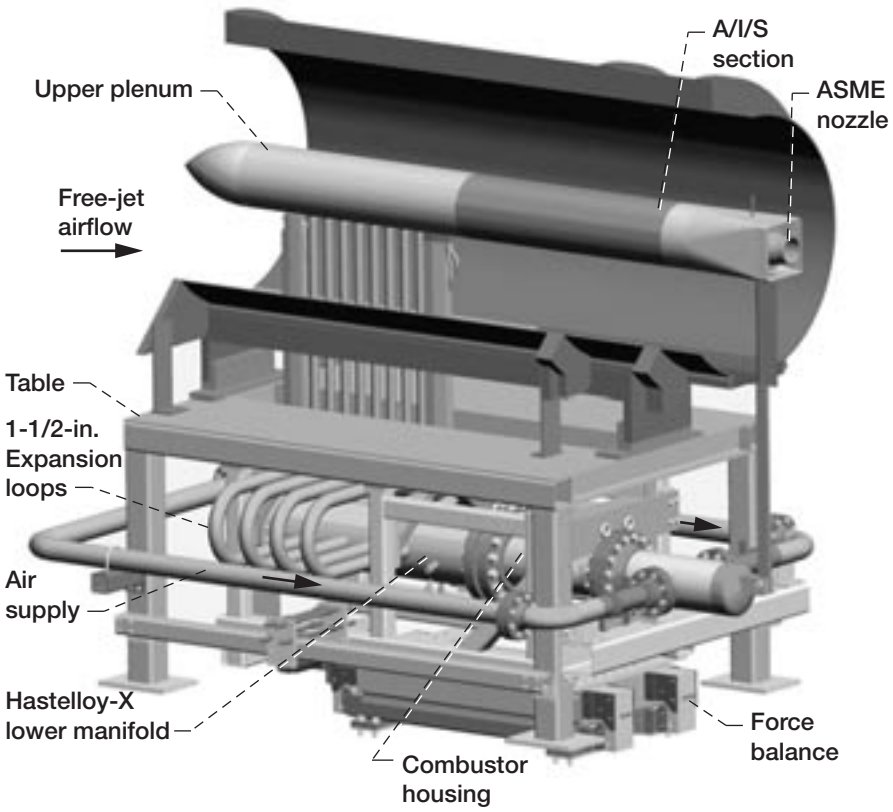

High-Flow Jet Exit Rig.

The combustor assembly checkout was successfully conducted in Glenn's Engine Component Research Laboratory in the spring of 2001. The combustor is a low-smoke version of the J–79 combustor used to power the F–4 Phantom military aircraft. The natural-gas-fueled combustor demonstrated high-efficiency combustion over a wide range of operating conditions. This wide operating envelope is required to support the testing of both single- and dual-flow nozzles.

Key research goals include providing simultaneous, highly accurate acoustic, flow, and thrust measurements on jet nozzle models in realistic flight conditions, as well as providing scaleable acoustic results. The High-Flow Jet Exit Rig is a second-generation high-flow test rig. Improvements include cleaner flow with reduced levels of particulate, soot, and odor. Choked-flow metering is required with ±0.25-percent accuracy. Thrust measurements from 0 to 2000 lbf are required with ±0.25-percent accuracy. Improved acoustics will be achieved by minimizing noise through large pipe bend radii, lower internal flow velocities, and microdrilled choke plates with thousands of 0.040-in.-diameter holes.

Glenn contacts:
Robert.J.Buehrle, 216–433–8735, Robert.J.Buehrle@grc.nasa.gov; and Paul A. Trimarchi, 216–433–3824, Paul.A.Trimarchi@grc.nasa.gov

Authors: Robert J. Buehrle and Paul A. Trimarchi

Headquarters program office: OAT

Programs/Projects: AAPL, UEET, QAT

Understanding of the Dynamics of the Stirling Convertor Advanced by Structural Testing

The NASA Glenn Research Center, the U.S. Department of Energy, and the Stirling Technology Company (STC) are developing a highly efficient, long-life, free-piston Stirling convertor for use as an advanced spacecraft power system for future NASA missions, including deep-space and Mars surface applications. As part of this development, four structural dynamic test programs were recently performed on Stirling Technology Demonstration Convertors (TDC's) that were designed and built by STC under contract to the Department of Energy. This testing was performed in Glenn's Structural Dynamics Laboratory and Microgravity Emissions Laboratory.

Dynamic emissions of a pair of Stirling convertors were measured in Glenn's Microgravity Emissions Laboratory.

The first test program, in November and December 1999, demonstrated that the Stirling TDC could withstand the harsh random vibration experienced during a typical spacecraft launch and survive with no structural damage or functional power performance degradation. This was a critical step in enabling the use of Stirling convertors for future spacecraft power systems. The most severe test was a $12.3g_{rms}$ random vibration test, with test durations of 3 min per axis. The random vibration test levels were chosen to simulate, with margin, the maximum anticipated launch vibration conditions.

The Microgravity Emissions Laboratory is typically used to measure the dynamics produced by operating space experiments and the resulting impact to the International Space Station's microgravity environment. For the second Stirling dynamic test program, performed in January 2001, the Microgravity Emissions Laboratory was used to characterize the structure-borne disturbances produced by the normal operation of a pair of Stirling convertors. The forces and moments produced by the normal operation of a Stirling system must be recognized and controlled, if necessary, so that other nearby spacecraft components, such as cameras, are not adversely affected. The Stirling convertor pair emitted relatively benign tonal forces at its operational frequency and associated harmonics. Therefore, Stirling power systems will not disturb spacecraft science experiments if minimal appropriate mounting efforts are made.

The third test program, performed in February and May 2001, resulted in a modal characterization of a Stirling convertor. Since the deflection of the TDC piston rod, under vibration excitation, was of particular interest, the outer pressure shell was removed to allow access to the rod. Through this testing, the Stirling TDC's natural frequencies and modes were identified. This knowledge advanced our understanding of the successful 1999 vibration test and may be utilized to optimize the output power of future Stirling designs.

The fourth test program, in April 2001, was conducted to characterize the structural response of a pair of Stirling convertors, as a function of their mounting interface stiffness. The test results provide guidance for the Stirling power package interface design. Properly designed, the interface may lead to increased structural capability and power performance beyond what was demonstrated in the successful 1999 vibration test.

Dynamic testing performed to date at Glenn has shown that the Stirling convertors can withstand liftoff random vibration environments and meet "good neighbor" vibratory emission requirements. Furthermore, the future utilization of the information obtained during the tests will allow the corporation selected to be the Stirling system integrator to optimize their convertor and system interfaces designs. Glenn's Thermo-Mechanical Systems Branch provides Stirling technology expertise under a Space Act Agreement with the Department of Energy. Additional vibration testing by Glenn's Structural Systems Dynamics Branch is planned to continue to demonstrate the Stirling power system's vibration capability as its technology and flight system designs progress.

Bibliography

Hughes, William O.; McNelis, Mark E.; and Goodnight, Thomas W.: Vibration Testing of an Operating Stirling Convertor. NASA/TM—2000-210526, 2000. http://gltrs.grc.nasa.gov/GLTRS/

Goodnight, Thomas W.; Hughes, William O.; and McNelis, Mark E.: Dynamic Capability of an Operating Stirling Convertor. NASA/TM—2000-210527 (AIAA Paper 2000–2839), 2000. http://gltrs.grc.nasa.gov/GLTRS/

Thieme, Lanny G.; and Schreiber, Jeffrey G.: Update on the NASA GRC Stirling Technology Development Project. NASA/TM—2000-210592, 2000. http://gltrs.grc.nasa.gov/GLTRS/

Suarez, et al.: Impact Testing of a Stirling Convertor's Linear Alternator. Proceedings of the Space Technology and Applications International Forum, Albuquerque, NM, Feb. 3–6, 2002 (NASA/TM—2002-211342, http://gltrs.grc.nasa.gov/GLTRS/).

Goodnight, T.W., et al.: Effect of Structural Mount Dynamics on a Pair of Operating Stirling Convertors. Proceedings of the Space Technology and Applications International Forum, Albuquerque, NM, Feb. 3–6, 2002.

Find out more about this research:

Structural Dynamics Laboratory:
http://www.grc.nasa.gov/WWW/SDL/Home.html

Microgravity Emissions Laboratory:
http://www.grc.nasa.gov/WWW/MEL/

Thermo-Mechanical Systems Branch:
http://www.grc.nasa.gov/WWW/tmsb/

Glenn contacts:
William O. Hughes, 216– 433–2597, William.O.Hughes@grc.nasa.gov; Thomas W. Goodnight, 216–433–2381, Thomas.W.Goodnight@grc.nasa.gov; and Anne M. McNelis, 216–433–8880, Anne.M.McNelis@grc.nasa.gov

Author: William O. Hughes

Headquarters program office:
OSS (Flight Program)

Programs/Projects: Power and On-Board Propulsion Division, Stirling Engine Technology

Preliminary Sizing Completed for Single-Stage-To-Orbit Launch Vehicles Powered By Rocket-Based Combined Cycle Technology

Single-stage-to-orbit (SSTO) propulsion remains an elusive goal for launch vehicles. The physics of the problem is leading developers to a search for higher propulsion performance than is available with all-rocket power. Rocket-based combined cycle (RBCC) technology provides additional propulsion performance that may enable SSTO flight.

Structural efficiency is also a major driving force in enabling SSTO flight. Increases in performance with RBCC propulsion are offset with the added size of the propulsion system. Geometrical considerations must be exploited to minimize the weight.

Integration of the propulsion system with the vehicle must be carefully planned such that aeroperformance is not degraded and the air-breathing performance is enhanced. Consequently, the vehicle's structural architecture becomes one with the propulsion system architecture. Geometrical considerations applied to the integrated vehicle lead to low drag and high structural and volumetric efficiency.

Sizing of the SSTO launch vehicle (GTX) is itself an elusive task. The weight of the vehicle depends strongly on the propellant required to meet the mission requirements. Changes in propellant requirements result in changes in the size of the vehicle, which in turn, affect the weight of the vehicle and change the propellant requirements. An iterative approach is necessary to size the vehicle to meet the flight requirements.

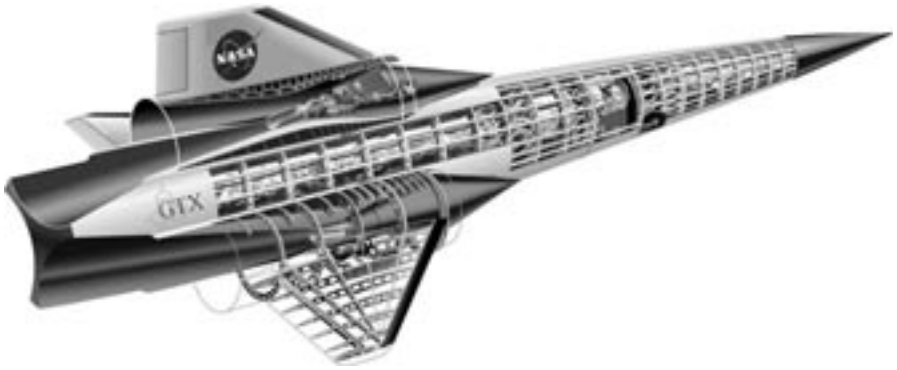

GTX reference vehicle. This figure is shown in color (i.e., more detail can be seen) in the online version of this article (http://www.grc.nasa.gov/WWW/RT2001/7000/7740roche.html).

GTXSizer was developed to do exactly this. The governing geometry was built into a spreadsheet model along with scaling relationships. The scaling laws attempt to maintain structural integrity as the vehicle size is changed. Key aerodynamic relationships are maintained as the vehicle size is changed. The closed weight and center of gravity are displayed graphically on a plot of the synthesized vehicle. In addition, comprehensive tabular data of the subsystem weights and centers of gravity are generated.

The model has been verified for accuracy with finite element analysis. The final trajectory was rerun using OTIS (Boeing Corporation's trajectory optimization software package), and the sizing output was incorporated into a solid model of the vehicle using PRO/Engineer computer-aided design software (Parametric Technology Corporation, Waltham, MA).

Glenn contact:
Joseph M. Roche, 216–433–2575,
Joseph.M.Roche@grc.nasa.gov

Author: Joseph M. Roche

Headquarters program office: OAT

Programs/Projects:
Gen Three, hypersonics

CORBASec Used to Secure Distributed Aerospace Propulsion Simulations

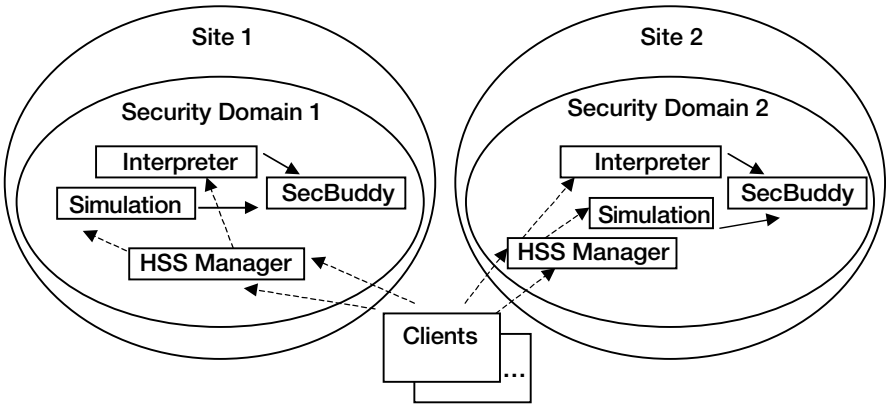

CORBASec multiple security domain, multiple ORB interceptor services, and application-invoked architecture.

The NASA Glenn Research Center and its industry partners are developing a Common Object Request Broker (CORBA) Security (CORBASec) test bed to secure their distributed aerospace propulsion simulations. Glenn has been working with its aerospace propulsion industry partners to deploy the Numerical Propulsion System Simulation (NPSS) object-based technology. NPSS is a program focused on reducing the cost and time in developing aerospace propulsion engines. It was developed by Glenn and is being managed by the NASA Ames Research Center as the lead center reporting directly to NASA Headquarters' Aerospace Technology Enterprise. Glenn is an active domain member of the Object Management Group: an open membership, not-for-profit consortium that produces and manages computer industry specifications (i.e., CORBA) for interoperable enterprise applications. When NPSS is deployed, it will assemble a distributed aerospace propulsion simulation scenario from proprietary analytical CORBA servers and execute them with security afforded by the CORBASec implementation.

The NPSS CORBASec test bed was initially developed with the TPBroker Security Service product (Hitachi Computer Products (America), Inc., Waltham, MA) using the Object Request Broker (ORB), which is based on the TPBroker Basic Object Adaptor, and using NPSS software across different firewall products. The test bed has been migrated to the Portable Object Adaptor architecture using the Hitachi Security Service product based on the VisiBroker 4.x ORB (Borland, Scotts Valley, CA) and on the Orbix 2000 ORB (Dublin, Ireland, with U.S. headquarters in Waltham, MA). Glenn, GE Aircraft Engines, and Pratt & Whitney Aircraft are the initial industry partners contributing to the NPSS CORBASec test bed. The test bed uses Security SecurID (RSA Security Inc., Bedford, MA) two-factor token-based authentication together with Hitachi Security Service digital-certificate-based authentication to validate the various NPSS users.

The test bed is expected to demonstrate NPSS CORBASec-specific policy functionality, confirm adequate performance, and validate the required Internet configuration in a distributed collaborative aerospace propulsion environment.

Glenn contact:
Tammy M. Blaser, 216–433–2699,
Tammy.M.Blaser@grc.nasa.gov

Author: Tammy M. Blaser

Management program office:
NASA Ames Research Center

Programs/Projects:
CICT, Aerospace Technology Enterprise

Observer-Based Magnetic Bearing Controller Developed for Aerospace Flywheels

A prototype of a versatile, observer-based magnetic bearing controller for aerospace flywheels was successfully developed and demonstrated on a magnetic bearing test rig (see the photograph) and an actual flywheel module.

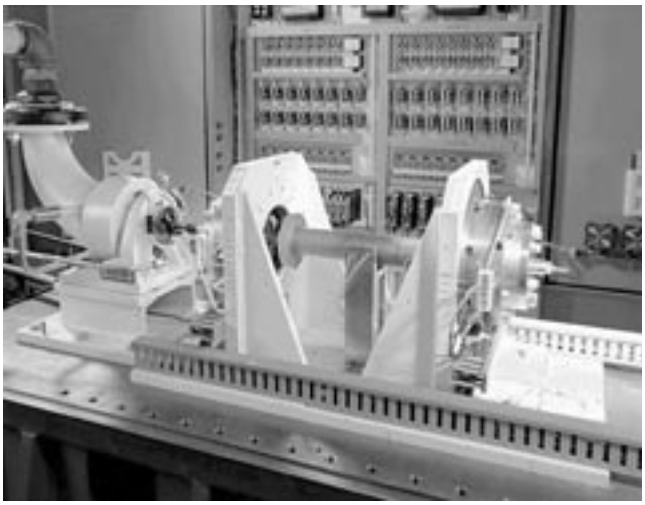

Simple test rig used to develop the observer-based controller.

The objective of this development included a fast, yet low risk, control development process, and a robust, high-performance controller for a large variety of flywheels. This required a good system model, an efficient development procedure, and a model-based controller that addressed the key problems associated with flywheel and bearing imbalance, sensor error, and vibration. The model used in this control development and tuning procedure included the flexible rotor dynamics and motor-induced vibrations. Such a model was essential for low-risk scheduling of speed-dependent control parameters and for reliable evaluation of novel control strategies. The successfully tested control prototype utilized an extended Kalman filter to estimate the true rotor principal-axis motion from the raw sensor position feedback. For control refinement, the extended Kalman filter also estimated and eliminated the combined effects of mass-imbalance and sensor runouts from the input data.

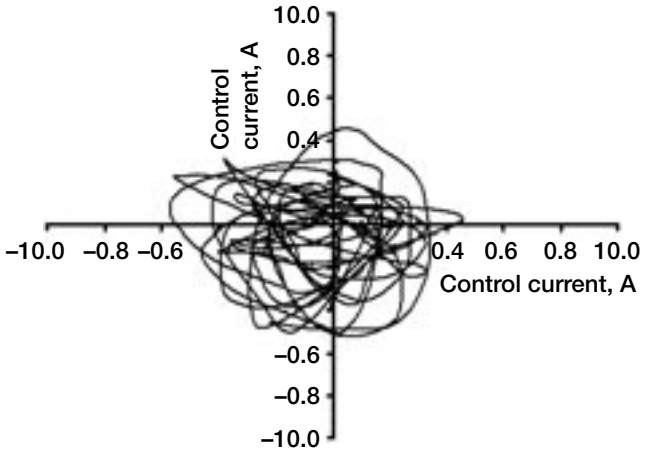

Test results of the observer-based controller on an actual flywheel module. Speed at 26,000 rpm; imbalance compensation, 0.83 of estimated total errors.

A key advantage of the design based on the extended Kalman filter is its ability to accurately estimate both the rotor's principal-axis position and gyroscopic rates with the least amount of phase lag. This is important for control parameter scheduling to dampen the gyroscopic motions. Because of large uncertainties in the magnetic bearing and imbalance characteristics, this state-estimation scheme alone is insufficient for containing the rotor motion within the desired 1-mil excursion radius. A nonlinear gain adjustment based on an estimation of the principal-axis orbit size was needed to provide a coarse (nonoptimal), but robust, control of the orbit growth. Control current minimization was achieved with a (steepest gradient) search of synchronous errors in the principal-axis position input data.

Actual flywheel tests of this observer-based controller (developed entirely in-house) at the NASA Glenn Research Center showed that the model correctly predicted the rotor orbit growth as a function of rotational speed, and it demonstrated the capability of gain adjustments to arrest this growth. Data from these tests on an actual flywheel module spun to 26,000 rpm proved that the controller was able to contain the shaft motion to within much less than 0.5 mils of radial excursion with axis currents less than 300 mA in root-mean-square estimate (see the graph). The test speed range was limited because of thermal

expansion concerns for this particular flywheel unit, not because of any deficiency in the controller. Simulations for this unit indicated that the controller should be robust up to its top operating speed of 60,000 rpm. Aside from these important achievements, and most significantly, it took less than 1 week to adapt this controller from the simple test rig to the actual flywheel and to demonstrate full five-axis levitation and control. This demonstration showed that both the controller and the model-based development and tuning framework are easily adaptable to a wide range of rotors and bearing configurations and, hence, are capable of reducing design risks and costs for many future flywheel technology developments.

Bibliography

Misawa, E.A.; and Hedrick, J.K.: Nonlinear Observers—A State-of-the-Art Survey. J. Dyn. Syst. Meas. Control, vol. 111, no. 3, 1989, pp. 344–352.

Glenn contacts:
Dr. Dzu K. Le, 216–433–5640, Dzu.K.Le@grc.nasa.gov; and Andrew J. Provenza, 216–433–6025, Andrew.J.Provenza@grc.nasa.gov

Authors: Dr. Dzu K. Le and Andrew J. Provenza

Headquarters program office: OAT

Programs/Projects: AFTP, SRF

Commercial-Off-The-Shelf Microelectromechanical Systems (MEMS) Flow-Measurement Probes Fabricated And Assembled

As an alternative to conventional tubing instrumentation for measuring airflow, designers and technicians at the NASA Glenn Research Center have been fabricating packaging components and assembling a set of unique probes using commercial-off-the-shelf microelectromechanical systems (MEMS) integrated circuits (computer chips).

Using MEMS as an alternative has some compelling advantages over standard measurement devices. Sensor technologies have matured through high-production usage in industries such as automotive and aircraft manufacturers. Currently, MEMS are the choice in applications such as tire pressure monitors, altimeters, pneumatic controls, cable leak detectors, and consumer appliances.

Conventional instrumentation uses tubing buried in the model aerodynamic surfaces or wind tunnel walls. The measurements are made when pressure is introduced at the tube opening. The pressure then must travel the tubing for lengths ranging from 20 to hundreds of feet before reaching an electronic signal conditioner. This condition causes a considerable amount of damping and requires measurements to be made only after the test rig has reached steady-state operation. The electronic MEMS pressure sensor is able to take readings continuously under dynamic states in nearly real time.

The use of stainless steel tubing for pressure measurements requires many tubes to be cleaned, cut to length, carefully installed, and delicately deburred and spliced for use. A cluster of a few hundred 1/16-in.- (0.0625-in.-) diameter tubes (not uncommon in research testing facilities) can be several inches in diameter and may weigh enough to require two men to handle. Replacing hard tubing with electronic chips can eliminate much of the bulk. Each sensor would fit on the tip of the 1/16-in. tubing with room to spare.

The P592 piezoresistive silicon pressure sensor (Lucas NovaSensor, Fremont, CA) was chosen for this project because of its cost, availability, and tolerance to extreme

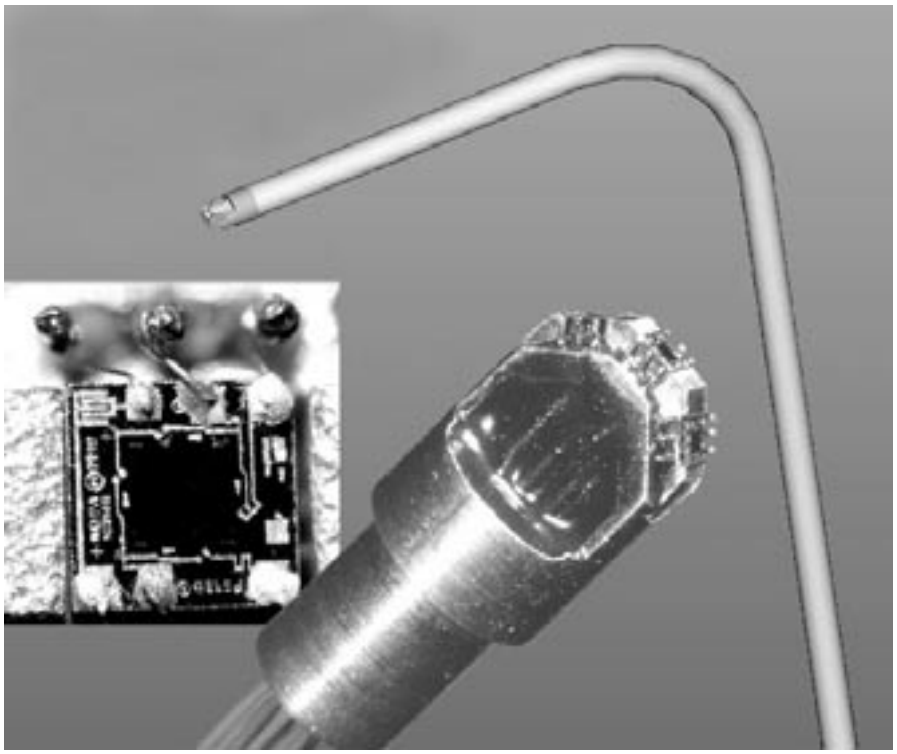

Commercial-off-the-shelf MEMS flow-measurement probes.

ambient conditions. The chip is 1 mm square by 0.6 mm thick (0.039 by 0.023 in.) with 0.12-mm (0.005-in.) wire connection tabs.

Three MEMS chips were used to build the first type of flow-angularity probe. This MEMS probe will be demonstrated as an alternative to a standard tube type "Cobra Probe" now used routinely in wind tunnel and aeronautical hardware applications. The response time and accuracy would allow the probe to be translated on an actuator across a flow field, yielding precision dynamic measurements not possible with conventional instrumentation.

The low profile, the minimal power requirement, the rugged construction, and the moderate cost all contribute to making MEMS sensors the enticing choice instrument in future research measurement needs.

The MEMS probe efforts are a continuation of work initiated by Brian Willis, without whose foresight and efforts this project would never have been realized. This task was funded through cooperation with the NASA Electronic Parts and Packaging (NEPP) program at the Jet Propulsion Laboratory.

Glenn contact:
Chip Redding, 216–433–3468,
Chip.Redding@grc.nasa.gov

Jet Propulsion Laboratory contact:
Reza Ghaffarian, 818–354–2059,
Reza.Ghaffarian@jpl.nasa.gov

Author: Chip Redding

Technical developers: Floyd A. Smith, Gregory C. Blank, and Charles T. Cruzan

Headquarters program office:
OA (Office of the Chief Engineer)

Programs/Projects: NEPP at JPL

2001

Commercial Technology

Numerical Propulsion System Simulation (NPSS): An Award Winning Propulsion System Simulation Tool

The Numerical Propulsion System Simulation (NPSS) is a full propulsion system simulation tool used by aerospace engineers to predict and analyze the aerothermodynamic behavior of commercial jet aircraft, military applications, and space transportation. The NPSS framework was developed to support aerospace, but other applications are already leveraging the initial capabilities, such as aviation safety, ground-based power, and alternative energy conversion devices such as fuel cells. By using the framework and developing the necessary components, future applications that NPSS could support include nuclear power, water treatment, biomedicine, chemical processing, and marine propulsion. NPSS will dramatically reduce the time, effort, and expense necessary to design and test jet engines. It accomplishes that by generating sophisticated computer simulations of an aerospace object or system, thus enabling engineers to "test" various design options without having to conduct costly, time-consuming real-life tests. The ultimate goal of NPSS is to create a numerical "test cell" that enables engineers to create complete engine simulations overnight on cost-effective computing platforms. Using NPSS, engine designers will be able to analyze different parts of the engine simultaneously, perform different types of analysis simultaneously (e.g., aerodynamic and structural), and perform analysis in a more efficient and less costly manner.

Numerical Propulsion System Simulation designated co-winner of the NASA Software of the Year Award for 2001.

NPSS will cut the development time of a new engine in half, from 10 years to 5 years. And NPSS will have a similar effect on the cost of development: new jet engines will cost about a billion dollars to develop rather than two billion. NPSS is also being applied to the development of space transportation technologies, and it is expected that similar efficiencies and cost savings will result.

Advancements of NPSS in fiscal year 2001 included enhancing the NPSS Developer's Kit to easily integrate external components of varying fidelities, providing the initial Visual-Based Syntax (VBS) capability, and developing additional capabilities to support space transportation. NPSS was supported under NASA's High Performance Computing and Communications Program.

Through the NASA/Industry Cooperative Effort agreement, NASA Glenn and its industry and Government partners are developing NPSS. The NPSS team consists of propulsion experts and software engineers from GE Aircraft Engines, Pratt & Whitney, The Boeing Company, Honeywell, Rolls-Royce Corporation, Williams International, Teledyne Continental Motors, Arnold Engineering Development Center, Wright Patterson Air Force Base, and the NASA Glenn Research Center.

Glenn is leading the way in developing NPSS—a method for solving complex design problems that's faster, better, and cheaper.

Find out more about this research:
http://hpcc.grc.nasa.gov/npssintro.shtml

Bibliography

Follen, G.J.: An Object Oriented Extensible Architecture for Affordable Aerospace Propulsion Systems. To be presented in Paris, France, Spring 2002.

Follen, G.; and auBuchon, M.: Numerical Zooming Between the NPSS Version 1 and a One-Dimensional Meanline Design Analysis Code. ISABE Paper 99–7196, 1999.

Binder, M.: Numerical Propulsion System Simulation Introduction. Multimedia CD, mbinder@reality-alt.com, Washington DC, 2001.

Evans, A.L., et al.: Numerical Propulsion System Simulation's National Cycle Program. AIAA Paper 98–3113, 1998.

Ashleman, Russell H., Jr.; Lavelle, Thomas; and Parsons, Frank: The National Cycle Program: A Flexible System Modeling Architecture. AIAA Paper 98–3114, 1998.

Glenn contacts:
Cynthia G. Naiman, 216–433–5238, Cynthia.G.Naiman@grc.nasa.gov and
Gregory J. Follen, 216–433–5193, Gregory.J.Follen@grc.nasa.gov

Authors: Laurel J. Stauber and Cynthia G. Naiman

Headquarters program office: OAT

Programs/Projects: HPCCP, CAS

Special recognition: In 2001, the NPSS team won the 2001 NASA Office of Aerospace Technology (OAT) Turning Goals into Reality (TGIR) Award for Goal 3 Pioneering Technology Innovation, was co-winner of the NASA 2001 Software of the Year Award (SOYA), and was a finalist to CrossTalk: The Journal of Defense Software Engineering TOP 5 Software Projects for 2001. NPSS Version 1.0 was selected as one of the top 16 Government Software Projects for 2001 out of 87 nominees.

Definitions of NASA Headquarters Program Offices

OAT Office of Aerospace Technology
- **CTD** Commercial Technology Division

OBPR Office of Biological and Physical Research

OSF Office of Space Flight
- **SOMO** Space Operations Management Office
- **OHEDS** Office of Human Exploration and Development of Space
- **OHSF** Office of Human Space Flight

OSS Office of Space Science
- **ATMS** Advanced Technology & Mission Studies Division

Definitions of Programs and Projects

AAPL	Aeroacoustic Propulsion Laboratory
Aero-SAPIENT	Aeronautical Satellite-Assisted Process for Information Exchange Through Network Technologies
AFTP	Aerospace Flywheel Technology Program
APOBP	Advanced Power & On-Board Propulsion Systems
ASTP	Advanced Space Transportation Program
AvSP	Aviation Safety Program
CAS	Computational Aerospace Sciences Project
CETDP	Cross-Enterprise Technology Development Program
CICT	Computing Information and Communications Technology Program
CloudSat	Cloud Cover Statistical Analysis Program
CTO	Glenn's Commercial Technology Office
DARPA	Defense Advanced Research Projects Agency
DDF	Director's Discretionary Fund (NASA Glenn)
EMRCE	ElectroMagnetic Radiation Control Experiment
FESS	Flywheel Energy Storage System
Galex	Galaxy Evolution Explorer
Gen Three	Third Generation Space Launch Vehicles
GMI	Glennan Microsystems Initiative
GEO	Geosynchronous Earth orbit
HEDS	Human Exploration and Development of Space
HITEMP	Advanced High Temperature Engine Materials Technology Program
HOTPC	High Operating Temperature Propulsion Components
HPCCP	High-Performance Computing and Communications Program
HRDD	High-Rate Data Delivery
HSR	High-Speed Research
HST	Hubble Space Telescope
ISE	Intelligent Synthesis Environment
ISS	International Space Station
JPL	Jet Propulsion Laboratory
IT Base	Information Technology Base Program
LTP	Learning Technologies Project
NEPAG	NASA Electronic Parts Assurance Group
NEPP	NASA Electronic Parts and Packaging
NGST	Next Generation Space Telescope
NSSK	North-South stationkeeping
NSTAR	NASA Solar Electric Propulsion Technology Application Readiness
PERS	Polymer Rechargeable System

QAT	Quiet Aircraft Technology
RAC	Revolutionary Aeropropulsion Concepts
RLV	Reusable Launch Vehicles
RSL	Rotor Safe Life
RTA	Revolutionary Turbine Accelerator
SBIR	Small Business Innovation Research
SEC	Smart Efficient Components
SEP	Solar Electric Propulsion
SILNT	Selected Integrated Low-Noise Transmissions for Rotorcraft
SLI	Strategic Launch Initiative
SRF	Glenn's Strategic Research Fund
SSP	Space Solar Power
STPO	Space Transportation Project Office
STR	Space Transportation Research
TPA	Technical Product Agreement
UEET	Ultra-Efficient Engine Technology Program
Ultra Safe	Ultra Safe Propulsion Project
X–38	Prototype crew return vehicle for ISS
ZCET	Zero CO_2 Emission Technology

Index of Authors and Contacts

Both authors and contacts are listed in this index. Articles start on the page numbers following the names.

A

Abel, Dr. Phillip B. 169
Abdul-Aziz, Dr. Ali 133, 134
Aboudi, Prof. Jacob 127, 131
Adamovsky, Dr. Grigory 83
Agui, Dr. Juan H. 185
Anderson, Robert C. 110
Andro, Monty 94
Ansari, Dr. Rafat R. 186
Ardent, Cory P. 27
Arnold, Dr. Steven M. 127, 128, 130, 131
Auping, Judith V. 37

B

Baaklini, Dr. George Y. 133, 134, 138, 140, 144
Baez, Anastacio N. 62
Bailey, Dr. Sheila G. 44, 45, 50
Bakhle, Dr. Milind A. 147
Banger, Dr. Kulbinder K. 49
Banks, Bruce A. 63, 65
Bansal, Dr. Narottam P. 17
Barrie, Robert L. 15
Bass, Jay D. 23
Bauer, Robert A. 174
Beach, Raymond F. 60, 204
Bednarcyk, Dr. Brett A. 130, 131
Bennett, William R. 29
Berton, Jeffrey J. 3
Bhatt, Dr. Ramakrishna T. 133
Bizon, Thomas P. 101
Blank, Gregory C. 224
Blaser, Tammy M. 222
Blech, Richard A. 122
Bonacuse, Peter J. 15, 136
Bond, Thomas H. 58
Bowman, Dr. Randy R. 12
Boyle, Dr. Robert L. 108
Bozzolo, Dr. Guillermo H. 169
Bream, Bruce L. 2
Breisacher, Kevin J. 109
Bridges, Dr. James E. 212
Buehrle, Robert J. 217
Button, Robert M. 61

C

Calomino, Dr. Anthony M. 39
Campbell, Sandi G. 25
Castro, Dr. Stephanie L. 44
Chang, Dr. Clarence T. 85
Chao, Dr. David F. 188
Chato, David J. 119
Chima, Dr. Rodrick V. 103, 104
Choi, Dr. Benjamin B. 149, 150
Choi, Dr. Sung R. 17, 137
Chuang, Dr. Kathy 27
Clark, Gregory W. 63
Clark, Dr. John I. 186
Claus, Russell W. 124
Cowen, Jonathan E. 49
Cruzan, Charles T. 224
Cunningham, Cameron C. 216

D

de Groh, Kim K. 63, 65, 66
DeGroot, Dr. Wilhemus A. 110
Decker, Dr. Arthur J. 82
DeLaat, John C. 85
DellaCorte, Dr. Christopher 2, 171, 172
Delleur, Ann M. 205
Delventhal, Rex A. 204
Dempsey, Paula J. 159
Dever, Joyce A. 66, 68
DiCarlo, Dr. James A. 8, 9, 33
Dietrich, Daniel L. 181, 182
Doehne, S. Michelle 57
Doherty, Michael P. 195
Dolce, James L. 62
Draper, Susan L. 13, 30
Duffy, Dr. Kirsten P. 151
Dunlap, Patrick H., Jr. 160

E

Ebihara, Ben T. 168
Eckel, Dr. Andrew J. 19a
Edmonds, Brian J. 172
Effinger, Michael R. 21
Elam, Sandra K. 21
Eichenberg, Dennis J. 214
Ellis, Dr. David L. 31

F

Falck, Robert D. 207
Farmer, Dr. Serene C. 19b, 23
Ferguson, Dr. Dale C. 46
Fine, Elizabeth 63, 65
Fite, E. Brian 157, 216
Follen, Gregory J. 228
Foltz, David A. 91
Foster, Dr. John E. 57
Fusaro, Robert L. 162, 168

G

Gabb, Dr. Timothy P. 15
Gaier, Dr. James R. 66, 69
Garces, Dr. Jorge E. 169
Garg, Dr. Anita 10
Gayda, Dr. John 16
Gennett, Dr. Tom 47
Gerber, Scott S. 71
Ghaffarian, Reza 224
Goldburg, Walter I. 192
Goodnight, Thomas W. 219
Greenbauer-Seng, Leslie A. 31
Griffin, Dr. DeVon W. 189, 202
Gummow, Jonathan D. 65, 66
Guo, Dr. Ten-Huei 87
Gyekenyesi, Dr. Andrew L. 138
Gyekenyesi, Dr. John P. 137

H

Haag, Thomas W. 57
Hamley, John A. 59b
Hammerstrom, Anne 63, 65
Hammoud, Ahmad 71
Harmon, Laura M. 140
Harris, Dr. Jerry D. 49

Handschuh, Dr. Robert F. 163
He, Charles C. 66
Hebsur, Mohan G. 143
Heidelberg, Laurence J. 157
Hepp, Dr. Aloysius F. 44, 47, 49, 52
Hicks, Dr. Yolanda R. 110
Hoffman, David J. 207
Hoffmann, Monica I. 198
Hojnicki, Jeffrey S. 205
Hopkins, Dale A. 155, 156
Horan, Richard 28
Hughes, William O. 219
Humphrey, Donald L. 31
Hunter, Dr. Gary W. 78
Hurst, Janet B. 22

I
Ivancic, William D. 92, 93

J
Jaskowiak, Martha H. 21
Jaworske, Dr. Donald A. 70
Jenkins, Phillip P. 50, 52
John, W. Trevor 84

K
Kacpura, Thomas J. 194
Kaminski, Carolyn 63, 65
Kantzos, Peter T. 15, 136, 143
Kenny, Barbara H. 60
Kerslake, Thomas W. 207
Kifle, Muli 101
Kinder, Dr. James D. 29
King, James F. 186
Kiser, J. Douglas 39
Klann, Gary A. 211
Kobayashi, Takahisa 88
Kolecki, Joseph C. 5
Kory, Carol L. 94
Krause, David L. 141, 143
Krawczyk, Richard J. 174
Kriven, Waltraud M. 23
Krupar, Martin J. 210

L
Laing, Peter 116
Landis, Dr. Geoffrey A. 50
LaPointe, Dr. Michael R. 53, 55
Le, Dr. Dzu K. 223
Lee, Dr. Ho-Jun 152
Lee, Dr. Kang N. 41
Leissler, George 28
Lekki, John D. 83
Lepicovsky, Dr. Jan 104
Lerch, Dr. Bradley A. 13, 30
Levine, Dr. Stanley R. 24
Lewicki, Dr. David G. 165
Linne, Alan A. 210
Linne, Diane 19a
Liou, Dr. Meng-Sing 126
Liu, Dr. Nan-Suey 115
Locci, Dr. Ivan E. 10, 34
Locke, Dr. Randy J. 110
Loh, Dr. Ching Y. 122

M
MacKay, Dr. Rebecca A. 10
Mansour, Adel 116
Martin, Richard E. 144
Marx, Laura 63, 65
Mason, Lee S. 72
McClendon, Mark W. 66
McDowell, Dr. Mark 200
McFarland, Dr. Eric R. 104
McNelis, Anne M. 219
McQuillen, John B. 190
Meador, Dr. Mary Ann B. 29
Mehmed, Oral 147, 151
Messer, Russell K. 66, 68
Mikellides, Dr. Pavlos G. 53, 55
Miller, Dr. Robert A. 41
Min, Dr. James B. 147, 153
Miranda, Dr. Félix A. 100
Miyoshi, Dr. Kazuhisa 13, 30
Montague, Gerald T. 149
Morscher, Gregory N. 22
Mortensen, Dale J. 101
Motil, Susan M. 202

N
Nahra, Henry K. 198
Naiman, Cynthia G. 228
Nayagam, Dr. Vedha 183
Needham, Kathleen K. 172
Nemeth, Noel N. 145
Nguyen, Nam T. 101
Nguyen, Dr. Quang-Viet 112

O
Oeftering, Richard 213
Okada, Don 58
Okojie, Dr. Robert S. 80
Oleson, Steven R. 207
Opila, Dr. Elizabeth J. 39
Oswald, Fred B. 162, 166, 168
Oyama, Dr. Akira 126

P
Patnaik, Dr. Surya N. 155
Patterson, Michael J. 57, 59b
Patterson, Richard L. 71
Palko, James W. 23
Pereira, Dr. J. Michael 13, 156
Petersen, Ruth A. 5
Phelps, Keith 58
Pietromica, Anthony J. 68
Pindera, Prof. Marek-Jerzy 127
Piñero, Luis R. 57, 58
Ponchak, Dr. George E. 96, 97
Provenza, Andrew J. 223
Pyter, Janusz 58

R
Raffaelle, Dr. Ryne P. 44, 45, 47, 49, 52
Raj, Dr. Sai V. 30, 34
Raju, Dr. Manthena S. 115
Rawlin, Vincent K. 57, 59a, 59b
Redding, Chip 224
Reddy, Dr. Dhanireddy R. 53, 55
Reveley, Mary S. 4
Revilock, Duane M. 156
Ritzert, Frank J. 10
Rivera, Osvaldo 212
Roche, Joseph M. 221

S
Salem, Dr. Jonathan A. 34
Sankaran, Dr. Subramanian 195
Sarver-Verhey, Timothy R. 207
Sawicki, Dr. Jerzy T. 138
Sayir, Dr. Ali 19b, 23
Scheiman, Daniel A. 66
Scheiman, David A. 52
Schreiber, Jeffrey G. 73
Sechkar, Edward A. 68

Sexton, J. Andrew 50
Shaltens, Richard K. 73
Shaw, Loretta M. 105
Shook, Tony D. 216
Sicker, Ronald J. 194
Siebert, Mark W. 168
Simon, Donald L. 88
Simons, Dr. Rainee N. 100
Singh, Dr. Mrityunjay 24
Sinogeiken, Sergey V. 23
Skoch, Gary J. 105
Smialek, Dr. James L. 37
Smith, Floyd A. 224
Smith, Dr. Mark A. 49
Smith, Stephen J. 141
Snead, John H. 202
Spuckler, Dr. Charles M. 108
Soulas, George C. 57
Sovey, James S. 59b
Srivastava, Dr. Rakesh 147
Stark, David E. 211
Stauber, Laurel J. 228
Steinetz, Dr. Bruce M. 160
Strazisar, Dr. Anthony J. 84, 105, 106
Stueber, Thomas J. 68
Suder, Dr. Kenneth L. 106
Sutliff, Daniel L. 157
Sutter, Dr. James K. 28, 66

T

Tacina, Robert R. 116
Telesman, Jack 15
Thieme, Lanny G. 73
Thomas-Ogbuji, Dr. Linus U. 31, 33
Thorp, Scott A. 106
Tomsik, Thomas M. 120
Tran, Quang K. 101
Trimarchi, Paul A. 217
Trudell, Jeffrey J. 134
Tyburski, Dr. Timothy E. 204

V

Vaden, Karl R. 98
Valco, Dr. Mark J. 171
Vancil, Bernard 99
Vander Wal, Dr. Randy L. 47
Verrilli, Michael J. 39
Viens, Michael J. 66

W

Wald, Lawrence W. 175
Wang, L. Len 66
Wernet, Dr. Mark P. 84
Wey, Changlie 116
Whittenberger, J. Daniel 34, 143
Wilbur, Paul 59a
Wilkinson, Dr. R. Allen 185
Williams, Forman A. 183
Williams, George J. 59a
Wilt, David M. 52
Wintucky, Edwin G. 99
Wiseman, Steve 58
Wnuk, Stephen P. 212
Wong, Wayne A. 74, 76
Wright, Douglas 65

Y

Youngstrom, Erica 63, 65
Yun, Dr. Hee Mann 8, 9

Z

Zaman, Dr. Khairul B. 117
Zhang, Dr. Nengli 188
Zernic, Michael J. 176
Zhu, Dr. Dongming 41
Zimmerli, Dr. Gregory A. 192

REPORT DOCUMENTATION PAGE

Form Approved
OMB No. 0704-0188

1. AGENCY USE ONLY (*Leave blank*)	2. REPORT DATE	3. REPORT TYPE AND DATES COVERED
	March 2002	Technical Memorandum

4. TITLE AND SUBTITLE

Research & Technology 2001

5. FUNDING NUMBERS

None

6. AUTHOR(S)

7. PERFORMING ORGANIZATION NAME(S) AND ADDRESS(ES)

National Aeronautics and Space Administration
John H. Glenn Research Center at Lewis Field
Cleveland, Ohio 44135–3191

8. PERFORMING ORGANIZATION REPORT NUMBER

E–13142

9. SPONSORING/MONITORING AGENCY NAME(S) AND ADDRESS(ES)

National Aeronautics and Space Administration
Washington, DC 20546–0001

10. SPONSORING/MONITORING AGENCY REPORT NUMBER

NASA TM—2002-211333

11. SUPPLEMENTARY NOTES

Responsible person, Walter S. Kim, organization code 9400, 216–433–3742.

12a. DISTRIBUTION/AVAILABILITY STATEMENT

Unclassified - Unlimited
Subject Categories: 01 and 31 Distribution: Nonstandard

Available electronically at http://gltrs.grc.nasa.gov/GLTRS
This publication is available from the NASA Center for AeroSpace Information, 301–621–0390.

12b. DISTRIBUTION CODE

13. ABSTRACT ***(Maximum 200 words)***

This report selectively summarizes NASA Glenn Research Center's research and technology accomplishments for fiscal year 2001. It comprises 156 short articles submitted by the staff scientists and engineers. The report is organized into five major sections: Aeronautics, Research and Technology, Space, Engineering and Technical Services, and Commercial Technology. A table of contents and author index have been developed to assist readers in finding articles of special interest. This report is not intended to be a comprehensive summary of all the research and technology work done over the past fiscal year. Most of the work is reported in Glenn-published technical reports, journal articles, and presentations prepared by Glenn staff and contractors. In addition, university grants have enabled faculty members and graduate students to engage in sponsored research that is reported at technical meetings or in journal articles. For each article in this report, a Glenn contact person has been identified, and where possible, a reference document is listed so that additional information can be easily obtained. The diversity of topics attests to the breadth of research and technology being pursued and to the skill mix of the staff that makes it possible. For more information about research at Glenn, visit us on the World Wide Web (http://www.grc.nasa.gov). This document is available online (http://www.grc.nasa.gov/www/RT). For publicly available reports, visit the Glenn Technical Report Server (http://gltrs.grc.nasa.gov/GLTRS).

14. SUBJECT TERMS	15. NUMBER OF PAGES
Aeronautics; Aerospace engineering; Space flight; Space power; Materials; Structures; Electronics; Space experiments; Technology transfer	247
	16. PRICE CODE

17. SECURITY CLASSIFICATION OF REPORT	18. SECURITY CLASSIFICATION OF THIS PAGE	19. SECURITY CLASSIFICATION OF ABSTRACT	20. LIMITATION OF ABSTRACT
Unclassified	Unclassified	Unclassified	